Systematic Studies of Oxoanionic Lanthanoid Salts in their +II and +IV Oxidation States

Inaugural-Dissertation

zur

Erlangung des Doktorgrades

der Mathematisch-Naturwissenschaftlichen Fakultät

der Universität zu Köln

vorgelegt von

Niko Thomas Flosbach

aus Wipperfürth

Erster Gutachter: Prof. Dr. Mathias S. Wickleder
Zweiter Gutachter: Prof. Dr. Uwe Ruschewitz

Bischof, ich kann fliegen
Sagte der Schneider zum Bischof.
Pass auf, wie ich's mach!
Und der stieg mit so'nen Dingen
Die aussahn wie Schwingen
Auf das große, große Kirchendach.
Der Bischof ging weiter.
Das sind lauter so Lügen
Der Mensch ist kein Vogel
Es wird nie ein Mensch fliegen
Sagte der Bischof vom Schneider.

Der Schneider ist verschieden
Sagten die Leute dem Bischof.
Es war eine Hatz.
Seine Flügel sind zerspellet
Und er liegt zerschellet
Auf dem harten, harten Kirchenplatz.
Die Glocken sollen läuten
Es waren nichts als Lügen
Der Mensch ist kein Vogel
Es wird nie ein Mensch fliegen
Sagte der Bischof den Leuten.

Ulm 1592
B. Brecht

Acknowledgement

First and foremost I thank Prof. M. Wickleder for the supervision of this work and the many scientific discussions that we had. I thank Prof. U. Ruschewitz as the second supervisor of this work. I also thank the current and former members of the research group of Prof. Wickleder. I thank Prof. G. Deacon for my research stay before my PhD that significantly contributed to my motivation to research the chemistry of the rare earth elements. I thank Prof. M. Jansen for our valuable scientific exchange.
I thank the students (L. Pantenburg, S. Brieger, K. Kanani, S. Kuang, N. Sander, M. Maslo and T. Lapic) who I supervised during my PhD and whose help with the practical work is greatly appreciated.
I also thank J. Bruns and Prof. B. Rasche for their support and the collaboration in joint projects. I also owe sincere gratitude to Prof. M. Bykov and his team for the help with high-pressure experiments that have added invaluable contributions to this work. I thank Prof. C. Wickleder, M. Adlung, J. Weiß and P. Fischer for sharing their expertise on optical spectroscopy and the collaboration. I also thank Prof. S. Disch and L. Rochels for the help with magnetochemical experiments.
I thank the staff of the institute of inorganic chemistry in Cologne for their help with routine measurements.
Lastly, I thank my friends and family for their support throughout my PhD time and beyond.

Zusammenfassung

Die vorliegende Arbeit befasst sich mit der Synthese neuer oxoanionischer Verbindungen der Lanthanoide in ungewöhnlichen Oxidationsstufen, sowie derer chemischen und physikalischen Charakterisierung.
Es gelang die Synthese der ersten strukturell charakterisierten oxoanionischen Verbindungen von Pr^{4+} in der Form von $PrSi_3O_8$, sowie $Pr_2Si_7O_{18}$ durch die Reaktion von PrO_2 und SiO_2 in einer Diamantstempelzelle bei ca. 29 GPa. Die Kristallstruktur beider Silikate konnte durch Einkristallstrukturanalyse aufgeklärt werden. Als Produkt einer konkurrierenden Reaktion, wurde ein Pr(IV)oxidperoxid mit der empirischen Formel Pr_2O_5 unter den gleichen Bedingungen erhalten. Die gezielte Synthese dieser Verbindung durch die Reaktion von PrO_2 mit Sauerstoff in einer Diamantstempelzelle bei ca. 27 GPa ermöglichte eine detaillierte Untersuchung der Struktur von Pr_2O_5, welches die bislang sauerstoffreichste binäre Verbindung eines Lanthonoids mit Sauerstoff darstellt. Analoge Experimente mit PrO_2 und P_2O_5 lieferten $PrPO_4$ in einer neuen Hochdruckmodifikation, welche der Barytstruktur entspricht.
Eine systematische Untersuchung verschiedener Solvate von $Ln(OTf)_2$ (Ln = Sm, Eu, Yb) wurde durchgeführt, in der die physikalischen Eigenschaften der Verbindungen insbesondere im Hinblick auf ihre Lumineszenz charakterisiert wurden. In weiterführenden Experimenten wurde die Anwendbarkeit der synthetischen Methoden im Hinblick auf weitere Anionen und Kationen geprüft. Um das hohe Potential der Triflate in chemischen Synthesen zu demonstrieren wurden die bisher unbekannten lösungsmittelfreien Azide $Ln(N_3)_2$ (Ln = Eu, Yb) durch Salzmetathese dargestellt und analytisch charakterisiert.

Abstract

The present work deals with the synthesis of new oxoanionic compounds of the lanthanoids in unusual oxidation states and their chemical and physical characterisation.
It was possible to obtain the first structurally characterised oxoanionic compounds of Pr^{4+} in the form of $PrSi_3O_8$ and $Pr_2Si_7O_{18}$ by reacting PrO_2 and SiO_2 in a diamond anvil cell at ca. 29 GPa. The crystal structure of both silicates could be solved by single crystal X-ray diffraction analysis. A unique praseodymium(IV) oxide peroxide with the empirical formula Pr_2O_5 formed as a product of a competing reaction under the same conditions. The intentional synthesis of this compound was possible by reacting PrO_2 and oxygen in a diamond anvil cell at ca. 27 GPa and enabled detailed studies the structure of Pr_2O_5 which constitutes the most oxygen rich binary phase of any lanthanoid and oxygen. Analogous experiments with PrO_2 and P_2O_5 afforded a new high-pressure modification of $PrPO_4$ which is equivalent to the barite-type structure.
A systematic investigation of various solvates of $Ln(OTf)_2$ (Ln = Sm, Eu, Yb) was conducted, in which the physical properties of the compounds were characterised with emphasis on their luminescence. In additional experiments, the applicability of the synthetic methods was examined with respect to different cations and anions. In order to demonstrate the high potential of the triflates in chemical synthesis, the thus far unknown solvent-free azides $Ln(N_3)_2$ (Ln = Eu, Yb) were synthesised by salt metathesis and characterised analytically.

Abbreviations

atm.	=	atmospheric
a. u.	=	arbitrary units
CN	=	coordination number
CV	=	cyclic voltammetry
comp.	=	compare
conc.	=	concentrated
cryst.	=	crystallographic
DAC	=	diamond anvil cell
DCM	=	dichloromethane
DME	=	dimethoxyethane
DSC	=	differential scanning calorimetry
e. g.	=	exempli gratia
eq.	=	equivalents or equation (depending on context)
equiv.	=	equivalents
exc.	=	excess
fig.	=	figure
GooF	=	goodness of fit
hp	=	high-pressure
IR	=	infrared
Laser	=	light amplification by the stimulated emission of radiation
LED	=	light emitting diode
Ln	=	lanthanoid
Max.	=	maximum
max.	=	maximal
Min.	=	minimum
min.	=	minimal
NHE	=	normal hydrogen electrode
PXRD	=	powder X-ray diffraction
Red.	=	reduction
rpm	=	rotations per minute
rt	=	room temperature
SCE	=	saturated calomel electrode
SC-XRD	=	single crystal X-ray diffraction
SI	=	supporting information
sim.	=	simulated
tab.	=	table
TBA	=	tetrabutylammonium
TGA	=	thermogravimetric analysis

THF	=	tetrahydrofuran
trig.	=	trigonal
UV-Vis	=	ultraviolet-visible
vs.	=	versus

Contents

1 Introduction **1**

2 State of Knowledge **2**
2.1 The Lanthanoids . . . 2
2.2 Tetravalent Lanthanoids . . . 2
2.2.1 General Considerations . . . 2
2.2.2 Tetravalent Praseodymium and Terbium . . . 3
2.2.3 Tetravalent Neodymium and Dysprosium . . . 5
2.3 Divalent Lanthanoids . . . 5
2.3.1 Physical Properties of Ln^{2+}-ions . . . 5
2.3.2 Chemistry of Divalent Lanthanoids . . . 7
2.3.2.1 Trifluoromethanesulphonates of Divalent Lanthanoids . . . 8

3 Objective **9**
3.1 Tetravalent Lanthanoids . . . 9
3.2 Divalent Lanthanoids . . . 9

4 Results and Discussion **11**
4.1 Tetravalent Lanthanoids . . . 11
4.1.1 Electrochemical Experiments . . . 11
4.1.2 Chemical Oxidation with XeF_2 in Acetonitrile . . . 13
4.1.3 Reactions of Ln^{3+}-salts with XeF_2 in SO_3 . . . 15
4.1.4 Attempted Syntheses of $Pr_2(S_2O_8)_3$ . . . 16
4.1.5 Reaction of $Pr_2(SO_4)_3$ and $K_2S_2O_8$ at High Pressure . . . 18
4.1.6 Reaction of PrO_2 and SiO_2 at High Pressure (***Manuscript 1***) . . . 19
4.1.7 $Ln_4(SiO_4)_3$ and Polymorphism of $Tb_4(SiO_4)(Si_3O_{10})$ . . . 30
4.1.8 Ternary Silicates . . . 34
4.1.9 Reaction of PrO_2 and P_2O_5 at High Pressure (***Manuscript 2***) . . . 35
4.1.10 High Pressure Synthesis of $Pr_2(O_2)O_3$ - A Unique Lanthanoid(IV) Oxide Peroxide (***Manuscript 3***) . . . 42
4.2 Divalent Lanthanoids . . . 52
4.2.1 Structure, Magnetism and Luminescence of $Eu(OTf)_2(CH_3CN)$ and $Sm(OTf)_2(CH_3CN)$ (***Manuscript 4***) . . . 52
4.2.2 $Yb(OTf)_2(MeCN)_2$ and $Ca(OTf)_2(MeCN)_{0.5}$ . . . 62
4.2.3 THF- and DME-Solvates of $Ln(OTf)_2$ . . . 65
4.2.4 Luminescence of Desolvated $Ln(OTf)_2$ . . . 70
4.2.5 Attempted Reduction of Thulium(III) . . . 71
4.2.6 Attempted Synthesis of Europium(II) Perchlorate . . . 74
4.2.7 Lanthanoid(II) Azides (***Manuscript 5***) . . . 76

5 Conclusion **85**
5.1 Tetravalent Lanthanoids . . . 85
5.2 Divalent Lanthanoids . . . 86

6 Experimental Section **87**
6.1 General Procedures . . . 87
6.1.1 Multi-Anvil Press . . . 87
6.1.2 Ball Mill . . . 87
6.1.3 Other Methods . . . 87
6.2 Experimental Procedures . . . 87
6.2.1 General Procedure for the Synthesis of $Ln(OTf)_3$ . . . 87
6.2.2 Synthesis of $Ca(OTf)_2$ . . . 88
6.2.3 General Procedure for the Synthesis of $Ln(ClO_4)_3$ . . . 88
6.2.4 Synthesis of SrO_2 . . . 89
6.2.5 Crystallisation of $Pr(ClO_4)_3(MeCN)_4$ . . . 89
6.2.6 Reaction of $Tb(OTf)_3$ and XeF_2 in Acetonitrile . . . 89
6.2.7 Reaction of $Tb(ClO_4)_3$ and XeF_2 in Acetonitrile . . . 90
6.2.8 Reaction of $Pr(ClO_4)_3$ and XeF_2 at Room Temperature . . . 90
6.2.9 Reaction of $Pr(ClO_4)_3$ and XeF_2 at Low Temperature . . . 90
6.2.10 Reactions of $Ln(OTf)_3$ and $Ln(ClO_4)_3$ with XeF_2 in SO_3 . . . 91
6.2.11 Synthesis of $Pr_2(SO_4)_3$ . . . 91
6.2.12 Treatment of $(NH_4)_2S_2O_8$ with $Pr(OH)_3$ at Elevated Temperature . . . 92
6.2.13 Treatment of $(NH_4)_2S_2O_8$ with $Pr(OH)_3$ at 0 °C . . . 92
6.2.14 Synthesis of $(TBA)_2S_2O_8$ . . . 92
6.2.15 Reaction $(TBA)_2S_2O_8$ and $Pr(OTf)_3$ in THF . . . 93
6.2.16 Multi-Anvil Press Experiments . . . 93
6.2.17 Synthesis of $Yb(OTf)_2(MeCN)_2$ . . . 94
6.2.18 Crystallisation of $Ca(OTf_2)(MeCN)_{0.5}$ . . . 94
6.2.19 Crystallisation of $Ca(OTf)_2(THF)_2$ . . . 94
6.2.20 Reaction of $Eu(OTf)_2$ and Eu in THF . . . 95
6.2.21 Synthesis of $Eu(OTf)_2(THF)_{1.5}$ . . . 95
6.2.22 Synthesis of $Sr(OTf)_2(THF)_{1.5}$ . . . 95
6.2.23 Attempted Synthesis of $Sm(OTf)_2(THF)_{1.5}$ . . . 96
6.2.24 Crystallisation of $Ln(OTf)_2(DME)_2$ . . . 96
6.2.25 Mechanochemical Synthesis of $Eu(OTf)_2$ . . . 96
6.2.26 Synthesis of KC_8 . . . 97
6.2.27 Attempted Mechanochemical Comproportionation of $Tm(OTf)_3$ and Tm . 97
6.2.28 Attempted Mechanochemical Comproportionation of $Tm(OTf)_3$ and Tm in Presence of THF . . . 97
6.2.29 Attempted Mechanochemical Comproportionation of $Tm(OTf)_3$ and Tm in Presence of Acetonitrile . . . 98

6.2.30 Attempted Mechanochemical Comproportionation of $Tm(OTf)_3$ and Tm in Presence of Acetonitrile at -40 °C . . . 98
6.2.31 Mechanochemical Treatment of $Tm(OTf)_3$ with KC_8 . . . 98
6.2.32 Treatment of $Tm(OTf)_3$ with *n*-BuLi . . . 98
6.2.33 Treatment of $Tm(OTf)_3$ with KC_8 in Acetonitrile . . . 99
6.2.34 Treatment of $Tm(OTf)_3$ with KC_8 and 18-Crown-6 in Acetonitrile . . . 99
6.2.35 Treatment of $Tm(OTf)_3$ with KC_8 in THF . . . 99
6.2.36 Reaction of $Tm(OTf)_3$ with KC_8 in THF / Diethylether . . . 100
6.2.37 Treatment of $Tm(OTf)_3$ with KC_8 in MeCN / Diethylether . . . 100
6.2.38 Reaction of $Tm(OTf)_3$ with KC_8 in Diethylether . . . 100
6.2.39 Treatment of $Eu(ClO_4)_3$ with Eu in Acetonitrile . . . 100
6.2.40 Mechanochemical Treatment of $Eu(ClO_4)_3$ with Eu . . . 101
6.2.41 Mechanochemical Reaction of $Eu(ClO_4)_3$ with Eu in Presence of Acetonitrile 101

7 Appendix 102
7.1 Supplementary Material of Manuscripts . . . 102
7.2 Supporting Analytical Data . . . 174
7.2.1 Powder X-Ray Diffraction Data . . . 174
7.2.2 IR-Spectra . . . 194
7.2.3 Thermogravimetric Analyses . . . 204
7.2.4 UV-Vis Spectra . . . 207
7.2.5 Luminescence Spectra . . . 211
7.2.6 Crystallographic Tables . . . 212

8 References 225

List of Figures

1 Dieke diagram of free Ln^{3+}-ions . . . 6
2 Reduction potentials and ionisation energies of lanthanoids . . . 8
3 CVs of $Tb(ClO_4)_3$ and $Tb(OTf)_3$ . . . 12
4 UV-Vis spectra of $Tb(OTf)_3$ and $Tb(ClO_4)_3$ with XeF_2 . . . 14
5 Crystal Structure of $(NH_4)[Pr(SO_4)_2(H_2O)_3]\cdot H_2O$ . . . 17
6 Crystal Structure of $(TBA)_2S_2O_8$ . . . 18
7 Single crystal of $KPr(SO_4)_2$ . . . 19
8 Luminescence spectra of $Pr_4(SiO_4)_3$ . . . 30
9 Crystal structure of $Tb(SiO_4)(Si_3O_{10})$ . . . 32
10 Luminescence spectra of $Tb_4(SiO_4)(Si_3O_{10})$ . . . 33
11 Single crystals of $Pr_4(SiO_4)_3$ . . . 34
12 Single crystal of SiO_2 next to $Pr_4(SiO_4)_3$ . . . 35
13 Single crystals of $Yb(OTf)_2(MeCN)_2$ . . . 62
14 Crystal structure of $Yb(OTf)_2(MeCN)_2$ . . . 63
15 Coordination polyhedron of Yb^{2+} in $Yb(OTf)_2(MeCN)_2$ . . . 63
16 Single crystals of $Ca(OTf)_2(MeCN)_{0.5}$ . . . 64
17 Crystal structure of $Ca(OTf)_2(MeCN)_{0.5}$ . . . 64
18 Coordination polyhedra of Ca^{2+} in $Ca(OTf)_2(MeCN)_{0.5}$ . . . 65
19 Single crystals of $Ca(OTf)_2(THF)_2$ . . . 67
20 Crystal structure of $Ca(OTf)_2(THF)_2$ . . . 67
21 Luminescence spectrum of $Eu(OTf)_2(THF)_{1.5}$ . . . 68
22 Crystal structure of $Sm(OTf)_2(DME)_2$ . . . 69
23 Luminescence spectra of $Eu(OTf)_2$ . . . 70
24 UV-Vis spectrum and photo of a Tm^{2+}-solution . . . 73
25 UV-Vis spectrum of the products from reacting $Eu(ClO_4)$ and Eu . . . 74
26 Single crystal structure of $Eu(ClO_4)_3(MeCN)_4$ . . . 75
27 PXRD data of $Ln(OTf)_3$ . . . 174
28 PXRD data of $Pr(ClO_4)_3$ . . . 175
29 PXRD data of $Eu(ClO_4)_3$ . . . 175
30 PXRD data of $Tb(ClO_4)_3$ . . . 176
31 PXRD data of SrO_2 . . . 176
32 PXRD data $Tb(ClO_4)_3 + XeF_2$ reacted in MeCN . . . 177
33 PXRD data $Pr(ClO_4)_3 + XeF_2$ reacted in MeCN . . . 177
34 PXRD data $Pr(ClO_4)_3 + XeF_2$ . . . 178
35 PXRD data $Tb(OTf)_3 + XeF_2 + SO_3$ . . . 178
36 PXRD data $Tb(ClO_4)_3 + XeF_2 + SO_3$ . . . 179
37 PXRD data $Pr(ClO_4)_3 + XeF_2 + SO_3$ . . . 179
38 PXRD data of $(TBA)_2S_2O_8$ . . . 180
39 PXRD data $Pr(OTf)_3 + (TBA)_2S_2O_8$ . . . 180

40 PXRD $K_2S_2O_8$ + $Pr_2(SO_4)_3$ reacted at 11 GPa . . . 181
41 PXRD data of $La_4(SiO_4)_3$ . . . 181
42 PXRD data of $Nd_4(SiO_4)_3$ . . . 182
43 PXRD data of $Pr_4(SiO_4)_3$ . . . 182
44 PXRD data of $Tb_4(SiO_4)(Si_3O_{10})$(1) . . . 183
45 PXRD data of $Tb_4(SiO_4)(Si_3O_{10})$(2) . . . 183
46 PXRD data PrO_2 + SiO_2 + Na_2O_2 reacted at 11 GPa . . . 184
47 PXRD data PrO_2 + SiO_2 + SrO_2 reacted at 11 GPa . . . 184
48 PXRD data of $PrPO_4$ . . . 185
49 PXRD pattern of impure $Yb(OTf)_2(MeCN)_2$ . . . 185
50 PXRD data of $Ca(OTf)_2$ . . . 186
51 PXRD data of amorphous products from reacting Eu and $Eu(OTf)_3$ in THF . . . 186
52 PXRD data of impure $Eu(OTf)_2(THF)_{1.5}$ . . . 187
53 PXRD data of $Eu(OTf)_2(THF)_{1.5}$ . . . 187
54 PXRD data of $Sr(OTf)_2(THF)_{1.5}$ . . . 188
55 PXRD data of impure $Sm(OTf)_2(THF)_{1.5}$ . . . 188
56 PXRD data of impure $Sm(OTf)_2(DME)_2$ . . . 189
57 PXRD data of impure $Eu(OTf)_2(DME)_2$ . . . 189
58 PXRD data of impure $Yb(OTf)_2(DME)_2$ . . . 190
59 PXRD data of KC_8 . . . 190
60 PXRD data of the products obtained from reacting $Tm(OTf)_3$ and KC_8 in a ball mill . . . 191
61 PXRD data of $Eu(ClO_4)_3(MeCN)_4$ . . . 191
62 PXRD data of $Eu(ClO_4)_3(MeCN)_4$ . . . 192
63 PXRD data of $Eu(ClO_4)_3(MeCN)_4$ . . . 192
64 PXRD data of impure $Eu(ClO_4)_3(MeCN)_4$ . . . 193
65 IR-spectra of $Ln(OTf)_3$ . . . 194
66 IR-spectra of $Ln(ClO_4)_3$ . . . 194
67 IR-spectrum of $Pr_2(SO_4)_3$ . . . 195
68 IR-spectrum $Tb(OTf)_3$ + XeF_2 reacted in MeCN . . . 195
69 IR-spectrum $Tb(ClO_4)_3$ + XeF_2 + SO_3 . . . 196
70 IR-spectrum $(TBA)_2S_2O_8$ + $Pr(OTf)_3$ in THF . . . 196
71 IR-spectrum $K_2S_2O_8$ + $Pr_2(SO_4)_3$ reacted at 11 GPa . . . 197
72 IR-spectrum of $La_4(SiO_4)_3$ . . . 197
73 IR-spectrum of $Nd_4(SiO_4)_3$. . . . 198
74 IR-spectrum of $Pr_4(SiO_4)_3$. . . . 198
75 IR-spectrum of $Tb_4(SiO_4)(Si_3O_{10})$ . . . 199
76 IR-spectrum PrO_2 + SiO_2 + Na_2O_2 reacted at 11 GPa . . . 199
77 IR-spectrum PrO_2 + SiO_2 + SrO_2 reacted at 11 GPa . . . 200
78 IR-spectrum of $Eu(OTf)_2(THF)_{1.5}$ . . . 200
79 IR-spectrum of $Sr(OTf)_2(THF)_{1.5}$ . . . 201

80 IR-spectrum of impure $Sm(OTf)_2(THF)_{1.5}$ . . . 201
81 IR-spectrum of impure $Sm(OTf)_2(DME)_2$ . . . 202
82 IR-spectrum of impure $Eu(OTf)_2(DME)_2$ . . . 202
83 IR-spectrum of impure $Yb(OTf)_2(DME)_2$ . . . 203
84 TGA-DSC data of $La_4(SiO_4)_3$ . . . 204
85 TGA-DSC data of $Nd_4(SiO_4)_3$ . . . 205
86 TGA-DSC data of $Pr_4(SiO_4)_3$ . . . 205
87 TGA-DSC data of $Tb_4(SiO_4)(Si_3O_{10})$ . . . 206
88 UV-Vis spectrum $Tm(OTf)_3$ + KC_8 after ball milling . . . 207
89 UV-Vis spectrum Tm + $Tm(OTf_3)$ after ball milling . . . 208
90 UV-Vis spectrum of $Eu(OTf)_2$ . . . 208
91 UV-Vis spectrum $Tm(OTf)_3$ + KC_8 after ball milling . . . 209
92 UV-Vis spectrum $Tm(OTf)_3$ + Tm + MeCN after ball milling . . . 209
93 UV-Vis spectrum $Tm(OTf)_3$ with KC_8 in DME + acetonitrile . . . 210
94 Luminescence spectrum of $Sm(OTf)_2$ . . . 211

List of Tables

1 Oxidation potentials of Ln^{4+}-ions and 4th ionisation energies . . . 3
2 Overview of THF-solvates of $M(OTf)_2$ (M = Sm, Eu, Sr, Yb, Ca) . . . 66
3 Overview of DME-solvates of $Ln(OTf)_2$ (Ln = Sm, Eu, Tm, and Yb) . . . 69
4 Summary of luminescence data of $Eu(OTf_2)$ and its solvates . . . 71
5 Summary of attempted reductions of $Tm(OTf)_3$ . . . 72
6 Quantities used for the synthesis of $Ln(OTf)_3$ . . . 88
7 Quantities used for the synthesis of $Ln(ClO_4)_3$ . . . 89
8 Quantities used for the reactions of $Ln(ClO_4)_3$ or $Ln(OTf)_3$ with XeF_2 in SO_3 . . . 91
9 Detailed information on syntheses in the multi-anvil press . . . 93
10 Experimental parameters for the syntheses of $Ln(OTf)_2(DME)_2$ . . . 96
11 Experimental parameters for the treatment of $Eu(ClO_4)_3$ with Eu in acetonitrile 101
12 Crystallographic data of $Tb(OTf)_3(MeCN)_3$ . . . 212
13 Crystallographic data of $(NH_4)Pr(SO_4)_2(H_2O)_4$ . . . 213
14 Crystallographic data of $(TBA)_2S_2O_8$ . . . 214
15 Crystallographic data of $Pr_4(SiO_4)_3$ . . . 215
16 Crystallographic data of $Tb_4(SiO_4)(Si_3O_{10})$ . . . 216
17 Crystallographic data of $Yb(OTf)_2(MeCN)_2$ . . . 217
18 Crystallographic data of $Ca(OTf)_2(MeCN)_{0.5}$ . . . 218
19 Crystallographic data of $Ca(OTf)_2(THF)_2$ . . . 219
20 Crystallographic data of $Sr(OTf)_2(THF)_{1.5}$ . . . 220
21 Crystallographic data of $Sm(OTf)_2(DME)_2$ . . . 221
22 Crystallographic data of $Eu(OTf)_2(DME)_2$ . . . 222
23 Crystallographic data of $Yb(OTf)_2(DME)_2$ . . . 223

24 Crystallographic data of $Pr(ClO_4)_3(MeCN)_4$ 224
25 Crystallographic data of $Eu(ClO_4)_3(MeCN)_4$ 225

1 Introduction

In the past decades, the lanthanoids have become integral constituents of many advanced technologies, such as LEDs, lasers, scintillators and telecommunication which play crucial roles in modern societies.[1] Because of the unique physical properties of the lanthanoid ions that are responsible for the many use cases thereof, they cannot simply be replaced by other elements. Despite being part of the so called *rare earth elements*, the natural abundance of most lanthanoids in the earth's crust is comparatively high. The most abundant lanthanoid cerium for example is more abundant than lead and copper.[2]
In most chemical compounds the lanthanoids are found in their +III oxidation state which is the most stable oxidation state for each individual element of the group. Altering the oxidation state of any element naturally influences its physical properties. Considering that most applications of the lanthanoids rely on their unique physical properties, expanding the redox chemistry of the lanthanoids yields the potential of not only expanding the fundamental knowledge of their chemistry but also to discover new materials with desirable properties. Because of the notorious stability of the +III oxidation state, the chemistry of lanthanoids in oxidation states other than +III still remains underdeveloped in certain respects. With the ever growing demand for new materials, the search for new compounds of lanthanoids, in particular those with unusual oxidation states, becomes a principle necessity for new technological inventions and developments.
The present work addresses the challenges associated with producing lanthanoids in unsusual oxidation states by systematically developing and examining new synthetic protocols. Furthermore, the investigation of the chemical and physical properties of novel compounds obtained hereby comprise central motives of this work. The contributions to the chemical knowledge of lanthanoids obtained herein might lay the foundation for further developments in the field.

2 State of Knowledge

2.1 The Lanthanoids

The chemical elements 57 (lanthanum) to 71 (lutetium) are typically referred to as the *lanthanoids*, emphasising the chemical similarities of the group's elements to the eponymous element lanthanum. Although lanthanum cannot be similar to itself, it is generally accepted to include it in the lanthanoids.[3] Within the series of the lanthanoids the 4f-orbitals are gradually filled, granting them a special position between the s-block and the d-block elements. Since the 4f-orbitals are well shielded from the chemical surrounding by being located closer to the nucleus than the 5s- and 5d-orbitals of the xenon core, the filling of the shell does not contribute to an increase in size of the atoms or ions.[4] Instead, the ionic radii of lanthanoid ions and atoms gradually decrease with increasing charge of the nucleus due to increased electrostatic forces, as well as relativistic contributions.[5] This well known effect is called the lanthanoid contraction and constitutes a fundamental concept, not only in the chemistry of the lanthanoids. The unique properties of the 4f-shell that is gradually being filled throughout the group lead to several consequences affecting the physical properties of the lanthanoids, as well as their chemical character. In most lanthanoid ions, the optical properties are dominated by weak intraconfigurational f-f-transitions that are very narrow and are only marginally influenced by the chemical environment.[6–8] Another important consequence of the character of the 4f-shell is that most lanthanoid ions possess localised magnetic moments that are also effectively inert to influences of the chemical environment.[9–12]

Among others, the aforementioned properties of the lanthanoids clearly distinguish them from the d-block elements as well as the actinoids and yield the potential for several technological applications which cannot easily be realised with other elements. Because of their irreplaceable functions in advanced technologies, the lanthanoids are widely considered to be key resources for modern societies.[13–17]

In chemical compounds the lanthanoids most often occur in their +III oxidation state which is the most stable oxidation state for all elements of the group.[18,19] Certain electronic configurations like the half occupied 4f-shell in the Eu^{2+}-ion (and the isoelectronic Tb^{4+}-ion) lead to a stabilisation of the +II and the +IV oxidation state which will be discussed in more detail in the following sections.

2.2 Tetravalent Lanthanoids

2.2.1 General Considerations

Removing an additional electron from Ln^{3+}-ions to form Ln^{4+}-ions generally requires much more energy than is needed for initial three individual ionisation steps, making the

preparation of compounds containing Ln^{4+}-ions a severe challenge for chemists.[20,21] In fact, the formation of Ln^{4+}-ions in condensed phases has only been proven for Ce, Pr, Nd, Tb and Dy that have the lowest fourth ionisation energies of all lanthanoids.[21,22] The 4th ionisation energies of the mentioned elements are shown in tab. 1, along with the standard oxidation potentials of the Ln^{4+}/Ln^{3+} pairs.

Tab. 1 Standard oxidation potentials[a] E_0 for the Ln^{IV}/Ln^{III} pairs and 4th ionisation energies of cerium, terbium, praseodymium, neodymium and dysprosium.

	4th Ionisation Energy / eV[21]	**$E_0(Ln^{3+}/Ln^{4+})$[a] / V**[18]
Ce	36.8	+1.74
Pr	39.0	+3.2
Tb	39.4	+3.1
Nd	40.4	+5.0
Dy	41.4	+5.2

[a] Potential relative to standard hydrogen electrode.

Ce^{4+} is by far the most stable Ln^{4+}-ion, receiving its stability from the closed-shell [Xe]-configuration. The Ce^{4+}-ion is the only representative of the Ln^{4+}-ions that occurs in a wide variety of compound classes and even is, in some cases, stable in aqueous media.[23,24] Although the standard oxidation potential (shown in tab. 1) suggests that the Ce^{4+}-ion is able to oxidise water to oxygen under standard conditions, the oxidation can be impeded due to kinetic reasons. The field of compounds containing Ce^{4+} ranges from simple binary compounds, like CeO_2 and CeF_4, over salts containing oxoanions (e. g. $Ce(SO_4)_2$, $CeSiO_4$, $(NH_4)_2Ce(NO_3)_6$) to metal-organic and organometallic complexes.[25–30] Although the chemistry of Ce^{4+} is comparatively rich and manifold it shall be emphasised that it still is a strong oxidant and is usually reduced to Ce^{3+} easily.

2.2.2 Tetravalent Praseodymium and Terbium

As opposed to Ce^{4+}, Pr^{4+} and Tb^{4+} are very difficult to obtain due to their extremely high oxidation potential and the resulting proclivity to be reduced to Pr^{3+} and Tb^{3+}. As the first succeeding element after cerium, the Pr^{4+}-ion possesses one f-electron (Pr^{4+}:[Xe] $4f^1$), while Tb^{4+} is isoelectronic to the [Xe] $4f^7$-configured ions Eu^{2+} and Gd^{3+}. The Pr^{4+}-ion is of particular interest due to its unusual properties that deviate from those typically expected for lanthanoid ions and more resemble those of early actinoid ions.[31] The unusual participation in chemical bonding of the 4f-electron of Pr^{4+} leads to a situation, where both spin orbit coupling and crystal field splitting have to be considered when describing the electronic structure of the ion. This unique property creates a certain flexibility that could be exploited for potential physical applications. Thus far however, the number of well characterised compounds of Pr^{4+} is still very small, as will be elaborated in more

detail below.

Both the fourth ionisation energies and the oxidation potentials of the Ln^{4+}/Ln^{3+}-pair (compare tab. 1) are similar for praseodymium and terbium, indicating that there will also be similarities in the redox chemistry of both elements. The chemical similarities of Pr^{4+} and Tb^{4+} become particularly obvious when comparing the pool of known compounds, in which both elements occur in their tetravalent oxidation state. Apart from the binary compounds LnO_2 (Ln = Ce, Pr, Tb),[32–34] which are either available through *'solvolytic disproportionation'*[1] or oxidation with molecular oxygen under high pressure, and LnF_4 (Ln = Ce, Pr, Tb),[35–39] that require fluorination with either molecular fluorine or krypton fluoride, several ternary oxides and fluorides are also known. Oxides of the form A_2LnO_3 (A = Li, Na, K, Rb, Cs and Ln = Ce, Pr, Tb) as well as Li_8LnO_6 (Ln = Ce, Pr, Tb) can be prepared by solid state reactions of the respective binary oxides or peroxides.[40–47] Similarly, fluorides of the composition A_2LnF_6 (A = Li, Na, K, Rb, Cs and Ln = Ce, Pr, Tb) and A_3LnF_7 (A = Na, Rb, K, Cs and Ln = Ce, Pr, Tb) form when subjecting ternary fluorides of the lanthanoids to fluorine at high pressure and high temperature.[48–54] Next to the mentioned examples, several other salts like the perovskites $BLnO_3$ (B = Sr, Ba and Ln = Ce, Pr, Tb) and $LnOF_2$ exist.[42,55–58]

Oxoanionic compounds of both Pr^{4+} and Tb^{4+} are more scarce than simple oxides and fluorides. In the 1960s, a series of communications was issued claiming the synthesis not only of various Pr^{4+}-sulphates ($Pr(SO_4)_2$, $Pr(SO_4)_2{\cdot}2\ H_2SO_4$ and $(NH_4)_8Pr(SO_4)_6{\cdot}5\ H_2O$) but even of the hexachloropraseodymates $A_2[PrCl_6]$ (A = NH_4, Na, K, Rb, Cs), praseodymium(IV) oxalate hydrates and $Pr(OH)_4$.[59–63] Although the methods and analyses described in the communications seem authentic, some remarks have to be made about the results.

The reported compounds have never again occurred anywhere in the scientific literature, although they were reported ca. 60 years ago, indicating issues with reproducing the results. Reports of analogous compounds of Tb^{4+} are also missing entirely, which is surprising, considering the similar chemical behaviour of both ions that was elucidated above. Furthermore, the characterisation of the Pr^{4+}-salts relied almost exclusively on elemental analyses and no structural evidence was presented. The synthetic procedure in aqueous media along with the presence of chloride ions next to Pr^{4+} have raised doubts in the scientific community about the validity of the results.[18,64]

Only as recent as 2017, the first oxoanionic compounds of Tb^{4+} were reported in the form of $K_2TbGe_2O_7$ and the mixed valent $Cs_8Tb_3Ge_9O_{27}$ that were obtained by hydroflux methods.[65,66] Following this discovery, a series of metal organic imidophosphoranes and siloxides were discovered that are able to support Tb^{4+} and Pr^{4+}.[22,67–72] This clearly demonstrates that both elements are accessible in their tetravalent oxidation states in

[1]The term'*solvolytic disproportionation* is misleading since the separation of Pr^{3+} and Pr^{4+} from Pr_6O_{11} does not involve redox processes. The term was used regardless in order to stay consistent with *Brauer's* terminology.[34]

compounds other than oxides and fluorides. Despite the recent advances in the field, still no oxoanionic compounds of Pr^{4+} have been structurally characterised, evoking the necessity for a concentrated effort of approching this target.

2.2.3 Tetravalent Neodymium and Dysprosium

In analogy to the Pr^{4+} and Tb^{4+} pair that was discussed in section 2.2.2, Nd^{4+} and Dy^{4+} are similar to each other in terms of their oxidation potential, but differ in their ionic radii due to the lanthanoid contraction. As presented in tab. 1, the Nd^{4+}- and Dy^{4+}-ions are even stronger oxidants than the Ln^{4+}-ions previously discussed. When reviewing the known compounds, in which these ions occur, the pool becomes even smaller than for Pr^{4+} and Tb^{4+}, with simple binary compounds like LnO_2 being entirely inaccessible. LnF_4 has been observed for both elements only in noble gas matrices.[73] Only ternary fluorides of the form Cs_2MLnF_7 (M = K, Rb, Cs; Ln = Nd, Dy) have been prepared by oxidation of ternary fluorides of the trivalent lanthanoids with fluorine, representing the only class of well characterised Nd^{4+}- and Dy^{4+}-compounds.[74,75]

2.3 Divalent Lanthanoids

2.3.1 Physical Properties of Ln^{2+}-ions

When changing the oxidation state of a lanthanoid ion from +III to +II, several consequences arise that alter the physical properties of the ion and thus provide the opportunity to develop new materials and applications. The discussion of the luminescent as well as the magnetic properties of the Ln^{3+}-ions is often conceptualised using *Dieke's* diagram, in which the electronic terms of each ion are listed according to their relative energies with respect to the ground term, as is illustrated in fig. 1.[76,77]

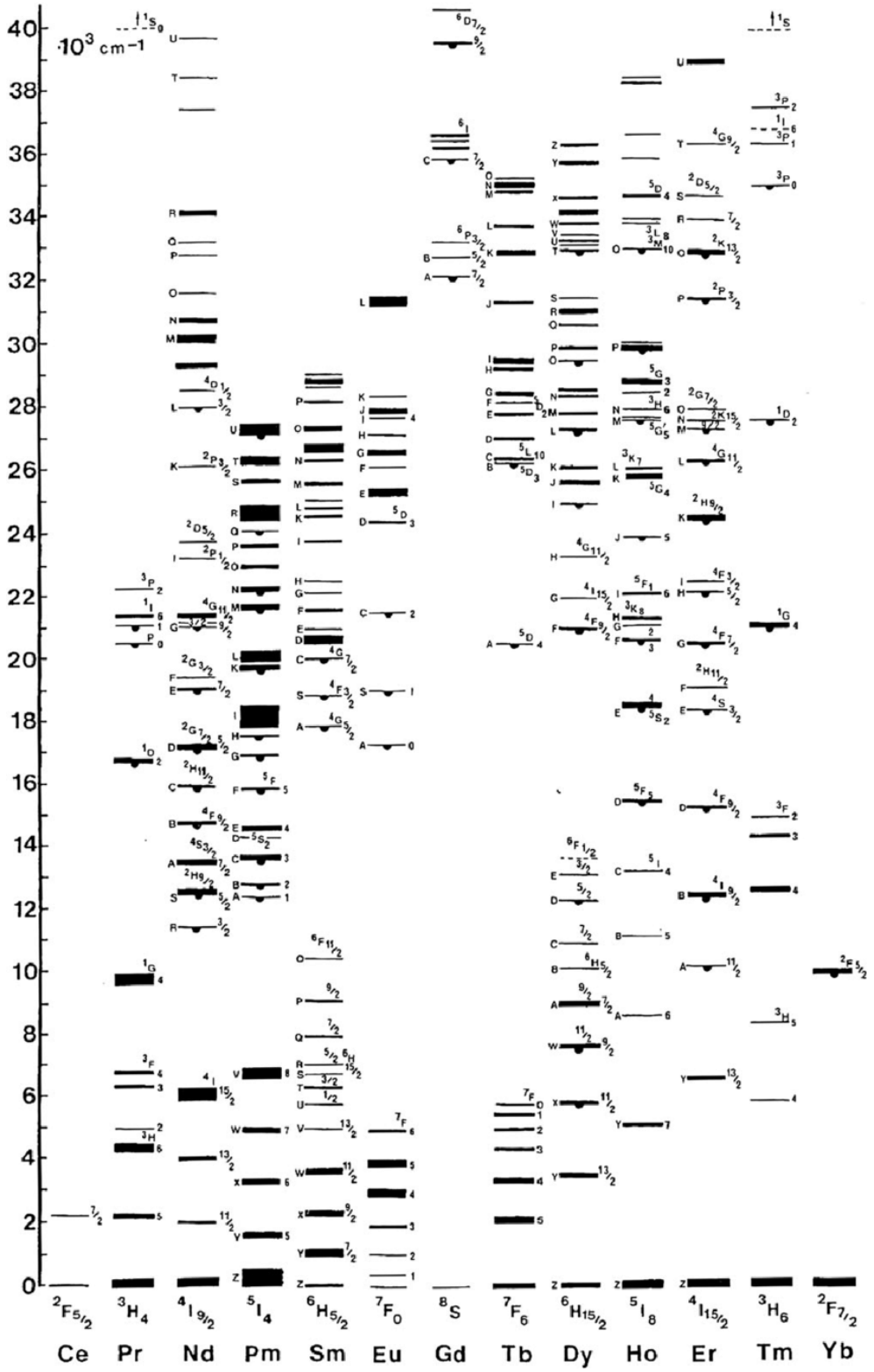


Fig. 1 Dieke diagram of free Ln^{3+}-ions reprinted from *Meijerink* et al.[77]

The concept relies on the assumption that the chemical environment does not interfere with the 4f-orbitals, and thus does not exhibit any influence on the respective relative energy levels. For the Ln^{2+}-ions the same concept is also applicable and can qualitatively

be deduced from the conventional *Dieke* diagram.[78,79] The same terms that describe the electronic configuration of a given Ln^{3+}-ion shift by one position to lower atomic numbers, but will also change in energy. For example, the terms used for the description of the Eu^{3+}-ion ([Xe] $4f^6$) are the same as for the isoelectronic Sm^{2+}-ion but will occur at different energy levels.
A second important change that has severe implications, in particular on the luminescence of the lanthanoid ions, is the lowering of the unoccupied 5d-orbitals in the case of Ln^{2+}-ions. For most Ln^{3+}-ions, intraconfigurational f-f-transitions dominate the luminescence that are typically very narrow, but also quite weak due to the violation of *Laporte's* rule.[80–82] Another main characteristic of the luminescence of most Ln^{3+}-ions is that the absorption and emission wavelengths are characteristic for each ion and cannot easily be varied by chemical engineering. For the Ln^{2+}-ions however, the lowered 5d-orbitals often allow interconfigurational f-d or d-f transitions that are very intense, resulting in strong colour and luminescence. Because the 5d-orbitals are strongly influenced by the chemical environment, the colour of absorption and emission can be adjusted by chemically engineering the compounds tailored to the demands for applications. Consequently, the energy terms of the d-orbitals can no longer be drawn as straight lines in *Dieke's* diagram and instead an energy range is typically given instead. Because of these unique features, divalent lanthanoid ions are of particular interest and have already been established successfully in phosphors.[83] Due to the challenging synthesis associated with most Ln^{2+}-salts, the pool of compounds engineers can select from is still comparatively small. The discovery of new salts of divalent lanthanoids, as well as establishing reliable synthetic protocols can therefore be considered essential for the progress of material science and technology in a broader context.

2.3.2 Chemistry of Divalent Lanthanoids

Like for tetravalent lanthanoids, the chemistry of divalent lanthanoids is essentially concentrated on a few elements. The *classical* divalent lanthanoids are europium, ytterbium and samarium that are the most easily accessible Ln^{2+}-ions. The $4f^7$-configured Eu^{2+}-ion is the most stable Ln^{2+}-ion ($E_0(Eu^{2+}/Eu^{3+}) = -0.35$ V), followed by the $4f^{14}$-configured Yb^{2+}-ion ($E_0(Yb^{2+}/Yb^{3+}) = -1.05$ V) and the $4f^6$-configured Sm^{2+}-ion ($E_0(Sm^{2+}/Sm^{3+}) = -1.55$ V) (potential relative to standard hydrogen electrode).[19,84] Other Ln^{2+}-ions are also known under certain conditions, but are less common due to their strongly reducing character. The reduction potentials of the Ln^{2+}-ions and the third ionisation energies are graphically summarised in fig. 2.

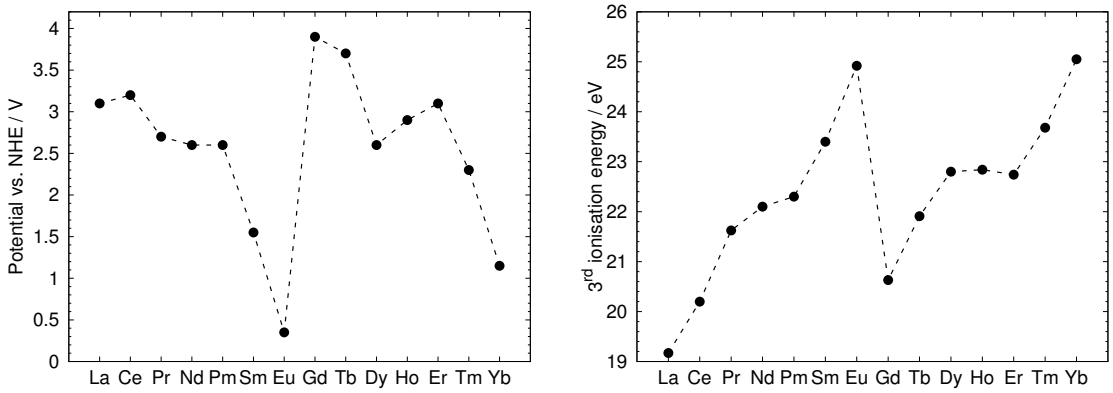


Fig. 2 Reduction potentials of divalent lanthanoid ions (left) and their third ionisation energies.[20,21,84]

Naturally, the possibility to prepare salts of divalent lanthanoids both correlates with the reduction potential of the cation, as well as the capability of the respective anion to oxidise the Ln^{2+}-ion back to its trivalent form. Hence, many simple binary and multinary halides are known for most lanthanoids.[64] While binary fluorides of the composition LnF_2 are only known for the *classical* divalent lanthanoids,[85–88] lanthanoid diiodides were discovered for Ln = La, Ce, Pr, Nd, Sm, Eu, Gd, Dy, Tm, and Yb.[89] Within the presented series of diiodides, only those of Nd, Sm, Eu, Dy, Tm and Yb actually contain Ln^{2+}-ions while the other iodides characteristically exhibit metallic properties which are caused by the third electron occupying the conduction band.[90,91] Consequently those diiodides contain Ln^{3+}-ions and therefore are not considered salts of divalent lanthanoids, despite their composition.

Compared to the halides and other systems with monoatomic anions, only few compounds are known with oxoanions with most of them only being known for Eu^{2+}. For example, the orthosilicate Eu_2SiO_4 was described in two different modifications and $EuSO_4$ can be prepared by precipitation from aqueous solution.[92–95] Even these simple systems have not been realised for other Ln^{2+}-ions, due to their sensitivity towards water.

The strategy pursued in this work to circumnavigate this issue was to synthesise salts of Ln^{2+}-ions with weakly coordinating anions in order to increase the solubility in organic solvents to overcome the limits posed by aqueous systems. Trifluoromethanesulphonate (triflate, OTf) appeared to be an ideal candidate for this endeavour given its low basicity and easy availability. Therefore, the following section is dedicated to reviewing the current state of research about trifluoromethanesulphonates of divalent lanthanoids.

2.3.2.1 Trifluoromethanesulphonates of Divalent Lanthanoids

A comprehensive overview of the literature on divalent lanthanoid triflates is provided in ***Manuscript 4*** (section 4.2.1).

3 Objective

The paramount objective of this work was to systematically study and develop protocols for the synthesis of new salts of divalent and tetravalent lanthanoids, with particular emphasis on oxoanions. This fundamental class of anions is ubiquitous in inorganic chemistry but is notoriously underrepresented for lanthanoids with oxidation states other than +III. As was pointed out in section 2.3.1, the discovery of such compounds is an elementary process in advancing the development of new materials and technologies. The present work is separated into two sections, the first addressing the chemistry of tetravalent lanthanoids (in particular Pr^{4+}) and the second dealing with salts of divalent lanthanoids.

3.1 Tetravalent Lanthanoids

The focus within the field of tetravalent lanthanoids was to be set on Pr^{4+} because of its $4f^1$-configuration that is, in contrast to the closed shell Ce^{4+}-ion and the $4f^7$-configured Tb^{4+}-ion, of particular interest for the reasons elaborated in section 2.2.2. In previous work several potential strategies for the synthesis of oxoanionic salts of Pr^{4+} were investigated,[96] including the reaction of PrO_2 with Brønstedt-acids, Lewis acid-base reactions with PrO_2 as well as oxidations of Pr^{3+}-salts, neither of which yielded a new salt of Pr^{4+} under the applied conditions.
In this work, two of these fundamental strategies were to be adapted and expanded. The first strategy was to investigate potential methods of oxidising Pr^{3+} to Pr^{4+} by employing strong oxidants under various experimental conditions as well as electrochemical methods. The second strategy involved reacting PrO_2 with acid anhydrides such as SiO_2, P_2O_5 and others under high pressure using a multi-anvil press or diamond anvil cells in order to force Lewis acid-base reactions.

3.2 Divalent Lanthanoids

For the reasons explained in section 2.3.2, the triflates of divalent lanthanoids presented an attractive synthetic target. Although some synthetic protocols were already known before this work (see section 4.2.1 for details), thorough characterisation of the lanthanoid(II) triflates in the solid state was missing with only few exceptions.[97,98] The literature procedures were to be reviewed, reproduced and optimised in order to find a feasible and effective way to produce the phase pure triflates, allowing the material to be properly characterised, in particular with regard to their luminescence.
Additionally, it was to be investigated if the synthetic protocols allowed for some flexibility with respect to solvent and other parameters to improve their utility. The crystallisation

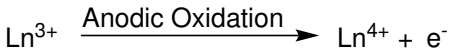
of the lanthanoid(II) triflates from different solvents would allow valuable insights into the relationship of the atomic structure and the physical properties of the Ln^{2+}-ions.
Once this milestone would be conquered, it was to be investigated if the protocols could be applied for the synthesis of other salts of Ln^{2+}, too. Additionally, experiments exploiting the reactivity of the compounds to explore their synthetic potential were also planned.

4 Results and Discussion

4.1 Tetravalent Lanthanoids

4.1.1 Electrochemical Experiments

In contrast to conventional chemical methods, the utilisation of electrochemistry permits to accurately apply a desired potential to a chemical system and therefore allows to induce redox reactions at the electrodes. Applying this principle to the challenge of obtaining tetravalent lanthanoids, a suitable system consisting of electrode, solvent, lanthanoid(III)-precursor, electrolyte etc. must first be found, for which several factors are to be considered. A general reaction equation for the electrochemical oxidation of Ln^{3+}-ions is presented in scheme 1. Since aqueous systems do not appear suitable due to their comparatively low electrochemical window and the resulting proclivity to produce oxygen at high positive potentials, organic solvents had to be used.



Scheme 1 Generalised reaction equation of the anodic oxidation of trivalent lanthanoids.

When reviewing available solvent-electrolyte combinations, ideally the combination with the highest possible stability towards positive potentials was to be selected. Thus, acetonitrile and tetrabutylammonium hexafluorophosphate ($TBAPF_6$) were chosen as the solvent-electrolyte system which is reportedly stable up to potentials of >+3 V (both vs. normal hydrogen electrode, NHE or saturated calomel electrode, SCE).[99,100] The second important decision was the choice of suitable precursors of Ln^{3+}-salts. The first contemplation in this discussion was to select an anion that itself is inert to oxidation within the applied range of potentials. In addition to that the resulting salts had to have sufficient solubility in acetonitrile for the planned experiments. Therefore, the triflate and the perchlorate anions were determined to be suitable candidates. Instead of starting with praseodymium, terbium was chosen because the oxidation potential of Tb^{4+} is slightly lower than that of Pr^{4+} (comp. tab. 1) and eventual oxidation events were expected to be close to the limit of the electrochemical window of the solvent-electrolyte system. $Tb(ClO_4)_3$ and $Tb(OTf)_3$ were synthesised as described in sections 6.2.1 and 6.2.3. Cyclic voltammograms (CVs) were measured of both compounds in order to establish a relationship between redox processes and applied potentials in the selected systems. The first two cycles of the CVs are shown in fig. 3.

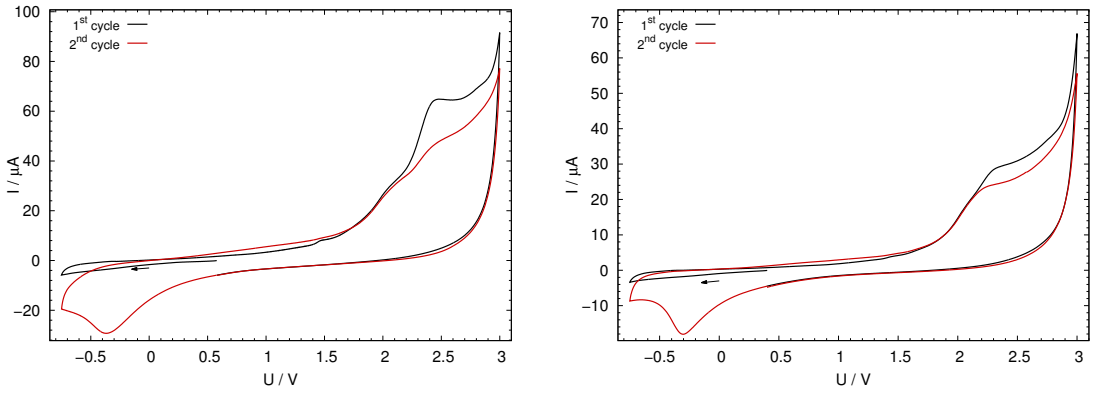


Fig. 3 Cyclic voltammograms of $Tb(ClO_4)_3$ (left) and $Tb(OTf)_3$ (right). Both analytes were measured with a sweeping velocity of 100 mV/s, an analyte concentration of 1 mmol/l, an electrolyte concentration ($TBAPF_6$) of 0.1 mol/l and against a Ag/AgCl reference electrode.

It is apparent that both curves are inherently similar to each other, indicating that the strategy of excluding redox processes involving the anion were successful and that the currents observed are indeed caused by terbium ions. When starting at the equilibrium potential and changing the potential towards reductive values, no current was observed, as was expected. When sweeping to oxidative potentials, a current was observed, peaking at ca. 2.4 V for $Tb(ClO_4)_3$ and 2.3 V for $Tb(OTf)_3$ indicating the oxidation of Tb^{3+} to Tb^{4+}. When reversing the sweeping direction soon after the oxidation event, no immediate reduction follows, from which it is concluded that the process is irreversible. In the second cycles of the CVs a reduction takes place, peaking at -0.4 V for $Tb(ClO_4)_3$ and -0.3 V for $Tb(OTf)_3$. These reductions must be attributed to the oxidised species that had formed in the first cycles since they were not observed in the first reductive sweeps. Visual inspection of the working electrode after completing the experiment revealed that a thin film had formed on the surface that could not be further characterised due to the microscopic quantities. When repeating the experiment and mixing the solution between cycles, the reductive current always reappeared, proving that the solid layer on the electrode contained oxidised species, possibly in the form of terbium oxides.

Conclusively, the cyclic voltammetry experiments of $Tb(ClO_4)_3$ and $Tb(OTf)_3$ have demonstrated that an oxidation event occurs when applying potentials close to the border of the electrochemical window, resulting in an unidentified solid that forms of the surface of the electrode but is insoluble in acetonitrile. These observations are consistent with the hypothesis of terbium oxides forming on the surface of the electrode. If the anticipated $Tb(OTf)_4$ or related species had formed, a reversible signal would have been expected. Since similar results are to be expected from analogous experiments with praseodymium, they were not conducted.

4.1.2 Chemical Oxidation with XeF_2 in Acetonitrile

The chemical oxidation of Pr^{3+} or Tb^{3+} to their tetravalent ions is generally expected to require a strong oxidant. XeF_2 is an attractive reagent for this purpose not only because of its commercial availability, but also because the formation of xenon as a gaseous byproduct ensures that oxidations proceed irreversibly. Another merit of XeF_2 is its solubility in organic solvents such as acetonitrile. The following section discusses the attempted oxidations of Ln^{3+} triflates and perchlorates with xenon difluoride. The triflates and perchlorates were synthesised following the procedures described in sections 6.2.1 and 6.2.3. $Tb(OTf)_3(MeCN)_3$ (Niggli-notation: $^1_\infty[Tb(OTf)_{6/2}(MeCN)_{3/1}]$) and $Pr(ClO_4)_3(MeCN)_4$ (Niggli-noatation: $^0_\infty[Pr(ClO_4)_{3/1}(MeCN)_{4/1}]$) were crystallised to obtain reference data for X-ray diffraction analysis. $Tb(OTf)_3(MeCN)_3$ (see tab. 12 for cryst. data) is isostructural to other Ln^{3+}-compounds of the same composition[101] and therefore does not require further analysis. $Pr(ClO_4)_3(MeCN)_4$ is isostructural to the Eu^{3+}-compound that will be discussed below (section 4.2.6).
The first attempts to oxidise Tb^{3+} were made by adding a solution of $Tb(OTf)_3$ to a solution of XeF_2 in acetonitrile, as shown in scheme 2.

$$2\ Tb(OTf)_3 + XeF_2 \xrightarrow[rt]{MeCN} Xe^0 + 2\ Tb^{4+} + 6\ OTf^- + 2\ F^-$$

Scheme 2 Expected reaction for the oxidation of $Tb(OTf)_3$ using XeF_2.

As soon as both solutions were combined, a gas started to evolve and the solution changed its colour from colourless to brown. The reaction was allowed to continue until the effervescence had eased and the tone of the colour remained constant. When subjecting the solution to a laser ($\lambda = 405$ nm), green fluorescence was observed which is characteristic for Tb^{3+} and suggests that Tb^{3+} still was, at least partially present in the solution. A UV-Vis spectrum (compare fig. 4) was recorded of the diluted solution showing a broad absorption band ranging from the UV-region into the visible range, explaining the brown colour. By comparison with a reference spectrum of pure $Tb(OTf)_3$ in acetonitrile, the peak at 240 nm can be assigned to the absorption of the triflate anion.

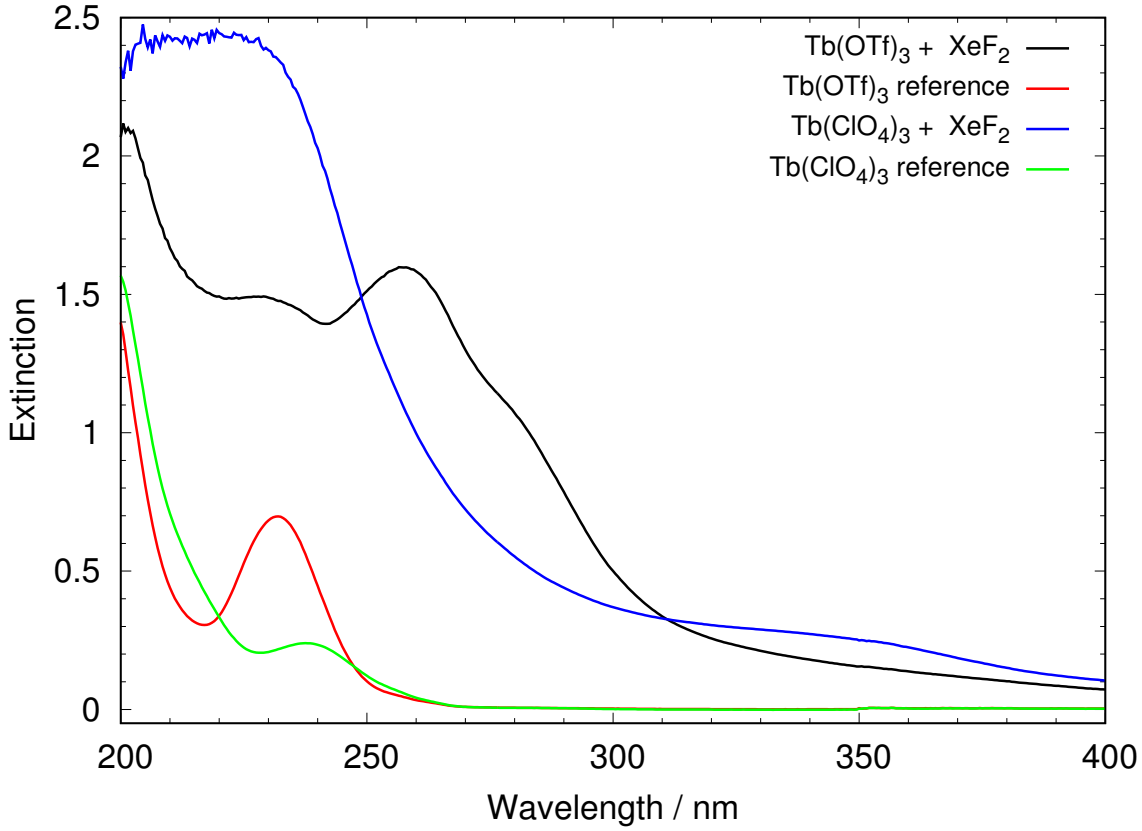


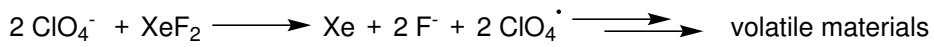
Fig. 4 UV-Vis spectra of the reaction mixtures of $Tb(OTf)_3$ and $Tb(ClO_4)_3$ with XeF_2, as well as the reference spectra of solutions of $Tb(OTf)_3$ and $Tb(ClO_4)_3$ in acetonitrile. The solutions were prepared with arbitrary concentrations.

In order to obtain more information about the products of the reaction, multiple attempts were undertaken to grow single crystals, all of which failed. Evaporation of volatile materials from the mixture afforded a sticky crude product that could not be analysed by powder X-ray diffraction (PXRD). The IR-spectrum of the material (see fig. 68) still showed characteristic vibrations of the triflate anion, next to some additional bands that cannot be unambiguously assigned.

The experiment was repeated with $Tb(ClO_4)_3$ instead of $Tb(OTf)_3$, again resulting in a deeply coloured solution (UV-Vis shown in fig. 4), with a broad absorption band peaking at <250 nm. The peak at ca. 260 nm, while present in the experiment with terbium triflate was missing in this experiment, proving that different chromophores have formed. After evaporation of the volatiles, an amorphous solid was obtained (comp. fig. 32). All attempts to recrystallise the materials failed so that the solid remained unidentified.

When attempting similar reactions with $Pr(ClO_4)_3$, it was noticed that the starting materials changed colour from green to orange when mixed at room temperature even without a solvent. The colour quickly intensified and was followed by a violent reaction concomitant with a bright flame. The residue, consisting of PrF_3 (see fig. 33 for PXRD

data) suggests that instead of oxidising the Pr^{3+}-ions, XeF_2 oxidises the perchlorate anion to yield volatile materials. One possible reaction pathway is illustrated in scheme 3.

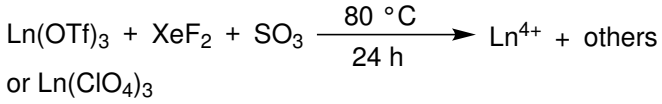


Scheme 3 Proposed reaction pathway explaining the formation of PrF_3 when reacting solid $Pr(ClO_4)_3$ and XeF_2.

In order to isolate the orange material that had formed before the solids spontaneously ignited, the reaction was repeated under more controlled conditions. The substrates were cooled to -78 °C and then combined at the same temperature. After no apparent change in colour could be observed, the mixture was carefully warmed up to room temperature, at which point an orange colour started to appear. Since no ignition occurred, the still orange products were analysed by PXRD, revealing that $Pr(ClO_4)_3$ was the only crystalline phase in the products (see fig. 34 for PXRD data). Furthermore, when subjecting the mixture to dynamic vacuum, orange substances were observed in the cooling trap of the Schlenk line, clearly showing that the orange colour was caused by volatile oxidation products of the perchlorate anions instead of Pr^{4+}-ions.

4.1.3 Reactions of Ln^{3+}-salts with XeF_2 in SO_3

By employing XeF_2 as the oxidant in combination with SO_3, *Wickleder* et al. successfully managed to stabilise Pd^{4+} in oxoanionic environment.[102] The following section describes the attempts to adapt this method for the synthesis of oxoanionic species of Pr^{4+} and Tb^{4+} by reacting the triflates and perchlorates of the trivalent lanthanoids with SO_3 in presence of XeF_2. Scheme 4 shows the general reaction scheme.



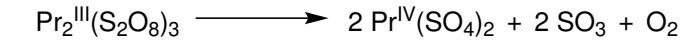
Scheme 4 Generalised reaction scheme for the reaction of $Ln(OTf)_3$ and $Ln(ClO_4)_3$ with SO_3 in presence of XeF_2 adapted from a procedure by *Wickleder* et al. that resulted in the stabilisation of Pd^{4+} in oxoanionic environment.[102]

Similar to the observations made by reacting the perchlorates of Pr^{3+} and Tb^{3+} with XeF_2 in the experiments described earlier in this section, an orange colour was observed when reacting them in presence of SO_3. Removing all volatiles from the mixtures resulted in the recovery of the pure perchlorates (see fig. 36, fig. 37 and fig. 69), proving that under the applied conditions, no oxidation of the Ln^{3+}-ions occurred.
Subjecting the triflates to the same conditions also failed to produce materials containing tetravalent lanthanoids. Unlike the reactions of the perchlorates, no change of colour was

observed, further corroborating the hypothesis that the orange colour is not caused by oxidation of the lanthanoids ions but is rather a result of competing processes involving the perchlorate ion.

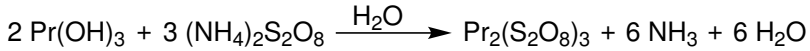
4.1.4 Attempted Syntheses of $Pr_2(S_2O_8)_3$

This section deals with the synthesis of praseodymium(III) peroxodisulphate that, if subjected to the right conditions might be susceptible to internal redox reactions resulting in the formation of $Pr(SO_4)_2$. One hypothesised reaction equation is shown in scheme 5.



Scheme 5 Hypothesised decomposition of $Pr_2(S_2O_8)_3$ yielding $Pr(SO_4)_2$.

Thus far, no lanthanoid peroxodisulphates are known in the solid state. In order to adress this issue, two synthetic strategies were attempted to obtain $Pr_2(S_2O_8)_3$. The first strategy was inspired by a method that can successfully be applied for the synthesis of group(I) metal peroxodisulphates and involves the reaction of $(NH_4)_2S_2O_8$ with basic salts of the metals.[103] In this particular case, $Pr(OH)_3$ was chosen as the basic precursor. The intended reaction is displayed in scheme 6.



Scheme 6 Intended reaction when converting $Pr(OH)_3$ and $(NH_4)_2S_2O_8$.

Instead of $Pr_2(S_2O_8)_3$, the ammonium sulphatopraseodymate $(NH_4)[Pr(SO_4)_2(H_2O)_3]\cdot H_2O$ (Niggli-notation: $(NH_4)^2_\infty[Pr(SO_4)_{4/2}(H_2O)_{3/1}]H_2O$) had formed, proving that the peroxodisulphate group decomposed into sulphate under the applied conditions. $(NH_4)[Pr(SO_4)_2(H_2O)_3]\cdot H_2O$ was identified by single crystal structure analysis ($P2_1/n$, $a = 665.61(2)$ pm, $b = 1882.52(9)$ pm, $c = 878.32(3)$ pm, $\beta = 97.603(3)°$). The atoms of the asymmetric unit and the unit cell are illustrated in fig. 5.

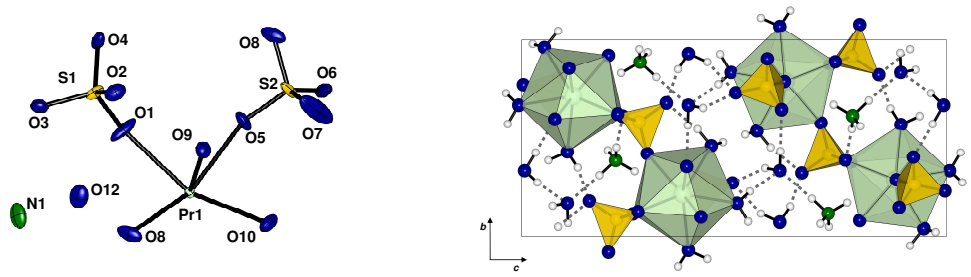


Fig. 5 Left: Atoms of the asymmetric unit of $(NH_4)[Pr(SO_4)_2(H_2O)_3]\cdot H_2O$ with displacement ellipsoids shown at 50% probability. Hydrogen atoms were omitted for clarity. Right: Unit cell of $(NH_4)[Pr(SO_4)_2(H_2O)_3]\cdot H_2O$ viewed along the crystallographic a-axis. Green = Pr; yellow = sulphur; blue = oxygen; green = nitrogen; white = hydrogen.

$(NH_4)[Pr(SO_4)_2(H_2O)_3]\cdot H_2O$ is isostructural to the analogous structures of La, Ce, Nd, Sm and Tb.[104–107] Further crystallographic data of $(NH_4)[Pr(SO_4)_2(H_2O)_3]\cdot H_2O$ is provided in tab. 13. Trying to prevent the decomposition of the peroxodisulphate group by cooling the reaction to 0 °C failed because the starting materials were not converted.
Since the peroxodisulphate anion decomposed during the acid base reaction between $Pr(OH)_3$ and $(NH_4)_2S_2O_8$, another strategy had to be employed. The metathesis of tetrabutylammonium peroxodisulphate and $Pr(OTf)_3$ in THF has the advantage over the previous attempts that reaction temperatures of <0 °C are possible. Furthermore, it was to be expected that $Pr_2(S_2O_8)_3$, if formed, would precipitate from solution, thus providing a driving force for the metathesis. This concept is shown in scheme 7.

$$3\ (Bu_4N)_2S_2O_8 + 2\ Pr(OTf)_3 \xrightarrow[-78\ °C]{THF} Pr_2(S_2O_8)_3 \downarrow + 6\ (Bu_4N)OTf$$

Scheme 7 Attempted metathesis of $(TBA)_2S_2O_8$ and $Pr(OTf)_3$ in THF.

$(TBA)_2S_2O_8$ was prepared following an adapted literature procedure (see section 6.2.14),[108] during which single crystals were obtained. $(TBA)_2S_2O_8$ crystallises in the monoclinic space group $P2_1/c$ (a = 2274.5(1) pm, b = 1518.28(9) pm, c = 2409.9(1) pm, β = 105.959(2)°) with eight formula units per cell. The atoms of the asymmetric unit are shown in fig. 6. Additional crystallographic data are summarised in tab. 14.

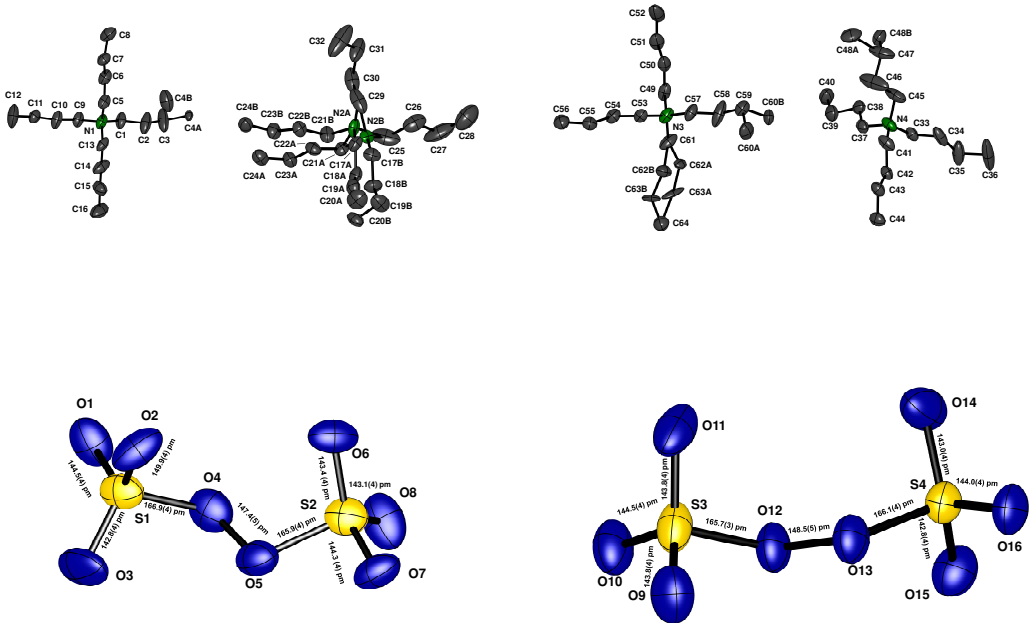


Fig. 6 Atoms of the asymmetric unit of $(TBA)_2S_2O_8$ with displacement ellipsoids shown at 50% probability. Hydrogen atoms were omitted.

With $(TBA)_2S_2O_8$ now being available, the planned metathesis (see scheme 7) was attempted. At low temperatures, the solubility of the substrates was insufficient so that the suspension had to be warmed up. When warming up the mixture however, a gas started to evolve, signalling the decomposition of the peroxodisulphate group. The resulting solids could not be identified unambiguously (see fig. 39 and fig. 70 for analytical data).
Considering the difficulties encountered when attempting to synthesise $Pr_2(S_2O_8)_3$, it was decided to resort to multinary systems with more easily available peroxodisulphates as starting materials, as will be described in section 4.1.5.

4.1.5 Reaction of $Pr_2(SO_4)_3$ and $K_2S_2O_8$ at High Pressure

Due to the unavailability of the binary $Pr_2(S_2O_8)_3$, the peroxodisulphate anion was combined with the Pr^{3+}-ion from external sources. The reaction of $K_2S_2O_8$ and $Pr_2(SO_4)_3$ was carried out at 11 GPa in order to favour the oxidation of Pr^{3+} over the disproportionation of the peroxodisulphate anion. The respective reaction equation is shown in scheme 8.

$$Pr_2(SO_4)_3 + K_2S_2O_8 \xrightarrow[1000\ W]{11\ GPa} K_2Pr_2^{IV}(SO_4)_5$$

Scheme 8 Anticipated reaction of $K_2S_2O_8$ and $Pr_2(SO_4)_3$.

From this reaction, green single crystals were obtained that had the same unit cell as $KPr(SO_4)_2$.[109] Microscopic photos of the crystals are shown in fig. 7.

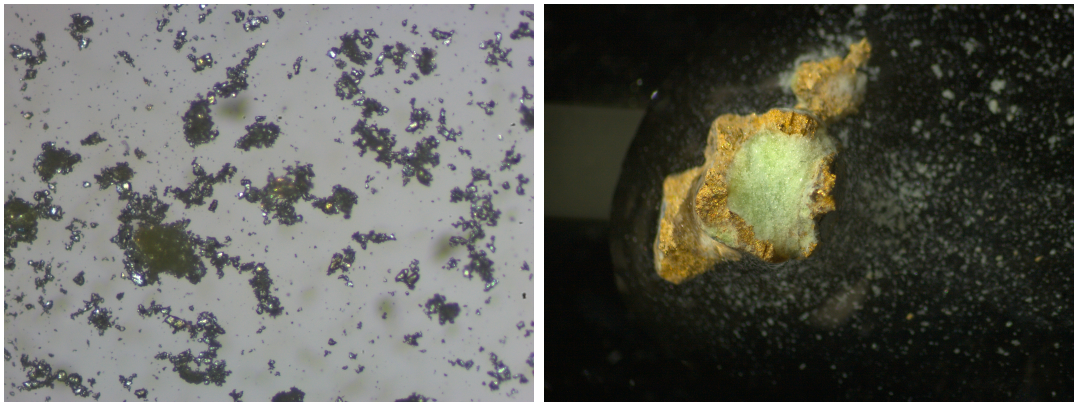


Fig. 7 Microscopic photos of the single crystals (left) obtained from reacting $K_2S_2O_8$ and $Pr_2(SO_4)_3$ at 11 GPa. The right image shows the bulk material still contained by the gold crucible.

The bulk material differs in composition from that of the investigated single crystal, as evidenced by PXRD (comp. fig. 40). It is likely that multiple phases have formed during the reaction and that next to $KPr(SO_4)_2$, other ternary sulphates of potassium and praseodymium were also present. However, the green colour of the bulk material is characteristic of Pr^{3+}, from which it is concluded that the experiment did not succeed in obtaining a sulphate containing Pr^{4+}. More analytical data are shown in fig. 71.

4.1.6 Reaction of PrO_2 and SiO_2 at High Pressure (*Manuscript 1*)

Like its analogue with Ce^{4+}, $PrSiO_4$ is expected to crystallise in the zircon structure that is characterised by strong ionic interactions due to the highly charged ions and high coordination numbers of the cations.[28] Both properties are beneficial for the stabilisation of Pr^{4+}. In fact, $CeSiO_4$ in the form of stetindite is one of the few minerals known to support Ce^{4+} and there even have been indications that Pr^{4+} is naturally contained in small concentrations in certain deposits.[110] A comprehensive overview of the current state of relevant research is contained in ***Manuscript 1***.

Manuscript 1 systematically describes the reaction of PrO_2 with SiO_2 at various pressure points up to 29 GPa in a diamond anvil cell (DAC). Generally, at pressures of up to 15 GPa $Pr_2Si_2O_7$ formed, whereas the reaction at 29 GPa produced the silicates $PrSi_3O_8$ and $Pr_2Si_7O_{18}$, both containing Pr^{4+}. Next to those two silicates, $Pr_4Si_3O_{12}$ and $Pr_2(O_2)O_3$ were also observed at 29 GPa. Theoretical calculations of the band structure supported the presence of Pr^{4+} in $PrSi_3O_8$ and $Pr_2Si_7O_{18}$. Both silicates are the first examples of structurally characterised salts of Pr^{4+} in oxoanionic environment, and therefore constitute a major milestone in the research of tetravalent lanthanoids.

The author's contributions include the experimental work, data analysis and writing

of the manuscript, all carried out in collaboration with the coauthors. Band structure calculations were performed by B. Rasche.
Supporting information of ***Manuscript 1*** is provided in section 7.1.

Stabilization of Pr^{4+} in Silicates – High Pressure Synthesis of $PrSi_3O_8$ and $Pr_2Si_7O_{18}$

Niko T. Flosbach*,[1] Maxim Bykov*,[1,2] Elena Bykova,[3] Bertold Rasche,[1,4] Mohamed Mezouar,[5] Timofey Fedotenko,[6] Stella Chariton,[7] Vitali B. Prakapenka,[7] Mathias S. Wickleder*[1]

[1]Institute of Inorganic Chemistry, University of Cologne, Greinstraße 6, 50939 Cologne, Germany

[2]Institute of Inorganic and Analytical Chemistry, Goethe University Frankfurt, Max-von-Laue-Straße 7, 60438 Frankfurt am Main, Germany

[3]Institute of Geosciences, Goethe University Frankfurt, Altenhöferallee 1, 60438 Frankfurt am Main, Germany

[4]Institute of Inorganic Chemistry, University of Stuttgart, 70569 Stuttgart, Germany

[5]European Synchrotron Radiation Facility (ESRF), Avenue des Martyrs 71, 38000 Grenoble, France

[6]Deutsches Elektronen-Synchrotron, Notkestr. 85, 22607 Hamburg, Germany

[7]Center for Advanced Radiation Sources, University of Chicago, Chicago, Illinois 60637, USA

ABSTRACT: The reaction between PrO_2 and SiO_2 was investigated at various pressure points up to 29 GPa in a diamond anvil cell using laser heating and *in situ* single crystal structure analysis. The pressure points at 5 and 10 GPa produced $Pr_2^{III}(Si_2O_7)$, whereas $Pr_4^{III}Si_3O_{12}$ and $Pr_2^{IV}(O_2)O_3$ were obtained at 15 GPa. $Pr_4^{III}Si_3O_{12}$ can be interpreted as a high-pressure modification of the still unknown orthosilicate $Pr_4^{III}(SiO_4)_3$. $Pr^{IV}Si_3O_8$ and $Pr_2^{IV}Si_7O_{18}$ that contain praseodymium in its rare +IV oxidation state were identified at 29 GPa. After releasing the pressure from the reaction chamber, the Pr(IV) silicates could be recovered, indicating that they are metastable at ambient pressure. Theoretical calculations of the electronic structure corroborate the oxidation state of praseodymium in both $Pr^{IV}Si_3O_8$ and $Pr_2^{IV}Si_7O_{18}$. Both silicates are the first structurally characterized representatives of Pr^{4+}-containing salts with oxoanions. All three silicates contain condensed networks of $[SiO_6]$-octahedra which is unprecedented in the rich chemistry of lanthanoid silicates.

INTRODUCTION

One of the most fundamental chemical properties of any element is the number of electrons it is able to either accept or donate to its binding partners. The number of electrons affected thereby is usually referred to as the oxidation state of the respective element. In the lanthanoid series the oxidation state of +III is paramount since it is the most stable for all elements of the series.

The physical behavior of most Ln^{3+} ions (Ln = lanthanoid) is dominated by the unique nature of the 4*f*-valence shell, which is well shielded from its chemical environment, resulting in sharp optical transitions, as well as localized magnetic moments. These properties are of great interest for a whole spectrum of different technical applications and thus a plethora of use cases has evolved that play an integral part in modern societies. The applications of lanthanoids range from catalysis over pharmaceutical use to optical or magnetic components of high-tech devices.[1-4] Since the physical properties of any ion are drastically altered when changing its oxidation state, compounds with lanthanoids in oxidation states other than +III are of particular interest, yielding the potential to discover new structures with desirable properties.[5-6]

The divalent oxidation state has been observed for all lanthanoids (except for the radioactive promethium), but is most commonly encountered in Sm^{2+}, Eu^{2+} and Yb^{2+}.[7-10] The chemistry of lanthanoids in their tetravalent oxidation states is far more restricted because of the strongly oxidizing character of the respective ions. Only Ce^{4+}, which is isoelectronic to the xenon

atom has been extensively studied.[11-14] Even high-pressure studies of compounds containing Ce^{4+} have been published.[15] Following Ce^{4+} in terms of oxidative potential are Pr^{4+} and Tb^{4+} that are much more strongly oxidizing than Ce^{4+}, which is directly reflected in the limited amount of respective compounds that are well characterized.

Recently, the meticulous analysis of the electronic structure of ternary Pr^{4+} oxides revealed that the electronic structure of the Pr^{4+} ion is not analogous to other lanthanoid ions, but shows rather unique behavior that is more similar to that of early actinoids in high oxidation states, granting the Pr^{4+} ion an exclusive role in the chemistry of lanthanoid oxides.[16] More general trends are yet to be established and their investigation has been impeded thus far by the scarcity of Pr^{4+} compounds which is attributed to their difficult synthesis. Establishing methods for the synthesis of Pr^{4+} salts, in particular of inorganic salts, would act as a catalyst for new developments in the field by triggering further investigations.

Until recently, when the first oxoanionic salts of Tb^{4+} and metal organic complexes of both ions were published, Pr^{4+} and Tb^{4+} were known to exist almost exclusively in solid oxides and fluorides.[17-24] Some oxoanionic salts of Pr^{4+} were reported in the 1960s in a series of communications by *Pajakoff* in form of various sulfates along with nitrates, oxalates and even carbonates.[25-29] Despite these early reports that contain no structural data, the published compounds were never reproduced until today and the proposed compositions were thus never confirmed by X-ray diffraction experiments or other techniques. Reports on analogous compounds of Tb^{4+} have also not been published, despite the similar oxidation potential of both tetravalent cations (Pr^{3+}/Pr^{4+}: E_0 = 3.2 V; Tb^{3+}/Tb^{4+}: E_0 = 3.1 V).[30-31] Hence, no oxoanionic salt containing Pr^{4+} has been structurally characterized thus far. There have been some indications that Pr^{4+} naturally occurs in stentindit, which is $CeSiO_4$ that crystallizes in the zircon type structure.[32-34] In fact, the hypothetical $PrSiO_4$ is expected to crystallize in the same structure type as the analogous silicate of Ce^{4+}, rendering it a promising candidate for the stabilization of Pr^{4+} in oxoanionic salts. The reaction of praseodymium oxides with silicon oxide has been investigated thoroughly at ambient pressure and elevated temperatures and typically results in the formation of $Pr_2(Si_2O_7)$, in which the praseodymium ions are found to carry a formal charge of +3.[35-39]

Generally, lanthanoid silicates are known to exhibit a structurally rich and diverse chemistry, with nesosilicates known for the oxidation states +II (for Eu), +III (for La) and +IV (for Ce).[32-34, 40-45] Sorosilicates of the form $Ln_2(Si_2O_7)$ have been reported in various structures for almost the entire series of lanthanoids, while silicates of the composition $Ln_4(SiO_4)(Si_3O_{10})$ that have the same empirical formula $Ln_2Si_2O_7$ are also known.[46-72] The longest chain of connected $[SiO_4]$-tetrahedra is found in $Ln_6(Si_4O_{13})(SiO_4)_2$ (Ln = La, Ce, Tm) where four $[SiO_4]$-tetrahedra are condensed to the $Si_4O_{13}^{10-}$ anion.[70-72] Despite the manifold library of lanthanoid silicates, thus far no silicates with infinite chains, layers or even three dimensionally expanding networks of silicon-oxide tetrahedra have been discovered. Applying high pressure to silicates typically results in the transformation of tetrahedral $[SiO_4]$ building blocks to octahedral $[SiO_6]$-units, offering the opportunity to further expand the structural chemistry of lanthanoid silicates beyond the conventional tetrahedral silicates.[73-76] Although many of the aforementioned compounds were synthesized under high pressure, no octahedrally coordinated silicates were discovered. In this work, the systematic investigation of the reaction between quartz and praseodymium dioxide at pressures up to 29 GPa resulted in the discovery of the three unprecedented lanthanoid silicates $Pr_4Si_3O_{12}$, $PrSi_3O_8$ and $Pr_2Si_7O_{18}$; all of which accommodate condensed $[SiO_6]$-octahedra forming intricate networks expanding in three dimensions. The latter two silicates contain praseodymium in its rare +IV oxidation state, thus adding the class of oxoanionic salts to the scarce number of structurally characterized Pr(IV) salts.

EXPERIMENTAL AND COMPUTATIONAL METHODS

Synthesis of PrO_2 250 mg (0.245 mmol, 6 eq.) of freshly prepared Pr_6O_{11} (calcination of $Pr(OH)_3$) were added to a quartz crucible that was inserted into a steel autoclave with an internal volume of approximately 20 ml. 9 ml of liquid oxygen were condensed into the autoclave, before it was sealed and heated to 500 °C for 12 hours. After allowing the autoclave to cool down to room temperature, the pressure was released and 254 mg of PrO_2 (1.47 mmol, 100%) were recovered as a black powder. The PXRD (powder X-ray diffraction) data of the product is shown in fig. S 1.

Analysis of Substrates The purity of PrO_2 and SiO_2 was verified by PXRD. The data was collected on a Rigaku MiniFlex benchtop diffractometer using Cu-K_α radiation (λ_1 = 1.541 Å; λ_2 = 1.544 Å), in steps of 0.02° and an exposure time of 0.2 to 0.24 seconds per step. The samples were mounted on glass holders. Rietveld refinements were performed with Topas.[77] The data is shown in the fig. S 1 and fig. S 2 (see SI).

Reaction of SiO_2 and PrO_2 Both starting materials were loaded into a diamond anvil cell after they were thoroughly homogenized in a mortar. No additional pressure transmitting medium was added, therefore conditions were not hydrostatic.[78] SiO_2 was used as supplied from commercial sources (*Riedel-de-Haën*). BX90-type diamond anvil cells equipped with Boehler-Almax type diamonds with culet size of 200 to 250 μm were used. A 100 to 125 μm hole drilled in a preindented rhenium gasket served as the sample chamber. The cell was compressed to pressure points 5, 10, 15 and 29 GPa (estimated errors ±1 GPa) as determined by ruby fluorescence and heated by using double-sided laser heating system of GSECARS (GeoSoilEnviro Center for Advanced Radiation Sources).[79-80] The pressure was determined before heating. The samples were heated locally with a heating time of 2 seconds and the temperature was determined by black body radiation.[81]

X-Ray Data Collection and Processing The heated region of the cell was mapped at individual pressure points by collecting X-ray diffraction images in a grid pattern. X-ray diffraction data at 15 and 29 GPa were collected at the synchrotron beamline P02.2 at DESY (Deutsches Elektronen Synchrotron, λ = 0.2903 Å, Perkin Elmer XRD1621 flat panel detector), the beamline ID-27 at ESRF (European Synchrotron Radiation Facility, λ = 0.3738 Å, Eiger2 X 9M CdTe detector) and X-ray diffraction data at the pressure points 5 and 10 GPa were collected at 13IDD of the APS (Advanced Photon Source, λ = 0.2952 Å, Pilatus 1M CdTe detector).[82-84]

Single crystal data collection was achieved by collecting ω-scans of ±30° or 35° with $\Delta\omega$ = 0.5° and an exposure time 2-5 s per frame. The resulting data was processed using the CrysAlisPro software in combination with DaFi.[85] The structures were

solved and refined using ShelX with Olex as the user interface.[86-87] CSD 2305371, 2305372, 2305373 and 2305374 (CSD = Cambridge structural database) contains the supplementary crystallographic data for this paper. These data can be obtained free of charge from FIZ Karlsruhe via www.ccdc.cam.ac.uk/structures.

Density Functional Theory (DFT) Calculations All DFT calculations were performed as scalar-relativistic calculations with the full-potential local-orbital (FPLO) code version 18.00,[88] within the local density approximation (LDA) using the parametrisation PW92.[89] The Blöchl corrected linear tetrahedron method was employed for $PrSi_3O_8$ and $Pr_2Si_7O_{18}$ with a 12×12×12 k-mesh (minimum 80 k-points Å), after checking for convergence with respect to the number of k-points. The structures were relaxed until the remaining forces were below 0.002 eV/Å, which involved only minor rearrangements in both cases. To account for the strong correlation of the praseodymium 4f-states, the latter were treated as open core (oc) states and consequently lowered in energy. The following states were treated as valence states: for praseodymium: 5s, 5p, 6s, 7s, 5d, 6d, 6p, 5f; for silicon: 2s, 2p, 3s, 4s, 3p, 4p, 3d; for oxygen: 1s, 2s, 3s, 2p, 3p, 3d. Mulliken population analysis[90] was directly provided by FPLO.

RESULTS AND DISCUSSION

At 5 GPa, $Pr_2(Si_2O_7)$ containing Pr^{3+} could be identified as the major phase, proving that the conditions were not suitable for praseodymium to retain its tetravalent oxidation state. The previously unheated part of the sample was reheated at lower temperatures in an attempt to stabilize Pr^{4+} through kinetic reaction control. The X-ray diffraction pattern revealed the formation of $Pr_2(Si_2O_7)$, along with unreacted starting materials. Consequently, the pressure was increased to 10 GPa, where the sample was reheated in a different location than before, where again $Pr_2(Si_2O_7)$ was observed as the main product. Since the Pr^{4+} ions were reduced during the reaction of PrO_2 and SiO_2, another oxidation product was expected. Possible reduction pathways of Pr^{4+} are formation of oxygen or peroxide species, neither of which could be detected.

$$2\ PrO_2 + 2\ SiO_2 \xrightarrow[1000\ \text{to}\ 4000\ \text{K}]{\text{DAC, 5 to 10 GPa}} Pr_2Si_2O_7 + \ldots \quad (1)$$

Because the pressure range between 5 to 10 GPa proved to be insufficient to stabilize Pr^{4+}, the pressure was increased to 29 GPa, where the experiment was repeated. The reaction of PrO_2 and SiO_2 at 29 GPa afforded two silicates ($Pr_2Si_7O_{18}$ and $PrSi_3O_8$) with similar compositions, both formally containing praseodymium in its tetravalent oxidation state. Next to the aforementioned phases, a silicate of Pr^{3+} with the composition $Pr_4Si_3O_{12}$ was found as well as the recently discovered oxide-peroxide $Pr_2(O_2)O_3$ (will be reported elsewhere).

$$PrO_2 + 3\ SiO_2 \xrightarrow[\text{ca. 2300 K}]{\text{DAC, 29 GPa}} PrSi_3O_8 \quad (2)$$

$$2\ PrO_2 + 7\ SiO_2 \xrightarrow[\text{ca. 2300 K}]{\text{DAC, 29 GPa}} Pr_2Si_7O_{18} \quad (3)$$

$$8\ PrO_2 + 3\ SiO_2 \xrightarrow[\text{ca. 2300 K}]{\text{DAC, 29 GPa}} Pr_4Si_3O_{12} + 2\ Pr_2(O_2)O_3 \quad (4)$$

As opposed to $Pr_2Si_7O_{18}$ and $PrSi_3O_8$, the valence of Pr^{4+} is not preserved in $Pr_4Si_3O_{12}$ which can be conceived as the high-pressure modification of the yet unknown orthosilicate $Pr_4(SiO_4)_3$. The reduction of the Pr^{4+} ions must be accompanied by the oxidation of oxygen atoms that is in fact observed in the formation of $Pr_2(O_2)O_3$.

Notably, the discovered phases in which Pr^{4+} is stabilized are more silicon rich than both $Pr_4Si_3O_{12}$ and the anticipated $PrSiO_4$. The Pr:Si:O ratios in the newly discovered compounds are visualized in fig. 1 as a ternary composition diagram along with previously published phases.

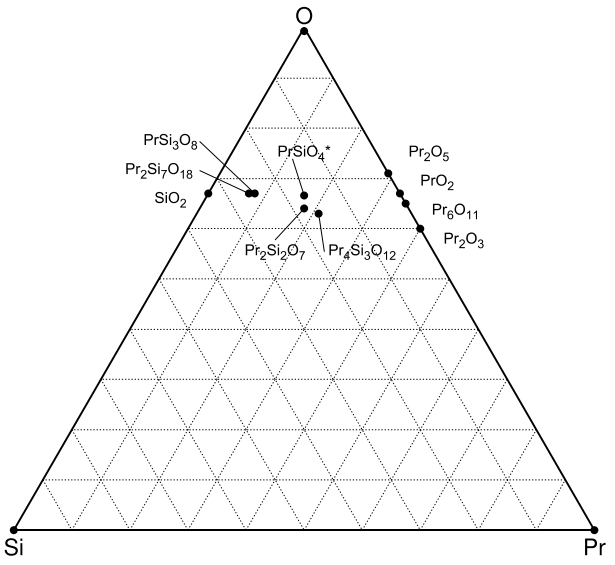


Figure 1. Ternary composition diagram of the Pr-Si-O system. The anticipated phase $PrSiO_4$ is highlighted since it has not yet been discovered. Phases only containing Pr and Si were omitted along with some binary phases between Pr and O since they are not subject of the present work. References: SiO_2[91], $Pr_2Si_2O_7$[35-39], $Pr_2(O_2)O_3$, PrO_2[92], Pr_6O_{11}[93], Pr_2O_3[94].

After decreasing the pressure to approximately 15 GPa, the cell was reheated in a different location, where neither $Pr_2Si_7O_{18}$ nor $PrSi_3O_8$ were unambiguously identified. Only $Pr_4Si_3O_{12}$ along with the oxidation product $Pr_2(O_2)O_3$ were found, suggesting that 15 GPa is insufficient for the stabilization of Pr^{4+} in a silicate compound.

$$8\ PrO_2 + 3\ SiO_2 \xrightarrow[\text{laser heating}]{\text{DAC, 15 GPa}} Pr_4Si_3O_{12} + 2\ Pr_2(O_2)O_3 \quad (5)$$

Furthermore, when analyzing the diffraction images of the spot that was heated at 29 GPa, all phases previously observed were still present. At ambient pressure, both Pr(IV) silicates could be identified while no evidence of $Pr_2(O_2)O_3$ was found, that was previously found to be unstable at ambient pressure. The data quality of the diffraction images of the decompressed cell did not allow for single crystal structure refinements.

Crystal Structures The crystal structures of the silicates $Pr_4Si_3O_{12}$, $PrSi_3O_8$ and $Pr_2Si_7O_{18}$ all consist of close packed sublattices of praseodymium ions and oxygen atoms, in which the silicon atoms occupy octahedral voids. In both, $PrSi_3O_8$ and $Pr_2Si_7O_{18}$ the sublattice of Pr^{4+} ions and oxygen atoms forms a distorted hexagonal close packing (hcp), where the silicon atoms occupy 1/3rd of the octahedral voids in $PrSi_3O_8$ and 7/20th

of the gaps in $Pr_2Si_7O_{18}$. As opposed to the hcp-sublattice (hexagonal close packing) in $PrSi_3O_8$ and $Pr_2Si_7O_{18}$, the Pr^{3+} ions and oxygen atoms in $Pr_4Si_3O_{12}$ form a close packing with a complex sequence of hexagonal and cubic close packing, which can be described as *hhcc* in the *Jagodzinski* notation (see fig. 2).

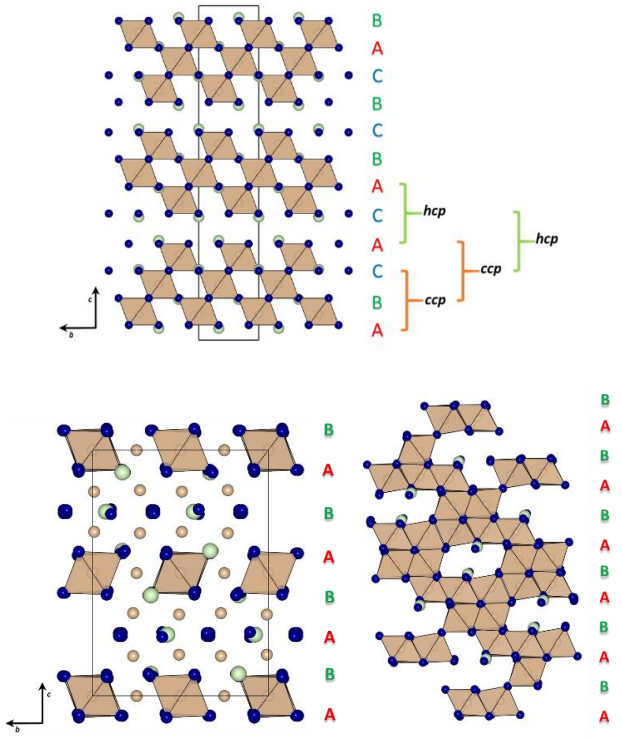
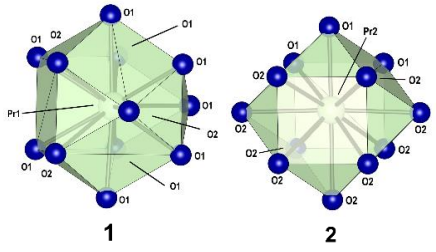


Figure 2. Crystal structures of $Pr_4Si_3O_{12}$ (top), $PrSi_3O_8$ (bottom left), $Pr_2Si_7O_{18}$ (bottom right) at 29 GPa and room temperature. Blue = oxygen, light green = praseodymium, ocher = silicon. For $PrSi_3O_8$ some $[SiO_6]$-octahedra are not shown. Colored letters indicate the stacking order of the layers forming the close packing. ccp = cubic close packing.

The silicon atoms are octahedrally coordinated by six oxygen atoms in all of the three compounds, which is typical for silicates under high pressure.[73-76] The coordination geometries of the praseodymium ions are determined by their role as constituents of the close packing, which results in twelve fold coordination numbers in all three compounds. The respective coordination polyhedra are shown in fig. 3.



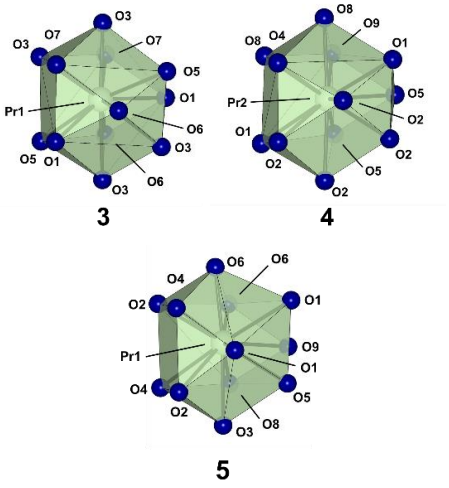


Figure 3. Coordination polyhedra of the praseodymium ions in $Pr_4Si_3O_{12}$ (**1** and **2**), $PrSi_3O_8$ (**3** and **4**) and $Pr_2Si_7O_{18}$ (**5**).

In $PrSi_3O_8$ and $Pr_2Si_7O_{18}$, where the Pr^{4+} ions are part of the hcp, the coordination geometries are slightly distorted anticuboctahedra, with average Pr-O distances of 255(1) pm (for Pr1) and 256(1) pm (for Pr2) in $PrSi_3O_8$ and 258(4) pm in $Pr_2Si_7O_{18}$. Because of the alternating stacking pattern in $Pr_4Si_3O_{12}$, there are two types of coordination geometries around the Pr^{3+} ions. Pr^{3+} ions within the hcp regions are coordinated in a distorted anticuboctahedral shape with an average Pr-O distance of 256(2) pm. Such Pr^{3+} ions that are located in areas of ccp, are found to be coordinated in a distorted cuboctahedral geometry, with an average Pr-O distance of 252(2) pm. Because of the high density of the structures along with the high coordination numbers of the cations, the average Pr-O distances are, within the margin of error, invariant to the charge of the praseodymium ions.

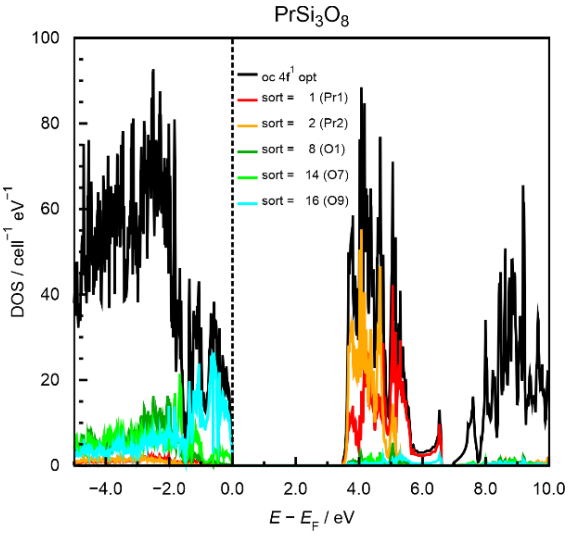
All three structures consist of networks of $[SiO_6]$-octahedra, which are partially edge- and partially vertex sharing in both $PrSi_3O_8$ and $Pr_2Si_7O_{18}$, whereas in $Pr_4Si_3O_{12}$ only vertex sharing octahedra occur. All three silicates therefore contain infinite networks of condensed ions, which is unprecedented in the large field of lanthanoid silicates.

Stabilization of Praseodymium(IV) Given the structural similarities between $Pr_2Si_7O_{18}$ and $PrSi_3O_8$ it is concluded that the structure type is beneficial for the stabilization of Pr^{4+} in silicates and hence a ratio of approximately 1:3 of Pr and Si appears to be advantageous. At a pressure of 29 GPa, the calculated densities of $Pr_2Si_7O_{18}$ (ρ_{calc} = 5.62 g/cm^3) and $PrSi_3O_8$ (ρ_{calc} = 5.71 g/cm^3) are significantly lower than the density of $Pr_4Si_3O_{12}$ (ρ_{calc} = 7.53 g/cm^3) due to the reduced content of praseodymium ions in the close packing. When considering the changes of molar volume for the suggested reaction equations , the formation of both $Pr_2Si_7O_{18}$ and $PrSi_3O_8$ is accompanied by an increase of molar volume (ΔV) of +0.41 Å^3 per atom (for $Pr_2Si_7O_{18}$) +0.47 Å^3 per atom (for $PrSi_3O_8$), whereby the formation of $Pr_4Si_3O_{12}$ and $Pr_2(O_2)O_3$ shows almost no change of molar volume per atom (ΔV = +0.04 Å^3 per atom). Translating the atomic volume changes into the change of *Gibbs* free energy ΔG, according to

$$\frac{d(\Delta G)}{dp} = \Delta V \qquad (6)$$

in which *dp* is the change in pressure, yields a change ΔG of +0.6 kJ/mol ($Pr_4Si_3O_{12}$ + $Pr_2(O_2)O_3$), +7.1 kJ/mol ($Pr_2Si_7O_{18}$) and +8.2 kJ/mol ($PrSi_3O_8$). If instead of stishovite and the cotunnite phase of PrO_2, the stishovite and fluorite phase are used as reference, the increase of molar volumes diminishes and even becomes negative (ΔV = -0.48 Å^3 per atom, translating to -8.4 kJ/mol) in the case of $Pr_4Si_3O_{12}$ and $Pr_2(O_2)O_3$. The changes in the ΔG-values that correspond to the volume changes of the formations of $PrSi_3O_8$ +5.1 kJ/mol and $Pr_2Si_7O_{18}$ +4.3 kJ/mol still remain positive. This comparison leads to the conclusion that the formation of $Pr_4Si_3O_{12}$ along with $Pr_2(O_2)O_3$ is the thermodynamically favored process at 29 GPa, whereby the formation of $Pr_2Si_7O_{18}$ and $PrSi_3O_8$ is kinetically enabled and/or triggered by local inhomogeneities in the distribution of the starting materials along with different temperature zones and cooling rates. The inhomogeneous distribution of the reaction products (see SI fig. S 29 to fig. S 31) further corroborates this hypothesis.

Band Structure Calculations DFT calculations (for details see 'Experimental and Computational Methods') of the electronic band structures of $PrSi_3O_8$ and $Pr_2Si_7O_{18}$ suggest a band gap of approximately 2 eV in both cases (fig. 4) and can therefore be considered non-conductive. As is common for DFT calculations, the calculated electronic band gap is a lower threshold, because the 5*d*-states of praseodymium are treated for correlation only via the exchange-correlation potential. As these states are directly above the Fermi level, the actual band gap is probably larger. Below the Fermi level, the states are dominated by the oxygen atoms of the silicate network. Mulliken charges are +2.9 for praseodymium (both structures), +1.9 and +1.8 for silicon ($PrSi_3O_8$ and $Pr_2Si_7O_{18}$, respectively), and –1.1 for oxygen (both structures). The substantial band gap together with these comparatively high Mulliken charges indicates that the nature of the chemical bonds between the silicate network and the praseodymium ions is strongly ionic in both compounds. This model of an ionic solid is also consistent with the expected behavior of Pr^{4+} cations embedded into a network of condensed silicate anions.



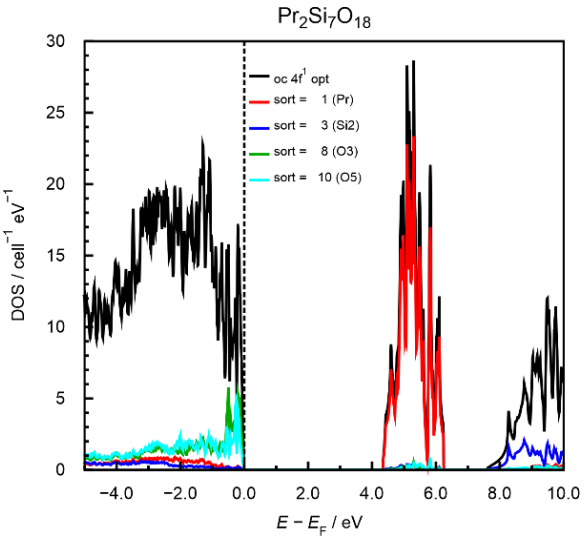


Figure 4. Density of states (total and projected, see legend) for $PrSi_3O_8$ (top) and $Pr_2Si_7O_{18}$ (bottom) as obtained by DFT calculations.

CONCLUSION

The reaction of PrO_2 and SiO_2 was investigated at various pressure points up to 29 GPa. While pressures up to 10 GPa failed to stabilize Pr^{4+} due to the formation of $Pr_2(Si_2O_7)$, further increase in pressure to 15 GPa afforded the praseodymium(IV) oxide-peroxide Pr_2O_5 next to $Pr_4Si_3O_{12}$, in which the praseodymium again is found to be trivalent. However, in contrast to $Pr_2(Si_2O_7)$, the pressure was sufficient to force the silicon atoms into octahedral coordination geometry, as is typical for silicates under high pressure. $Pr_4Si_3O_{12}$ is interpreted as a high-pressure modification of $Pr_4(SiO_4)_3$, which has not been discovered yet.

Additionally, at 29 GPa two new silicates of the composition $Pr_2Si_7O_{18}$ and $PrSi_3O_8$ could be identified next to the aforementioned $Pr_4Si_3O_{12}$ and $Pr_2(O_2)O_3$ by *in situ* X-ray diffraction. Both $Pr_2Si_7O_{18}$ and $PrSi_3O_8$ formally contain Pr^{4+} ions, rendering them the first structurally characterized oxoanionic salts of Pr^{4+}. The charge of the Pr^{4+} ions in both silicates is supported by DFT-calculations. Since both silicates are structurally closely related and the structure type allows for some flexibility, it is postulated that there might be more silicates containing Pr^{4+} with similar compositions that are obtainable under similar conditions. Both silicates survived after releasing the pressure from the cell, indicating metastability under ambient conditions, laying the foundation for further studies aiming at their synthesis on a preparative scale. This work therefore provides a synthetic method to obtain silicates of tetravalent praseodymium for the first time and offers the exclusive opportunity to expand the knowledge about the physical properties of the Pr^{4+} cation in the future.

The observation of octahedrally coordinated silicon atoms in lanthanoid silicates is unprecedented, as is the formation of three dimensionally condensed silicates, thus adding a completely new class of compounds to the already diverse structural chemistry of lanthanoid silicates.

ASSOCIATED CONTENT

Supporting Information Supporting Information. Analytical data of substrates, crystal structures, precession images, XRD-maps, calculated structures. (PDF).

AUTHOR INFORMATION

Corresponding Author

*Niko T. Flosbach - Greinstr. 6, 50939 Cologne, Germany;
Email: n.flosbach@uni-koeln.de

*Maxim Bykov – Max-von-Laue-Straße 7, D-60438 Frankfurt am Main, Germany;
Email: bykov@chemie.uni-frankfurt.de

*Mathias S. Wickleder - Greinstr. 6, 50939 Cologne, Germany;
Email: mathias.wickleder@uni-koeln.de

Author Contributions

The manuscript was written through contributions of all authors. All authors have given approval to the final version.

Notes

The authors declare no competing financial interest.

ACKNOWLEDGEMENTS

M. B. acknowledges the support of Deutsche Forschungsgemeinschaft (DFG Emmy-Noether Program project BY112/2-1). Co-funded by the European Union (ERC, HIPMAT, 101077963). Views and opinions expressed are however those of the author(s) only and do not necessarily reflect those of the European Union or the European Research Council. Neither the European Union nor the granting authority can be held responsible for them. We acknowledge DESY (Hamburg, Germany), a member of the Helmholtz Association HGF, for the provision of experimental facilities. Parts of this research were carried out at PETRAIII and we would like to thank Nico Giordano for assistance in using beamline P02.2. Beamtime was allocated for proposal(s) I-20230654, I-20220041, I-20211466 and I-20221160. We acknowledge the European Synchrotron Radiation Facility (ESRF) for provision of synchrotron radiation facilities under proposal numbers MA5485, CH6476, CH6817.

Portions of this work were performed at GeoSoilEnviroCARS (The University of Chicago, Sector 13), Advanced Photon Source (APS), Argonne National Laboratory. GeoSoilEnviroCARS was supported by the National Science Foundation – Earth Sciences (EAR – 1634415). This research used resources of the Advanced Photon Source, a U.S. Department of Energy (DOE) Office of Science User Facility operated for the DOE Office of Science by Argonne National Laboratory under Contract No. DE-AC02-06CH11357.

B.R. acknowledges funding via a Liebig-group from the "Fond der Chemischen Industrie" (FCI). We are indebted to IFW Dresden, particularly Ulrike Nitzsche and Manuel Richter for the provided resources for the DFT calculations and fruitful discussions.

N. F. and M. W. thank Prof. Martin Jansen for the donation of the oxygen autoclaves used for the synthesis of praseodymium dioxide.

ABBREVIATIONS

APS, Advanced Photon Source; bcc, body centered cubic; ccp, cubic close packing; CSD, Cambridge structure database; DAC, diamond anvil cell; DESY, Deutsches Elektronen Synchrotron; DFG, Deutsche Forschungsgemeinschaft; DFT, density functional theory; DOE, US-Department of Energy; DOS, density of states; ESRF, European Synchrotron Radiation Facility; FCI, Fonds der Chemischen Industrie; fig., figure; FPLO, full-potential local-orbital; GSECARS, GeoSoilEnviro Center for Advanced Radiation Sources; hcp, hexagonal close packing; HGF, Helmholtz-Gemeinschaft Deutscher Forschungszentren; IWF, Leibniz Institut für Festkörper- und Werkstoffforschung Dresden; LDA, local density approximation; Ln, lanthanoid; PETRAIII, Positron-Elektron-Tandem-Ring-Anlage; PXRD, powder X-ray diffraction; SI, supporting information; tab., table; XRD, X-ray diffraction

References

[1] *Rare earth elements: A review of applications, occurrence, exploration, analysis, recycling, and environmental impact*, V. Balaram, *Geosci. Front.* **2019**, *10*, 1285-1303.

[2] *Novel polymerization catalysts and hydride clusters from rare-earth metal dialkyls*, M. Nishiura, Z. Hou, *Nat. Chem.* **2010**, *2*, 257-268.

[3] *Application of rare earths in fluid catalytic cracking: A review*, A. Akah, *J. Rare Earths* **2017**, *35*, 941-956.

[4] *Rare earths: jewels for functional materials of the future*, S. V. Eliseeva, J.-C. G. Bünzli, *New J. Chem.* **2011**, *35*, 1165-1176.

[5] *Synthesis, spectroscopic properties and applications of divalent lanthanides apart from* Eu^{2+}, M. Suta, C. Wickleder, *J. Lumin.* **2019**, *210*, 210-238.

[6] *The chemical and physical properties of tetravalent lanthanides: Pr, Nd, Tb, and Dy*, T. P. Gompa, A. Ramanathan, N. T. Rice, H. S. La Pierre, *Dalton Trans.* **2020**, *49*, 15945-15987.

[7] *Lanthanum does form stable molecular compounds in the +2 oxidation state*, P. B. Hitchcock, M. F. Lappert, L. Maron, A. V. Protchenko, *Angew. Chem. Int. Ed.* **2008**, *120*, 1510-1513.

[8] *Expanding rare-earth oxidation state chemistry to molecular complexes of holmium(II) and erbium(II)*, M. R. MacDonald, J. E. Bates, M. E. Fieser, J. W. Ziller, F. Furche, W. J. Evans, *J. Am. Chem. Soc.* **2012**, *134*, 8420-8423.

[9] *Completing the series of +2 ions for the lanthanide elements: synthesis of molecular complexes of* Pr^{2+}, Gd^{2+}, Tb^{2+}, *and* Lu^{2+}, M. R. MacDonald, J. E. Bates, J. W. Ziller, F. Furche, W. J. Evans, *J. Am. Chem. Soc.* **2013**, *135*, 9857-9868.

[10] *Simple and complex halides*, G. Meyer, M. S. Wickleder, *Handbook on the Physics and Chemistry of Rare Earths* **2000**, *28*, 53-129.

[11] F. Sroor, F. T. Edelmann, in *Cerium - Molecular Structure, Technological Applications and Health Effects*, Nova Science Publishers, New York, **2012**, pp. 73-106.

[12] *Recent advances in the coordination chemistry of cerium (IV) complexes*, Y.-M. So, W.-H. Leung, *Coord. Chem. Rev.* **2017**, *340*, 172-197.

[13] *The difficult search for organocerium(IV) compounds*, R. Anwander, M. Dolg, F. T. Edelmann, *Chem. Soc. Rev.* **2017**, *46*, 6697-6709.

[14] K. Binnemans, in *Handbook on the Physics and Chemistry of Rare Earths, Vol. 36* (Eds.: K. A. Gschneidner, J.-C. G. Bunzli, V. K. Pecharsky), Elsevier, **2006**, pp. 281-392.

[15] *New high-pressure phase and equation of state of $Ce_2Zr_2O_8$*, D. Errandonea, R. Kumar, S. Achary, O. Gomis, F. Manjón, R. Shukla, A. Tyagi, *J. Appl. Phys.* **2012**, *111*.

[16] *Chemical design of electronic and magnetic energy scales of tetravalent praseodymium materials*, A. Ramanathan, J. Kaplan, D.-C. Sergentu, J. A. Branson, M. Ozerov, A. I. Kolesnikov, S. G. Minasian, J. Autschbach, J. W. Freeland, Z. Jiang, *Nat. Commun.* **2023**, *14*, 3134.

[17] *One-pot hydrothermal synthesis of $Tb^{III}{}_{13}(GeO_4)_6O_7(OH)$ and $K_2Tb^{IV}Ge_2O_7$: preparation of a stable terbium(4+) complex*, K. Fulle, L. D. Sanjeewa, C. D. McMillen, Y. Wen, A. C. Rajamanthrilage, J. N. Anker, G. Chumanov, J. W. Kolis, *Inorg. Chem.* **2017**, *56*, 6044-6047.

[18] *$Cs_3RE^{III}Ge_3O_9$ (RE= Pr, Nd, and Sm–Yb) and $Cs_8Tb^{III2}Tb^{IV}Ge_9O_{27}$: a rare example of a mixed-valent Tb(III)/Tb(IV) oxide*, G. Morrison, N. R. Spagnuolo, S. G. Karakalos, H.-C. Zur Loye, *Inorg. Chem.* **2019**, *58*, 8702-8709.

[19] *Molecular complex of Tb in the +4 oxidation state*, C. T. Palumbo, I. Zivkovic, R. Scopelliti, M. Mazzanti, *J. Am. Chem. Soc.* **2019**, *141*, 9827-9831.

[20] *Design, isolation, and spectroscopic analysis of a tetravalent terbium complex*, N. T. Rice, I. A. Popov, D. R. Russo, J. Bacsa, E. R. Batista, P. Yang, J. Telser, H. S. La Pierre, *J. Am. Chem. Soc.* **2019**, *141*, 13222-13233.

[21] *Stabilization of the oxidation state+ IV in siloxide-supported terbium compounds*, A. R. Willauer, C. T. Palumbo, R. Scopelliti, I. Zivkovic, I. Douair, L. Maron, M. Mazzanti, *Angew. Chem. Int. Ed.* **2020**, *59*, 3549-3553.

[22] *Accessing the +IV oxidation state in molecular complexes of praseodymium*, A. R. Willauer, C. T. Palumbo, F. Fadaei-Tirani, I. Zivkovic, I. Douair, L. Maron, M. Mazzanti, *J. Am. Chem. Soc.* **2020**, *142*, 5538-5542.

[23] *Comparison of tetravalent cerium and terbium ions in a conserved, homoleptic imidophosphorane ligand field*, N. T. Rice, I. A. Popov, D. R. Russo, T. P. Gompa, A. Ramanathan, J. Bacsa, E. R. Batista, P. Yang, H. S. La Pierre, *Chem. Sci.* **2020**, *11*, 6149-6159.

[24] *Structure, reactivity and luminescence studies of triphenylsiloxide complexes of tetravalent lanthanides*, A. R. Willauer, I. Douair, A.-S. Chauvin, F. Fadaei-Tirani, J.-C. G. Bünzli, L. Maron, M. Mazzanti, *Chem. Sci.* **2022**, *13*, 681-691.

[25] *Über die vierwertigen Verbindungen des Praseodyms, 1. Mitt.: Komplexe Chloride, Nitrate und Sulfate des vierwertigen Praseodyms*, S. Pajakoff, *Monatsh. Chem.* **1963**, *94*, 482-496.

[26] *Über die vierwertigen Verbindungen des Praseodyms, 2. Mitt.: Komplexe Oxalate des vierwertigen Praseodyms*, S. Pajakoff, *Monatsh. Chem.* **1963**, *94*, 527-529.

[27] *Über die vierwertigen Verbindungen des Praseodyms, 3. Mitt.: Untersuchungen der Praseodym (IV)-und Terbium (IV)-Fluorkomplexe: Kurze Mitteilung*, S. Pajakoff, *Monatsh. Chem.* **1964**, *95*, 1002-1004.

[28] *Über die vierwertigen Verbindungen des Praseodyms, 4. Mitt.: Die thermische Dissoziation des Praseodymcarbonats*, S. Pajakoff, *Monatsh. Chem.* **1966**, *97*, 733-743.

[29] *Über die vierwertigen Verbindungen des Praseodyms, 5. Mitt.: Die Bildung des Praseodym (IV)-Oxalats bei der thermischen Zersetzung des Praseodym (III)-Oxalats in Sauerstoff-Atmosphäre und Ausnützung dieses Effektes bei der Trennung der Seltenerdmetalle*, S. Pajakoff, *Monatsh. Chem.* **1968**, *99*, 484-500.

[30] *Electron-transfer and f→d absorption bands of some lanthanide and actinide complexes and the standard (III–IV) oxidation potentials for each member of the lanthanide and actinide series*, L. Nugent, R. Baybarz, J. Burnett, J. Ryan, *J. Inorg. Nucl. Chem.* **1971**, *33*, 2503-2530.

[31] *Thermochemical properties of yttrium, lanthanum, and the lanthanide elements and ions*, L. R. Morss, *Chem. Rev.* **1976**, *76*, 827-841.

[32] *Quadrivalent praseodymium in planetary materials*, M. Anenburg, A. D. Burnham, J. L. Hamilton, *Am. Mineral.* **2020**, *105*, 1802-1811.

[33] *The crystal structures of $CeSiO_4$ and $Ca_2Ce_8(SiO_4)_6O_2$*, J. Skakle, C. Dickson, F. Glasser, *Powder Diffr.* **2000**, *15*, 234-238.

[34] *The role of water and hydroxyl groups in the structures of stetindite and coffinite, $MSiO_4$ (M= Ce, U)*, A. C. Strzelecki, T. Barral, P. Estevenon, A. Mesbah, V. Goncharov, J. Baker, J. Bai, N. Clavier, S. Szenknect, A. Migdisov, *Inorg. Chem.* **2021**, *60*, 718-735.

[35] *The crystal structure of α-$Pr_2Si_2O_7$*, J. Felsche, *Naturwissenschaften* **1970**, *57*, 452-452.

[36] *The crystal structure of β-$Pr_2Si_2O_7$*, J. Felsche, *Naturwissenschaften* **1970**, *57*, 669-670.

[37] *The crystal structures of the dimorphic rare earth disilicate, $Pr_2Si_2O_7$*, J. Felsche, *Z. Kristallogr. Cryst. Mater.* **1971**, *133*, 364-385.

[38] *Solid state reactions in highly dispersed praseodymium oxide–SiO_2 system*, M. A. Małecka, L. Kępiński, *J. Alloys Compd.* **2007**, *430*, 282-291.

[39] J. Felsche, in *Rare Earths*, Springer Berlin Heidelberg, Berlin, Heidelberg, **1973**, pp. 99-197.

[40] *Structure cristalline de $Eu_2(II)SiO_4\beta$*, R. Marchand, P. l'Haridon, Y. Laurent, *J. Solid State Chem.* **1978**, *24*, 71-76.

[41] *The crystal structure of the low form of Eu_2SiO_4*, J. Felsche, *Naturwissenschaften* **1971**, *58*, 218-219.

[42] *High-pressure rare earth silicates: Lanthanum silicate with barium phosphate structure, holmium silicate apatite, and lutetium disilicate type X*, M. E. Fleet, X. Liu, *J. Solid State Chem.* **2005**, *178*, 3275-3283.

[43] *Inorganic Lanthanide Compounds with Complex Anions*, M. S. Wickleder, *Chem. Rev.* **2002**, *102*, 2011-2088.

[44] M. Wickleder, in *Rare Earth Chemistry* (Eds.: P. Rainer, J. Thomas, A. S. Cristian), De Gruyter, Berlin, Boston, **2020**, pp. 117-136.

[45] *Old and New Insights into Structure and Properties of $Eu_2[SiO_4]$*, C. Funk, J. Köhler, I. Lazar, D. Kajewski, K. Roleder, J. Nuss, A. Bussmann-Holder, H. Bamberger, J. van Slageren, D. Enseling, T. Jüstel, T. Schleid, *Cryst. Growth Des.* **2018**, *18*, 6316-6325.

[46] *Investigation by the use of profile refinement of neutron powder diffraction data of the geometry of the $[Si_2O_7]^{6-}$ ions in the high temperature phases of rare earth disilicates prepared from the melt in crucible-free synthesis*, A. Nørlund Christensen, *Z. Kristallogr. Cryst. Mater.* **1994**, *209*, 7-13.

[47] *X-Ray Crystallographic Study of $Ce_2Si_2O_7$*, A. N. Christensen, R. Hazell, E. Øvreeide, K. Aaby, C. E. Olsen, J. Springborg, H. Weihe, M. Zehnder, G. W. Francis, *Acta. Chem. Scand.* **1994**, *48*, 1012-1014.

[48] *Dicerium disilicate, $Ce_2[Si_2O_7]$*, B. Deng, J. A. Ibers, *Acta Cryst.* **2005**, *E61*, i76-i78.

[49] *Crystal Structures of the High-Temperature Forms of $Ln_2Si_2O_7$ (Ln= La, Ce, Pr, Nd, Sm) Revisited*, A. C. Tas, M. Akinc, *J. Am. Ceram. Soc.* **1994**, *77*, 2968-2970.

[50] *Rare earth disilicates $R_2Si_2O_7$ (R= Gd, Tb, Dy, Ho): type B*, M. E. Fleet, X. Liu, *Z. Kristallogr. Cryst. Mater.* **2003**, *218*, 795-801.

[51] *A new rare earth disilicate ($REE_2Si_2O_7$; REE= Dy, Tm, Lu; type-L): Evidence for non-quenchable 10 GPa polymorph with silicon in fivefold trigonal bipyramidal coordination?*, M. E. Fleet, X. Liu, *Am. Mineral.* **2004**, *89*, 396-404.

[52] *Structure and complex twinning of dysprosium disilicate ($Dy_2Si_2O_7$), Type B*, M. E. Fleet, X. Liu, *Acta Cryst.* **2000**, *B56*, 940-946.

[53] *The crystal structures of the rare earth pyrosilicates*, Y. I. Smolin, Y. F. Shepelev, *Acta Cryst.* **1970**, *B26*, 484-492.

[54] *Synthesis and crystal structure of $Er_2Si_2O_7$*, H.-Y. C. Chi Lisheng, H.-H. Zhuang, H. Jinshun, *Jiegou Huaxue* **1998**, *17*, 24-26.

[55] *High-pressure rare earth disilicates $REE_2Si_2O_7$ (REE= Nd, Sm, Eu, Gd): type K*, M. E. Fleet, X. Liu, *J. Solid State Chem.* **2001**, *161*, 166-172.

[56] *The determination of the structure of gadolinium pyrosilicate*, Y. I. Smolin, Y. F. Shepelev, *Izv. Akad. Nauk SSSR, Neorg. Mater. Inorg. Mater. (USSR)* **1967**, *3*, 1034-1038.

[57] *A new silicate structure containing linear $[Si_3O_{10}]$ groups*, J. Felsche, *Naturwissenschaften* **1972**, *59*, 35-36.

[58] *$La_2Si_2O_7$. Hydrothermal synthesis and crystal structure*, A. M. Dago, D. Y. Pushcharovskij, E. Strelkova, E. A. Pobedimskaya, N. V. Belov, *Dokl. Akad. Nauk* **1980**, *252*, 1117-1121.

[59] *Über den H-und A-Typ von $La_2[Si_2O_7]$*, H. Müller-Bunz, T. Schleid, *Z. Anorg. Allg. Chem.* **2000**, *626*, 2549-2556.

[60] O. Greis, H. Bossemeyer, P. Greil, B. Breidenstein, A. Haase, in *Mater. Sci. Forum, Vol. 79*, Trans Tech Publ, **1991**, pp. 803-808.

[61] *The mineralogy of the historical Mochalin Log REE deposit, South Urals, Russia. Part III. Percleveite-(La), $La_2Si_2O_7$, a new REE disilicate mineral*, A. V. Kasatkin, N. V. Zubkova, I. V. Pekov, N. V. Chukanov, R. Škoda, A. A. Agakhanov, D. I. Belakovskiy, D. A. Ksenofontov, J. Plášil, A. M. Kuznetsov, *Mineral. Mag.* **2020**, *84*, 913-920.

[62] *Crystal structure and luminescent properties of Eu^{3+}-doped A-$La_2Si_2O_7$ tetragonal phase stabilized by spray pyrolysis synthesis*, A. J. Fernandez-Carrion, M. Ocana, P. Florian, J. Garcia-Sevillano, E. Cantelar, A. N. Fitch, M. R. Suchomel, A. I. Becerro, *J. Phys. Chem. C* **2013**, *117*, 20876-20886.

[63] *Helical chain observed under transmission electron microscope: Synthesis and structure refinement of lutetium disilicate $Lu_2Si_2O_7$*, C. Wang, X. Liu, M. Fleet, J. Li, S. Feng, R. Xu, Z. Jin, *CrystEngComm* **2010**, *12*, 1617-1620.

[64] *Crystal structure of lutetium disilicate, $Lu_2Si_2O_7$*, F. Soetebier, W. Urland, *Z. Kristallogr. - New Cryst. Struct.* **2002**, *217*, 22-22.

[65] *Synthesis and crystal structure of $Nd_2Si_2O_7$ in low temperature form*, H.-Y. C. C. Lisheng, D. Shui-Quan, H.-H. Zhuang, J.-S. Huang, *Jiegou Huaxue* **1997**, *16*, 177-180.

[66] *Crystal structure of low-temperature form of samarium pyrosilicate, $Sm_2Si_2O_7$*, Y. I. Smolin, Y. F. Shepelev, I. Butikova, *Sov. Phys. Crystallogr.* **1970**, *15*, 214.

[67] *Thortveitite-type $Tm_2Si_2O_7$*, P. A. V. Kahlenberger, *Acta Cryst.* **2014**, *E70*, i34-i35.

[68] *Crystalline structure of ytterbium pyrosilicate $Yb_2Si_2O_7$*, Y. I. Smolin, Y. F. Shepelev, I. Butikova, *Zh. Struk. Khim* **1971**, *12*, 272.

[69] O. g. V. Yakubovich, M. Simonov, A. V. e. Voloshin, Y. A. Pakhomovskii, in *Dokl. Akad. Nauk SSSR, Vol.*

291, Russian Academy of Sciences, **1986**, pp. 863-867.

[70] *Structure evolution of nanocrystalline CeO_2 supported on silica: effect of temperature and atmosphere*, L. Kępiński, M. Wołcyrz, M. Marchewka, *J. Solid State Chem.* **2002**, *168*, 110-118.

[71] *Crystal Structure of B-Type $Tm_2Si_2O_7$ (≡ $Tm_4[Si_3O_{10}][SiO_4]$)*, I. Hartenbach, F. Lissner, T. Schleid, *Z. Naturforsch. B* **2003**, *58*, 925-927.

[72] *$La_2Si_2O_7$ im I—Typ: Gemäß $La_6[Si_4O_{13}][SiO_4]_2$ kein echtes Lanthandisilicat*, H. Müller-Bunz, T. Schleid, *Z. Anorg. Allg. Chem.* **2002**, *628*, 564-569.

[73] *High-pressure framework silicates*, R. M. Hazen, R. T. Downs, L. W. Finger, *Science* **1996**, *272*, 1769-1771.

[74] *Rietveld analysis of a new high-pressure strontium silicate $SrSi_2O_5$*, H. Kojitani, M. Kido, M. Akaogi, *Phys. Chem. Miner.* **2005**, *32*, 290-294.

[75] *High pressure phase transitions of paracelsian $BaAl_2Si_2O_8$*, L. A. Gorelova, A. S. Pakhomova, S. V. Krivovichev, L. S. Dubrovinsky, A. V. Kasatkin, *Sci. Rep.* **2019**, *9*, 12652.

[76] *High-pressure crystal chemistry of stishovite*, N. L. Ross, J. Shu, R. M. Hazen, *Am. Mineral.* **1990**, *75*, 739-747.

[77] *TOPAS: an innovative proton Monte Carlo platform for research and clinical applications*, J. Perl, J. Shin, J. Schumann, B. Faddegon, H. Paganetti, *Med Phys* **2012**, *39*, 6818-6837.

[78] *Comment on "High-pressure x-ray diffraction study of YBO_3/Eu^{3+}, $GdBO_3$, and $EuBO_3$: Pressure-induced amorphization in $GdBO_3$" [J. Appl. Phys. **115,** 043507 (2014)]*, D. Errandonea, A. Muñoz, J. Gonzalez-Platas, *J. Appl. Phys.* **2014**, *115*, 216101.

[79] *Compression curves of transition metals in the Mbar range: Experiments and projector augmented-wave calculations*, A. Dewaele, M. Torrent, P. Loubeyre, M. Mezouar, *Phys. Rev. B* **2008**, *78*, 104102.

[80] *Toward an international practical pressure scale: A proposal for an IPPS ruby gauge (IPPS-Ruby2020)*, G. Shen, Y. Wang, A. Dewaele, C. Wu, D. E. Fratanduono, J. Eggert, S. Klotz, K. F. Dziubek, P. Loubeyre, O. V. Fat'yanov, P. D. Asimow, T. Mashimo, R. M. M. Wentzcovitch, *High Press. Res.* **2020**, *40*, 299-314.

[81] *A portable laser heating microscope for high pressure research*, S. Guoyin, W. Lin, F. Richard, M. Ho-kwang, J. H. Russell, *J. Phys.: Conf. Ser.* **2010**, *215*, 012191.

[82] *Single-crystal diffractometer coupled with double-sided laser heating system at the Extreme Conditions Beamline P02.2 at PETRAIII*, E. Bykova, G. Aprilis, M. Bykov, K. Glazyrin, M. Wendt, S. Wenz, H.-P. Liermann, J. T. Roeh, A. Ehnes, N. Dubrovinskaia, L. Dubrovinsky, *Rev. Sci. Instrum.* **2019**, *90*, 073907.

[83] *The Extreme Conditions Beamline P02.2 and the Extreme Conditions Science Infrastructure at PETRA III*, H.-P. Liermann, Z. Konopkova, W. Morgenroth, K. Glazyrin, J. Bednarcik, E. E. McBride, S. Petitgirard, J. T. Delitz, M. Wendt, Y. Bican, A. Ehnes, I. Schwark, A. Rothkirch, M. Tischer, J. Heuer, H. Schulte-Schrepping, T. Kracht, H. Franz, *J. Synchrotron Rad.* **2015**, *22*, 908-924.

[84] *Strategies for in situ laser heating in the diamond anvil cell at an X-ray diffraction beamline*, S. Petitgirard, A. Salamat, P. Beck, G. Weck, P. Bouvier, *J. Synchrotron Rad.* **2014**, *21*, 89-96.

[85] *Domain Auto Finder (DAFi) program: the analysis of single-crystal X-ray diffraction data from polycrystalline samples*, A. Aslandukov, M. Aslandukov, N. Dubrovinskaia, L. Dubrovinsky, *J. Appl. Crystallogr.* **2022**, *55*, 1383-1391.

[86] *A short history of SHELX*, G. Sheldrick, *Acta Crystallogr. A* **2008**, *64*, 112-122.

[87] *OLEX2: a complete structure solution, refinement and analysis program*, O. V. Dolomanov, L. J. Bourhis, R. J. Gildea, J. A. K. Howard, H. Puschmann, *J. Appl. Crystallogr.* **2009**, *42*, 339-341.

[88] *Full-potential nonorthogonal local-orbital minimum-basis band-structure scheme*, K. Koepernik, H. Eschrig, *Phys. Rev. B* **1999**, *59*, 1743.

[89] *Accurate and simple analytic representation of the electron-gas correlation energy*, J. P. Perdew, Y. Wang, *Phys. Rev. B* **1992**, *45*, 13244.

[90] *Electronic population analysis on LCAO–MO molecular wave functions. I*, R. S. Mulliken, *J. Chem. Phys.* **1955**, *23*, 1833-1840.

[91] *The cristobalite structures*, T. F. W. Barth, *Am. J. Sci.* **1932**, *5*, 350-356.

[92] *An X-ray study of the rare-earth oxide systems: Ce^{IV}—Nd^{III}, Cr^{IV}—Pr^{III}, Ce^{IV}—Pr^{IV} and Pr^{IV}—Nd^{III1}*, J. D. McCullough, *J. Am. Chem. Soc.* **1950**, *72*, 1386-1390.

[93] *The emergence of bifunctional catalytic properties by the introduction of Bi^{3+} in defect fluorite-structured $PrO_{1.833}$*, R. Nagarajan, J. Pandey, *Dalton Trans.* **2020**, *49*, 12707-12715.

[94] *On the phase interval $PrO_{1.50}$ to $PrO_{1.71}$ in the praseodymium oxide-oxygen system*, R. P. Turcotte, J. M. Warmkessel, R. J. Tilley, L. Eyring, *J. Solid State Chem.* **1971**, *3*, 265-272.

4.1.7 $Ln_4(SiO_4)_3$ and Polymorphism of $Tb_4(SiO_4)(Si_3O_{10})$

Initially observed as a product of the reaction between PrO_2 and SiO_2 in presence of Na_2O_2 at 11 GPa (see section 4.1.8 for more information), $Pr_4(SiO_4)_3$ presented the first orthosilicate of Pr^{3+} and only the second orthosilicate of any trivalent lanthanoid ion.[111,112] When subjecting PrO_2 and SiO_2 to analogous conditions as the initial reaction that included Na_2O_2, $Pr_4(SiO_4)_3$ formed again and could be recovered as green single crystals. $Pr_4(SiO_4)_3$ is isostructural to $La_4(SiO_4)_3$ and can be described as a defect $Ba_3(PO_4)_2$ structure.[111,112] Although the data set produced a reasonable structural model, some crystallographic issues like the ambiguous assignment of the space group could not be resolved due to twinning next to superstructures that also occurred in the previously described lanthanum silicate. The structural model was generated and refined in the trigonal space group $R\bar{3}m$ ($a = b = 536.19(3)$ pm, $c = 1909.8(2)$ pm). Because the structure is already described elsewhere (for La)[111,112] it is not shown on this occasion.

Despite the unsatisfactory single crystal data sets, the PXRD-data (see fig. 43) demonstrated that the material can be isolated with good purity, allowing further analytical studies. Notably, $Pr_4(SiO_4)_3$ is luminescent and shows emission bands at 569 nm and 420 nm. The absorption and emission spectra are shown in fig. 8.

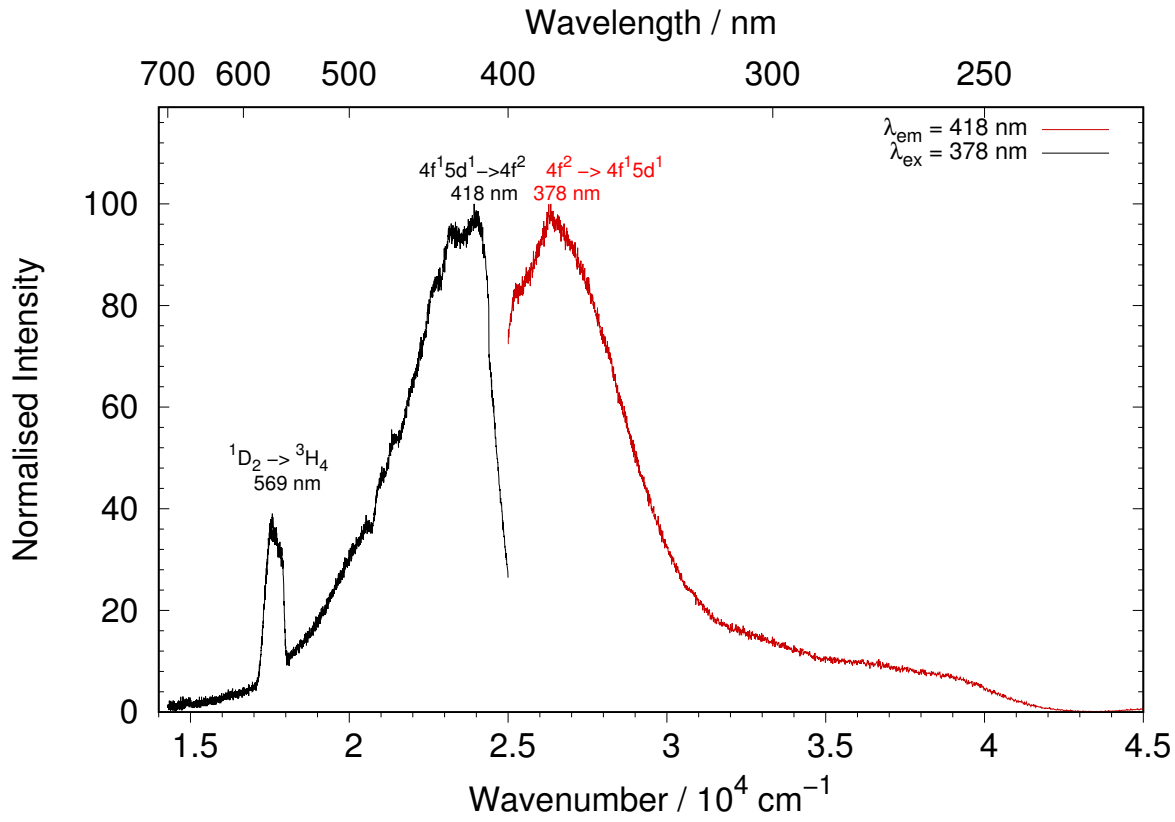


Fig. 8 Emission and excitation spectra of $Pr_4(SiO_4)_3$ at room temperature.

Next to the sharp emission at 569 nm that was assigned to the intraconfigurational $^1D_2 \rightarrow {}^3H_4$-transition (comp. fig. 1), a broader emission band was found at ca. 420 nm. This band, along with the corresponding excitation band can be attributed to interconfigurational $4f^2 \rightarrow 4f^1 5d^1$ (or vice versa in the excitation) transition which are typical for Pr^{3+}.[113]

Apart from $Pr_4(SiO_4)_3$, other lanthanoid orthosilicates with Ln = La and Nd, were also synthesised by the same method and could be produced in good purity. The materials are thermally stable to at least 1000 °C (see fig. 84 to fig. 86) and all crystallise isostructurally, as evidenced by PXRD fig. 41 to fig. 43.

When repeating the experiment with Tb_4O_7, triclinic $Tb_4(SiO_4)(Si_3O_{10})$[2] was obtained as single crystals ($P\bar{1}$, $a = 655.61(9)$ pm, $b = 668.9(1)$ pm, $c = 2412.2(4)$ pm, $\alpha = 93.777(6)°$, $\beta = 90.114(6)°$, $\gamma = 91.876(6)°$) instead of $Tb_4(SiO_4)_3$. As was the case with praseodymium, the Tb^{4+}-ions contained in Tb_4O_7 were reduced during the reaction. A proposed reaction equation is shown in scheme 9.

$$Tb_4O_7 + 4\,SiO_2 \xrightarrow[1000\ W]{11\ GPa} Tb_4(SiO_4)(Si_3O_{10}) + 1/2\,O_2$$

Scheme 9 Hypothesised reaction equation for the formation of $Tb_4(SiO_4)(Si_3O_{10})$ at high pressure.

Despite the weak data set, the relationship to structurally extremely similar lanthanoid 'disilicates'[3] can be assessed by comparing the arrangement of the $[SiO_4]$-tetrahedra within the structure (see fig. 9).[114–120] Although the structural model is sufficient to recognise general differences in the arrangement of the anions, it does not allow for a detailed description of interatomic distances etc.

[2]Niggli-notation was not provided due to the presence of eight crystallographically independent Tb-centres.

[3]Although the discussed structures have the empirical formula $Ln_2Si_2O_7$, no $Si_2O_7^{6-}$-ions are contained therein. The term is commonly used in the contemporary literature nonetheless, and was therefore adapted.

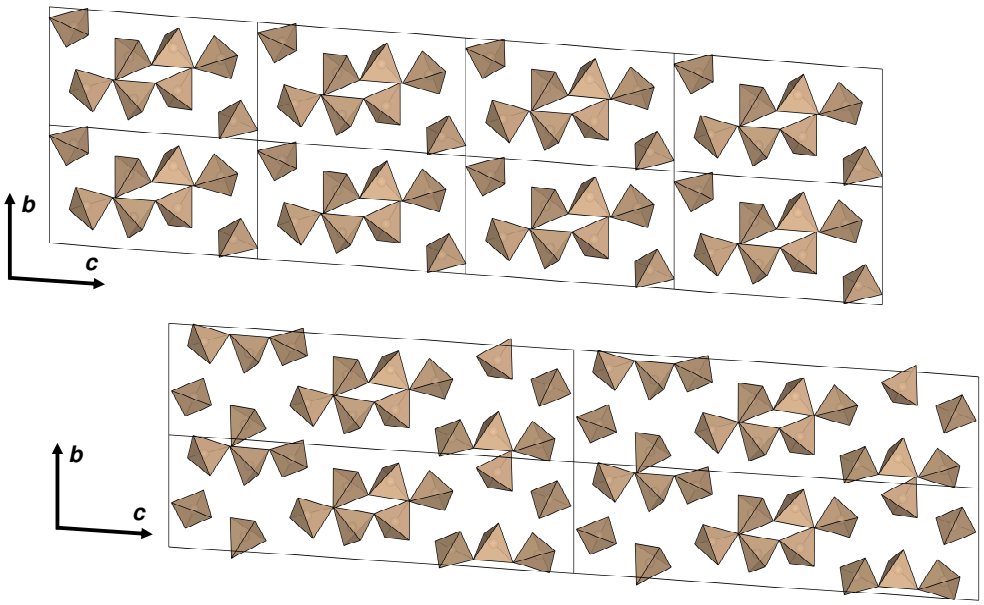


Fig. 9 Top: B-type $Ln(SiO_4)(Si_3O_{10})$. Bottom: New structure type of $Ln(SiO_4)(Si_3O_{10})$ for Ln = Tb, synthesised by reacting Tb_4O_7 and SiO_2 at 11 GPa. Metal cations and oxygen atoms are not shown in order to illustrate the arrangement of the $[SiO_4]$-tetrahedra.

The claim that the newly found polymorph of $Tb_4(SiO_4)(Si_3O_{10})$ is in fact different from that reported in the literature[119] is additionally supported by PXRD data that showed good agreement with the simulated data of the new structure (fig. 44) but poor agreement with the simulated data from the known structure (fig. 45).
Upon excitation in the UV-region, $Tb_4(SiO_4)(Si_3O_{10})$ showed four emission bands in the visible range which correspond to the transitions of the $^5D_4$-term to different ^7F_J-terms. The luminescence spectrum is displayed in fig. 10.

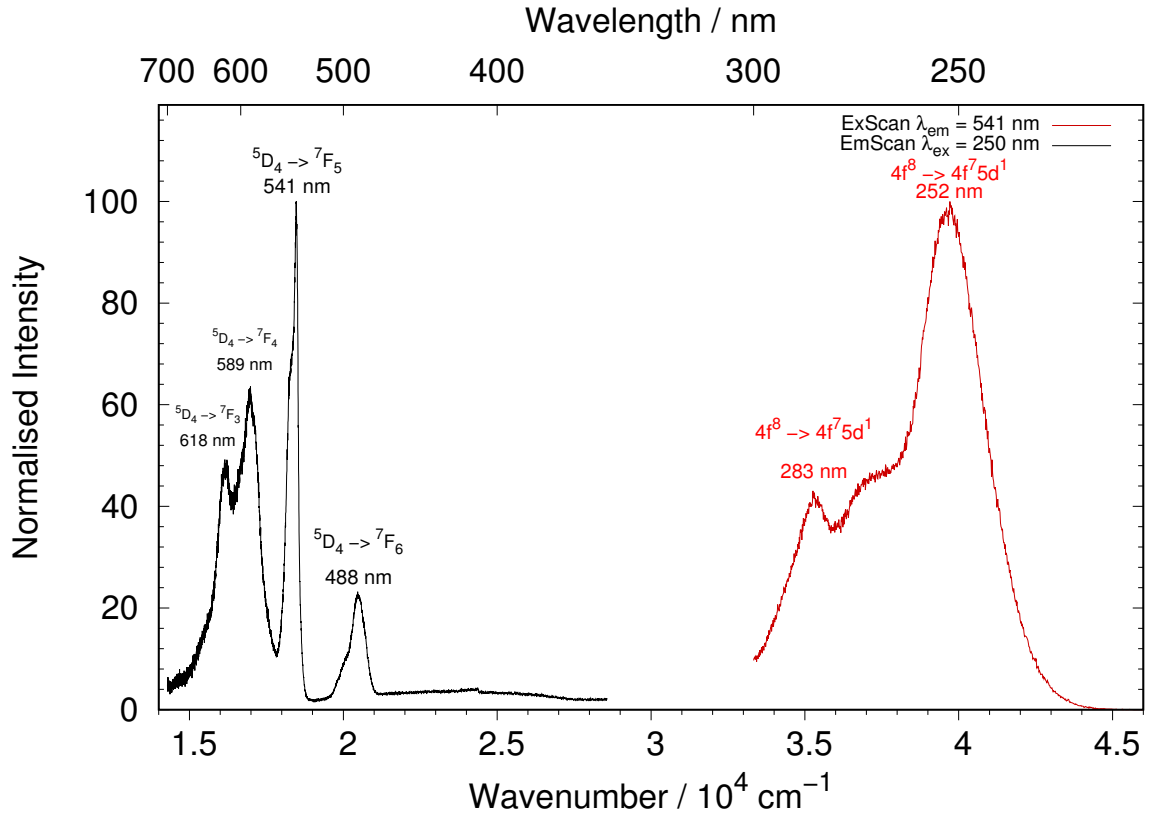


Fig. 10 Emission and excitation spectrum of $Tb_4(SiO_4)(Si_3O_{10})$ at room temperature.

The excitation spectrum is dominated by two broad bands at 283 nm and 252 nm that are indicative of interconfigurational excitation mechanisms according to $4f^8 \rightarrow 4f^7 5d^1$. The splitting into two bands can be explained by crystal field splitting of the involved d-orbitals. In comparison to the orthosilicate $Pr_4(SiO_4)_3$, the d-orbitals are found at higher energies. Since no direct comparison between the two structures with the same metal cation is possible, no conclusive arguments can be made about the difference in influence of the two structures on the crystal field splitting.

The experiments and their results elucidated in this section allow the conclusion that Pr^{4+} can be stabilised in the form of $PrSi_3O_8$ and $Pr_2Si_7O_{18}$ if extremely high pressure is applied in the synthesis. Remarkably, once these phases have formed, they can theoretically be recovered at ambient pressure. At lower pressure points of 11 GPa and 15 GPa the phases $Pr_4(SiO_4)_3$ and its high pressure modification $Pr_4Si_3O_{12}$ had formed, with the latter containing a condensed network of $[SiO_6]$-octahedra, which is unprecedented for lanthanoid silicates. $Pr_4(SiO_4)_3$ and $Nd_4(SiO_4)_3$ could be synthesised on a preparative scale in a multi-anvil press as the first orthosilicates of the respective lanthanoids. Next to its characteristic f-f-transition, $Pr_4(SiO_4)_3$ showed a broad interconfigurational absorption and emission at an unusually low energy that is located at the transitional region of the

UV- and visible range of the optical spectrum, indicating strong ligand field splitting. When recreating the same experimental conditions used in the synthesis of the lanthanoid(III) orthosilicates, $Tb_4(SiO_4)(Si_3O_{10})$ could be obtained as a new polymorph that is structurally similar to the B-Type $Ln_2Si_2O_7$-structure. The different reactivity observed for terbium implies that the $Ln_4(SiO_4)_3$-structure type is more stable for the lighter lanthanoids under the applied conditions. However, as with praseodymium, terbium could not retain its +IV oxidation state due to competing reactions.

4.1.8 Ternary Silicates

As elaborated in the previous section, Pr^{4+} could only be stabilised in silicates if the reaction of PrO_2 and SiO_2 if extreme pressure of ca. 29 GPa was applied during the synthesis, which was too much to be transferred to experiments on a preparative scale. It was therefore decided to investigate if Pr^{4+} can be stabilised in the form of ternary silicates by reacting PrO_2 and SiO_2 in presence of Na_2O_2 or SrO_2 using a multi-anvil press. On this occasion it shall be emphasised that ternary oxides of the form Na_2PrO_3 or $SrPrO_3$ can be obtained even at ambient pressure from the same, or similar reactants.[42,47] The reaction of PrO_2, SiO_2 and Na_2O_2 at 11 GPa afforded green single crystals of $Pr_4(SiO_4)_3$ that are displayed in fig. 11. A more detailed discussion of $Pr_4(SiO_4)_3$ is already provided in the previous section.

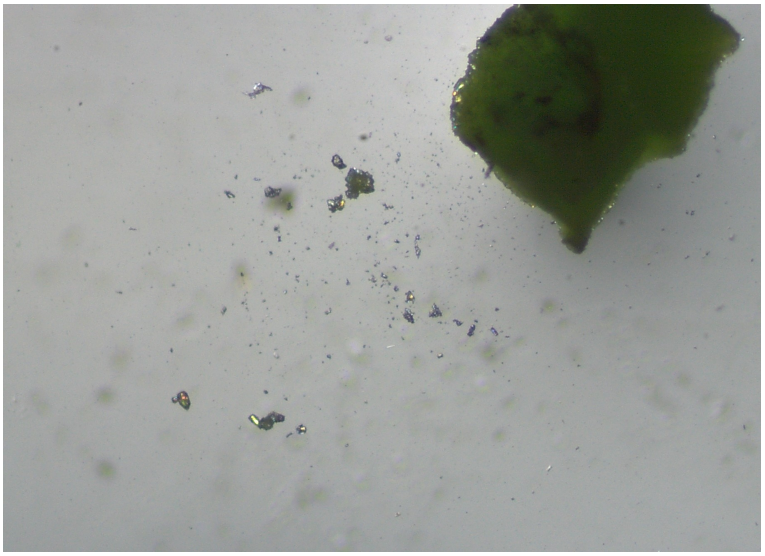


Fig. 11 Single crystals of $Pr_4(SiO_4)_3$ under a polarised light microscope.

The fate of the Na^+-ions remained uncertain. The PXRD-data (see fig. 46) almost exclusively showed reflections that are attributed to $Pr_4(SiO_4)_3$. Reflections not belonging to $Pr_4(SiO_4)_3$, could not be assigned due to their weak intensity. Although more detailed investigations to address the fate of Na_2O_2 seemed appealing, it must be concluded that the applied strategy of synthesising a ternary silicate of Pr^{4+} failed. Neither the first

and most important goal of having Pr^{4+} retain its oxidation state, nor the second goal of synthesising a ternary silicate succeeded.
SrO_2 releases oxygen at temperatures as low as 380 °C at ambient pressure,[121] allowing the interpretation that it is more strongly oxidising than Na_2O_2 which can even be melted before decomposing.[122] Additionally, the presence of Sr^{2+}-cations changes the structural chemistry of the potential products. Resulting from the experiments were a mixture of colourless single crystals and a green powder, as illustrated in fig. 12.

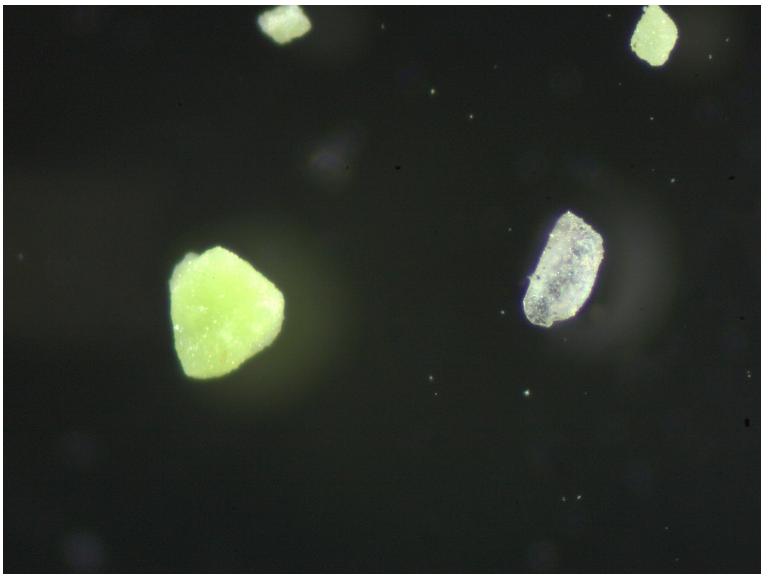


Fig. 12 Single crystals of SiO_2 (right) next to $Pr_4(SiO_4)_3$ (left) under a polarised light microscope.

The colourless phase could be identified as quartz by single crystal structure analysis, whereas the green powder consisted of $Pr_4(SiO_4)_3$ (comp. fig. 47). Like in the previous experiment including Na_2O_2, no ternary silicate could be obtained and the addition of the peroxide could not prevent the reduction of Pr^{4+}. The reoccurring formation of the orthosilicate $Pr_4(SiO_4)_3$ demonstrates that it is exceptionally stable under the applied conditions and that its formation is preferred over the formation of ternary phases with sodium or strontium.

4.1.9 Reaction of PrO_2 and P_2O_5 at High Pressure (*Manuscript 2*)

In analogy to the successful stabilisation of Pr^{4+} in silicates (see ***Manuscript 1***, section 4.1.6), the reaction of PrO_2 and P_2O_5 was investigated under similar conditions. Because the reaction at 11 GPa (see section 6.2.16) afforded monazite-type $PrPO_4$, containing Pr^{3+}, the reaction was repeated under higher pressures of up to 33.5 GPa in a diamond anvil cell to afford *hp*-$PrPO_4$ (*hp* = high-pressure) that crystallises in the barite structure. The crystal structure was determined by *in situ* single crystal diffraction analysis at pressure points 33.5, 27, 16 GPa and at ambient pressure. At ambient pressure,

a distorted barite variant was found.
The author's contributions include the experimental work, data analysis and writing of the manuscript in cooperation with the coauthors.
Supporting information of ***Manuscript 2*** is provided in section 7.1.

A New High-Pressure Polymorph of $PrPO_4$

Niko T. Flosbach*,[1] M. Bykov*,[1,2] L. Brüning,[1,2] P. Jurzick,[1,2] Mohamed Mezouar,[3] Timofey Fedotenko,[4] M. S. Wickleder*[1]

[1]Institute of Inorganic Chemistry, University of Cologne, Greinstraße 6, 50939 Cologne, Germany

[2]Institute of Inorganic and Analytical Chemistry, Goethe University Frankfurt, Max-von-Laue-Straße 7, 60438 Frankfurt am Main, Germany

[3]European Synchrotron Radiation Facility (ESRF), Avenue des Martyrs 71, 38000 Grenoble, France

[4]Deutsches Elektronen-Synchrotron, Notkestr. 85, 22607 Hamburg, Germany

ABSTRACT: The reaction of PrO_2 and phosphorus(V) oxide at 26 GPa in a diamond anvil cell afforded a new high-pressure polymorph of $PrPO_4$ that crystallizes in the barite-type structure with the space group *Pnma* (a = 785.75(8), b = 491.4(2) pm, c = 640.21(9) pm, V = 247.18(9) · 10^6 pm^3), along with the praseodymium(IV) oxide peroxide $Pr_2(O_2)O_3$. Both compounds could be identified by single crystal diffraction. When releasing the pressure, *hp*-$PrPO_4$ retains its structure to at least 16 GPa, but transforms into a distorted barite variant in the monoclinic space group $P2_1/n$ at ambient pressure. An attempt to produce additional *hp*-polymorphs at a higher pressure of 33.5 GPa reproduced the barite-type polymorph of $PrPO_4$. We herein report the first structural characterization of a lanthanoid orthophosphate in the orthorhombic barite structure.

INTRODUCTION

Compounds of the composition ABO_4 are ubiquitous in mineralogy, material science and chemistry and have been studied in great detail.[1-5] Their structural chemistry offers a rich variety of different structure types which generally depend on the ratios of atomic or ionic radii of the elements involved.[6-7] Typical ABO_4 structure types are barite ($BaSO_4$), monazite ($LaPO_4$), zircon ($ZrSiO_4$) and scheelite ($CaWO_4$), all of which are eponymous to the respective minerals. Monazite is the most important commercial source of lanthanoids and has been subject to several high-pressure (*hp*) studies due to its geological, physical and economic relevance.[8-15] Lanthanoid orthophosphates do not only constitute the most important class of lanthanoid containing minerals in the form of monazite and xenotime but have also proven to be pivotal for many technological applications, corroborating the necessity to study their chemical and physical properties.[16-20] The crystal structures of ABO_4 compounds can systematically be categorized by comparing the ratio of ionic radii of A, B and O to yield regions in which certain structure types are preferred. This concept is often visualized using *Bastide's* diagram (see fig. 1).[6-7, 21-22]

Since A, B and O usually differ in their compressibility within the structure, pressure induced phase transitions can be predicted by extrapolating the change of the ratio of ionic radii, which is manifested by drawing diagonal lines in *Bastide's* diagram. By applying this method, monazite-type ABO_4 structures are generally expected to transition to a barite structure for such monazites that are located close to the barite-monazite border. Structures with larger B-ions (e.g. $LaVO_4$, $PbCrO_4$…) are expected to transition to the scheelite-type at high pressure. Despite the manifold library of ABO_4 structures that are located in the monazite area in *Bastide's* diagram, actual transitions to *hp*-polymorphs were rarely proven experimentally.[9, 12, 23-30] Single crystal X-ray diffraction of $LaPO_4$ allowed the determination of the structure at 26 GPa, revealing a post-barite type structure in the space group $P2_12_12_1$, instead of the anticipated *Pnma* barite structure.[12] Recent studies of natural monazite at >30 GPa demonstrated that after decompression, a new structure in the space group $P2_1/n$ is obtained, that resembles a distorted barite structure.[15] Despite these sophisticated studies, no structural evidence of lanthanoid orthophosphates in the barite structure is known. We herein report the crystal structure of *hp*-$PrPO_4$ in the space group *Pnma* that was observed when reacting PrO_2 and phosphorus(V) oxide in a diamond anvil cell at >26 GPa.

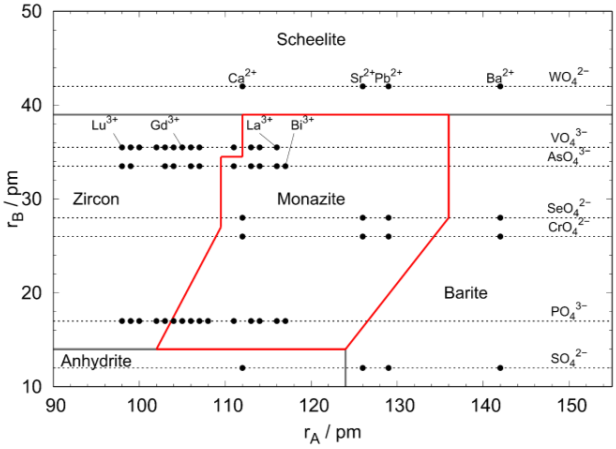


Figure 1. *Bastide's* diagram for ABO_4 structures.[7]

EXPERIMENTAL METHODS

Praseodymium dioxide was synthesized by oxidation of freshly calcinated Pr_6O_{11} with supercritical oxygen at 2.5 kbar. Phosphorus(V) oxide was obtained through commercial sources

(*Sigma Aldrich*, 99%) and was purified by sublimation before use. For the reaction at high pressure, the starting materials were homogenized and loaded into BX90-type diamond anvil cells with Boehler-Almax type diamonds with culet size of 200 µm. Preindented rhenium with a hole of ca. 100 µm was used to contain the materials. The cell was compressed to 26 ±1 GPa as determined by Raman bands of the diamonds, and then heated with an IR-laser. The generated temperature was estimated by detection the black body radiation.[31] *In situ* X-ray diffraction experiments were carried out at the high-pressure beam line P02.2 at *DESY (Deutsches Elekronen Synchrotron)*. X-ray diffraction experiments were repeated at 16 GPa and ambient pressure in the heated region of the sample. The experiment was repeated at a pressure of 33.5 ±1 GPa. X-Ray diffraction data of this experiment was collected at beam line ID27 at the *European Synchrotron Radiation Facility* (*ESRF*) and P02.2 at *DESY*.

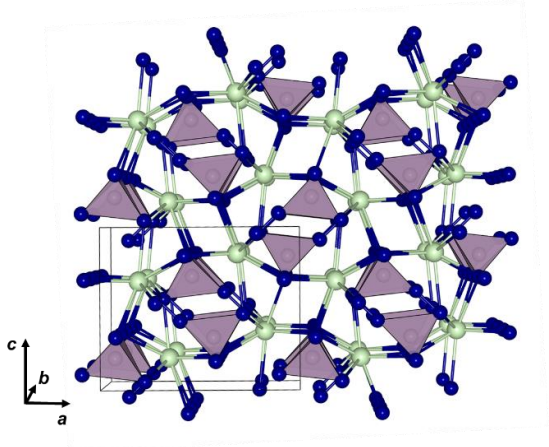
RESULTS AND DISCUSSION

The reaction of praseodymium dioxide and phosphorus(V) oxide at 26 GPa resulted in the formation of praseodymium(III) orthophosphate in the orthorhombic space group *Pnma*, along with praseodymium(IV) oxide peroxide with the composition $Pr_2(O_2)O_3$.

$$8\ PrO_2 + P_4O_{10} \xrightarrow[\text{ca. 4200 K}]{\text{DAC, 26 GPa}} 4\ PrPO_4 + 2\ Pr_2(O_2)O_3 \qquad (1)$$

Both products could be identified by single crystal X-ray diffraction of polycrystalline samples. Under the given conditions, the Pr^{4+} cations were partially reduced to Pr^{3+}, while some oxygen atoms were found oxidized in the form of peroxide anions in $Pr_2(O_2)O_3$. The formation of $Pr_2(O_2)O_3$ along with salts of Pr^{3+} follows the same pattern that was recently observed when the reaction between silicon dioxide and praseodymium dioxide was investigated under similar conditions.[32]

At 26 GPa, $PrPO_4$ crystallizes in the barite structure (*Pnma*, a = 785.75(8), b = 491.4(2) pm, c = 640.21(9) pm, V = 247.18(9) · 10^6 pm^3) with four formula units per cell. Images of the structure are shown in fig. 2. The Pr^{3+}-ions are coordinated by ten oxygen atoms with Pr-O distances ranging from 230(1) pm to 271.3(5) pm (compare tab. 1), with an average bond length of 252(1) pm. When considering that the distances between Pr1 and O1, as well as Pr1 and O2 exceed the sum of ionic radii (for ambient pressure), the coordination number decreased from ten to eight.[33] The coordination geometry for the case of the 10-fold coordination of Pr^{3+} is shown in fig. 3, with a summary of selected distances provided in tab. 1.



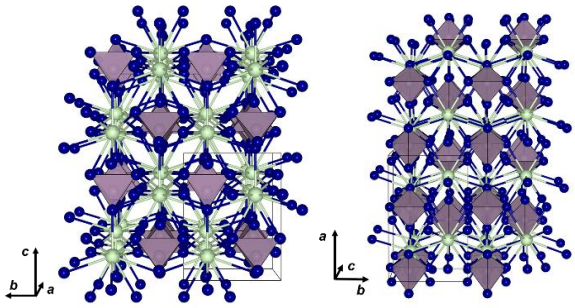


Figure 2. Crystal structure of $PrPO_4$ at 26 GPa viewed along various axes. Pr = light green; O = blue; phosphorus = purple.

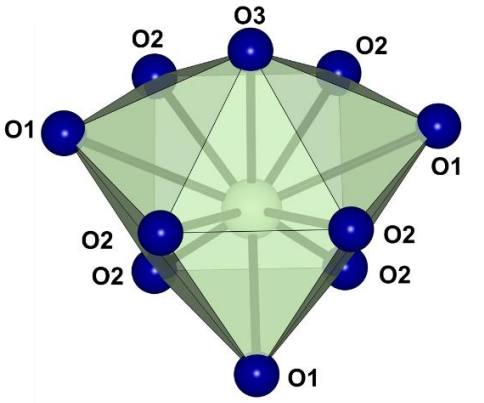


Figure 3. Coordination polyhedron of Pr1 in the orthorhombic $PrPO_4$ structure.

After decompression of the cell to 16 GPa, $PrPO_4$ was still found in the orthorhombic barite structure with a slightly larger cell compared to the structure at 26 GPa. The Pr^{3+}-ions are still coordinated by eight plus two oxygen atoms with distances ranging from 227(3) pm to 283(1) pm, with an average distance of 256(1) pm. As expected, the bond lengths slightly increase when decreasing the pressure, resulting in the Pr1-O1 and Pr1-O2 distances exceeding the sum of ionic radii even more. All Pr-O and P-O distances are summarized in tab. 1.

Table 1. Selected interatomic distances in $PrPO_4$ at different pressures as determined by single crystal X-ray diffraction. All values are given in units of pm.

Pnma	**33.5 GPa**	**26 GPa**	**16 GPa**	***P*2$_1$/*n***	**Ambient Pressure**
Pr1-O1	269.2(5)	271.3(5)	283(1)	Pr1-O1	253(2)
				Pr1-O1’	353(2)
Pr1-O2	246.0(7)	247.9(7)	252(1)	Pr1-O3	255(4)
				Pr1-O2	281(4)
Pr1-O3	227(1)	230(1)	227(3)	Pr1-O3’	237(3)
Pr1-O2’	261.2(5)	262.6(7)	267.1(1)	Pr1-O4	267(3)

				Pr1-O3''	333(3)
Pr1-O1'	241(1)	242(1)	238(4)	Pr1-O2	272(2)
Pr1-O2''	237.9(7)	239.9(6)	246(1)	Pr1-O4'	250(5)
				Pr1-O3'''	245(4)
P1-O1	149(1)	150(1)	149(3)	P1-O1	152(4)
P1-O2	150.7(9)	150.0(8)	151(1)	P1-O3	153(2)
				P1-O4	153(2)
P1-O3	149(1)	148(1)	148(3)	P1-O2	157(4)

At 26 GPa and 16 GPa, the orthorhombic structure was the most prominent phase in the heated area, as illustrated by the XRD maps shown in fig. S4 and S5. In those locations, in which single crystal data were collected, the majority of grains were identified as the barite-type $PrPO_4$ phase, which is confirmed by XRPD patterns obtained from the same locations. The patterns are displayed in fig. 4 and 5 and show a good match to the structures obtained from single crystal diffraction data at all three pressure points.

After decreasing the pressure to ambient pressure, instead of the orthorhombic *Pnma* structure of $PrPO_4$, a distorted variant of the barite structure in the monoclinic space group $P2_1/n$ was obtained, that was previously described by *Wang* for the case of natural monazite.[15]

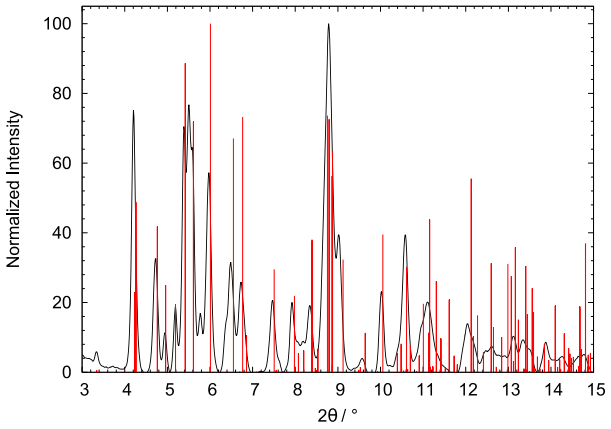


Figure 4. XRPD pattern of the products obtained after heating the cell at 26 GPa. The red lines indicate the theoretical positions of the peaks of the orthorhombic $PrPO_4$ at 26 GPa.

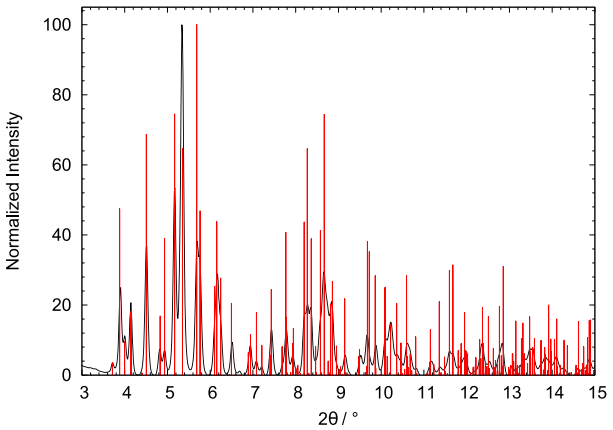


Figure 5. XRPD pattern of the products obtained after heating the cell at ambient pressure. The red lines indicate the theoretical positions of the peaks of the distorted barite structure of $PrPO_4$ at ambient pressure.

In order to investigate potential post-barite phases that were described for $LaPO_4$ by *Ruiz-Fuertes* et al.,[12] the experiment was repeated at 33.5 GPa. However, instead of observing the non-centrosymmetric $P2_12_12_1$ structure, $PrPO_4$ was found to crystallize in the barite structure under the given conditions.

CONCLUSION

Although several studies have addressed high-pressure polymorphism of lanthanoid orthophosphates and have even predicted the transition to a barite structure, no crystallographic evidence of an actual *hp*-barite polymorph has been reported. In this work, a new *hp*-polymorph of $PrPO_4$ was obtained by reacting PrO_2 and phosphorus(V) oxide at 26 and 33.5 GPa that were characterized by single crystal X-Ray diffraction. *hp*-$PrPO_4$ crystallizes in the orthorhombic space group *Pnma* and is isostructural to barite. Upon decompression of the cell to 16 GPa, the *Pnma* structure was conserved, whereas decompression to ambient pressure resulted in the formation of a distorted variant of barite, that was previously reported only for natural monazite.[15] In the future, this knowledge could be utilized to investigate the physical properties of *hp*-$PrPO_4$ and other lanthanoid orthophosphates under high pressure in order to establish systematic trends and thereby expand the knowledge of this fundamental class of materials.

ASSOCIATED CONTENT

Supporting Information

Supporting Information. Analytical data of starting materials, XRD-maps, single crystal refinements, PXRD patterns of $PrPO_4$, precession images of $Pr_2(O_2)O_3$. (PDF).

AUTHOR INFORMATION

Corresponding Author

*Niko T. Flosbach - Greinstr. 6, 50939 Cologne, Germany;
Email: n.flosbach@uni-koeln.de

*Maxim Bykov – Max-von-Laue-Straße 7, D-60438 Frankfurt am Main, Germany;
Email: bykov@chemie.uni-frankfurt.de

*Mathias S. Wickleder - Greinstr. 6, 50939 Cologne, Germany;
Email: mathias.wickleder@uni-koeln.de

Notes

The authors declare no competing financial interest.

ACKNOWLEDGEMENTS

N. F. and M. W. thank Prof. Martin Jansen for the donation of the oxygen autoclaves used for the synthesis of praseodymium dioxide.

ABBREVIATIONS

DESY, Deutsches Elektronen Synchrotron; ESRF, European synchrotron radiation facility; fig., figure; tab., table; XRD, X-ray diffraction

REFERENCES

[1] *Structure maps of ABX_4 inorganic compounds*, V. E. Lashin, N. A. Khritokhin, O. V. Andreev, *Russ. J. Inorg. Chem.* **2012**, *57*, 1584-1587.

[2] *Two Selective Sites Control of Cr^{3+}-Doped ABO_4 Phosphors for Tuning Ultra-Broadband Near-Infrared Photoluminescence and Multi-Applications*, Q. Zhang, D. Liu, P. Dang, H. Lian, G. Li, J. Lin, *Laser Photonics Rev.* **2022**, *16*, 2100459.

[3] *Novel Structural Motif To Promote Mg-Ion Mobility: Investigating ABO_4 Zircons as Magnesium Intercalation Cathodes*, A. Rutt, D. Sari, Q. Chen, J. Kim, G. Ceder, K. A. Persson, *ACS Appl. Mater. Interfaces* **2023**, *15*, 34983-34991.

[4] *A review on mechanochemical syntheses of functional materials*, Q. Zhang, F. Saito, *Adv. Powder Technolog.* **2012**, *23*, 523-531.

[5] *Crystal chemistry of the monazite structure*, N. Clavier, R. Podor, N. Dacheux, *J. Eur. Ceram. Soc.* **2011**, *31*, 941-976.

[6] *Pressure effects on the structural and electronic properties of ABX_4 scintillating crystals*, D. Errandonea, F. J. Manjón, *Prog. Mater. Sci.* **2008**, *53*, 711-773.

[7] *Systématique simplifiée des composés ABX_4 ($X = O^{2-}$, F^-) et evolution possible de leurs structures cristallines sous pression*, J. P. Bastide, *J. Solid State Chem.* **1987**, *71*, 115-120.

[8] *Study of monazite under high pressure*, T. Huang, J.-S. Lee, J. Kung, C.-M. Lin, *Solid State Commun.* **2010**, *150*, 1845-1850.

[9] *High-pressure stability and compressibility of APO_4 (A = La, Nd, Eu, Gd, Er, and Y) orthophosphates: An x-ray diffraction study using synchrotron radiation*, R. Lacomba-Perales, D. Errandonea, Y. Meng, M. Bettinelli, *Phys. Rev. B* **2010**, *81*, 064113.

[10] *Structural characterization of (Sm,Tb)PO_4 solid solutions and pressure-induced phase transitions*, J. M. Heuser, R. I. Palomares, J. D. Bauer, M. J. L. Rodriguez, J. Cooper, M. Lang, A. C. Scheinost, H. Schlenz, B. Winkler, D. Bosbach, N. S., D. G., *J. Eur. Ceram. Soc.* **2018**, *38*, 4070-4081.

[11] *Shock-produced high-pressure (La, Ce, Th)PO_4 polymorph revealed by microstructural phase heritage of monazite*, T. M. Erickson, N. E. Timms, M. A. Pearce, C. Cayron, A. Deutsch, L. P. Keller, D. A. Kring, *Geology* **2019**, *47*, 504-508.

[12] *High-pressure phase of $LaPO_4$ studied by x-ray diffraction and second harmonic generation*, J. Ruiz-Fuertes, A. Hirsch, A. Friedrich, B. Winkler, L. Bayarjargal, W. Morgenroth, L. Peters, G. Roth, V. Milman, *Phys. Rev. B* **2016**, *94*, 134109.

[13] *High-pressure phase transitions and properties of MTO_4 compounds with the monazite-type structure*, D. Errandonea, *physica status solidi (b)* **2017**, *254*, 1700016.

[14] *Monazite trace-element and isotopic signatures of (ultra) high-pressure metamorphism: Examples from the Western Gneiss Region, Norway*, R. M. Holder, B. R. Hacker, A. R. C. Kylander-Clark, J. M. Cottle, *Chem. Geol.* **2015**, *409*, 99-111.

[15] *Pressure-induced structural phase transitions in natural monazite*, B. Wang, *Phys. Rev. B* **2023**, *107*, 104102.

[16] *Effect of Al Dopant Al-$LaPO_4$ as an Interfacial Layer of Cu/Al-LaPO4/n-Si-Based MIS Schottky Barrier Diode for Optoelectronic Applications*, R. Mariappan, R. Priya, R. N. Jayaprakash, *J. Electron. Mater.* **2023**, *52*, 3831-3840.

[17] *Monitoring decomposition of Eu^{3+} doped $LaPO_4$ nanocrystals in glass using Eu^{3+} as an optical probe for applications in temperature sensing*, B. Bondzior, C. Nguyen, T. H. Q. Vu, P. J. Dereń, L. Petit, *Mater. Chem. Phys.* **2024**, *311*, 128493.

[18] *Review on rare earth metals doped $LaPO_4$ for optoelectronic applications*, R. Priya, R. Mariappan, A. Karthikeyan, E. Palani, E. Krishnamoorthy, G. Gowrisankar, *Solid State Commun.* **2021**, *339*, 114457.

[19] *Synthesis and sintering of $LaPO_4$ powder and its application*, W. Ruigang, P. Wei, C. Jian, F. Minghao, C. Zhenzhu, L. Yongming, *Mater. Chem. Phys.* **2003**, *79*, 30-36.

[20] *Rare earth elements: A review of applications, occurrence, exploration, analysis, recycling, and environmental impact*, V. Balaram, *Geosci. Front.* **2019**, *10*, 1285-1303.

[21] *Crystal stability and pressure-induced phase transitions in scheelite AWO_4 (A = Ca, Sr, Ba, Pb, Eu) binary oxides. II: Towards a systematic understanding*, F. J. Manjón, D. Errandonea, J. López-Solano, P. Rodríguez-Hernández, S. Radescu, A. Mujica, A. Muñoz, N. Garro, J. Pellicer-Porres, A. Segura, C. Ferrer-Roca, R. S. Kumar, O. Tschauner, G. Aquilanti, *phys. stat. sol. (b)* **2007**, *244*, 295-302.

[22] *Pressure-induced phase transformations of zircon-type $LaVO_4$ nanorods*, H. Yuan, K. Wang, C. Wang, B. Zhou, K. Yang, J. Liu, B. Zou, *J. Phys. Chem. C* **2015**, *119*, 8364-8372.

[23] *Exploring the high-pressure behavior of the three known polymorphs of $BiPO_4$: Discovery of a new polymorph*, D. Errandonea, O. Gomis, D. Santamaría-Perez, B. García-Domene, A. Muñoz, P. Rodríguez-Hernández, S. N. Achary, A. K. Tyagi, C. Popescu, *J. Appl. Phys.* **2015**, *117*, 105902.

[24] *Phase stability of lanthanum orthovanadate at high pressure*, D. Errandonea, J. Pellicer-Porres, D. Martinez-Garcia, J. Ruiz-Fuertes, A. Friedrich, W. Morgenroth, C. Popescu, P. Rodriguez-Hernandez, A.

Munoz, M. Bettinelli, *J. Phys. Chem. C* **2016**, *120*, 13749-13762.

[25] *Monazite-type $SrCrO_4$ under compression*, J. Gleissner, D. Errandonea, A. Segura, J. Pellicer-Porres, M. A. Hakeem, J. E. Proctor, S. V. Raju, R. S. Kumar, P. Rodríguez-Hernández, A. Muñoz, S. Lopez-Moreno, M. Bettinelli, *Phys. Rev. B* **2016**, *94*, 134108.

[26] *High-pressure structural transformations of $PbCrO_4$ up to 51.2 GPa: An angle-dispersive synchrotron X-ray diffraction study*, D. Errandonea, R. S. Kumar, *Mater. Res. Bull.* **2014**, *60*, 206-211.

[27] *In situ high-pressure synchrotron x-ray diffraction study of $CeVO_4$ and $TbVO_4$ up to 50 GPa*, D. Errandonea, R. S. Kumar, S. Achary, A. K. Tyagi, *Phys. Rev. B* **2011**, *84*, 224121.

[28] *Evidence for monazite-, barite-, and $AgMnO_4$ (distorted barite)-type structures of $CaSO_4$ at high pressure and temperature*, W. A. Crichton, J. B. Parise, S. M. Antao, A. Grzechnik, *Am. Mineral.* **2005**, *90*, 22-27.

[29] *Complex high-pressure polymorphism of barium tungstate*, O. Gomis, J. A. Sans, R. Lacomba-Perales, D. Errandonea, Y. Meng, J. C. Chervin, A. Polian, *Phys. Rev. B* **2012**, *86*, 054121.

[30] *High-pressure investigations of lanthanoid oxoarsenates: I. Single crystals of scheelite-type $Ln[AsO_4]$ phases with Ln= La–Nd from monazite-type precursors*, S. J. Metzger, F. Ledderboge, G. Heymann, H. Huppertz, T. Schleid, *Z. Naturforsch. B* **2016**, *71*, 439-445.

[31] *A portable laser heating microscope for high pressure research*, S. Guoyin, W. Lin, F. Richard, M. Ho-kwang, J. H. Russell, *J. Phys.: Conf. Ser.* **2010**, *215*, 012191.

[32] *Stabilization of Pr^{4+} in Silicates – High Pressure Synthesis of $PrSi_3O_8$ and $Pr_2Si_7O_{18}$*, N. T. Flosbach, M. Bykov, E. Bykova, B. Rasche, M. Mezouar, T. Fedotenko, S. Chariton, V. B. Prakapenka, M. S. Wickleder, *Inorg. Chem.* **2024**, submitted.

[33] *Revised effective ionic radii and systematic studies of interatomic distances in halides and chalcogenides*, R. D. Shannon, *Acta crystallographica section A: crystal physics, diffraction, theoretical and general crystallography* **1976**, *32*, 751-767.

4.1.10 High Pressure Synthesis of $Pr_2(O_2)O_3$ - A Unique Lanthanoid(IV) Oxide Peroxide (*Manuscript 3*)

As already elucidated in ***Manuscript 1*** and ***2*** (sections 4.1.6 and 4.1.9), $Pr_2(O_2)O_3$ forms at high pressure when reacting PrO_2 with SiO_2 or P_2O_5. ***Manuscript 3*** deals with the intentional synthesis of $Pr_2(O_2)O_3$ by reacting PrO_2 with oxygen at 27 GPa. $Pr_2(O_2)O_3$ presents the most oxygen rich compound of any binary phase of a lanthanoid and oxygen and is, after $Nd_2(O_2)O_2$[123], only the second structurally characterised oxide peroxide of a lanthanoid. Furthermore, $Pr_2(O_2)O_3$ contains Pr^{4+} next to peroxide anions, which is entirely unprecedented.

$Pr_2(O_2)O_3$ was identified by *in situ* single crystal X-ray diffraction at pressure points of 27 , 20 and 11 GPa, while decomposition into unknown phases occurred when releasing the pressure to ambient pressure. In a control experiment the role of oxygen as a reactant was confirmed. Next to Raman-spectroscopy that corroborated the presence of a peroxide group, the electronic structure of $Pr_2(O_2)O_3$ was assessed by theoretical calculations that support the presence of tetravalent praseodymium.

The author's contributions include the experimental work, data analysis as well as writing of the manuscript in collaboration with the coauthors. M. Ekholm, M. Amirabbasi and I. A. Abrikosov performed the theoretical calculations and wrote the corresponding sections of the manuscript.

Supporting information of ***Manuscript 3*** is provided in section 7.1.

High Pressure Synthesis of Pr_2O_5 – A Unique Lanthanoid(IV) Oxide Peroxide

N. T. Flosbach*[1], M. Bykov*[1,2], L. Brüning[1], P. L. Jurzick[1], E. Bykova[3], M. Ekholm[4], I. A. Abrikosov[4], M. Amirabbasi[5], M. Mezouar[6], B. Wehinger[6], N. Giordano[7], T. Fedotenko[7], V. Prakapenka[8], S. Chariton[8], M. S. Wickleder*[1]

[1]University of Cologne, Institute of Inorganic Chemistry, Greinstr. 6, 50939 Cologne, Germany

[2]Institute of Inorganic and Analytical Chemistry, Goethe University Frankfurt, Max-von-Laue-Str. 7, 60438 Frankfurt am Main, Germany

[3]Institute of Geosciences, Goethe University Frankfurt, Altenhöferallee 1, 60438 Frankfurt am Main, Germany

[4]Department of Physics, Chemistry and Biology, Linköping University, SE-581 83, Sweden

[5]Theory of Magnetic Materials, Institut für Materialwissenschaft, Technische Universität Darmstadt, 64289 Darmstadt, Germany

[6]European Synchrotron Radiation Facility, Grenoble Cedex F-38043, France

[7]Deutsches Elektronen-Synchrotron DESY, Notkestr. 85, 22607 Hamburg, Germany

[8]Center for Advanced Radiation Sources, University of Chicago, Chicago, IL, USA

ABSTRACT: Reacting praseodymium(IV) oxide with oxygen at 27 GPa in a diamond anvil cell afforded the oxide peroxide $Pr_2^{IV}(O_2)O_3$, which was characterized by single crystal X-ray diffraction on multi-grain samples, Raman spectroscopy and quantum theoretical calculations at various pressure points. The presence of tetravalent praseodymium ions is supported by electronic structure calculations, showing a band gap of ca. 1.5 eV, which is consistent with the anticipated chemical model of an ionic solid. $Pr_2(O_2)O_3$ thus far represents the most oxygen rich phase of any binary compound of a lanthanoid and oxygen. Additionally, these results demonstrate that instead of oxidizing the praseodymium ions past their +IV oxidation state, oxygen undergoes a comproportionation to form peroxide anions. Direct oxidation of the oxide anions by Pr^{4+}-ions was ruled out by a control experiment in argon instead of oxygen, where no oxidation of oxide ions was observed.

INTRODUCTION

Because of their distinct physical and chemical properties, the lanthanoids have evolved to form an integral constituent of modern technologies like electronics, optical devices, and magnetic components, in which they serve irreplaceable functions.[1] The chemistry of the lanthanoids is dominated by the +III oxidation state that is the most stable for all elements of the series. Naturally, differences in the electronic configuration of a given element in different oxidation states manifest themselves in the physical properties of the respective ions. Consequently, the search for new compounds containing lanthanoids in oxidation states other than +III is not only an endeavor of expanding the fundamental knowledge of their chemistry but is also motivated by the potential of developing novel materials of unprecedented physical and chemical properties.

Next to the +III oxidation state, some elements of the series can form stable compounds in their divalent oxidation states. The *classical* divalent lanthanoids are samarium, europium and ytterbium. Due to their chemical availability, research of divalent lanthanoids has historically been concentrated on these three elements, albeit recent studies have shown that the entire series, except for radioactive promethium, is accessible in their divalent oxidation state, at least in metal organic complexes.[2-4] Additionally, several *non-classical* lanthanoids can be found in the form of reduced halides.[5]

In contrast to the divalent lanthanoids, the accessibility of their tetravalent counterparts is much more difficult because of

the strongly oxidizing character of the respective ions. In fact, the Ce^{4+}-ion is the only Ln^{4+}-ion that is available in a wide variety of compounds, albeit it is still strongly oxidizing. When comparing the standard oxidation potentials E_0 for the Ln^{3+}/Ln^{4+} pairs, Pr^{3+}/Pr^{4+} (E_0 = +3.2 V) and Tb^{3+}/Tb^{4+} (E_0 = +3.1 V) follow Ce^{4+} (E_0 = +1.74 V) in the row of the most stable Ln^{4+}-ions.[6-7] As expected for such strongly oxidizing cations, the chemistry of Pr^{4+} and Tb^{4+} is almost exclusively limited to oxides and fluorides.[8-24] Even simple salts of the form LnO_2 or LnF_4 (for Ln = Pr, Tb) usually require harsh conditions to be synthesized.[25] The recent discovery of metal organic complexes containing Pr^{4+} and Tb^{4+}, as well as the synthesis of $K_2Tb^{V}Ge_2O_7$ and the mixed valent $Cs_8Tb_2^{III}Tb^{IV}Ge_9O_{27}$ present irrevocable evidence that the chemistry of tetravalent praseodymium and terbium can be expanded beyond simple oxides and fluorides, thus providing the opportunity to investigate their optical and magnetic behavior in more detail.[26-35] Combined theoretical and experimental studies of selected examples of Pr^{4+} containing compounds have shown that the $4f^1$-configured ion does not follow the general trends typically observed in $4f^n$-configured ions but rather behaves more similar to the early actinoids.[36] Given the scarcity of materials containing Pr^{4+}, such studies thus far have to remain focused on very few systems, limiting the opportunity to establish new trends and to research potential applications.

Although Nd^{4+} and Dy^{4+} show an even higher proclivity to be reduced to their respective trivalent ions (E_0 = +5.0 V for Nd^{3+}/Nd^{4+} and E_0 = +5.2 V for Dy^{3+}/Dy^{4+}),[6-7] fluorides of the form $Cs_2MLn^{IV}F_7$ (M = K, Rb, Cs; Ln = Nd, Dy) have been prepared by oxidation with fluorine under extreme pressure.[37-38] The binary fluorides $Ln^{IV}F_4$ (Ln = Nd, Dy) have thus far only been observed in noble gas matrices.[39] When attempting to synthesize a perovskite of the form $BaNd^{IV}O_3$ by reacting barium peroxide with neodymium(III) oxide at 4 GPa and 1500 °C Range *et al.* obtained an oxide peroxide with the empirical formula NdO_2, which is to be conceived as $Nd_2^{III}(O_2)O_2$, as evidenced by single crystal structure analysis and vibrational spectra.[40-42]

As of today, no evidence of higher oxidation states than +IV has been reported for the lanthanoids in condensed phases. Removing the last 4f-electron from the $4f^1$-configured Pr^{4+}-ion would result in the closed shell configuration of Pr^{5+}: [Xe], analogous to Ce^{4+} or La^{3+}. Attempts to stabilize Pr^{5+} in the form of PrF_5 in a noble gas matrix were reported to be unsuccessful.[43] Recent studies have demonstrated for the first time that Pr^{5+} is accessible in the gas phase.[44-46]

Recent studies have revealed that a multitude of unique compounds like CaO_3, Xe_3O_2, Xe_2O_5 or FeO_2, which are unattainable by other methods, can be synthesized by utilizing the reactivity of oxygen at high pressure.[47-49] Additionally, several studies predicted that many elements can be oxidized beyond their current highest oxidation states by high-pressure methods, posing the question if Pr^{5+} is also accessible under high pressure.[50-52] We herein report the discovery of the unique oxide peroxide $Pr_2^{IV}(O_2)O_3$ with the empirical formula Pr_2O_5 that was obtained by oxidation of PrO_2 at 27 GPa in a diamond anvil cell.

RESULTS AND DISCUSSION

By reacting PrO_2 with oxygen under similar conditions, $Pr_2(O_2)O_3$ was obtained.

$$2\ PrO_2 + 0.5\ O_2 \xrightarrow[\text{ca. 1600 K}]{\text{DAC, 27 GPa}} Pr_2^{IV}(O_2)O_3 \qquad (1)$$

The title compound could be identified by single crystal X-ray diffraction of multi grain samples at three different pressure points (27 GPa, 20 GPa and 11 GPa, see tab. S 1). The crystal structure is discussed in more detail below. Raman spectroscopy of the DAC revealed two weak signals at 820 cm^{-1} and 850 cm^{-1} that are assigned to characteristic vibrations of the peroxide anion based on comparison of similar compounds.[53-54] The Raman spectrum is depicted in fig. 1.

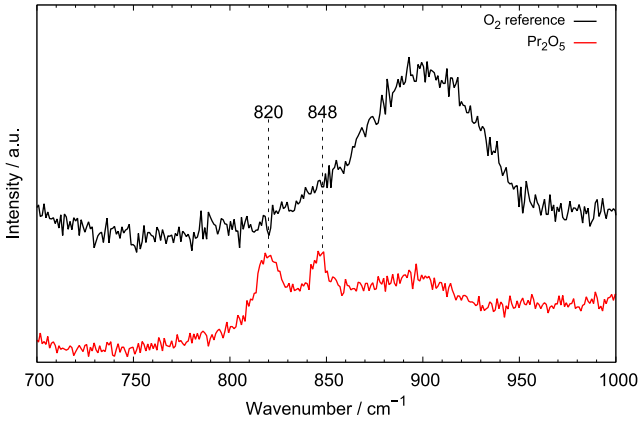


Figure 1. Excerpt of the Raman spectrum of the reaction chamber at 27 GPa. Vibrations assigned to the peroxide group of $Pr_2(O_2)O_3$ are highlighted. The spectra were recorded with an excitation wavelength of 532 nm. The black spectrum is a reference spectrum of only oxygen without praseodymium oxides that was measured using the same experimental setup.

The weak signal to noise ratio is caused by the small quantities of $Pr_2(O_2)O_3$ next to other materials as a result of local heating. In order to exclude autooxidation of praseodymium dioxide as a possible reaction pathway to $Pr_2(O_2)O_3$, the experiment was repeated using argon as the pressure transmitting medium instead of oxygen, where the cotunnite-type PrO_2 was observed as the main phase, proving that a second reactant is needed for the formation of $Pr_2(O_2)O_3$.[55]

Crystal Structure of Pr2(O2)O3 Because the general structure motifs are the same for all three pressure points (27, 20 and 11 GPa), the details are discussed exemplarily for the structure at 11 GPa which is the closest to ambient pressure. $Pr_2(O_2)O_3$ crystallizes in the orthorhombic space group *Pbcn* (no. 60) with four formula units per unit cell. The Pr^{4+}-ions form a distorted body-centered cubic (*bcc*) sublattice in which the oxide ions O2 and O3 occupy tetrahedral voids and the peroxide ions occupy octahedral voids. The coordination geometries of the oxide ions O2 and O3 are depicted in fig. 2.

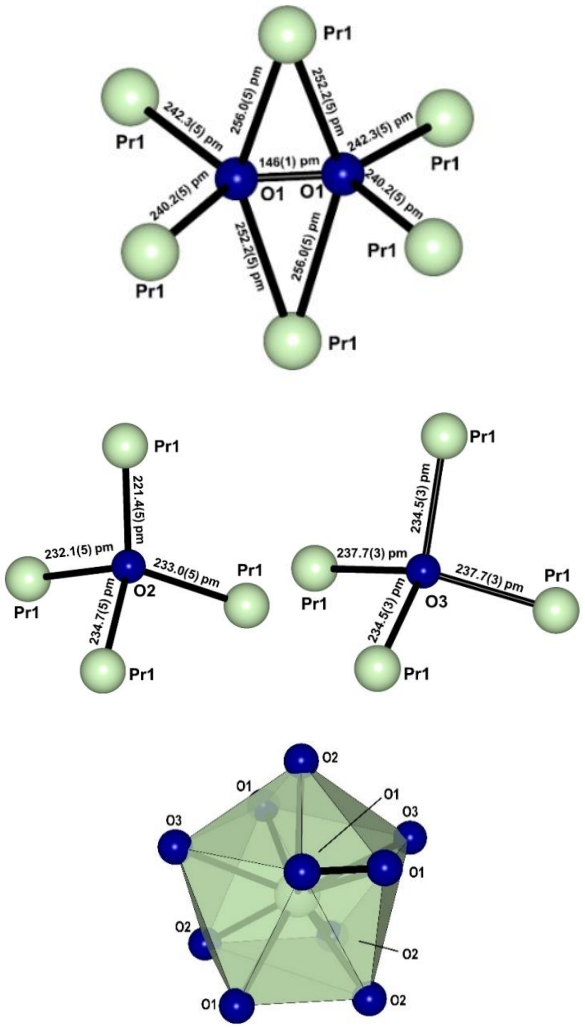


Figure 2. Coordination geometries of the peroxide anion (top), the oxide anions O2 (middle left) and O3 (middle right) and the Pr^{4+}-ion (bottom). The displayed interatomic distances refer to the structure at 11 GPa.

The [OPr_4]-polyhedra of O2 and O3 deviate significantly from the ideal tetrahedral geometry. In the coordination polyhedron of O2 the Pr1-O2-Pr1 angles reach as high as 123.8(3)° and as low as 99.6(2)° with an average angle of 109.4°. The Pr-O distances of O2 range from 234.7(5) pm to 221.4(5) pm with an average value of 230.3 pm across all four bonds. The Pr-O distances of O3 are similar, if slightly longer. Because O3 lies on a twofold rotational axis (Wyckoff Symbol = *4c*), there are only two different Pr-O distances to be discussed. The shorter one is 234.5(3) pm and the longer one is 237.7(3) pm, which is slightly longer than the longest Pr-O distance in the polyhedron of O2. The deviation of the [OPr_4]-polyhedron around O3 from ideal tetrahedral geometry is even more pronounced than in the polyhedron of O2. The largest Pr1-O3-Pr1 angle found at 11 GPa is 137.3(3)°, which is much larger than the ideal tetrahedral angle of ca. 109.5°. On the contrary, the smallest angle in the same polyhedron is only 97.73(1)°, further indicating a strong distortion when compared to ideal tetrahedral geometry. This distortion is a result of the significant deviation of the sublattice of Pr^{4+}-ions from the ideal body centered cubic packing, which in turn is caused by packing effects. The peroxide anions constituted of O1 atoms occupy octahedral voids in the *bcc* sublattice of Pr^{4+}-ions, as illustrated in fig. 2. On two opposing sides the peroxide anions coordinate to one Pr1 site with both atoms (η^2) each, with Pr-O distances 256.0(5) pm and 252.3(5) pm. The terminal coordination to Pr1 includes four Pr^{4+}-ions, two for each oxygen atom, where the distances are found to be 242.3(5) pm and 240.2(5) pm. The discrepancy is merely a result of the different denticity in both cases. The average Pr-O distance in the polyhedron is 247.9 pm. With an O-O distance of 146(1) pm, the O-O-bond lies within the distance typically observed for peroxide bonds, even when high pressure is accounted for.[53-54, 56]

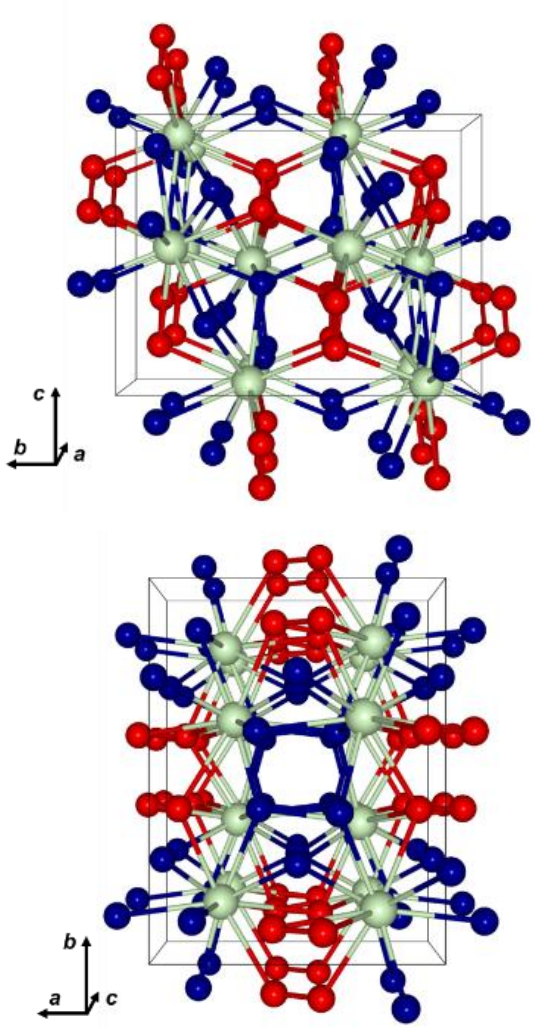


Figure 3. Crystal structure of $Pr_2(O_2)O_3$ at 11 GPa viewed along the crystallographic *a*- and *c*-axes. Green = praseodymium; blue = oxide; red = peroxide.

The coordination polyhedron of Pr1 involves ten oxygen atoms, wherein four are constituents of peroxide anions while the remaining six are constituents of oxide anions. The coordination polyhedron of the Pr^{4+}-ions can be labeled as a distorted augmented sphenocorona (*Johnson*-solid no. 87) with a distortion coefficient of 2.427, as suggested by CShM-calculations.[57] The average Pr-O distance in the polyhedron is 238.4 pm, where the shortest distance is found between Pr1 and O2 at 221.4(5) pm and the longest between the η^2-coordinating per-

oxide ion and Pr1 (256.0(5) pm). Despite the higher coordination number of the Pr^{4+}-ion, compared to the 8-fold coordination of Nd^{3+} in $Nd_2^{III}(O_2)O_2$ (d_{avg}(Nd-O) = 247 pm), the distances between lanthanoid ion and oxygen atoms are significantly shorter, suggesting a higher charge of the cation, even when considering the higher pressure.[40] The ionic radius of Pr^{3+} is approximately 118 pm for the case of 9-fold coordination (no value is available for 10-fold coordination) and that of a 4-fold coordinated oxide anion 138 pm,[58] yielding an expected Pr^{3+}-O^{2-}-distance of 256 pm, which is much longer than that observed in the title compound (compare fig. 2).

Pressure Dependence of Structural Motifs At higher pressures $Pr_2(O_2)O_3$ still crystallizes in the same orthorhombic space group *Pbcn*, with the same structure that was found at 11 GPa. A comprehensive overview of systematic trends of the pressure dependence of selected structural motifs is provided in the following abstract.

The most fundamental change at higher pressure is the compression of the entire structure, resulting in shortening of the lattice parameters and hence the molar volume of its contents. The lattice parameters are plotted for all experimental pressure points along with theoretically calculated data in fig. 4. The cell volume decreases from 305.33(7)·10^6 pm^3 to 286.19(1)·10^6 pm from 11 GPa to 27 GPa by ca. 6.3%.

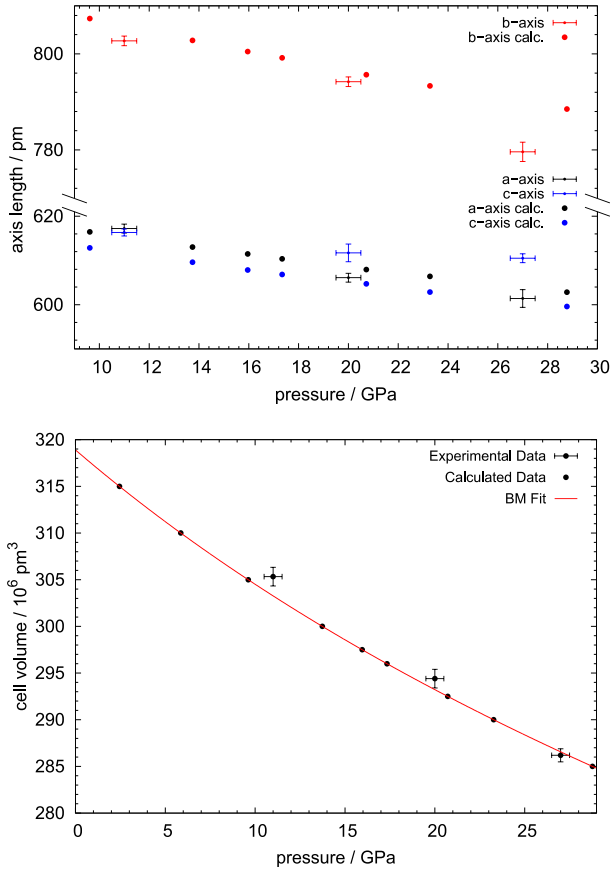


Figure 4. Lattice parameters of $Pr_2(O_2)O_3$ at different pressure points (top) and cell volume of the unit cell at different pressures (bottom). Calculated values are displayed at points, whereas experimental data is shown as crosses. The red line in the right graphic symbolizes the Birch-Murnaghan equation of state obtained by theoretical calculations.

While the *c*-axis length only decreases from 616.33(8) pm at 11 GPa to 610.5(5) pm at 27 GPa, which is equivalent to a relative compression of ca. 1.0%, the *a*- and *b*-axes are more strongly compressed. The *a*-axis length decreases from 617.2(1) pm to 601.4(2) pm, corresponding to a relative change of ca. 2.5%, whereas the *b*-axis undergoes a slightly larger relative change of 2.9% from 802.7(1) ppm to 779.6(2) ppm. The decline of axis length along the *a*- and *b*-axes does not follow a linear trend, whereby the compression of the *c*-axis is linear within the margin of error. Naturally, the compression of the cell is facilitated by shortening of chemical bonds. The O-O distance of the peroxide group is shortened by ca. 2% from 147(1) pm at 11 GPa to 144.1(7) pm at 27 GPa, as is depicted in fig. 5.

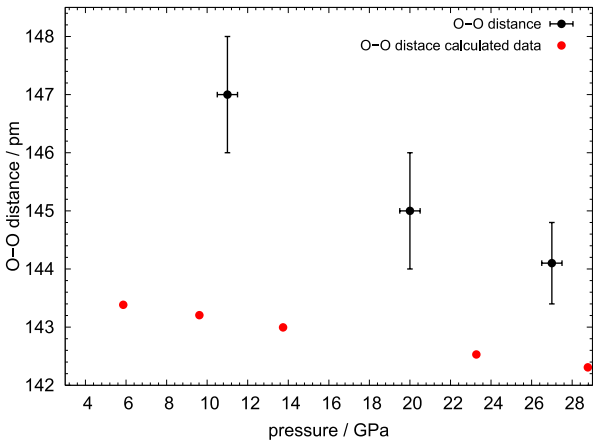


Figure 5. Pressure dependence of the O-O-distance in the peroxide anion in $Pr_2(O_2)O_3$. Calculated data is shown in red.

With increasing pressure, the $[PrO_{10}]$-polyhedron loses approximately 6.2% of its volume between 11 to 27 GPa (285.1(2)·10^6 pm^3 to 267.3(2)·10^6 pm^3). Likewise, the average Pr-O distance in the polyhedron decreases from 238.4 pm at 11 GPa to 233.3 pm at 27 GPa. All discussed distances are shown in tab. S 2 in the SI.

The ab-initio calculations recover the orthorhombic *Pbcn* structure at all volumes. With U_{eff} = 2.5 eV we also obtain good quantitative agreement with the experimental lattice parameters. Nevertheless, the monotonic pressure dependence of the theoretically predicted lattice parameters deviate slightly from the experimentally observed trends, which is likely due to the non-hydrostatic conditions in the cell. By fitting the the Birch-Murnaghan equation of state to the calculated pressure-volume data we obtain the bulk modulus B_0 = 192.8 GPa and B_0' = 5.0, with the equilibrium volume V_0 = 319.2·10^6 pm^3.[59] The calculations also reproduce a decreased peroxide distance with pressure, as seen in fig. 6, in support of the experiments.

The electronic structure calculations (see fig. S 5) reveal an insulating band gap of 1.2 eV and a local Pr magnetic moment of ~1 μ_B. This is consistent with the model of an ionic salt containing $4f^1$-configured Pr^{4+} ions, along with oxide and peroxide anions each carrying localized negative charges. We suggest that the formation of the +IV oxidation state is possible due to the peroxide dimers, which form antibonding states and prevent oxidation of Pr beyond +IV. This is supported by the calculated electronic density of states which shows the antibonding states

of the peroxide anions, accommodating two electrons per formula unit (see SI).

CONCLUSION

The reaction of praseodymium dioxide with oxygen at 27 GPa afforded the unprecedented lanthanoid(IV) oxide peroxide $Pr_2^{IV}(O_2)O_3$ with the empirical formula Pr_2O_5 with the highest oxygen content of any binary phase of any lanthanoid and oxygen. $Pr_2(O_2)O_3$ is only the second oxide peroxide to be discovered, adding another member to this exclusive group of compounds. Its structure was determined by single crystal X-ray diffraction techniques and further corroborated by quantum theoretical calculation as well as Raman spectroscopy. Upon decompression of the sample, the title compound decomposed into unknown products between 11 GPa and ambient pressure. Investigation of the compound at different pressure points between 11 GPa and 27 GPa, along with theoretical calculations allowed for the determination of the Birch-Murnaghan equation of state of $Pr_2(O_2)O_3$.

The presence of tetravalent praseodymium ions next to peroxide anions has not been reported before and to the best of our knowledge has never been reported for any other tetravalent lanthanoid cation. The electronic structure was assessed by band structure calculations that support the assignment of charge distribution within the solid. These discoveries set the foundation for further studies of the physical and chemical properties of the $4f^1$-configured Pr^{4+}-ion that have recently been demonstrated to deviate from the general trends observed in lanthanoids.[36] Even under the extreme conditions applied in our experiments, no evidence of oxidation of praseodymium past the +IV oxidation state was observed, indicating that the +V oxidation state is not accessible under the applied experimental parameters, at least not in binary oxides.

EXPERIMENTAL AND COMPUTATIONAL DETAILS

Synthesis of Praseodymium Dioxide 250 mg of Pr_6O_{11} (obtained from calcination of freshly precipitated $Pr(OH)_3$) (0.245 mmol, 6 eq.) were added to a silica crucible that was inserted into a steel autoclave with an internal volume of ca. 20 ml. 9 ml of liquid oxygen were condensed into the autoclave before it was closed and heated to 500 °C for 12 hours. After allowing the autoclave to cool to room temperature, the pressure was released and 254 mg of PrO_2 (1.47 mmol, 100%) were retrieved from the silica crucible as a black powder.

Reaction of Praseodymium Dioxide and Oxygen Praseodymium dioxide was loaded in a BX90-type diamond anvil cell equipped with Boehler-Almax-type diamonds (culet diameter 250 μm) together with oxygen under cryogenic loading. Oxygen served both as a pressure transmitting medium and a reactant. The sample was compressed to 27 GPa and laser heated to ca. 1400 °C. The structure was solved by single crystal X-ray diffraction of multi grain samples at beam line P02.2 at DESY. The pressure was then reduced to 20 GPa, 11 GPa and finally to ambient pressure without further heating. At both 20 GPa and 11 GPa, the title compound could be identified by single crystal diffraction data. At ambient pressure, the diffraction patterns did not allow for satisfactory structure solution.

Raman data of the cell was recorded at 27 GPa using the advanced integrated optical spectroscopy system at GSECARS.[60]

Control Experiment Praseodymium dioxide was loaded in a BX90 diamond anvil cell equipped with Boehler-Almax-type diamonds (culet diameter 250 μm) together with argon. The cell was compressed to 33 GPa and heated to >1500 K. The cell was decompressed to first 28 GPa and then to ambient pressure. At all three pressure points single crystal diffraction data was collected. The cotunnite-type PrO_2 phase was identified at 33 GPa and 28 GPa, whereas no satisfactory structure solutions could be obtained at ambient pressure.[61]

X-Ray Diffraction Data Collection and Processing X-Ray diffraction data was collected at the synchrotron beamline P02.2 at DESY (λ = 0.2903 Å, Perkin Elmer XRD1621 flat panel detector).[62-63] The control experiment was conducted at the synchrotron beam line ID27 at ESRF (λ = 0.3738 Å, Eiger2 X 9M CdTe flat panel detector).[64] After increasing the cell pressure to the target pressure (pressure determined by Raman shift of the diamond D-band),[65] a two dimensional grid of the heated area was produced by collecting XRD images at selected positions. ω-scans of ±35° were collected at respective positions within the grid. The diffraction data was processed and analysed with the CrysAlisPro software in combination with DaFi.[66] Structures were solved and refined using ShelX with the Olex user interface.[67-68] The full data sets were deposited in the Cambridge crystal structure database (CCDC) with the numbers 2303283 (27 GPa), 2303282 (20 GPa) and 2303284 (11 GPa).

Quantum Theoretical Calculations Ab-initio density functional theory (DFT)[69-70] calculations were performed with the projector augmented waves (PAW) method[71-72] as implemented in the Vienna ab-initio simulation package (VASP) [73-75]. We used the revised Perdew-Burke-Ernzerhof generalized gradient approximation (PBEsol)[76] with the on-site effective Coulomb parameter U_{eff} in the parametrization by Dudarev et al. [77-78]. Structural relaxation was performed with the plane wave expansion up to 525 eV and a 8x6x8 k-point grid. Total energy was converged within 10^{-6} eV and the forces were converged within 0.01 eV / Å. Presented calculations were done for an antiferromagnetically ordered cell within the scalar-relativistic approximation. Test calculations show that the magnetic configuration and spin-orbit coupling only have a very minor impact on the quantities of interest.

ASSOCIATED CONTENT

Supporting Information

Crystallographic data of $Pr_2(O_2)O_3$ (tab. S 1); Summary of selected interatomic distances (tab. S 2); Full Raman spectrum (fig. S 1), XRD-map at 27 GPa (fig. S 2); XRD-map at 20 GPa (fig. S 3); XRD-map at 11 GPa (fig. S 4); Calc. density of states plots (fig. S 5).

AUTHOR INFORMATION

Corresponding Author

*Niko T. Flosbach - Greinstr. 6, 50939 Cologne, Germany;
Email: n.flosbach@uni-koeln.de

*Maxim Bykov – Max-von-Laue-Straße 7, D-60438 Frankfurt am Main, Germany;
Email: bykov@chemie.uni-frankfurt.de

*Mathias S. Wickleder - Greinstr. 6, 50939 Cologne, Germany;
Email: mathias.wickleder@uni-koeln.de

Author Contributions

The manuscript was written through contributions of all authors. All authors have given approval to the final version.

Notes

The authors declare no competing financial interest.

ACKNOWLEDGEMENTS

Funded/Co-funded by the European Union (ERC, HIPMAT, 101077963). Views and opinions expressed are however those of the author(s) only and do not necessarily reflect those of the European Union or the European Research Council. Neither the European Union nor the granting authority can be held responsible for them.

M. B. acknowledges the support of Deutsche Forschungsgemeinschaft (DFG Emmy-Noether project BY112/2-1). E. B. acknowledges the support of Deutsche Forschungsgemeinschaft (DFG Emmy-Noether project No. BY101/2-1). We acknowledge the European Synchrotron Radiation Facility (ESRF) for provision of synchrotron radiation facilities under proposal number CH6475. We acknowledge DESY (Hamburg, Germany), a member of the Helmholtz Association HGF, for the provision of experimental facilities. Parts of this research were carried out at the beamline P02.2 of PETRA III. Beamtime was allocated for proposal I-20220041. Use of the GSECARS Raman Lab System was supported by the NSF MRI Proposal (EAR-1531583). Portions of this work were performed at GeoSoilEnviroCARS (The University of Chicago, Sector 13), Advanced Photon Source (APS), Argonne National Laboratory. GeoSoilEnviroCARS is supported by the National Science Foundation – Earth Sciences (EAR – 1634415). This research used resources of the Advanced Photon Source, a U.S. Department of Energy (DOE) Office of Science User Facility operated for the DOE Office of Science by Argonne National Laboratory under Contract No. DE-AC02-06CH11357.

M. E. and I. A. acknowledge support by the Knut and Alice Wallenberg Foundation (Wallenberg Scholar grant no. KAW-2018.0194). Support from the Swedish Research Council (VR) grant no. 2019-05600, the Swedish Government Strategic Research Area in Materials Science on Functional Materials at Linköping University (Faculty Grant SFO-Mat-LiU no. 2009 00971) and the Swedish Government Strategic Research Area the Swedish e-Science Research Centre is gratefully acknowledged. National Academic Infrastructure for Supercomputing in Sweden (NAISS) and the Swedish National Infrastructure for Computing (SNIC) partially funded by the Swedish Research Council through grant agreements no. 2022-06725 and no. 2018-05973 are acknowledged for awarding this project access to the LUMI supercomputer, owned by the EuroHPC Joint Undertaking, hosted by CSC (Finland) and the LUMI consortium.

The computations were also enabled by resources provided by the National Academic Infrastructure for Supercomputing in Sweden (NAISS) and the Swedish National Infrastructure for Computing (SNIC) at the National Supercomputer Centre (NSC) and PDC Center for High Performance Computing, partially funded by the Swedish Research Council through grant agreements no. 2022-06725 and no. 2018-05973.

N. F. and M. W. thank Prof. Martin Jansen for the donation of oxygen autoclaves used for the synthesis of PrO_2.

ABBREVIATIONS

APS, advanced photon source, bcc, body centered cubic; CCDC, Cambridge crystal structure database; CShM, calc., calculated, continuous shape measurements; DAC, diamond anvil cell; DESY, Deutsches Elektronen Synchrotron; DFG, Deutsche Forschungsgemeinschaft, DFT, density functional theory; DOE, Department of Energy; ESRF, European synchrotron radiation facility; fig., figure; GSECARS, GeoSoilEnviro Center for Advanced Radiation Sources; Ln, lanthanoid; NAISS, National Academic Infrastructure for Supercomputing in Sweden PAW, projection augmentor waves, PBEsol, Perdew-Burke-Ernzerhof generalized gradient approximation; PETRAIII, Positron-Elektron-Tandem-Ring-Anlage; SNIC, Swedish National Infrastructure for Computing tab., table; XRD, X-ray diffraction

REFERENCES

[1] S. T. Liddle, D. P. Mills, L. S. Natrajan, *Lanthanides And Actinides, The: Synthesis, Reactivity, Properties And Applications*, World Scientific, **2021**.

[2] *Lanthanum does form stable molecular compounds in the +2 oxidation state*, P. B. Hitchcock, M. F. Lappert, L. Maron, A. V. Protchenko, *Angew. Chem. Int. Ed.* **2008**, *120*, 1510-1513.

[3] *Expanding rare-earth oxidation state chemistry to molecular complexes of holmium (II) and erbium (II)*, M. R. MacDonald, J. E. Bates, M. E. Fieser, J. W. Ziller, F. Furche, W. J. Evans, *J. Am. Chem. Soc.* **2012**, *134*, 8420-8423.

[4] *Completing the series of +2 ions for the lanthanide elements: synthesis of molecular complexes of Pr^{2+}, Gd^{2+}, Tb^{2+}, and Lu^{2+}*, M. R. MacDonald, J. E. Bates, J. W. Ziller, F. Furche, W. J. Evans, *J. Am. Chem. Soc.* **2013**, *135*, 9857-9868.

[5] *Simple and complex halides*, G. Meyer, M. S. Wickleder, *Handbook on the Physics and Chemistry of Rare Earths* **2000**, *28*, 53-129.

[6] *Electron-transfer and f⟶ d absorption bands of some lanthanide and actinide complexes and the standard (III–IV) oxidation potentials for each member of the lanthanide and actinide series*, L. J. Nugent, R. D. Baybarz, J. L. Burnett, J. L. Ryan, *J. Inorg. Nucl. Chem.* **1971**, *33*, 2503-2530.

[7] *Thermochemical properties of yttrium, lanthanum, and the lanthanide elements and ions*, L. R. Morss, *Chem. Rev.* **1976**, *76*, 827-841.

[8] *Higher Oxides of the Lanthanide Elements. Terbium Dioxide*, D. M. Gruen, W. C. Koehler, J. J. Katz, *J. Am. Chem. Soc.* **1951**, *73*, 1475-1479.

[9] *Terbium Tetrafluoride: Preparation and Properties*, B. B. Cunningham, D. C. Feay, M. A. Rollier, *J. Am. Chem. Soc.* **1954**, *76*, 3361-3363.

[10] *Krypton difluoride reaction with cerium-, praseodymium- and terbium dioxides*, Y. M. Kiselev, V. B. Sokolov, *Zh. Neorg. Khim.* **1984**, *29*, 857-859.

[11] *Komplexe Fluoride seltener Erden: Cs_3TbF_7*, R. Hoppe, K.-M. Rödder, *Z. Anorg. Allg. Chem.* **1961**, *312*, 277-281.

[12] *Neue ternäre Oxide vierwertiger Seltener Erden und des Thoriums*, E. Paletta, R. Hoppe, *Naturwissenschaften* **1966**, *53*, 611-612.

[13] *Neue Oxoterbate (IV)*, R. Hoppe, K. Seeger, *Naturwissenschaften* **1968**, *55*, 297-297.

[14] *Über Li_8PrO_6 und Li_8TbO_6 (mit einer Bemerkung über Li_8CeO_6)*, R. Wolf, R. Hoppe, *Z. Anorg. Allg. Chem.* **1985**, *522*, 39-47.

[15] *Über Na_2PrO_3 und Na_2TbO_3*, R. Wolf, R. Hoppe, *Z. Anorg. Allg. Chem.* **1988**, *556*, 97-108.

[16] *Determination of the crystal structure of Li_2TbF_6 from X-ray and neutron powder diffraction. An example of lithium in five-fold coordination*, Y. Laligant, A. Le Bail, G. Ferey, D. Avignant, J. C. Cousseins, *Eur. J. Solid State Inorg. Chem.* **1988**, *25*.

[17] *Studies on the Higher Oxides of Some Rare-Earth Elements*, H. A. Pagel, P. H. M.-P. Brinton, *J. Am. Chem. Soc.* **1929**, *51*, 42-54.

[18] *The preparation of praseodymium tetrafluoride*, J. Soriano, M. Givon, J. Shamir, *Inorg. Nucl. Chem. Lett*, **1966**, *2*, 13-14.

[19] *Reactions of Lanthanide Atoms with Oxygen Difluoride and the Role of the Ln Oxidation State*, T. Mikulas, M. Chen, D. A. Dixon, K. A. Peterson, Y. Gong, L. Andrews, *Inorg. Chem.* **2014**, *53*, 446-456.

[20] *The structures of $BaCeO_3$, $BaPrO_3$ and $BaTbO_3$ by neutron diffraction: lattice parameter relations and ionic radii in O-perovskites*, A. J. Jacobson, B. C. Tofield, B. E. F. Fender, *Acta Cryst.* **1972**, *28*, 956-961.

[21] *Structure and Magnetic Properties of Tetravalent Praseodymium Perovskite $SrPrO_3$*, Y. Hinatsu, M. Itoh, N. Edelstein, *J. Solid State Chem.* **1997**, *132*, 337-341.

[22] *Ein neues Oxopraseodymat(IV): Li_2PrO_3*, V. R. Wolf, R. Hoppe, *J. Solid State Chem.* **1987**, *70*, 12-18.

[23] *Über Ordnungsvarianten des NaCl-Typs. Neue kubische Formen von $NaMO_2$ (M= Sc, Y, Dy, Tm, Yb, Lu), K_2MO_3 Rb_2MO_3,(M= Ce, Pr, Th) und Cs_2ThO_3*, H. Brunn, R. Hoppe, *Z. Anorg. Allg. Chem.* **1977**, *430*, 144-154.

[24] L. B. Asprey, J. S. Coleman, M. J. Reisfeld, in *Advances in Chemistry, Vol. 71*, ACS Publications, **1967**, pp. 122-126.

[25] G. Meyer, L. R. Morss, *Synthesis of lanthanide and actinide compounds, Vol. 2*, Springer Science & Business Media, **2012**.

[26] *One-pot Hydrothermal Synthesis of $Tb^{III13}(GeO_4)_6O_7(OH)$ and $K_2Tb^{IV}Ge_2O_7$: Preparation of a Stable Terbium (4+) Complex*, K. Fulle, L. D. Sanjeewa, C. D. McMillen, Y. Wen, A. C. Rajamanthrilage, J. N. Anker, G. Chumanov, J. W. Kolis, *Inorg. Chem.* **2017**, *56*, 6044-6047.

[27] *$Cs_3RE^{III}Ge_3O_9$ (RE= Pr, Nd, and Sm–Yb) and $Cs_8Tb^{III2}Tb^{IV}Ge_9O_{27}$: a Rare Example of a Mixed-Valent Tb (III)/Tb (IV) Oxide*, G. Morrison, N. R. Spagnuolo, S. G. Karakalos, H.-C. Zur Loye, *Inorg. Chem.* **2019**, *58*, 8702-8709.

[28] *Molecular Complex of Tb in the +4 Oxidation state*, C. T. Palumbo, I. Zivkovic, R. Scopelliti, M. Mazzanti, *J. Am. Chem. Soc.* **2019**, *141*, 9827-9831.

[29] *Design, Isolation, and Spectroscopic Analysis of a Tetravalent Terbium Complex*, N. T. Rice, I. A. Popov, D. R. Russo, J. Bacsa, E. R. Batista, P. Yang, J. Telser, H. S. La Pierre, *J. Am. Chem. Soc.* **2019**, *141*, 13222-13233.

[30] *Stabilization of the Oxidation State +IV in Siloxide-Supported Terbium Compounds*, A. R. Willauer, C. T. Palumbo, R. Scopelliti, I. Zivkovic, I. Douair, L. Maron, M. Mazzanti, *Angew. Chem. Int. Ed.* **2020**, *59*, 3549-3553.

[31] *Accessing the+ IV Oxidation State in Molecular Complexes of Praseodymium*, A. R. Willauer, C. T. Palumbo, F. Fadaei-Tirani, I. Zivkovic, I. Douair, L. Maron, M. Mazzanti, *J. Am. Chem. Soc.* **2020**, *142*, 5538-5542.

[32] *Comparison of tetravalent cerium and terbium ions in a conserved, homoleptic imidophosphorane ligand field*, N. T. Rice, I. A. Popov, D. R. Russo, T. P. Gompa, A. Ramanathan, J. Bacsa, E. R. Batista, P. Yang, H. S. La Pierre, *Chem. Sci.* **2020**, *11*, 6149-6159.

[33] *The chemical and physical properties of tetravalent lanthanides: Pr, Nd, Tb, and Dy*, T. P. Gompa, A. Ramanathan, N. T. Rice, H. S. La Pierre, *Dalton Trans.* **2020**, *49*, 15945-15987.

[34] *Structure, reactivity and luminescence studies of triphenylsiloxide complexes of tetravalent lanthanides*, A. R. Willauer, I. Douair, A.-S. Chauvin, F. Fadaei-Tirani, J.-C. G. Bünzli, L. Maron, M. Mazzanti, *Chem. Sci.* **2022**, *13*, 681-691.

[35] *Spectroscopic and electrochemical characterization of a Pr^{4+} imidophosphorane complex and the redox chemistry of Nd^{3+} and Dy^{3+} complexes*, N. T. Rice, I. A. Popov, R. K. Carlson, S. M. Greer, A. C. Boggiano, B. W. Stein, J. Bacsa, E. R. Batista, P. Yang, H. S. La Pierre, *Dalton Trans.* **2022**, *51*, 6696-6706.

[36] *Chemical design of electronic and magnetic energy scales of tetravalent praseodymium materials*, A. Ramanathan, J. Kaplan, D.-C. Sergentu, J. A. Branson, M. Ozerov, A. I. Kolesnikov, S. G. Minasian, J. Autschbach, J. W. Freeland, Z. Jiang, M. Mourigal, H. S. La Pierre, *Nat. Commun.* **2023**, *14*, 3134.

[37] R. Hoppe, in *The Rare Earths in Modern Science and Technology: Volume 3* (Eds.: G. J. McCarthy, H. B. Silber, J. J. Rhyne, F. M. Kalina), Springer US, Boston, MA, **1982**, pp. 315-315.

[38] *Core-level spectroscopy of the tetravalent lanthanide compounds M_3LnF_7 (with M = Cs, Rb; Ln = Ce, Pr, Nd, Tb, Dy)*, Z. Hu, G. Kaindl, B. G. Müller, *J. Alloys Compd.* **1997**, *246*, 177-185.

[39] *Extending the Row of Lanthanide Tetrafluorides: A Combined Matrix-Isolation and Quantum-Chemical*

Study, T. Vent-Schmidt, Z. Fang, Z. Lee, D. Dixon, S. Riedel, *Chem. Eur. J.* **2016**, *22*, 2406-2416.

[40] *High-Pressure Synthesis and Crystal Structure of Neodymium(III) Oxide Peroxide, $Nd_2O_2(O_2)$*, K.-J. Range, M. Stadler, F. Rau, U. Klement, *Angew. Chem. Int. Ed.* **1987**, *26*, 1174-1175.

[41] *A raman study of neodymium(III) oxide peroxide, $Nd_2O_2(O_2)$, at ambient and high pressures*, A. M. Heyns, K.-J. Range, *J. Alloys Compd.* **1991**, *176*, L17-L21.

[42] *Raman and infrared study of neodymium oxide peroxide, $Nd_2O_2(O_2)$*, A. M. Heyns, K.-J. Range, *J. Raman Spectrosc.* **1994**, *25*, 855-859.

[43] *Investigation of Praseodymium Fluorides: A Combined Matrix-Isolation and Quantum-Chemical Study*, T. Vent-Schmidt, S. Riedel, *Inorg. Chem.* **2015**, *54*, 11114-11120.

[44] *Pentavalent Lanthanide Compounds: Formation and Characterization of Praseodymium(V) Oxides*, Q. Zhang, S.-X. Hu, H. Qu, J. Su, G. Wang, J.-B. Lu, M. Chen, M. Zhou, J. Li, *Angew. Chem. Int. Ed.* **2016**, *55*, 6896-6900.

[45] *Pentavalent lanthanide nitride-oxides: NPrO and $NPrO^-$ complexes with N-Pr triple bonds*, S.-X. Hu, J. Jian, J. Su, X. Wu, J. Li, M. Zhou, *Chem. Sci.* **2017**, *8*, 4035-4043.

[46] *Chemical evidence of the stability of praseodymium(V) in gas-phase oxide nitrate complexes*, B. Monteiro, N. A. Bandeira, C. Lourenço, A. F. Lucena, J. M. Carretas, J. K. Gibson, J. Marçalo, *Chem. Commun.* **2019**, *55*, 14139-14142.

[47] *Pressure-stabilized divalent ozonide CaO_3 and its impact on Earth's oxygen cycles*, Y. Wang, M. Xu, L. Yang, B. Yan, Q. Qin, X. Shao, Y. Zhang, D. Huang, X. Lin, J. Lv, D. Zhang, H. Gou, H.-K. Mao, C. Chen, Y. Ma, *Nat. Commun.* **2020**, *11*, 4702.

[48] *Synthesis and stability of xenon oxides Xe_2O_5 and Xe_3O_2 under pressure*, A. Dewaele, N. Worth, C. J. Pickard, R. J. Needs, S. Pascarelli, O. Mathon, M. Mezouar, T. Irifune, *Nat. Chem.* **2016**, *8*, 784-790.

[49] *FeO_2 and FeOOH under deep lower-mantle conditions and Earth's oxygen–hydrogen cycles*, Q. Hu, D. Y. Kim, W. Yang, L. Yang, Y. Meng, L. Zhang, H.-K. Mao, *Nature* **2016**, *534*, 241-244.

[50] *Gold with +4 and +6 Oxidation States in AuF_4 and AuF_6*, J. Lin, S. Zhang, W. Guan, G. Yang, Y. Ma, *J. Am. Chem. Soc.* **2018**, *140*, 9545-9550.

[51] *IrF_8 Molecular Crystal under High Pressure*, J. Lin, Z. Zhao, C. Liu, J. Zhang, X. Du, G. Yang, Y. Ma, *J. Am. Chem. Soc.* **2019**, *141*, 5409-5414.

[52] *Caesium in high oxidation states and as a p-block element*, M.-S. Miao, *Nat. Chem.* **2013**, *5*, 846-852.

[53] *Stable magnesium peroxide at high pressure*, S. S. Lobanov, Q. Zhu, N. Holtgrewe, C. Prescher, V. B. Prakapenka, A. R. Oganov, A. F. Goncharov, *Sci. Rep.* **2015**, *5*, 13582.

[54] *Stability of the peroxide group in BaO_2 under high pressure*, X. Zhang, X. Luo, M. Bykov, E. Bykova, I. Chuvashova, D. Butenko, S. Chariton, V. Prakapenka, D. Smith, H. Wang, Y. Wang, J. Lv, A. F. Goncharov, *Phys. Rev. B* **2021**, *103*, 094104.

[55] A. Haberer, H. Huppertz, Wiley Online Library, **2010**.

[56] *Calcium peroxide from ambient to high pressures*, J. R. Nelson, R. J. Needs, C. J. Pickard, *Phys. Chem. Chem. Phys.* **2015**, *17*, 6889-6895.

[57] *Continuous Shape Measures as a Stereochemical Tool in Organometallic Chemistry*, J. Cirera, E. Ruiz, S. Alvarez, *Organometallics* **2005**, *24*, 1556-1562.

[58] *Revised effective ionic radii and systematic studies of interatomic distances in halides and chalcogenides*, R. D. Shannon, *Acta Crystallogr. A* **1976**, *32*, 751-767.

[59] *Finite elastic strain of cubic crystals*, F. Birch, *Phys. Rev.* **1947**, *71*, 809.

[60] *Advanced integrated optical spectroscopy system for diamond anvil cell studies at GSECARS*, N. Holtgrewe, E. Greenberg, C. Prescher, V. B. Prakapenka, A. F. Goncharov, *High Press. Res.* **2019**, *39*, 457-470.

[61] *Orthorhombic HP-PrO_2 – High-Pressure Synthesis and Crystal Structure*,, A. Haberer, H. Huppertz, *Z. Anorg. Allg. Chem.* **2010**, *636*, 363-367.

[62] *Single-crystal diffractometer coupled with double-sided laser heating system at the Extreme Conditions Beamline P02.2 at PETRAIII*, E. Bykova, G. Aprilis, M. Bykov, K. Glazyrin, M. Wendt, S. Wenz, H.-P. Liermann, J. T. Roeh, A. Ehnes, N. Dubrovinskaia, L. Dubrovinsky, *Rev. Sci. Instrum.* **2019**, *90*, 073907.

[63] *The Extreme Conditions Beamline P02.2 and the Extreme Conditions Science Infrastructure at PETRA III*, H.-P. Liermann, Z. Konopkova, W. Morgenroth, K. Glazyrin, J. Bednarcik, E. E. McBride, S. Petitgirard, J. T. Delitz, M. Wendt, Y. Bican, A. Ehnes, I. Schwark, A. Rothkirch, M. Tischer, J. Heuer, H. Schulte-Schrepping, T. Kracht, H. Franz, *J. Synchrotron Rad.* **2015**, *22*, 908-924.

[64] *Strategies for in situ laser heating in the diamond anvil cell at an X-ray diffraction beamline*, S. Petitgirard, A. Salamat, P. Beck, G. Weck, P. Bouvier, *J. Synchrotron Rad.* **2014**, *21*, 89-96.

[65] *Pressure calibration of diamond anvil Raman gauge to 310 GPa*, Y. Akahama, H. Kawamura, *J. Appl. Phys.* **2006**, *100*, 043516.

[66] *Domain Auto Finder (DAFi) program: the analysis of single-crystal X-ray diffraction data from polycrystalline samples*, A. Aslandukov, M. Aslandukov, N. Dubrovinskaia, L. Dubrovinsky, *J. Appl. Crystallogr.* **2022**, *55*, 1383-1391.

[67] *A short history of SHELX*, G. M. Sheldrick, *Acta Crystallogr. A* **2008**, *64*, 112-122.

[68] *OLEX2: a complete structure solution, refinement and analysis program*, O. V. Dolomanov, L. J. Bourhis, R.

J. Gildea, J. A. K. Howard, H. Puschmann, *J. Appl. Crystallogr*. **2009**, *42*, 339-341.

[69] *Inhomogeneous Electron Gas*, P. Hohenberg, W. Kohn, *Phys. Rev.* **1964**, *136*, B864-B871.

[70] *Self-Consistent Equations Including Exchange and Correlation Effects*, W. Kohn, L. J. Sham, *Phys. Rev.* **1965**, *140*, A1133-A1138.

[71] *Projector augmented-wave method*, P. E. Blöchl, *Phys. Rev. B* **1994**, *50*, 17953-17979.

[72] *From ultrasoft pseudopotentials to the projector augmented-wave method*, G. Kresse, D. Joubert, *Phys. Rev. B* **1999**, *59*, 1758.

[73] *Ab initio molecular dynamics for liquid metals*, G. Kresse, J. Hafner, *Phys. Rev. B* **1993**, *47*, 558.

[74] *Efficiency of ab-initio total energy calculations for metals and semiconductors using a plane-wave basis set*, G. Kresse, J. Furthmüller, *Comput. Mater. Sci.* **1996**, *6*, 15-50.

[75] *Efficient iterative schemes for ab initio total-energy calculations using a plane-wave basis set*, G. Kresse, J. Furthmüller, *Phys. Rev. B* **1996**, *54*, 11169.

[76] *Restoring the Density-Gradient Expansion for Exchange in Solids and Surfaces*, J. P. Perdew, A. Ruzsinszky, G. I. Csonka, O. A. Vydrov, G. E. Scuseria, L. A. Constantin, X. Zhou, K. Burke, *Phys. Rev. Lett.* **2008**, *100*, 136406.

[77] *Band theory and Mott insulators: Hubbard U instead of Stoner I*, V. I. Anisimov, J. Zaanen, O. K. Andersen, *Phys. Rev. B* **1991**, *44*, 943.

[78] *Electron-energy-loss spectra and the structural stability of nickel oxide: An LSDA+ U study*, S. L. Dudarev, G. A. Botton, S. Y. Savrasov, C. J. Humphreys, A. P. Sutton, *Phys. Rev. B* **1998**, *57*, 1505.

4.2 Divalent Lanthanoids

4.2.1 Structure, Magnetism and Luminescence of $Eu(OTf)_2(CH_3CN)$ and $Sm(OTf)_2(CH_3CN)$ (*Manuscript 4*)

The first milestone to be accomplished within the field of divalent lanthanoids was to establish an efficient and reliable method of producing their triflates. As described in ***Manuscript 4***, $Eu(OTf)_2$ and $Sm(OTf)_2$ were synthesised by comproportionation of $Ln(OTf)_3$ and Ln^0 (Ln = Sm, Eu) and subsequently crystallised as solvates with acetonitrile. In order to obtain a suitable host-lattice for optical spectroscopy, the isostructural strontium triflate $Sr(OTf)_2(MeCN)$ was synthesised, as well. Next to the crystallographic description, the triflates were characterised with respect to their thermal decomposition, by vibrational spectroscopy, electrochemically and magnetochemically. Additionally, their optical properties were investigated by luminescence and reflectance spectroscopy.

The author's contribution include the experimental work, data analysis and writing of the manuscript in collaboration with the coauthors. Electrochemical experiments were performed in collaboration with B. Rasche, magnetochemical measurements were carried out in collaboration with L. Rochels and S. Disch. Experiments addressing the luminescence of the triflates were conducted by P. Fischer and M. Adlung who also wrote the respective sections of the manuscript. Most parts of the introduction of ***Manuscript 4*** were written by M. Wickleder and M. Adlung.

Supporting information of ***Manuscript 4*** is provided in section 7.1.

The Divalent Lanthanoid Triflates $Ln(CF_3SO_3)_2(CH_3CN)$ (Ln = Sm, Eu): Structure, Luminescence and Magnetism

Niko T. Flosbach[1], Bertold Rasche[2], Leonhard Rochels[3], Sabrina Disch[3], Claudia Wickleder[4], Matthias Adlung[4], Pia Fischer[4], Mathias S. Wickleder*[1]

[1]University of Cologne, Institute of Inorganic Chemistry, Greinstr. 6, 50939 Cologne, Germany

[2]Institute of Inorganic Chemistry, University of Stuttgart, Pfaffenwaldring 55, 70569 Stuttgart, Germany

[3]Anorganische Chemie und Center for Nanointegration Duisburg-Essen (CENIDE), University of Duisburg-Essen, Universitätsstraße 5-7, 45141 Essen, Germany

[4]Institute of Inorganic Chemistry, University of Siegen, Adolf-Reichwein-Straße, 57068 Siegen, Germany

ABSTRACT: The reaction of the trivalent lanthanide triflates $Ln(OTf)_3$ (Ln = Sm, Eu) with the respective metals in acetonitrile leads to the Ln(II)-triflates $Eu(OTf)_2(CH_3CN)$ (monoclinic, $P2_1/n$, $Z = 4$, $a = 1053.54(1)$, $b = 610.28(5)$, $c = 1946.92(2)$ pm, $\beta = 98.611(4)$) and $Sm(OTf)_2(CH_3CN)$ (monoclinic, $P2_1/n$, $Z = 4$, $a = 1054.41(4)$, $b = 612.16(2)$, $c = 1952.65(7)$ pm, $\beta = 98.524(2)$). The isotypic strontium compound $Sr(OTf)_2(CH_3CN)$ (monoclinic, $P2_1/n$, $Z = 4$, $a = 1056.39(5)$, $b = 610.05(3)$, $c = 1950.1(1)$ pm, $\beta = 98.900(2)°$) has been obtained from $SrCO_3$ and triflic acid. The compounds have been investigated by X-ray diffraction, vibrational spectroscopy, luminescence spectroscopy, cyclic voltammetry, thermal analysis, and magnetic measurements.

INTRODUCTION

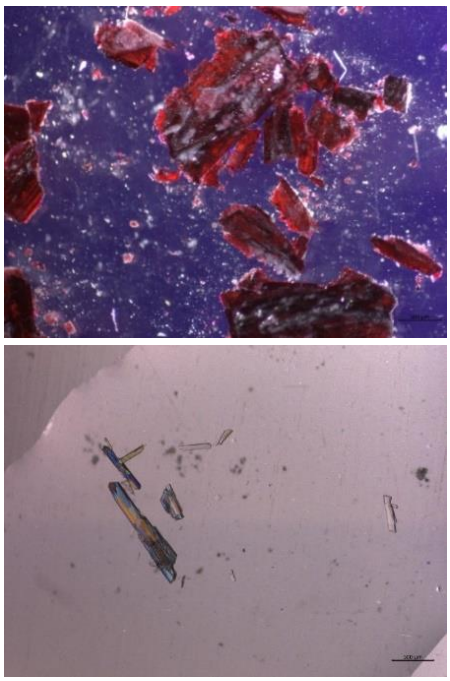
The chemistry of the lanthanoids is strongly stamped by the trivalent oxidation state because the *f*-electrons of these elements are strongly shielded and are essentially not involved in chemical bonding.[1-4] On the other hand, the well-shielded electrons lead to unique physical properties of the Ln^{3+}-ions, and especially their luminescence and their magnetism have attracted significant attention that has led to various applications.[5-9] The luminescence of most Ln^{3+}-ions is based on *f-f*-transitions which are very sharp due to the shielding of the electrons and almost independent of the nature of the host lattice. On the other hand, *f-f*-transitions are parity forbidden and thus their intensities are low.[1-4] For some of the lanthanoids the divalent oxidation state is also known. The Ln^{2+} ions are especially stable if this oxidations state leads to a filled (f^{14}, Yb^{2+}) or half-filled (f^7, Eu^{2+}) *f*-shell. Moreover, the metals neighboring Yb and Eu, namely Tm and Sm are known to be fairly stable in this oxidation state, as well.[10-12] The optical spectroscopy of Ln^{2+}-ions is highly interesting because they show not only *f-f*- but also *f-d*-transitions. The latter are parity allowed transitions, i.e. their intensities are strong compared to those of the *f-f*-transitions. However, in contrast to the latter, *f-d*-transitions are strongly influenced by the ion's surrounding because the *d*-states are not shielded.[13] Thus, the spectroscopic properties of divalent lanthanoids can vary significantly in different host lattices. The most well-researched class of compounds of divalent lanthanoids are certainly halides. The dihalides LnX_2 are known for Ln = Sm, Eu, Tm, Yb with X = Cl, Br, I and for Sm and Eu also for X = F. Moreover, several ternary Ln^{2+} halides have been reported.[14] The luminescence properties of various halides have been investigated, including measurements on "diluted" samples using the Sr^{2+} and Ca^{2+} halides as host lattices.[15-16] It turned out that the competition between *f-f*- and *f-d*-transitions is not only a question of the host lattice but also depends on the temperature. In a joint project we now started the investigation of divalent lanthanoid ions in oxoanionic environments. Compared to the halides mentioned above, the number of reliably characterized oxoanionic Ln^{2+}-species is very limited. The most well-known compounds are probably $EuSO_4$ and $EuCO_3$, which have been reported almost 60 years ago for the first time.[17] Subsequently, $EuSO_4$ and its properties have been characterized various times. However, a single crystal structure determination is still missing.[18-19] Another class of oxoanionic Ln^{2+}-compounds that has attracted considerable interest is that of the trifluoromethanesulfonates, the so-called "triflates". By far the most of the reports are devoted to the reactions of samarium triflate, $Sm(OTf)_2$. These investigations are inspired by *Kagan´*s break-through observation, that samarium diiodide, SmI_2, is a suitable chemical reagent for single electron reduction reactions in organic chemistry.[20] $Sm(OTf)_2$ can be generated in organic solvents by various methods, for example by *Grignard* reactions,[21] comproportionation routes,[22] and electrochemical synthesis.[23] The tetrahydrofuran (C_5H_8O, THF) solvate $Sm(OTf)_2(THF)_{1.5}$ has been obtained in crystalline form by reacting metallic samarium with a triflate derived from 1,5-dithioniabicyclo[3.3.0]octane, so that its crystal structure could be determined.[24] Further reactions have been carried out in acetonitrile (CH_3CN) and dimethoxyethane (DME), however without structural investigations.[25-26] A valuable review on coupling

reactions based on Sm^{2+} was published in 2012.[27] Quite recently, DME turned out to be also a suitable solvent for the reduction of $Tm(OTf)_3$ by KC_8, and the solvate $Tm(OTf)_2(DME)_2$ was characterized.[28]

In this work we show that the triflates of divalent europium and samarium can be conveniently prepared in acetonitrile in form of the solvates $Ln(OTf)_2(CH_3CN)$ (Ln = Sm, Eu). The crystal structure of the compounds has been elucidated. Moreover, their magnetic and luminescence properties were studied and electrochemical investigations were performed. Furthermore, the isotypic strontium triflate, $Sr(OTf)_2(CH_3CN)$, has been characterized as a host lattice for Sm^{2+} and Eu^{2+}, respectively.

RESULTS AND DISCUSSION

Syntheses $Eu(OTf)_3$ and $Sm(OTf)_3$ were synthesized by dissolving the commercially available sesquioxides in aqueous triflic acid, yielding the respective nonahydrates. The hydrates were heated to 275 °C under dynamic vacuum until no more vibrational bands of water could be detected by IR-spectroscopy. $Sr(OTf)_2$ was prepared by dissolving $SrCO_3$ in aqueous triflic acid and subsequent dehydration under dynamic vacuum at 275 °C until the absence of water was confirmed by IR-spectroscopy. The anhydrous triflates were reacted with freshly filed Ln^0 metal in acetonitrile. In the case of Sm, one drop of mercury was added to the mixture. Sonication of the mixtures afforded deeply colored solutions. Filtration of excess metal and evaporation of the filtrate yielded $Ln(OTf)_2(CH_3CN)$ (Ln = Sm, Eu) in excellent yields. Single crystals of the compounds were obtained by slow evaporation of the solvent. $Sr(OTf)_2(CH_3CN)$ could be crystallized from solutions of $Sr(OTf)_2$ in CH_3CN. The Sm(II) compound is deep-red, the Eu(II) and the Sr(II) triflate are colorless (fig. 1). Details of the syntheses are given in the supporting information.



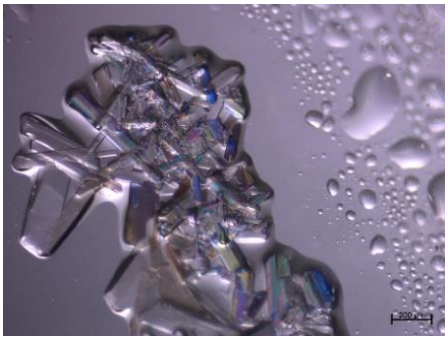


Figure 1. Microscopic photos of single crystals of $Sm(OTf)_2(CH_3CN)$ (top), $Eu(OTf)_2(CH_3CN)$ (middle) and $Sr(OTf)_2(CH_3CN)$ (bottom).

Crystal structures The triflates $Ln(OTf)_2(CH_3CN)$ (Ln = Sm, Eu, **1-Sm** and **1-Eu**) and $Sr(OTf)_2(CH_3CN)$ (**1-Sr**) are isotypic and crystallize in the monoclinic crystal system with the space group $P2_1/n$. All atoms are situated on a general site of this space group (Wyckoff symbol 4*e*). The structure will be discussed on the example of the samarium compound. Detailed data for all compounds are summarized in tab. 1. and tab. 2. Further information can be found in the SI (supplementary material).

In the crystal structure of $Sm(OTf)_2(CH_3CN)$ the Sm^{2+}-ions are coordinated by oxygen atoms of six monodentate triflate anions and by the nitrogen atom of the CH_3CN solvent molecule. The triflate anions belong to two crystallographically different species. The resulting $[SmO_6N]$ polyhedron is best described as a distorted mono-capped trigonal prism (continuous shape measures, $CShM^{29}$ = 0.886). The Sm-O distances range from 249.6(1) pm (Sm1-O2) to 257.7(1) pm (Sm1-O6), averaging at 254(3) pm. The Sm-N distance is significantly longer and found at 271.6(2) pm.

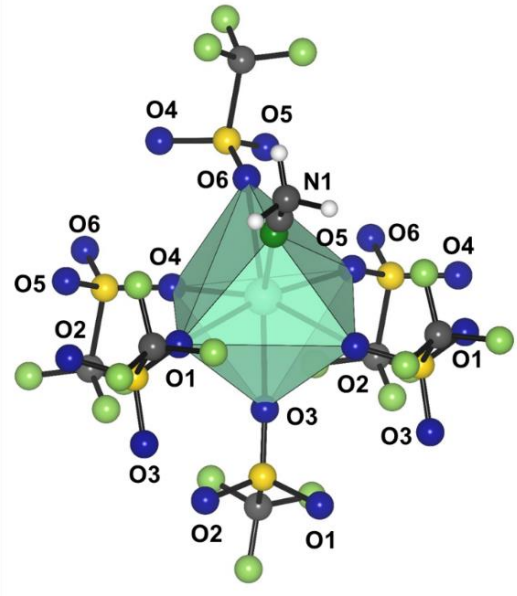


Figure 2. Coordination polyhedron around the Sm^{2+}-ions in the crystal structure of $Sm(OTf)_2(CH_3CN)$.

The distances between the Sm^{2+}-ion and the coordinating atoms are significantly longer than those in comparable com-

plexes of Sm^{3+}, which agrees with the expected behavior for divalent samarium.[30] The same argument is made for **1-Eu**.[31] The coordination geometries of **1-Sm, 1-Eu** and **1-Sr** are shown in fig. 3.

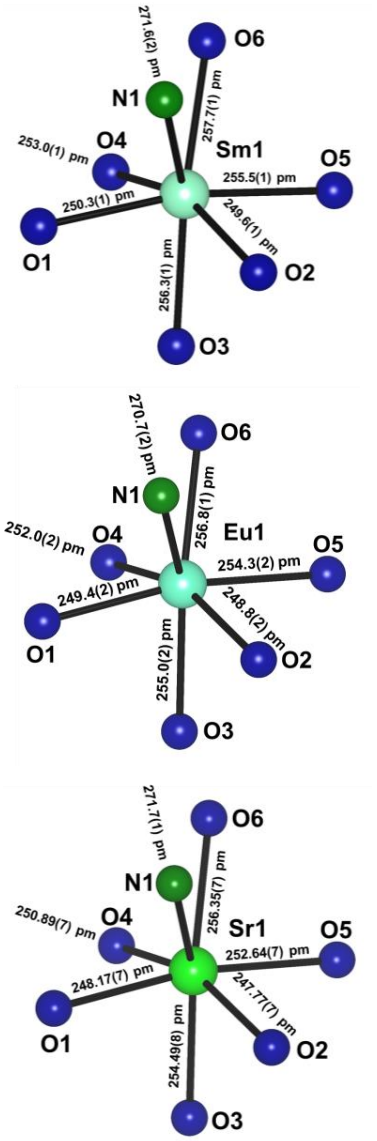


Figure 3. Coordination polyhedra around Sm^{2+}, Eu^{2+} and Sr^{2+} in $Ln(OTf)_2(CH_3CN)$ and $Sr(OTf)_2(CH_3CN)$.

The bond lengths in the coordination sphere of the different metal ions are very similar to each other, although most of them marginally decrease from Sm^{2+} over Eu^{2+} to Sr^{2+} because of their slightly different ionic radii ($r(Sm^{2+})$ = 122 pm; $r(Eu^{2+})$ = 120 pm; $r(Sr^{2+})$ = 121 pm, all values given for 7-fold coordination).[32]

Each triflate anion acts as a μ_3-bridging ligand between three adjacent metal centers, resulting in a two-dimensional network of $[SmO_6N]$-polyhedra that forms curved layers along the crystallographic *b*-axis and the [101]-direction. The layers are connected by interactions of CF_3-groups of the triflate anions, as evidenced by the short distance of fluorine atoms of neighboring triflate anions reaching as low as 275.0(2) pm (F2-F4).

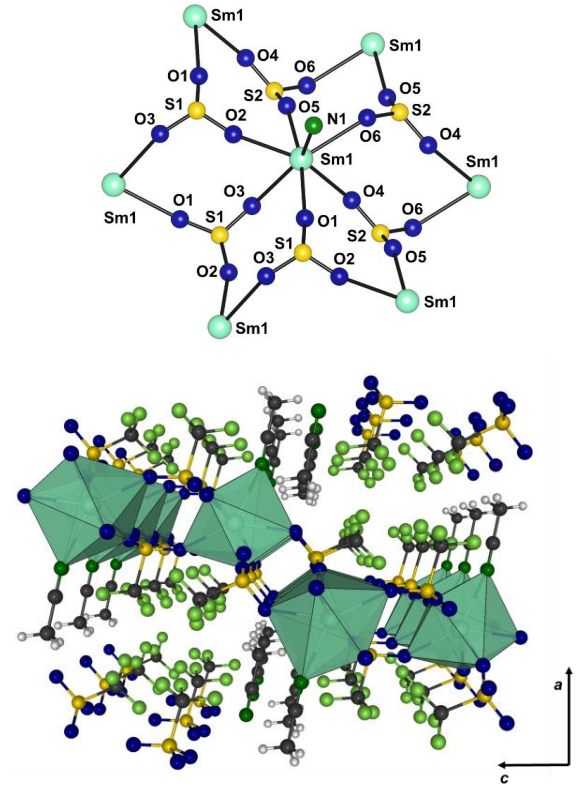


Figure 4. Top: Bridging modes of the triflate anions between the metal ions (CF_3-groups were omitted for clarity). Bottom: Three-dimensional view of the unit cell viewed along the crystallographic *b*-axis.

Table 1. Summary of selected interatomic distances in $Sm(OTf)_2(CH_3CN)$, $Eu(OTf)_2(CH_3CN)$ and $Sr(OTf)_2(CH_3CN)$. All data are given in units of pm.

1-Sm		**1-Eu**		**1-Sr**	
Sm1-O1	250.3(1)	Eu1-O1	249.4(2)	Sr1-O1	248.17(7)
Sm1-O2	249.6(1)	Eu1-O2	248.8(2)	Sr1-O2	247.77(7)
Sm1-O3	256.3(1)	Eu1-O3	255.0(2)	Sr1-O3	254.49(8)
Sm1-O4	253.0(1)	Eu1-O4	252.0(2)	Sr1-O4	250.89(7)
Sm1-O5	255.5(1)	Eu1-O5	254.3(2)	Sr1-O5	252.64(7)
Sm1-O6	257.7(1)	Eu1-O6	256.8(1)	Sr1-O6	256.35(7)
Sm1-N1	271.6(2)	Eu1-N1	270.7(2)	Sr1-N1	271.7(1)
F1-F4	309.1(2)	F1-F4	308.6(3)	F1-F4	309.15(9)
F2-F4	275.0(2)	F2-F4	274.1(3)	F2-F4	274.67(9)
F2-F6	279.5(1)	F2-F6	278.3(2)	F2-F6	278.03(9)
F3-F4	290.5(2)	F3-F4	289.8(3)	F3-F4	292.6(1)

F3-F6	315.7(2)	F3-F6	314.3(2)	F3-F6	311.5(1)

Crystallographic Data

Table 2. Selected crystallographic data of $Sm(OTf)_2(MeCN)$, $Eu(OTf)_2(MeCN)$ and $Sr(OTf)_2(MeCN)$.

Compound	**1-Sm**	**1-Eu**	**1-Sr**
Chemical Formula	$C_4H_3SmF_6NO_6S_2$	$C_4H_3EuF_6NO_6S_2$	$C_4H_3SrF_6NO_6S_2$
Molar Mass	489.54 g/mol	491.15 g/mol	426.81 g/mol
Temperature	100(2) K	100(2) K	100(2) K
Crystal System	monoclinic	monoclinic	monoclinic
Space Group	$P2_1/n$	$P2_1/n$	$P2_1/n$
Lattice Parameters	a = 1054.41(4) pm	a = 1053.54(1) pm	a = 1056.39(5) pm
	b = 612.16(2) pm	b = 610.28(5) pm	b = 610.05(3) pm
	c = 1952.65(7) pm	c = 1946.92(2) pm	c = 1950.1(1) pm
	β = 98.524(2)°	β = 98.611(4)°	β = 98.900(2)°
Cell Volume	1246.45(8) Å^3	1237.7(2) Å^3	1241.6(1) Å^3
Formula Units	4	4	4
Calculated Density	2.609 g/cm^3	2.636 g/cm^3	2.283 g/cm^3
Absorption Correction	multi-scan	multi-scan	multi-scan
Absorption Coefficient	5.146 mm^{-1}	5.506 mm^{-1}	4.779 mm^{-1}
F(000)	920.0	924.0	824.0
Crystal Size	0.428 mm × 0.175 mm × 0.133 mm	0.22 mm × 0.05 mm × 0.02 mm	0.424 mm × 0.236 mm × 0.067 mm
Radiation	Mo-Kα (λ = 0.71073)	Mo-Kα (λ = 0.71073)	Mo-Kα (λ = 0.71073)
2θ-Range	4.218° to 68.674°	4.232° to 71.262°	4.228° to 78.744°
Index Range	-16 ≤ h ≤ 16; -9 ≤ k ≤ 9; -30 ≤ l ≤ 30	-17 ≤ h ≤ 12; -8 ≤ k ≤ 9; -31 ≤ l ≤ 26	-16 ≤ h ≤ 16; -9 ≤ k ≤ 10; -33 ≤ l ≤ 33
Reflections Collected	119850	12133	39557
Independent Reflections	5214 (R_{int} = 0.0492, R_σ = 0.0182)	4954 (R_{int} = 0.0446, R_σ = 0.0455)	5630 (R_{int} = 0.0418, R_σ = 0.0274)
Data/Restraints/Parameters	5214/0/183	4954/0/182	5630/3/193
Goodness of Fit	1.226	1.076	1.065
R_1; wR_2 ($I \geq 2\sigma(I_o)$)	0.0157; 0.0385	0.0249; 0.0511	0.0194; 0.0469
R_1; wR_2 (All Data)	0.0158; 0.0385	0.0350; 0.0526	0.0238; 0.0478
Largest Diff. Peak/Hole	1.55 e/Å^3; -0.94 e/Å^3	1.78 e/Å^3; -0.97 e/Å^3	0.68 e/Å^3; -0.63 e/Å^3

Thermal Decomposition In order to research the thermal stability of the title compounds, differential thermal analysis coupled with thermogravimetry (DTA-TG) experiments were performed. The thermal decompositions of **1-Eu** and **1-Sm** are very similar and will be discussed exemplarily for **1-Sm** for which the DTA-TG diagram is depicted in fig. 5.

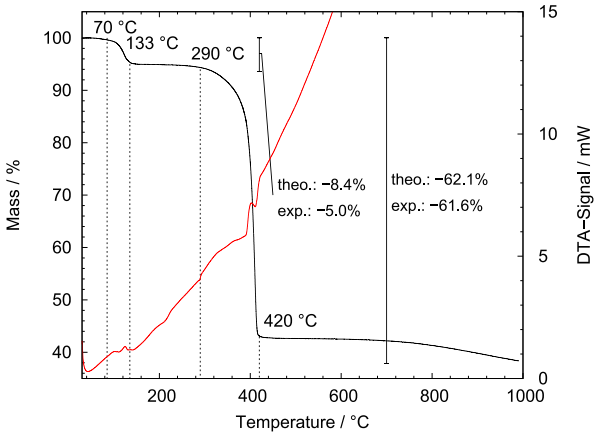
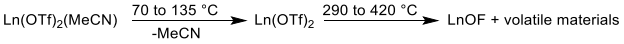


Figure 5. DTA-TG of $Sm(OTf)_2(CH_3CN)$. The mass curve is shown in black and the DTA-signal is depicted as a red curve. Mass differences shown in the diagram correspond to the theoretical mass losses for the proposed decomposition pathway to $Sm(OTf)_2$ and SmOF, and the experimental mass losses, respectively. The data were collected under nitrogen flow with a constant heating rate of 5 °C/min.

The decomposition of **1-Sm** proceeds via two steps. The first step begins at approximately 70 °C and can be attributed to the loss of acetonitrile from the lattice. The DTA-signal shows a very weak endothermic peak for the desolvation, indicating that the acetonitrile is only weakly bound in the structure. The experimental mass loss (ca. 5%) is marginally smaller than the calculated mass loss, which is likely to be a result of acetonitrile escaping from the structure during the preparation or storage of the material.



Scheme 1: Proposed decomposition pathway of $Ln(OTf)_2(CH_3CN)$ (Ln = Sm, Eu).

The desolvated triflates are metastable to ca. 290 °C in the case of **1-Sm** and 350 °C in the case of **1-Eu** (see SI). Both solvent-free triflates were isolated by heating the acetonitrile adducts to 220 °C under dynamic vacuum (see SI for analytical data), proving the metastability of the +II oxidation state in the triflates, even under elevated temperatures. However, when ac-

etonitrile solutions of $Sm(OTf)_2$ were heated in sealed glass ampoules, their characteristic green color faded and slowly disappeared even at temperatures as low as 60 °C.

The desolvated triflate of Sm^{2+} starts to decompose at ca. 290 °C (350 °C for **1-Eu**) and converts into SmOF, along with volatile components that were not further analyzed. Notably, the Ln^{2+}-cations are oxidized to their trivalent oxidation states during this final process. The differences in thermal stability of $Ln(OTf)_2$ are in line with the expected behavior of Sm^{2+} being the more strongly reducing ion, hence leading to higher fragility of its compounds.

The thermal decomposition of **1-Sr** is very similar to those of **1-Sm** and **1-Eu**, with the obvious difference that the decomposition of the desolvated triflate does not accompany redox processes. Instead of converting into LnOF, SrF_2 is formed. For more details, refer to fig. S 22 and S 23 in the SI.

Electrochemistry Cyclic Voltammetry of **1-Sm** and **1-Eu** (dissolved in acetonitrile) was used to study the redox pairs of Ln^{2+}/Ln^{3+} in more detail. The experimental setup consisted of a three-electrode setup with a leakless Ag/AgCl reference electrode, a graphite counter electrode and a glassy carbon working electrode. Tetrabutylammonium hexafluorophosphate was used in 0.1 M concentration as the supporting electrolyte.

The experiments were started at the respective equilibrium states (open circuit potential, OCP) from where the potential was first swept reductively and subsequently oxidatively in three cycles. On the first reductive sweep for europium no and for samarium a very week reductive current was observed. On the first and second oxidative cycle, both curves show a similar oxidative current that peaks at ca. 0.4 V for europium and at ca. -0.5 V for samarium (all potentials vs. reference). On the second reductive cycle, a similarly strong reductive current is observed for both the samarium and the europium sample. The reductive currents peak at -0.2 V for europium and at -1.3 V for samarium. We assign the oxidative peak to the oxidation of the Ln^{2+}-ions to Ln^{3+} and the reductive peak to the reduction of the trivalent to the divalent form of samarium and europium, respectively. Consequently, as we start from the divalent species, only after the Ln^{3+}-ions have formed electrochemically, the reductive signal can be observed. The initial week reductive signal in case of samarium is most likely due to small traces being oxidized when preparing the solutions. This illustrates the higher sensitivity of the Sm(II)-compounds. Overall both redox processes appear to be quasi-reversible in solution with the setup used ($\Delta E(Eu^{2+}/Eu^{3+})$ = 0.57 V, $\Delta E(Sm^{2+}/Sm^{3+})$ = 0.78 V; reversible limit ΔE = 57 mV).

As was expected for the more strongly reducing Sm^{2+}-ion, the redox processes occur at much more negative potentials than for europium. A direct comparison of both cyclovoltamograms is shown in fig. 8.

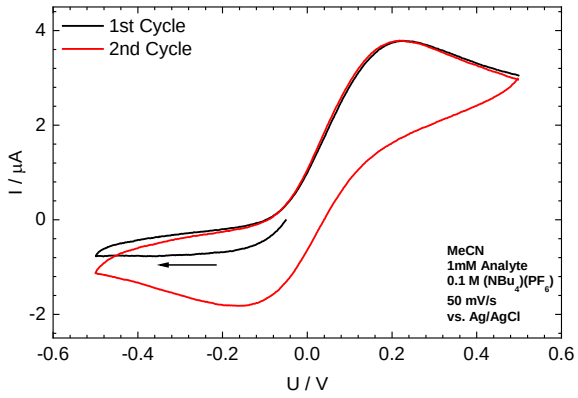


Figure 6. Cylcovoltamogram of $Eu(OTf)_2$ in acetonitrile.

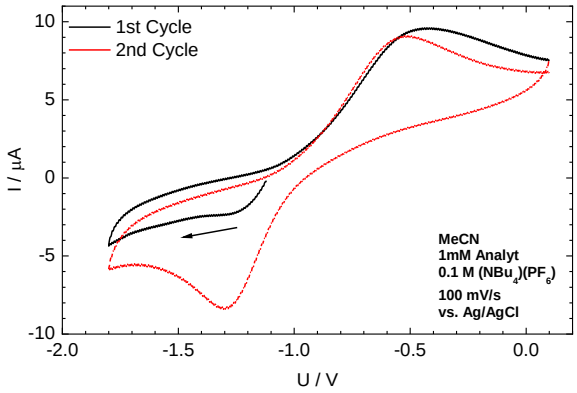


Figure 7. Cylcovoltamogram of $Sm(OTf)_2$ in acetonitrile.

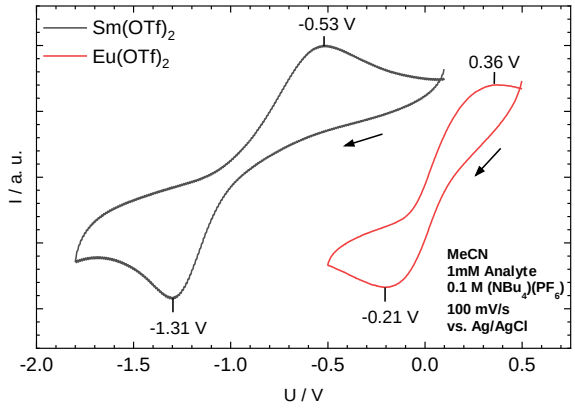


Figure 8. Comparison of cyclovoltamograms of $Sm(OTf)_2$ and $Eu(OTf)_2$ in acetonitrile. Only the second cycles are shown.

Magnetism Temperature dependent susceptibility measurements of **1-Eu** demonstrate that the compound is a classic Curie-paramagnet across the whole temperature range considered (5 K to 350 K) (compare fig. 9). A Curie-Weiss fit delivers the effective magnetic moment of 8.3 μ_B, which is just marginally larger than both the literature values (lit:[33] 7.8-7.9 μ_B [33]) and the theoretical spin-only value for a $4f^7$ system (7.94 μ_B). The determined Weiss temperature of -0.7 K can be regarded as negligible. These results not only confirm the +II oxidation state of europium, but also demonstrate the absence of cooperative magnetic effects between the europium ions in the solid state.

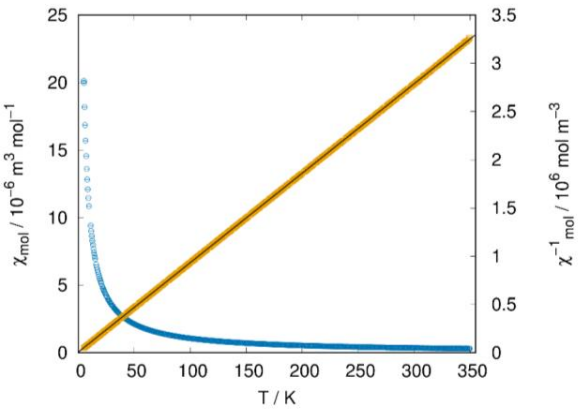


Figure 9. Molar susceptibility (blue circles) and inverse molar susceptibility (orange squares) of $Eu(OTf)_2(CH_3CN)$ with fit according to the Curie-Weiss law (black solid line).

In contrast to Eu^{2+}, the Sm^{2+} ion does not possess a thermally isolated electronic ground state, because the ^7F_J terms are very close to each other so that thermal population of higher J-states than $^7F_0$ is possible. Since each of the ^7F_J terms has its own unique contribution to the effective magnetic moment of the Sm^{2+}-ion, a temperature dependency of the effective magnetic moment is expected, and in fact observed in **1-Sm**. Naturally, given its temperature dependent paramagnetism, **1-Sm** does not obey Curie's law. The calculated effective magnetic moment at room temperature of 3.49 μ_B is in excellent agreement with the experimental literature value of 3.5 μ_B.[33] The dependence of the effective magnetic moment of **1-Sm** is illustrated in fig. 10.

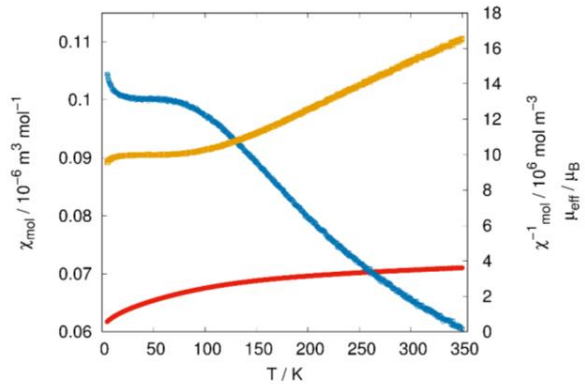


Figure 10. Molar susceptibility (blue circles) and inverse molar susceptibility (orange squares) of $Sm(OTf)_2(CH_3CN)$. The red curve represents the effective magnetic moment μ_{eff} (in μ_B).

The almost constant susceptibility at below 100 K is typical for $4f^6$-configured ions and further corroborates the +II oxidation state of Sm in $Sm(OTf)_2(CH_3CN)$.[34-37]

Luminescence $Eu(OTf)_2(CH_3CN)$ and $Sm(OTf)_2(CH_3CN)$ both show intense luminescence of Eu^{2+} and Sm^{2+}, respectively. All spectra were measured at low temperature since at room temperature, the luminescence was much less intense. The excitation and emission curve of $Eu(OTf)_2(MeCN)$ are shown in fig. 11. The emission spectrum consists of one intense emission band with a maximum of 25090 cm^{-1} (399 nm), a full width at half maximum (FWHM) of 1233 cm^{-1} and a Stokes shift of 2133 cm^{-1}. The high emission energy is confirmed by other complex anions like sulfates or phosphates which also have similar Stokes shifts.[38-39] The emission band can be assigned to the parity-allowed $4f^65d^1 \rightarrow 4f^7(^8S_{7/2})$ transition. Excitation takes place from the $4f^7(^8S_{7/2})$ ground state of Eu^{2+} into the $4f^65d^1$ excited state which leads a broad excitation band between 41670 cm^{-1} and 26320 cm^{-1} (240 nm and 380 nm).

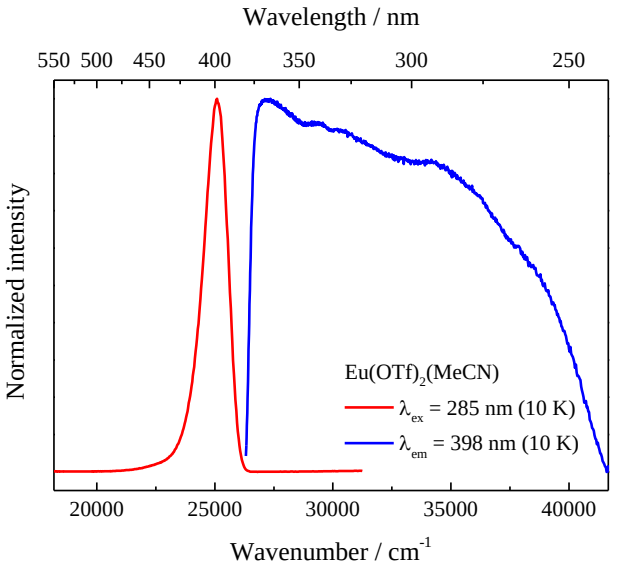
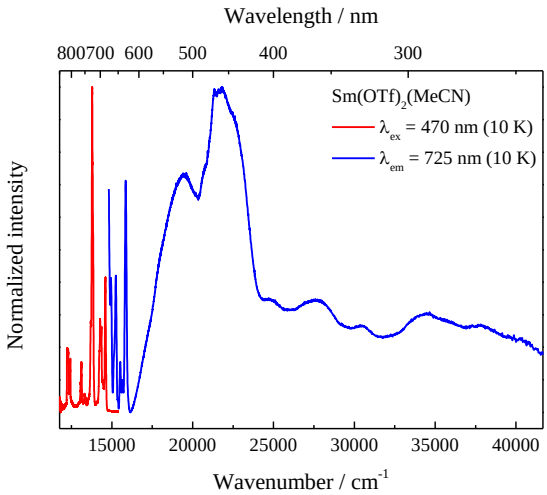


Figure 11. Excitation (blue curve) and emission (red curve) spectrum of $Eu(OTf)_2(MeCN)$ measured at 10 K.

Excitation and emission spectra of $Sm(OTf)_2(MeCN)$ are presented in fig. 12 (top graph) whereas the emission spectrum is shown in a more detailed way in fig. 12 (bottom graph). Excitation occurs from the $4f^6(^7F_0)$ ground state of Sm^{2+} into the $4f^55d^1$ excited state. The spectrum consists of broad transitions including multiple excitation bands. This can be explained by the excitation into several 5*d*-orbitals with different energies by crystal field splitting and 4*f*-5*d*-spin orbit interactions. Additionally, there are several sharp excitation bands that can be assigned to the $4f^6(^7F_J) \rightarrow 4f^6(^5D_1)$-transition. A more detailed assignment of the excitation bands is shown in the figure. These sharp and very intense transition bands, compared with other parity forbidden transitions can be explained by a mixing of the excited 4*f*- and 5*d*-levels in the excited state. Due to this mixing, the $4f \rightarrow 4f$ transitions become less parity forbidden and therefore, more intense.



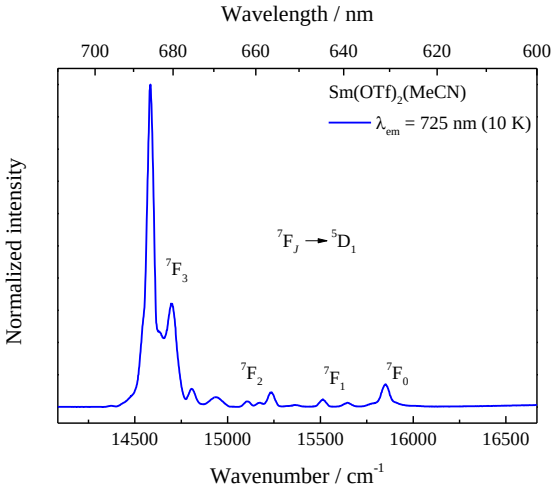


Figure 12. Results from the luminescence measurements of $Sm(OTf)_2(MeCN)$ at a temperature of 10 K. Emission is presented in red whereas the blue curve shows the excitation spectrum. The sharp $4f^6(^7F_J)\rightarrow 4f^6(^5D_1)$ excitation bands are shown separately (bottom spectrum) together with an assignment of the respective transitions.

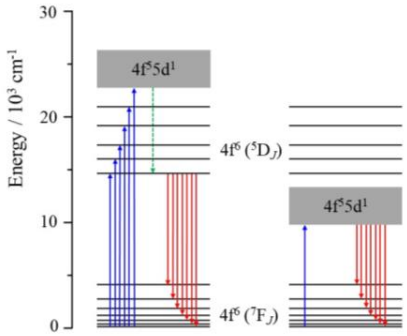
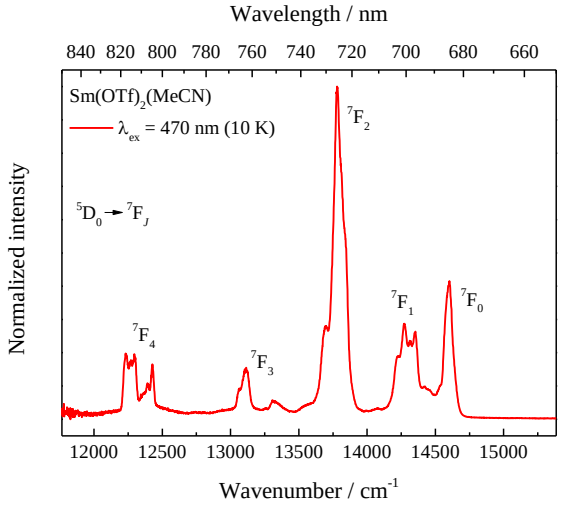


Figure 13. Energy diagram of Sm^{2+} whereas the excited 5*d*-level can be energetically above (left) or below (right) the excited 4*f*-levels. Therefore, emission can take place either from excited $4f^6$- or $4f^55d^1$-states.

In the emission spectrum at low temperature (fig. 14, top) as well as room temperature several sharp transitions can be observed. These emission bands can be assigned to the intraconfigurational $4f^6(^5D_0)\rightarrow 4f^6(^7F_J)$-transitions. In this work, for **1-Sm** no broad $4f^55d^1 \rightarrow 4f^6$ emission band could be detected. Here, excitation takes place into the 5*d*-orbitals followed by a nonradiative transition to the energetically lower $4f^6$-levels. This is shown schematically in fig. 13. Since only $4f^6(^5D_0)\rightarrow 4f^6(^7F_J)$-transitions take place, the excited $4f^55d^1$-state is energetically higher than the excited $4f^6$-levels. The temperature dependent emission spectrum shows that the intensity of the $4f^6(^5D_0)\rightarrow 4f^6(^7F_J)$-transitions strongly decreases with increasing temperature and the resolution of the single transitions also decreases due to thermal quenching by multi phonon emission of the luminescence (fig. 14, bottom).



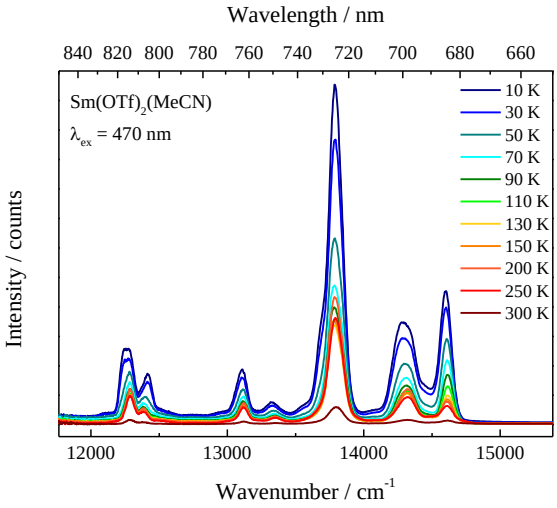


Figure 14. Emission spectrum of $Sm(OTf)_2(CH_3CN)$ at 10 K and an excitation wavelength of 470 nm with an assignment of the $4f^6(^5D_0)\rightarrow 4f^6(^7F_J)$ transitions (top) and temperature dependent emission in the range between 10 K and 300 K (bottom).

CONCLUSION

The divalent lanthanoid triflates $Ln(OTf)_2(CH_3CN)$ (Ln = Sm, Eu) were synthesized by reduction of $Ln(OTf)_3$ and the respective metal in acetonitrile. For the first time, an adequate description of divalent europium and samarium triflates was carried out in their solid state. The phase-pure triflates could be isolated as their acetonitrile solvates and were analyzed with respect to their thermal, electrochemical, magnetic and optical properties. Additionally $Sr(OTf)_2(CH_3CN)$ was prepared and characterized as a host lattice for optical studies.

All three compounds are thermally instable towards loss of acetonitrile, whereas the desolvated triflates proved to be remarkably stable to temperatures of up to almost 300 °C. Electrochemical experiments of the dissolved compounds demonstrated the absence of trivalent ions in **1-Ln** and allowed for a direct comparison of the redox events between Sm and Eu.

1-Eu is a classic Curie paramagnet, due to its isolated $4f^7$-configured ground state. Unlike **1-Eu**, **1-Sm** showed temperature dependent paramagnetism, that is typical for $4f^6$-configured ions. Like the magnetic measurements, the optical spectra allowed for a direct correlation of the electronic configuration of

the Ln^{2+}-ions to the physical properties of their compounds. The luminescence of **1-Eu** is dominated by a broad interconfigurational *d-f*-emission in the near UV-region, peaking at 399~nm that can be excited over a large spectral region between ca. 240 to 380~nm. In **1-Sm**, the emission spectrum showed several sharp *f-f*-transitions that were attributed as $4f^6(^5D_0) \rightarrow 4f^6(^7F_J)$ transitions. Although interconfigurational excitation into the *d*-states was possible, no corresponding emission could be observed.

The presented results clearly demonstrate that divalent lanthanoid triflates are not only useful tools in synthetic chemistry, but also attractive materials with remarkable physical properties. Future studies addressing related compounds, such as other solvates, might help to expand this new class of materials and the knowledge thereof and there hereby lay the foundation for future applications.

ASSOCIATED CONTENT

Supporting Information

General experimental details; synthetic procedures; further analytical data.

AUTHOR INFORMATION

Corresponding Author

*Mathias S. Wickleder - Greinstr. 6, 50939 Cologne, Germany; Email: mathias.wickleder@uni-koeln.de

Author Contributions

The manuscript was written through contributions of all authors. All authors have given approval to the final version.

Notes

The authors declare no competing financial interest.

ACKNOWLEDGEMENTS

B. R. thanks the “Fond der Chemischen Industrie” (FCI) for funding via a Liebig-Group.

L. R. and S. D. acknowledge funding by the Deutsche Forschungsgemeinschaft (DFG: Emmy Noether grant DI 1788/2-1).

N. F. and M. W. thank Alisha Mertens for measuring DTA-TG data.

ABBREVIATIONS

calc., calculated, CShM, continuous shape measurements; DFG, Deutsche Forschungsgemeinschaft, DTA-TG, differential thermal analysis coupled with thermogravimetry; fig., figure; Ln, lanthanoid; tab., table; XRD, X-ray diffraction.

REFERENCES

[1] G. H. Dieke, *Spectra and Energy Levels of Rare Earth in Crystals*, John Wiley and Sons, New York, **1968**.

[2] *Electronic Energy Levels in the Trivalent Lanthanide Aquo Ions. I. Pr^{3+}, Nd^{3+}, Pm^{3+}, Sm^{3+}, Dy^{3+}, Ho^{3+}, Er^{3+}, and Tm^{3+}*, W. T. Carnall, P. R. Fields, K. Rajnak, *J. Chem. Phys.* **2003**, *49*, 4424-4442.

[3] C. Görller-Walrand, K. Binnemans, in *Handbook on the Physics and Chemistry of Rare Earths, Vol. 25*, Elsevier, **1998**, pp. 101-264.

[4] *Optical Properties of Lanthanides in Condensed Phase, Theory and Applications*, R. Reisfeld, *AIMS Mater. Sci.* **2015**, *2*, 37-60.

[5] *Challenges in Application of Luminescent Materials, a Tutorial Overview (Invited Review)*, C. Ronda, *Prog. Electromagn. Res.* **2014**, *147*, 81-93.

[6] *Luminescent Ions in Advanced Composite Materials for Multifunctional Applications*, G. Bai, M.-K. Tsang, J. Hao, *Adv. Funct. Mater.* **2016**, *26*, 6330-6350.

[7] *Permanent magnet applications*, J. M. D. Coey, *J. Magn. Magn. Mater.* **2002**, *248*, 441-456.

[8] *Rare earth (RE) doped phosphors and their emerging applications: A review*, I. Gupta, S. Singh, S. Bhagwan, D. Singh, *Ceram. Int.* **2021**, *47*, 19282-19303.

[9] *Lanthanides: Applications in Cancer Diagnosis and Therapy*, R. D. Teo, J. Termini, H. B. Gray, *J. Med. Chem.* **2016**, *59*, 6012-6024.

[10] *Synthesis, spectroscopic properties and applications of divalent lanthanides apart from Eu^{2+}*, M. Suta, C. Wickleder, *J. Lumin.* **2019**, *210*, 210-238.

[11] *Valence Stability of Lanthanide Ions in Inorganic Compounds*, P. Dorenbos, *Chem. Mater.* **2005**, *17*, 6452-6456.

[12] *Stabilization of the Divalent State for the Lanthanides and Actinides in Solutions, Melts and Clusters*, N. B. Mikheev, I. A. Rumer, *Radiochim. Acta* **1999**, *85*, 49-56.

[13] *Energy of the first $4f^7 \rightarrow 4f^6 5d$ transition of Eu^{2+} in inorganic compounds*, P. Dorenbos, *J. Lumin.* **2003**, *104*, 239-260.

[14] G. Meyer, M. S. Wickleder, in *Handbook on the Physics and Chemistry of Rare Earths, Vol. 28* (Eds.: L. Eyring, K. Gschneidner), Elsevier Science Publishers, New York, **2000**, pp. 53-129.

[15] *$f \rightarrow d$ transition energies of divalent lanthanides in inorganic compounds*, P. Dorenbos, *J. Phys.: Condens. Matter* **2003**, *15*, 575.

[16] *Doubly-valent rare-earth ions in halide crystals*, J. R. O., *J. Phys. Chem. Solids* **1991**, *52*, 101-174.

[17] *The crystal structure of $EuSO_4$ and $EuCO_3$*, I. Mayer, E. Levy, A. Glasner, *Acta Crystallogr.* **1964**, *17*, 1071-1072.

[18] *Europium (II) Sulfate $EuSO_4$: Synthesis Methods, Crystal and Electronic Structure, Luminescence Properties*, Y. G. Denisenko, A. E. Sedykh, A. S. Oreshonkov, M. S. Molokeev, N. O. Azarapin, E. I. Sal'nikova, O. D. Chimitova, O. V. Andreev, I. A. Razumkova, K. Müller-Buschbaum, *Eur. J. Inorg. Chem.* **2022**, *2022*, e202200043.

[19] *Thermal decomposition of europium sulfates $Eu_2(SO_4)_3 \cdot 8H_2O$ and $EuSO_4$*, Y. G. Denisenko, N. A. Khritokhin, O. V. Andreev, S. A. Basova, E. I. Sal'nikova, A. A. Polkovnikov, *J. Solid State Chem.* **2017**, *255*, 219-224.

[20] *Divalent lanthanide derivatives in organic synthesis. 1. Mild preparation of samarium iodide and ytterbium iodide and their use as reducing or coupling agents*, P. Girard, J. L. Namy, H. B. Kagan, *J. Am. Chem. Soc.* **1980**, *102*, 2693-2698.

[21] *Samarium(II) Triflate as a New Reagent for the Grignard-Type Carbonyl Addition Reaction*, S.-i. Fukuzawa, K. Mutoh, T. Tsuchimoto, T. Hiyama, *J. Org. Chem.* **1996**, *61*, 5400-5405.

[22] *Generation of Sm^{II} Reductants Using High Intensity Ultrasound*, J. A. Teprovich Jr., P. K. S. Antharjanam, E. Prasad, E. N. Pesciotta, R. A. Flowers II, *Eur. J. Inorg. Chem.* **2008**, *2008*, 5015-5019.

[23] *Electrochemical generation of low-valent lanthanides*, J. D. Parrish, R. D. Little, *Tetrahedron Lett.* **2001**, *42*, 7767-7770.

[24] *The First Oxidative Addition of a Hypervalent Compound to Metallic Lanthanoid: Synthesis, Characterization, and Reaction of Samarium(II) Bis(trifluoromethanesulfonate) Derived from Metallic Samarium and 1,5-Dithioniabicyclo[3.3.0]octane Bis(trifluoromethanesulfonate)*, K. Mashima, T. Oshiki, K. Tani, *J. Org. Chem.* **1998**, *63*, 7114-7116.

[25] *A convenient pathway to Sm(II)-mediated chemistry in acetonitrile*, T. Maisano, K. E. Tempest, D. V. Sadasivam, I. I. R. A. Flowers, *Org. Biomol. Chem.* **2011**, *9*, 1714-1716.

[26] *Small molecule activation with divalent samarium triflate: a synergistic effort to cleave O_2*, M. Xémard, M. Cordier, E. Louyriac, L. Maron, C. Clavaguéra, G. Nocton, *Dalton Trans.* **2018**, *47*, 9226-9230.

[27] *Beyond Samarium Diiodide: Vistas in Reductive Chemistry Mediated by Lanthanides(II)*, M. Szostak, D. J. Procter, *Angew. Chem. Int. Ed.* **2012**, *51*, 9238-9256.

[28] *Divalent Thulium Triflate: A Structural and Spectroscopic Study*, M. Xémard, A. Jaoul, M. Cordier, F. Molton, O. Cador, B. Le Guennic, C. Duboc, O. Maury, C. Clavaguéra, G. Nocton, *Angew. Chem. Int. Ed.* **2017**, *56*, 4266-4271.

[29] *Continuous Shape Measures as a Stereochemical Tool in Organometallic Chemistry*, J. Cirera, E. Ruiz, S. Alvarez, *Organometallics* **2005**, *24*, 1556-1562.

[30] *CCDC 959305: Experimental Crystal Structure Determination*, J. C. Berthet, P. Thuery, M. Ephritikhine, **2013**.

[31] *Ionic Liquids as Crystallization Media: Weakly-Coordinating Anions Do Coordinate in $^1{}_\infty[Eu(OTf)_3(CH_3CN)_3]$*, S. Tang, A.-V. Mudring, *Cryst. Growth Des.* **2011**, *11*, 1437-1440.

[32] *Revised effective ionic radii and systematic studies of interatomic distances in halides and chalcogenides*, R. Shannon, *Acta Crystallogr. A* **1976**, *32*, 751-767.

[33] H. Lueken, *Magnetochemie*, B. G. Teubner, Stuttgart, **1999**.

[34] *The paramagnetic susceptibility of C-type europium sesquioxide*, P. Caro, P. Porcher, *J. Magn. Magn. Mater.* **1986**, *58*, 61-66.

[35] *Effect of the Anisotropic Exchange and the Crystalline Field on the Magnetic Susceptibility of Eu_2O_3*, N. L. Huang, J. H. Van Vleck, *J. Appl. Phys.* **2003**, *40*, 1144-1146.

[36] *Van Vleck paramagnetism of the trivalent Eu ions*, Y. Takikawa, S. Ebisu, S. Nagata, *J. Phys. Chem. Solids* **2010**, *71*, 1592-1598.

[37] *Synthesis and characterization of the divalent samarium Zintl-phases $SmMg_2Bi_2$ and $SmMg_2Sb_2$*, D. Ramirez, A. Gallagher, R. Baumbach, T. Siegrist, *J. Solid State Chem.* **2015**, *231*, 217-222.

[38] *Luminescence of Eu^{2+} in host lattices with three alkaline earth ions in a row*, S. H. M. Poort, Krevel, J. W. H. van, Stomphorst, R, Vink, A P, and Blasse, G., *J. Solid State Chem.* **1996**, *122*, 432–435.

[39] *Investigation of TLD Phosphors by Optical Excitation –Luminescence of Eu^{2+} Centers in $MgSO_4$, $CaSO_4$, $SrSO_4$, $BaSO_4$*, N. Yamashita, I. Yamamoto, K. Ninagawa, T. Wada, Y. Yamashita, Y. Nakao, *Jpn. J. Appl. Phys.* **1985**, *24*, 1174.

While the previous section deals with the acetonitrile solvates of $M(OTf)_2$ (M = Sm, Eu, Sr), the following discussion is dedicated to acetonitrile solvates of $M(OTf)_2$ (M = Yb, Ca), as well as solvates with other polar aprotic solvents of $M(OTf)_2$ (M = Sm, Eu, Sr, Ca, Yb).[4]

4.2.2 $Yb(OTf)_2(MeCN)_2$ and $Ca(OTf)_2(MeCN)_{0.5}$

In analogy to the methods described in ***Manuscript 4*** (section 4.2.1), $Yb(OTf)_2$ could be generated from reducing $Yb(OTf)_3$ with metallic ytterbium. When slowly crystallised from solution, single crystals of $Yb(OTf)_2(MeCN)_2$ were obtained,[5] that slowly converted into $Yb(OTf)_2$, even at ambient pressure. By PXRD it was proven that $Yb(OTf)_2$ is isostructural to $Ca(OTf)_2$ (for more details on $Yb(OTf)_2$ see section 7.1, ***Manuscript 5 SI***).

$Yb(OTf)_2(MeCN)_2$ (Niggli-notation: $^1_\infty[Yb(OTf)_{3/3}(OTf)_{2/2}(MeCN)_{2/1}]$) crystallises in the monoclinic space group $C2/m$ (a = 2520.2(2) pm, b = 5.9465(5) pm, c = 1039.29(9) pm, β = 99.518(3)° with four formula units per cell. A microscopic photo of the single crystals is shown in fig. 13, next to the atoms of the asymmetric unit.

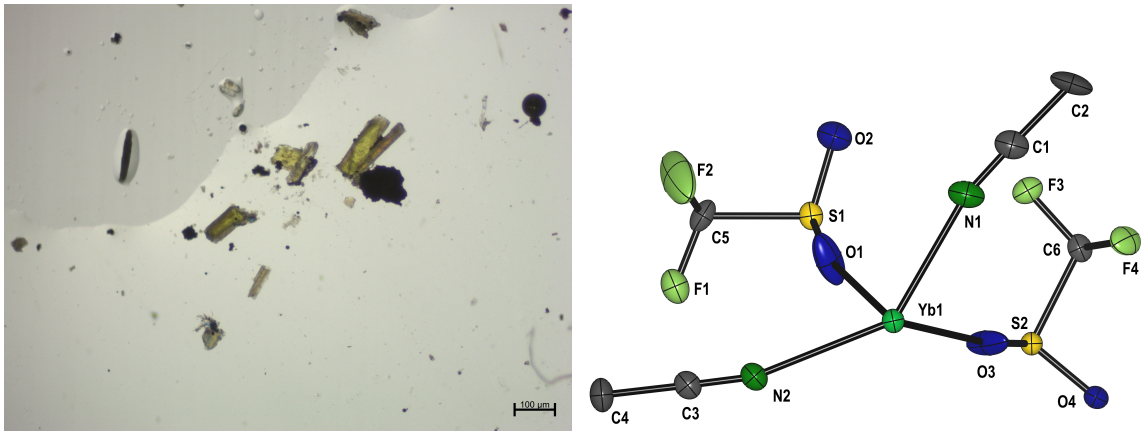


Fig. 13 Microscopic photo of single crystals of $Yb(OTf)_2(MeCN)_2$ (left) and atoms of the asymmetric unit (right). Displacement ellipsoids are shown at 50% probability level. Hydrogen atoms were omitted for clarity.

Notably, all atoms except for O1, O3, F2 and F4 and some hydrogen atoms are located on the mirror plane (Wyckoff site 4*i*). The structure consists of $[YbO_5N_2]$-polyhedra that are connected to each other by μ_3-bridging triflate groups, resulting in zig-zag chains that propagate along the crystallograpic *b*-axis (comp. fig. 14).

[4]Parts of this work was carried out as part of a bachelor thesis that was supervised by the author.[124] The affected results are labelled as such.

[5]Experimental work was partially carried out in by S. Brieger and partially by the author; data analysis and discussion of the results are not contained in[124] and were thus included into the present work.

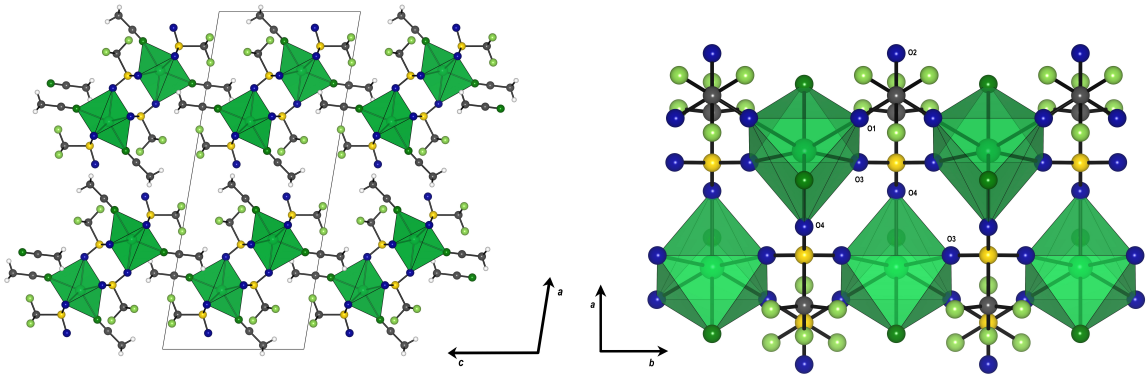


Fig. 14 Crystal structure of $Yb(OTf)_2(MeCN)_2$ viewed along the crystallographic *b*-axis (left) and along the crystallographic *c*-axis. Green = ytterbium, yellow = sulphur, light green = fluorine, blue = oxygen, dark gree = nitrogen, grey = carbon, white = hydrogen.

The Yb^{2+}-ions are coordinated by five oxygen atoms that are constituents of triflate anions and two nitrogen atoms of acetonitrile with bond lengths ranging from 235(1) pm between Yb1 and O1 and 255(1) pm between Yb1 and O2. The coordination polyhedron of the Yb^{2+}-ion is depicted in fig. 15.

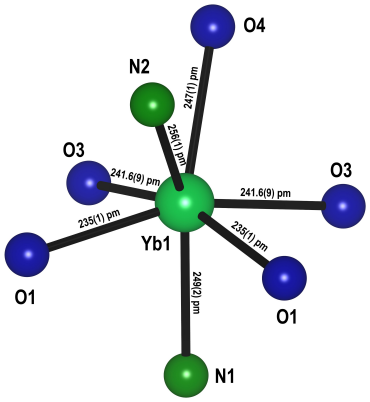


Fig. 15 Coordination polyhedron of Yb^{2+} in $Yb(OTf)_2(MeCN)_2$.

The high residual electronic densities between the fluorine atoms of adjacent chains could be a result of disordering, paired with high conformational flexibility of the CF_3-group. Additional crystallograhpic data are provided in tab. 17. Due to the high volatility of the acetonitrile embedded into the structure of $Yb(OTf)_2(MeCN)_2$, it was not possible to produce the pure material and thus further studies of the material were prevented.
Parallel to the work on $Yb(OTf)_2(MeCN)_2$, it was attempted to generate an analogous compound of calcium as a potential host lattice for photophysical investigations of the Yb^{2+}-ion. However, instead of $Ca(OTf)_2(MeCN)_2$, $Ca(OTf)_2(MeCN)_{0.5}$ was obtained (see section 6.2.18) that crystallises in the triclinic space group $P\bar{1}$ ($a = 1183.75(8)$ pm, $b = 1500.54(9)$ pm, $c = 1506.21(9)$ pm, $\alpha = 80.520(2)°$, $\beta = 68.189(2)°$, $\gamma = 68.725(2)°$) with

four formula units per unit cell.[6] In contrast to $Yb(OTf)_2(MeCN)_2$, $Ca(OTf)_2(MeCN)_{0.5}$ exhibits a layered strucutre, which is a direct consequence of the reduced content of acetonitrile in the structure. Single crystals of $Ca(OTf)_2(MeCN)_{0.5}$ are shown in fig. 16.

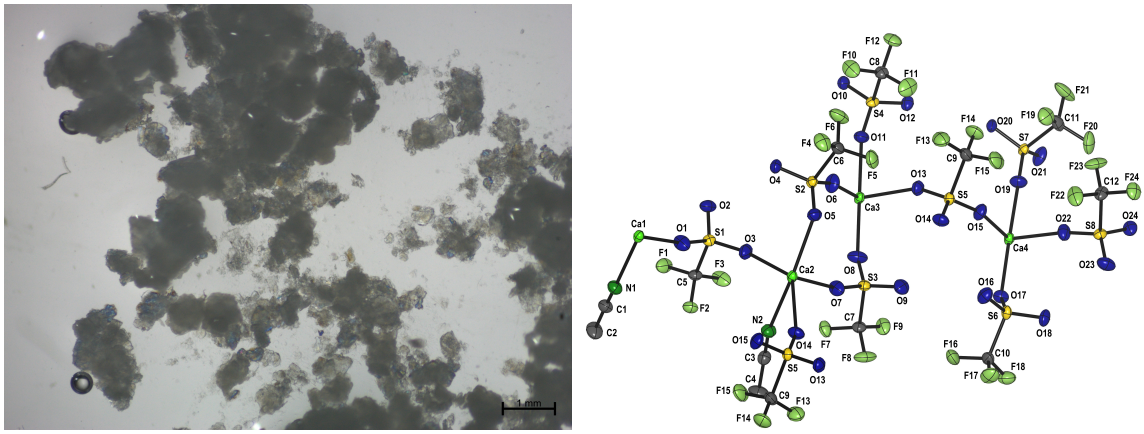


Fig. 16 Microscopic photo of single crystals of $Ca(OTf)_2(MeCN)_{0.5}$ (left) and atoms of the asymmetric unit (right). Hydrogen atoms were omitted. Ellipsoids are shown at 50% probability level.

Structurally and stoichiometrically, $Ca(OTf)_2(MeCN)_{0.5}$ can be considered an intermediate between the previously discussed $M(OTf)_2(MeCN)$ (M = Sr, Sm, Eu) (see ***Manuscript 4***, section 4.2.1) and desolvated $Ca(OTf)_2$ that was described by *Jansen* et al.[125] As in $Ca(OTf)_2$, the structure of $Ca(OTf)_2(MeCN)_{0.5}$ consists of layers of coordinated Ca^{2+}-ions that are bridged by triflate groups, as illustrated in fig. 17.

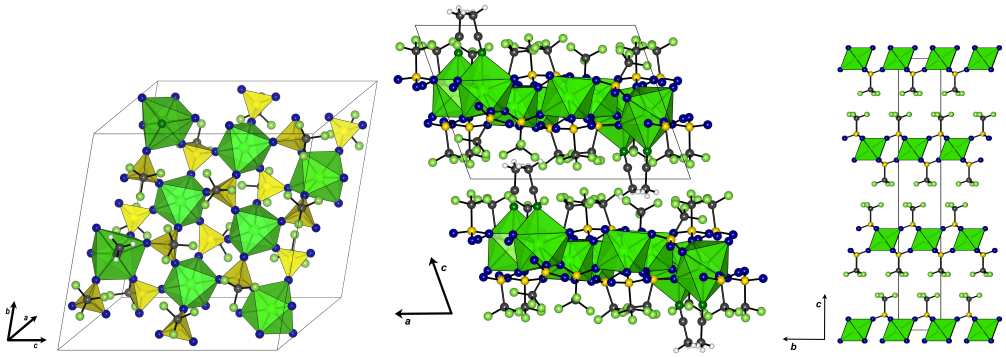


Fig. 17 Crystal structure of $Ca(OTf)_2(MeCN)_{0.5}$ (left and middle) and crystal structure of $Ca(OTf)_2$ (right).[125] Green = calcium, yellow = sulphur, light green = fluorine, blue = oxygen, dark gree = nitrogen, grey = carbon, white = hydrogen.

Only every second Ca^{2+}-ion is coordinated by acetonitrile, resulting in similar 7-fold coordination geometries to that observed around Yb^{2+} in $Yb(OTf)_2(MeCN)_2$. Such Ca^{2+}-ions that are not coordinated by acetonitrile, are surrounded by six oxygen atoms of triflate groups that form distorted octahedra, as shown in fig. 18.

[6] Niggli-notation was not provided because of the high complexity of the structure.

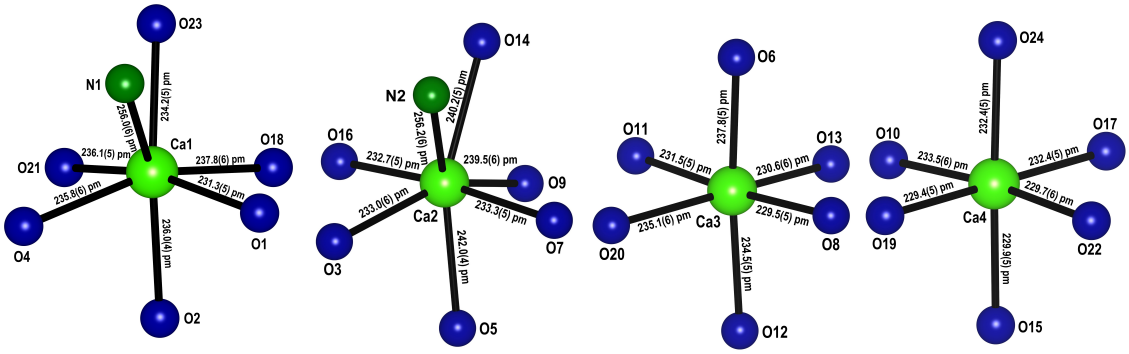


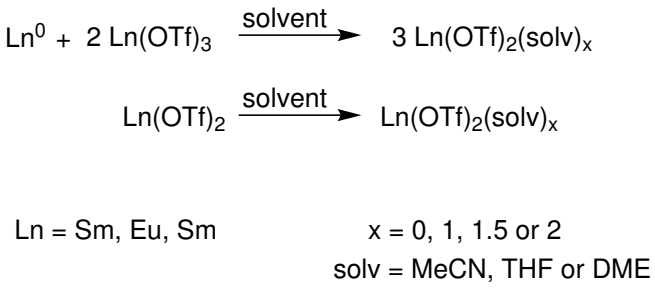
Fig. 18 Coordination polyhedra of Ca^{2+} in $Ca(OTf)_2(MeCN)_{0.5}$.

As displayed in fig. 18, the bond lengths between Ca^{2+} and coordinating atoms range from 229.4(5) between Ca4 and O19 to 256.2(6) pm between Ca2 and N2, which is comparable to the distances found in $Yb(OTf)_2(MeCN)_2$ (comp. fig. 15), at least for the polyhedra aroud Ca1 and Ca2. Additional crystallographic data of $Ca(OTf)_2(MeCN)_{0.5}$ is provided in tab. 18.

Because the Ca- and Yb-compounds were found not to be isostructural and due to the difficulties encountered when attempting to produce pure $Yb(OTf)_2(MeCN)_2$, it was decided to not pursue further analytical characterisation of $Ca(OTf)_2(MeCN)_{0.5}$.

4.2.3 THF- and DME-Solvates of $Ln(OTf)_2$

The methods described in the previous sections of producing $Ln(OTf)_2$ (Ln = Sm, Eu or Yb) by comproportionating $Ln(OTf)_3$ and the respective lanthanoid metal were generalised beyond acetonitrile to other aprotic polar solvents such as THF and DME to yield different solvates. Alternatively, the same adducts can be accessed by recrystallising the desolvated triflates from the respective solvents, as is illustrated in scheme 10.



Scheme 10 Two possible methods of synthesising various solvates of $Ln(OTf)_2$.

Since the adducts with acetonitrile were already thoroughly discussed in ***Manuscript 4***, the following section deals with the solvates of THF and DME. At the start of this work $Sm(OTf)_2(THF)_{1.5}$ and $Tm(OTf)_2(DME)_2$ were the only structurally known solvates of divalent lanthanoid triflates.[97,98] The THF-adducts of $Eu(OTf)_2$ and $Yb(OTf)_2$ were

synthesised as elucidated above and their crystal structures could be solved to complete the series of $Ln(OTf)_2(THF)_n$ (n = 1.5 for Ln = Sm and Eu; n = 2 for Ln = Yb). Additionally, the analogous compounds of calcium and strontium were produced by recrystallisation of $M(OTf)_2$ (M = Ca, Sr) from THF. A summary of the THF-adducts is presented in tab. 2.

Tab. 2 Overview of structurally characterised THF-solvates of $Ln(OTf)_2$ and their analogues with strontium and calcium.

	Sm[97]	**Eu**[a]	**Sr**	**Yb**[a]	**Ca**
n(THF)	1.5	1.5	1.5	2	2
Space Group	$P2_1/n$	$P2_1/n$	$P2_1/n$	$P2_12_12_1$	$P2_1/c$
a / pm	1783(1)	1669.7(2)	1737.99(7)	1092.73(7)	544.04(5)
b / pm	1025(2)	1008.95(8)	1012.57(2)	1182.28(9)	1197.7(1)
c / pm	2031(2)	2055.8(2)	2015.52(8)	1479.8(1)	1450.1(1)
β / °	109.05(5)	109.304(3)	109.513(4)	90	99.62(1)
V / 10^6 pm^3	3507(7)	3268.6(5)	3343.3(2)	1911.8(2)	931.6(1)
CN[b]	7	7	7	7	6
d_{avg}(M-O) / pm	256.4(2)	255.4(3)	257.3(2)	243.1(3)	321.5(1)

[a]Compounds were prepared by S. Brieger.[124]

[b]CN = Coordination number of the metal.

$Sr(OTf)_2(THF)_{1.5}$ is isostructural to the Sm^{2+}- and Eu^{2+}-analogues, whereas the Yb^{2+}- and Ca^{2+}-structures crystallise in different structure types which are closely related to each other.

The crystal structure of $Yb(OTf)_2(THF)_2$ has already been discussed in detail elsewhere.[124] Single crystals of $Ca(OTf)_2(THF)_2$ (Niggli-notation: $^1_\infty[Ca(OTf)_{4/2}(THF)_{2/1}]$) and the atoms of the asymmetric unit are shown in fig. 19 and its structure will be discussed in the following section.

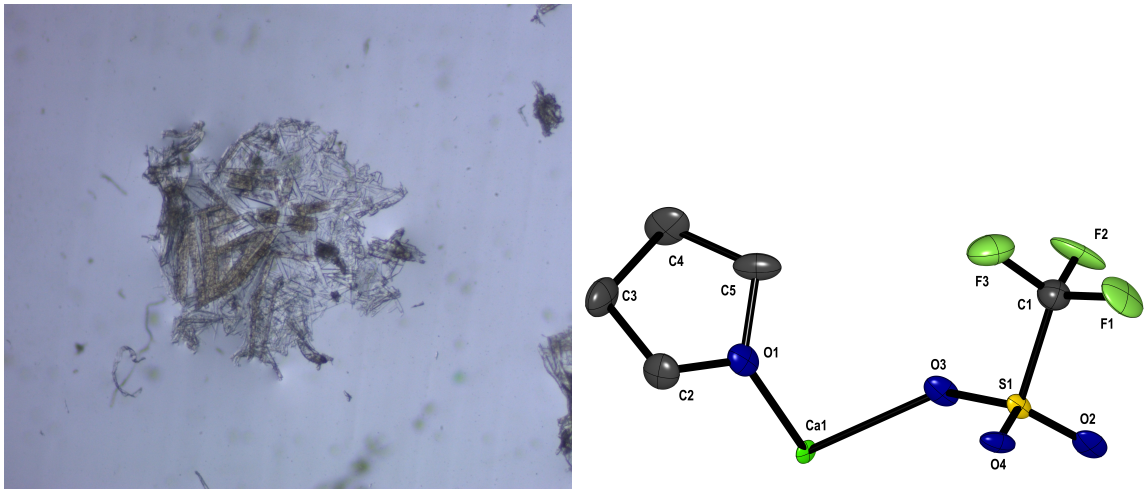


Fig. 19 Microscopic photo of single crystals of $Ca(OTf)_2(THF)_2$ (left) and atoms of the asymmetric unit (right). Hydrogen atoms were omitted. Displacement ellipsoids are shown at 50% probability level.

Both structures consist of chains of $[MO_n]$-polyhedra (n = 6 for Ca and n = 7 for Yb) that are connected via bridging triflate groups, as illustrated in fig. 20.

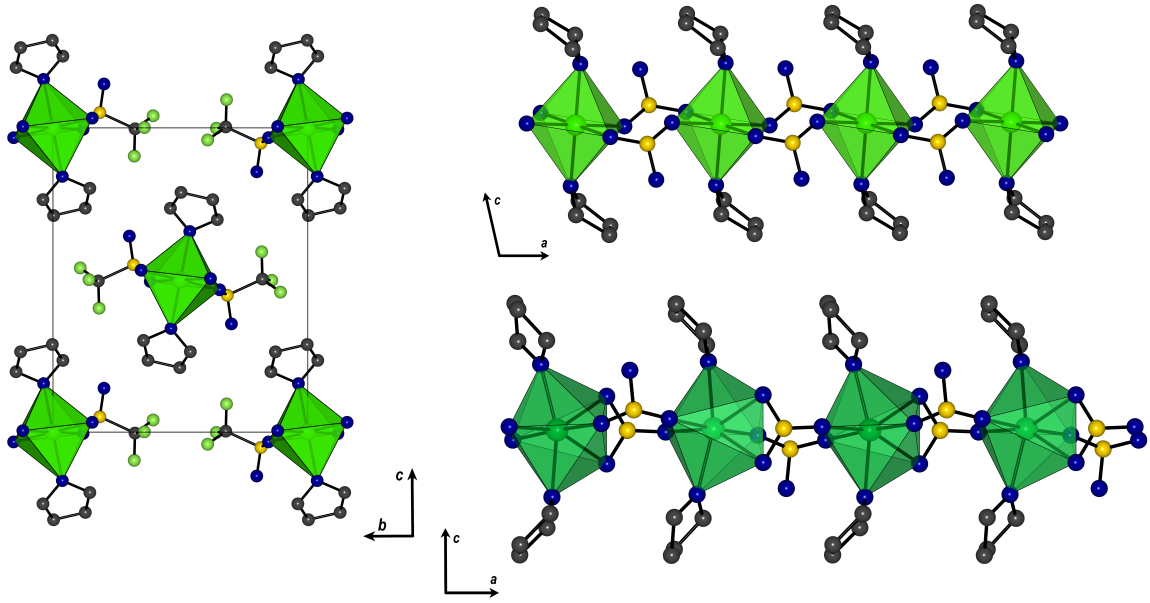


Fig. 20 Left: Crystal structure of $Ca(OTf)_2(THF)_2$ viewed along the crystallographic *a*-axis. Top right: Chain of $[CaO_6]$-polyhedra viewed along the crystallographic *b*-axis. Bottom right: Chain of $[YbO_6]$-polyhedra viewed along the crystallographic *b*-axis. Hydrogen atoms were omitted in all three graphics; CF_3-groups were omitted in the right graphics. Dark green = ytterbium, green = calcium, yellow = sulphur, light green = fluorine, blue = oxygen, grey = carbon.

The marginally larger ionic radius of the Yb^{2+}-ion causes the coordination sphere to expand from a 6-fold coordination, observed in $Ca(OTf)_2(THF)_2$ to a seven-fold coordination in $Yb(OTf)_2(THF)_2$.[126] The expansion of the coordination sphere in the case of Yb^{2+} is

facilitated by rotation of the triflate groups to establish a chelating coordination for every second group, as opposed to the strictly η_1-coordinating triflate groups in $Ca(OTf)_2(THF)_2$. Phase pure $M(OTf)_2(THF)_{1.5}$ (M = Sr or Eu) could be obtained after careful recrystallisation of the desolvated triflates from THF (see sections 6.2.21 and 6.2.22). If the evaporation of the solvent was not conducted carefully however, impure products or amorphous solids (comp. sections 6.2.20 and 6.2.23) were obtained, demonstrating the difficulties when handling these materials. Both solvates were not stable when stored at room temperature and all manipulations had to be carried out immediately. Undiluted $Eu(OTf)_2(THF)_{1.5}$ shows intense emission in the violet to blue region (ca. 420 nm) of the colour spectrum when excited at 378 nm. The emission and excitation spectrum are shown in fig. 21.

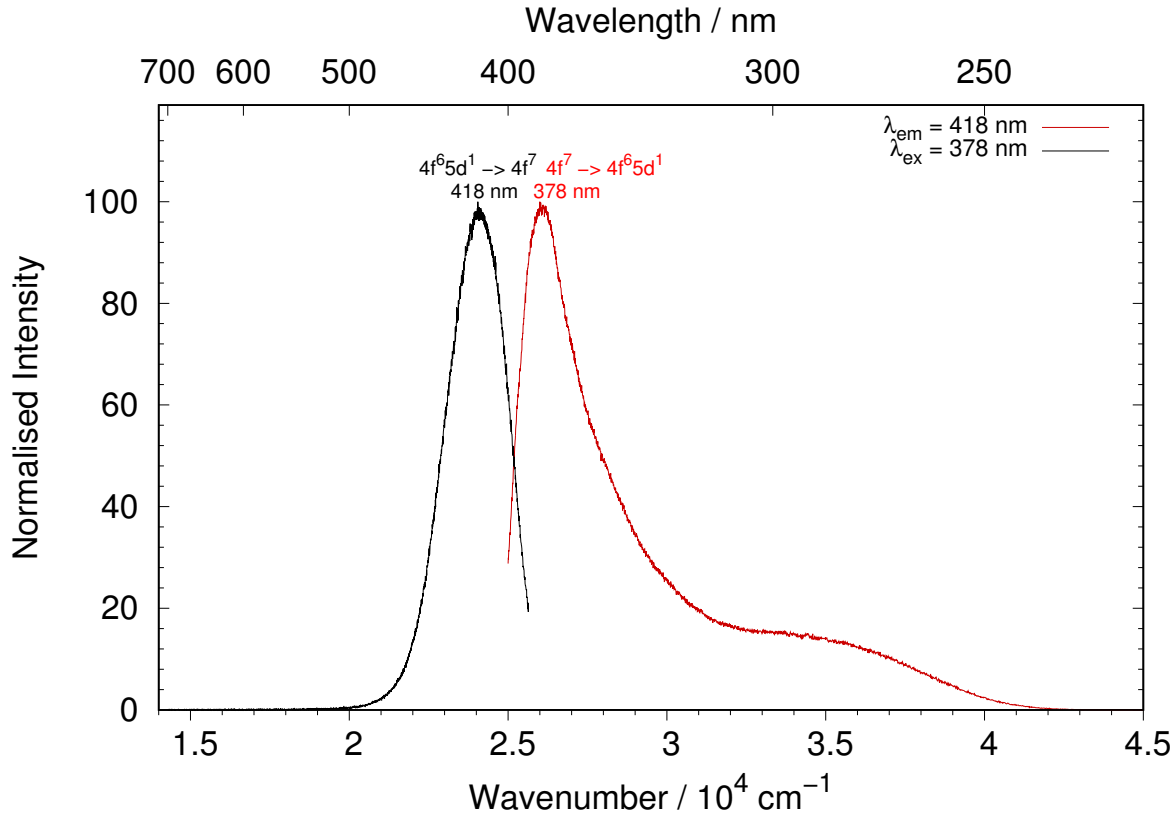


Fig. 21 Emission and excitation spectrum of $Eu(OTf)_2(THF)_{1.5}$ measured at room temperature.

Both emission and excitation data are typical for interconfigurational f-d-and d-f-transitions of Eu^{2+}-ion, as explained in sections 2.3.1 and 4.2.1. In comparison to the acetonitrile solvate of $Eu(OTf)_2$, the $4f^65d^1 \rightarrow 4f^7$-emission is shifted to lower energies, allowing the conclusion that the d-orbitals are more strongly affected by the crystal field found in the THF-solvate.

Similar to the crystallisation of the THF-solvates of the divalent metal triflates, solvates of DME could also be obtained by analogous methodology (see scheme 10). A summary

of selected structural parameters of the DME-solvates is provided in tab. 3.

Tab. 3 Overview of structurally characterised DME-solvates of $Ln(OTf)_2$.

	Sm	**Eu**[a]	**Tm**[98]	**Yb**
n(DME)	2	2	2	2
Space Group	$I2/a$	$I2/a$	$I2/a$	$I2/a$
a / pm	1198.05(7)	1198.73(7)	1195.4(2)	1191.010
b / pm	1075.37(7)	1072.22(6)	1078.4(2)	1078.430
c / pm	1676.3(1)	1668.8(1)	1719.0(2)	1657.991
β / °	99.685(2)	99.505(2)	106.61(1)	102.103(3)
V / 10^6 pm^3	2128.9(2)	2115.4(2)	2123.7(6)	2082.2(2)
CN[b]	8	8	8	8
d_{avg}(M-O) / pm	259.6(5)	258.5(6)	247(1)	248.8(4)

[a]Compound was initially prepared by S. Brieger.[124] In this work a new data set was produced which the presented data refers to.

[b]CN = Coordination number of the lanthanoid.

Other than observed for the THF- and acetonitrile solvates, in the series of DME-solvates no structural transition occurs when moving though the series towards the heavier lanthanoids. In fact, all four compounds are isostructural and consist of $[LnO_8]$-polyhedra that form chains along the crystallographic a-axis, as shown in fig. 22.

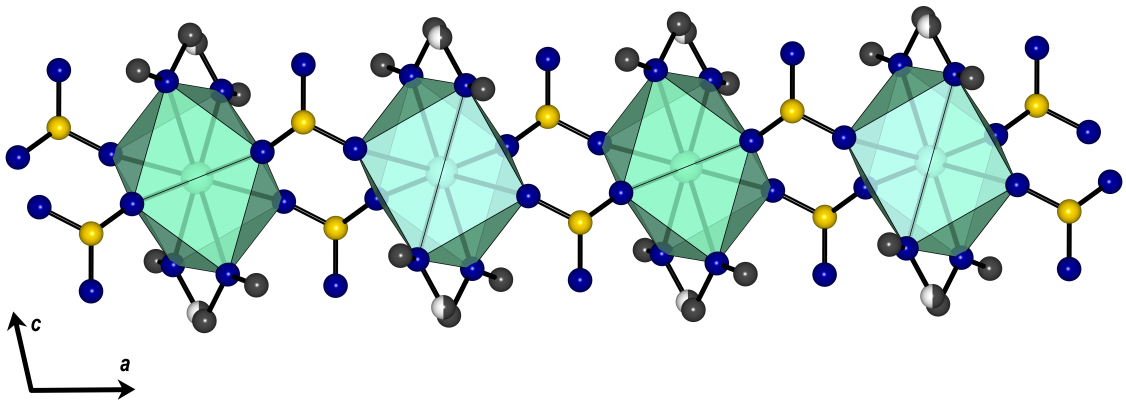


Fig. 22 Crystal structure of $Ln(OTf)_2(DME)_2$ (Ln = Sm, Eu, Tm, Yb), exemplary shown for $Sm(OTf)_2(DME)_2$ as viewed along the crystallographic b-axis. Hydrogen atoms and CF_3-groups were omitted. Half-filled spheres indicate 50% occupation of the respective site due to disordering. Green = samarium, yellow = sulphur, blue = oxygen, grey = carbon.

Structurally, the DME-solvates (Niggli-notation: $^1_\infty[Ln(OTf)_{4/2}](DME)_{2/1}$) are closely related to the THF-solvates of $Yb(OTf)_2$ and $Ca(OTf)_2$, where the THF ligands are located at similar positions as the DME ligands in this case (comp. fig. 20). The structure type of the DME-solvates is evidently more flexible towards accommodating cations of different sizes, which can be explained by the expansion of the coordination sphere to an

8-fold-coordinationwhich is facilitated by the chelating character of the DME-moieties. Because the structure type has already been reported,[98] a more detailed description is not required.
Unlike the acetonitrile-solvates and some of the THF-solvates, it was not possible to prepare the pure materials of $Ln(OTf)_2(DME)_2$ since the crystallisation of the triflates from DME lead to mixtures with yet unidentified crystalline phases (see section 6.2.24 for exp. data).

4.2.4 Luminescence of Desolvated $Ln(OTf)_2$

The desolvated triflates $Ln(OTf)_2$ (Ln = Sm, Eu, Yb) were produced according to methods described in section 4.2.1. While $Yb(OTf)_2$ did not show emission in the range from 200 nm to 800 nm, luminescence spectra of $Eu(OTf)_2$ and $Sm(OTf)_2$ could be measured and will be discussed in the follwoing section.
Like the solvates with THF and acetonitrile, $Eu(OTf)_2$ exhibits intense emission in the transitional region between UV and the visible ranges of the electromagnetic spectrum. More precisely, the emission maximum is found at 393 nm, which is almost identical to the emission peak of $Eu(OTf)_2(MeCN)$. The emission and excitation spectra of $Eu(OTf)_2$ are shown in fig. 23.

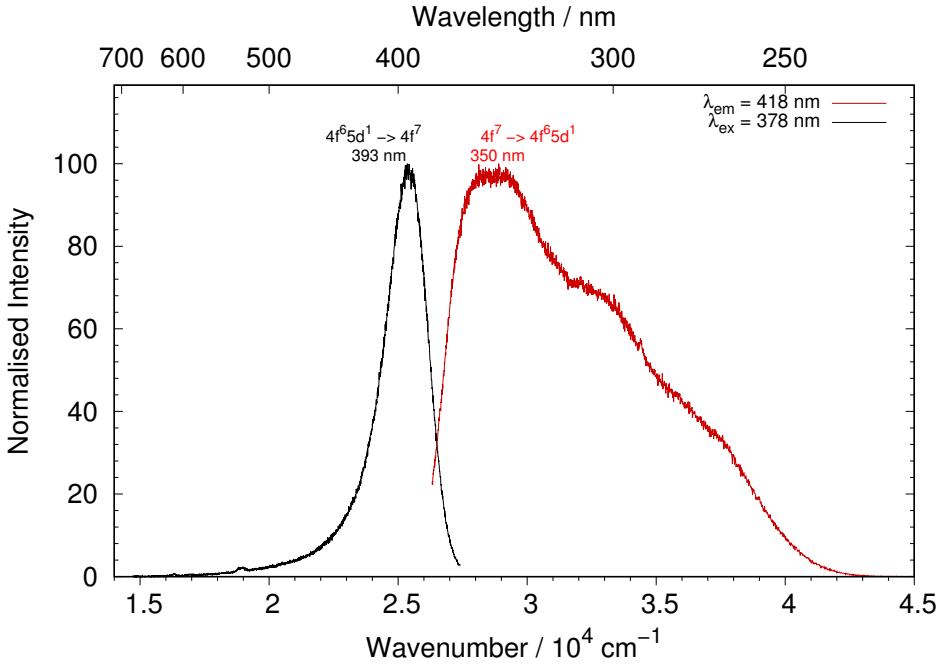


Fig. 23 Emission and excitation spectra of $Eu(OTf)_2$ at room temperature.

Again, the broad nature of the emission and excitation bands are typical for interconfigurational $4f^7 \rightarrow 4f^6 5d^1$-transitions (or vice versa). As opposed to the solvated triflates, the crystal structure of $Eu(OTf)_2$ remains unknown and thus, the influence of the structure on

the luminescence can only be assessed indirectly. While the precise coordination polyhedra of the Eu^{2+}-ions are unknown, it must be coordinated only by oxygen atoms of the triflate anions. Considering the similar emission wavelengths of $Eu(OTf)_2$ and $Eu(OTf_2)(MeCN)$, it can be concluded that the potentially different coordination geometry, along with the nephelauxetic effects of exchanging nitrogen for oxygen lead to very similar crystal field splitting. A summary of spectroscopic data of the Eu^{2+} triflates is provided in tab. 4.

Tab. 4 Summary of emission- and excitation wavelengths of $Eu(OTf)_2$ and its solvates.

Compound	Emission Max. / nm	Excitation Max. / nm	Stokes Shift / cm^{-1}	Spectral Data
$Eu(OTf)_2$	393	350	3126	fig. 23
$Eu(OTf)_2(MeCN)$	398	370	1901	contained in section 4.2.1
$Eu(OTf)_2(THF)_{1.5}$	418	378	2531	fig. 21

Since the emission spectra of both $Sm(OTf)_2$ (see fig. 94) and $Sm(OTf)_2(MeCN)$ (see section 4.2.1) are dominated by intraconfigurational f-f-transitions, their emission spectra are inherently similar and do not require a more detailed disquisition.

4.2.5 Attempted Reduction of Thulium(III)

The synthetic protocol that was established for the syntheses of $Ln(OTf)_2$ by reducing $Ln(OTf)_3$ with the respective metals worked well for Ln = Sm, Eu and Yb (see section 4.2.1). For Tm however, the protocol did not result in conversion of the starting materials.[124] Given the more strongly reducing character of the Tm^{2+}-ion, when compared to the other Ln^{2+}-ions mentioned above, the conversion is simply missing a thermodynamic driving force. In other words the reduction potential of metallic thulium under the given conditions is not sufficient to reduce Tm^{3+} to Tm^{2+}.
The synthesis of $Tm(OTf)_2(DME)_2$ was accomplished by reduction of $Tm(OTf)_3$ with KC_8 at low temperatures, as demonstrated by *Nocton* et al., proving that $Tm(OTf)_2$ is practically accessible.[98] The following section deals with the attempted synthesis of different solvates of $Tm(OTf)_2$. The challenges therein already become evident when reviewing *Nocton's* work who claimed that solutions of $Tm(OTf)_2$ are instable at room temperature due to disproportionation, further corroborating the hypothesis that the equilibrium between metallic thulium, $Tm(OTf)_3$ and $Tm(OTf)_2$ is located on the side of Tm^{3+} and Tm^0. Initial attempts of reducing $Tm(OTf)_3$ with metallic thulium under mechanochemical conditions confirm this claim. In order to validate the mechanochemical approach, $Eu(OTf)_2$ was synthesised by analogous methods (see section 6.2.25 for exp. details).

Adapting *Nocton's* method, the reduction of $Tm(OTf)_3$ with KC_8 was attempted at low temperatures in THF or acetonitrile, neither of which resulted in the conversion of the substrates. The lack of conversion in this case could be a result of differences in the complexation of Tm-ions in the different solvents, where DME seemingly is beneficial for the stablisation of the Tm^{2+}-ion. Likewise, adding 18-crown-6 to the reaction mixture did not result in the reduction of Tm^{3+}. All relevant experiments of this section are summarised in tab. 5.

Tab. 5 Summary of attempted reductions of $Tm(OTf)_3$ that were conducted in this work. Calculated eq. are referring to the ratio of the reducing agent and $Tm(OTf)_3$.

Reducing Agent	**Eq.**	**Solvent**	**Conditions**	**Exp. Details**	**Conv. to Tm^{2+}**
Tm	0.5	ball mill	rt	6.2.27	no
Tm	2.6	ball mill + THF	rt	6.2.26	no
Tm	2	ball mill + MeCN	rt	6.2.29	no
Tm	0.5	ball mill + MeCN	-40 °C	6.2.30	no
KC_8	1	ball mill	rt	6.2.31	no
n-BuLi	1.1	THF	-78 °C to rt	6.2.32	no
KC_8	3	MeCN	-40 °C to rt	6.2.33	no
KC_8 + 18-crown-6	4.6	MeCN	-40 °C	6.2.34	no
KC_8	3	THF	-78 °C	6.2.35	no
KC_8	1.1	THF / Et_2O	-78 °C	6.2.36	yes
KC_8	2	MeCN / Et_2O	-40 °C	6.2.37	no
KC_8	1.2	Et_2O	sonication	6.2.38	yes

It was known that $Sm(OTf)_3$ can be reduced by butyl lithium (BuLi),[127] hence it was attempted with thulium as well, where again no conversion was observed. Finally, repeating the attempted reduction in THF with the addition of diethylether resulted in a violet solution that was obtained after filtration. At room temperature, the solution lost its colour within seconds, preventing further analytical experiments. A photo of the solution is shown in fig. 24. When combining acetonitrile and diethylether, no conversion was observed.

Using pure diethylether proved problematic due to the low solubility of $Tm(OTf)_3$. However, when sonicating a mixture of $Tm(OTf)_3$ and KC_8, followed by quick evaporation of the volatile materials resulted in a crude mixture of solids containing Tm^{2+}. By suspending the solids in cold THF, followed by immediate filtration, a UV-Vis spectrum could be measured which is shown in fig. 24.

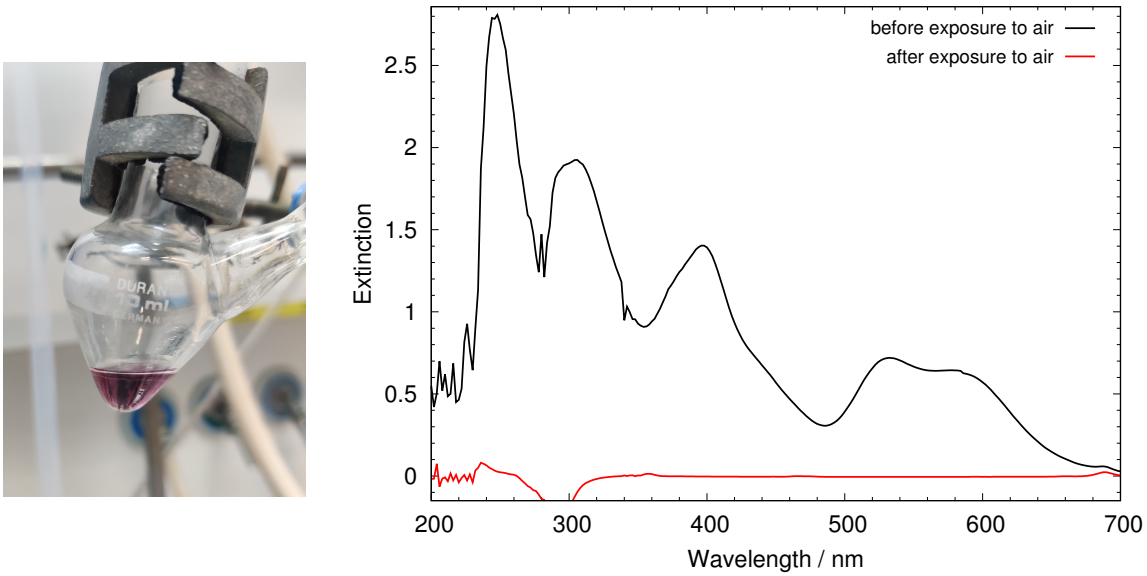


Fig. 24 Photo of a violet solution containing Tm^{2+} (left) and UV-Vis spectrum (right), obtained from reacting $Tm(OTf)_3$ and KC_8 in diethylether. The spectrum was measured in THF.

The UV-Vis spectrum had to be recorded as quickly as possible, due to the thermal instability of the solution. Thus a large step size had to be chosen, diminishing the resolution of the spectrum. Nonetheless, five strong absorption bands can be identified with peaks at ca. 248, 305, 394, 529 and 589 nm that are indicative of Tm^{2+} for the reasons elaborated in section 2.3.1. After exposure to air, all bands quickly disappeared due to the oxidation of Tm^{2+}. Negative intensities in the second spectrum might be a result of fingerprints on the cuvette when measuring the background or other external factors. The validity of the arguments made previously are not affected hereby.

While the presented results are qualitative indicators for the formation of Tm^{2+}, they cannot provide information about how much of the initial $Tm(OTf)_3$ was converted. All attempts to crystallise $Tm(OTf)_2$ from solution failed due to its notorious instability, even at low temperatures.

The results gathered in this section demonstrate that it is in principle possible to obtain Tm^{2+} by reduction with KC_8 in solvents other than DME. However, the problems encountered by *Nocton* et al. during their work on $Tm(OTf)_2$ in DME[98] appear to become even more challenging, when transitioning to other solvents. As mentioned above, the complexation of the Tm-ions by the solvent seems to have a decisive influence on the reactivity of Tm^{2+}-species. Although theoretically possible, the practical difficulties encountered in this work when dealing with Tm^{2+}-species, render further studies of new solvates such as single crystal XRD, or luminescence spectroscopy practically impossible.

4.2.6 Attempted Synthesis of Europium(II) Perchlorate

In the previous sections, the methods introduced in section 4.2.1 of producing $Ln(OTf)_2$ were explored with respect to different solvents, as well as different lanthanoid metals in order to establish the limits of their applicability. The question if the methods can also be transferred to the synthesis of salts containing other anions remained open. Hence, the following section is dedicated to the synthesis of $Eu(ClO_4)_2$. Both anions (triflate and perchlorate) are similarly weakly coordinating, but the perchlorate ion is potentially more sensitive towards reduction. Therefore the least reducing Ln^{2+}-ion was chosen in the form of Eu^{2+}. The anticipated reaction equation is shown in scheme 11.

$$Eu + 2\,Eu(ClO_4)_3 \xrightarrow{MeCN} 3\,Eu(ClO_4)_2(MeCN)_n$$

Scheme 11 Anticipated reaction of $Eu(ClO_4)_3$ and Eu, where n is an arbitrary number.

Reacting metallic europium with $Eu(ClO_4)_3$ in acetonitrile indeed produced yellow solutions (see section 6.2.39 for exp. details), as was the case for the triflate. A UV-Vis spectrum of the yellow solution is shown in fig. 25 next to a reference spectrum of $Eu(OTf)_2$.

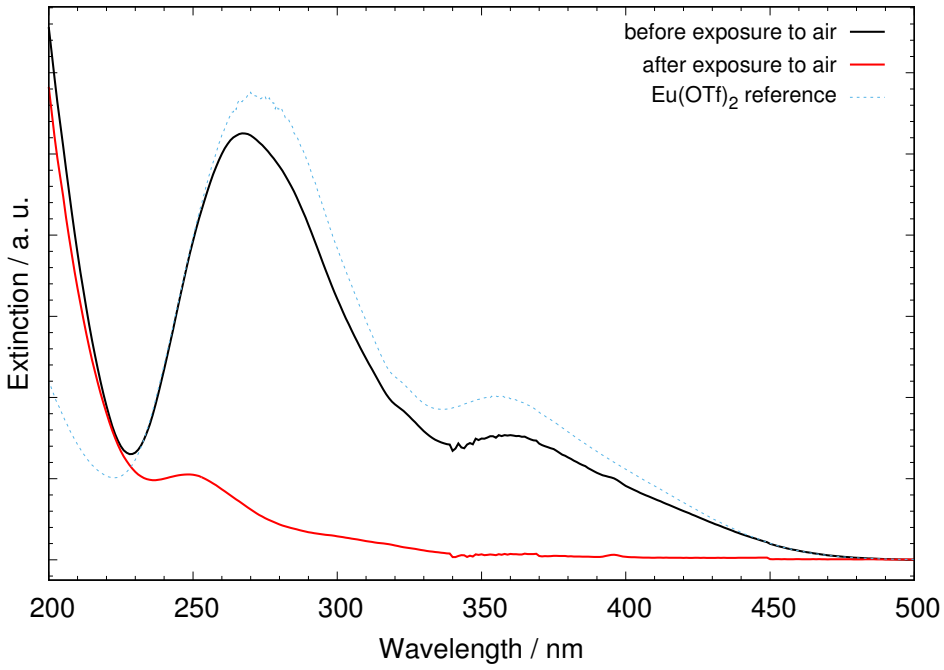


Fig. 25 UV-Vis spectrum of the solution obtained from reacting $Eu(ClO_4)_3$ and Eu in acetonitrile, next to a reference spectrum of $Eu(OTf)_2$. The spectrum was measured in acetonitrile.

The absorption bands of the solution are almost identical to those previously observed for $Eu(OTf)_2$ and peak at ca. 270 and 360 nm. After exposure to atmospheric oxygen

both bands vanish, signalling the oxidation of Eu^{2+} to Eu^{3+}. Despite this observation, evaporation of the solution yielded $Eu(ClO_4)_3(MeCN)_4$, in which europium is still found in its trivalent oxidation state.

Although no high-quality data set could be produced, the structural model of the compound allows for a brief description of the structure, which is partially supported by the observation that the analogous compound of Pr^{3+} is isostructural (see section 4.1.2). The structure of $Eu(ClO_4)_3(MeCN)_4$ (Niggli-notation: ${}^{0}_{\infty}[Eu(ClO_4)_{3/1}(MeCN)_{4/1}]$) was solved and refined in the monoclinic space group Cc ($a = 1201.56(2)$ pm, $b = 1068.27(1)$ pm, $c = 1572.70(2)$ pm, $\beta = 105.575(2)°$). The structure consists of molecular units of $[Eu(ClO_4)_3(MeCN)_4]$, in which two of the perchlorate anions act as chelating ligands, whereas the third perchlorate anion coordinates terminally. The coordination sphere of the central ion is saturated by four units of acetonitrile, resulting in an irregular 9-fold coordination geometry. The complex is shown in fig. 26.

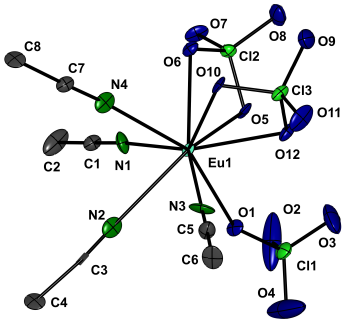


Fig. 26 Single crystal structure of $Eu(ClO_4)_3(MeCN)_4$. Hydrogen atoms are omitted and displacement ellipsoids are shown at 50% probability level.

When redissolving the solids in acetonitrile, again yellow solutions were obtained, proving that presence of Eu^{3+} was not a result of oxidation during the crystallisation process but instead proved the incomplete conversion of $Eu(ClO_4)_3$. In order to increase the conversion rate of the reaction, the experiment was repeated several times with varying concentration, with and without the addition of mercury, and even using excess of metallic europium (see section 6.2.39 for exp. details). In all cases, pure $Eu(ClO_4)_3(MeCN)_4$ was recovered, from which it is concluded that Eu^{2+} was only present in small quantities in the investigated solutions, but because of its comparably high molar extinction coefficient, still caused intense colours.

Since $Eu(OTf)_2$ could not only be obtained by comproportionation in organic solvents, but also mechanochemically (see section 6.2.25 for exp. details), the same was attempted for $Eu(ClO_4)_2$. After grinding $Eu(ClO_4)_3$ and metallic europium in a ball mill, a grey powder formed which when dissolved in acetonitrile produced yellow solutions. Recrystallisation of the crude products afforded $Eu(ClO_4)_3(MeCN)_4$ once more (see section 6.2.40 for exp. details), allowing a similar conclusion as was made for the experiments in acetonitrile.

In an effort to further increase the conversion rate, a small amount of acetonitrile was added to the ball mill and the experiment was repeated. As soon as the ball mill was started, the contents detonated so violently that further mechanochemical experiments were considered unsafe and were therefore not repeated.
In conclusion, the experiments have shown that the methods that proved successful for the synthesis of $Ln(OTf)_2$ (Ln = Sm, Eu, Yb), could not simply be transfered to the perchlorate ion, due to a lack of conversion of the substrates. If the conversion rate was forcefully increased by adding solvent to the ball mill, the reactants exploded, which is likely to be a result of competing redox reactions between the perchlorate anion and metallic europium or acetonitrile.

4.2.7 Lanthanoid(II) Azides (*Manuscript 5*)

The previous sections dealt with the synthesis and characterisation of lanthanoid(II) triflates, as well as the exploration of the limits of the applied synthetic methods. The final section of this chapter finally addresses their chemical applications. One of the major advantages of triflates over most other inorganic salts of divalent lanthanoids is their high solubility in organic solvents that can be exploited to perform metatheses with other soluble salts. In order to proof this concept, the following manuscript describes the synthesis and characterisation of the binary divalent lanthanoid azides which have historically been particularly difficult synthetic targets.[128,129]
More precisely, solvent-free $Eu(N_3)_2$ and $Yb(N_3)_2$ could be synthesised by salt metathesis of $TBAN_3$ and $Ln(OTf)_2$ (Ln = Eu, Yb) in acetonitrile. It was shown that both azides are isostructural to $Sr(N_3)_2$.[130] The thermogravimetric data suggest the formation of the metals as was indirectly verified by the presence of the sesquioxides after the experiments. Optical spectroscopy revealed that undiluted $Eu(N_3)_2$ is strongly luminescent at low temperature with an emission wavelength of $\lambda_{max} = 576$ nm.
The author's contribution include the experimental work, data analysis and writing of the manuscript in collaboration with the coauthors. Optical measurements were conducted by J. Weiß who also wrote the respective sections of the manuscript.
Supporting information of ***Manuscript 5*** is provided in section 7.1.

Synthesis and Optical Properties of Solvent-Free Binary Azides $Eu(N_3)_2$ and $Yb(N_3)_2$

N. T. Flosbach[1], P. L. Jurzick[1], M. Bykov[1,2], J. W. Weiß[3], C. Wickleder[3], M. S. Wickleder[1]

[1]University of Cologne, Institute of Inorganic Chemistry, Greinstr. 6, 50939 Cologne, Germany

[2]Institute of Inorganic and Analytical Chemistry, Goethe University Frankfurt, Max-von-Laue-Str. 7, 60438 Frankfurt am Main, Germany

[3]University of Siegen, Institute of Inorganic Chemistry, Adolf-Reichwein-Straße, 57068 Siegen, Germany

ABSTRACT: The metathesis of divalent lanthanoid triflates and tetrabutylammonium azide afforded the pure solvent-free binary azides $Eu(N_3)_2$ and $Yb(N_3)_2$. The two compounds not only present the first examples of true binary lanthanoid azides, but also the first examples of binary phases between divalent lanthanoids and nitrogen. The azides were obtained in crystalline form and characterized by PXRD, IR-spectroscopy, thermal analysis as well as advanced optical spectroscopy. Both $Eu(N_3)_2$ and $Yb(N_3)_2$ are isostructural to $Ca(N_3)_2$ and $Sr(N_3)_2$ and decompose into the respective metals at relatively mild conditions. $Eu(N_3)_2$ emits in the yellow to green region of the color spectrum (λ_{max} = 576 nm) when exited with blue light (λ_{max} = 450 nm) at T = 10 K. The emission is quenched strongly upon heating, due to a combination of vibrational influence of the N_3^--ion and a small band gap. The band gaps of both compounds were determined from reflectance spectra with the aid of a Tauc plot.

INTRODUCTION

One of the most important features in the chemistry of the lanthanoids is the ubiquity of the +III oxidation state, that is the most stable for each individual element of the series.[1-2] Many applications of lanthanoid elements utilize the unique physical properties of their ions that are directly related to the nature of the 4f-orbitals that are gradually filled throughout the series.[3-5] Changing the oxidation state of a lanthanoid naturally results in different physical properties that can be exploited to address the ever increasing demand for new materials exhibiting novel properties.[6-7] Although metal organic complexes for most lanthanoids in their +II oxidation state have been discovered, simple salts of divalent lanthanoids remain limited to only a few elements with samarium, europium and ytterbium being the most prominent ones.[8-12] The highest reduction potential of divalent lanthanoids is found for the $4f^7$-configured Eu^{2+}-ion ($E_0(Eu^{2+}/Eu^{3+}) \approx -0.35$ V)[1-2] making it the only Ln^{2+}-ion that can in principle be handled under aqueous conditions. The closed shell Yb^{2+}-ion and the $4f^6$-configured Sm^{2+}-ion follow Eu^{2+} in the row of least reducing Ln^{2+}-ions with standard reduction potentials of $E_0(Yb^{2+}/Yb^{3+}) \approx -1.05$ V and $E_0(Sm^{2+}/Sm^{3+}) \approx -1.55$.[1-2] The Eu^{2+}-ion is of particular interest due to its relatively easy accessibility, along with its optical properties that are fundamentally different from those of most Ln^{3+}-ions.[13-17] Its luminescence is typically dominated by parity allowed interconfigurational $4f^65d^1 \rightarrow 4f^7$ emission and respective absorption that are, in contrast to the intraconfigurational transitions in most Ln^{3+}-ions, much more intense. Another advantage of interconfigurational transitions in Eu^{2+} is the possibility to tailor the emission and absorption wavelengths by influencing the energy levels of the d-orbitals by chemically engineering the crystal field.[18-20] The variation of the coordinating atoms around a central metal ion thus alters the luminescent properties. As opposed to oxygen-based donor systems, inorganic compounds in which divalent lanthanoid ions are coordinated solely by nitrogen atoms are rare.[21-22]

When reviewing simple binary phases of lanthanoids and nitrogen, the only structurally characterized examples are the lanthanoid(III) nitrides that crystallize in the cubic NaCl-structure type along with the phases LnN_2 (Ln = Ce, Pr, Nd) and Ln_2N_3 (Ln = Tb, Dy, Ho, Tm, Lu).[23-30] Another possibility of creating binary phases between metals and nitrogen are azides of the general form $M(N_3)_n$. Binary metal azides and homoleptic azido complexes are known for almost all transition metals, as well as for many main group elements but are comparatively underdeveloped in the chemistry of lanthanoids.[31] Polyazidolanthanoid(III) complexes have been prepared in various forms and

even solvates of binary $Gd(N_3)_3$ with DMSO have been reported.[32-37] Azides of divalent europium and ytterbium were first discovered by *Kraus* et al. who reacted the lanthanoid metals with silver azide in liquid ammonia to obtain the respective ammonia adducts.[38] We herein present a facile synthetic route to obtain solvent-free $Eu(N_3)_2$ and $Yb(N_3)_2$ and report structural data for the first time, along with advanced characterization including luminescence and reflectance spectroscopy in the solid state.

RESULTS AND DISCUSSION

Synthesis and Structure The metathesis of lanthanoid(II) triflates with tetrabutylammonium azide in acetonitrile resulted in the precipitation of the solvent-free azides $Ln(N_3)_2$. When attempting the synthesis with $Sm(OTf)_2$ to obtain $Sm(N_3)_2$, the green solution immediately lost its intense colour after the addition of the $(Bu_4N)N_3$-solution, indicating that the Sm^{2+}-ions were oxidized to Sm^{3+}.

$$\underset{(solv)}{Ln(OTf)_2} + 2\ \underset{(solv)}{(Bu_4N)N_3} \xrightarrow[rt]{MeCN} \underset{(s)}{Ln(N_3)_2} + 2\ \underset{(solv)}{(Bu_4N)OTf} \qquad (1)$$

Both azides precipitated as crystalline powders and could easily be removed from the reaction mixtures either by filtration or centrifugation. Powder X-ray diffraction (PXRD) patterns of both products are shown in fig. 1. When exposing the azides to atmospheric oxygen, the intense color vanished within minutes in the case of $Yb(N_3)_2$ but lasted several weeks in the case of $Eu(N_3)_2$.

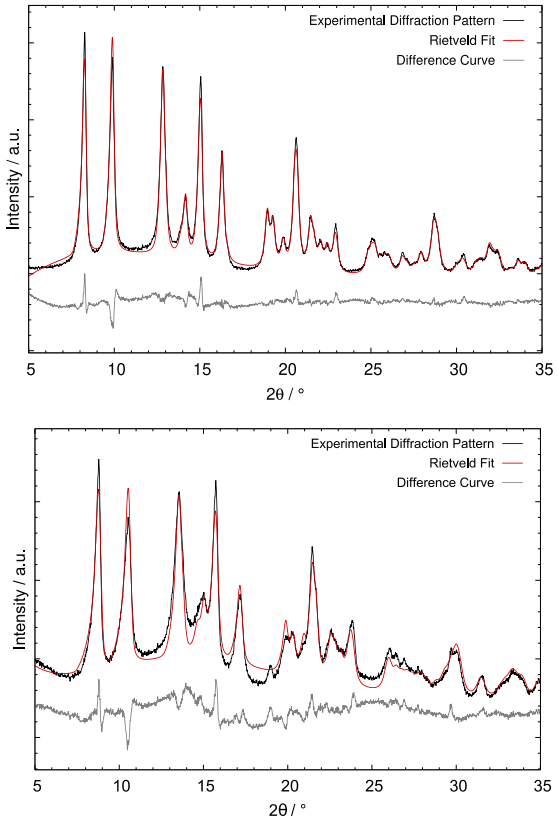


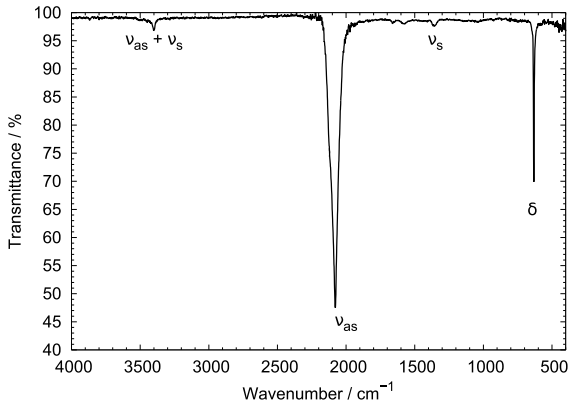
Figure 1. PXRD data and Rietveld refinements of $Eu(N_3)_2$ (top) and $Yb(N_3)_2$ (bottom). For $Eu(N_3)_2$, $Sr(N_3)_2$ was used as a reference structure, whereas $Ca(N_3)_2$ was used for the refinement of $Yb(N_3)_2$.[39] The data were produced using Mo-Kα_1-radiation.

Both compounds are isostructural to $Sr(N_3)_2$ and $Ca(N_3)_2$. The lattice parameters of $Eu(N_3)_2$ are very close to those of the related $Sr(N_3)_2$ that was used as a reference model for the Rietveld refinement. Likewise, the lattice parameters obtained from the Rietveld refinement of $Yb(N_3)_2$ and $Ca(N_3)_2$ are almost identical. For both pairs of ions the similarities were expected due to the similarities in ionic radii between Sr^{2+}/Eu^{2+} and Ca^{2+}/Yb^{2+}. The lattice parameters are summarized in tab. 1.

Table 1. Lattice parameters of $Ln(N_3)_2$ obtained from Rietveld refinement and corresponding data of $Sr(N_3)_2$ and $Ca(N_3)_2$ taken from *Simon* et al.[39]

	$Eu(N_3)_2$	**$Sr(N_3)_2$**	**$Yb(N_3)_2$**	**$Ca(N_3)_2$**
a / pm	612.17(7)	612.02(9)	597.5(1)	595.4(2)
b / pm	1149.2(2)	1154.6(2)	1102.9(3)	1103.6(5)
c / pm	1174.2(2)	1182.6(2)	1133.0(3)	1133.1(6)
V / 10^6 pm^3	826.0(2)	835.7(2)	746.6(4)	744.5(6)
R_{wp}	6.36	-	6.20	-
R_{exp}	2.12	-	5.41	-
R_p	4.94	-	4.69	-
GoF	3.00	-	1.15	-

Vibrational Spectroscopy As expected, the IR-spectra of the title compounds are very similar to each other and both are dominated by a strong absorption at ca. 2100 cm^{-1} that is typical for azides and can be assigned to the asymmetric stretching vibration (ν_{as}) of the azide anion.[37-38] The symmetric stretching vibration (ν_s) is very weak and found at ca. 1400 cm^{-1}. Additionally, a deformational vibration (δ) of the azide group causes a sharp absorption band at ca. 620 cm^{-1}. A fourth band at ca. 3400 cm^{-1} is attributed to a combinational vibration of ν_{as} and ν_s. The assignment was done by comparison to literature data of similar azides.[39-41] Both IR-spectra are shown in fig. 2 and their vibrational frequencies are summarized in tab. 2. The weak features between 1500 and 1700 cm^{-1} cannot be assigned unambiguously but possibly are the result of additional combination vibrations.



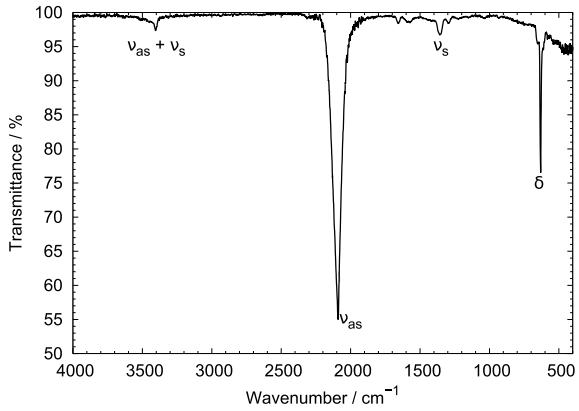


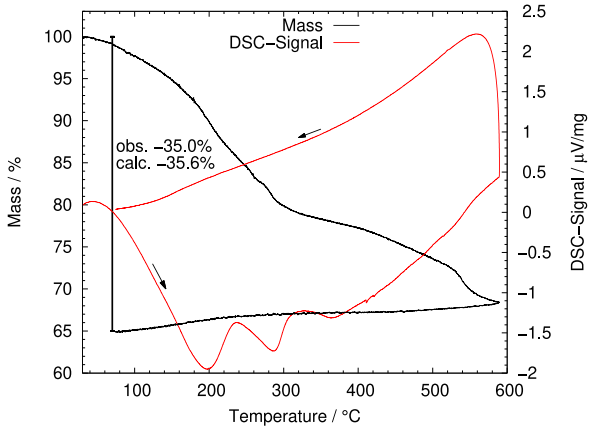
Figure 2. IR-spectra of $Eu(N_3)_2$ (top) and $Yb(N_3)_2$ (bottom).

Table 2. Summary of IR-data of $Eu(N_3)_2$ and $Yb(N_3)_2$ and literature data of $Sr(N_3)_2$ and $Ca(N_3)_2$.[39] All values are given in units of cm^{-1}.

	$Eu(N_3)_2$	**$Sr(N_3)_2$**	**$Yb(N_3)_2$**	**$Ca(N_3)_2$**
δ	633	635	630	636
ν_s	1356	1371	1356	1379
ν_{as}	2076	2112	2090	2166/2114/ 2101
$\nu_{as} + \nu_s$	3401	-[a]	3405	-[a]

[a]Values were not provided in the publication.

Thermal Decomposition Decomposition of both $Eu(N_3)_2$ and $Yb(N_3)_2$ already begins at temperatures <100 °C and continues under gradual loss of mass until ca. 600 °C. In the mass curves of the TGA-DSC diagrams (fig. 3) no distinct steps are recognizable, but the DSC-curves show at least three distinguishable exothermic signals that are indicative of a complex multi-step decomposition pathway.



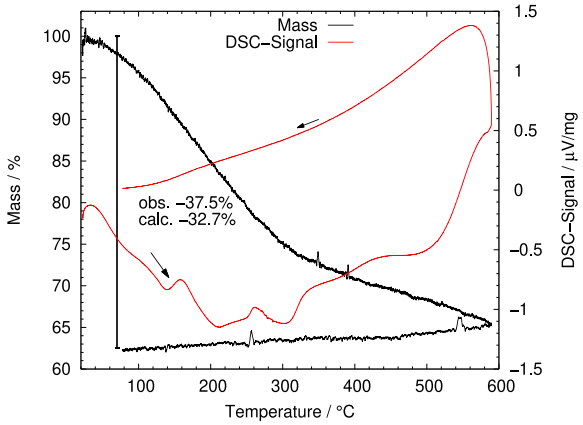


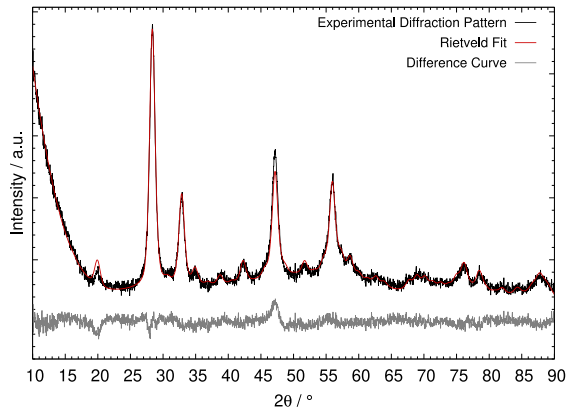
Figure 3. TGA-DSC data of $Eu(N_3)_2$ (top) and $Yb(N_3)_2$ (bottom) measured with a heating rate of 5 K/min and a continuous flow of argon. Small pikes in the bottom diagram are a result of external influences of the measurement.

After the decomposition was completed, ca. 65.0% of the initial mass remained in the case of $Eu(N_3)_2$ and ca. 62.5% in the case of $Yb(N_3)_2$, which is – within the margin of error (ca. 5-10%) – consistent with the formation of the metallic elements. The formation of the elements is typical for metal azides and has been reported for many examples, including the earth alkaline metal azides.[42]

$$Ln(N_3)_2 \xrightarrow[\text{multiple steps}]{\Delta T} Ln + 3\,N_2 \qquad (2)$$

Ln = Eu, Yb

PXRD data of the residues revealed the formation of the pure sequioxides, as was expected after exposure of the metals to atmospheric oxygen, corroborating the proposed decomposition reaction. The diffraction data of the oxides are shown in fig 4.



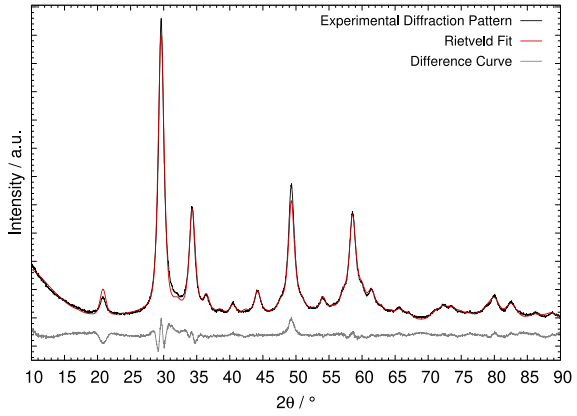


Figure 4. PXRD data of Eu_2O_3 (top) and Yb_2O_3 (bottom) obtained from thermally decomposing $Eu(N_3)_2$ and $Yb(N_3)_2$ and subsequent exposure to atmospheric oxygen. Rietveld refinements were performed using starting models by *Kato* et al.[43] The refined parameters are provided in the supporting information (SI). The data were produced using Cu-Kα-radiation.

It was attempted to isolate metallic europium by repeating the thermal decomposition of $Eu(N_3)_2$ on a preparative scale choosing the same parameters (continuous flow of argon and heating rate of 5 K/min) as were applied in the TGA-DSC measurements. Unlike in the TGA-DSC experiments, the azide exploded and no material could be recovered. Hence, the experiment was repeated with a slower heating rate of 1 K/min that again resulted in a detonation from which no leftovers could be analyzed.

Optical Spectroscopy Upon irradiation with UV-light (λ = 450 nm), $Eu(N_3)_2$ shows intense, yellow-green $4f^6 5d^1 \rightarrow 4f^7$ emission (λ_{max} = 576 nm) at T = 10 K (fig. 5, top). The excitation spectrum features one broad band between 350 nm and 520 nm and its shape indicates possible indirect excitation via the azide unit. As this is not a doped sample, observing any emission at all is very rare due to usually strong concentration quenching. Temperature-dependent emission spectra with an excitation wavelength of λ = 450 nm were recorded and show strong thermal quenching (fig. 5, bottom. By analyzing the integrated intensities, a quenching temperature of T_{50} = ~95 K was determined (fig. S 3). To further characterize the observed Eu^{2+}-emission, a decay time measurement was performed at 10 K with an excitation wavelength of λ = 355 nm. A tri-exponential decay function was fitted to the decay signal to obtain a decay time of τ_1 = (409.0 ± 1.3) ns (fig. S 4). The second time (τ_2 = (112.3 ± 0.4) ns) could indicate an indirect excitation process via the host material while the third time (τ_3 = (19.3 ± 0.1) ns) can be assigned to the pulse width of the laser used for excitation.

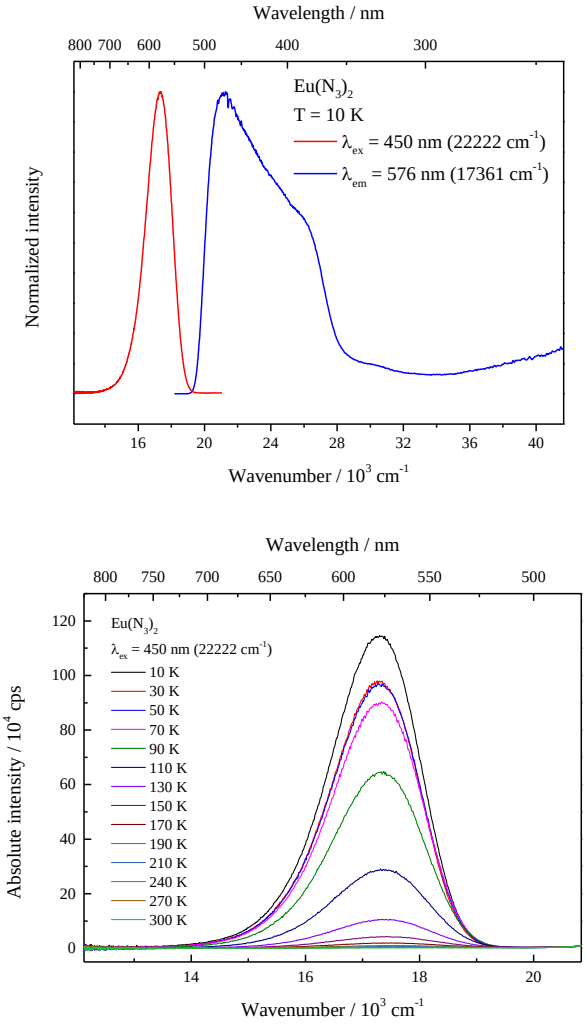


Figure 5. Emission and excitation spectra of $Eu(N_3)_2$ (top) and temperature-dependent emission spectra of $Eu(N_3)_2$ with an excitation energy of 450 nm (bottom).

The determined value of 409 ns fits very well into the range between 400-1500 ns known for Eu^{2+} containing compounds,[44] even though $Eu(N_3)_2$ is not a doped compound. Compared to $Eu(N_3)_2$, $Yb(N_3)_2$ does not show any luminescence at all. One reason might be a too narrow band gap, leading to excitation into the conduction band and quenching via photoionization. Additionally, the high vibrational energy determined from IR-spectra for both compounds likely leads to additional quenching processes (e.g. via multi-phonon transitions). To further investigate these observations, reflectance measurements were performed on both compounds (fig. 6).

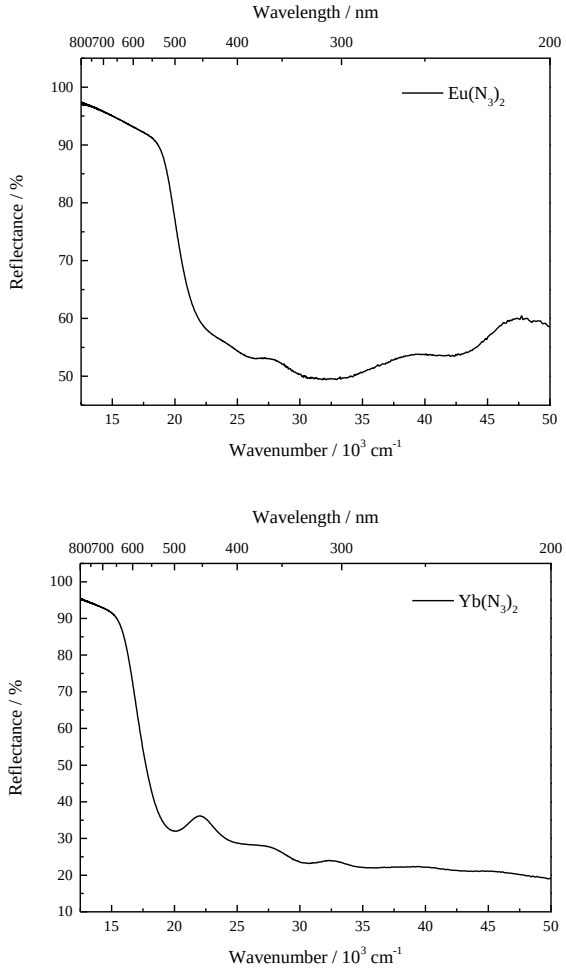


Figure 6. Reflectance spectra of $Eu(N_3)_2$ (top) and $Yb(N_3)_2$ (bottom).

Similar absorption bands can be seen which might be attributed to the presence of the $[(N_3)_2]^{2-}$ unit, whereas the colors of the powders ($Eu(N_3)_2$ - yellow, $Yb(N_3)_2$ - orange) are clearly represented by the absorption behavior. In the case of $Eu(N_3)_2$, some of the absorption bands can be correlated to the excitation spectra (fig. S 5). By using the Kubelka-Munk function,[45] Tauc plots of both samples were constructed (fig. S 6+7).[46] Using a linear fitting function, the respective band gaps can be derived from the interception with the x-axis at y = 0. Direct band gaps of 2.42 eV for $Eu(N_3)_2$ and 2.12 eV for $Yb(N_3)_2$ could be determined. The smaller band gap for $Yb(N_3)_2$ and other processes mentioned before might be the reason why no luminescence can be observed for this compound.

CONCLUSION

The binary solvent-free lanthanoid(II) azides $Eu(N_3)_2$ and $Yb(N_3)_2$ were synthesized by metathesis of $TBAN_3$ and $Ln(OTf)_2$ and present the first binary phases between divalent lanthanoids and nitrogen, as well as the first structurally characterized true binary azides of lanthanoids. Attempts to generate $Sm(N_3)_2$ failed due to competing redox processes. Both compounds are isostructural to $Sr(N_3)_2$ and $Ca(N_3)_2$ and show complex thermal decomposition pathways commencing at temperatures even below 100 °C, ultimately resulting in the formation of the metals. The formation of metallic europium and ytterbium is supported by the observation of the respective oxides after intentional exposure to atmospheric oxygen.

While $Yb(N_3)_2$ did not show luminescence, $Eu(N_3)_2$ showed characteristic interconfigurational emission ($4f^6 5d^1 \rightarrow 4f^7$) with λ_{max} = 576 nm at 10 K. This emission is strongly quenched by temperature, likely due to vibrational influence of the N_3^- anion and a small band gap, leading to non-radiative relaxation. The determined decay time of τ_1 = (409.0 ± 1.3) ns fits in the range known for Eu^{2+}. Band gaps of 2.42 eV and 2.12 eV for $Eu(N_3)_2$ and $Yb(N_3)_2$ were determined from reflectance spectra with the aid of a Tauc plot. Finally, it must be concluded that the successful synthesis of $Eu(N_3)_2$ and $Yb(N_3)_2$ prove the remarkable efficacy of the applied procedure and the value of divalent lanthanoid triflates as precursors in synthetic chemistry. The method is expected to be much more versatile and relevant research thereof is in progress.

EXPERIMENTAL METHODS

CAUTION! The materials produced in this procedure might decompose violently and suitable protective safety measures are recommended when reproducing the experiments.

Synthesis of Starting Materials $Eu(OTf)_2$ and $Yb(OTf)_2$ were synthesized according to a literature procedure (will be published elsewhere). Tetrabutylammonium azide ($TBAN_3$) was purchased from TCI (>95%) and was used without additional purification. All manipulations were conducted under strict exclusion of oxygen and water using standard Schlenk-techniques and argon-filled gloveboxes. Acetonitrile was dried over activated molecular sieves (3 Å) for at least three days and degassed by three to four consecutive freeze-thaw-pump-cycles prior to use.

Synthesis of $Eu(N_3)_2$ 188 mg (0.661 mmol, 2.2 eq.) of $TBAN_3$ was dissolved in 1.5 ml of acetonitrile and slowly added to a solution of 150 mg (0.305 mmol, 1 eq.) of $Eu(OTf)_2(MeCN)$ in acetonitrile. The reaction mixture was stirred for 16 h at room temperature and the precipitate was separated by centrifuging the suspension for 10 min at 4000 rpm. The solids were washed with 5 ml of acetonitrile and centrifuged three more times, with additional washing steps in between. The solids were dried under reduced pressure to obtain 70 mg (0.30 mmol, 96%) of $Eu(N_3)_2$ as a yellow powder.

Synthesis of $Yb(N_3)_2$ 134 mg (0.471 mmol, 2.2 eq.) of $TBAN_3$ was dissolved in 1.5 ml of acetonitrile and slowly added to a solution of 100 mg (0.212 mmol, 1 eq.) of $Yb(OTf)_2$ in acetonitrile. The reaction mixture was treated as described for the synthesis of $Eu(N_3)_2$, yielding 42 mg (0.16 mmol, 78%) of $Yb(N_3)_2$ as an orange powder.

X-Ray Diffraction Data X-ray diffraction data were collected on a Stadi-P ($MoK\alpha_1$-radiation) in Debye-Scherrer geometry in sealed glass capillaries (diameter = 0.5 mm). Residues from thermal analyses were analyzed using a Rigaku Miniflex 600-C (Cu-Kα-radiation) with a scanning speed of 2 °/min. Samples were prepared on flat silicon holders.

IR-Spectroscopy IR-spectra were recorded on a *Bruker Alpha II* that was set up inside of an argon filled glovebox.

Thermogravimetric Analysis Thermogravimetric experiments were performed on a STA 409 (*Netzsch*). The samples were loaded into corundum crucibles and layered with *n*-hexane

inside a glove box before transferring the samples to the instrument. The hexane layer was evaporated under isothermal conditions in an argon stream before the measurements were started.

Photoluminescence Photoluminescence emission and excitation measurements were conducted using a Fluorolog3 FL3-22 spectrometer (Jobin Yvon) equipped with a 450 W Xenon arc lamp. The samples were sealed in small, optical grade quartz ampoules to protect them from air and moisture. Spectral resolution down to 0.05 nm was achieved using double Czerny-Turner monochromators and for signal detection, a photomultiplier tube (R928P, Hamamatsu) was used. Measurements down to 10 K and temperature-dependent luminescence measurements were performed with the aid of a closed-cycle Helium cryostat (Advanced Research Systems, Inc.). All emission spectra were corrected for the photomultiplier sensitivity, whereas the excitation spectra were corrected for the background spectrum of the lamp.

For decay time measurements in the ns to µs region, a frequency-shifted Nd:YAG laser (Spectra Physics Quanta Ray Indi 40) with a repetition rate of 10 Hz was used. A single monochromator (Jobin Yvon) with a resolution down to 5 nm was utilized to select the desired emission wavelength. The decay signal was recorded with a photomultiplier attached to an oscilloscope (Rohde & Schwarz RTM 2052, 500 MHz 5G Sa/s).

Reflectance spectroscopy The reflectance spectra were measured with a Cary 5000 UV/Vis spectrometer (Agilent) equipped with a deuterium (D_2) lamp as excitation source in a range of 175 nm and 350 nm as well as a halogen lamp in the range of 350 nm and 3300 nm. Precise selection of the desired wavelength was achieved by double Littrow monochromators. The reflected light was detected with a photomultiplier up to 800 nm.

Diffuse reflectance was accounted for by usage of an integrating sphere with a diameter of d = 110 mm in the sample compartment that is covered with fully reflecting Spectralon™ and functions in the range of 200 nm and 2500 nm. Powdered samples were filled into a sample holder in the Ar glove box. Afterwards, the sample holder was tightly sealed to minimize air and moisture contact.

ASSOCIATED CONTENT

Supporting Information Supporting Information. Analytical data of $Yb(OTf)_2$, refined parameters of Ln_2O_3, determination of the quenching temperature, decay time measurement of $Eu(N_3)_2$, references. (PDF).

AUTHOR INFORMATION

Corresponding Author

*Mathias S. Wickleder - Greinstr. 6, 50939 Cologne, Germany; Email: mathias.wickleder@uni-koeln.de

Author Contributions

The manuscript was written through contributions of all authors.

Notes

The authors declare no competing financial interest.

ACKNOWLEDGEMENTS

The authors thank Tobias Rennebaum for performing the TGA-DSC experiments.

ABBREVIATIONS

DMSO, dimethyl sulfoxide; DSC, differential scanning calorimetry; eq., equivalents; Ln, lanthanoid; PXRD, powder X-ray diffraction; TBA, tetrabutylammonium; TGA, thermogravimetric analysis.

REFERENCES

[1] *Electron-transfer and f-d absorption bands of some lanthanide and actinide complexes and the standard (II-III) oxidation potential for each member of the lanthanide and actinide series*, L. J. Nugent, R. D. Baybarz, J. L. Burnett, J. L. Ryan, *J. Phys. Chem.* **1973**, *Materials*, 1528-1539.

[2] *Thermochemical properties of yttrium, lanthanum, and the lanthanide elements and ions*, L. R. Morss, *Chem. Rev.* **1976**, *76*, 827-841.

[3] *Rare earths: jewels for functional materials of the future*, S. V. Eliseeva, J.-C. G. Bünzli, *New J. Chem.* **2011**, *35*, 1165-1176.

[4] *Rare earth elements: A review of applications, occurrence, exploration, analysis, recycling, and environmental impact*, V. Balaram, *Geosci. Front.* **2019**, *10*, 1285-1303.

[5] T. Behrsing, G. B. Deacon, P. Junk, in *Lanthanides And Actinides, The: Synthesis, Reactivity, Properties And Applications*, World Scientific, London, **2021**.

[6] *Synthesis, spectroscopic properties and applications of divalent lanthanides apart from Eu^{2+}*, M. Suta, C. Wickleder, *J. Lumin.* **2019**, *210*, 210-238.

[7] *The chemical and physical properties of tetravalent lanthanides: Pr, Nd, Tb, and Dy*, T. P. Gompa, A. Ramanathan, N. T. Rice, H. S. La Pierre, *Dalton Trans.* **2020**, *49*, 15945-15987.

[8] *Simple and complex halides*, G. Meyer, M. S. Wickleder, *Handbook on the Physics and Chemistry of Rare Earths* **2000**, *28*, 53-129.

[9] *Lanthanum does form stable molecular compounds in the +2 oxidation state*, P. B. Hitchcock, M. F. Lappert, L. Maron, A. V. Protchenko, *Angew. Chem. Int. Ed.* **2008**, *120*, 1510-1513.

[10] *Expanding Rare-Earth Oxidation State Chemistry to Molecular Complexes of Holmium(II) and Erbium(II)*, M. R. MacDonald, J. E. Bates, M. E. Fieser, J. W. Ziller, F. Furche, W. J. Evans, *J. Am. Chem. Soc.* **2012**, *134*, 8420-8423.

[11] *Completing the Series of +2 Ions for the Lanthanide Elements: Synthesis of Molecular Complexes of Pr^{2+}, Gd^{2+}, Tb^{2+}, and Lu^{2+}*, M. R. MacDonald, J. E. Bates, J. W. Ziller, F. Furche, W. J. Evans, *J. Am. Chem. Soc.* **2013**, *135*, 9857-9868.

[12] *All the Lanthanides Do It and Even Uranium Does Oxidation State +2*, G. Meyer, *Angew. Chem. Int. Ed.* **2014**, *53*, 3550-3551.

[13] *UV, Blue, Green, Yellow, Red, and Small: Newest Developments on Eu^{2+}-doped nanophosphors*, H. Terraschke, C. Wickleder, *Chem. Rev.* **2015**, *115*, 11352-11378.

[14] *Persistent Luminescence in Eu^{2+}-Doped Compounds: A Review*, K. Van den Eeckhout, P. F. Smet, D. Poelman, *Mater.* **2010**, *3*, 2536-2566.

[15] *Anomalous luminescence of Eu^{2+} and Yb^{2+} in inorganic compounds*, P. Dorenbos, *J. Phys.: Condens. Matter* **2003**, *15*, 2645.

[16] *Mixed Microscopic Eu^{2+} Occupancies in the Next-Generation Red LED Phosphor $Sr[Li_2Al_2O_2N_2]$: Eu^{2+} (SALON: Eu^{2+})*, F. Ruegenberg, A. García-Fuente, M. Seibald, D. Baumann, G. Hoerder, T. Fiedler, W. Urland, H. Huppertz, A. Meijerink, M. Suta, *Adv. Opt. Mater.* **2023**, *11*, 2202732.

[17] *Chasing Down the Eu^{2+} Ions: The Delicate Structure − Property Relationships in the Ultra-Narrow Band Phosphor $K_{1.6}Na_{2.1}Li_{0.3}[Li_3SiO_4]_4$: Eu^{2+}*, F. Ruegenberg, A. García-Fuente, M. Seibald, D. Baumann, S. Peschke, W. Urland, A. Meijerink, H. Huppertz, M. Suta, *Adv. Opt. Mater.* **2021**, *9*, 2101643.

[18] *Tailoring of Deep-Red Luminescence in Ca_2SiO_4: Eu^{2+}*, Y. Sato, H. Kato, M. Kobayashi, T. Masaki, D. H. Yoon, M. Kakihana, *Angew. Chem. Int. Ed.* **2014**, *53*, 7756-7759.

[19] *Tailoring Emission Characteristics: Narrow-Band Red Luminescence from SLA to $CaBa[Li_2Al_6N_8]$:Eu^{2+}*, P. Wagatha, V. Weiler, P. J. Schmidt, W. Schnick, *Chem. Mater.* **2018**, *30*, 7885-7891.

[20] *Narrow Bandwidth Luminescence in $Sr_2Li(Al,Ga)O_4$: Eu^{2+} by Selective Site Occupancy Engineering for High Definition Displays*, J. Qiao, Y. Zhou, M. S. Molokeev, Q. Zhang, Z. Xia, *Laser Photonics Rev.* **2021**, *15*, 2100392.

[21] *Mixed Valence Europium Nitridosilicate Eu_2SiN_3*, M. Zeuner, S. Pagano, P. Matthes, D. Bichler, D. Johrendt, T. Harmening, R. Pöttgen, W. Schnick, *J. Am. Chem. Soc.* **2009**, *131*, 11242-11248.

[22] *$Eu_2Si_5N_8$ and $EuYbSi_4N_7$. The First Nitridosilicates with a Divalent Rare Earth Metal*, H. Huppertz, W. Schnick, *Acta Cryst.* **1997**, *C53*, 1751-1753.

[23] *Über Mononitride und stickstoffreichere Nitride der Seltenerdmetalle (Mitt. I)*, R. Kieffer, P. Ettmayer, S. Pajakoff, *Monatsh. Chem.* **1972**, *103*, 1285-1298.

[24] *Über die Mischkristallbildung von ThN mit LaN, CeN, PrN, NdN, SmN, GdN, DyN und ErN*, P. Ettmayer, J. Waldhart, A. Vendl, G. Banik, *Monatsh. Chem.* **1980**, *111*, 945-948.

[25] *Europium nitride synthesized by direct nitridation with ammonia*, T. Suehiro, N. Hirosaki, T. Wada, Y. Yajima, M. Mitomo, *Powder Diffr.* **2005**, *20*, 40-42.

[26] *Mischnitride von Thorium mit seltenen Erden*, H. Holleck, E. Smailos, *J. Nucl. Mater.* **1980**, *91*, 237-239.

[27] *Composition limits and vaporization behaviour of rare earth nitrides*, R. C. Brown, N. J. Clark, *J. Inorg. Nucl. Chem.* **1974**, *36*, 2507-2514.

[28] *Neutron Diffraction Investigation of the Magnetic Properties of Compounds of Rare-Earth Metals with Group V Anions*, H. R. Child, M. K. Wilkinson, J. W. Cable, W. C. Koehler, E. O. Wollan, *Phys. Rev.* **1963**, *131*, 922-931.

[29] *F.c.c. type-III antiferromagnetism in YbN*, A. Dönni, P. Fischer, A. Furrer, W. Bacsa, P. Wachter, *Z. Phys. B - Condensed Matter* **1990**, *80*, 269-274.

[30] *Phase relations in the ternary systems rare-earth metal (RE)-boron-nitrogen, where RE = Tb, Dy, Ho, Er, Tm, Lu, Sc, and Y*, H. P. Klesnar, P. Rogl, *HTHP* **1990**, *22*, 453-457.

[31] *Physics and chemistry of the inorganic azides*, B. L. Evans, A. D. Yoffe, P. Gray, *Chem. Rev.* **1959**, *59*, 515-568.

[32] *Spectroscopic studies on unexpected complex azides of lanthanum(III) and neodymium(III)*, A. Popitsch, A. Mautner, H. P. Fritzer, *J. Mol. Struct.* **1982**, *79*, 313-318.

[33] *The crystal structure of a many-fold connected complex of lanthanum in $Cs_3La(N_3)_6$*, F. A. Mautner, H. Krischner, H. P. Fritzer, C. Kratky, *J. Mol. Struct.* **1989**, *213*, 169-174.

[34] *The crystal structure of $Cs_2Nd(N_3)_5$*, F. A. Mautner, H. Krischner, H. P. Fritzer, C. Kratky, *Z. Kristallogr.* **1989**, *188*, 279-286.

[35] *The crystal structure of $Cs_5Eu(N_3)_8$*, F. A. Mautner, H. Krischner, *Monatsh. Chem.* **1990**, *121*, 781-786.

[36] *Lanthanide Clusters with Azide Capping Ligands*, B. F. Moore, T. J. Emge, J. G. Brennan, *Inorg. Chem.* **2013**, *52*, 6021-6027.

[37] *Binary Polyazides of Cerium and Gadolinium*, K. Rosenstengel, A. Schulz, O. Niehaus, O. Janka, R. Pöttgen, A. Villinger, *Eur. J. Inorg. Chem.* **2018**, *2018*, 778-790.

[38] *Octaammine Eu^{II} and Yb^{II} Azides and Their Thermal Decompositions to the Nitrides*, T. G. Müller, J. Mogk, M. Conrad, F. Kraus, *Eur. J. Inorg. Chem.* **2016**, *2016*, 4162-4169.

[39] *Azide und Cyanamide – ähnlich und doch anders/Azides and Cyanamides – Similar and Yet Different*, O. Reckeweg, A. Simon, *Z. Naturforsch. B* **2003**, *58*, 1097-1104.

[40] *Infrared Vibrations of Crystalline Potassium Azide*, J. I. Bryant, *J. Chem. Phys.* **1963**, *38*, 2845-2854.

[41] *Infrared Spectra of Alkali Metal Azide Crystals*, H. A. Papazian, *J. Chem. Phys.* **1961**, *34*, 1614-1616.

[42] *Mechanism of thermal decomposition of metal azides*, B. V. L'Vov, *Thermochim. Acta* **1997**, *291*, 179-185.

[43] *Structural Change of C-Rare Earth Sesquioxides Yb_2O_3 and Er_2O_3 as a Function of Temperature*, A. Saiki, N. Ishizawa, N. Mizutani, M. Kato, *J. Ceram. Soc. Jpn.* **1985**, *93*, 649-654.

[44] *Lifetime measurements in Eu^{2+}-doped host lattices*, S. H. M. Poort, A. Meyerink, G. Blasse, *J. Phys. Chem. Solids* **1997**, *58*, 1451-1456.

[45] *Ein Beitrag zur Optik der Farbanstriche*, P. Kubelka, F. Munk, *Zeitschr. f. techn. Physik* **1931**, *11a*, 593-601.

[46] *Optical properties and electronic structure of amorphous Ge and Si*, J. Tauc, *Mater. Res. Bull.* **1968**, *3*, 37-46.

5 Conclusion

5.1 Tetravalent Lanthanoids

Attempts to synthesise new salts of tetravalent praseodymium (and terbium) by oxidation of the Ln^{3+}-ions failed, even when thermodynamical parameters such as electrochemical potential or pressure were adjusted to the very limits of preparative possibilities.
Only at the extremely high pressure of 29 GPa, it was possible to identify the first structurally characterised oxoanionic salts of Pr^{4+} in the form of $PrSi_3O_8$ and $Pr_2Si_7O_{18}$ by reacting PrO_2 and SiO_2 in a diamond anvil cell. Next to that a Pr^{3+}-silicate of the composition $Pr_4Si_3O_{12}$ had formed that can be conceived as a high-pressure polymorph of $Pr_4(SiO_4)_3$ which also was synthesised for the first time in this work (in separate experiments). The discovery of the Pr^{4+}-silicates constitutes a major milestone in the chemistry of lanthanoids, adding the class of oxoanionic salts to the still very limited collection of Pr^{4+}-compounds. Since both compounds can in principle be recovered at ambient pressure, future research should focus on optimising the procedure to that they can be produced in quantitative scale in order to study their chemical and physical properties at ambient pressure.
When trying to apply this procedure to stabilise Pr^{4+} in phosphates, a new high pressure modification of $PrPO_4$ formed which adapts the barite structure. The structural transition of ambient pressure monazite-type $LnPO_4$ to the barite-type at high pressure has often been hypothesised (see references of ***Manuscript 2***, section 4.1.9), but never been proven by XRD data. The lack of phosphates containing Pr^{4+} in this experiment emphasises the advantages of silicates for its stabilisation once more.
Both the formation of $Pr_4Si_3O_{12}$ and *hp*-$PrPO_4$ at ca. 30 GPa were accompanied by the formation of the oxide peroxide $Pr_2(O_2)O_3$ which is the first lanthanoid(IV) oxide peroxide and the most oxygen rich phase of any lanthanoid and oxygen. Its formation proved that even at high pressures, the oxidation of oxide anions to peroxide is preferred over Pr^{4+} retaining its +IV oxidation state. The intentional synthesis of $Pr_2(O_2)O_3$ by reacting PrO_2 and oxygen at ca. 27 GPa allowed for more detailed studies of this unique compound (see ***Manuscript 3***, section 4.1.10).
Complementing the results described above, ternary systems might enable the synthesis of oxoanionic Pr^{4+}-salts at lower pressure by providing a higher structural variability, so that their synthesis might become feasible on a preparative scale. Preliminary work pursuing this strategy was already conducted in this work.

5.2 Divalent Lanthanoids

Divalent lanthanoid triflates were produced by reducing $Ln(OTf)_3$ (Ln = Sm, Eu, Yb) with the respective metals in organic solvents. Solvates with acetonitrile, THF and DME were obtained and structurally characterised. The acetonitrile solvates of $Eu(OTf)_2$ and $Sm(OTf)_2$ could be synthesised in pure form and were analysed structurally and physically by magnetic measurements and luminescence spectroscopy. Solvates with THF and DME could only partially be obtained in pure form. For the case of desolvated $Eu(OTf)_2$ and for its THF and acetonitrile solvates, it was demonstrated that the emission wavelength can be tailored by incorporating different solvents into the structure.
For thulium the method failed and a systematic investigation on different procedures to produce new solvates of $Tm(OTf)_2$ was conducted. Although solutions containing Tm^{2+} could be reproducibly generated, the isolation of new solvates of $Tm(OTf)_2$ proved to be too difficult in any practical sence due to the temperature sensitivity of the materials. Additionally it was attempted to apply the synthetic protocol to other anions, for which $Eu(ClO_4)_2$ was selected as a synthetic target. After trying to optimise the reaction conditions, it was noticed that either the conversion rate was insufficient or the conditions were too harsh, either resulting in the recovery of $Eu(ClO_4)_3$ in the form of its acetonitrile solvate, or in the reduction of the perchlorate anions. Lanthanoid(II) perchlorates could therefore not be synthesised, but it is possible that other synthetic approaches such as electrochemical reduction or salt metatheses might be worth to pursue. Furthermore, salts with oxoanions such as nitrate, trifluoroacetate and other challenging synthetic targets could potentially be approached by comproportionation in acetonitrile.
Finally the synthetic utility of divalent lanthanoid triflates was demonstrated by converting them into the binary azides $Eu(N_3)_2$ and $Yb(N_3)_2$ (see ***Manuscript 5***, section 4.2.7) by metathesis with $TBAN_3$. These materials provide the unique opportunity to study the reactivity of lanthanoid azides under high pressure that is expected to result in the formation of new nitrides or diazenides.
Although only one example is presented in this work, it is to be expected that the metathesis can be expanded to other salts, such as cyanides, providing new access to a whole plethora of new salts of divalent lanthanoids.

6 Experimental Section

6.1 General Procedures

6.1.1 Multi-Anvil Press

High-pressure experiments were, if not explicitly mentioned otherwise, conducted in a *Voggenreiter* multi-anvil press using a standard *Walker*-type module.[131,132] Samples were compacted in gold- or platinum crucibles that were loaded into a standard 14/8-assembly. A detailed describtion of the used *Walker*-type setup was provided by *Huppertz.*[133]

6.1.2 Ball Mill

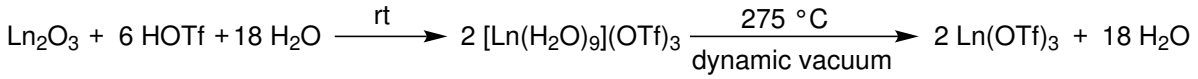
Mechanochemical experiments were carried out in a *Retsch 400 MM* mill using a steel ball and container (V = 5 ml).

6.1.3 Other Methods

Detailed description of all other materials and devices that were used in this work can be found in section 7.1.

6.2 Experimental Procedures

6.2.1 General Procedure for the Synthesis of $Ln(OTf)_3$



Two equivalents of lanthanoid(III) oxide[7] were suspended in a small amount of water and conc. triflic acid was added until all of the solids were dissolved. The solvent was then boiled off by heating the solution. The resulting solids were dehydrated at 275 °C and $1.5 \cdot 10^{-5}$ bar until no more vibrational bands of water could be detected by IR-spectroscopy. All quantitative data are summarised in tab. 6. Analytical data are displayed in fig. 27 and fig. 65.

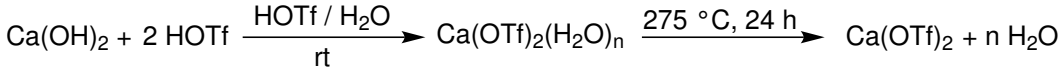
[7] For the synthesis of $Pr(OTf)_3$ and $Tb(OTf)_3$, the oxides Pr_6O_{11} and Tb_4O_7 were used in the respective quantities.

Tab. 6 Summary of quantities used for the synthesis of $Ln(OTf)_3$ according to the general procedure described in section 6.2.1.

Product	Mass Oxide	Mass Product	Yield / %
$Nd(OTf)_3$	5.00 g	12.95 g	70
$Pr(OTf)_3$	1.05 g	730 mg	20[a]
$Sm(OTf)_3$	1.03 g	2.99 g	85
$Eu(OTf)_3$	500 mg	1.39 g	82
$Tb(OTf)_3$	500 mg	1.52 g	93
$Tm(OTf)_3$	250 mg	685 mg	86
$Yb(OTf)_3$	1.50 g	4.50 g	95

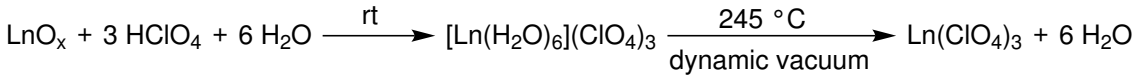
[a]Most of the material was spilled during operations, explaining the low yield.

6.2.2 Synthesis of $Ca(OTf)_2$



5.00 g (67.5 mmol, 1 eq.) of $Ca(OH)_2$ was suspended in ca. 20 ml of water before conc. triflic acid was added until all solids had dissolved. The volatiles were removed by heating and the resulting solids were heated to 275 °C for 24 hours to obtain 21.6 g (63.9 mmol, 95%). PXRD data of $Ca(OTf)_2$ is shown in fig. 50.

6.2.3 General Procedure for the Synthesis of $Ln(ClO_4)_3$



The lanthanoid oxide (Eu_2O_3, Pr_6O_{11} or Tb_4O_7) was suspended in a small amount of water and conc. perchloric acid was added until a homogeneous solution was obtained. The solvents were evaporated through heating at ambient pressure and the resulting solids were dehydrated at 245 °C and $1.5 \cdot 10^{-5}$ bar until no more vibrational bands of water could be detected by IR-spectroscopy. Quantitative data of individual experiments is summarised in tab. 7. Analytical data can be found in fig. 28, fig. 29, fig. 30 and fig. 66.

Tab. 7 Summary of quantities used for the synthesis of $Ln(ClO_4)_3$ according to the general procedure described in 6.2.3.

Product	Mass Oxide / g	Mass Product / g	Yield / %	Analytical Data
$Pr(ClO_4)_3$	1.33	2.32	67	fig. 28 + 66
$Eu(ClO_4)_3$	1.00	1.75	69	fig. 29 + 66
$Tb(ClO_4)_3$	0.51	0.74	60	fig. 30 + 66

6.2.4 Synthesis of SrO_2

$$2\ SrO + O_2 \xrightarrow[400\ °C]{5\ kbar} 2\ SrO_2$$

200 mg (1.93 mmol, 1 eq.) of SrO (obtained by calcination of $Sr(OH)_2{\cdot}(H_2O)_8$) was added to a quartz crucible that was inserted into an oxygen autoclave. The sample was then heated to 400 °C at 5 kbar for 12 hours. After releasing the pressure, 190 mg (1.59 mmol, 82%) of SrO_2 was obtained as a colourless powder. PXRD data are shown in fig. 31.

6.2.5 Crystallisation of $Pr(ClO_4)_3(MeCN)_4$

$$Pr(ClO_4)_3 + 4\ MeCN \xrightarrow[MeCN]{rt} Pr(ClO_4)_3(MeCN)_4$$

30 mg (0.068 mmol, 1 eq.) of $Pr(ClO_4)_3$ were dissolved in ca. 2 ml of acetonitrile. Slow evaporation of the solvent afforded green single crystals (ca. 20 mg) that were identified as $Pr(ClO_4)_3(MeCN)_4$. For crystallographic data see tab. 24.

6.2.6 Reaction of $Tb(OTf)_3$ and XeF_2 in Acetonitrile

$$Tb(OTf)_3 + 2\ XeF_2 \xrightarrow[MeCN]{rt} \text{unidentified products}$$

250 mg (0.414 mmol, 1 eq.) of $Tb(OTf)_3$ were dissolved in 1 ml of acetonitrile. The resulting solution was combined with a solution of 140 mg (0.823 mmol, 2 eq.) XeF_2 in 1 ml acetonitrile. After ca. 1 minute a gas started to evolve and the solution changed from colourless to brown. After employing several techniques to obtain single crystals (slow

evaporation, solvent layering, cooling, etc.) have failed, the solvents were removed under reduced pressure. A sticky residue (ca. 200 mg) was obtained that could not be analysed by PXRD. The IR-spectrum is shown in fig. 68.

6.2.7 Reaction of $Tb(ClO_4)_3$ and XeF_2 in Acetonitrile

$$Tb(ClO_4)_3 + 2\,XeF_2 \xrightarrow[MeCN]{rt} \text{unidentified products}$$

100 mg (0.219 mmol, 1 eq.) of $Tb(ClO_4)_3$ was dissolved in 1 ml of acetonitrile and added to a solution of 74 mg (0.44 mmol, 2 eq.) of XeF_2 in acetonitrile. When no more gasses were evolving, the reaction mixture was allowed to stand over night, after which solids had formed that were filtered off, washed with 1 ml of acetonitrile and dried under reduced pressure. 55 mg of an amorphous solid were obtained (comp. fig. 32).

6.2.8 Reaction of $Pr(ClO_4)_3$ and XeF_2 at Room Temperature

$$Pr(ClO_4)_3 + 3\,XeF_2 \xrightarrow{rt} PrF_3 + \text{unidentified products}$$

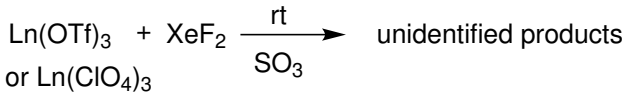
100 mg of $Pr(ClO_4)_3$ (0.228 mmol, 1 eq.) and 116 mg of XeF_2 were combined at ambient pressure. The solids immediately turned orange before igniting. After the reaction, ca. 5 mg of PrF_3 (0.03 mmol, 13%) could be recovered. PXRD data of the products are shown in fig. 33.

6.2.9 Reaction of $Pr(ClO_4)_3$ and XeF_2 at Low Temperature

$$Pr(ClO_4)_3 + 2\,XeF_2 \xrightarrow{-78\ ^\circ C \text{ to rt}} \text{unidentified products}$$

50 mg of $Pr(ClO_4)_3$ (0.14 mmol, 1 eq.) and 39 mg of XeF_2 (0.23 mmol, 2 eq.) were combined at -78 °C. The mixture was allowed to warm to 0 °C, when a yellow colouring occurred. Slowly warming the mixture to room temperature resulted in an intense orange colouring of the mixture. After removing the volatiles under reduced pressure, 35 mg of $Pr(ClO_4)_3$ were recovered as a green powder. PXRD data are shown in fig. 34.

6.2.10 Reactions of $Ln(OTf)_3$ and $Ln(ClO_4)_3$ with XeF_2 in SO_3



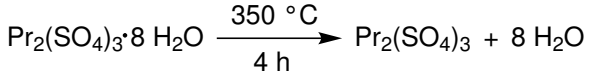
1 eq. of $Ln(OTf)_3$ or $Ln(ClO_4)_3$ and XeF_2 were added to an ampoule, before 0.5 to 1 ml of SO_3 was added at -196 °C. The ampoules were torch sealed under reduced pressure and heated to 80 °C for 24 h. After cooling to room temperature, the ampoules were opened and the volatiles were removed under reduced pressure to obtain the products as powders. A summary of experimental parameters is provided in tab. 8.

Tab. 8 Summary of quantitative data used for the reactions of $Ln(OTf)_3$ and $Ln(ClO_4)_3$ with XeF_2 in SO_3.

Substrate	Amount	Amount XeF_2	Volume SO_3 / ml	Recovered Amount / mg	Analytical Data
$Tb(OTf)_3$	50 mg 83 μmol, 1 eq.	14 mg 83 μmol, 1 eq.	1	15	fig. 35 + 68
$Pr(OTf)_3$	50 mg 85 μmol, 1 eq.	14 mg 85 μmol, 1 eq.	0.5	5	-[a]
$Tb(ClO_4)_3$	100 mg 219 μmol, 1 eq.	74 mg 437 μmol, 2 eq.	1	67	fig. 36 + 69
$Pr(ClO_4)_3$	50 mg 0.11 mmol, 1 eq.	19 mg 0.11 mmol, 1 eq.	0.5	20	fig. 37

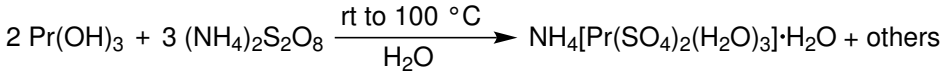
[a]Material (green powder) was insufficient for analytical measurements.

6.2.11 Synthesis of $Pr_2(SO_4)_3$



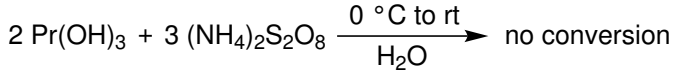
650 mg (0.908 mmol, 1 eq.) of $Pr_2(SO_4)_3{\cdot}(H_2O)_8$ were heated to 350 °C for 4 h under reduced pressure. 497 mg (0.872 mmol, 96%) of $Pr_2(SO_4)_3$ were recovered as a green powder. For IR-data see fig. 67.

6.2.12 Treatment of $(NH_4)_2S_2O_8$ with $Pr(OH)_3$ at Elevated Temperature



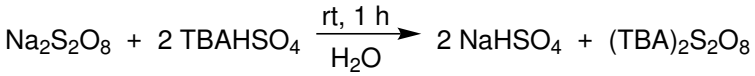
356 mg (1.56 mmol, 3 eq.) of $(NH_4)_2S_2O_8$ was added to a suspension of 200 mg (1.04 mmol, 2 eq.) of $Pr(OH)_3$ in 10 ml of water, causing immediate effervescence. The reaction mixture was heated to 100 °C and boiled until all volatile materials had evaporated. The resulting solids were suspended in 10 ml of water and filtered off to afford a green filtrate. Slow evaporation of the filtrate afforded $(NH_4)[Pr(SO_4)_2(H_2O)_3]\cdot H_2O$ as single crystals. For crystallographic data see tab. 13.

6.2.13 Treatment of $(NH_4)_2S_2O_8$ with $Pr(OH)_3$ at 0 °C



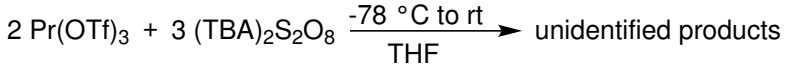
10 ml of an aqueous solution of 356 mg (1.56 mmol, 3 eq.) of $(NH_4)_2S_2O_8$ was added to a suspension of 200 mg (1.04 mmol, 2 eq.) of $Pr(OH)_3$ and stirred for 5 h at 0 °C. The reaction mixture was then stirred for another 16 h at room temperature to find the substrate still undissolved.

6.2.14 Synthesis of $(TBA)_2S_2O_8$



In analogy to a literature procedure (here $Na_2S_2O_8$ was used instead of $K_2S_2O_8$),[108] a solution of 175 mg (0.736 mmol, 1 eq.) in 1 ml of water was combined with 1 ml of an aqueous solution of 500 mg (1.47 mmol, 2 eq.). The mixture was stirred at room temperature for 1 h and then extracted three times with 10 ml of DCM. The combined organic layers were washed three times with 10 ml of water. The solvents were evaporated under reduced pressure and the product was recrystallised from an ethanol/water mixture to obtain 423 mg (0.625 mmol, 85%) of $(TBA)_2S_2O_8$ as colourless crystals. XRD data are provided in tab. 14 and fig. 38.

6.2.15 Reaction $(TBA)_2S_2O_8$ and $Pr(OTf)_3$ in THF



87 mg (0.15 mmol, 2 eq.) of $Pr(OTf)_3$ was suspended in 12 ml of THF. The suspension was combined with a suspension of 150 mg (0.222 mmol, 3 eq.) of $(TBA)_2S_2O_8$ in THF at -78 °C and stirred for one hour. The reaction mixture was then warmed to room temperature, when gasses started to evolve. The mixture was stirred for another 16 h at room temperature before the volatile materials were removed under reduced pressure to obtain ca. 100 mg of an unidentified solid. For analytical data see fig. 39 and fig. 70.

6.2.16 Multi-Anvil Press Experiments

The starting materials were homogenised and compactly loaded into a gold (or platinum) crucible that was compressed to 11 GPa. At 11 GPa the sample was heated for with a heating power of 1000 W before the pressure was slowly released. The samples were manually separated from the crucible as well as other materials. Details of individual experiments are summarised in tab. 9.

Tab. 9 Summary of syntheses conducted using a multi anvil press. All syntheses were carried out at 11 GPa and were heated for 15 min with a heating power of 1000 W.

Reactants			Equiv.			Product	Analytical Data
A	**B**	**C**	**A**	**B**	**C**		
La_2O_3	SiO_2	-	1	2	-	$La_4(SiO_4)_3$	fig. 41 + 72 + 84
Nd_2O_3	SiO_2	-	1	2	-	$Nd_4(SiO_4)_3$	fig. 42 + 73 + 85
PrO_2	SiO_2	-	1	1	-	$Pr_4(SiO_4)_3$	fig. 8 + 43 + 74 + 86
Tb_4O_7	SiO_2	-	1	4	-	$Tb_4(SiO_4)(Si_3O_{10})$	fig. 10 + 44 + 45 + 75 + 87
PrO_2	SiO_2	Na_2O_2	1	1	1	$Pr_4(SiO_4)_3$ +others	fig. 46 + 76
PrO_2	SiO_2	SrO_2	1	1	1	$Pr_4(SiO_4)_3$ +others	fig. 47 + 77
$Pr_2(SO_4)_3$	$K_2S_2O_8$	-	1	1	-	$KPr(SO_4)_2$	fig. 40 + 71
PrO_2	P_2O_5	-	3	2	-	$PrPO_4$	fig. 48

6.2.17 Synthesis of $Yb(OTf)_2(MeCN)_2$

$$Yb + Yb(OTf)_3 + 2\,MeCN \xrightarrow[MeCN]{Hg,\ sonication,\ 18\ h} 3\,Yb(OTf)_2(MeCN)_2$$

62 mg (0.36 mmol, 1.5 eq.) of freshly filed ytterbium and one drop of mercury were added to a solution of 300 mg (0.48 mmol, 2 eq.) of $Yb(OTf)_3$ in 12 ml of acetonitrile. The solution was sonicated for 18 hours, before the solids were filtered off. The filtrate was slowly concentrated at -10 to -15 °C. The precipitated solids were recrystallised to yield 143 mg of impure $Yb(OTf_2)(MeCN)_2$ (see fig. 49 for PXRD data).

6.2.18 Crystallisation of $Ca(OTf_2)(MeCN)_{0.5}$

$$Ca(OTf)_2 + 0.5\,MeCN \xrightarrow[MeCN]{100\ °C,\ 24\ h} Ca(OTf)_2(MeCN)_{0.5}$$

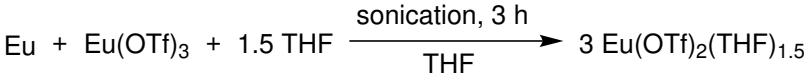
200 mg (0.592 mmol, 1 eq.) of $Ca(OTf)_2$ and 2 ml of acetonitrile were added to an ampoule, that was then torch-sealed. The ampoule was heated to 100 °C for 24 h and cooled to room temperature over 72 h. Colourless crystals had formed, from which $Ca(OTf)_2(MeCN)_{0.5}$ was identified by SC-XRD. After opening the ampoule, the crystals quickly decomposed into unknown products (comp. fig. 16). Crystallographic data of $Ca(OTf)_2(MeCN)_{0.5}$ is provided in tab. 18.

6.2.19 Crystallisation of $Ca(OTf)_2(THF)_2$

$$Ca(OTf)_2 + 2\,THF \xrightarrow[THF]{rt} Ca(OTf)_2(THF)_2$$

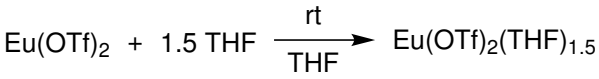
50 mg (0.15 mmol, 1 eq.) of $Ca(OTf)_2$ was dissolved in ca. 2 ml of THF. The solvents were slowly evaporated to afford colourless single crystals (ca. 40 mg) that were identified as $Ca(OTf)_2(THF)_2$ by single crystal X-ray diffraction. For crystallographic data see tab. 19.

6.2.20 Reaction of $Eu(OTf)_2$ and Eu in THF



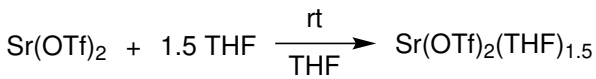
300 mg (0.501 mmol, 2 eq.) of $Eu(OTf)_3$ and 46 mg (0.30 mmol, 1.2 eq.) of freshly filed europium were added to 20 ml of THF. The reaction mixture was sonicated for 3 h before the solids were filtered off. The volatiles were removed from the filtrate under reduced pressure to obtain 280 mg of a yellow, amorphous solid. A saturated solution of the solids in THF was layered with *n*-hexane and stored at -40 °C for seven days. The solution was the slowly evaporated at room temperature and ambient pressure to obtain ca. 250 mg of impure $Eu(OTf)_2(THF)_{1.5}$ as a yellow powder. Analytical data are shown in fig. 51 and fig. 52.

6.2.21 Synthesis of $Eu(OTf)_2(THF)_{1.5}$



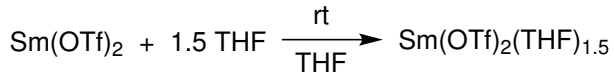
50 mg (0.11 mmol, 1 eq.) of $Eu(OTf)_2$ was dissolved in 5 ml of THF. The solvent was slowly evaporated at ambient pressure and room temperature to obtain 42 mg (0.075 mmol, 68%) of $Eu(OTf)_2(THF)_{1.5}$ as a pale yellow powder. For analytical data see fig. 53 and fig. 78.

6.2.22 Synthesis of $Sr(OTf)_2(THF)_{1.5}$



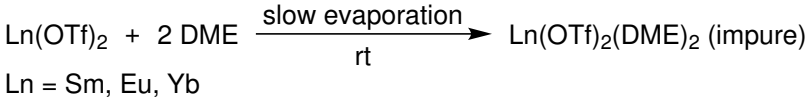
100 mg (0.259 mmol, 1 eq.) of $Sr(OTf)_2$ was suspended in 5 ml of THF. The solvent was slowly evaporated at ambient pressure and room temperature to obtain 110 mg (0.223 mmol, 86%) of $Sr(OTf)_2(THF)_{1.5}$ as a colourless powder. For analytical data see fig. 54 and fig. 79.

6.2.23 Attempted Synthesis of $Sm(OTf)_2(THF)_{1.5}$



50 mg (0.11 mmol, 1 eq.) of $Sm(OTf)_2$ was dissolved in 5 ml of THF. The solvent was slowly evaporated at ambient pressure and room temperature to obtain ca. 40 mg of impure $Sm(OTf)_2(THF)_{1.5}$ as a violet powder. For analytical data see fig. 55 and fig. 80.

6.2.24 Crystallisation of $Ln(OTf)_2(DME)_2$

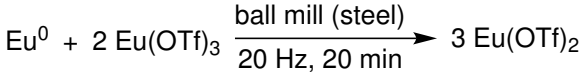


Between 50 and 91 mg of $Ln(OTf)_2$ (Ln = Sm, Eu, Yb) were dissolved in ca. 5 to 10 ml of DME. The solvent was slowly evaporated to yield between 60 and 100 mg of impure $Ln(OTf)_2(DME)_2$ as single crystals or polycrystalline samples. More precise data can be found in tab. 10.

Tab. 10 Summary of crystallisations of $Ln(OTf)_2$ in DME to obtain impure $Ln(OTf)_2(DME)_2$.

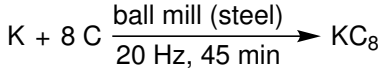
Substrate	Quantity of $Ln(OTf)_2$	Yield	Colour	Analytical Data
$Sm(OTf)_2$	91 mg (0.20 mmol)	100 mg	violet	fig. 56 + 81, tab. 21
$Eu(OTf)_2$	85 mg (0.19 mmol)	95 mg	yellow	fig. 57 + fig. 82, tab. 22
$Yb(OTf)_2$	50 mg (0.11 mmol)	60 mg	colourless	fig. 58 + 83, tab. 23

6.2.25 Mechanochemical Synthesis of $Eu(OTf)_2$



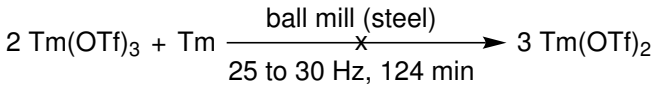
262 mg (0.437 mmol, 1 eq.) of $Eu(OTf)_3$ and 73 mg (0.48 mmol, 1.1 eq.) of freshly filed europium were added to a steel ball mill (V = 5 ml) and reacted at 20 Hz for 20 min. 244 mg of a grey powder was obtained. A small sample of the powder was dissolved in THF and analysed by UV-Vis spectroscopy (see fig. 90).

6.2.26 Synthesis of KC_8



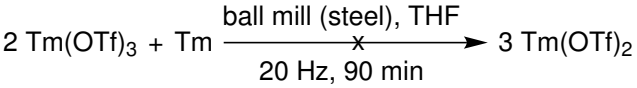
193 mg (4.93 mmol, 1 eq.) of freshly cut potassium and 473 mg (39.4 mmol, 8 eq.) of degassed graphite were reacted at 20 Hz for 45 min in a steel ball mill (V = 5 ml) to obtain 552 mg (4.08 mmol, 83%) of KC_8 as a golden powder (see fig. 59 for PXRD data).

6.2.27 Attempted Mechanochemical Comproportionation of $Tm(OTf)_3$ and Tm



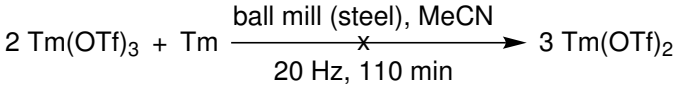
271 mg (0.440 mmol, 2 eq.) of $Tm(OTf)_3$ and 37 mg (0.22 mmol, 1 eq.) of Tm were ground at 25 Hz for 25 min in a steel ball mill (V = 5 ml), followed by an additional cycle of grinding at 30 Hz for 99 min. Ca. 230 mg of a black powder was obtained. The products were analysed by UV-Vis spectroscopy (see fig. 89).

6.2.28 Attempted Mechanochemical Comproportionation of $Tm(OTf)_3$ and Tm in Presence of THF



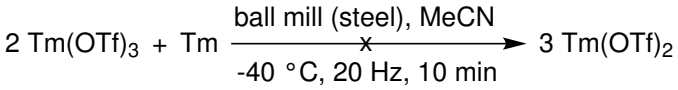
350 mg (0.568 mmol, 1 eq.) of $Tm(OTf)_3$, 250 mg (1.48 mmol, 2.6 eq.) of thulium and 1.5 ml of THF were ground at 20 Hz for 90 min in a steel ball mill (V = 5 ml), followed by an additional cycle of grinding at 30 Hz for 99 min. After evaporation of the solvent, ca. 230 mg of a black powder was obtained. The products were analysed by UV-Vis spectroscopy (see fig. 88).

6.2.29 Attempted Mechanochemical Comproportionation of $Tm(OTf)_3$ and Tm in Presence of Acetonitrile



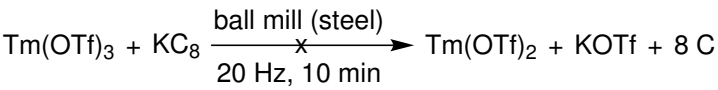
547 mg (0.888 mmol, 1 eq.) of $Tm(OTf)_3$, 150 mg (0.88 mmol, 1 eq.) of freshly filed thulium and 2 ml of acetonitrile were ground at 20 Hz for 110 min in a steel ball mill (V = 5 ml). After evaporation of the solvent, ca. 550 mg of a black powder was obtained. The products were analysed by UV-Vis spectroscopy (see fig. 92).

6.2.30 Attempted Mechanochemical Comproportionation of $Tm(OTf)_3$ and Tm in Presence of Acetonitrile at -40 °C



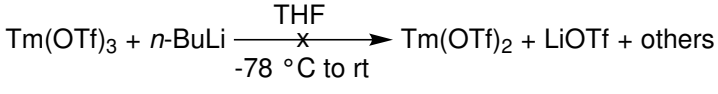
300 mg (1 mmol, 0.487 eq.) of $Tm(OTf)_3$ and 250 mg (1.48 mmol, 3 eq.) of freshly filed thulium were ground at -40 °C for 10 min at 20 Hz in a steel ball mill (V = 5 ml). No conversion of the substrates was observed.

6.2.31 Mechanochemical Treatment of $Tm(OTf)_3$ with KC_8



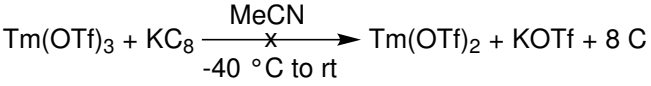
150 mg (0.244 mmol, 1 eq.) of $Tm(OTf)_3$ and 32 mg (0.24 mmol, 1 eq.) of KC_8 were ground at 20 Hz for 10 min in a steel ball mill (V = 5 ml) to obtain ca. 150 mg of an amorphous powder (comp. fig. 60). The products were analysed by UV-Vis spectroscopy (see fig. 91).

6.2.32 Treatment of $Tm(OTf)_3$ with *n*-BuLi



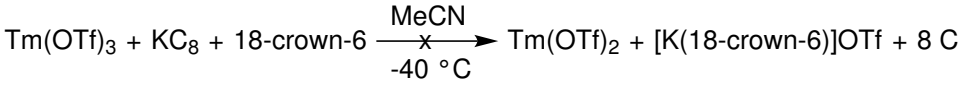
73 mg (0.12 mmol, 1 eq.) of $Tm(OTf)_3$ was dissolved in 5 ml of THF. 0.05 ml of a 2.5 M (1.1 eq.) solution of *n*-butyllithum was added to the Tm^{3+} solution at 78 °C. The reaction mixture was stirred at -78 °C for 3 h and another 16 h at room temperature, after which no conversion to Tm^{2+} was observed. By slow evaporation of the solvent, $Li_4(OTf)_4(THF)_6$ which was reported before by *Anwander* et al.[134] was identified by single crystal structure analysis.

6.2.33 Treatment of $Tm(OTf)_3$ with KC_8 in Acetonitrile



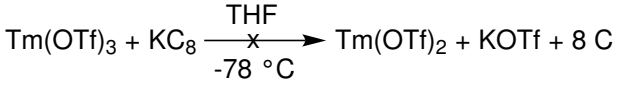
150 mg (0.244 mmol, 1 eq.) of $Tm(OTf)_3$ and 97 mg (0.72 mmol, 3 eq.) of KC_8 were added to 8 ml of acetonitrile at -40 °C. The reaction mixture was stirred at -41 °C for 4 h, before it was allowed to warm to room temperature, at which it was stirred for another 72 h. No conversion of Tm^{3+} to Tm^{2+} was observed.

6.2.34 Treatment of $Tm(OTf)_3$ with KC_8 and 18-Crown-6 in Acetonitrile



80 mg (0.13 mmol, 1 eq.) of $Tm(OTf)_3$ and 80 mg (0.59 mmol, 4.6 eq.) of KC_8 were added to 6 ml of acetonitrile. The reaction mixture was stirred for 4 h at -40 °C, upon which no conversion was observed. Then, 156 mg (0.59 mmol, 4.6 eq.) of 18-crown-6 were added. After stirring the reaction mixture for another 4 h, no conversion was observed.

6.2.35 Treatment of $Tm(OTf)_3$ with KC_8 in THF



150 mg (0.244 mmol, 1 eq.) of $Tm(OTf)_3$ and 97 mg (0.72 mmol, 3 eq.) of KC_8 were added to 8 ml of THF at -78 °C. The reaction mixture was stirred for 4 hours at -78 °C. No conversion of Tm^{3+} to Tm^{2+} was observed.

6.2.36 Reaction of $Tm(OTf)_3$ with KC_8 in THF / Diethylether

$$Tm(OTf)_3 + KC_8 \xrightarrow[-78\ °C]{THF\ /\ Et_2O} Tm(OTf)_2 + KOTf + 8\ C$$

200 mg (0.325 mmol, 1 eq.) of $Tm(OTf)_3$ and 50 mg (0.37 mmol, 1.1 eq.) of KC_8 were added to a mixture of 2 ml of THF and 2 ml of Diethylether at -78 °C. After stirring the reaction mixture for 10 min a sample was taken and filtered to yield a violet solution, that lost its colour within seconds at room temperature. A photograph of the solution is shown in fig. 24.

6.2.37 Treatment of $Tm(OTf)_3$ with KC_8 in MeCN / Diethylether

$$Tm(OTf)_3 + KC_8 \xrightarrow[-40\ °C]{MeCN\ /\ Et_2O} Tm(OTf)_2 + KOTf + 8\ C$$

120 mg (0.195 mmol, 1 eq.) of $Tm(OTf)_3$ and 50 mg (0.37 mmol, 2 eq.) of KC_8 were added to 4 ml of acetonitrile. The reaction mixture was stirred for 2 h at -40 °C, before 2 ml of diethylether were added. The mixture was stirred for an additional 2 h at -40 °C, when a sample of the reaction mixture was analysed by UV-Vis spectroscopy (see fig. 93).

6.2.38 Reaction of $Tm(OTf)_3$ with KC_8 in Diethylether

$$Tm(OTf)_3 + KC_8 \xrightarrow[sonication,\ 30\ min]{Et_2O} Tm(OTf)_2 + KOTf + 8\ C$$

250 mg (0.406 mmol, 1 eq.) of $Tm(OTf)_3$ and 65 mg (0.48 mmol, 1.2 eq.) of KC_8 were added to 3 ml of diethylether. The reaction mixture was sonicated for 30 min, before the volatile materials were removed under reduced pressure to obtain ca. 200 mg of a black powder. If treated with THF and subsequent filtration, a violet solution was obtained that lost its colour within minutes of storing. A UV-Vis spectrum is shown in fig. 24.

6.2.39 Treatment of $Eu(ClO_4)_3$ with Eu in Acetonitrile

$$Eu + 2\ Eu(ClO_4)_3 \xrightarrow{MeCN} 3\ Eu(ClO_4)_2(MeCN)_n$$

Freshly filed europium (varying amounts) were added to a solution of 100 mg (0.222 mmol, 2 eq.) of $Eu(ClO_4)_3$ in acetonitrile. The reaction mixture was sonicated and immediately turned yellow in all experiments. Individual experimental parameters are summarised in tab. 11. After filtration of the reaction mixture, evaporation of the solvent under reduced pressure produced $Eu(ClO_4)_3(MeCN)_4$ as colourless powders or single crystals. When attempting to analyse the solid residues that remained from the filtration, they exploded when touched with a metal spatula.

Tab. 11 Summary of experimental parameters used for the treatment of $Eu(ClO_4)_3$ with Eu in acetonitrile.

V(MeCN) / ml	Eq. of Eu	Addition of Hg	Reaction Time	Analytical Data
5	0.5	no	16 h	fig. 61
0.7	0.5	no	16 h	tab. 25
10[a]	0.5	yes	17 h	fig. 62 + 25
0.5	0.75	no	21 h	fig. 63

[a]Twice the amount of $Eu(ClO_4)_3$ and Eu was used.

6.2.40 Mechanochemical Treatment of $Eu(ClO_4)_3$ with Eu

$$Eu + 2\,Eu(ClO_4)_3 \xrightarrow[20\ Hz,\ 60\ min]{\text{ball mill (steel)}} 3\,Eu(ClO_4)_2$$

100 mg (0.222 mmol, 2 eq.) of $Eu(ClO_4)_3$ and 17 mg (0.11 mmol, 1 eq.) of freshly filed europium were ground for 60 min at 20 Hz in a steel ball mill (V = 5 ml). The materials were then suspended in ca. 5 ml of acetonitrile and filtered. The solvent was removed from the filtrate to yield ca. 60 mg of impure $Eu(ClO_4)_3(MeCN)_4$ as a colourless powder (see fig. 64 for PXRD data).

6.2.41 Mechanochemical Reaction of $Eu(ClO_4)_3$ with Eu in Presence of Acetonitrile

$$Eu + 2\,Eu(ClO_4)_3 \xrightarrow[25\ Hz,\ <1\ s]{\text{ball mill (steel), MeCN}} \text{unidentified products}$$

200 mg (0.444 mmol, 2 eq.) of $Eu(ClO_4)_3$, 34 mg (0.22 mmol, 1 eq.) of freshly filed europium and 1 ml of acetonitrile were added to a steel ball mill (V = 5 ml). As soon as the program (25 Hz) was started, a violent detonation occurred, from which no materials could be recovered.

7 Appendix

7.1 Supplementary Material of Manuscripts

Supporting Information

Stabilization of Pr^{4+} in Silicates - High Pressure Synthesis of $PrSi_3O_8$ and $Pr_2Si_7O_{18}$

Niko T. Flosbach*,[1] Maxim Bykov*,[1,2] Elena Bykova,[3] Bertold Rasche,[1,4] Mohamed Mezouar,[5] Timofey Fedotenko,[6] Stella Chariton,[7] Vitali B. Prakapenka,[7] Mathias S. Wickleder*[1]

[1] Institute of Inorganic Chemistry, University of Cologne, Greinstraße 6, 50939 Cologne, Germany

[2] Institute of Inorganic and Analytical Chemistry, Goethe University Frankfurt, Max-von-Laue-Straße 7, 60438 Frankfurt am Main, Germany

[3] Institute of Geosciences, Goethe University Frankfurt, Altenhöferallee 1, 60438 Frankfurt, Germany

[4] Institute of Inorganic Chemistry, University of Stuttgart, 70569 Stuttgart, Germany

[5] European Synchrotron Radiation Facility (ESRF), Avenue des Martyrs 71, 38000 Grenoble, France

[6] Deutsches Elektronen-Synchrotron, Notkestr. 85, 22607 Hamburg, Germany

[7] Center for Advanced Radiation Sources, University of Chicago, Chicago, Illinois 60637, USA

Corresponding Authors

*Niko T. Flosbach - Greinstr. 6, 50939 Cologne, Germany;

Email: n.flosbach@uni-koeln.de

*Maxim Bykov – Max-von-Laue-Straße 7, D-60438 Frankfurt am Main, Germany;

Email: bykov@chemie.uni-frankfurt.de

*Mathias S. Wickleder - Greinstr. 6, 50939 Cologne, Germany;

Email: mathias.wickleder@uni-koeln.de

Table of Contents

Analytical Data of the Substrates 3

Crystal Structures 3

Crystal Structure of $Pr_4Si_3O_{12}$ 3

Crystal Structure of $Pr_4Si_3O_{12}$ at 15 GPa 6

Crystal Structure of $PrSi_3O_8$ 6

Crystal Structure of $Pr_2Si_7O_{18}$ 9

Crystallographic Tables 11

Precession Images 15

$Pr_2(O_2)O_3$ at 29 GPa 15

$Pr_2(O_2)O_3$ at 15 GPa 16

$PrSi_3O_8$ at 15 GPa 17

$Pr_2Si_2O_7$ at 10 GPa 18

$Pr_2Si_2O_7$ at 5 GPa 20

$PrSi_3O_8$ at Ambient Pressure 21

$Pr_2Si_7O_{18}$ at Ambient Pressure 22

XRD Maps 24

Calculated Structures 25

Analytical Data of the Substrates

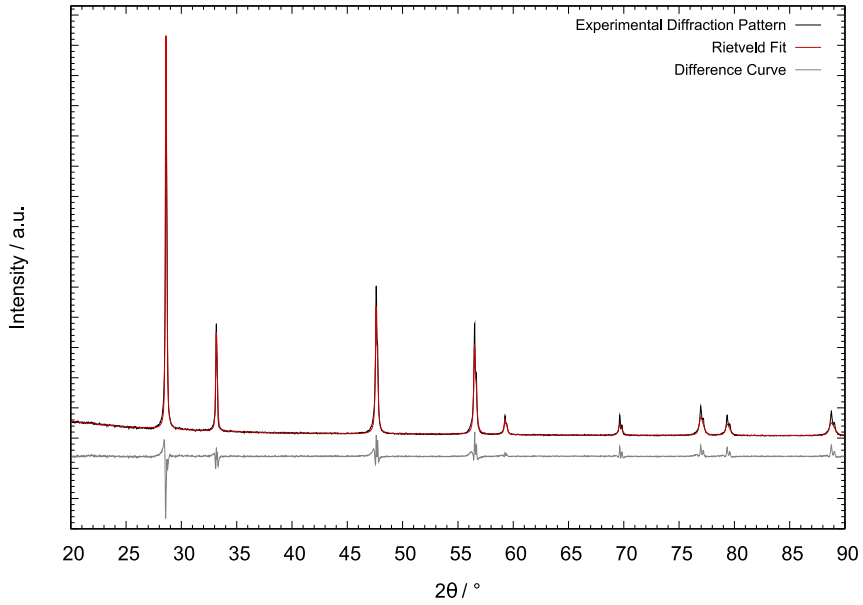


Fig. S 1: PXRD data of PrO_2. Lattice parameter obtained from Rietveld refinement: a = 539.41(6) pm.

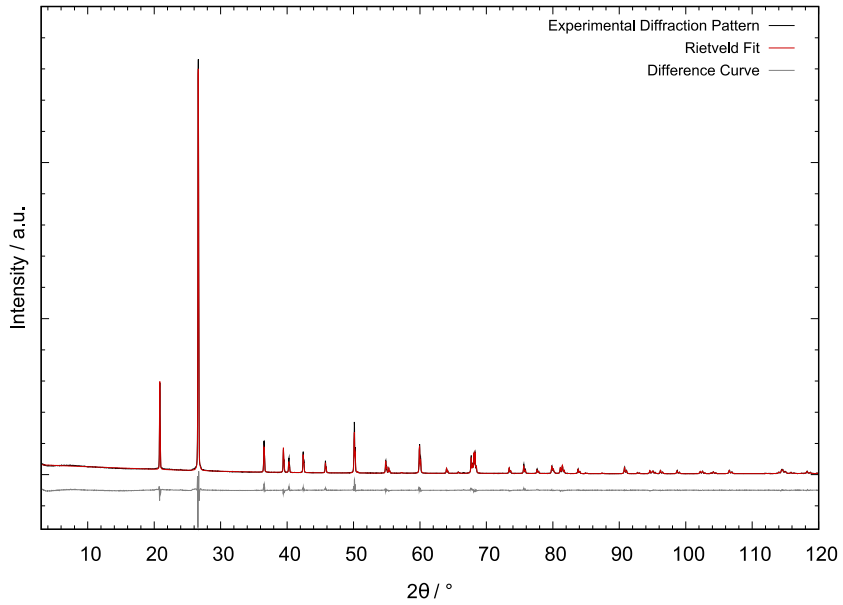


Fig. S 2: PXRD data of SiO_2. Lattice parameters obtained from Rietveld refinement: $a = b$ = 491.482(4); c = 540.659(8).

Crystal Structures

Crystal Structure of $Pr_4Si_3O_{12}$

$Pr_4Si_3O_{12}$ crystallizes in the trigonal space group $R\bar{3}m$ ($a = b$ = 510.0(1) pm, c = 2462(1) pm; values given for the structure at 29 GPa) with three formula units per cell. The structure consists

of trivalent praseodymium ions that are located within an intricate network of corner sharing [SiO_6]-octahedra. Together with the oxygen atoms, the praseodymium ions form a close packing with alternating regions of cubic close (ccp) and hexagonal close packing (hcp), as illustrated in Fig. S 3.

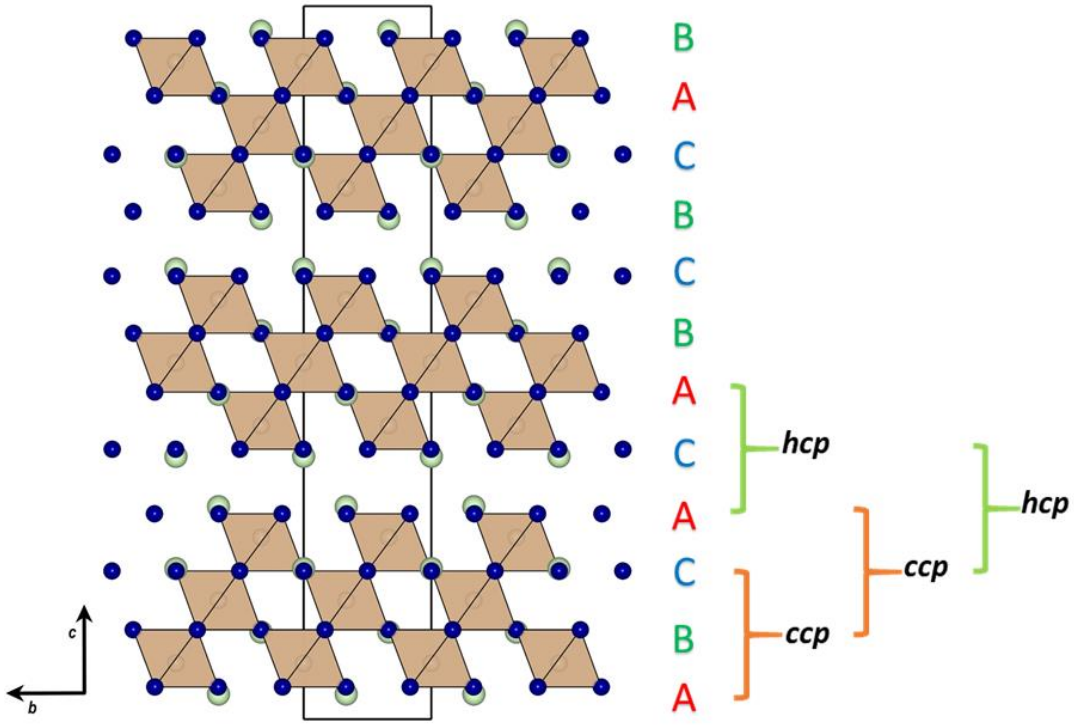


Fig. S 3: Crystal structure of $Pr_4Si_3O_{12}$ viewed along the crystallographic *a*-axis.

Two layers of cubic close packing are followed by two layers of hexagonal close packing, which are then followed by another two layers of cubic close packing, resulting in an alternating pattern (*Jagodzinski*-symbol = *hhcc*). The silicon atoms occupy one fourth of the octahedral voids in the first three layers of the unit cell, while the octahedral voids remain unoccupied in every fourth layer, so that three sixteenth of all octahedral voids are occupied by silicon atoms. Because every fourth layer of octahedral voids is unoccupied, the silicate anions form layers of corner sharing [SiO_6]-octahedra, which are separated by the unoccupied layers.

Both praseodymium ions (Pr1 and Pr2) are each coordinated by 12 oxygen atoms. Since Pr1 is located within layers that form hexagonal close packing, its coordination polyhedron is a slightly distorted anticuboctahedron, in which the Pr-O distances range from 248(1) pm to 266(1) pm with an average value of 256(2) pm.

In contrast to Pr1, Pr2 is located within domains of cubic close packing, resulting in a cuboctahedral coordination geometry of the Pr2 site. The Pr-O distances in the coordination sphere of Pr2 are within a similar range compared to that of Pr1 varying from 241(1) pm to 258(1) pm, yielding an average Pr-O distance of 252(2) pm.

The coordination polyhedra of both Pr1 and Pr2 are shown in Fig. S 4**Fig. S 4** for the structure at 29 GPa.

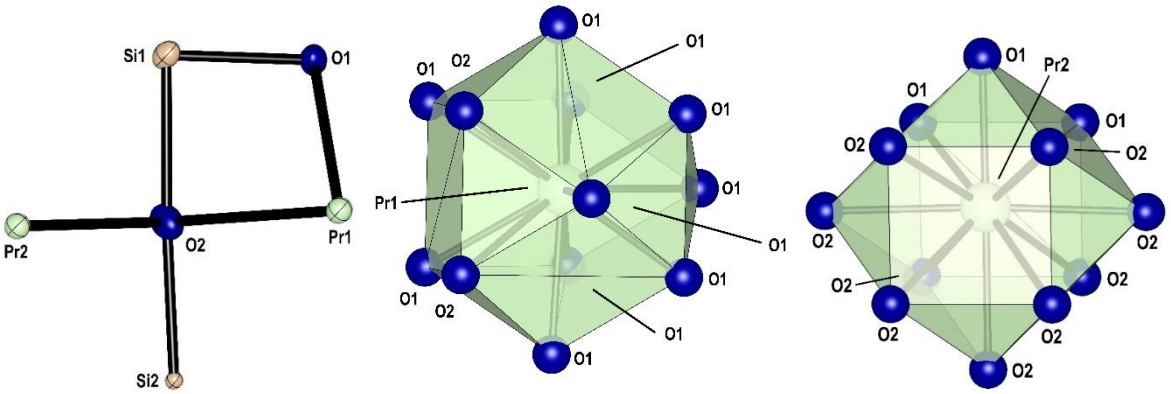


Fig. S 4: Excerpts of the crystal structure of $Pr_4Si_3O_{12}$. Left: Atoms of the asymmetric units shown as displacement ellipsoids with a probability level of 50%; middle: coordination environment of Pr1; right: coordination environment of Pr2. Images were generated from the dataset at 29 GPa.

The crystal structure of $Pr_4Si_3O_{12}$ hosts two different sites of Si atoms. Si1 occupies the *6c* site, while Si2 sits on a position with lower multiplicity (Wyckoff Symbol = *3b*). Both Si atoms are surrounded by six oxygen atoms yielding octahedral geometry. In the $[SiO_6]$-octahedron around Si1 two different Si-O distances are found (188(1) pm and 167(1) pm) that average at 178(2) pm, whereby all Si-O distances are equivalent for Si2 (178(1) pm).

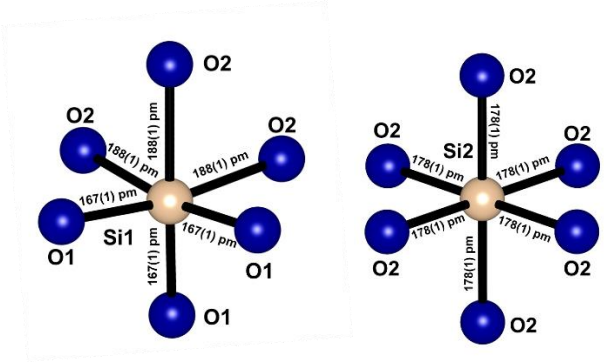


Fig. S 5: Octahedrally coordinated silicon atoms in $Pr_4Si_3O_{12}$. All distances refer to the structure at 29 GPa.

Crystal Structure of $Pr_4Si_3O_{12}$ at 15 GPa

Reheating the cell at 15 GPa afforded the same compound ($Pr_4Si_3O_{12}$) that was described in the previous abstract. The crystal structure of $Pr_4Si_3O_{12}$ undergoes minor changes when exposed to different pressure. Some of the most obvious differences will be discussed briefly in the following section.

When compared to the structure at 29 GPa (see above), the cell axes and hence the volume of the unit cell are marginally increased. The *a*- and *b*-axes change from 510.0(1) pm at 29 GPa to 513.2(3) pm at 15 GPa, which corresponds to a relaxation of ca. 0.6%. The *c*-axis is proportionally less affected changing only by ca. 0.2% to 2467.7(8) pm. The cell volume increases by ca. 1.5% from 554.6(3) $\cdot 10^6$ pm^3 to 562.9(5) $\cdot 10^6$ pm^3. The relatively small changes in the lattice parameters of $Pr_4Si_3O_{12}$ are manifested by minor changes in the coordination polyhedra of both praseodymium and silicon. In fact, most distances and polyhedral volumes do not change within the margin of error. Given that $Pr_4Si_3O_{12}$ forms a densely packed structure, its compressibility is expected to be low, explaining the low differences observed. Additionally, any relative changes in the interatomic distances are attenuated by the high coordination numbers. A direct comparison of selected crystallographic data of both data sets of $Pr_4Si_3O_{12}$ is provided in Tab. S 1.

Although the existence of $Pr_4Si_3O_{12}$ could still be proven at ambient pressure by determination of the unit cell, no satisfactory structural model could be generated due to the poor data quality.

Crystal Structure of $PrSi_3O_8$

$PrSi_3O_8$ crystallizes in the orthorhombic space group *Cmce* (*a* = 1506.3(7) pm, *b* = 881.9(4) pm, *c* = 1237.1(3) pm) with 16 formula units per cell. Similar to $Pr_4Si_3O_{12}$, there is a sublattice of

oxygen atoms and praseodymium ions that are arranged in a distorted close packing. In contrast to the alternating stacking of layers in $Pr_4Si_3O_{12}$, the praseodymium ions and oxygen atoms form an ABA-type stacking that results in a slightly distorted hexagonal close packing (hcp), as illustrated in Fig. S 6.

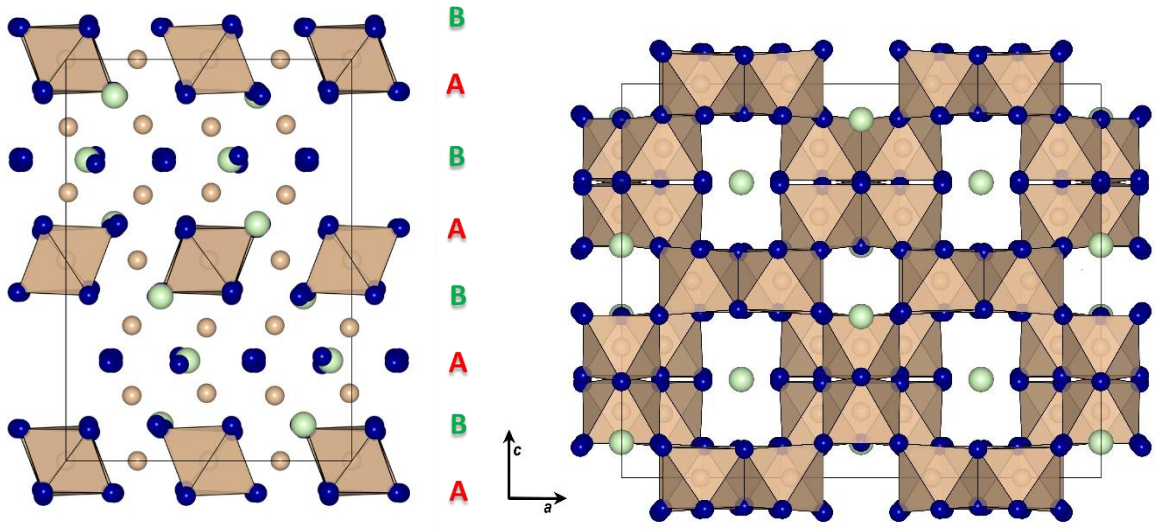


Fig. S 6: Crystal structure of $PrSi_3O_8$ seen along the crystallographic *a*-axis (left) and along the crystallographic *b*-axis (right). Some $[SiO_6]$-octahedra are not shown in the left image.

The occupancy of the octahedral voids in the *hcp*-sublattice with silicon atoms leads to the formation of a three dimensionally distributed network of $[SiO_6]$-octahedra, that are edge sharing with either two, three or four other $[SiO_6]$-octahedra within one layer. The connection to other layers is established by common corners of the octahedra. Both crystallographically distinguishable Pr-ions are each coordinated by twelve oxygen atoms forming a distorted anticuboctahedron in both cases (compare Fig. S 7).

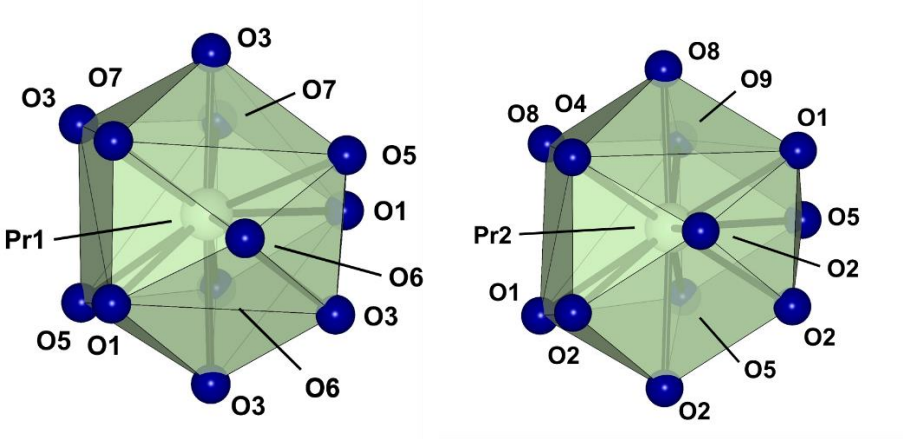


Fig. S 7: Anticuboctahedral coordination geometries of Pr1 (left) and Pr2 (right) in $PrSi_3O_8$.

The average Pr-O distance in the coordination polyhedron of Pr1 is 255.4(3) pm. The shortest Pr-O distance in the polyhedron around Pr1 is found between Pr1 and O3 (245(1) pm), whereby the longest is found between Pr1 and O7 (261.9(9) pm). The values for the respective polyhedron around Pr2 are similar ranging between 249(1) pm and 262(1) pm (average value of 256(3) pm). Because of the high coordination number and the high pressure, no definitive arguments can be made about the valence of the praseodymium ions based on the distances to the coordinating atoms alone. In fact, the distances are essentially the same as for the previously discussed $Pr_4Si_3O_{12}$ at the same pressure. It was already discussed that the Pr-O distances in $Pr_4Si_3O_{12}$ do not undergo significant changes when changing the pressure, which was interpreted to be a result of the low structural flexibility of the densely packed structure. The same structural inflexibility now leads to the apparent invariance of the Pr-O bond lengths when changing the valence from Pr^{3+} to Pr^{4+}.

Each of the five distinguishable silicon atoms in $PrSi_3O_8$ are octahedrally coordinated by six oxygen atoms. All five polyhedra are depicted in Fig. S 8. The degree to which the coordination geometry deviates from the ideal octahedron varies between the polyhedra. The Si-O distances range from 166(1) pm to 186(1) pm and are comparable to those observed in $Pr_4Si_3O_{12}$. Si-O distances are summarized in Tab. S 5.

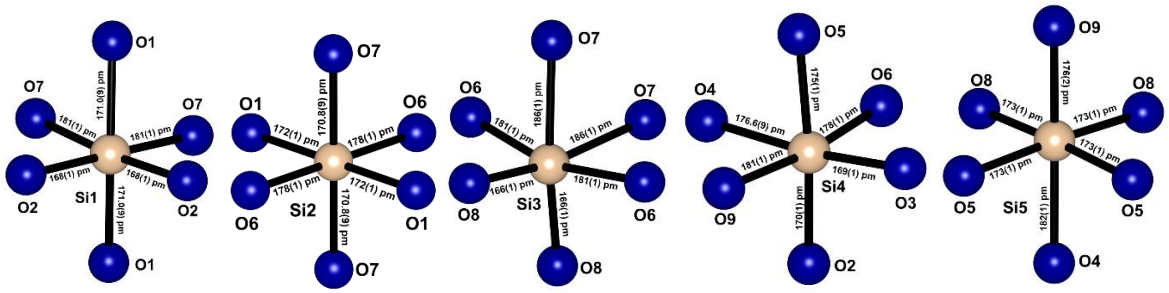


Fig. S 8: [SiO_6] polyhedra in $PrSi_3O_8$ at 29 GPa.

After releasing the pressure from the cell, $PrSi_3O_8$ could be identified by unit cell comparison at lower pressure points (15 GPa and ambient pressure). However due to the poor quality of the data sets not satisfactory structure solution was possible.

Crystal Structure of $Pr_2Si_7O_{18}$

$Pr_2Si_7O_{18}$ crystallizes in the triclinic space group $P\bar{1}$ (a = 607(1) pm, b = 633.5(6) pm, c = 656.9(3) pm, α = 94.21(6)°, β = 93.7(1)°, γ = 115.3(1)°) with one formula unit per cell. Similar to the previously discussed crystal structures of $Pr_4Si_3O_{12}$ and $PrSi_3O_8$ the structural foundation of $Pr_2Si_7O_{18}$ is formed by a close packing of praseodymium ions and oxygen atoms in which the silicon atoms occupy octahedral gaps. More precisely, the structure consists of a distorted hexagonal closest packing of Pr^{4+}-ions and oxygen atoms, where seven 20th of the octahedral gaps are occupied by silicon atoms. As in $PrSi_3O_8$, the [SiO_6]-octahedra form a three dimensional network in which they are partially corner sharing and partially edge sharing.

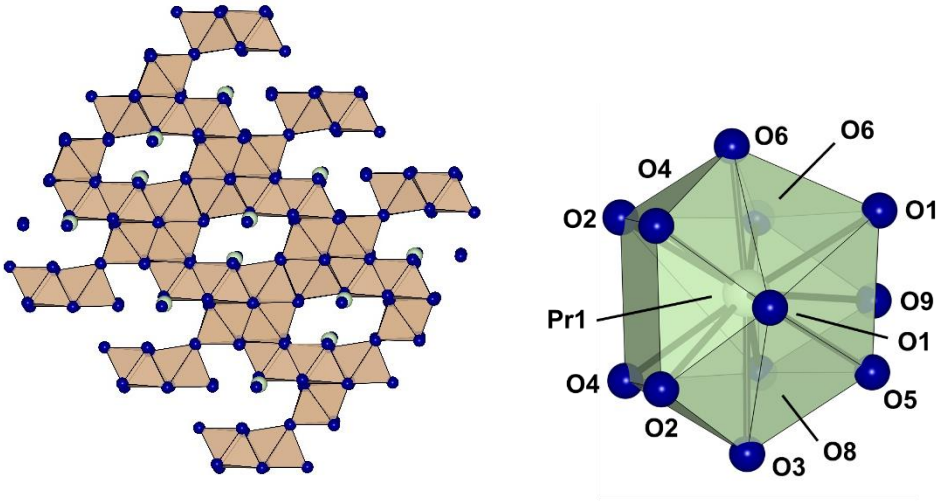


Fig. S 9: Left: Three dimensional network of $[SiO_6]$-octahedra in $Pr_2Si_7O_{18}$. Right: Anticuboctahedral coordination geometry of Pr1 in $Pr_2Si_7O_{18}$.

Given its role as a constituent of the hexagonal close packing, the Pr1 site is coordinated by 12 oxygen atoms in a distorted anticuboctahedral environment as depicted in Fig. S 9. The average Pr-O distance of 258(4) pm is comparable to that of the $[PrO_{12}]$-polyhedra of $PrSi_3O_8$ (255.6(1) pm), however the poor data quality does not allow for a more detailed discussion of interatomic distance or angles in $Pr_2Si_7O_{18}$. Nonetheless, the structural similarities between $Pr_2Si_7O_{18}$ and $PrSi_3O_8$ are obvious since both structures contain a sublattice of hexagonally close packed Pr^{4+}-ions and oxygen atoms that hosts silicon atoms in its octahedral voids. Even the degree to which these voids are occupied is strikingly similar from 3/8 to 7/20 of all voids, which are both close to 1/3 evoking the necessity to briefly compare the structures to the simple BiI_3 structure type. In the BiI_3 structure type the octahedral gaps are filled such that all $[BiI_6]$-octahedra are edge sharing, as opposed to the mix of corner- and edge sharing condensation pattern in the aforementioned praseodymium silicates. Furthermore, in the BiI_3 structure every second layer remains unoccupied, resulting in two dimensional sheets of condensed $[BiI_6]$-octahedra, which is not observed either in the three dimensionally connected silicates.

Crystallographic Tables

Tab. S 1: Crystallographic data of $Pr_4Si_3O_{12}$ at 15 GPa and 29 GPa.

Pressure	**15 GPa**	**29 GPa**
Chemical Formula	$Pr_4Si_3O_{12}$	$Pr_4Si_3O_{12}$
Molar Mass	839.91 g/mol	839.91 g/mol
Temperature	293(2) K	293(2) K
Crystal System	trigonal	trigonal
Space Group	$R\bar{3}$m	$R\bar{3}$m
Lattice Parameters	$a = b$ = 513.2(3) pm	$a = b$ = 510.0(1) pm
	c = 2467.7(8) pm	c = 2462(1) pm
Cell Volume	562.9(6) 10^6 pm^3	554.6(3) 10^6 pm^3
Formula Units	3	3
Calculated Density	7.434 g/cm^3	7.544 g/cm^3
Absorption Correction	multi scan	multi scan
Absorption Coefficient	12.401	12.585
F(000)	1122.0	1122.0
Crystal Size	0.01 x 0.01 x 0.01 mm	0.01 x 0.01 x 0.01 mm
Radiation	synchrotron (λ = 0.2916 nm)	synchrotron (λ = 0.2916 nm)
2θ-Range	4.064° to 35.692°	3.844° to 36.212°
Index Range	$-5 \le h \le 2$, $-7 \le k \le 9$, $-43 \le l \le 41$	$-6 \le h \le 7$, $-10 \le k \le 8$, $-40 \le l \le 32$
Reflections Collected	572	646
Independent Reflections	310 [R_{int} = 0.0456, R_{sigma} = 0.0525]	349 [R_{int} = 0.0470, R_{sigma} = 0.0514]
Data/Restraints/Parameters	310/0/24	349/0/24
Goodness of Fit	1.043	1.100
R_1; wR_2 ($I \ge 2\sigma(I_o)$)	R_1 = 0.0524, wR_2 = 0.1337	R_1 = 0.0618, wR_2 = 0.1553
R_1; wR_2 (all data)	R_1 = 0.0610, wR_2 = 0.1391	R_1 = 0.0652, wR_2 = 0.1595
Largest Diff. Peak/Hole	4.54/-3.80 e/Å^3	5.48/-4.07 e/Å^3

Tab. S 2: Overview of selected interatomic distances in $Pr_3Si_4O_{12}$ at 29 GPa.

Atoms	**Distance / pm**
Pr1-O1	256.2(6)
Pr1-O1’	248.1(9)
Pr1-O1’’	256.3(6)
Pr1-O2	265.5(7)
Pr2-O1	239.9(9)
Pr2-O2	255.1(3)
Pr2-O2’	258.2(7)
Si1-O1	167.5(8)
Si1-O2	187.3(7)
Si2-O2	178.5(6)

Tab. S 3: Overview of selected interatomic distances in $Pr_3Si_4O_{12}$ at 15 GPa.

Atoms	Distance / pm
Pr1-O1	256.6(6)
Pr1-O1’	247.0(6)
Pr1-O1’’	257.7(6)
Pr1-O2	267.3(5)
Pr2-O1	241.1(6)
Pr2-O2	256.8(6)
Pr2-O2’	256.9(6)
Si1-O1	171.2(7)
Si1-O2	188.3(7)
Si2-O2	177.7(6)

Tab. S 4: Crystallographic data of $PrSi_3O_8$ at 29 GPa.

Pressure	**29 GPa**
Chemical Formula	$PrSi_3O_8$
Molar Mass	353.18 g/mol
Temperature	293(2) K
Crystal System	orthorhombic
Space Group	*Cmce*
Lattice Parameters	a = 1506.3(7) pm
	b = 881.9(4) pm
	c = 1237.1(3) pm
Cell Volume	1643(1) 10^6 pm^3
Formula Units	16
Calculated Density	5.710 g/cm^3
Absorption Correction	multi scan
Absorption Coefficient	2.382
F(000)	2640.0
Crystal Size	0.01 x 0.01 x 0.01 mm
Radiation	synchrotron (λ = 0.3738 nm)
2θ-Range	3.304° to 39.502°
Index Range	$-18 \leq h \leq 17$, $-13 \leq k \leq 11$, $-20 \leq l \leq 20$
Reflections Collected	1379
Independent Reflections	816 [R_{int} = 0.0398, R_{sigma} = 0.0452]
Data/Restraints/Parameters	816/0/110
Goodness of Fit	1.000
R_1; wR_2 ($I \geq 2\sigma(I_o)$)	R_1 = 0.0591, wR_2 = 0.1593
R_1; wR_2 (all data)	R_1 = 0.0828, wR_2 = 0.1788
Largest Diff. Peak/Hole	2.02/-1.61 e/Å^3

Tab. S 5: Overview of selected interatomic distances in $PrSi_3O_8$ at 29 GPa.

Atoms	Distance / pm
Pr1-O1	251(1)
Pr1-O3	245(1)
Pr1-O3’	259(1)
Pr1-O5	256(1)
Pr1-O6	260(1)
Pr1-O7	261.9(9)
Pr2-O1	262(1)
Pr2-O2	254(1)
Pr2-O2’	258(1)
Pr2-O4	259(1)
Pr2-O5	249(1)
Pr2-O8	252(1)
Pr2-O9	260(1)
Si1-O1	171.0(9)
Si1-O2	168(1)
Si1-O7	181(1)
Si2-O1	172(1)
Si2-O6	178(1)
Si2-O7	170.8(9)
Si3-O6	181(1)
Si3-O7	186(1)
Si3-O8	166(1)
Si4-O2	170(1)
Si4-O3	169(1)
Si4-O4	176.6(9)
Si4-O5	175(1)
Si4-O6	178(1)
Si4-O9	181(1)
Si5-O4	182(1)
Si5-O5	173(1)
Si5-O8	173(1)
Si5-O9	176(2)

Tab. S 6: Crystallographic data of $Pr_2Si_7O_{18}$ at 29 GPa.

Pressure	**29 GPa**
Chemical Formula	$Pr_2Si_7O_{18}$
Molar Mass	766.45 g/mol
Temperature	293(2) K
Crystal System	triclinic
Space Group	$P\bar{1}$
Lattice Parameters	a = 607(1) pm
	b = 633.5(6) pm
	c = 656.9(3) pm
	α = 94.21(6)°
	β = 93.7(1)°
	γ = 115.3(1)°
Cell Volume	226.4(6) 10^6 pm^3
Formula Units	1

Calculated Density	5.620 g/cm^3
Absorption Correction	multi scan
Absorption Coefficient	5.242
F(000)	360.0
Crystal Size	0.01 x 0.01 x 0.01 mm
Radiation	synchrotron (λ = 0.2916 nm)
2θ-Range	3.676° to 28.112°
Index Range	$-3 \leq h \leq 3$, $-9 \leq k \leq 9$, $-10 \leq l \leq 10$
Reflections Collected	798
Independent Reflections	494 [R_{int} = 0.1216, R_{sigma} = 0.2371]
Data/Restraints/Parameters	494/0/58
Goodness of Fit	0.827
R_1; wR_2 ($I \geq 2\sigma(I_o)$)	R_1 = 0.0716, wR_2 = 0.1634
R_1; wR_2 (all data)	R_1 = 0.1133, wR_2 = 0.1732
Largest Diff. Peak/Hole	1.13/-1.21 e/Å^3

Tab. S 7: Overview of selected interatomic distances in $Pr_2Si_7O_{18}$ at 29 GPa.

Atoms	**Distance / pm**
Pr1-O1	265(5)
Pr1-O1’	262(4)
Pr1-O2	269(7)
Pr1-O2’	254(2)
Pr1-O3	267(5)
Pr1-O4	257(7)
Pr1-O5	254(2)
Pr1-O6	255(6)
Pr1-O6’	245(4)
Pr1-O8	265(2)
Pr1-O9	255(5)
Si1-O1	152(7)
Si1-O2	172(1)
Si1-O7	182(3)
Si2-O1	182(3)
Si2-O3	173(2)
Si2-O4	166(3)
Si2-O5	180(7)
Si2-O7	187(8)
Si2-O9	186(2)
Si3-O5	171(6)
Si3-O6	170(3)
Si3-O7	164(6)
Si3-O8	181(5)
Si3-O8’	178(4)
Si3-O9	176(2)
Si4-O2	167(2)
Si4-O3	167(5)
Si4-O4	173(5)
Si4-O6	171(5)
Si4-O8	178(3)
Si4-O9	185(6)

Precession Images

Precession images were generated after after harvesting all peaks, separation of individual domains, followed by indexing individual domain and determination of the unit cell.

$Pr_2(O_2)O_3$ at 29 GPa

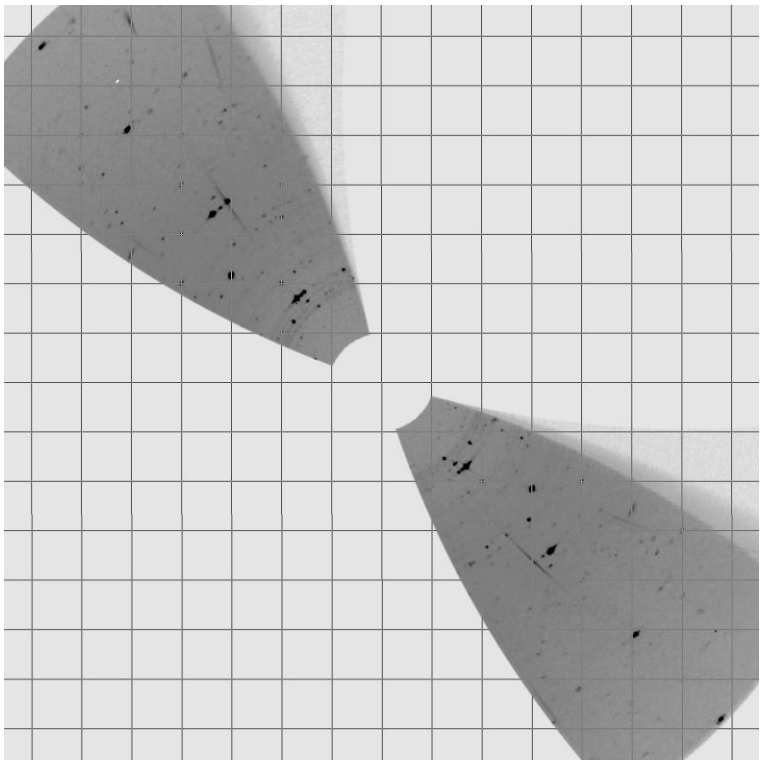


Fig. S 10: Precession image of the h0l-layer of $Pr_2(O_2)O_3$ at 29 GPa. Cell parameters: a = 603.7(2) pm, b = 788.28(9) pm, c = 611.0(2) pm, V = 290.7(1)•10^6 pm^3.

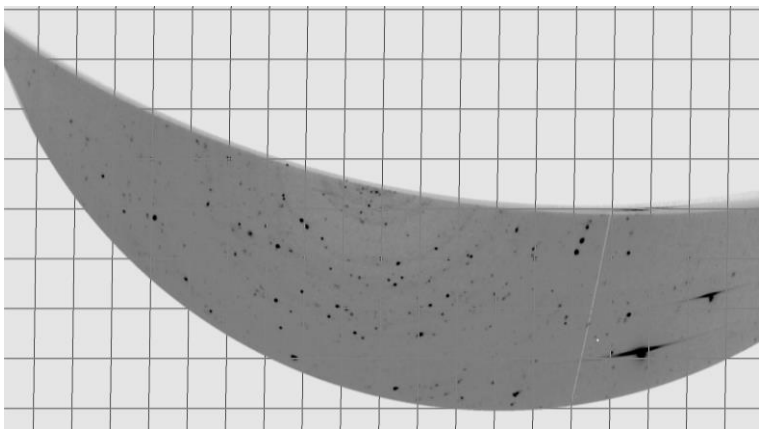


Fig. S 11: Precession image of the 2kl-layer of $Pr_2(O_2)O_3$ at 29 GPa. Cell parameters: a = 603.7(2) pm, b = 788.28(9) pm, c = 611.0(2) pm, V = 290.7(1)•10^6 pm^3.

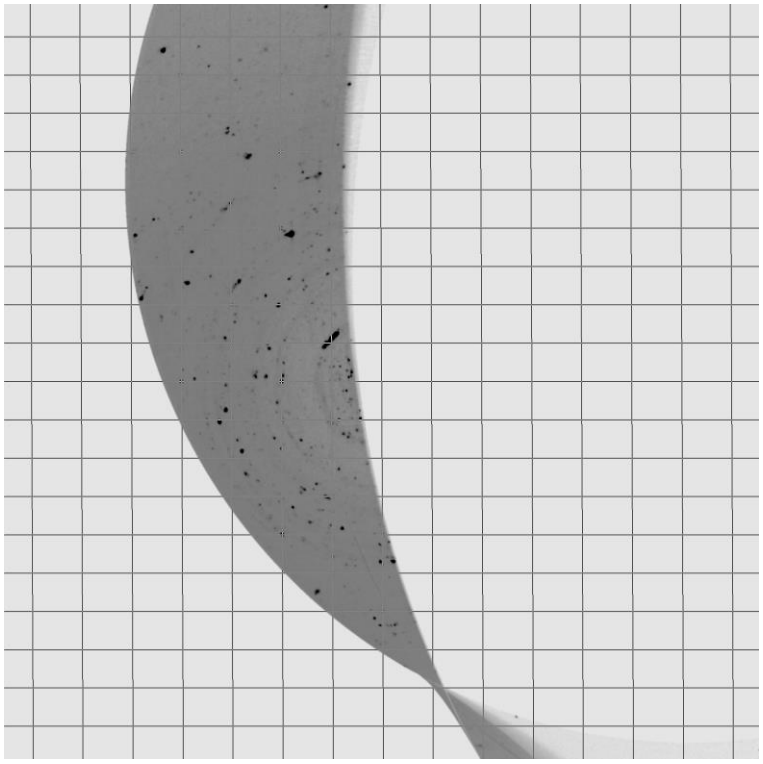


Fig. S 12: Precession image of the hk2-layer of $Pr_2(O_2)O_3$ at 29 GPa. Cell parameters: a = 603.7(2) pm, b = 788.28(9) pm, c = 611.0(2) pm, V = 290.7(1)•10^6 pm^3.

$Pr_2(O_2)O_3$ at 15 GPa

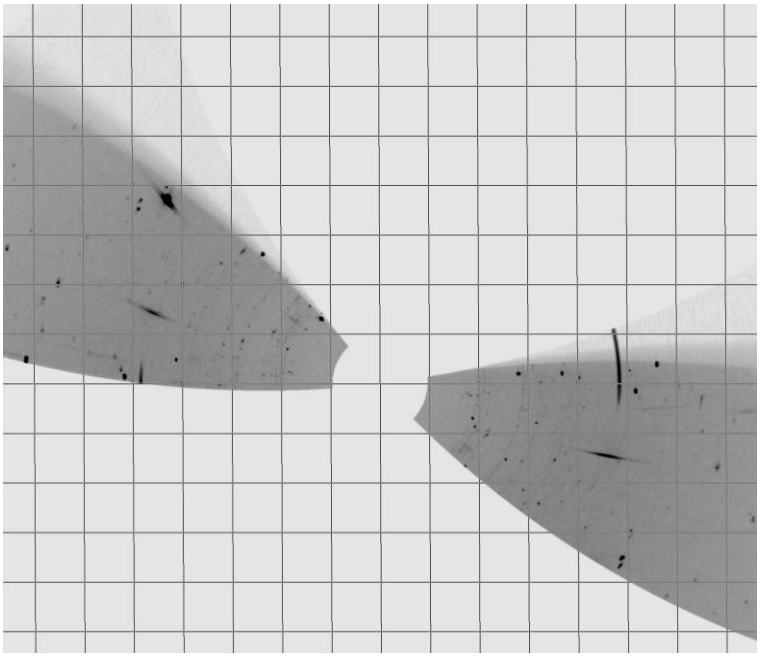


Fig. S 13: Precession image of the h0l-layer of $Pr_2(O_2)O_3$ at 15 GPa. Cell parameters: a = 610.8(2) pm, b = 800.2(2) pm, c = 612.9(3) pm, V = 299.5(2)•10^6 pm^3.

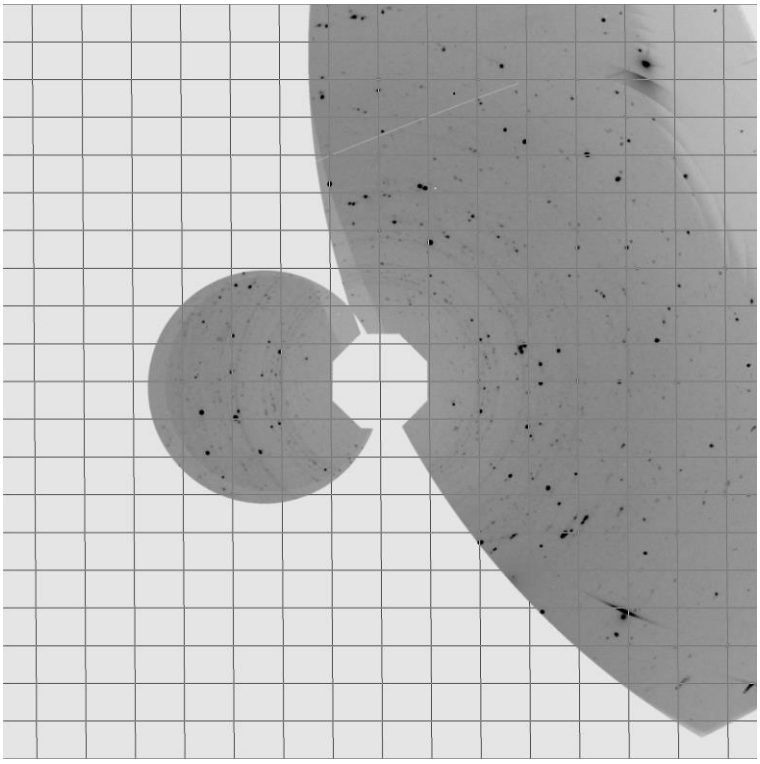


Fig. S 14: Precession image of the hk0-layer of $Pr_2(O_2)O_3$ at 15 GPa. Cell parameters: a = 610.8(2) pm, b = 800.2(2) pm, c = 612.9(3) pm, V = 299.5(2)•10^6 pm^3.

$PrSi_3O_8$ at 15 GPa

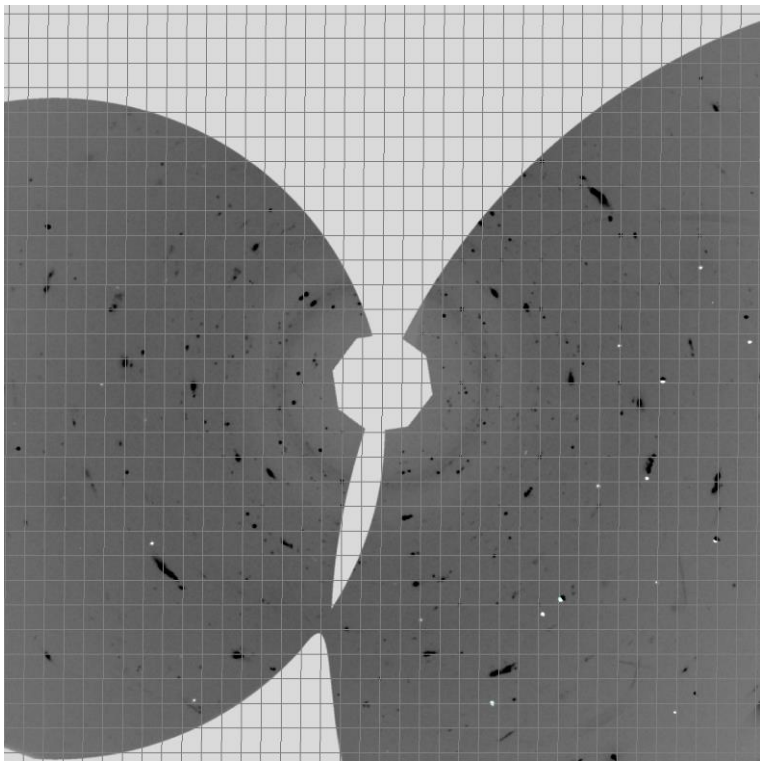


Fig. S 15: Precession image of the h0l-layer of $PrSi_3O_8$ at 15 GPa. Cell parameters: a = 1528.3(4) pm, b = 891.1(9) pm, c = 1228.6(3) pm, V = 1673(2)•10^6 pm^3.

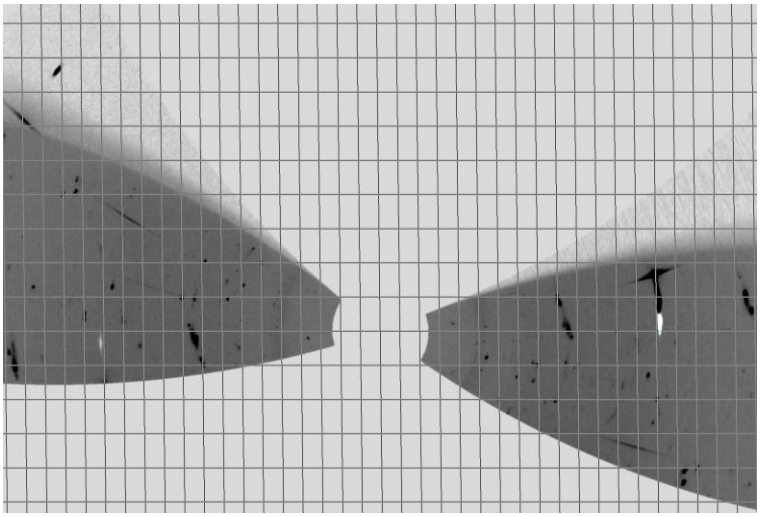


Fig. S 16: Precession image of the hk0-layer of $PrSi_3O_8$ at 15 GPa. Cell parameters: a = 1528.3(4) pm, b = 891.1(9) pm, c = 1228.6(3) pm, V = 1673(2)•10^6 pm^3.

$Pr_2Si_2O_7$ at 10 GPa

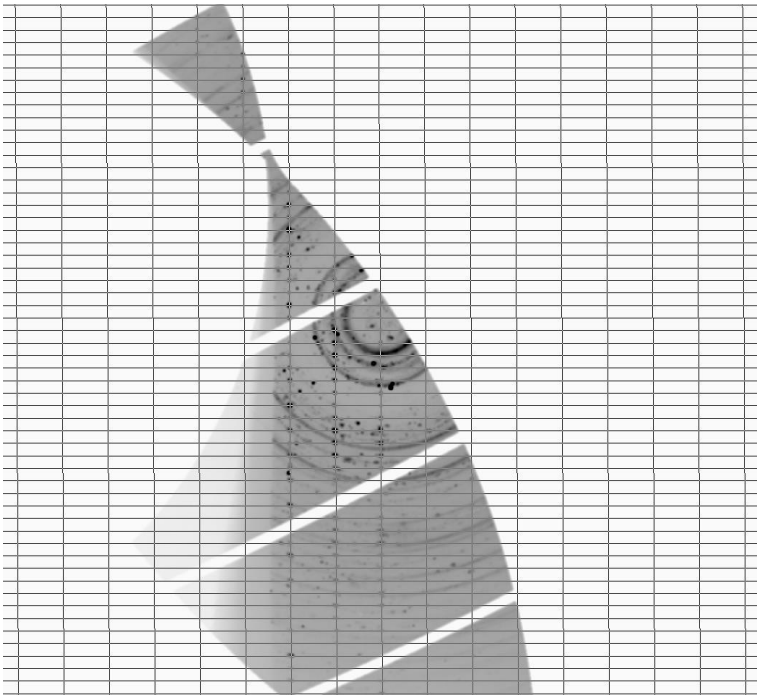


Fig. S 17: Precession image of the 2kl-layer of $Pr_2Si_2O_7$ at 10 GPa. Cell parameters: a = b = 662.85(6) pm, c = 2420.0(2) pm, V = 1063.3(2)•10^6 pm^3.

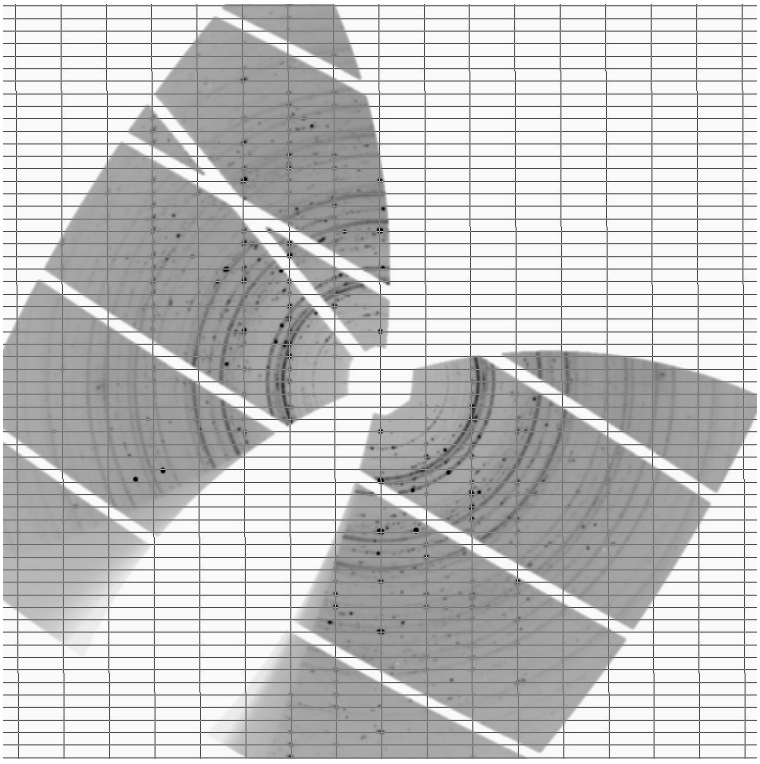


Fig. S 18: Precession image of the h0l-layer of $Pr_2Si_2O_7$ at 10 GPa. Cell parameters: $a = b = 662.85(6)$ pm, $c = 2420.0(2)$ pm, $V = 1063.3(2) \cdot 10^6$ pm^3.

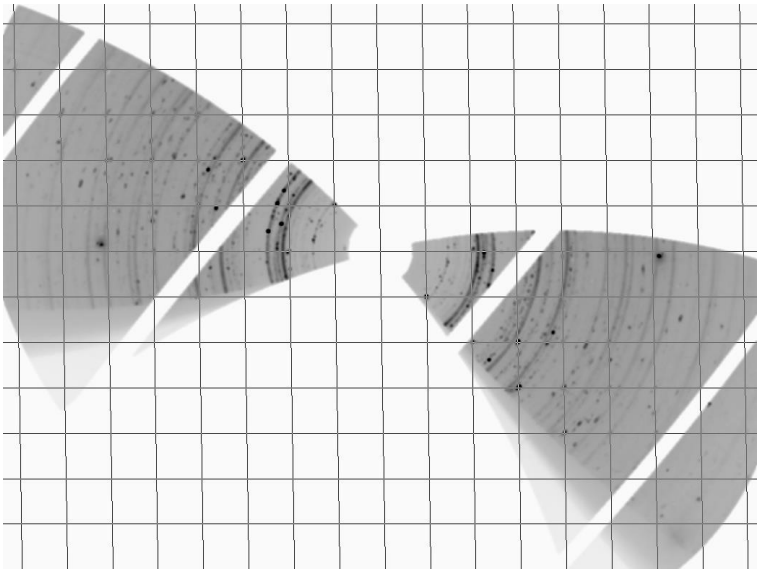


Fig. S 19: Precession image of the hk0-layer of $Pr_2Si_2O_7$ at 10 GPa. Cell parameters: $a = b = 662.85(6)$ pm, $c = 2420.0(2)$ pm, $V = 1063.3(2) \cdot 10^6$ pm^3.

$Pr_2Si_2O_7$ at 5 GPa

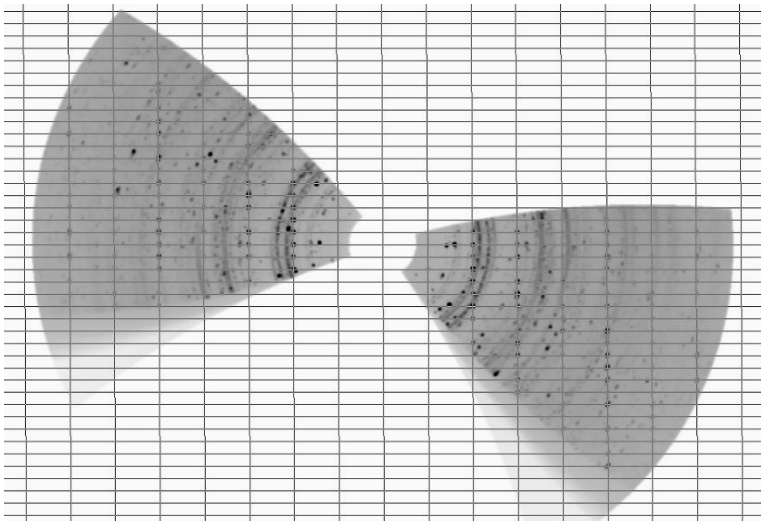


Fig. S 20: Precession image of the 0kl-layer of $Pr_2Si_2O_7$ at 5 GPa. Cell parameters: a = 677.26(4) pm, b = 677.26(4) pm, c = 2452(1) pm, V = 1124.9(4)•10^6 pm^3.

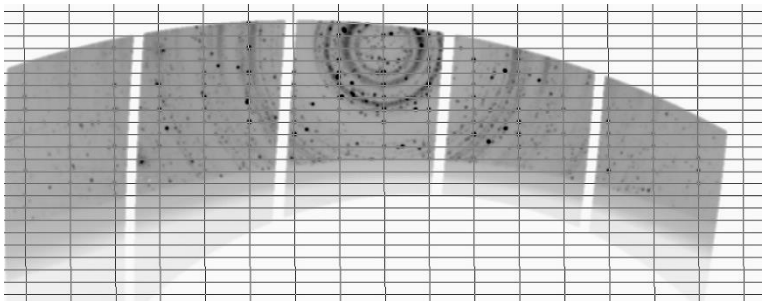


Fig. S 21: Precession image of the h2l-layer of $Pr_2Si_2O_7$ at 5 GPa. Cell parameters: a = 677.26(4) pm, b = 677.26(4) pm, c = 2452(1) pm, V = 1124.9(4)•10^6 pm^3.

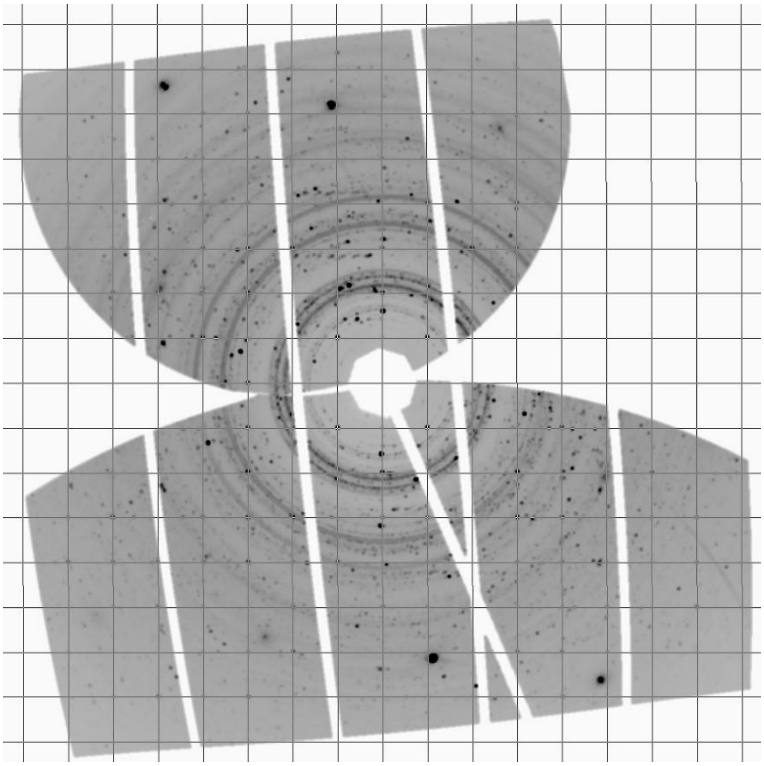


Fig. S 22: Precession image of the hk0-layer of $Pr_2Si_2O_7$ at 5 GPa. Cell parameters: a = 677.26(4) pm, b = 677.26(4) pm, c = 2452(1) pm, V = 1124.9(4)•10^6 pm^3.

$PrSi_3O_8$ at Ambient Pressure

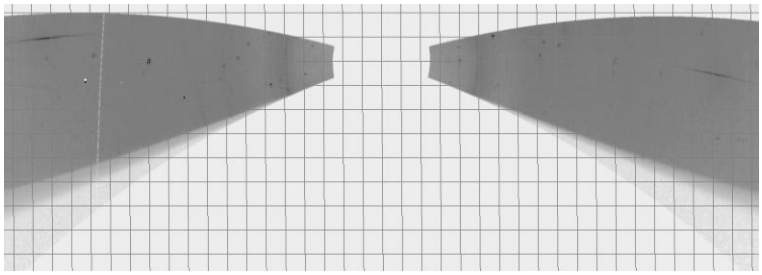


Fig. S 23: Precession image of the h0l-layer of $PrSi_3O_8$ at ambient pressure. Cell parameters: a = 1553.8(5) pm, b = 905.7(3) pm, c = 1259(1) pm, V = 1772(2)•10^6 pm^3.

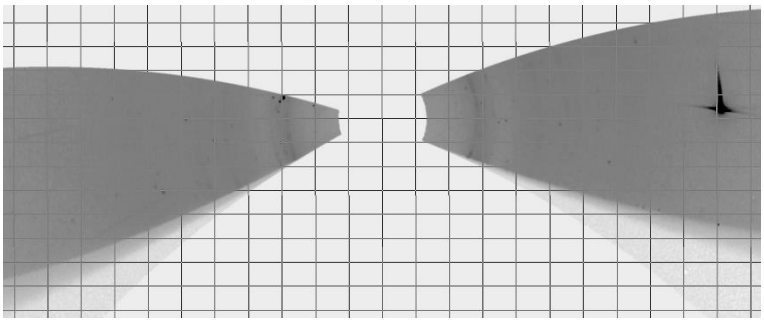


Fig. S 24: Precession image of the 1kl-layer of $PrSi_3O_8$ at ambient pressure. Cell parameters: a = 1553.8(5) pm, b = 905.7(3) pm, c = 1259(1) pm, V = 1772(2)•10^6 pm^3.

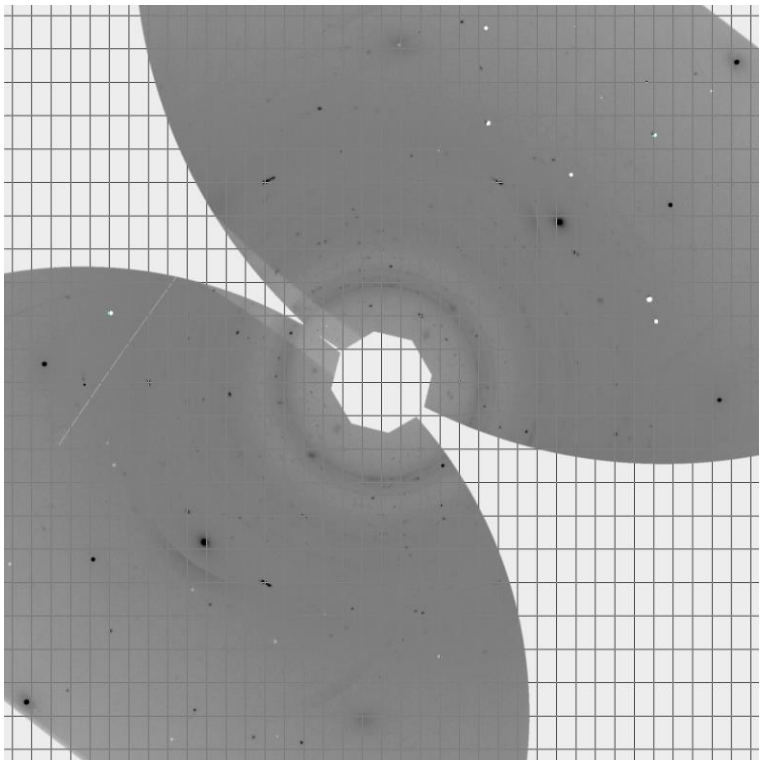


Fig. S 25: Precession image of the hk0-layer of $PrSi_3O_8$ at ambient pressure. Cell parameters: a = 1553.8(5) pm, b = 905.7(3) pm, c = 1259(1) pm, V = 1772(2)•10^6 pm^3.

$Pr_2Si_7O_{18}$ at Ambient Pressure

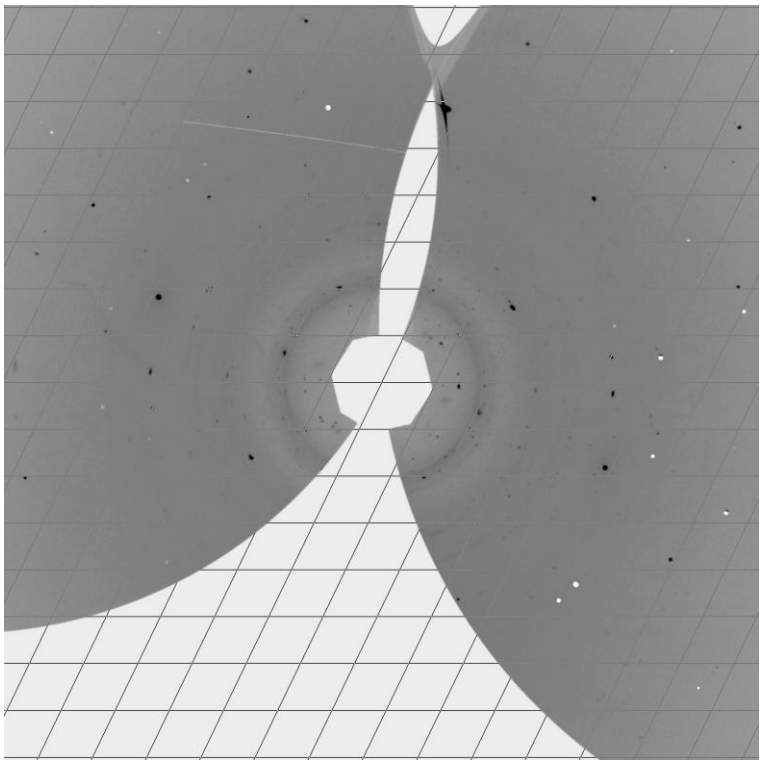


Fig. S 26: Precession image of the hk0-layer of $Pr_2Si_7O_{18}$ at ambient pressure. Cell parameters: a = 619.5(2) pm, b = 645.8(3) pm, c = 677.7(7) pm, V = 243.3(3)•10^6 pm^3.

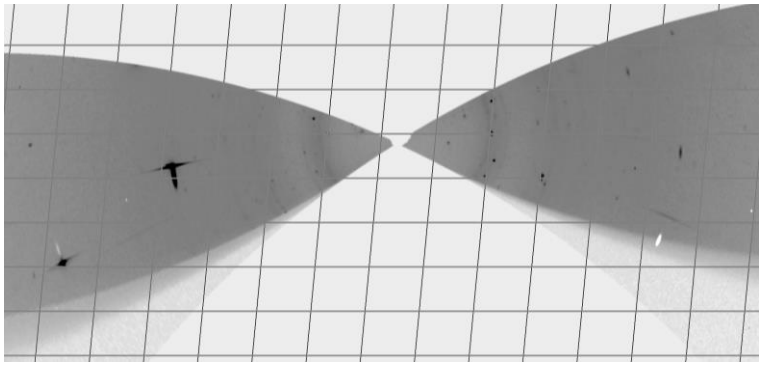


Fig. S 27: Precession image of the h-1l-layer of $Pr_2Si_7O_{18}$ at ambient pressure. Cell parameters: a = 619.5(2) pm, b = 645.8(3) pm, c = 677.7(7) pm, V = 243.3(3)•10^6 pm^3.

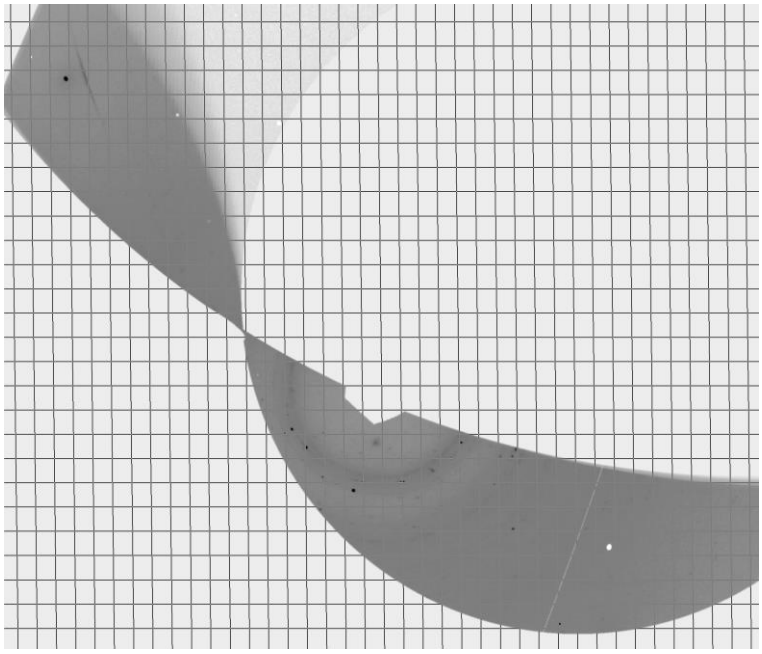


Fig. S 28: Precession image of the 1kl-layer of $Pr_2Si_7O_{18}$ at ambient pressure. Cell parameters: a = 619.5(2) pm, b = 645.8(3) pm, c = 677.7(7) pm, V = 243.3(3)•10^6 pm^3.

XRD Maps

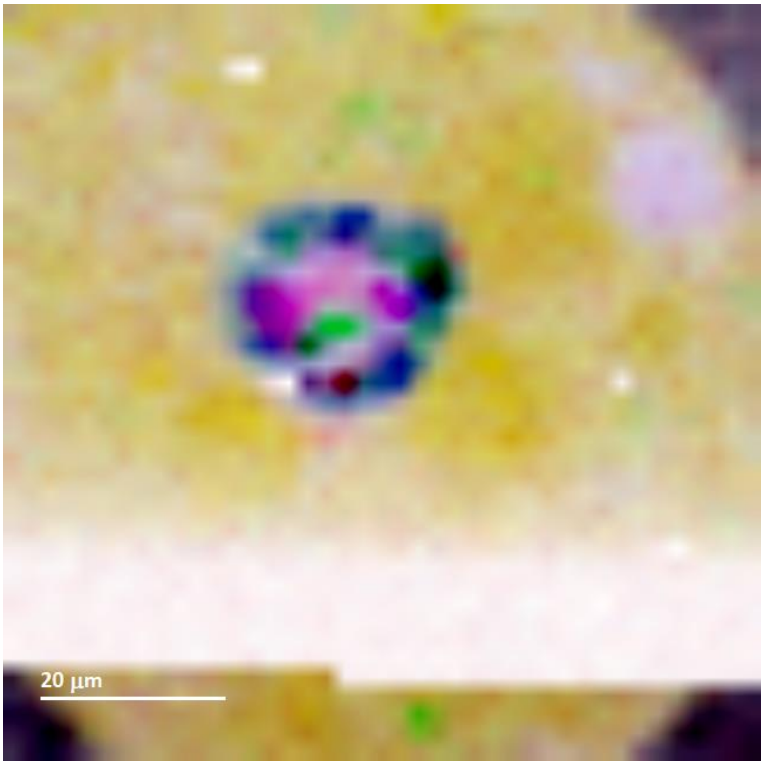


Fig. S 29: X-ray diffraction map of the cell at 29 GPa. Yellow = PrO_2 (fluorite structure); blue = $PrSi_3O_8$; green = $Pr_4Si_3O_{12}$; pink = $Pr_2Si_7O_{18}$; red = Pr_2O_5; black: = rhenium gasket.

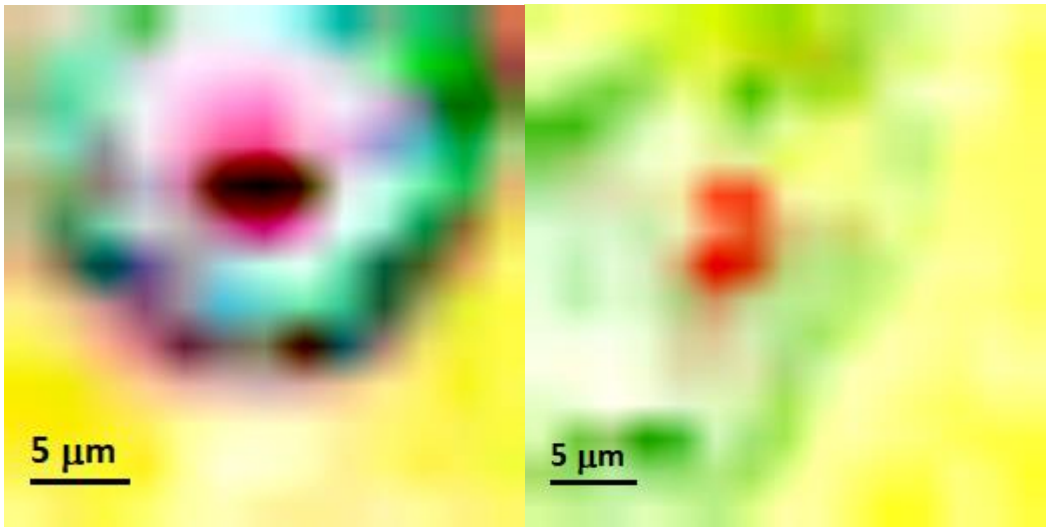


Fig. S 30: X-ray diffraction map of the cell at 15 GPa. Left: heated spot from the first pressure point at 29 GPa; right: area heated at 15 GPa. Yellow = PrO_2 (fluorite structure); blue = $PrSi_3O_8$; green = $Pr_4Si_3O_{12}$; pink = $Pr_2Si_7O_{18}$; red = Pr_2O_5.

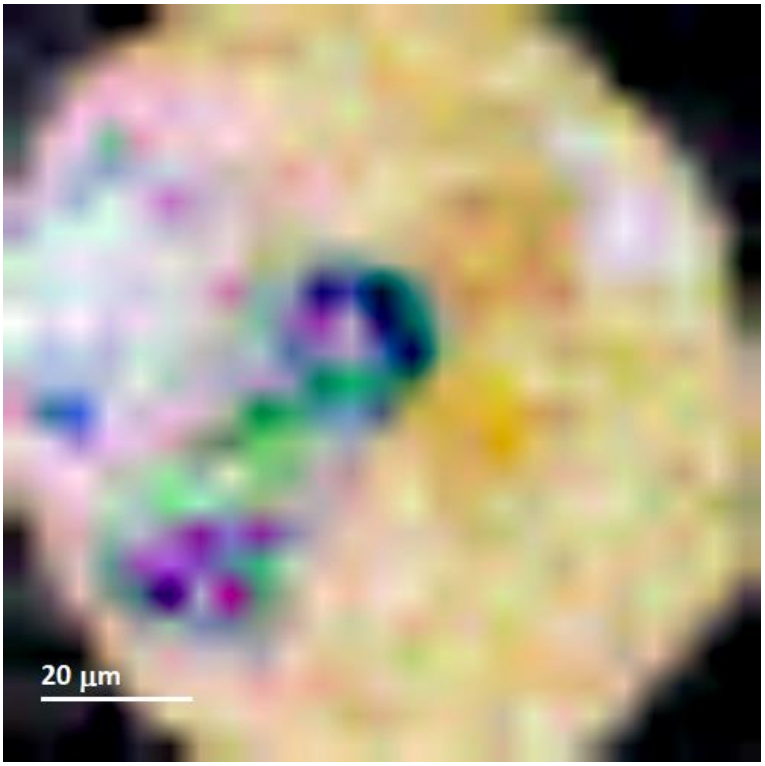


Fig. S 31: X-ray diffraction map of the cell at ambient pressure. Yellow = PrO_2 (fluorite structure); blue = $PrSi_3O_8$; green = $Pr_4Si_3O_{12}$; pink = $Pr_2Si_7O_{18}$; red = Pr_2O_5; black: = rhenium gasket.

Calculated Structures

Tab. S 8: Atomic coordinates $PrSi_3O_8$ after relaxation of the structure. Occ. = Occupancy, U = isotropic displacement parameter. All coordinate values are given in the units of 10^{-2} pm.

	x	y	z	Occ.	U	Site
Pr1	0.25000	-0.06419	-0.25000	1.000	0.015	8*e*
Pr2	0.00000	-0.17886	-0.08979	1.000	0.014	8*f*
Si3	-0.14674	0.00000	-0.50000	1.000	0.012	8*d*
Si2	0.25000	0.25000	-0.50000	1.000	0.010	8*c*
Si5	0.00000	-0.01078	-0.33254	1.000	0.013	8*f*
Si1	0.33425	0.00000	-0.50000	1.000	0.012	8*d*
Si4	-0.09108	-0.27591	-0.33147	1.000	0.013	16*g*
O5	-0.08108	-0.10448	-0.25616	1.000	0.018	16*g*
O4	0.00000	-0.18926	-0.40543	1.000	0.005	8*f*
O1	0.32815	0.15808	0.41971	1.000	0.012	16*g*
O6	-0.16429	-0.16725	-0.42191	1.000	0.015	16*g*
O7	-0.24332	-0.08281	0.42789	1.000	0.009	16*g*
O2	0.41661	0.07775	-0.42369	1.000	0.011	16*g*
O8	-0.07792	0.07702	-0.41156	1.000	0.015	16*g*
O9	0.00000	0.14689	-0.24500	1.000	0.012	8*f*
O3	0.32824	0.16703	-0.25867	1.000	0.014	16*g*

Tab. S 9: Atomic coordinates $PrSi_3O_8$ of the experimental structure. Occ. = Occupancy, U = isotropic displacement parameter. All coordinate values are given in the units of 10^{-2} pm.

	x	y	z	Occ.	U	Site
Pr1	0.25000	0.07536	0.25000	1.000	0.014	8e
Pr2	0.50000	0.83107	0.59034	1.000	0.013	8f
Si1	0.33510	0.00000	0.50000	1.000	0.012	8d
Si2	0.25000	0.25000	0.50000	1.000	0.011	8c
Si3	0.35240	0.50000	0.50000	1.000	0.013	8d
Si4	0.41230	0.23050	0.66260	1.000	0.014	16g
Si5	0.50000	0.49200	0.66830	1.000	0.014	8f
O9	0.50000	0.14910	0.74390	1.000	0.013	8f
O1	0.32660	0.15780	0.42030	1.000	0.014	16g
O2	0.41420	0.07890	0.57800	1.000	0.012	16g
O3	0.33020	0.16560	0.74380	1.000	0.015	16g
O4	0.50000	0.31700	0.59060	1.000	0.006	8f
O5	0.41910	0.39610	0.74040	1.000	0.019	16g
O6	0.33570	0.33040	0.58010	1.000	0.017	16g
O7	0.25650	0.41480	0.42790	1.000	0.010	16g
O8	0.42140	0.57920	0.58790	1.000	0.015	16g

Tab. S 10: Atomic coordinates $Pr_2Si_7O_{18}$ after relaxation of the structure. Occ. = Occupancy, U = isotropic displacement parameter. All coordinate values are given in the units of 10^{-2} pm.

	x	y	z	Occ.	U	Site
Pr1	-0.31336	0.30911	0.36599	1.000	0.008	2i
Si1	0.00000	0.00000	0.50000	1.000	0.003	1b
Si2	-0.18788	0.12771	-0.17880	1.000	0.006	2i
Si3	0.39349	0.27358	-0.12103	1.000	0.006	2i
Si4	-0.17921	-0.38329	-0.19239	1.000	0.007	2i
O1	0.27709	0.00565	0.44053	1.000	0.007	2i
O2	0.08509	0.27940	0.42126	1.000	0.005	2i
O3	-0.09862	0.22693	0.06680	1.000	0.004	2i
O4	-0.09983	0.39548	-0.27424	1.000	0.001	2i
O5	-0.49095	0.08167	-0.17542	1.000	0.003	2i
O6	-0.48093	0.43565	-0.32098	1.000	0.002	2i
O7	0.10104	0.12826	-0.24385	1.000	0.007	2i
O8	0.31672	-0.48867	-0.02584	1.000	0.007	2i
O9	-0.29280	-0.17379	-0.11746	1.000	0.004	2i

Tab. S 11: Atomic coordinates $Pr_2Si_7O_{18}$ of the experimental structure. Occ. = Occupancy, U = isotropic displacement parameter. All coordinate values are given in the units of 10^{-2} pm.

	x	y	z	Occ.	U	Site
Pr1	0.69070	0.31790	0.37790	1.000	0.008	Pr1
Si1	100.000	0.00000	0.50000	1.000	0.003	Si1

Si2	0.81200	0.12850	0.81040	1.000	0.006	Si2
Si3	0.39100	0.28320	0.88150	1.000	0.006	Si3
Si4	0.81400	0.61350	0.80150	1.000	0.007	Si4
O1	124.800	0.01600	0.45000	1.000	0.007	O1
O2	111.400	0.27600	0.42100	1.000	0.005	O2
O3	0.91100	0.22500	106.800	1.000	0.004	O3
O4	0.89700	0.39200	0.73000	1.000	0.001	O4
O5	0.50200	0.08000	0.83700	1.000	0.003	O5
O6	0.53000	0.42500	0.68200	1.000	0.002	O6
O7	0.11400	0.13100	0.76300	1.000	0.007	O7
O8	0.32200	0.51900	0.98100	1.000	0.007	O8
O9	0.68800	0.82200	0.88100	1.000	0.004	O9

Supporting Information

A New High-Pressure Polymorph of $PrPO_4$

Niko T. Flosbach*,[1] M. Bykov*,[1,2] L. Brüning,[1,2] P. Jurzick,[1,2] Mohamed Mezouar,[3] Timofey Fedotenko,[4] M. S. Wickleder*[1]

[1]Institute of Inorganic Chemistry, University of Cologne, Greinstraße 6, 50939 Cologne, Germany

[2]Institute of Inorganic and Analytical Chemistry, Goethe University Frankfurt, Max-von-Laue-Straße 7, 60438 Frankfurt am Main, Germany

[3]European Synchrotron Radiation Facility (ESRF), Avenue des Martyrs 71, 38000 Grenoble, France

[4]Deutsches Elektronen-Synchrotron, Notkestr. 85, 22607 Hamburg, Germany

Corresponding Authors

*Niko T. Flosbach - Greinstr. 6, 50939 Cologne, Germany;

Email: n.flosbach@uni-koeln.de

*Maxim Bykov – Max-von-Laue-Straße 7, D-60438 Frankfurt am Main, Germany;

Email: bykov@chemie.uni-frankfurt.de

*Mathias S. Wickleder - Greinstr. 6, 50939 Cologne, Germany;

Email: mathias.wickleder@uni-koeln.de

Table of Contents

Analytical Data of Starting Materials 2
XRD-Maps 3
Single Crystal Refinements 5
PXRD Patterns of $PrPO_4$ 7
Precession Images of $Pr_2(O_2)O_3$ 8

Analytical Data of Starting Materials

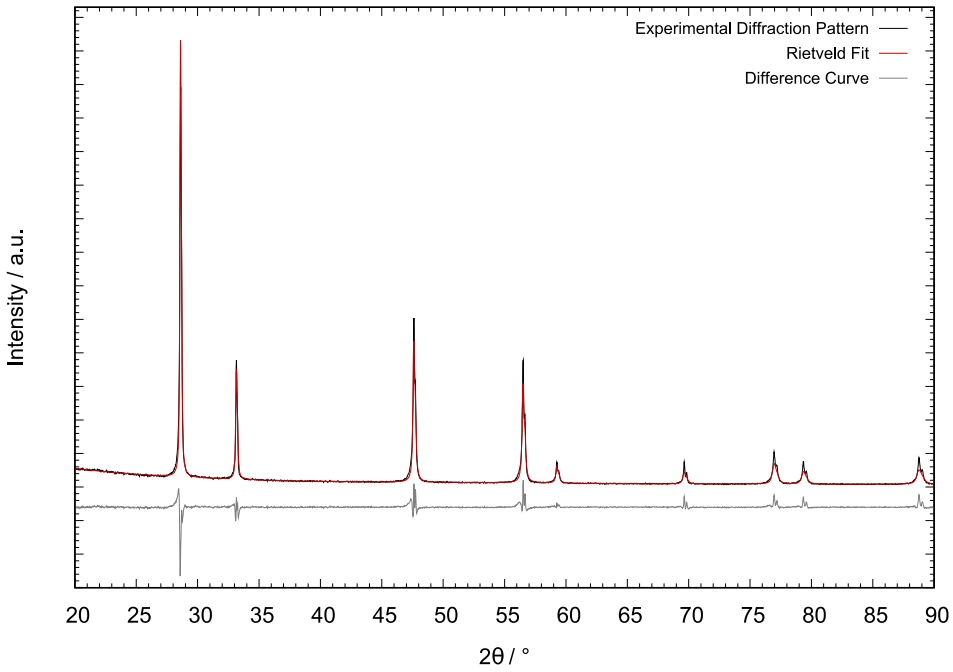


Fig. S 1: PXRD data of PrO_2. Lattice parameter obtained from Rietveld refinement: a = 539.41(6) pm.

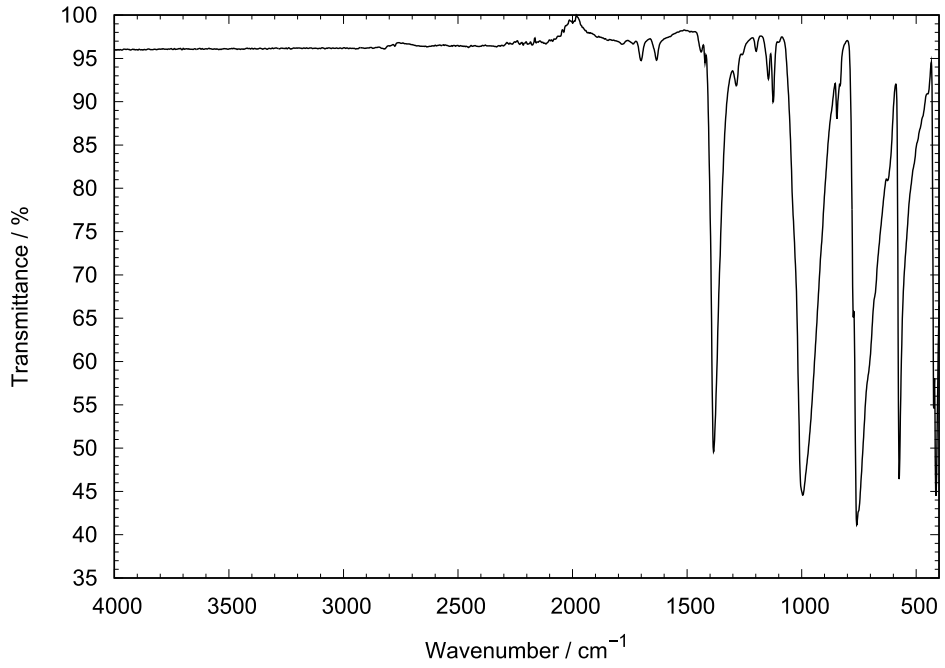


Fig. S 2: IR-spectrum of freshly sublimed phosphorus(V) oxide.

XRD-Maps

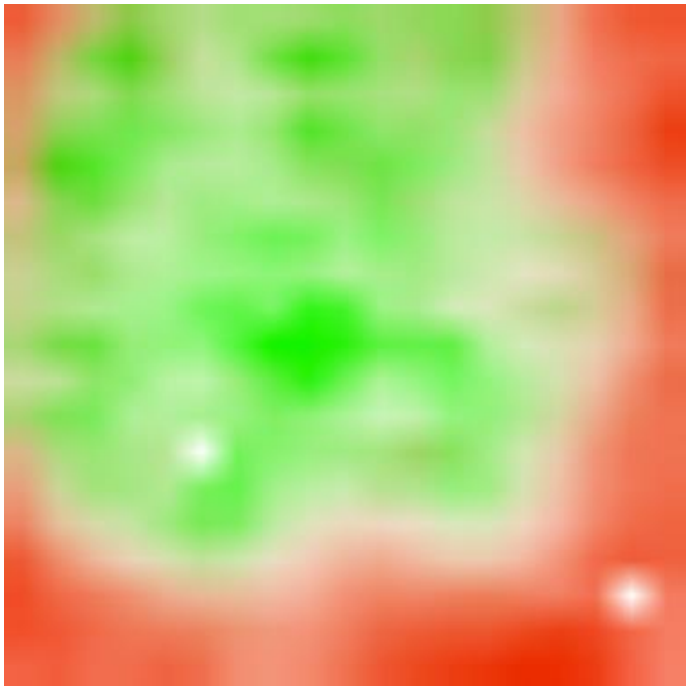


Fig. S 3: XRD map of the heated cell at 33.5 GPa. PrO_2 = red; $PrPO_4$ = green. Each edge of the graphic corresponds to 76 μm.



Fig. S 4: XRD map of the heated cell at 26 GPa. PrO_2 = red; $PrPO_4$ = green. Each edge of the graphic corresponds to 34 μm.



Fig. S 5: XRD map of the heated cell at 16 GPa. PrO_2 = red; $PrPO_4$ = green. Each edge of the graphic corresponds to 30 μm.



Fig. S 6: XRD map of the heated cell at ambient pressure. PrO_2 = red; $PrPO_4$ = green. Each edge of the graphic corresponds to 22 μm.

Single Crystal Refinements

Tab. S 1: Summary of crystallographic data of *hp*-$PrPO_4$ at different pressure points.

Pressure	**16 GPa**	**26 GPa**	**33.5 GPa**
Chemical Formula	$PrPO_4$	$PrPO_4$	$PrPO_4$
Molar Mass	471.76 g/mol	471.76 g/mol	471.76 g/mol
Temperature	293(2) K	293(2) K	293(2) K
Crystal System	orthorhombic	orthorhombic	orthorhombic
Space Group	*Pnma*	*Pnma*	*Pnma*
Lattice Parameters	a = 796.7(1) pm	a = 785.75(8) pm	a = 782.56(7) pm
	b = 502.2(2) pm	b = 491.4(2) pm	b = 488.6(2) pm
	c = 650.4(2) pm	c = 640.21(9) pm	c = 635.60(9)pm
Cell Volume	260.2(1) 10^6 pm^3	247.18(9) 10^6 pm^3	243.05(9) 10^6 pm^3
Formula Units	4	4	4
Calculated Density	6.022 g/cm^3	6.339 g/cm^3	6.446
Absorption Correction	multi scan	multi scan	multi scan
Absorption Coefficient	8.893 mm^{-1}	9.361 mm^{-1}	3.821 mm^{-1}
F(000)	424.0	424.0	424.0
Crystal Size	0.01 x 0.01 x 0.01 mm	0.01 x 0.01 x 0.01 mm	0.01 x 0.01 x 0.01 mm
Radiation	synchrotron (λ = 0.2901 Å)	synchrotron (λ = 0.2901 Å)	synchrotron (λ = 0.3738 Å)
2θ-Range	4.182° to 35.024°	3.35° to 34.704°	5.476° to 41.484°
Index Range	$-16 \le h \le 15$, $-8 \le k \le 7$, $-11 \le l \le 10$	$-14 \le h \le 13$, $-6 \le k \le 5$, $-11 \le l \le 11$	$-14 \le h \le 12$, $-5 \le k \le 3$, $-9 \le l \le 9$
Reflections Collected	1250	1148	452
Independent Reflections	541 [R_{int} = 0.0974, R_σ = 0.0790]	551 [R_{int} = 0.0204, R_σ = 0.0309]	312 [R_{int} = 0.0120, R_σ = 0.0180]
Data/Restraints/Parameters	541/0/34	551/0/34	312/0/34
Goodness of Fit	1.285	1.163	1.068
R_1; wR_2 ($I \ge 2\sigma(I_o)$)	R_1 = 0.0812, wR_2 = 0.1837	R_1 = 0.0491, wR_2 = 0.1234	R_1 = 0.0395, wR_2 = 0.1112
R_1; wR_2 (All Data)	R_1 = 0.1060, wR_2 = 0.1934	R1 = 0.0676, wR2 = 0.1323	R_1 = 0.0453, wR_2 = 0.1137
Largest Diff. Peak/Hole	2.59/-32.51 e/$Å^3$	1.84/-2.18 e/$Å^3$	2.37/-1.56 e/$Å^3$

Tab. S 2: Summary of crystallographic data of $PrPO_4$ at ambient pressure, obtained by decompression of *hp*-$PrPO_4$.

Pressure	**Ambient Pressure**
Chemical Formula	$PrPO_4$
Molar Mass	471.76 g/mol
Temperature	293(2) K
Crystal System	monoclinic
Space Group	$P2_1/n$
Lattice Parameters	a = 540.30(9) pm
	b = 800.9(8) pm
	c = 674.4(1) pm
Cell Volume	291.7(3) 10^6 pm^3
Formula Units	4
Calculated Density	5.371 g/cm^3
Absorption Correction	multi scan
Absorption Coefficient	7.931 mm^{-1}
F(000)	424.0
Crystal Size	0.01 x 0.01 x 0.01 mm
Radiation	synchrotron (λ = 0.2901 nm)
2θ-Range	3.712 to 35.314
Index Range	$-10 \leq h \leq 10$, $-7 \leq k \leq 8$, $-12 \leq l \leq 11$
Reflections Collected	1404
Independent Reflections	790 [R_{int} = 0.1260, R_σ = 0.1767]
Data/Restraints/Parameters	790/0/50
Goodness of Fit	1.107
R_1; wR_2 ($I \geq 2\sigma(I_o)$)	R_1 = 0.1035, wR_2 = 0.2008
R_1; wR_2 (All Data)	R_1 = 0.1776, wR_2 = 0.2243
Largest Diff. Peak/Hole	2.46/-2.41 e/$Å^3$

PXRD Patterns of $PrPO_4$

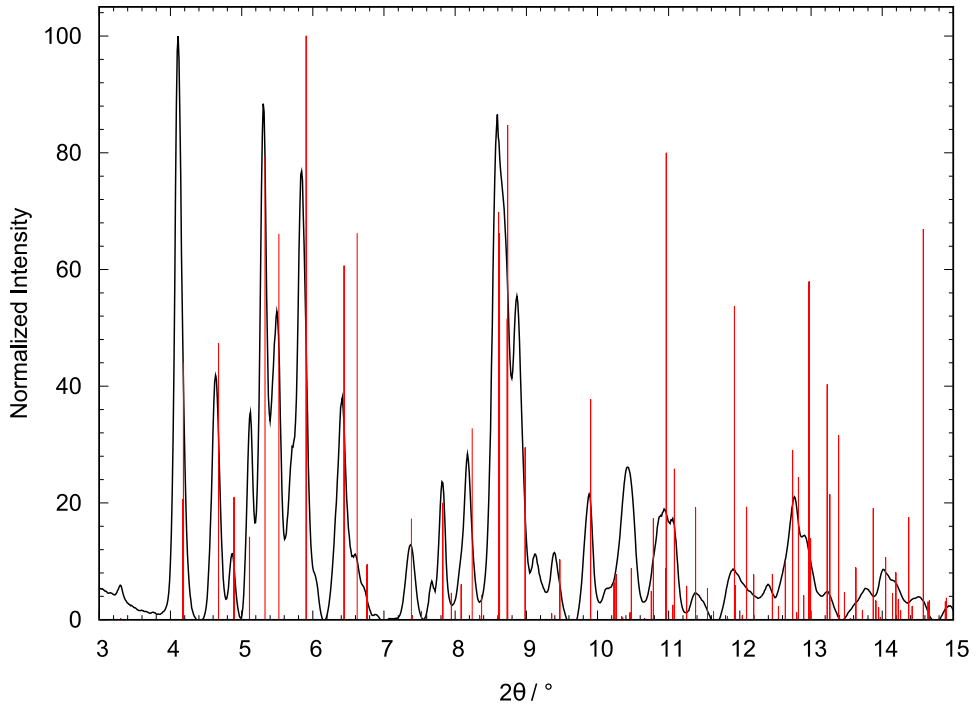


Fig. S 7: XRPD pattern of the products obtained after heating the cell at 16 GPa. The red lines indicate the theoretical positions of the peaks of the orthorhombic $PrPO_4$ structure at 16 GPa.

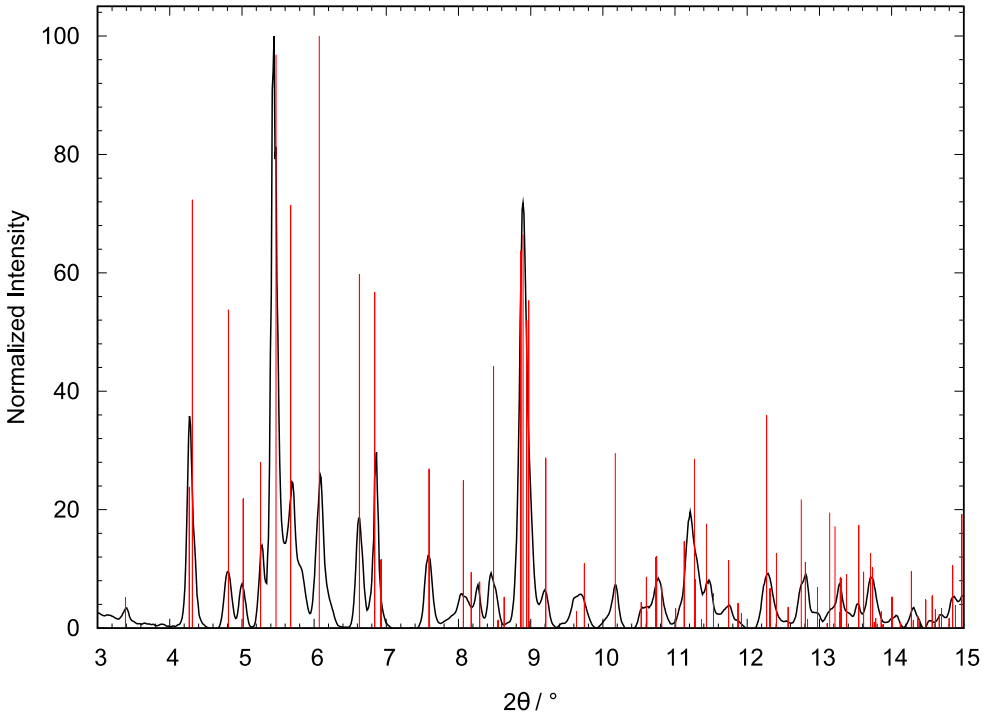


Fig. S 8: XRPD pattern of the products obtained after heating the cell at 33.5 GPa. The red lines indicate the theoretical positions of the peaks of the orthorhombic $PrPO_4$ structure at 33.5 GPa.

Precession Images of $Pr_2(O_2)O_3$

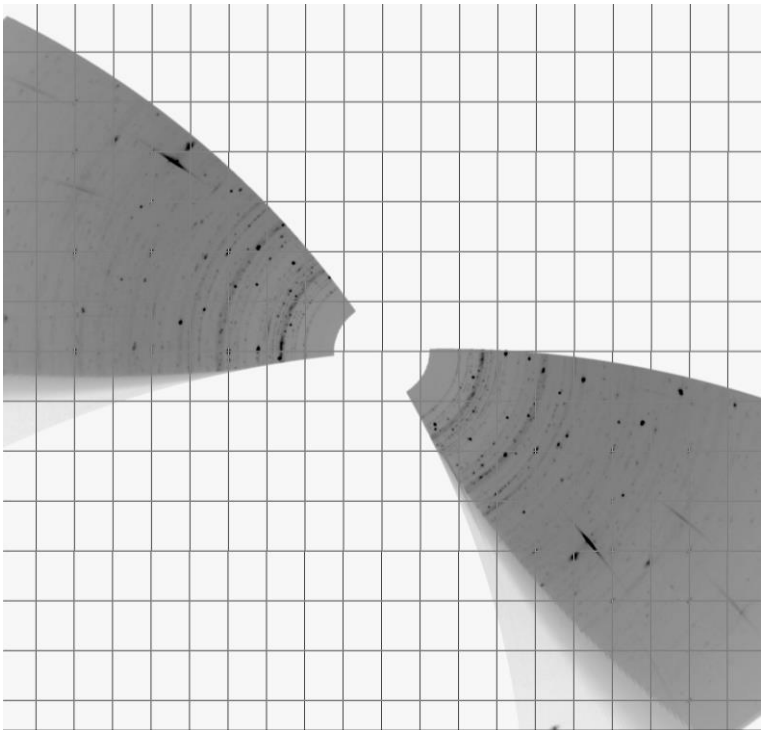


Fig. S 9: Precession image of the 0kl-layer of $Pr_2(O_2)O_3$ at 26 GPa. Cell parameters: a = 606.41(5) pm, b = 789.07(9) pm, c = 606.7(1) pm, V = 290.28(7)•10^6 pm^3.

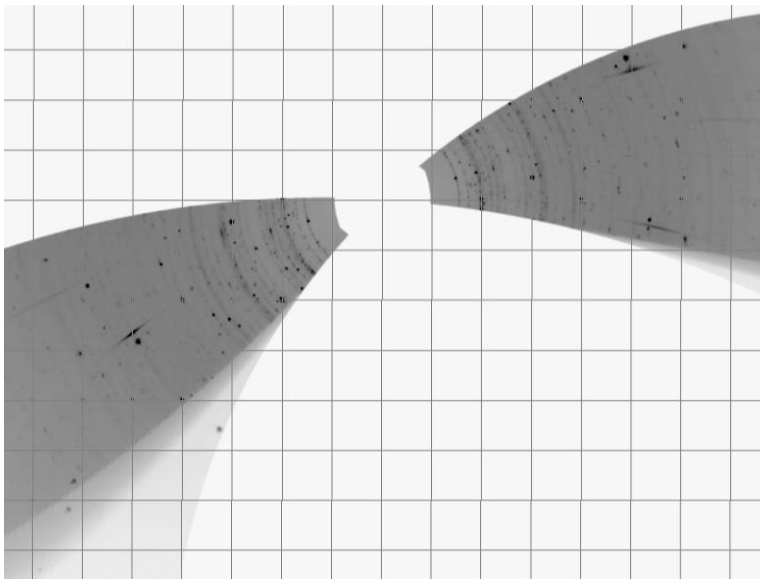


Fig. S 10: Precession image of the h0l-layer of $Pr_2(O_2)O_3$ at 26 GPa. Cell parameters: a = 606.41(5) pm, b = 789.07(9) pm, c = 606.7(1) pm, V = 290.28(7)•10^6 pm^3.

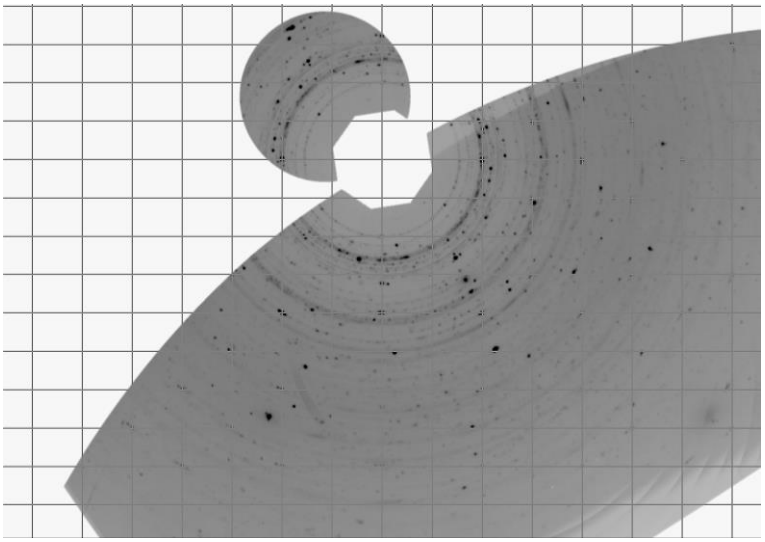


Fig. S 11: Precession image of the hk0-layer of $Pr_2(O_2)O_3$ at 26 GPa. Cell parameters: a = 606.41(5) pm, b = 789.07(9) pm, c = 606.7(1) pm, V = 290.28(7)•10^6 pm^3.

Supporting Information

High Pressure Synthesis of Pr_2O_5 – A Unique Lanthanoid(IV) Oxide Peroxide

N. T. Flosbach[1], M. Bykov[1,2], L. Brüning[1], P. L. Jurzick[1], E. Bykova[3], M. Ekholm[4], I. A. Abrikosov[4], M. Amirabbasi[5], M. Mezouar[6], B. Wehinger[6], N. Giordano[7], T. Fedotenko[7], V. Prakapenka[8], S. Chariton[8], M. S. Wickleder[1]

[1]University of Cologne, Institute of Inorganic Chemistry, Greinstr. 6, 50939 Cologne, Germany

[2]Institute of Inorganic and Analytical Chemistry, Goethe University Frankfurt, Max-von-Laue-Str. 7, 60438 Frankfurt am Main, Germany

[3]Institute of Geosciences, Goethe University Frankfurt, Altenhöferallee 1, 60438 Frankfurt am Main, Germany

[4]Department of Physics, Chemistry and Biology, Linköping University, SE-581 83, Sweden

[5]Theory of Magnetic Materials, Institut für Materialwissenschaft, Technische Universität Darmstadt, 64289 Darmstadt, Germany

[6]European Synchrotron Radiation Facility, Grenoble Cedex F-38043, France

[7]Deutsches Elektronen-Synchrotron DESY, Notkestr. 85, 22607 Hamburg, Germany

[8]Center for Advanced Radiation Sources, University of Chicago, Chicago, IL, USA

Corresponding Authors

*Niko T. Flosbach - Greinstr. 6, 50939 Cologne, Germany;

Email: n.flosbach@uni-koeln.de

*Maxim Bykov – Max-von-Laue-Straße 7, D-60438 Frankfurt am Main, Germany;

Email: bykov@chemie.uni-frankfurt.de

*Mathias S. Wickleder - Greinstr. 6, 50939 Cologne, Germany;

Email: mathias.wickleder@uni-koeln.de

Table of Contents

Crystallographic Data 2
Raman Spectrum 4
XRD Maps 4

Crystallographic Data

Tab. S 1: Selected crystallographic data of $Pr_2(O_2)O_3$ at three different pressure points.

	11 GPa	**20 GPa**	**27 GPa**
Chemical Formula	Pr_2O_5	Pr_2O_5	Pr_2O_5
Molar Mass	361.82 g/mol	361.82 g/mol	361.82 g/mol
Temperature	293(2) K	293(2) K	293(2) K
Crystal System	orthorhombic	orthorhombic	orthorhombic
Space Group	*Pbcn*	*Pbcn*	*Pbcn*
Lattice Parameters	*a* = 617.2(1) pm *b* = 802.7(1) pm *c* = 616.33(8) pm	*a* = 606.1(1) pm *b* = 794.2(1) pm *c* = 611.7(2) pm	*a* = 601.4(2) pm *b* = 779.6(2) pm *c* = 610.5(1) pm
Cell Volume	$305.33(3)\cdot10^6$ pm^3	$294.4(1)\cdot10^6$ pm^3	$286.19(1)\cdot10^6$ pm^3
Formula Units	4	4	4
Calculated Density	7.871 g/cm^3	8.162 g/cm^3	8.397 g/cm^3
Absorption Correction	multi scan	multi scan	multi scan
Absorption Coefficient	15.035 mm^{-1}	15.592 mm^{-1}	16.040 mm^{-1}
F(000)	632.0	632.0	632.0
Crystal Size	0.001 × 0.001 × 0.001 mm^3	0.001 × 0.001 × 0.001 mm^3	0.001 × 0.001 × 0.001 mm^3
Radiation	synchrotron (λ = 0.2901)	synchrotron (λ = 0.2901)	synchrotron (λ = 0.2901)
2θ-Range	3.398 to 35.17°	3.45 to 35.544°	3.492 to 34.54°

Index Range	$-8 \le h \le 8$, $-12 \le k \le 13$, $-9 \le l \le 10$	$-10 \le h \le 9$, $-15 \le k \le 14$, $-9 \le l \le 9$	$-8 \le h \le 8$, $-11 \le k \le 13$, $-10 \le l \le 9$
Reflections Collected	1472	1530	1447
Independent Reflections	708 [R_{int} = 0.0150, R_σ = 0.0178]	667 [R_{int} = 0.0179, R_σ = 0.0236]	642 [R_{int} = 0.0083, R_σ = 0.0090]
Data/Restraints/Parameters	708/0/33	667/0/33	642/0/34
Goodness of Fit	1.087	1.283	1.125
R_1; wR_2 ($I \ge 2\sigma(I_o)$)	R_1 = 0.0388, wR_2 = 0.1094	R_1 = 0.0361, wR_2 = 0.0901	R_1 = 0.0252, wR_2 = 0.0676
R_1; wR_2 (All Data)	R_1 = 0.0488, wR_2 = 0.1173	R_1 = 0.0486, wR_2 = 0.0940	R_1 = 0.0277, wR_2 = 0.0685
Largest Diff. Peak/Hole	7.10/-2.78	2.65/-2.98	2.34/-2.75

Tab. S 2: Summary of selected interatomic distances as well as other structural parameters of $Pr_2(O_2)O_3$ at different pressures.

	11 GPa	**20 GPa**	**27 GPa**
Cell Volume / 10^6 pm^3	305.33(3)	294.4(1)	286.19(1)
a / pm	617.2(1)	606.1(1)	601.4(2)
b / pm	802.7(1)	794.2(1)	779.6(2)
c / pm	616.33(8)	611.7(2)	610.5(1)
d(O1-O1) / pm	147(1)	145(1)	144.1(7)
$V_{Polyhedron}$ [PrO_{10}] / 10^6 pm^3	285.09(6)	275.03(7)	267.29(2)
d_{avg}(Pr-O) / pm	238.4(5)	235.5(6)	233.3(4)
d_1(Pr1-O1) / pm	240.2(5)	238.5(6)	235.5(4)
d_1(Pr1-O2) / pm	233.0(5)	231.4(7)	228.0(4)
d_2(Pr1-O2) / pm	232.1(5)	228.7(6)	229.7(4)
d_1(Pr1-O3) / pm	237.7(3)	234.3(3)	230.6(2)
d_3(Pr1-O2) / pm	221.4(5)	219.1(6)	235.2(4)
d_4(Pr1-O2) / pm	234.7(5)	231.8(6)	228.1(4)
d_2(Pr1-O1) / pm	256.0(5)	253.5(7)	245.3(4)
d_3(Pr1-O1) / pm	242.3(5)	238.5(6)	265(4)
d_2(Pr1-O3) / pm	234.5(3)	231.9(3)	232.4(2)
d_4(Pr1-O1) / pm	252.2(5)	247.4(6)	252.0(4)

Raman Spectrum

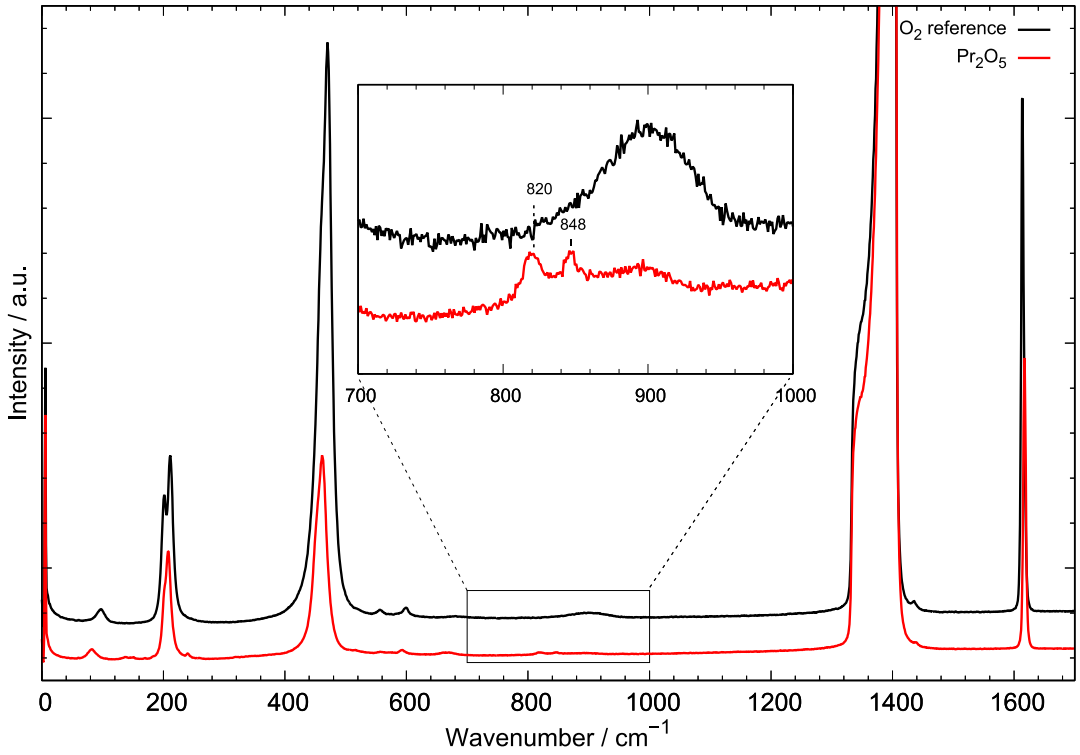


Fig. S 1: Raman spectrum of the reaction chamber at 27 GPa. Vibrations assigned to the peroxide group of $Pr_2(O_2)O_3$ are highlighted. The spectra were recorded with an excitation wavelength of 532 nm. The black spectrum is a reference spectrum of only oxygen without praseodymium oxides that was measured using the same experimental setup.

XRD Maps

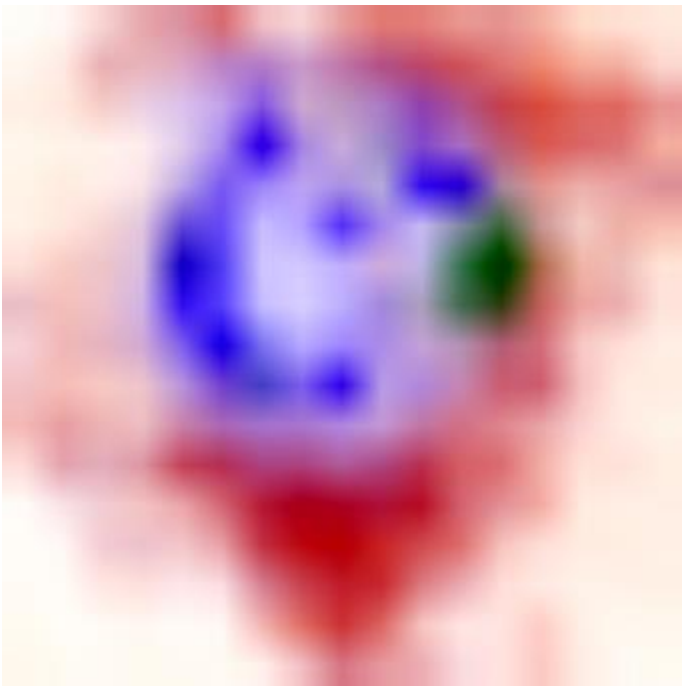


Fig. S 2: X-Ray diffraction map of the heated area in the diamond anvil cell at 27 GPa. Each edge of the graphic corresponds to 300 µm in the actual cell. Red = fluorite PrO_2; blue = $Pr_2(O_2)O_3$; green = ruby.



Fig. S 3: X-Ray diffraction map of the heated area in the diamond anvil cell at 20 GPa. Each edge of the graphic corresponds to 220 µm in the actual cell. Red = fluorite PrO_2; blue = $Pr_2(O_2)O_3$.

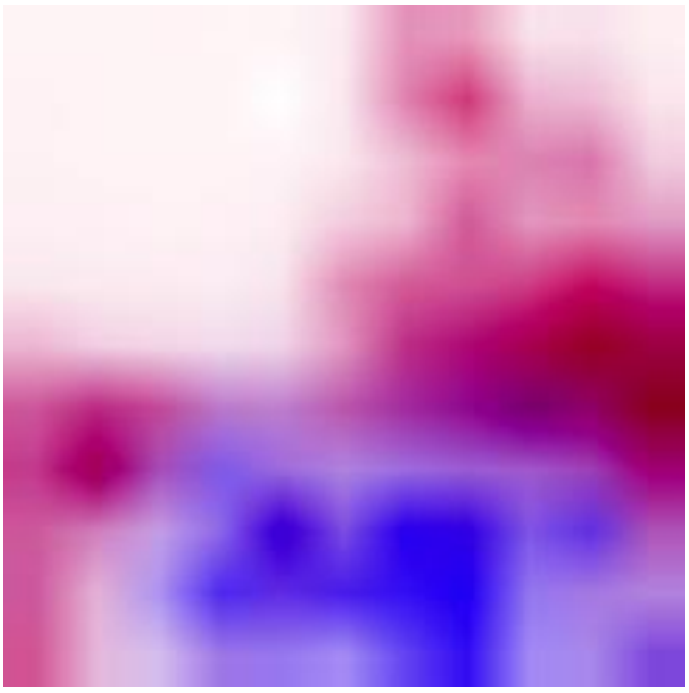


Fig. S 4: X-Ray diffraction map of the heated area in the diamond anvil cell at 11 GPa. Each edge of the graphic corresponds to 220 µm in the actual cell. Red = fluorite PrO_2; blue = $Pr_2(O_2)O_3$.

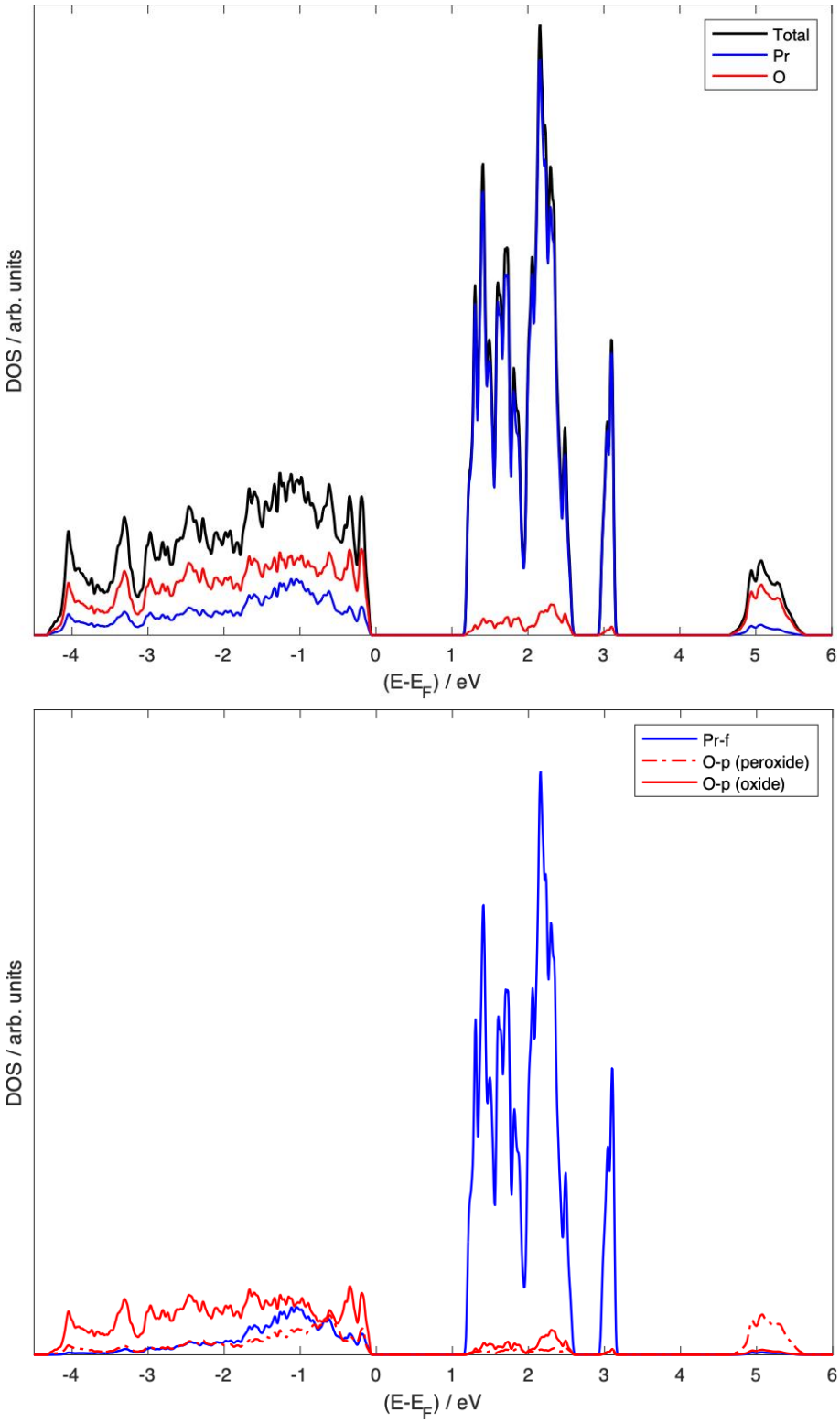


Fig. S 5: Calculated density of states (DOS) at the volume 290 Å^3. Top: total DOS and site-projected DOS with respect to the Fermi energy. Bottom: orbital resolved DOS showing Pr f-states and p-states of oxide and peroxide anions. Note the antibonding peroxide states at $E\text{-}E_F = 5$ eV. The peak contains exactly 2 electron states per formula unit.

Supporting Information

The Divalent Lanthanoid Triflates $Ln(CF_3SO_3)_2(CH_3CN)$ (Ln = Sm, Eu): Structure, Luminescence and Magnetism

Niko T. Flosbach[1], Bertold Rasche[2], Leonhard Rochels[3], Sabrina Disch[3], Claudia Wickleder[4], Matthias Adlung[4], Pia Fischer[4], Mathias S. Wickleder*[1]

[1] Institute of Inorganic Chemistry, University of Cologne, Greinstraße 6, 50939 Cologne, Germany

[2] Institute of Inorganic Chemistry, University of Stuttgart, Pfaffenwaldring 55, 70569 Stuttgart, Germany

[3] Anorganische Chemie und Center for Nanointegration Duisburg-Essen (CENIDE), University of Duisburg-Essen, Universitätsstraße 5-7, 45141 Essen, Germany

[4] Institute of Inorganic Chemistry, University of Siegen, Adolf-Reichwein-Straße, 57068 Siegen, Germany

Table of Contents

General Experimental Details 2

Single Crystal X-Ray Diffraction 2

Powder X-Ray Diffraction 3

Thermogravimetric Analysis 3

UV-Vis Spectra 3

IR-Spectra 4

Magnetic Measurements 4

Cyclic Voltammetry 4

Luminescence 4
Syntheses 5
Synthesis of $Sm(OTf)_3$ 5
Synthesis of $Eu(OTf)_3$ 6
Synthesis of $Sr(OTf)_2$ 8
Synthesis of $Sm(OTf)_2(CH_3CN)$ 9
Synthesis of $Eu(OTf)_2(CH_3CN)$ 10
Synthesis of $Sr(OTf)_2(CH_3CN)$ 10
Synthesis of $Sm(OTf)_2$ 10
Synthesis of $Eu(OTf)_2$ 11
Synthesis of $Sr(OTf)_2(CH_3CN):Sm^{2+}$ 12
Synthesis of $Sr(OTf)_2(CH_3CN):Eu^{2+}$ 13
Further Analytical Data 14
Rietveld Refinements 14
UV-Vis Spectra 16
Luminescence Spectra 17
Thermogravimetric Analyses 19
IR-Spectra 21
References 22

General Experimental Details

Single Crystal X-Ray Diffraction

Single crystal diffraction data were collected from a shock-cooled single crystal**s** at 100.0 K on a *BRUKER D8 Venture* three-circle diffractometer with a microfocus sealed tube using a multilayer mirror as monochromator and a *Bruker PHOTON III* detector. The diffractometer was equipped with an *Oxford Cryostream 800* low temperature device and used Mo-$K\alpha_1$ radiation (λ = 0.71073 Å). All data were integrated with *SAINT* and a multi-scan absorption

correction using SADABS was applied.[1,2] The structure was solved by dual methods using XT and refined by full-matrix least-squares methods against F2 by XL.[3,4] All non-hydrogen atoms were refined with anisotropic displacement parameters. All hydrogen atoms were refined isotropic on calculated positions using a riding model with their U_{iso} values constrained to 1.5 times the U_{eq} of their pivot atoms for terminal sp^3-carbon atoms and 1.2 times for all other carbon atoms. Crystallographic data for the structures reported in this paper have been deposited with the Cambridge Crystallographic Data Centre.[5] CCDC 2086582, 2086583 and 2328609, contain the supplementary crystallographic data for this paper. These data can be obtained free of charge from The Cambridge Crystallographic Data Centre via *www.ccdc.cam.ac.uk/structures*. This report was generated using FinalCif.[6]

Structures were visualized using *Vesta 3.5.5*.[7] Coordination polyhedra were calculated using continuous shape measurements (CShM) using *Shape 2.1*.[8]

Powder X-Ray Diffraction

Standard XRD measurements were conducted on a *P-XRD STOE Stadi-P* with a *Mythen 1 K* detector from 0 to 60° in steps of 1° and 120 s exposure time in Debye-Scherrer geometry. Mo-Kα_1 was used as a radiation source. Samples were prepared in glass capillaries with a diameter of 0.3 mm.

Residual material of TGA measurements were analyzed using a *Rigaku Miniflex* with a *HyPix-400 MF 2D* hybrid detector. Samples were mounted on a flat silicon holder and measured with 1.2 °/min in varying ranges.

Rietveld refinements were performed using *Topas* in combination with *Jedit*.[9] Theoretical patterns were simulated from literature data with *WinXPow*.[10]

Thermogravimetric Analysis

Thermogravimetric analyses were performed on a *Perkin Elmer STA 6000*, equipped with an autosampler. A constant gas stream of 19 ml/min was applied during the measurements.

UV-Vis Spectra

UV-Vis-spectra were measured in quartz cuvettes on a *UV-1600 PC Spectrophotometer*.

IR-Spectra

IR-spectra were measured on a *Bruker Alpha II* that was set up inside of an argon filled glovebox.

Magnetic Measurements

The temperature dependent magnetic susceptibility was measured using a Quantum Design PPMS Evercool II with vibrating sample magnetometer (VSM) option. 15.6 mg ($Eu(OTf)_2(CH_3CN)$) and 11.3 mg ($Sm(OTf)_2(CH_3CN)$) of sample material were transferred into powder capsules in inert atmosphere and fixed in a brass sample holder. Temperature dependent magnetization was measured in an applied magnetic field of 100 mT in a temperature range of 5-350 K with a heating rate of 1 K/min. A small background from the sample holder was determined in reference measurements and subtracted from the data. The magnetic susceptibility data were corrected for a diamagnetic susceptibility of $\chi_{dia} = -196 \times 10^{-11}$ m^3 mol^{-1} [13]. The temperature dependence of the effective magnetic moment μ_{eff} was derived assuming Curie behavior according to $\mu_{eff} = 797.7 \sqrt{\chi T} \mu_B$.

Cyclic Voltammetry

Cyclic voltammograms were measured under the exclusion of air using a three electrode setup with a glassy carbon working electrode, a leakless Ag/AgCl reference electrode and a graphite counter electrode. The electrolyte (tetrabutylammonium hexafluorophosphate) was recrystallised before use to ensure sufficient purity. The potential was controlled by a *Gamry* I1010B potentiostat together with the *Gamry* Framework software. The working electrode was polished three times between experiments on wet soft pads using aluminium oxide powder of decreasing grain sizes.

Luminescence

For the luminescence spectroscopy, a Fluorolog3 FL3-22 spectrometer (Horiba Jobin Yvon) containing a 450 W Xenon arc lamp was used. The exact wavelength for excitation and emission measurements was reached with double Czerny-Turner monochromators including 1200 grooves/nm. Within this, a spectral resolution of up to 0.05 nm can be reached. The emitted light was detected with a photomultiplier tube R928P (Hamamatsu) between 240 nm

and 850 nm. Emission spectra were corrected concerning the detector sensitivity whereas excitation spectra were corrected due to the background spectra of the lamp. Low temperature measurements were performed in a closed-cycle with cryostat CCS (Janis Research) with an external temperature control unit (LakeShore). Data collection was conducted with FluoroEssence 3.5 implemented in OriginPro 8.1. OriginPro 9.0 was used for posterior data evaluation.

Syntheses

All manipulations involving air sensitive materials were carried out in argon filled glove boxes or using standard schlenk-techniques. Rare earth oxides, metals and strontium carbonate were purchased from commercial suppliers. Solvents were dried over molecular sieves (300 pm) for at least one week and degassed by freeze-thaw-pump cycles.

Synthesis of $Sm(OTf)_3$

$$Sm_2O_3 + 6\ HOTf\ (aq) \xrightarrow{200\ °C} 2\ Sm(OTf)_3(H_2O)_9 \xrightarrow[\text{dynamic vac.}\ -18\ H_2O]{275\ °C} 2\ Sm(OTf)_3$$

1.03 g (2.95 mmol, 2 eq.) of Sm_2O_3 was suspended in 5 ml of water. 5 ml of concentrated triflic acid was added before the mixture was heated to 200 °C. After excess triflic acid was boiled off, the solids were transferred to a schlenk flask and heated to 275 °C under dynamic vacuum until vibrational bands of water had completely disappeared in the IR-spectrum (compare Fig. S 1). 2.99 g (5.00 mmol, 85%) of $Sm(OTf)_3$ was obtained as a colourless powder. For XRD-data see Fig. S 2.

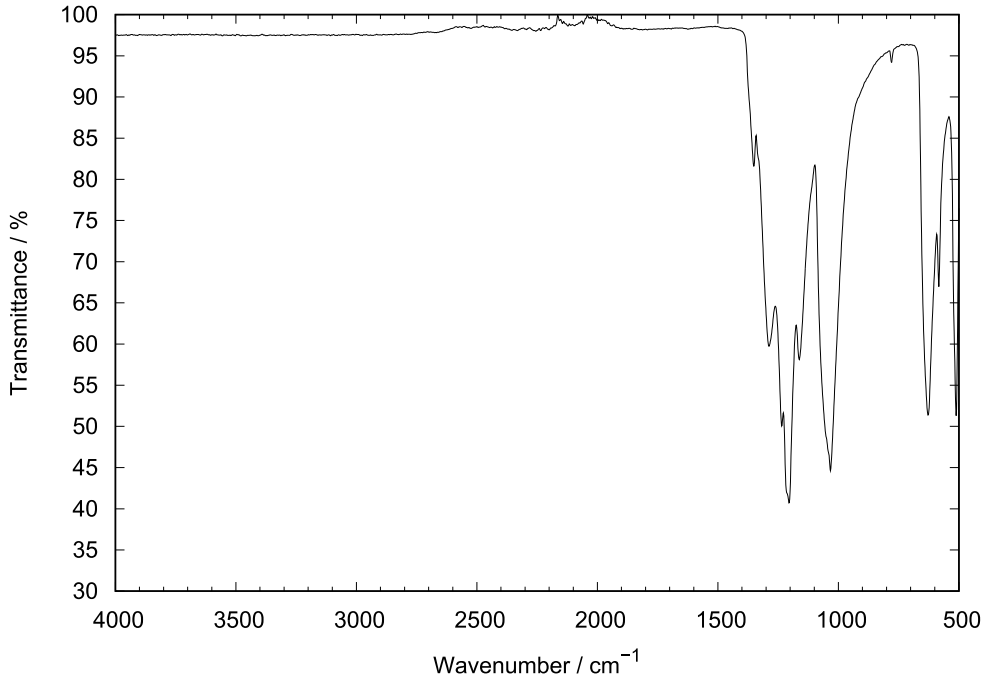


Fig. S 1: IR-spectrum of $Sm(OTf)_3$.

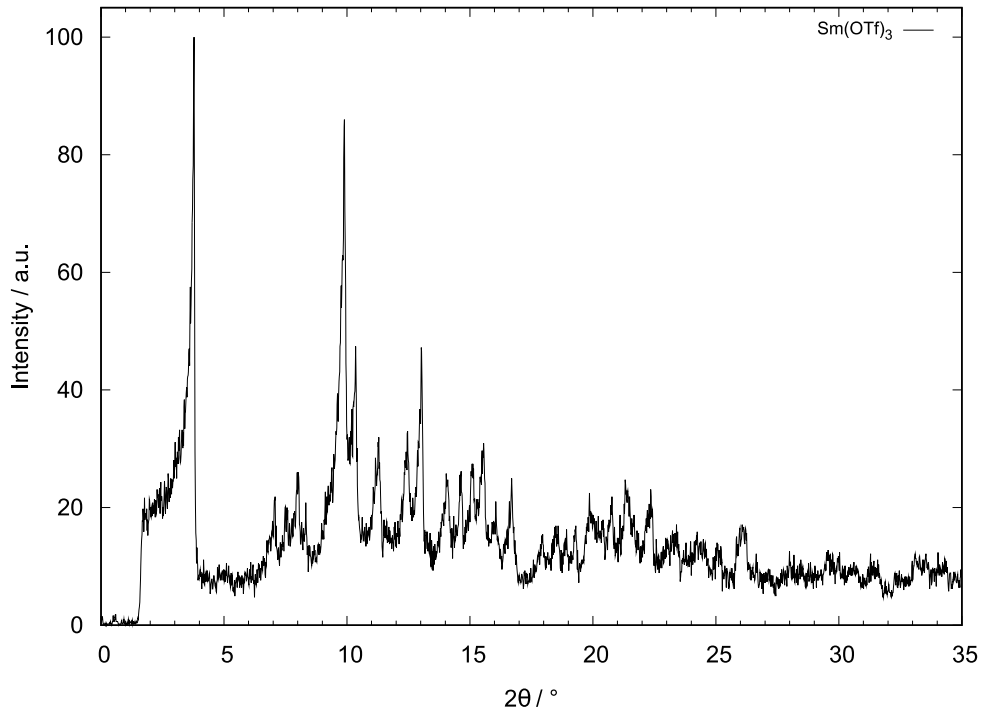


Fig. S 2: XRD pattern of $Sm(OTf)_3$. The data were generated using Mo-Kα_1 radiation.

Synthesis of $Eu(OTf)_3$

$$Eu_2O_3 + 6\ HOTf\ (aq) \xrightarrow{200\ °C} 2\ Eu(OTf)_3(H_2O)_9 \xrightarrow[\text{dynamic vac.}\ -18\ H_2O]{275\ °C} 2\ Eu(OTf)_3$$

500 mg (1.42 mmol, 2 eq.) of Eu_2O_3 was suspended in 10 ml of water. 0.75 ml (8.52 mmol, 3 eq.) of concentrated triflic acid were added before the mixture was heated to 200 °C. After all volatiles were boiled off, the solids were transferred to a schlenk flask and heated to 275 °C under dynamic vacuum until vibrational bands of water had completely disappeared in the IR-spectrum (compare Fig. S 3). 1.39 g (2.32 mmol, 82%) of $Eu(OTf)_3$ were obtained as a colourless powder. For XRD-data see Fig. S 4.

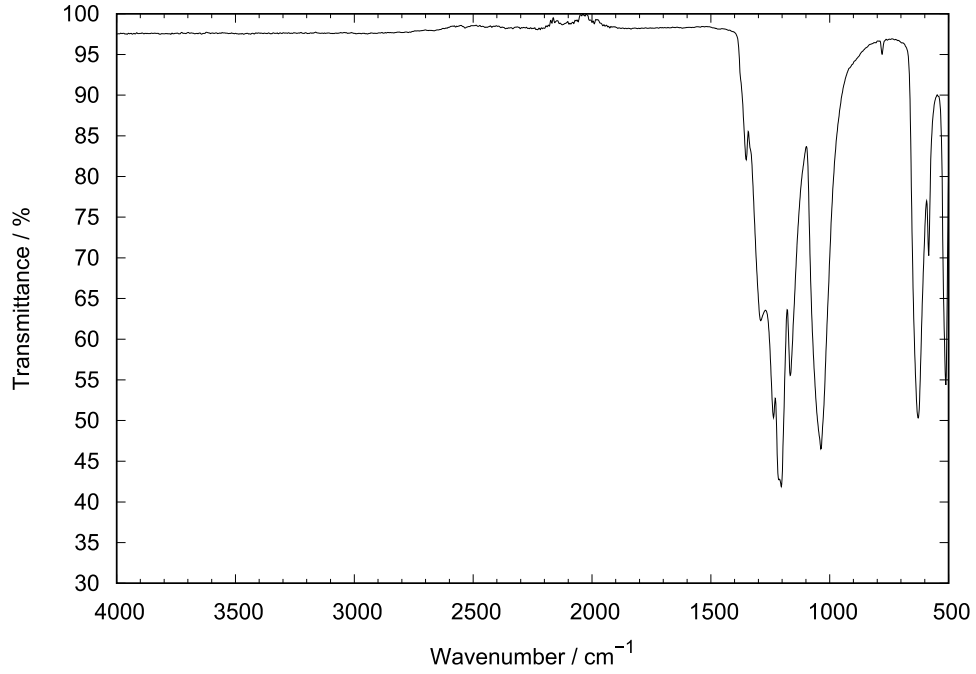


Fig. S 3: IR-Spectrum of $Eu(OTf)_3$.

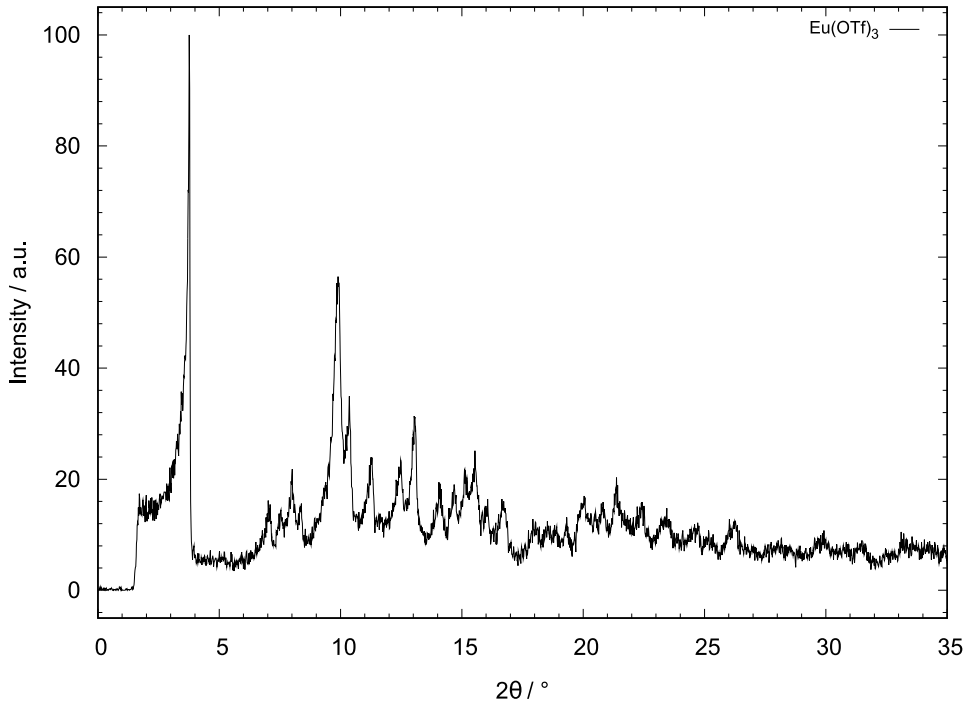
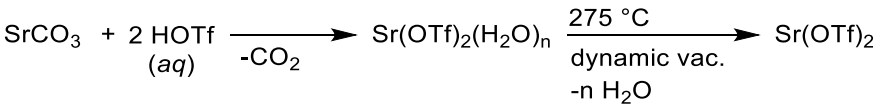


Fig. S 4: XRD pattern of $Eu(OTf)_3$. The data were generated using Mo-Kα_1 radiation.

Synthesis of $Sr(OTf)_2$



2.00 g (13.6 mmol, 1 eq.) of $SrCO_3$ was suspended in 10 ml of water. Conc. triflic acid was added until all solids had dissolved. The solution was boiled until all volatiles were removed. The resulting solids were transferred to a schlenk flask and heated to 275 °C under dynamic vacuum until no more vibrational band of water could be detected by IR-spectroscopy (compare Fig. S 6). 3.61 g (8.19 mmol, 60%) of $Sr(OTf)_2$ was obtained as a colourless powder. PXRD data of $Sr(OTf)_2$ is displayed in Fig. S 14.

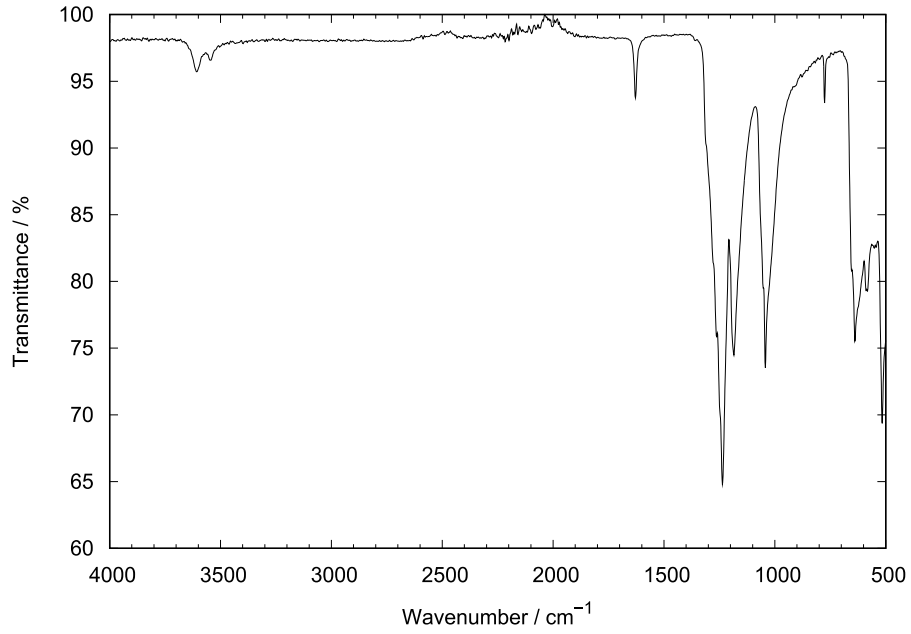


Fig. S 5: IR-Spectrum of $Sr(OTf)_2(H_2O)_n$ before heating to 275 °C.

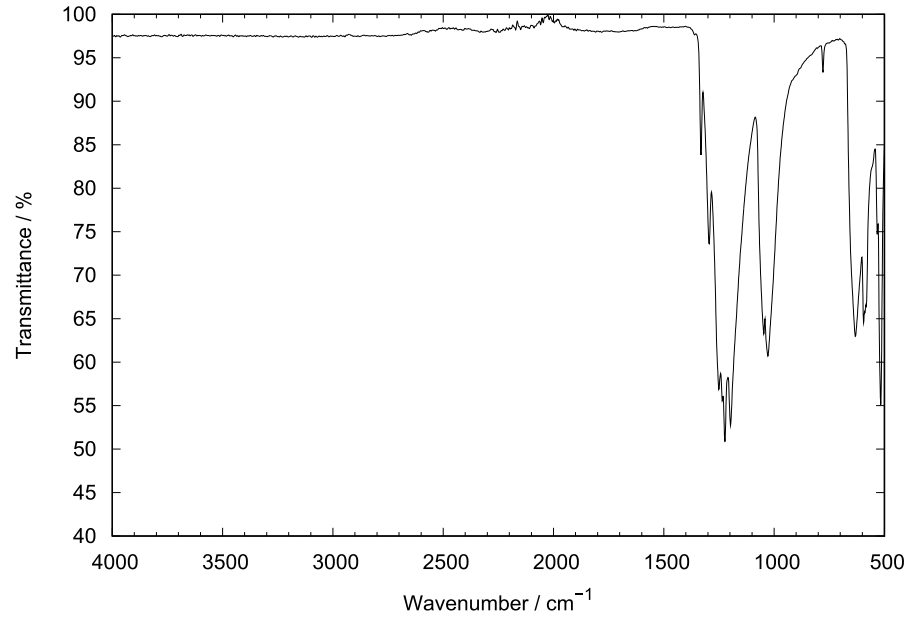


Fig. S 6: IR-Spectrum of $Sr(OTf)_2$ after dehydration at 275 °C.

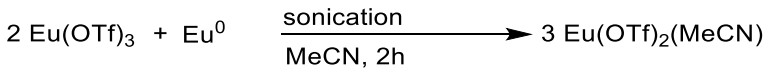
Synthesis of $Sm(OTf)_2(CH_3CN)$

$$2\ Sm(OTf)_3 + Sm^0 \xrightarrow[MeCN,\ 2h]{\text{cat. Hg, sonication}} 3\ Sm(OTf)_2(MeCN)$$

200 mg (0.335 mmol, 2 eq.) of $Sm(OTf)_3$ was dissolved in 15 ml of acetonitrile. 38 mg (0.25 mmol, 1.5 eq.) of freshly filed samarium was added along with two drops of mercury.

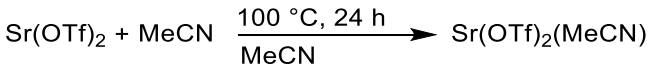
The reaction mixture was sonicated for two hours. Excess samarium and mercury were filtered off and the filtrate was evaporated to dryness under reduced pressure to yield 210 mg (0.429 mmol, 85%) of $Sm(OTf)_2(CH_3CN)$ as a purple powder.

Synthesis of $Eu(OTf)_2(CH_3CN)$



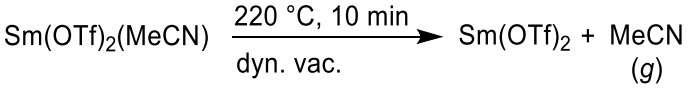
200 mg (0.334 mmol, 2 eq.) of $Eu(OTf)_3$ was dissolved in 15 ml of acetonitrile. 38 mg (0.25 mmol, 1.5 eq.) of freshly filed europium was added. The reaction mixture was sonicated for two hours. Excess europium was filtered off and the filtrate was evaporated to dryness under reduced pressure to yield 210 mg (0.428 mmol, 85%) of $Eu(OTf)_2(CH_3CN)$ as a colourless powder.

Synthesis of $Sr(OTf)_2(CH_3CN)$



500 mg (1.30 mmol, 1 eq.) of $Sr(OTf)_2$ was dissolved in 7.5 ml of acetonitrile. The solution was torch sealed in a glass ampoule and heated to 100 °C for 24 h and subsequently cooled to room temperature over another 72 h to obtain 350 mg (0.82 mmol, 63%) of $Sr(OTf)_2(CH_3CN)$ as colorless crystals.

Synthesis of $Sm(OTf)_2$



30 mg (61 μmol, 1 eq.) of $Sm(OTf)_2(CH_3CN)$ was heated to 220 °C under dynamic vacuum for 10 minutes. 25 mg (5.6 μmol, 92%) of $Sm(OTf)_2$ was obtained as a red powder. See Fig. S 14 for PXRD data.

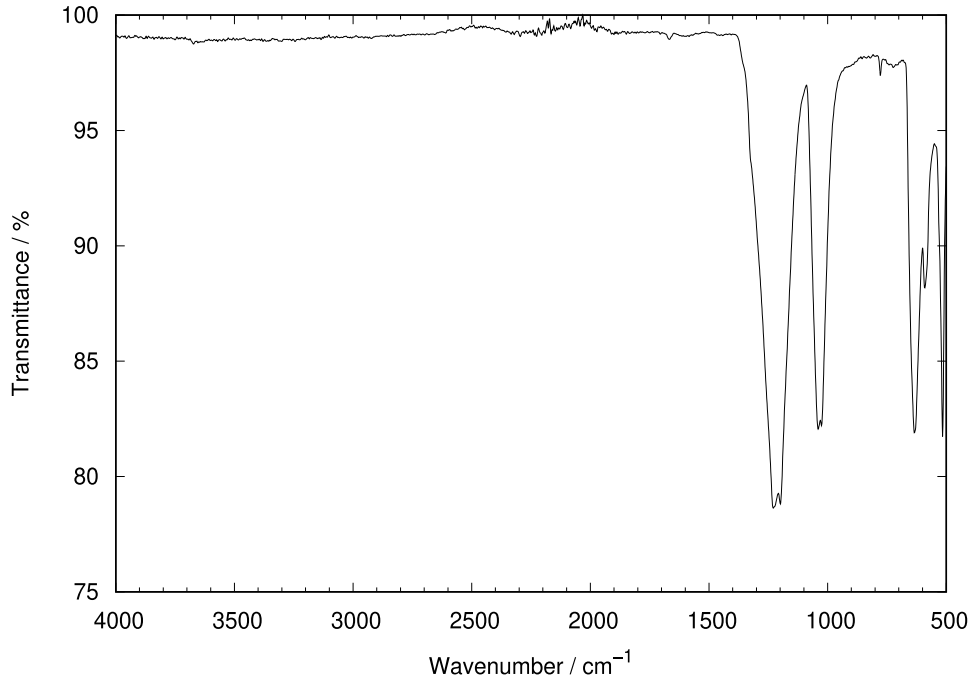


Fig. S 7: IR-spectrum of $Sm(OTf)_2$.

Synthesis of $Eu(OTf)_2$

$$Eu(OTf)_2(MeCN) \xrightarrow[\text{dyn. vac.}]{\text{220 °C, 10 min}} Eu(OTf)_2 + MeCN\,(g)$$

30 mg (61 µmol, 1 eq.) of $Eu(OTf)_2(CH_3CN)$ was heated to 220 °C under dynamic vacuum for 10 minutes. 25 mg (5.6 µmol, 92%) of $Eu(OTf)_2$ was obtained as a colourless powder. See Fig. S 14 for XRD data.

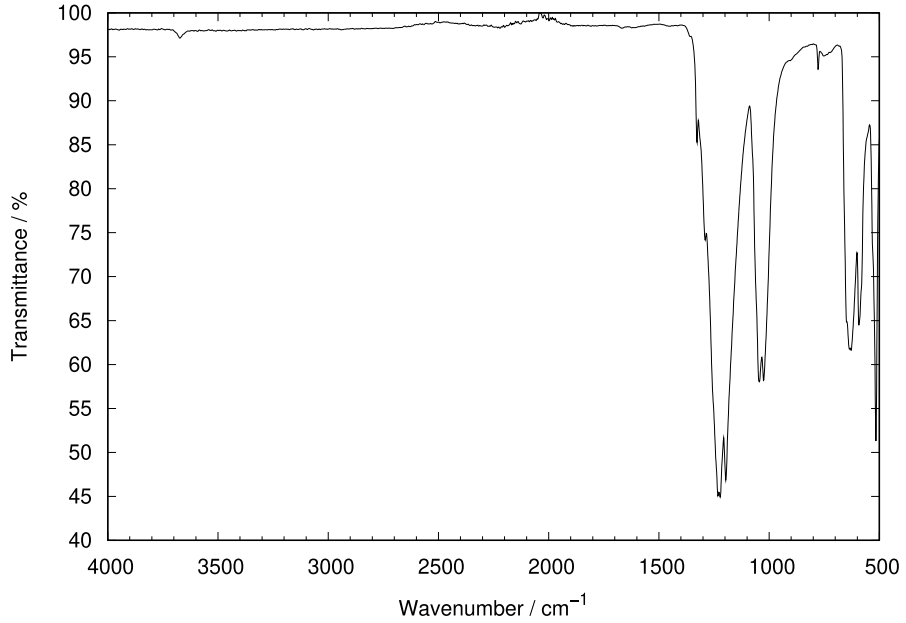


Fig. S 8: IR-spectrum of $Eu(OTf)_2$.

Synthesis of $Sr(OTf)_2(CH_3CN):Sm^{2+}$

$$Sr(OTf)_2 + 1\%\ Sm(OTf)_2(MeCN) \xrightarrow{MeCN,\ rt} Sr(OTf)_2(MeCN):Sm^{2+}$$

100 mg (0.259 mmol, 99 eq.) of $Sr(OTf)_2$ and 1.3 mg (2.6 µmol, 1 eq.) of $Sm(OTf)_2(CH_3CN)$ were dissolved in 15 ml of acetonitrile. The solvent was removed under reduced pressure to obtain 100 mg (0.256 mmol, 99%) of $Sr(OTf)_2(CH_3CN):Sm^{2+}$ as a pink powder.

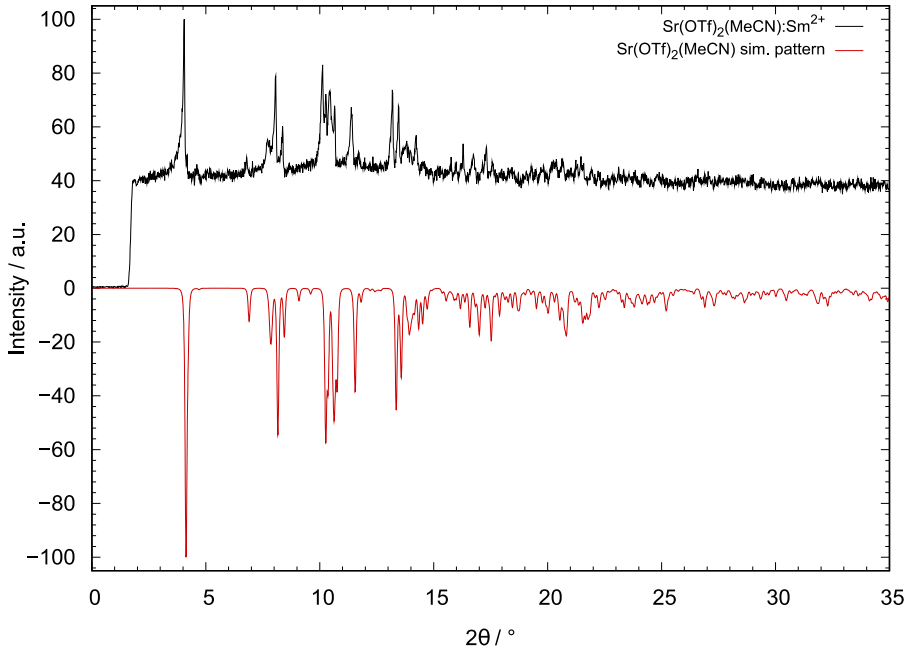


Fig. S 9: XRD pattern of $Sr(OTf)_2(CH_3CN):Sm^{2+}$, next to the simulated data of $Sr(OTf)_2(CH_3CN)$. The data were obtained using Mo-Kα_1 radiation.

Synthesis of $Sr(OTf)_2(CH_3CN):Eu^{2+}$

$$Sr(OTf)_2 + 1\%\ Eu(OTf)_2(MeCN) \xrightarrow{MeCN,\ rt} Sr(OTf)_2(MeCN):Eu^{2+}$$

100 mg (0.259 mmol, 99 eq.) of $Sr(OTf)_2$ and 1.3 mg (2.6 µmol, 1 eq.) of $Eu(OTf)_2(CH_3CN)$ were dissolved in 15 ml of acetonitrile. The solvent was removed under reduced pressure to obtain 100 mg (0.256 mmol, 99%) of $Sr(OTf)_2(CH_3CN):Eu^{2+}$ as a colourless powder.

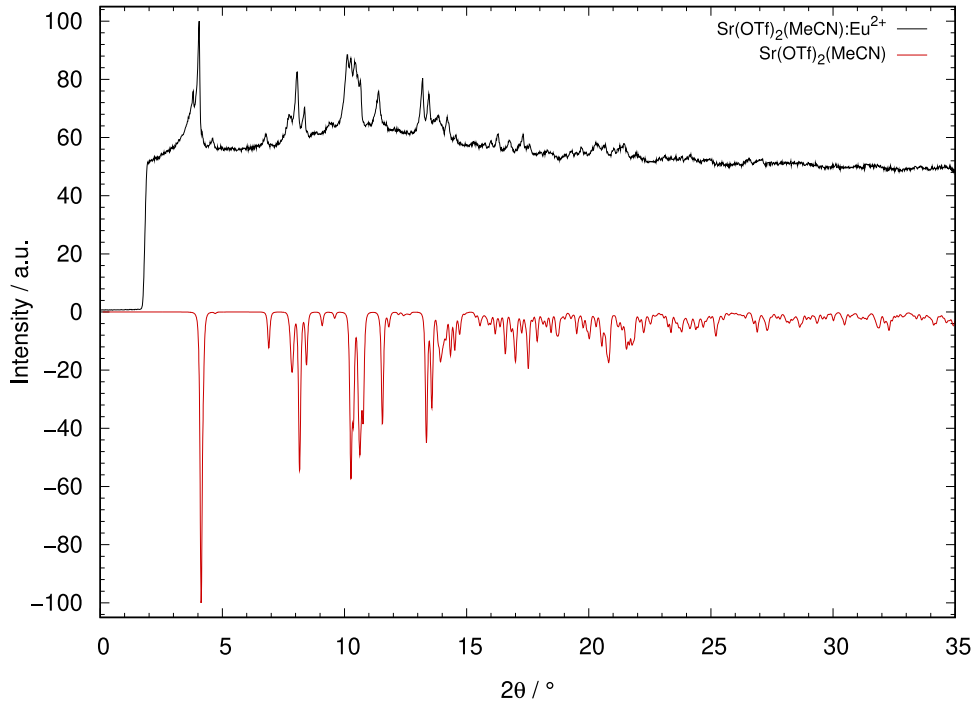


Fig. S 10: XRD pattern of $Sr(OTf)_2(CH_3CN):Eu^{2+}$, next to the simulated data of $Sr(OTf)_2(CH_3CN)$. The data were obtained using Mo-Kα_1 radiation.

Further Analytical Data

Rietveld Refinements

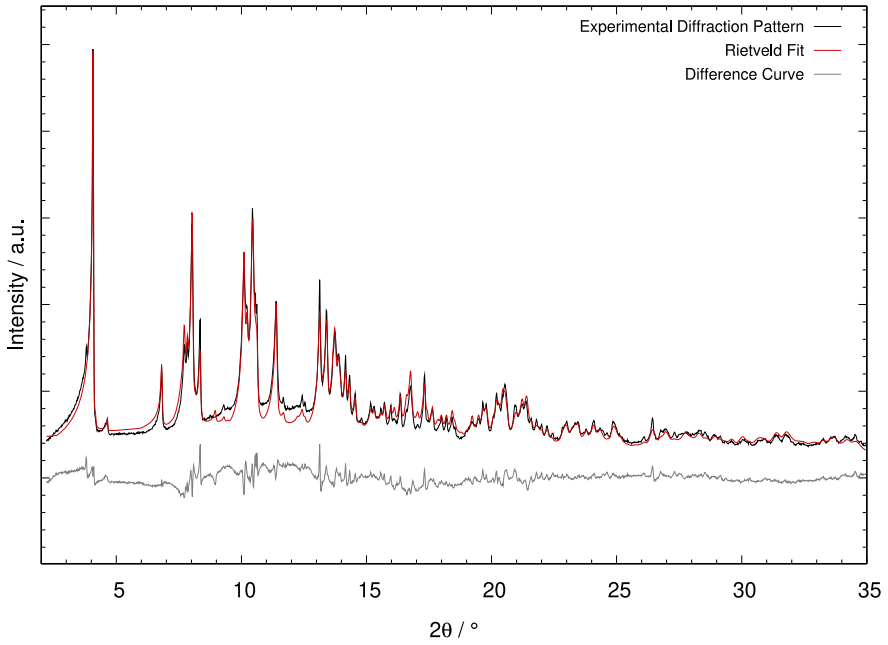


Fig. S 11: Rietveld refinement of $Sm(OTf)_2(CH_3CN)$. PXRD data were generated using Mo-Kα_1 radiation. R-values and refined lattice parameters are given in Table S 1.

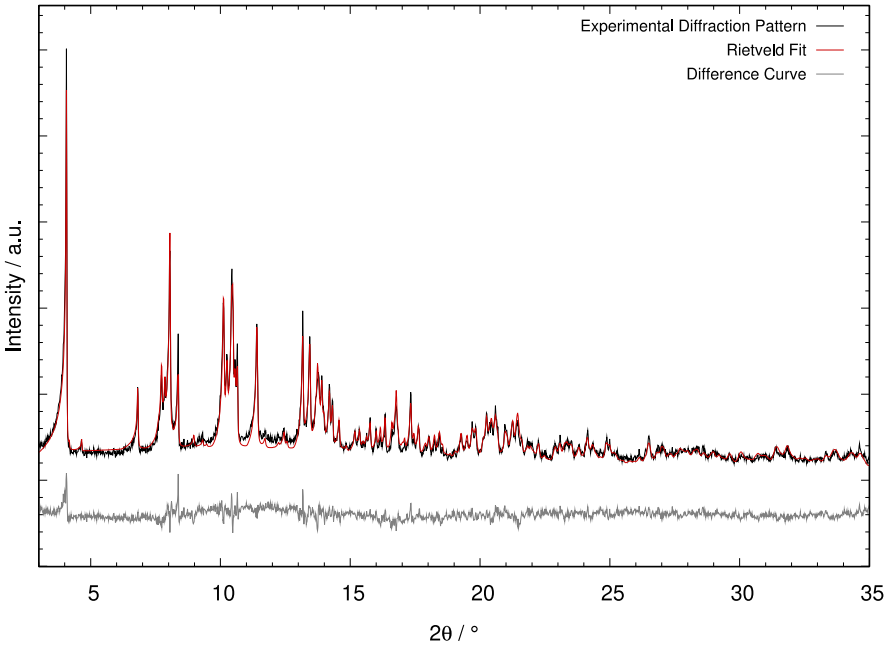


Fig. S 12: Rietveld refinement of $Eu(OTf)_2(CH_3CN)$. PXRD data were generated using Mo-Kα_1 radiation. R-values and refined lattice constants are given in Table S 1.

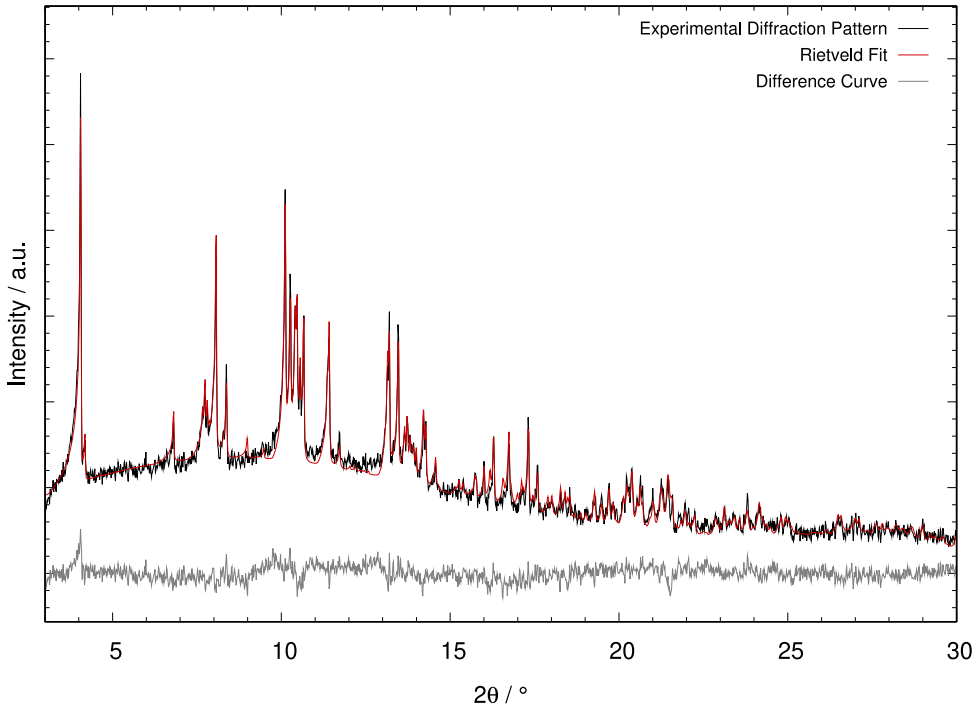


Fig. S 13: Rietveld refinement of $Sr(OTf)_2(CH_3CN)$. PXRD data were generated using Mo-Kα_1 radiation. R-values and refined lattice constants are given in Table S 1.

Table S 1: R-values and refined lattice parameters of the *Rietveld* refinements of $Sm(OTf)_2(CH_3CN)$, $Eu(OTf)_2(CH_3CN)$ and $Sr(OTf)_2(CH_3CN)$. For the refinements see Fig. S 11, Fig. S 12 and Fig. S 13.

	$Sm(OTf)_2(CH_3CN)$	**$Eu(OTf)_2(CH_3CN)$**	**$Sr(OTf)_2(CH_3CN)$**
Space Group	$P2_1/n$	$P2_1/n$	$P2_1/n$
a / pm	1073.1(2)	1072.9(1)	1074.20(6)
b / pm	620.9(1)	618.76(7)	619.92(5)
c / pm	1972.7(4)	1970.0(2)	1966.9(1)
β / °	98.92(2)	99.09(1)	99.28(1)
R_{wp}	10.79	9.42	2.65
R_{exp}	9.75	11.05	5.72
R_p	8.51	7.55	2.11
Gof	1.11	0.85	0.46

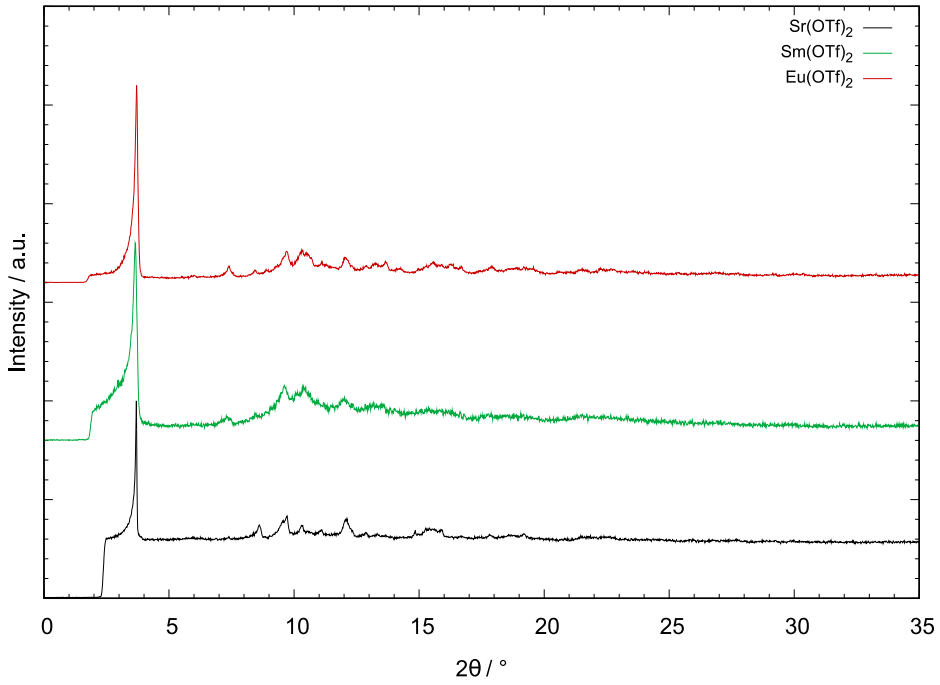


Fig. S 14: XRD patterns of $Sr(OTf)_2$, $Sm(OTf)_2$ and $Eu(OTf)_2$. The data were generated using Mo-Kα_1 radiation.

UV-Vis Spectra

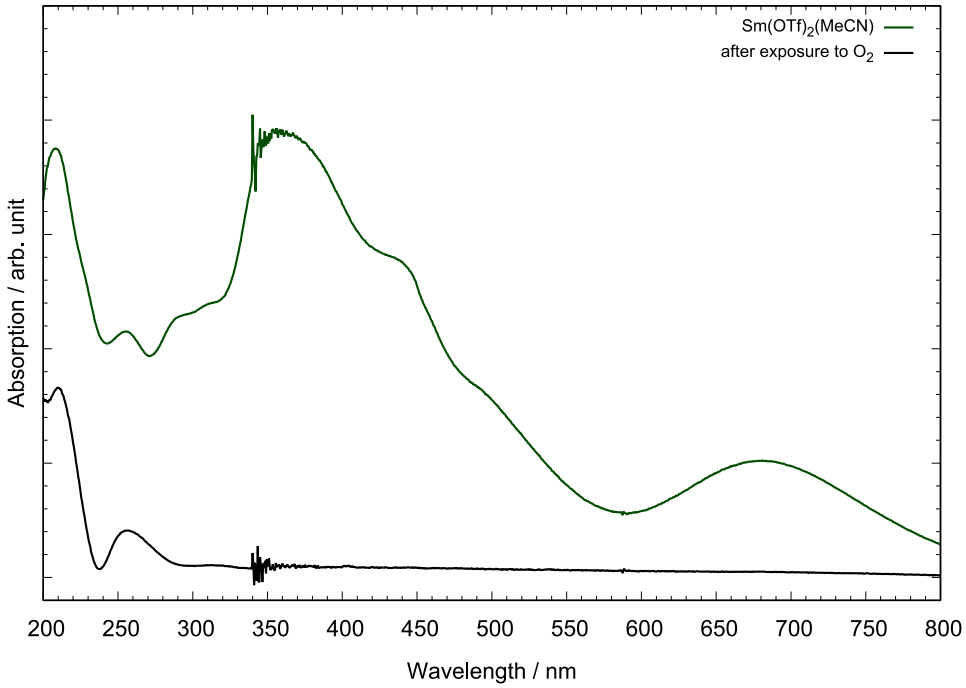


Fig. S 15: UV-Vis absorption spectrum of $Sm(OTf)_2(CH_3CN)$ dissolved in acetonitrile before (green) and after exposing the solution to atmospheric oxygen.

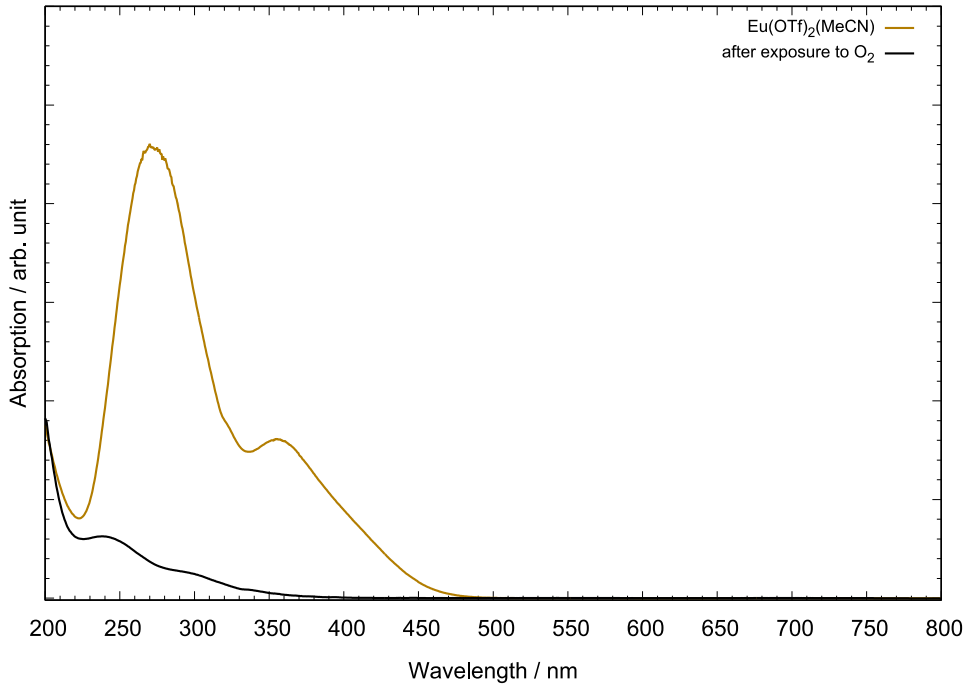


Fig. S 16: UV-Vis absorption spectrum of Eu(OTf)2(CH_3CN) dissolved in acetonitrile before (green) and after exposing the solution to atmospheric oxygen.

Luminescence Spectra

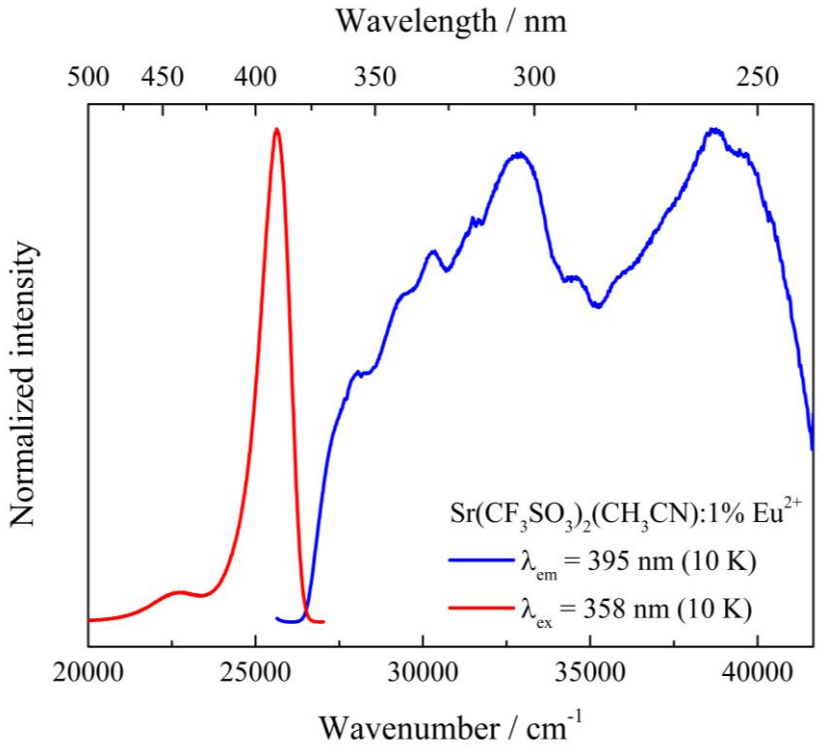


Fig. S 17: Luminescence spectrum of $Sr(OTf)_2(CH_3CN):Eu^{2+}$. The emission spectrum is shown in red and excitation spectrum is shown in blue.

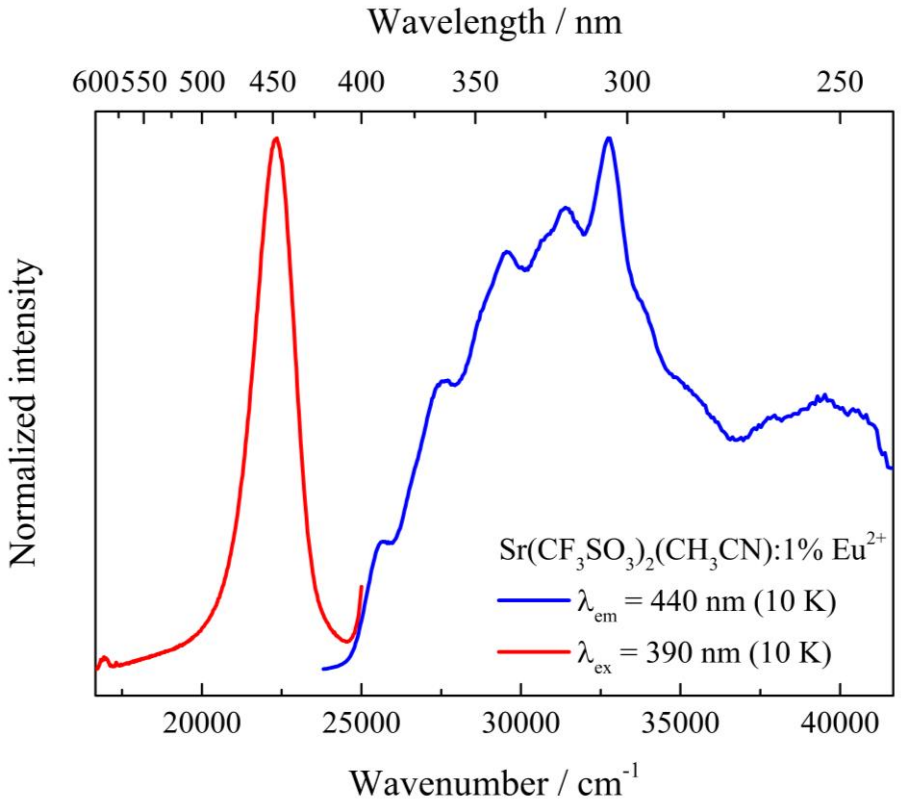


Fig. S 18: Luminescence spectrum of $Sr(OTf)_2(CH_3CN):Eu^{2+}$. The emission spectrum is shown in red and excitation spectrum is shown in blue.

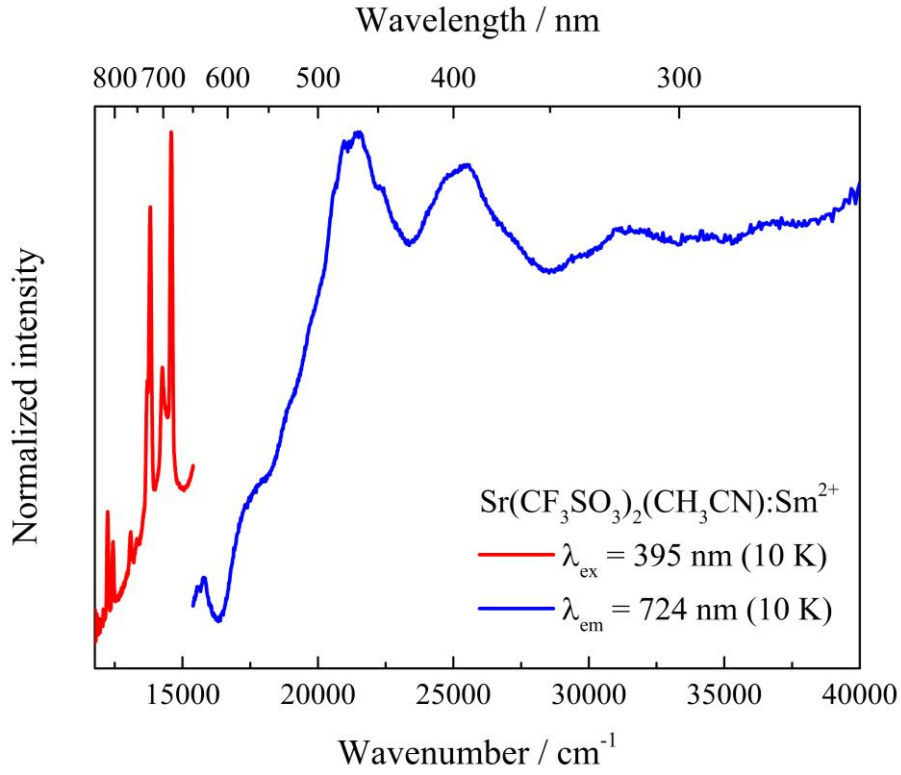


Fig. S 19: Luminescence spectrum of $Sr(OTf)_2(CH_3CN):Eu^{2+}$. The emission spectrum is shown in red and excitation spectrum is shown in blue.

Thermogravimetric Analyses

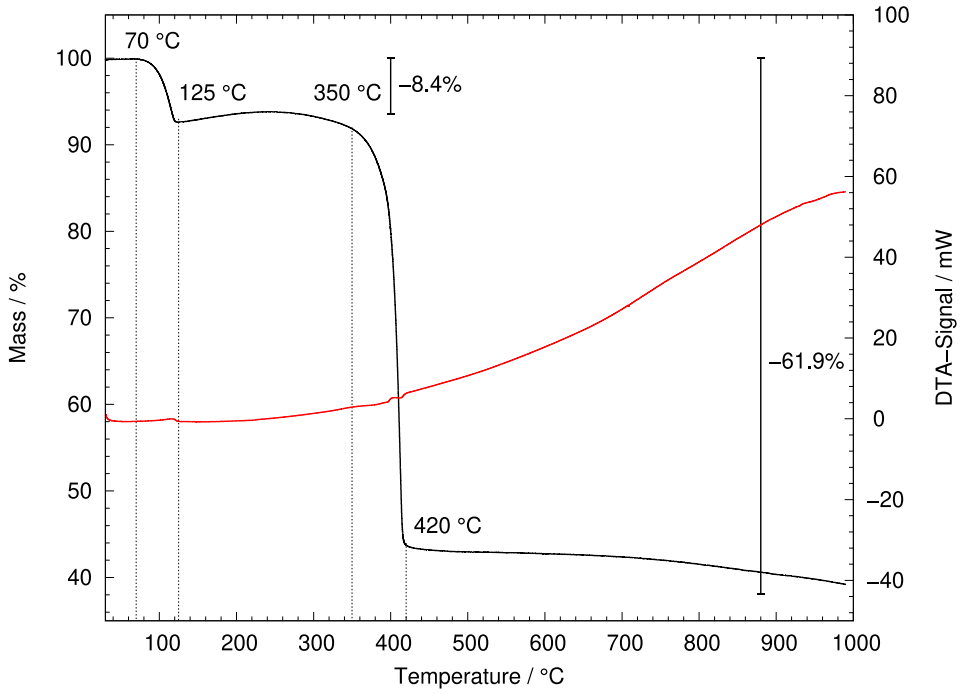


Fig. S 20: TGA-DTA of $Eu(OTf)_2(CH_3CN)$. The mass curve is shown in black and the DTA signal is depicted as a red curve. Mass differences shown in the diagram correspond to the theoretical mass losses for the proposed decomposition pathway. The data were collected under nitrogen flow with a constant heating rate of 5 °C/min.

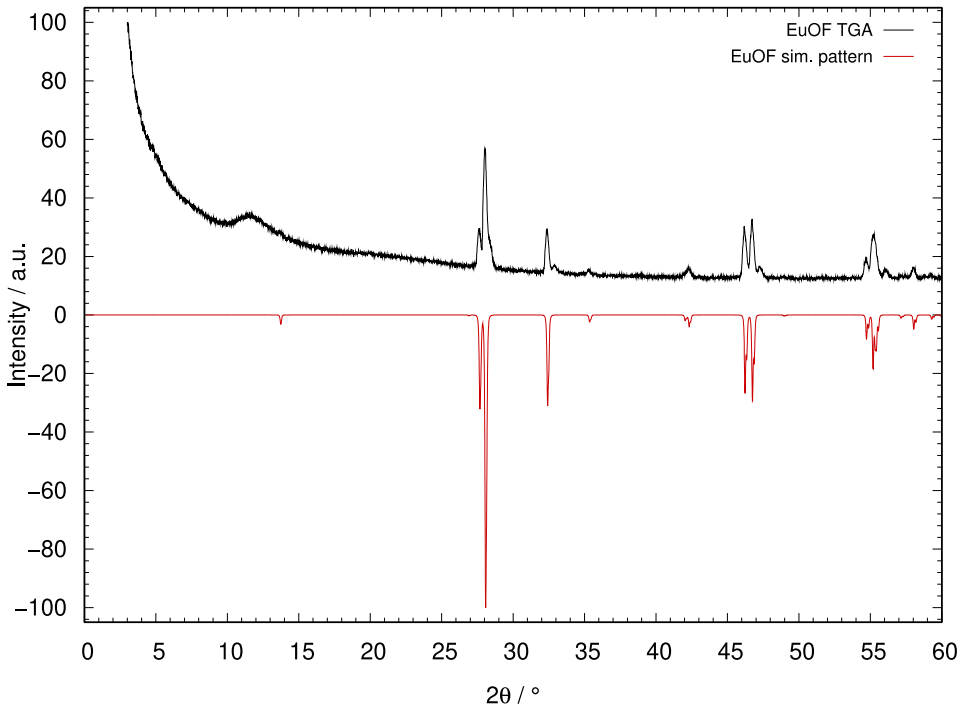


Fig. S 21: XRD pattern of EuOF obtained from thermal decomposition of $Eu(OTf)_2(CH_3CN)$, next to the simulated data obtained from [11]. The data were obtained using Cu-Kα radiation.

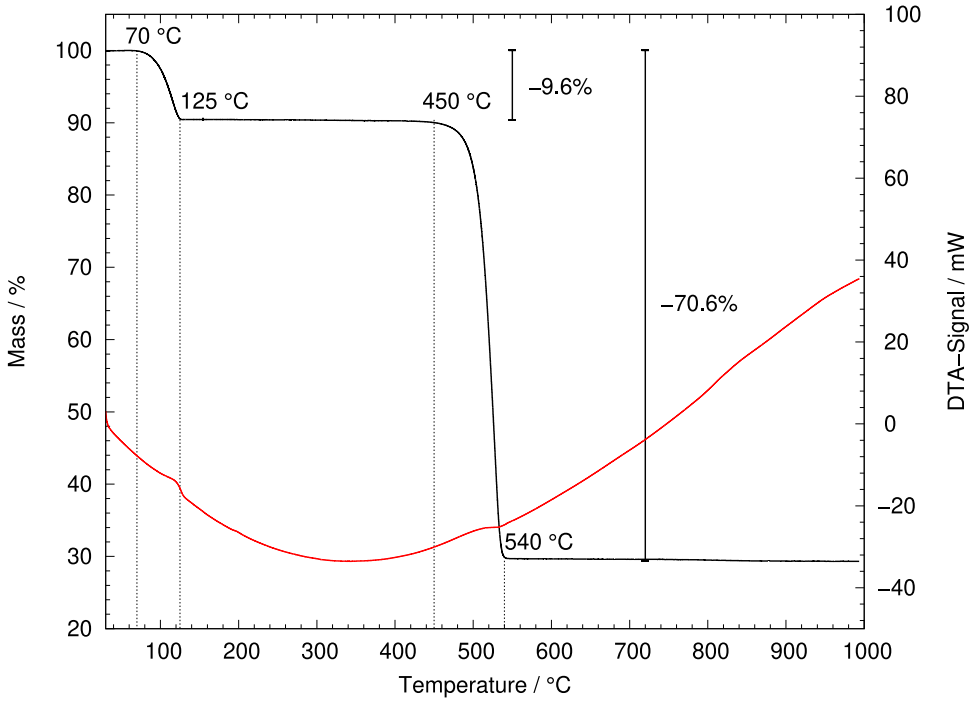


Fig. S 22: TGA-DTA of $Sr(OTf)_2(CH_3CN)$. The mass curve is shown in black and the DTA signal is depicted as a red curve. Mass differences shown in the diagram correspond to the theoretical mass losses for the proposed decomposition pathway. The data were collected under nitrogen flow with a constant heating rate of 5 °C/min.

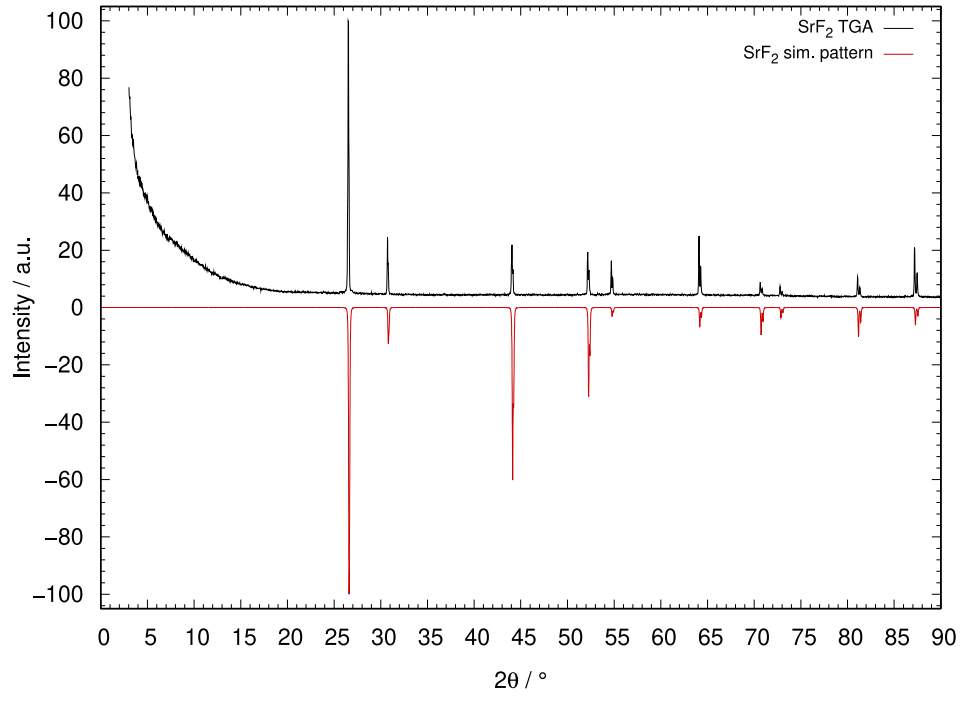


Fig. S 23: XRD pattern of SrF_2 obtained from thermal decomposition of $Sr(OTf)_2(CH_3CN)$, next to the simulated data obtained from [12]. The data were obtained using Cu-K_α radiation.

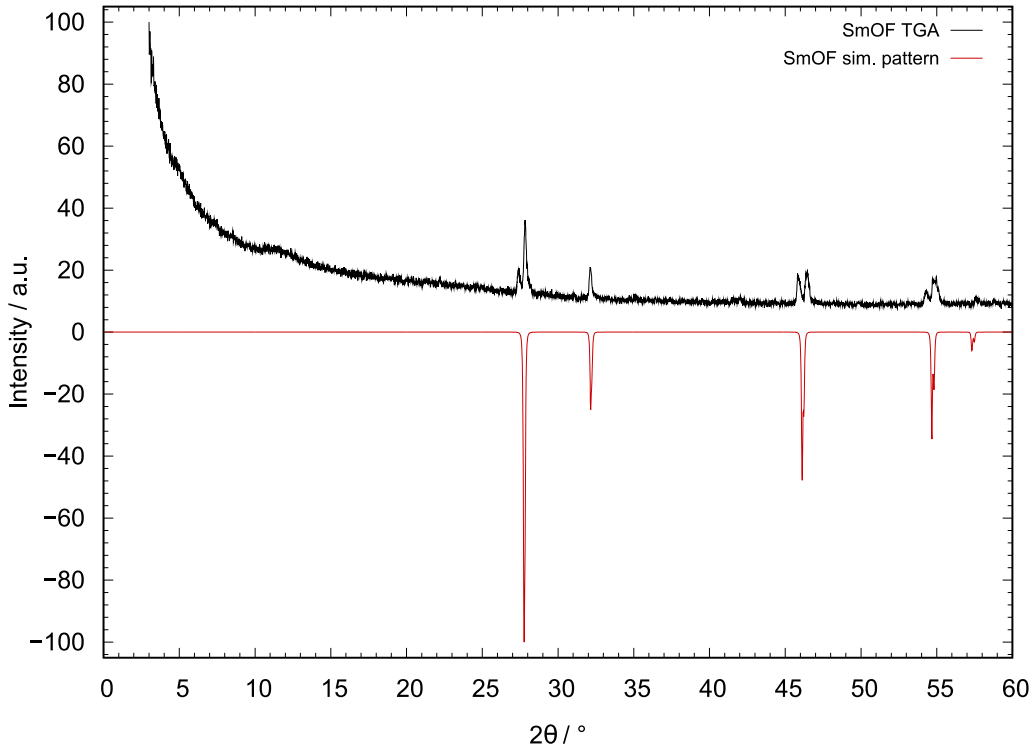


Fig. S 24: XRD pattern of SmOF obtained from thermal decomposition of $Sm(OTf)_2(CH_3CN)$, next to the simulated data obtained from [13]. The data were obtained using Cu-K_α radiation.

IR-Spectra

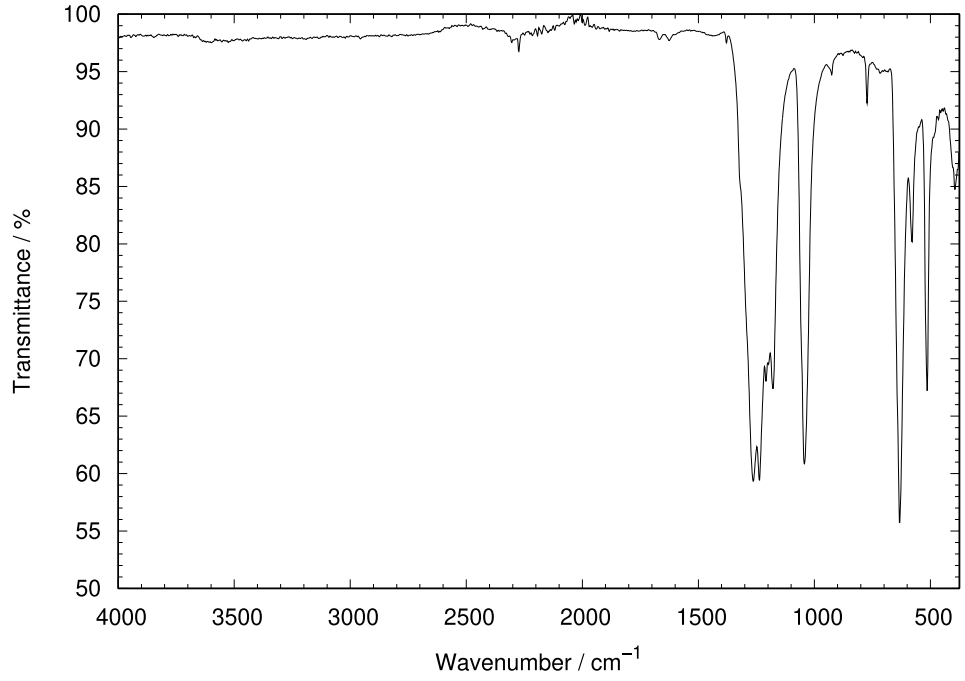


Fig. S 25: IR-spectrum of $Sm(OTf)_2(CH_3CN)$.

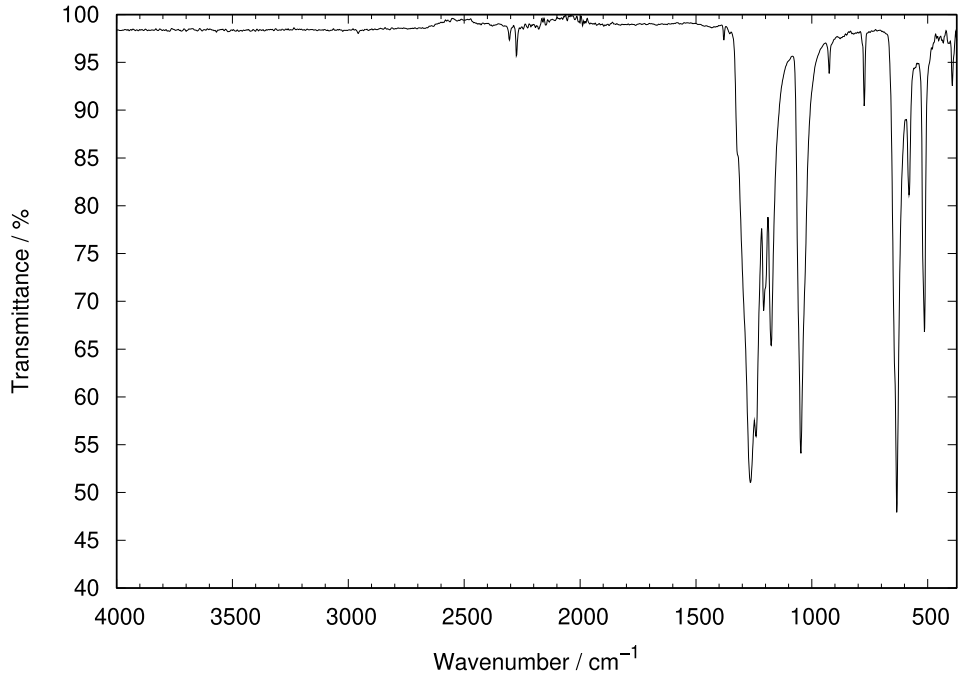


Fig. S 26: IR-spectrum of $Eu(OTf)_2(CH_3CN)$.

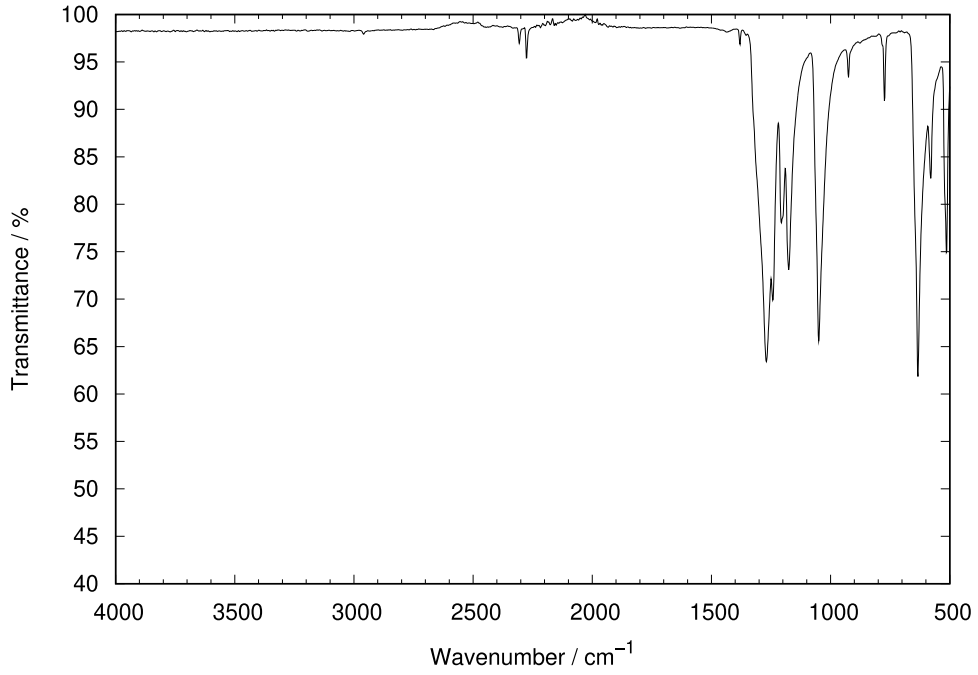


Fig. S 27: IR-spectrum of $Sr(OTf)_2(CH_3CN)$.

References

[1] Bruker, *SAINT*, V8.40B, Bruker AXS Inc., Madison, Wisconsin, USA.

[2] L. Krause, R. Herbst-Irmer, G. M. Sheldrick, D. Stalke, *J. Appl. Cryst.* **2015**, *48*, 3-10.

[3] G. M. Sheldrick, *Acta Cryst.* **2015**, *A71*, 3-8.

[4] G. M. Sheldrick, *Acta Cryst.* **2015**, *C71*, 3-8.

[5] C. R. Groom, I. J. Bruno, M. P. Lightfoot, S. C. Ward, *Acta Cryst.* **2016**, *B72*, 171-179.

[6] D. Kratzert, *FinalCif*, V107, *https://dkratzert.de/finalcif.html*.

[7] K. Momma, F. Izumi, *J. Appl. Cryst.* **2011**, *44*, 1272-1276.

[8] M. Pinsky, D. Avnir, *Inorg. Chem*. **1998**, *37*, 5575-5582; D. Casanova, J. Cirera, M. Llunell, P. Alemany, D. Avnir, S. Alvarez. *J. Am. Chem. Soc.* **2004**, *126*, 1755-1763; J. Cirera, E. Ruiz, S. Alvarez. *Chem. Eur. J.* **2006**, *12*, 3162-3167.

[9] J. S. O. Evans, *Mater. Sci. Forum* **2010**, *651*, 1-9.

[10] Stoe, WinXPOW 1.06; *STOE Powder Diffraction Software* (Stoe & Cie GmbH, Darmstadt), **1999**.

[11] R. J. Cava, D. Hirai, S. E. Dutton, *Mater. Res. Bull.* **2012**, *47*, 714-718.

[12] J. B. Forsyth, C. C. Wilson, T. M. Sabine, *Acta Cryst.* **1989**, *A45*, 244-247.

[13] C. Buyer, T. Schleid, *Acta Cryst.* **2021**, *A77*, C1036.

Supporting Information

Synthesis and Optical Properties of Solvent-Free Binary Azides $Eu(N_3)_2$ and $Yb(N_3)_2$

N. T. Flosbach[1], P. L. Jurzick[1], M. Bykov[1,2], J. W. Weiß[3], C. Wickleder[3], M. S. Wickleder[1]

[1]University of Cologne, Institute of Inorganic Chemistry, Greinstr. 6, 50939 Cologne, Germany

[2]Institute of Geosciences, Goethe University Frankfurt, Altenhöferallee 1, 60438 Frankfurt, Germany

[3]University of Siegen, Institute of Inorganic Chemistry, Adolf-Reichwein-Straße, 57068 Siegen, Germany

Table of Contents

Analytical Data of $Yb(OTf)_2$ 2
Refined Parameters of Ln_2O_3 3
Determination of the Quenching Temperature 4
Decay time measurement of $Eu(N_3)_2$ 4
Reflectance Measurement and Tauc Plots 5
References 6

Analytical Data of $Yb(OTf)_2$

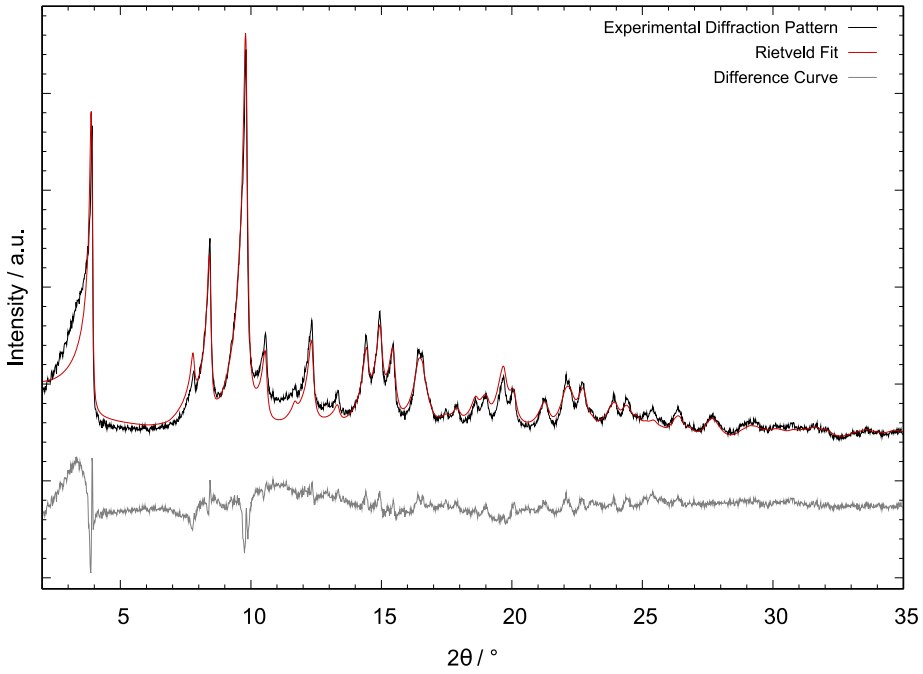


Fig. S 1 PXRD data and Rietveld refinements of of $Yb(OTf)_2$. The structure of $Ca(OTf)_2$ was using as a geometric starting model.[1] The data were produced using Mo-Kα_1-radiation.

Tab. S 1 Lattice parameters of $Yb(OTf)_2$ obtained from Rietveld refinement and corresponding data of $Ca(OTf)_2$ taken from *Jansen* et al.[1]

	$Yb(OTf)_2$	**$Ca(OTf)_2$**
Space Group	$R\bar{3}$	$R\bar{3}$
a / pm	564.3(1)	560.549(3)
c / pm	3132(1)	3114.17(2)
V / 10^6 pm^3	863.8(6)	847.42(1)
R_{wp}	10.11	-
R_{exp}	7.96	-
R_p	7.86	-
GoF	1.27	-

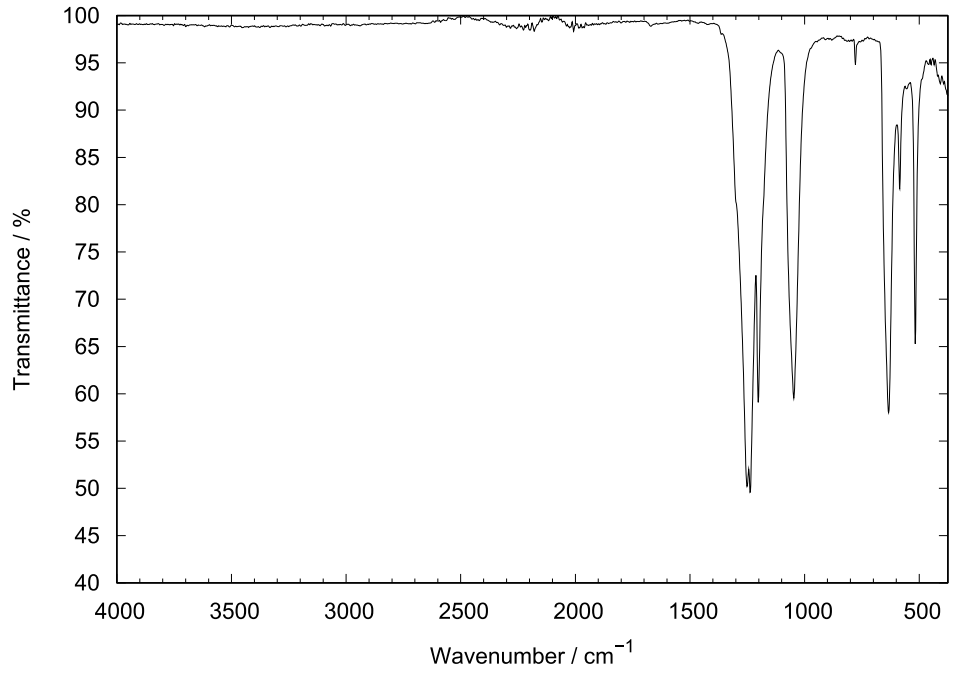


Fig. S 2: IR-spectrum of $Yb(OTf)_2$.

Refined Parameters of Ln_2O_3

Tab. S 2: Lattice parameters of Eu_2O_3 and Yb_2O_3 obtained from Rietveld refinement and corresponding literature (lit.) data.[2]

	Eu_2O_3	**Eu_2O_3 (lit.)[2]**	**Yb_2O_3**	**Yb_2O_3 (lit.)[2]**
Space Group	$Ia\bar{3}$	$Ia\bar{3}$	$Ia\bar{3}$	$Ia\bar{3}$
a / pm	1089.1(2)	1085.9(1)	1045.5(1)	1043.22(5)
V / 10^6 pm^3	1291.6(5)	1280.47[a]	1142.8(4)	1135.34[a]
R_{wp}	4.66	-	2.35	-
R_{exp}	2.39	-	2.58	-
R_p	3.54	-	1.82	-
GoF	1.95	-	0.91	-

[a] No standard deviation was provided in the literature data.

Determination of the Quenching Temperature

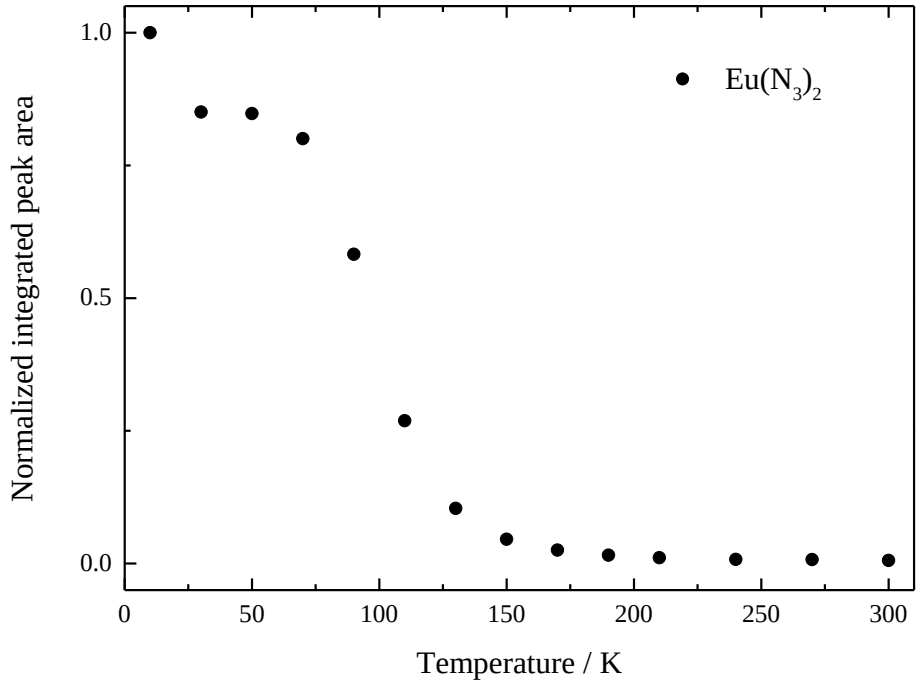


Fig. S 3: Temperature-dependent normalized integrated emission intensities reveal a quenching temperature of ~95 K.

Decay time measurement of $Eu(N_3)_2$

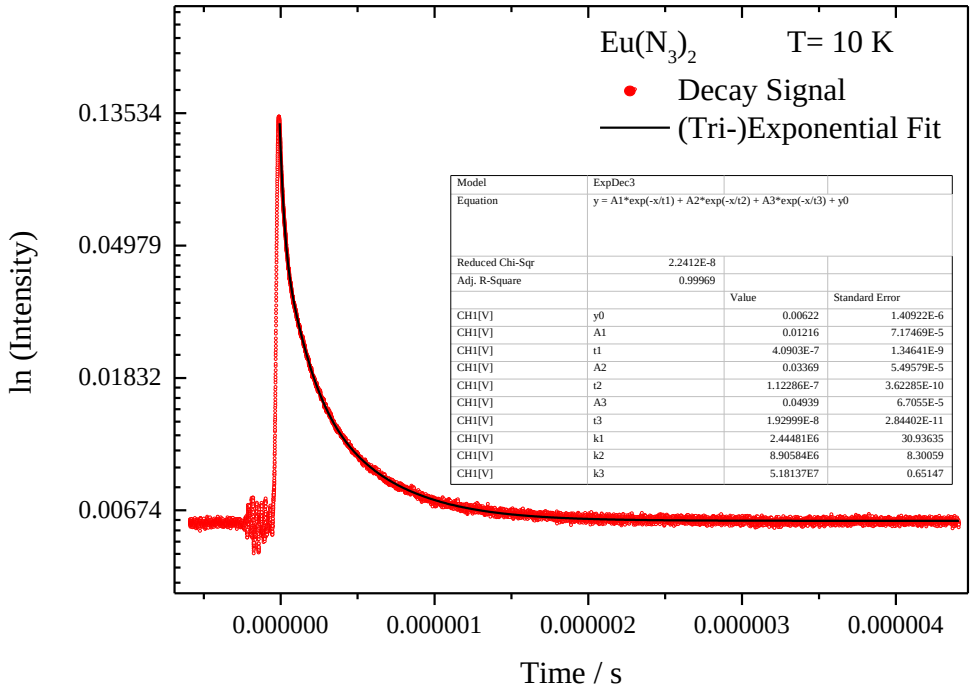


Fig. S 4: Decay signal of $Eu(N_3)_2$ recorded at λ = 576 nm with an excitation wavelength of λ = 355 nm. A tri-exponential fit is necessary to fit the decay signal to determine the decay time.

Reflectance Measurement and Tauc Plots

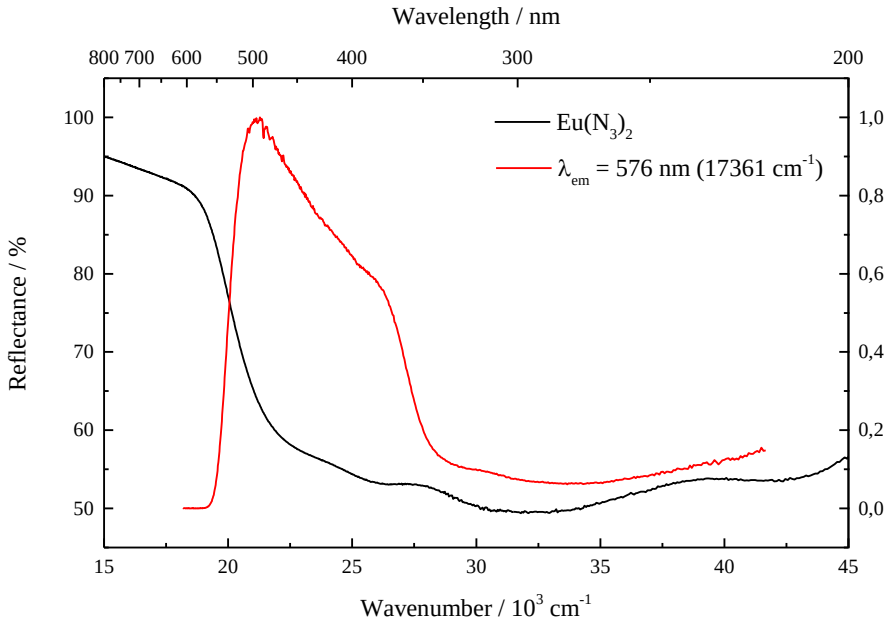


Fig. S 5: Reflectance spectrum of $Eu(N_3)_2$ with overlayed excitation spectrum recorded at $\lambda = 576$ nm. A correspondence between some absorption bands and the excitation spectrum can be seen.

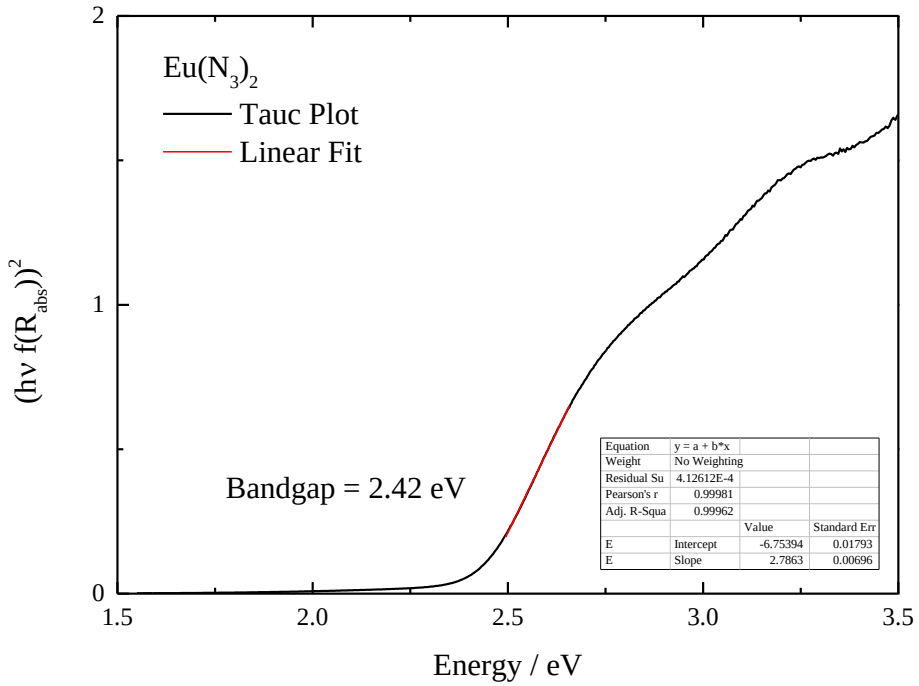


Fig. S 6: Tauc plot of $Eu(N_3)_2$ with linear fit to determine the band gap.

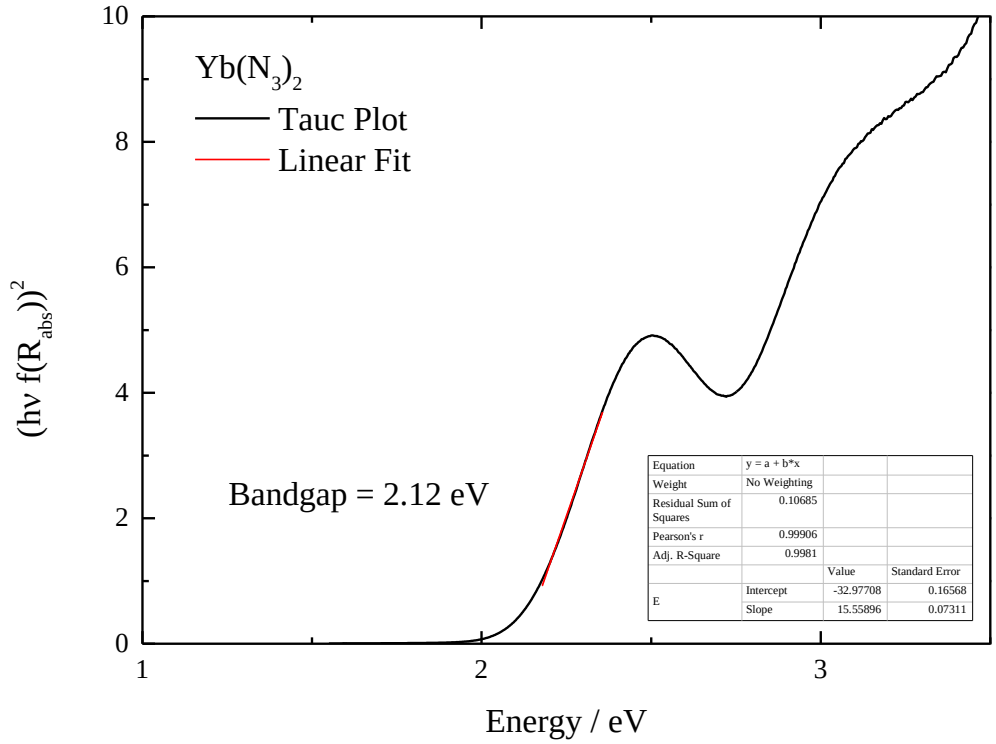


Fig. S 7: Tauc plot of $Yb(N_3)_2$ with linear fit to determine the band gap.

References

[1] R. Dinnebier, N. Sofina, L. Hildebrandt, M. Jansen, *Acta Cryst.* **2006**, *62*, 467-473.

[2] A. Saiki, N. Ishizawa, N. Mizutani, M. Kato, *J. Ceram. Soc. Jpn.* **1985**, *93*, 649-654.

7.2 Supporting Analytical Data

Raw files of analytical data and cif-files are available upon request.

7.2.1 Powder X-Ray Diffraction Data

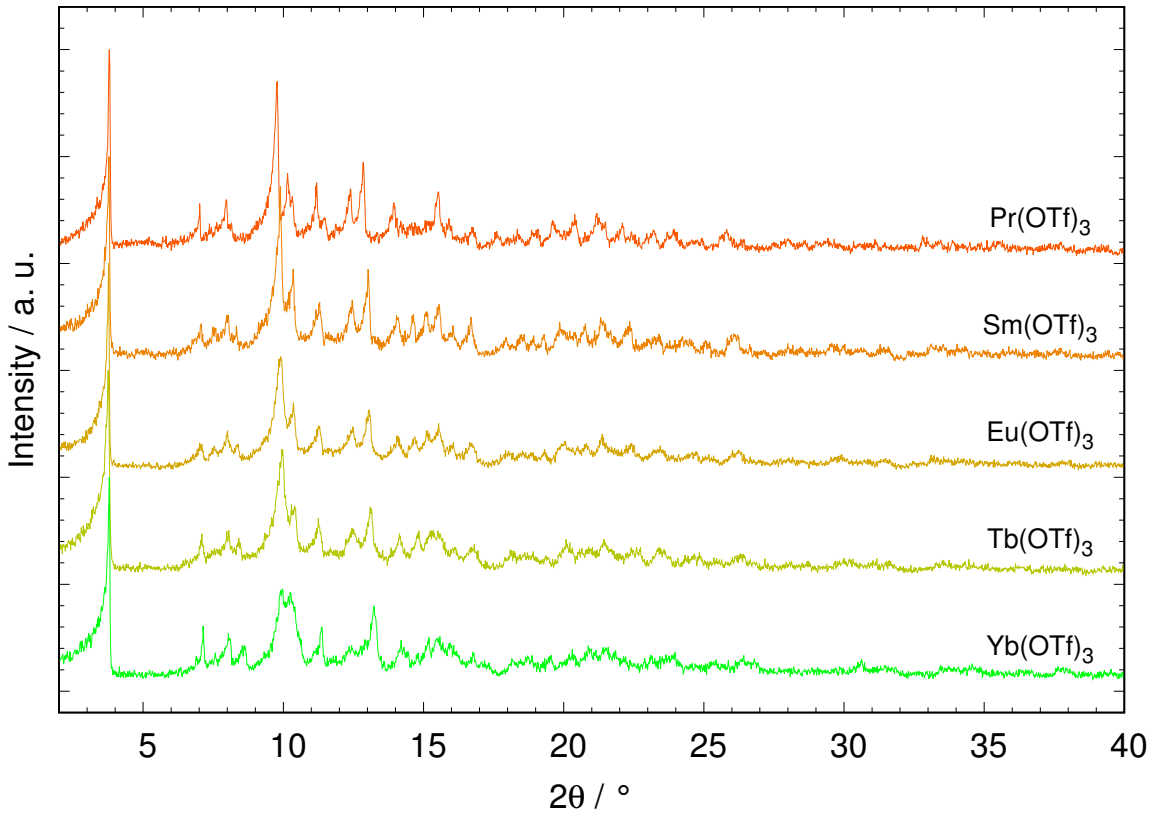


Fig. 27 Powder X-ray diffractogram of various lanthanoid triflates used in this work. For exp. details see section 6.2.1. The data were collected using Mo-Kα_1-radiation.

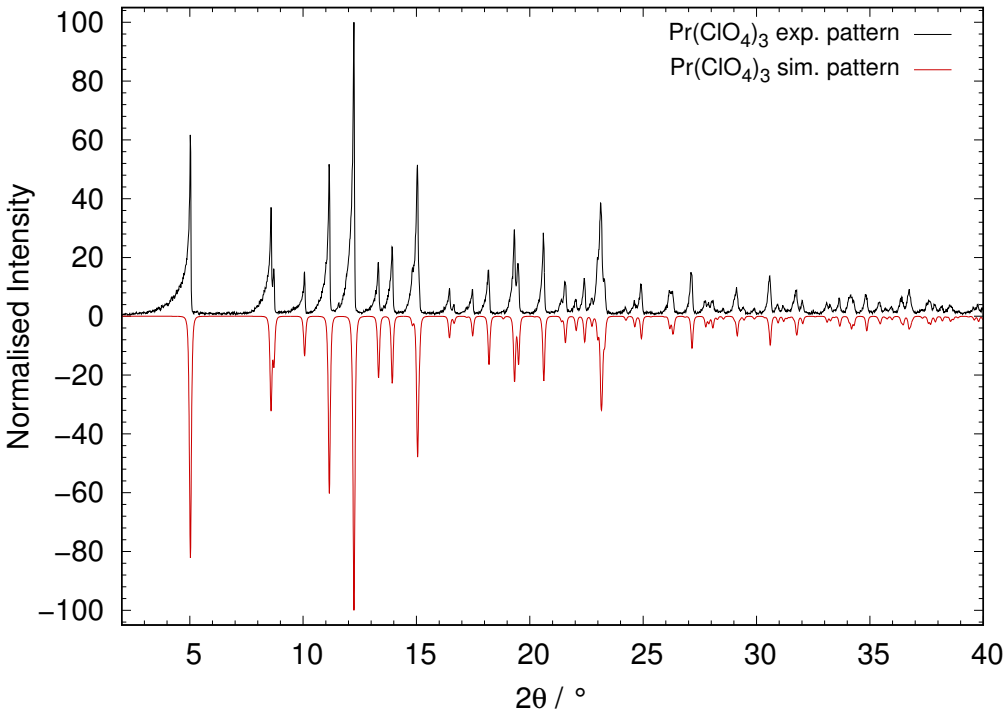


Fig. 28 Powder X-ray diffractogram $Pr(ClO_4)_3$. For detailed exp. data of the synthesis refer to section 6.2.3. The data were collected using Mo-Kα_1-radiation. The simulated data were generated from *Wickleder* et al.[135]

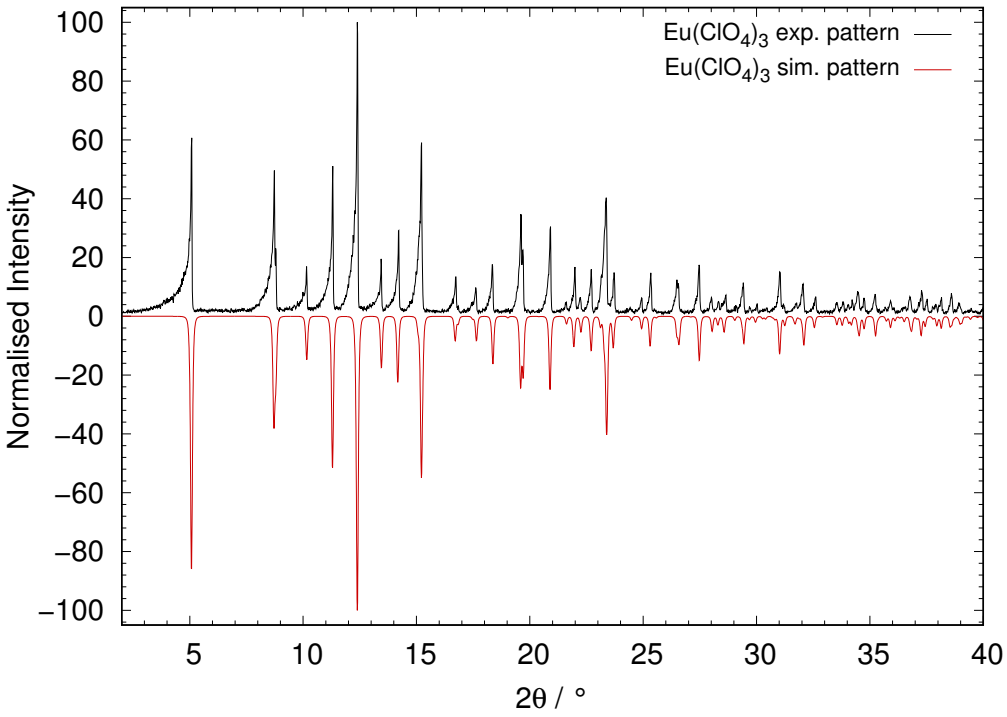


Fig. 29 Powder X-ray diffractogram $Eu(ClO_4)_3$. The data were collected using Mo-Kα_1-radiation. For detailed exp. data of the synthesis refer to section 6.2.3. The simulated data were generated from *Wickleder*.[136]

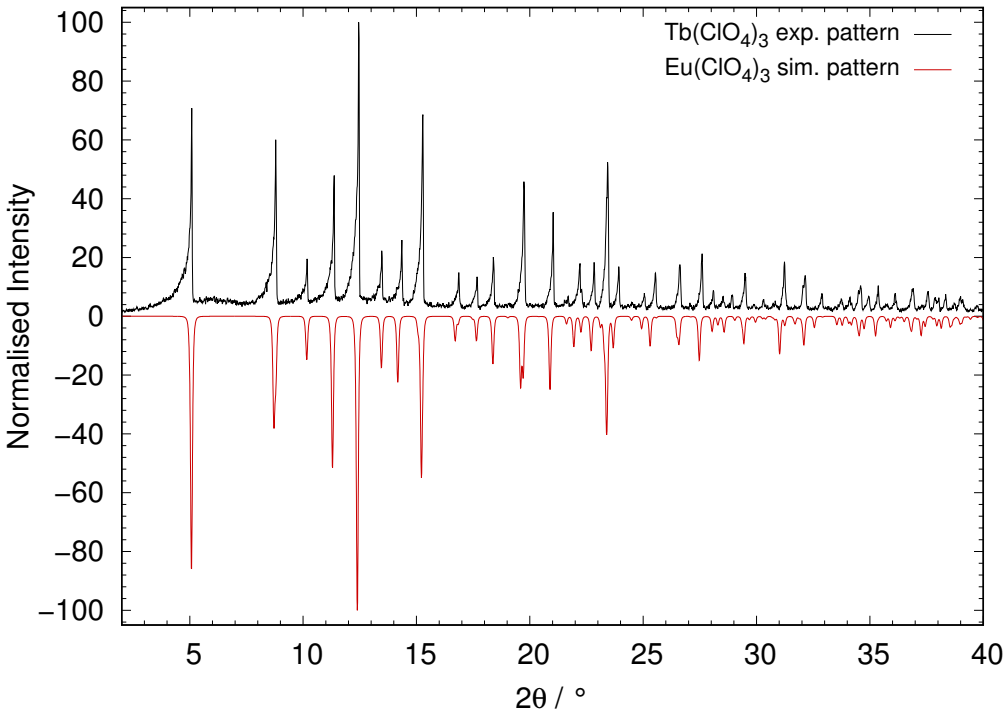


Fig. 30 Powder X-ray diffractogram $Tb(ClO_4)_3$. The data were collected using Mo-Kα_1-radiation. For detailed exp. data of the synthesis refer to section 6.2.3. The simulated data were generated from *Wickleder*.[136]

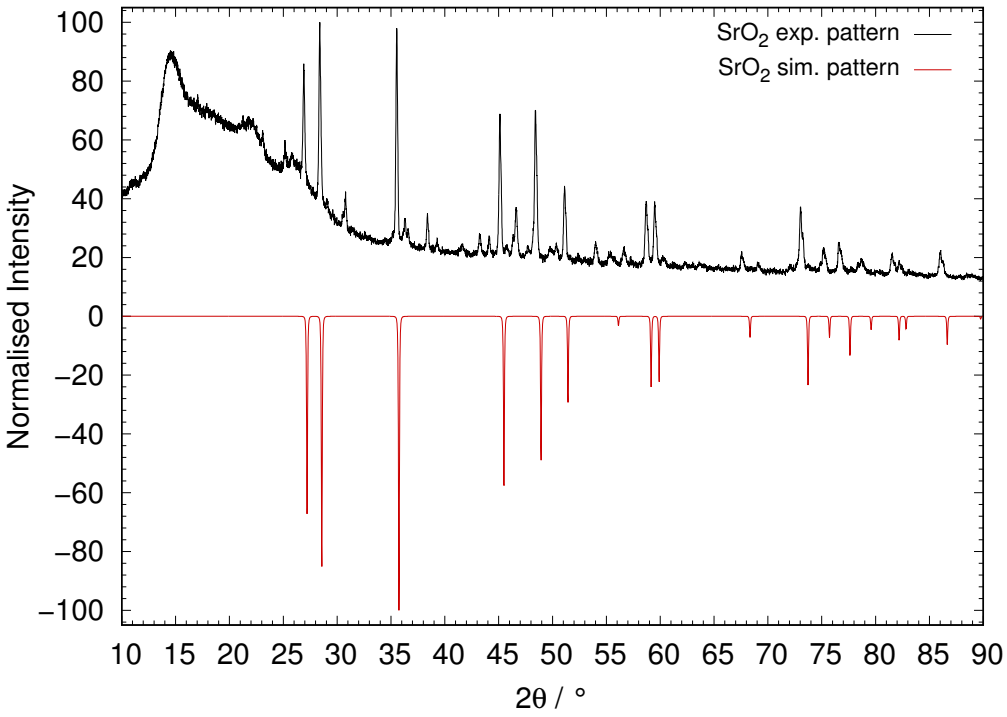


Fig. 31 Powder X-ray diffractogram SrO_2. The data were collected using Cu-Kα-radiation. For detailed exp. data of the synthesis refer to section 6.2.4. The simulated data were generated from *Bernal* et al.[137]

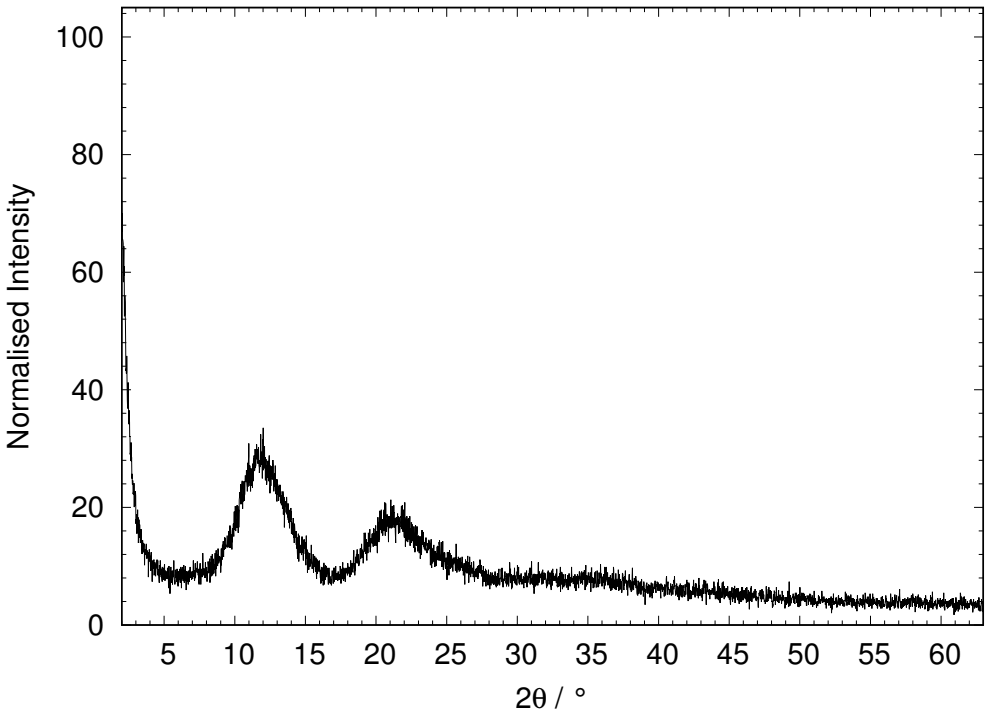


Fig. 32 Powder X-ray diffractogram of the crude product obtained from reacting $Tb(ClO_4)_3$ and XeF_2 in acetonitrile. For exp. details see section 6.2.7. The data were collected using Mo-Kα_1-radiation.

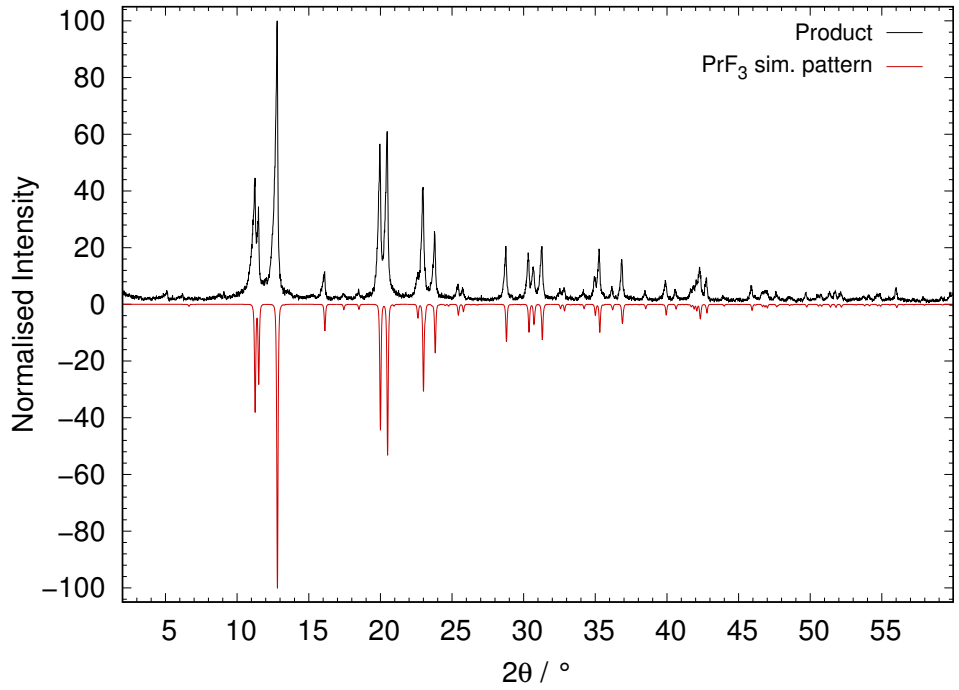


Fig. 33 Powder X-ray diffractogram $Pr(ClO_4)_3$ and XeF_2 without solvents after the solids ignited. For exp. details see section 6.2.8. The data were collected using Mo-Kα_1-radiation. The simulated data were generated from *Maksimov* et al.[138]

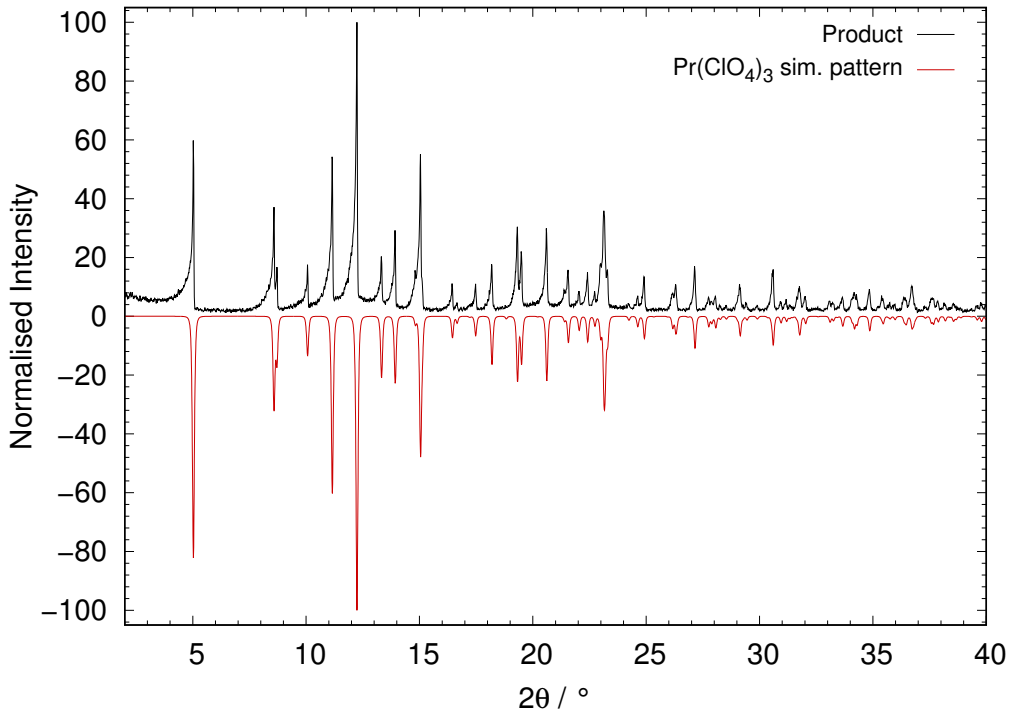


Fig. 34 Powder X-ray diffractogram of the product obtained from reacting $Pr(ClO_4)_3$ and XeF_2 without solvents. For exp. details see 6.2.9. The data were collected using Mo-Kα_1-radiation. The simulated data were generated from *Wickleder* et al.[135]

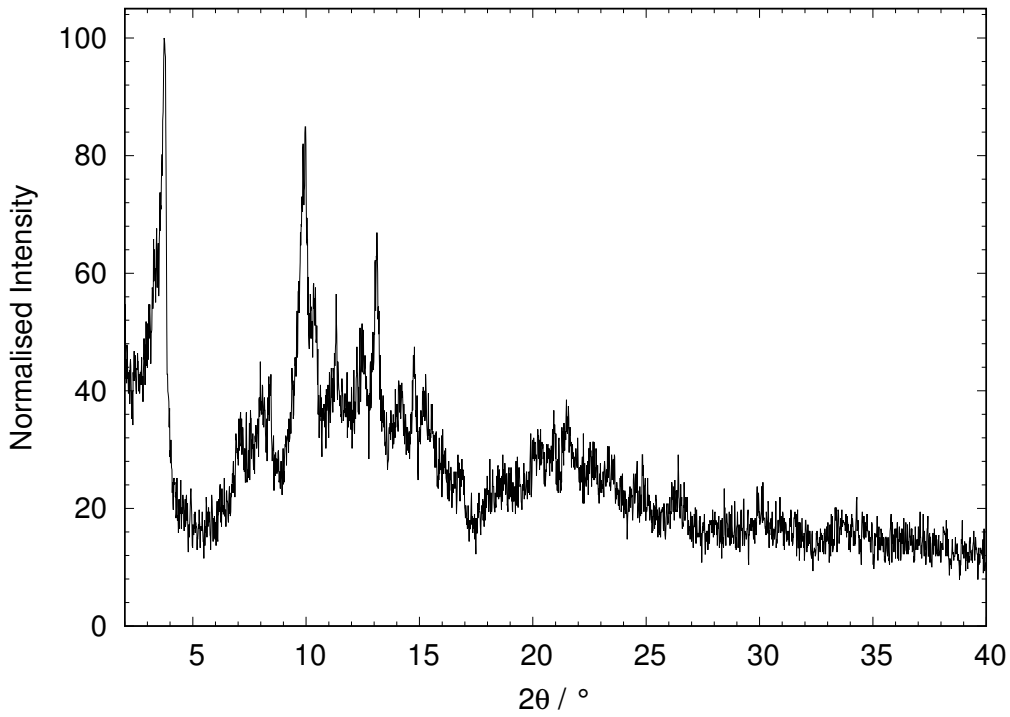


Fig. 35 Powder X-ray diffractogram of the product obtained from reacting $Tb(OTf)_3$ and XeF_2 in SO_3. For exp. details section 6.2.10. The data were collected using Mo-Kα_1-radiation.

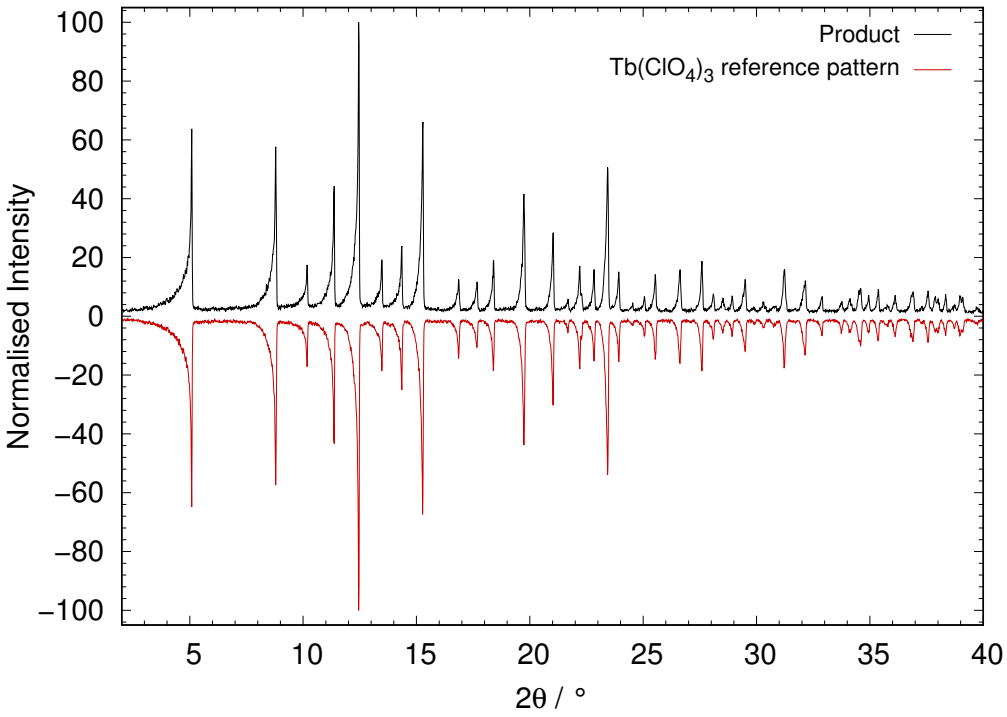


Fig. 36 Powder X-ray diffractogram of the product obtained from reacting $Tb(ClO_4)_3$ and XeF_2 in SO_3, along with an reference diffractogram of the starting material. For exp. details see section 6.2.10. The data were collected using Mo-Kα_1-radiation.

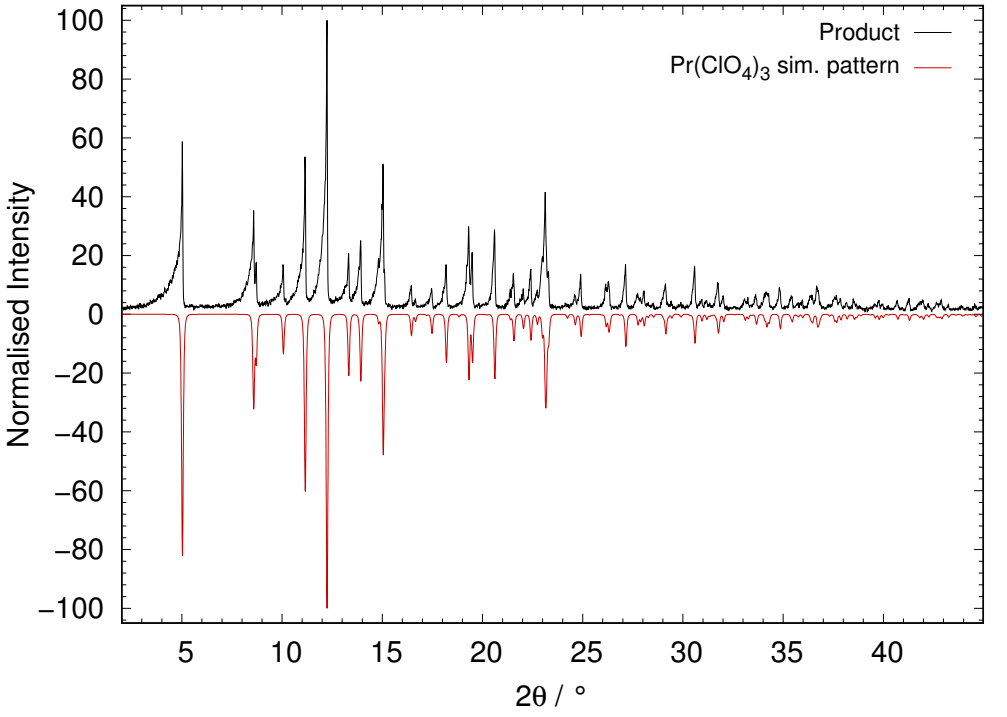


Fig. 37 Powder X-ray diffractogram of the product obtained from reacting $Pr(ClO_4)_3$ and XeF_2 in SO_3. For exp. details see section 6.2.10. The data were collected using Mo-Kα_1-radiation. The simulated data was generated from *Wickleder* et al.[135]

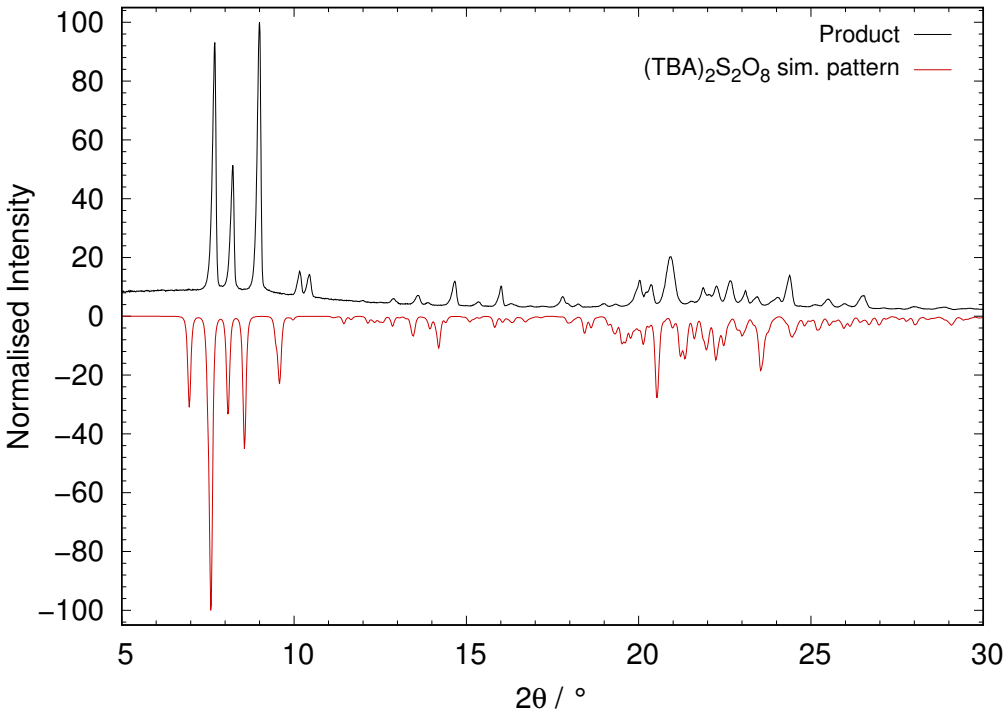


Fig. 38 Powder X-ray diffractogram of $(TBA)_2S_2O_8$ For exp. details section 6.2.14. The data were collected using Cu-Kα-radiation.

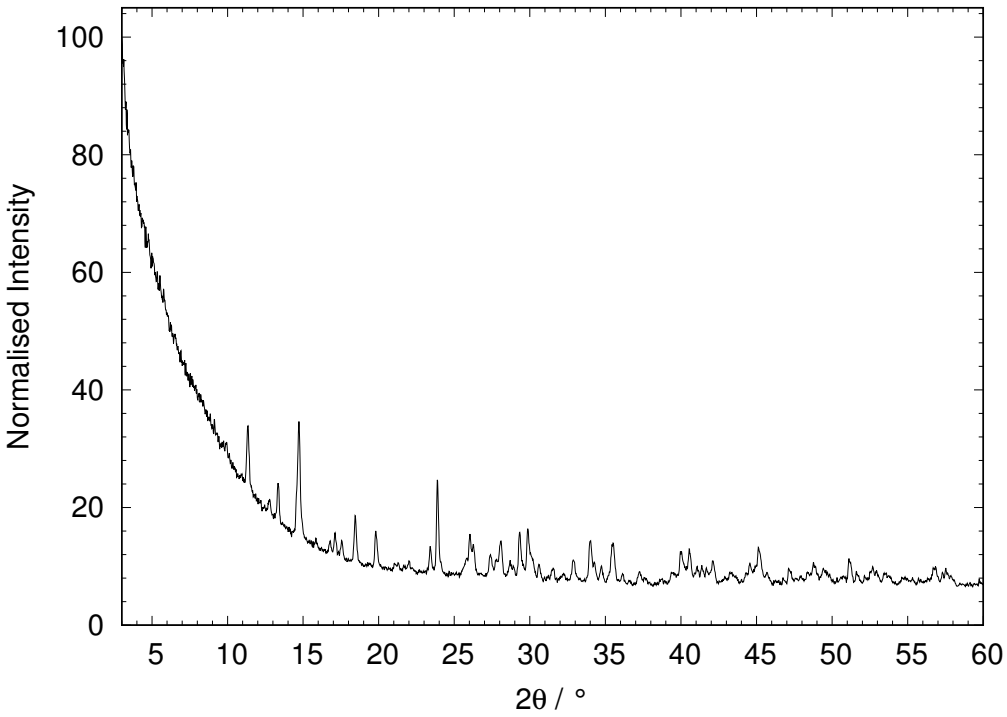


Fig. 39 Powder X-ray diffractogram of the product obtained from reacting $Pr(OTf)_3$ and $(TBA)_2S_2O_8$ in THF. For exp. details see section 6.2.15. The data were collected using Cu-Kα-radiation.

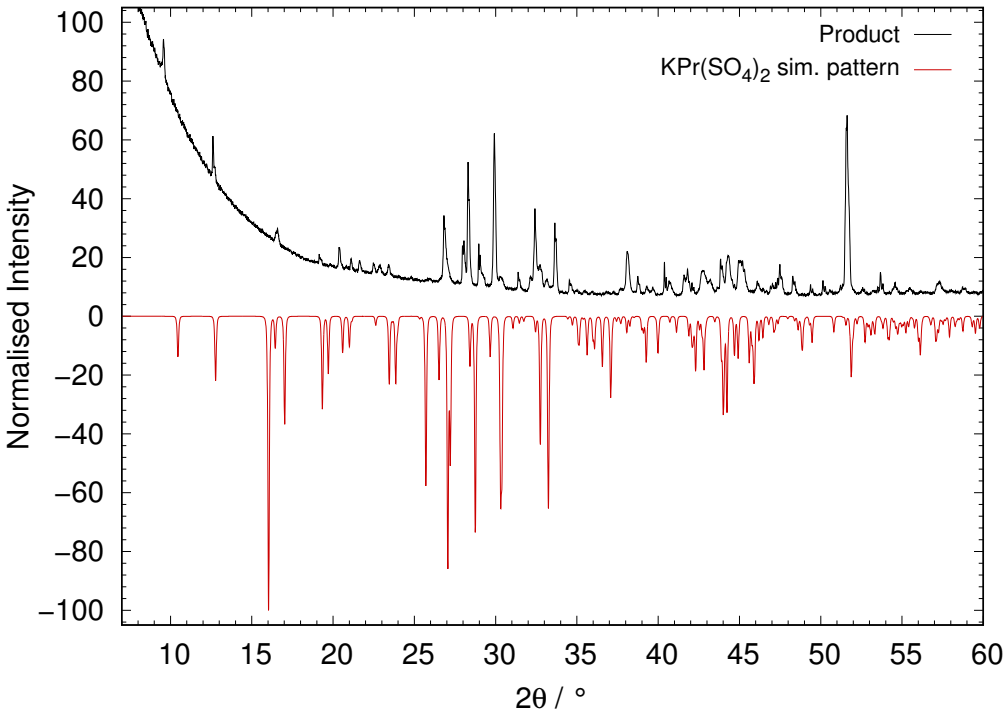


Fig. 40 Powder X-ray diffractogram of the products obtained from reacting $K_2S_2O_8$ and $Pr_2(SO_4)_3$ at 11 GPa. For detailed exp. data of the synthesis refer to section 6.2.16. The data were collected using Cu-Kα-radiation. The simulated data were generated from *Degtyarev* et al.[109]

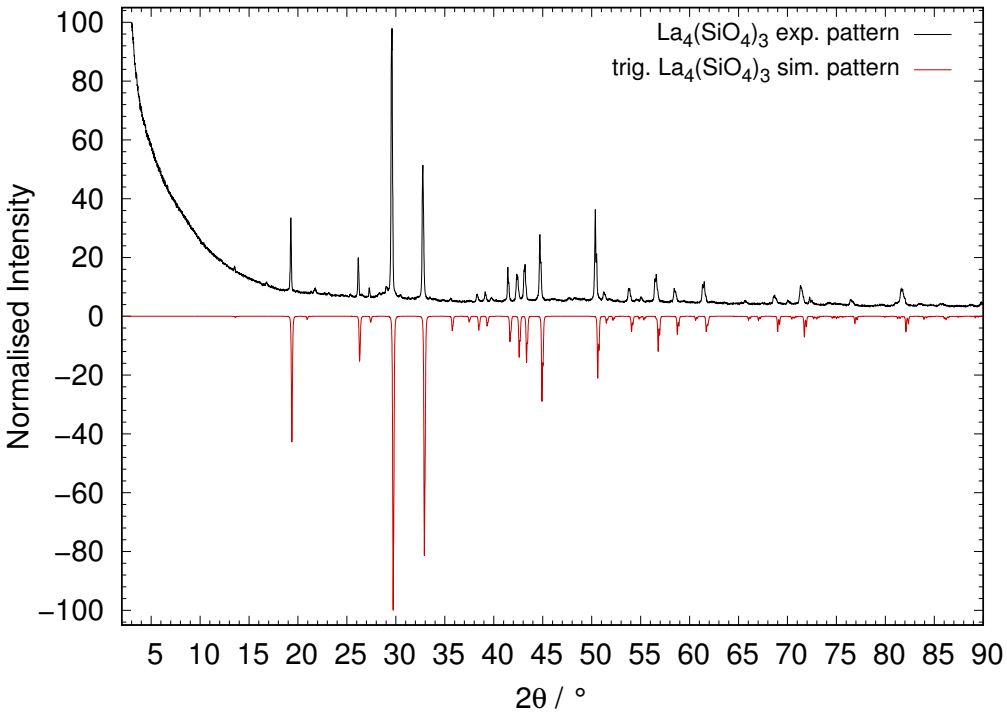


Fig. 41 Powder X-ray diffractogram of $La_4(SiO_4)_3$ obtained from reacting La_2O_3 and SiO_2 at 11 GPa. For detailed exp. procedure refer to section 6.2.16. The data were collected using Cu-Kα-radiation. The simulated data were generated from *Fleet* et al.[112]

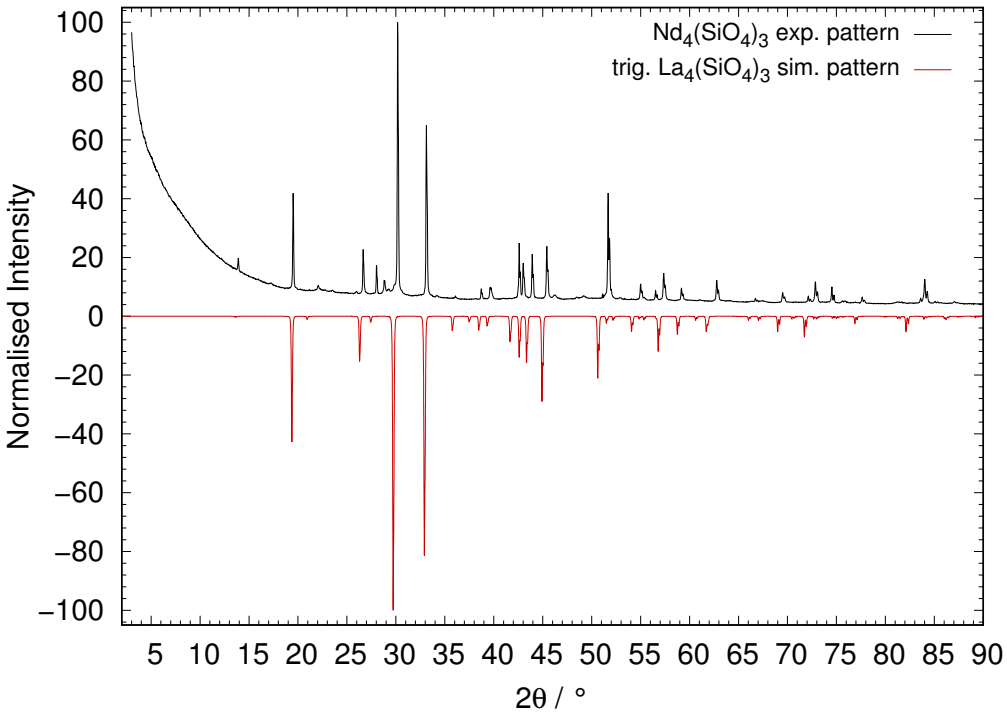


Fig. 42 Powder X-ray diffractogram of $Nd_4(SiO_4)_3$ obtained from reacting Nd_2O_3 and SiO_2 at 11 GPa. For detailed exp. procedure refer to section 6.2.16. The data were collected using Cu-Kα-radiation. The simulated data were generated from *Fleet* et al. [112]

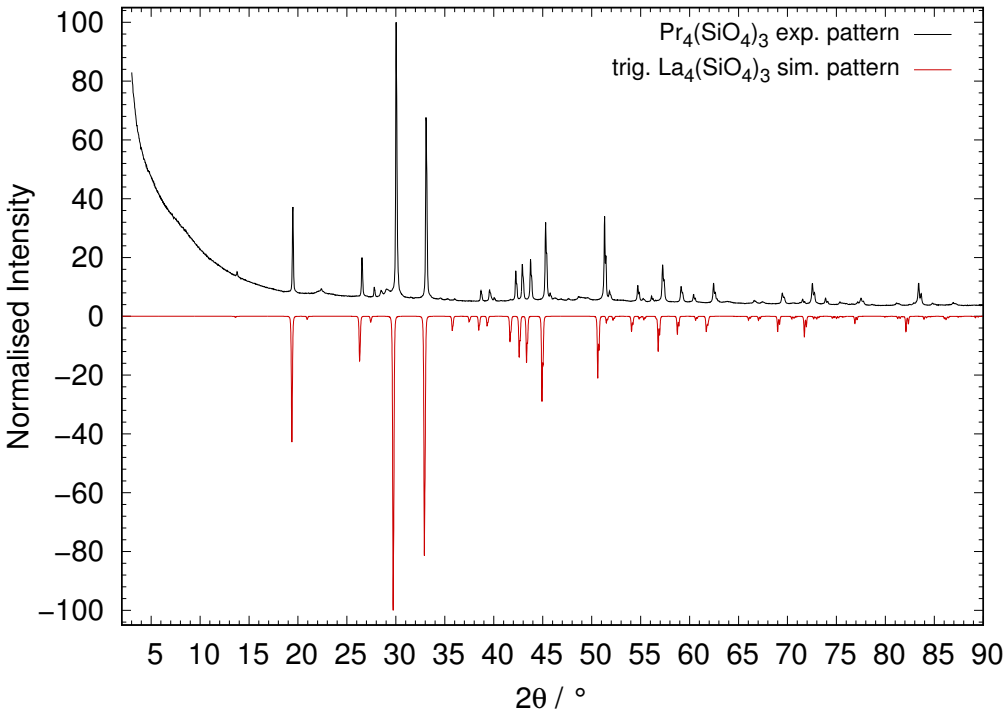


Fig. 43 Powder X-ray diffractogram of $Pr_4(SiO_4)_3$ obtained from reacting PrO_2 and SiO_2 at 11 GPa. For detailed exp. procedure refer to section 6.2.16. The data were collected using Cu-Kα-radiation. The simulated data were generated from *Fleet* et al. [112]

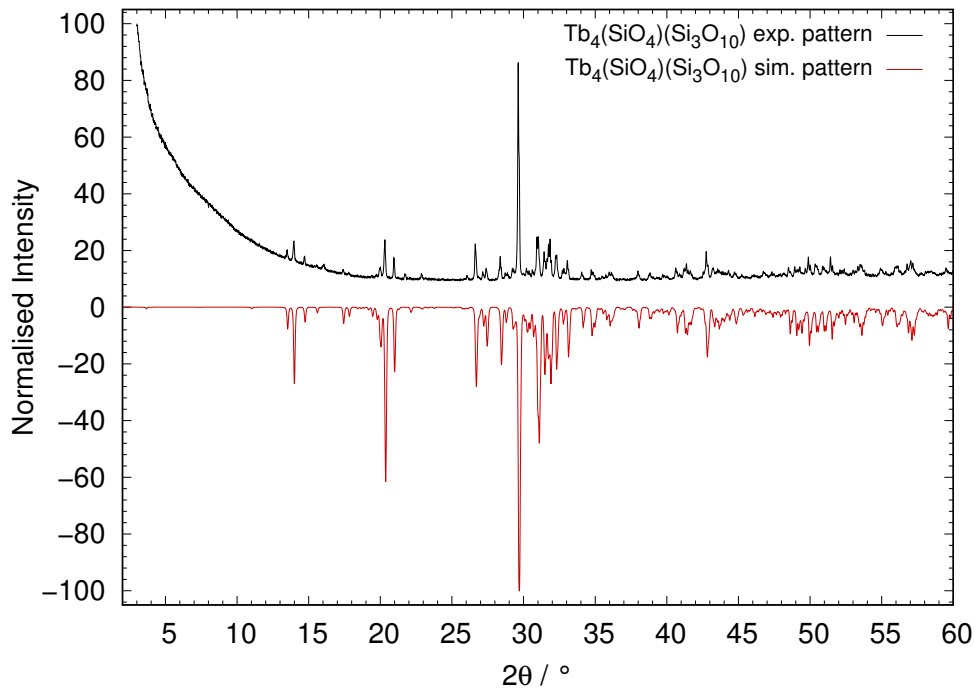


Fig. 44 Powder X-ray diffractogram of $Tb_4(SiO_4)(Si_3O_{10})$ obtained from reacting Tb_4O_7 and SiO_2 at 11 GPa. For detailed exp. procedure refer to section 6.2.16. The data were collected using Cu-Kα-radiation. The simulated data were generated the single crystal data set generated in this work.

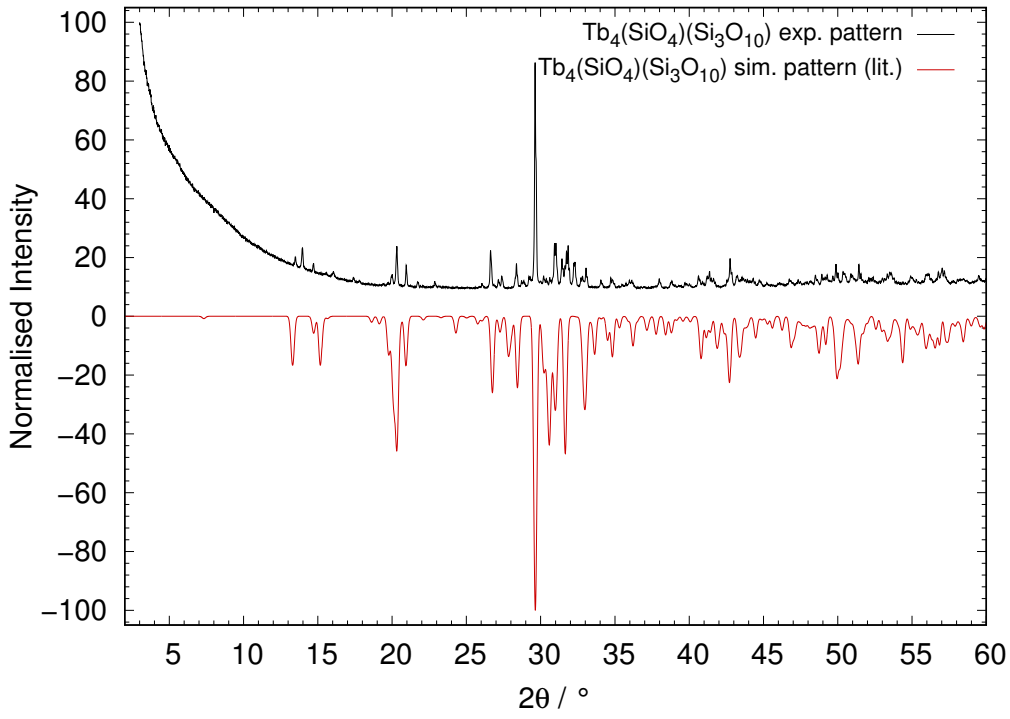


Fig. 45 Powder X-ray diffractogram of $Tb_4(SiO_4)(Si_3O_{10})$ obtained from reacting Tb_4O_7 and SiO_2 at 11 GPa. For detailed exp. procedure refer to section 6.2.16. The data were collected using Cu-Kα-radiation. The simulated data were generated from *Fleet* et al.[112]

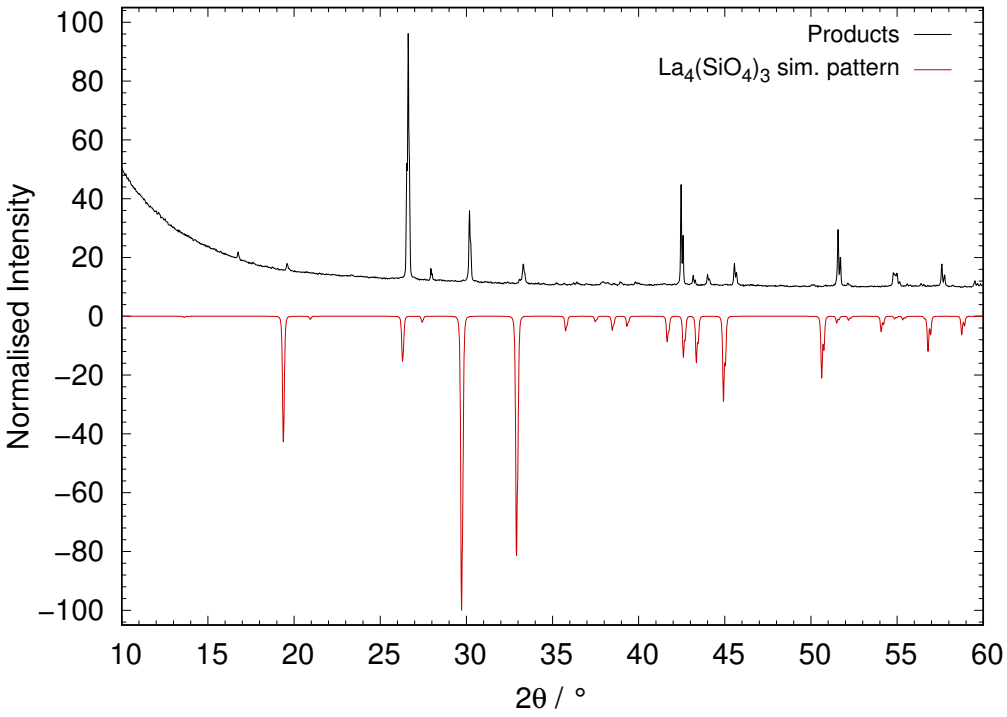


Fig. 46 Powder X-ray diffractogram of the products obtained by reacting PrO_2 and SiO_2 in presence of Na_2O_2 reacted at 11 GPa. For detailed exp. procedure refer to section 6.2.16. The data were collected using Cu-Kα-radiation. The simulated data were generated from *Fleet* et al.[112]

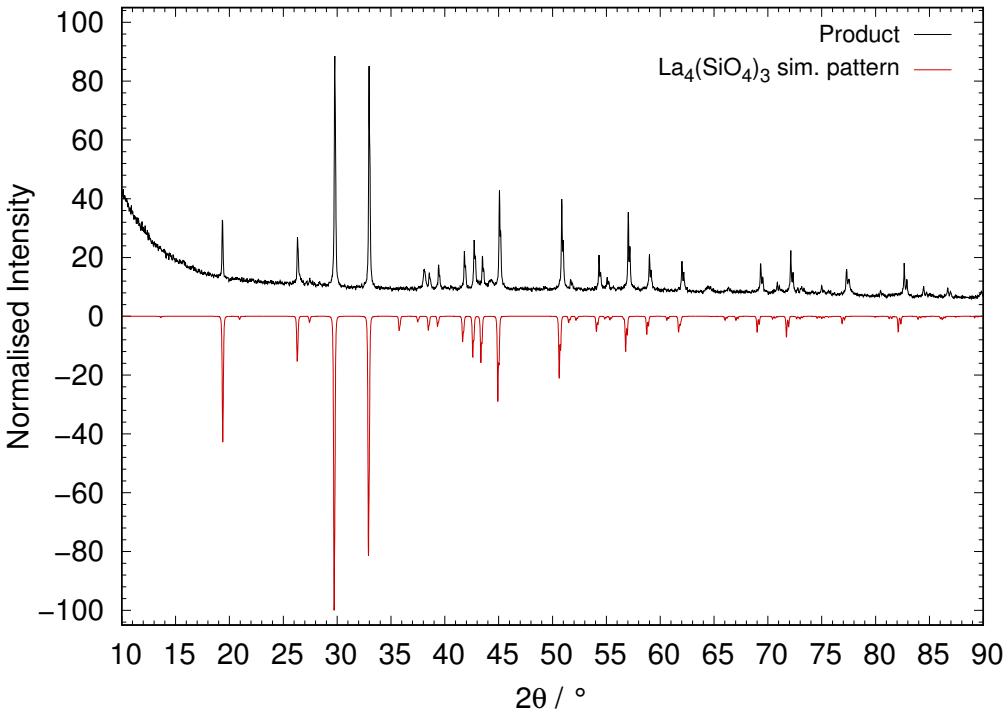


Fig. 47 Powder X-ray diffractogram of the products obtained by reacting PrO_2 and SiO_2 in presence of SrO_2 reacted at 11 GPa. For detailed exp. procedure refer to section 6.2.16. The data were collected using Cu-Kα-radiation. The simulated data were generated from *Fleet* et al.[112]

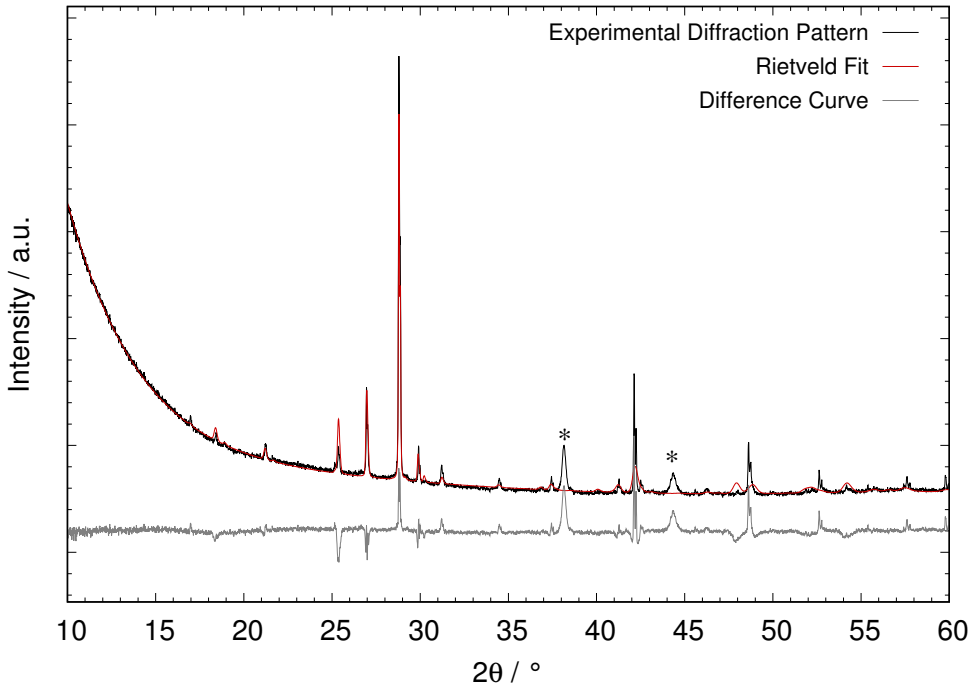


Fig. 48 Rietveld refinement of $PrPO_4$ obtained from reacting PrO_2 and P_2O_5 at 11 GPa. For exp. details see section 6.2.16. The structural model was adapted from *Hirsch* et al.[139] $a = 677.7(2)$ pm, $b = 699.1(2)$ pm, c = 643.5(4) pm, $\beta = 103.74(3)°$, Preferred Orientation Factor(001) = 1.72(5), $R_{wp} = 6.00$, $R_p = 3.72$, $R_p = 3.19$, Goof = 1.61. The data were collected using Cu-Kα-radiation. Marked reflections are a result of contamination with MgO from the octahedron.

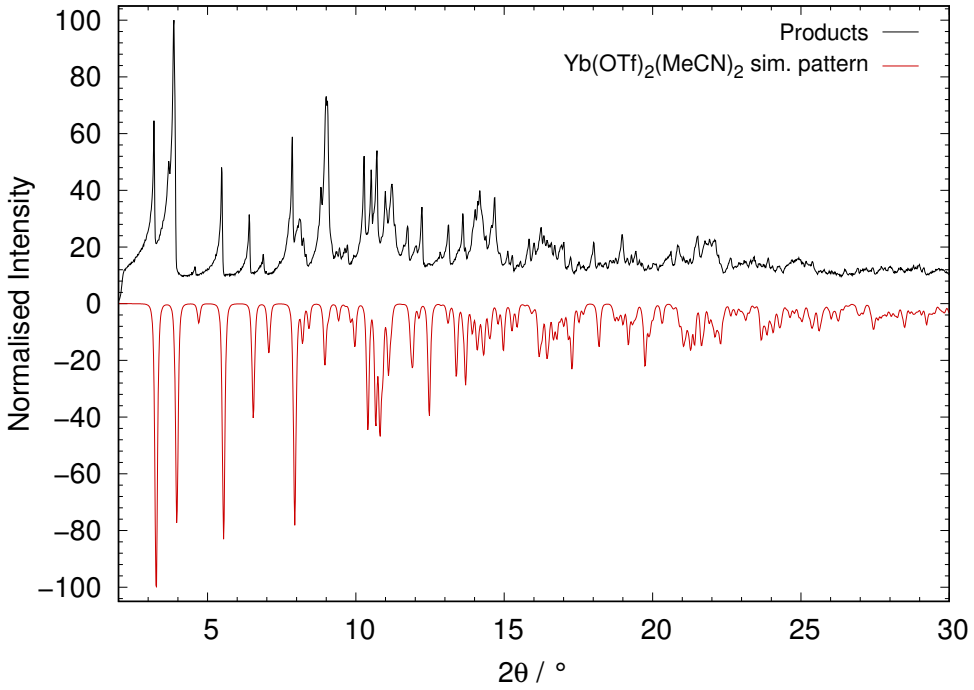


Fig. 49 PXRD data of impure $Yb(OTf)_2(MeCN)_2$. For exp. details see section 6.2.17. The data were collected using Mo-Kα_1-radiation. The simulated data were generated from own data (comp. tab. 17).

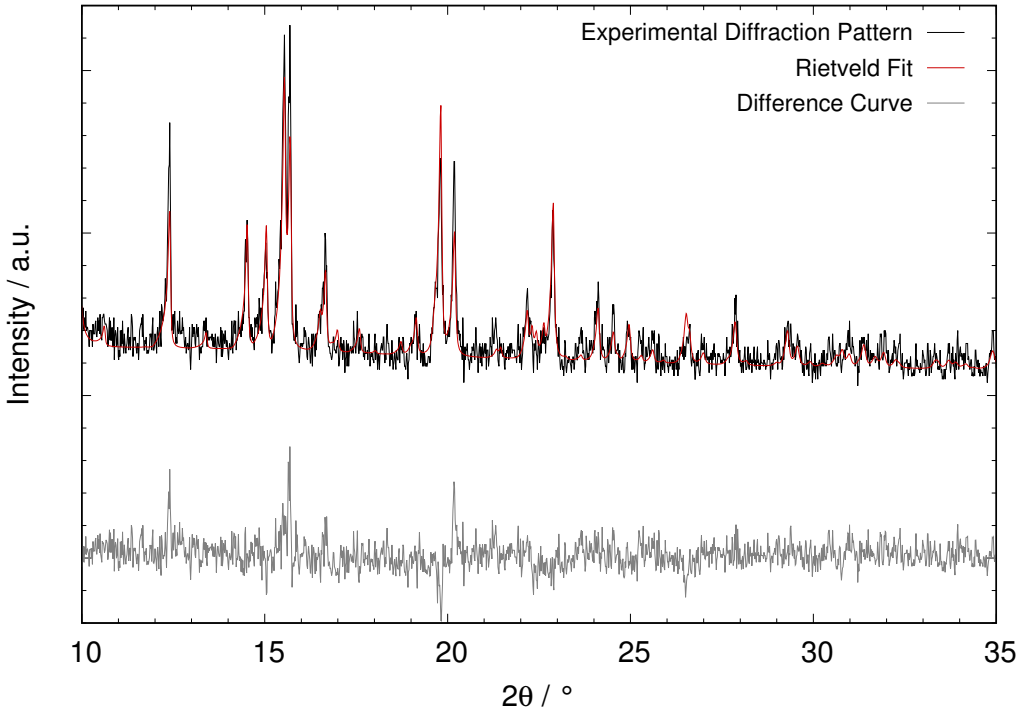


Fig. 50 Rietveld refinement of $Ca(OTf)_2$. For exp. details see section 6.2.2. The structural model was adapted from *Jansen* et al.[125] $R\bar{3}$,$a = b = 560.7$ pm, $c = 3113.9(5)$ pm, $R_{wp} = 26.2$, $R_p = 26.0$, $R_p = 19.8$, Goof = 1.00. The data were collected using Mo-Kα_1-radiation.

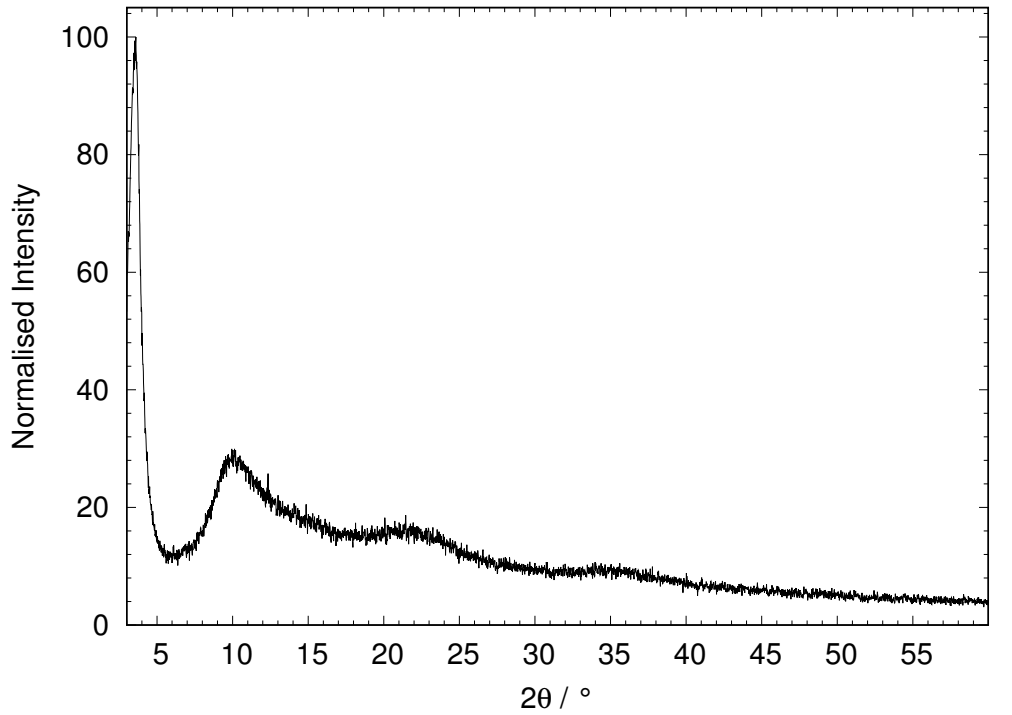


Fig. 51 PXRD data of the solids obtained from comproportionation of $Eu(OTf)_3$ and Eu in THF and immediate evaporation of the solvent. For detailed exp. procedure refer to section 6.2.20. The data were collected using Mo-Kα_1-radiation.

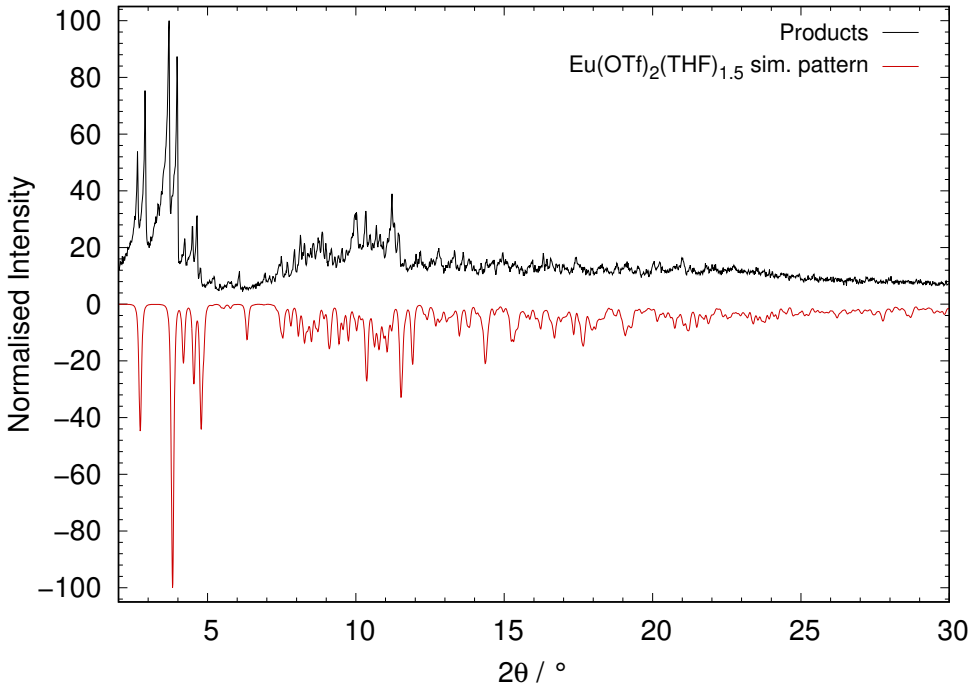


Fig. 52 Powder X-ray diffractogram of impure $Eu(OTf)_2(THF)_{1.5}$ obtained from comproportionation of $Eu(OTf)_3$ and Eu in THF and subsequent recrystallisation. For detailed exp. procedure refer to section 6.2.20. The data were collected using Mo-Kα_1-radiation. The simulated data were generated from own data.[124]

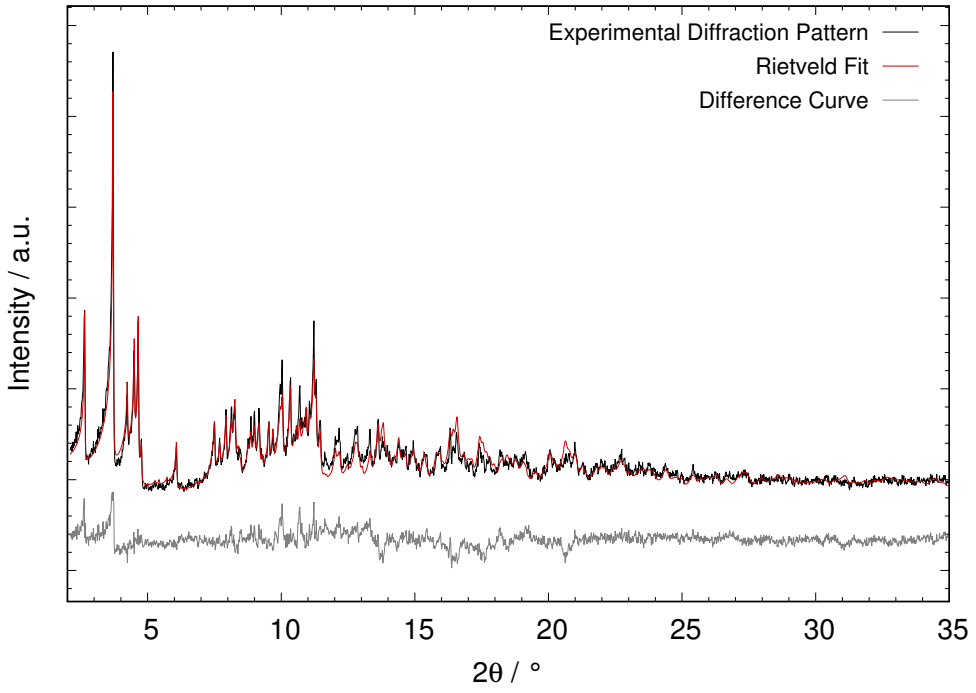


Fig. 53 Rietveld refinement of $Eu(OTf)_2(THF)_{1.5}$ obtained from recrystallisation of $Eu(OTf)_2$ from THF. For exp. details see section 6.2.21. The structural model was adapted from own data.[124] $P2_1/n$, a = 1778.6(3) pm, b = 1025.4(2) pm, c =2034.5(4) pm, β = 109.22(1)°, R_{wp} = 13.04, R_p = 7.92, R_p = 10.38, Goof = 1.65. The data were collected using Mo-Kα_1-radiation.

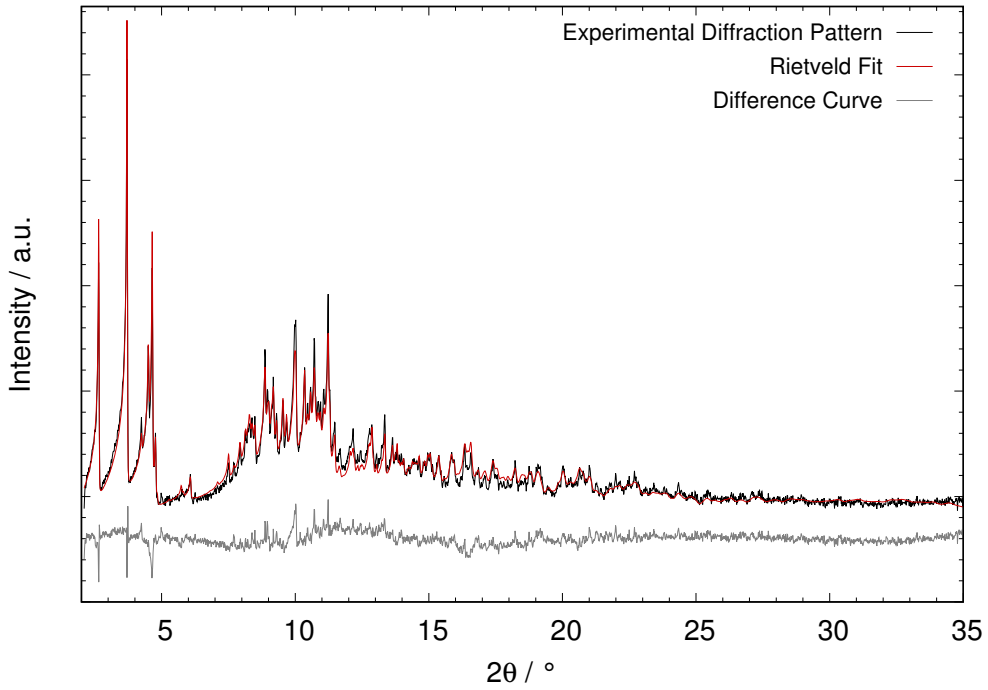


Fig. 54 Rietveld refinement of $Sr(OTf)_2(THF)_{1.5}$ obtained from recrystallisation of $Sr(OTf)_2$ from THF. For exp. details see section 6.2.22. The structural model was adapted own data (see tab. 20). $P2_1/n$, $a = 1781.2(3)$ pm, $b = 1024.6(1)$ pm, $c = 2029.8(3)$ pm, $\beta = 109.151(7)°$, $R_{wp} = 1.76$, $R_{exp} = 1.76$, $R_p = 1.32$, Goof = 1.00. The data were collected using Mo-Kα_1-radiation.

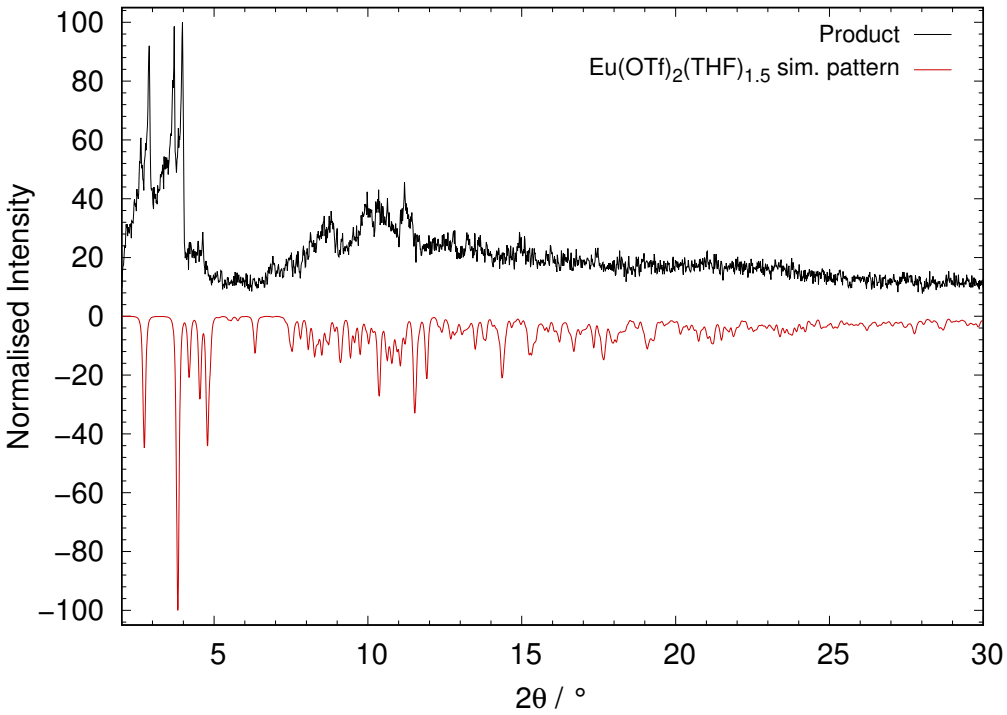


Fig. 55 PXRD data of impure $Sm(OTf)_2(THF)_{1.5}$ obtained from recrystallisation of $Sm(OTf)_2$ from THF. The simulated data were generated from own data.[124] For exp. details see section 6.2.23. The data were collected using Mo-Kα_1-radiation.

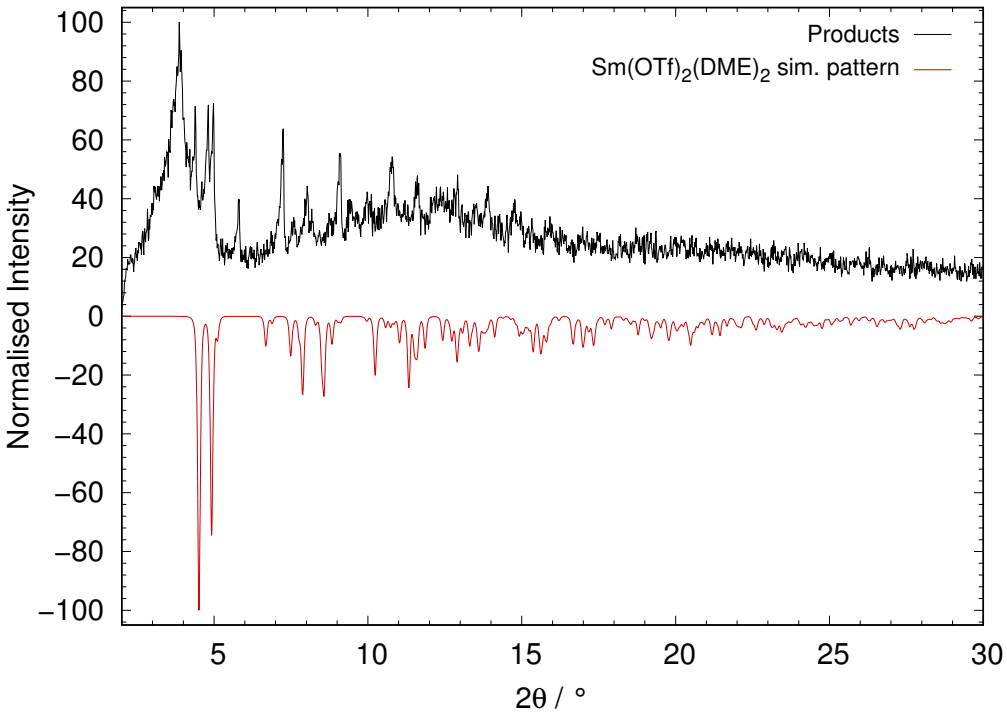


Fig. 56 PXRD data of impure $Sm(OTf)_2(DME)_2$ obtained from recrystallisation of $Sm(OTf)_2$ from DME. The simulated data were generated from own data (see tab. 21) For exp. details see section 6.2.24. The data were collected using Mo-Kα_1-radiation.

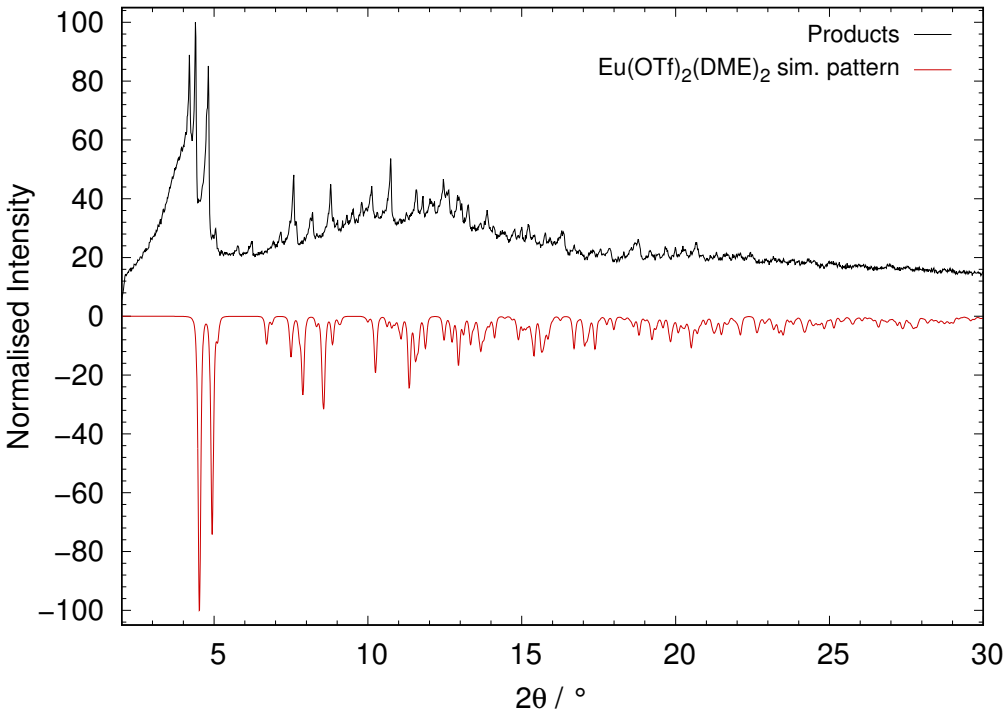


Fig. 57 PXRD data of impure $Eu(OTf)_2(DME)_2$ obtained from recrystallisation of $Eu(OTf)_2$ from DME. The simulated data were generated from own data (see tab. 22) For exp. details see section 6.2.24. The data were collected using Mo-Kα_1-radiation.

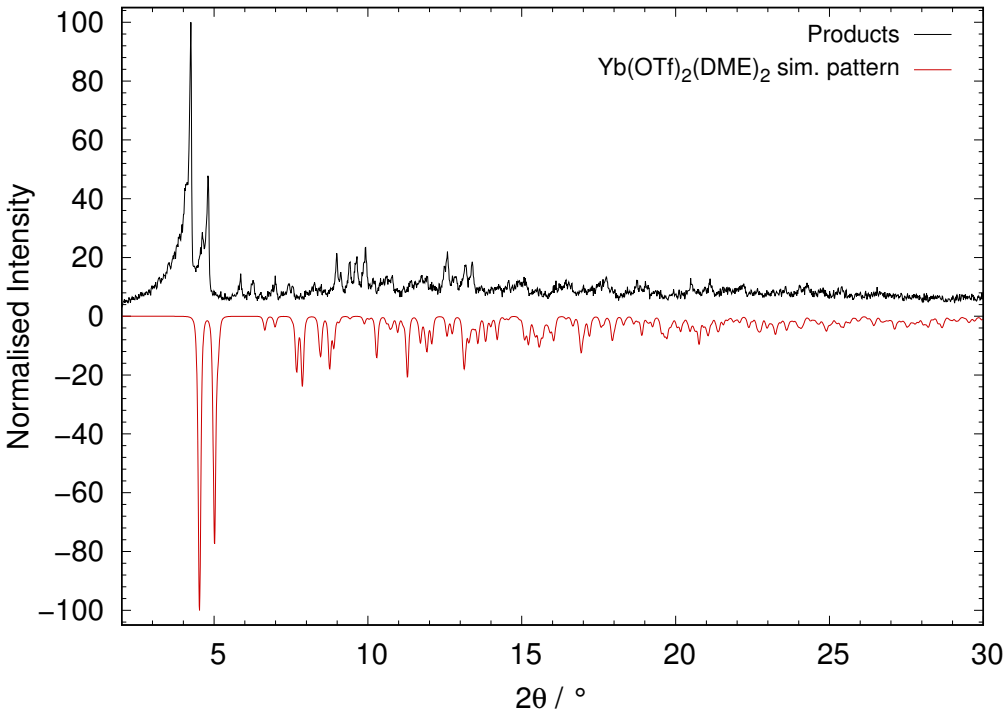


Fig. 58 PXRD data of impure $Yb(OTf)_2(DME)_2$ obtained from recrystallisation of $Yb(OTf)_2$ from DME. The simulated data were generated from own data (see tab. 23) For exp. details see section 6.2.24. The data were collected using Mo-Kα_1-radiation.

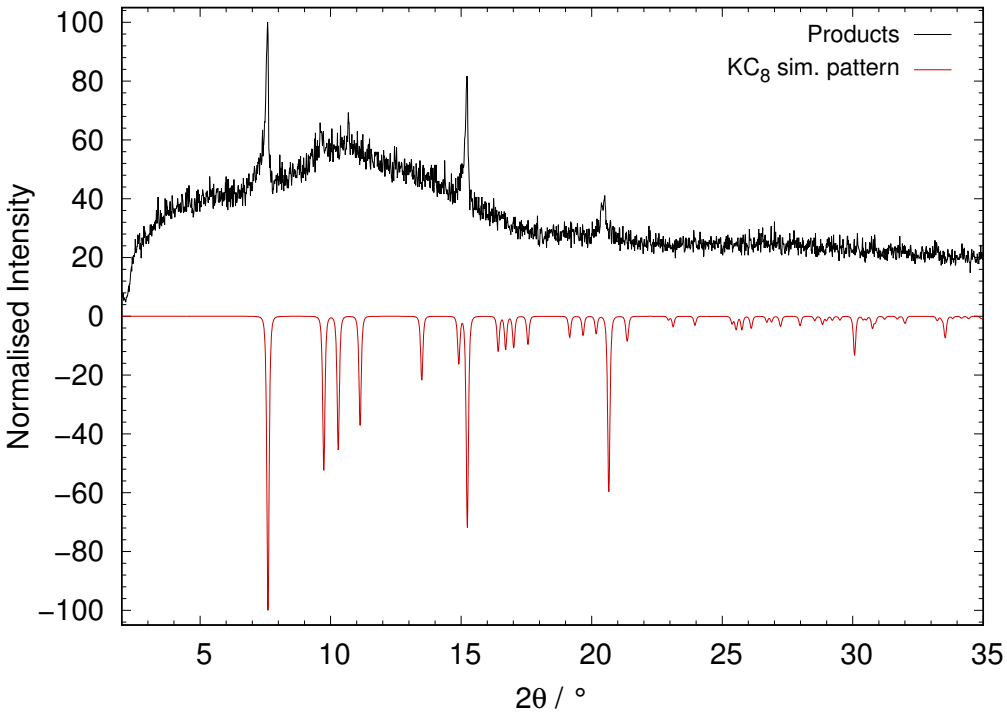


Fig. 59 PXRD data of KC_8 obtained from mechanochemical synthesis (see section 6.2.26 for exp. details). Simulated data were generated from literature data.[140] The data were collected using Mo-Kα_1-radiation.

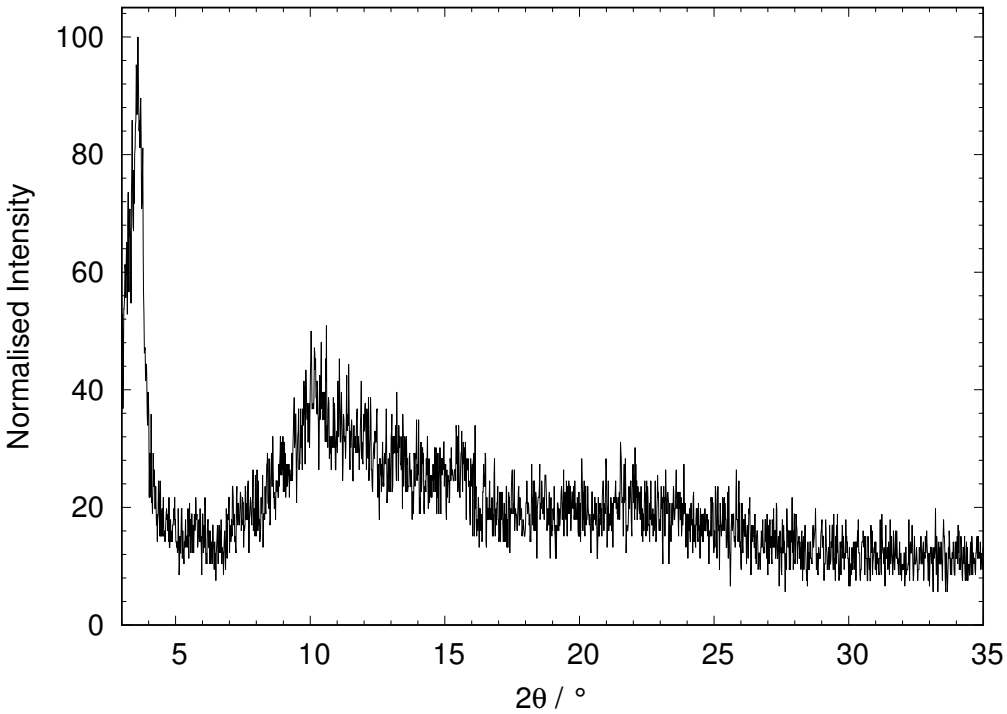


Fig. 60 PXRD data of of the products obtained from reacting $Tm(OTf)_3$ and KC_8 in a ball mill (see section 6.2.31 for exp. details). The data were collected using Mo-Kα_1-radiation.

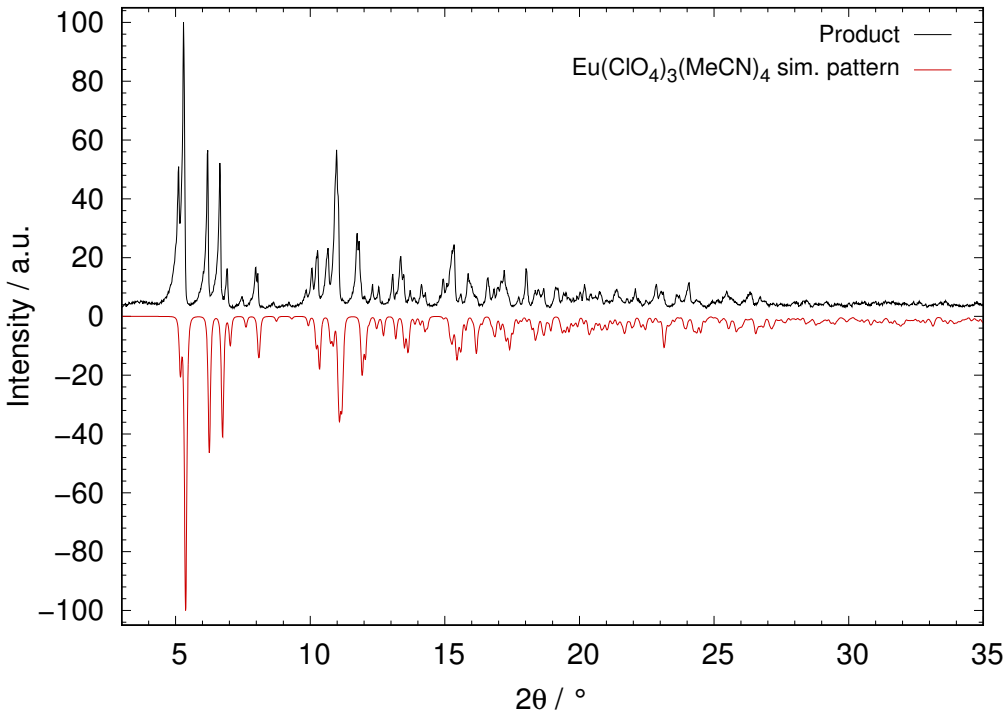


Fig. 61 PXRD data of $Eu(ClO_4)_3(MeCN)_4$ obtained from treating $Eu(ClO_4)_3$ with Eu in acetonitrile. For exp. details see 6.2.39. The simulated data were generated from own data (see section tab. 25). The data were collected using Mo-Kα_1-radiation.

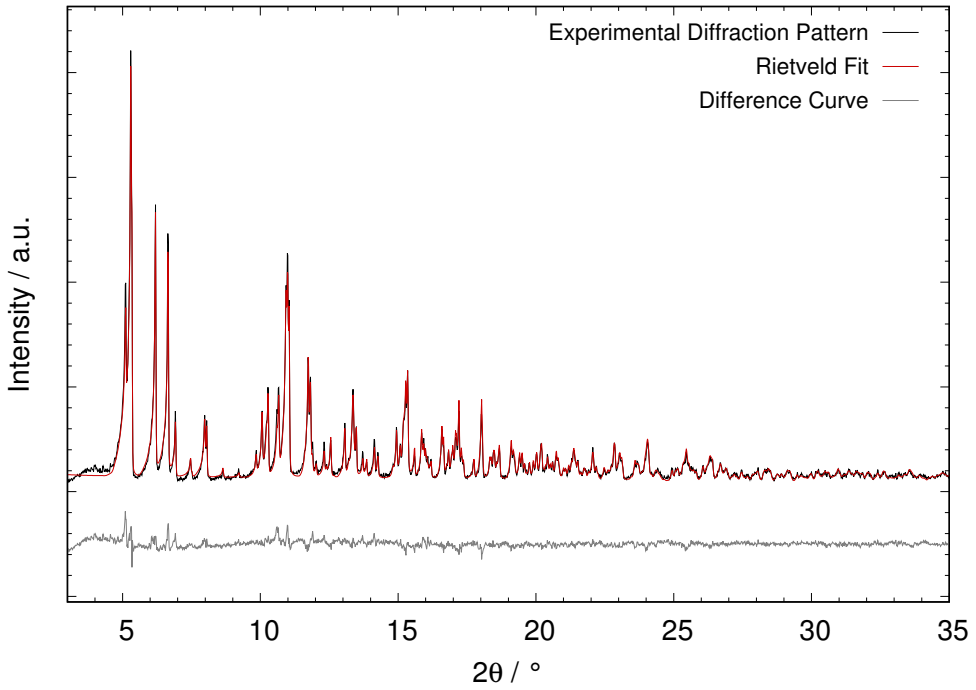


Fig. 62 Rietveld refinement of $Eu(ClO_4)_3(MeCN)_4$ obtained from treating $Eu(ClO_4)_3$ with Eu in acetonitrile. For exp. details see section 6.2.39. The structural model was adapted own data (see tab. 25). *Cc*, a = 1224.97(6) pm, b = 1082.45(5) pm, c =1588.76(8) pm, β = 106.211(3)°, R_{wp} = 10.52, R_{exp} = 6.26, R_p = 7.97, Goof = 1.68. The data were collected using Mo-Kα_1-radiation.

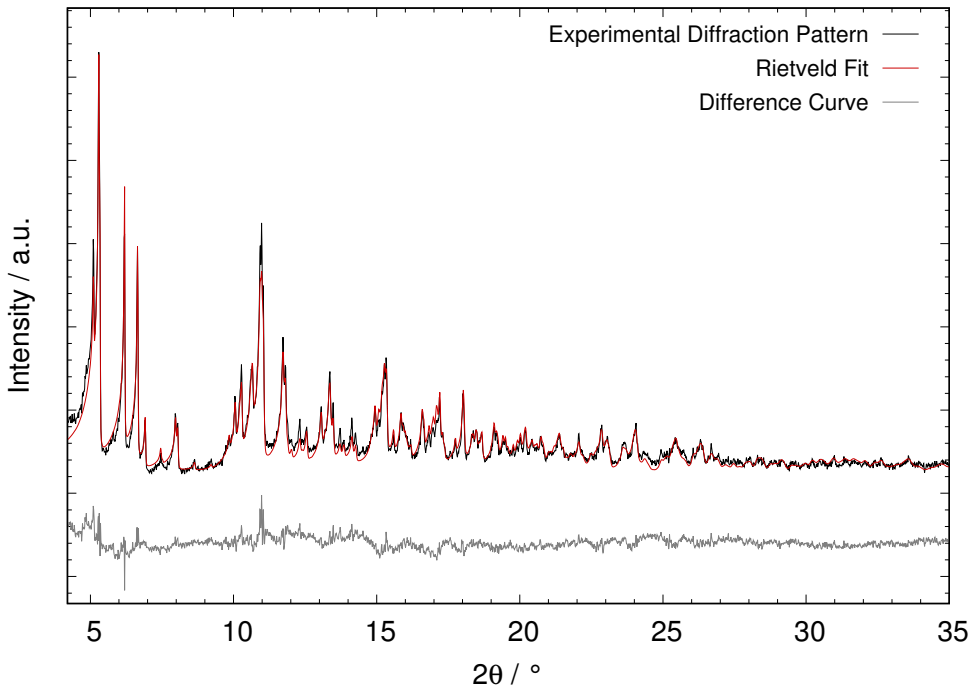


Fig. 63 Rietveld refinement of $Eu(ClO_4)_3(MeCN)_4$ obtained from treating $Eu(ClO_4)_3$ with Eu in acetonitrile. For exp. details see section 6.2.39. The structural model was adapted own data (see tab. 25). *Cc*, a = 1224.5(2) pm, b = 1081.8(1) pm, c =1588.2(2) pm, β = 106.23(8)°, R_{wp} = 11.16, R_{exp} = 5.79, R_p = 8.90, Goof = 1.93. The data were collected using Mo-Kα_1-radiation.

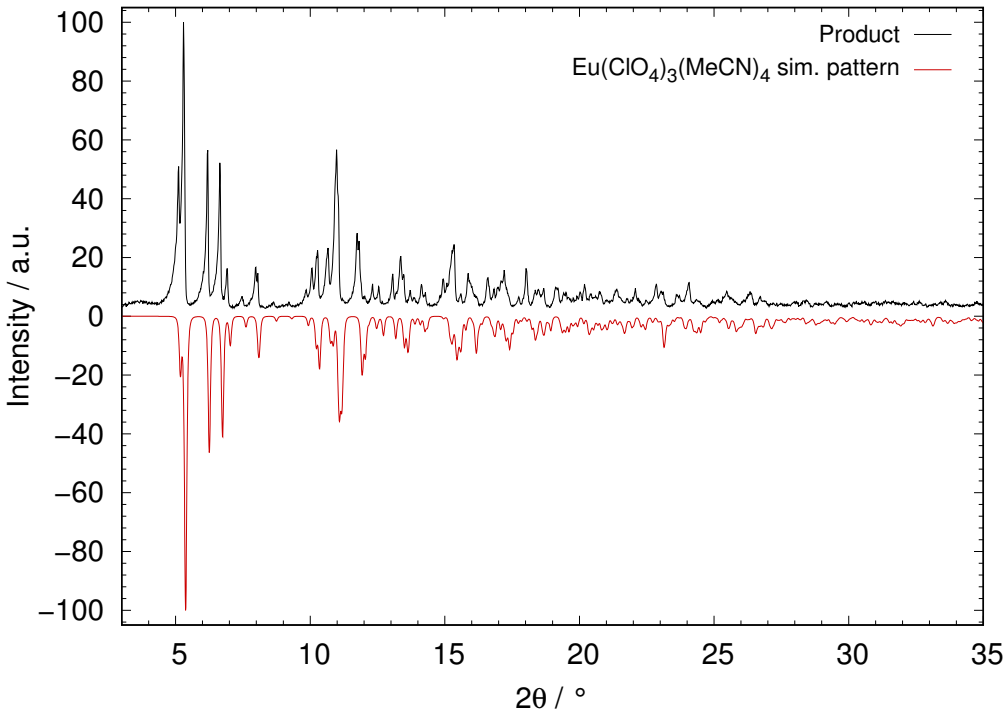


Fig. 64 PXRD data of impure $Eu(ClO_4)_3(MeCN)_4$ obtained from treating $Eu(ClO_4)_3$ with Eu in a steel ball mill. For exp. details see section 6.2.40. The simulated data were generated from own data (see tab. 25). The data were collected using Mo-Kα_1-radiation.

7.2.2 IR-Spectra

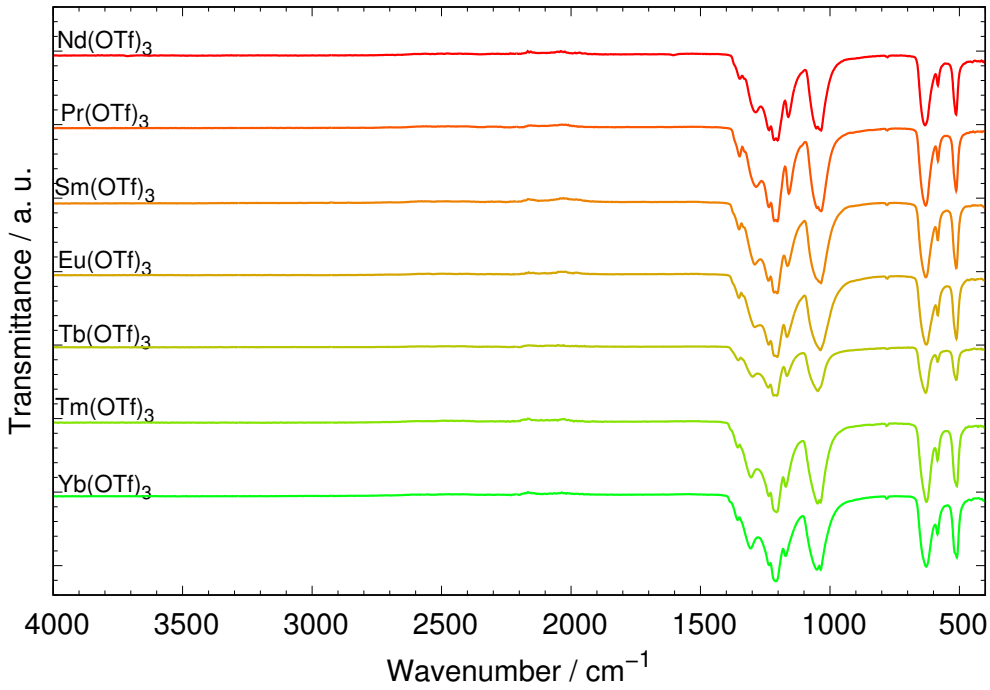


Fig. 65 IR-spectra of lanthanoid(III) triflates used in this work. For experimental details of their synthesis see section 6.2.1.

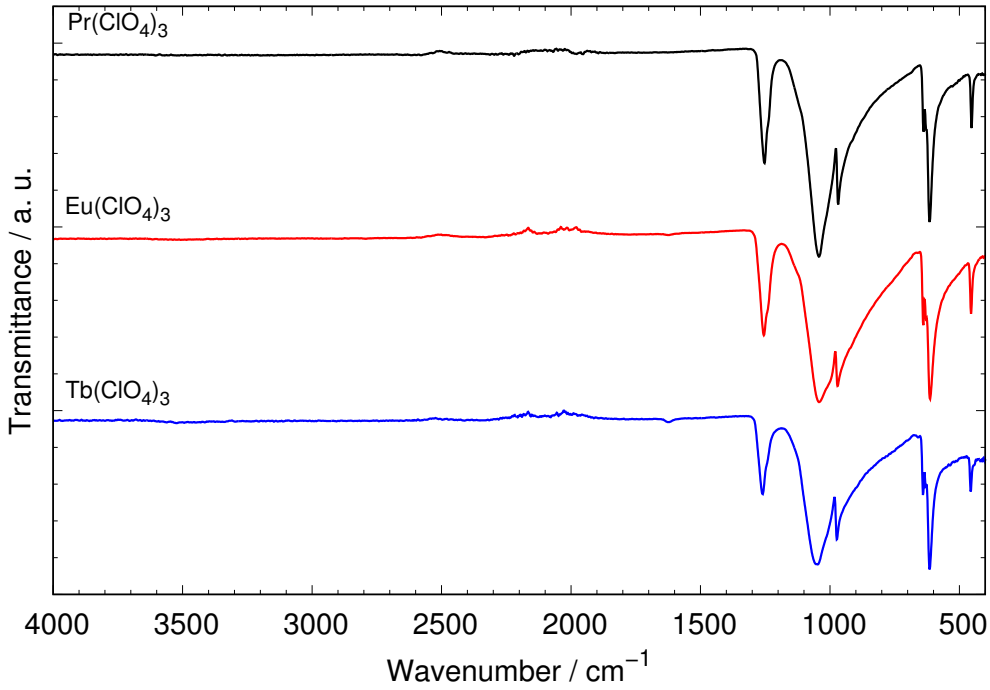


Fig. 66 IR-spectra of lanthanoid perchlorates synthesised in this work. For exp. details see section 6.2.3.

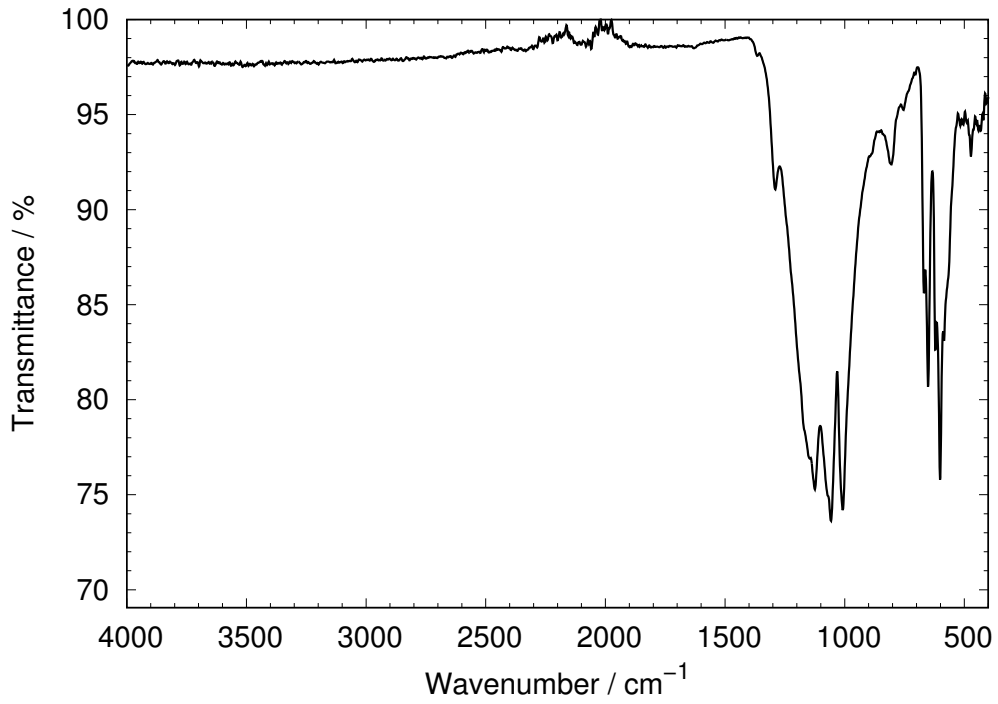


Fig. 67 IR-spectrum of $Pr_2(SO_4)_3$. For exp. details see section 6.2.11.

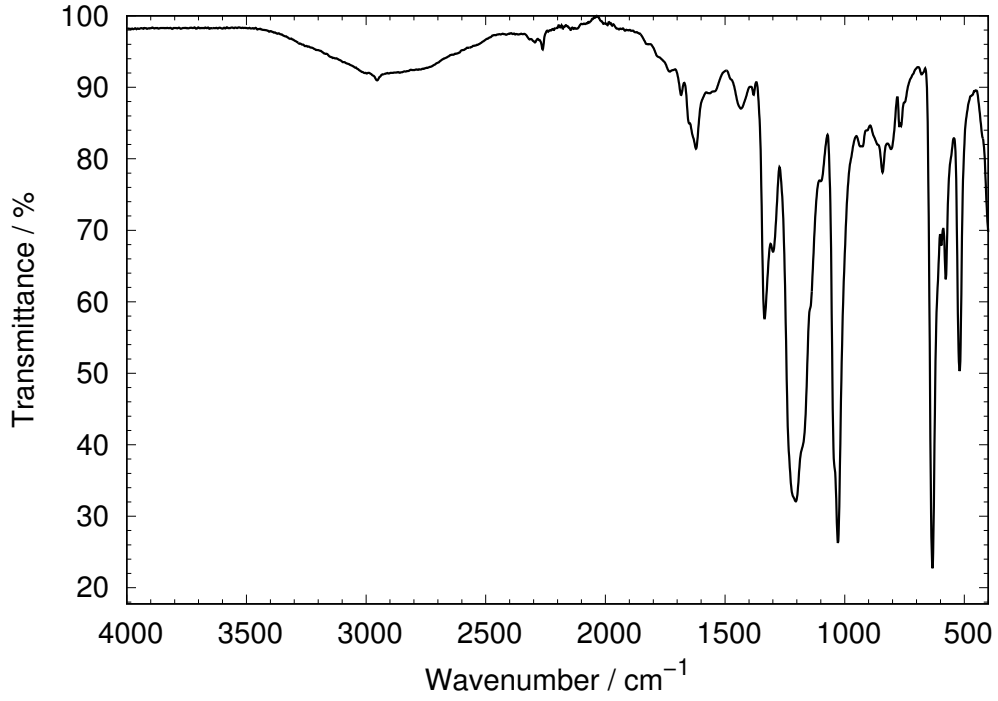


Fig. 68 IR-spectrum of the crude product obtained by reacting $Tb(OTf)_3$ and XeF_2 in acetonitrile. For exp. details see section 6.2.6.

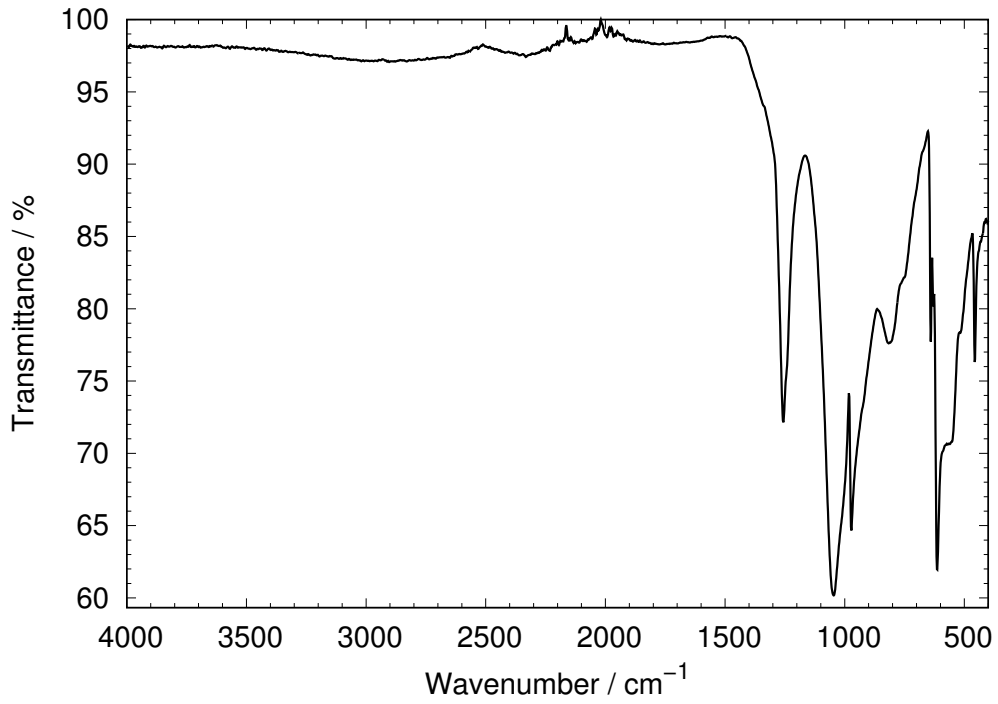


Fig. 69 IR-spectrum of the crude product obtained by reacting $Tb(ClO_4)_3$ and XeF_2 in SO_3. For exp. details see section 6.2.10.

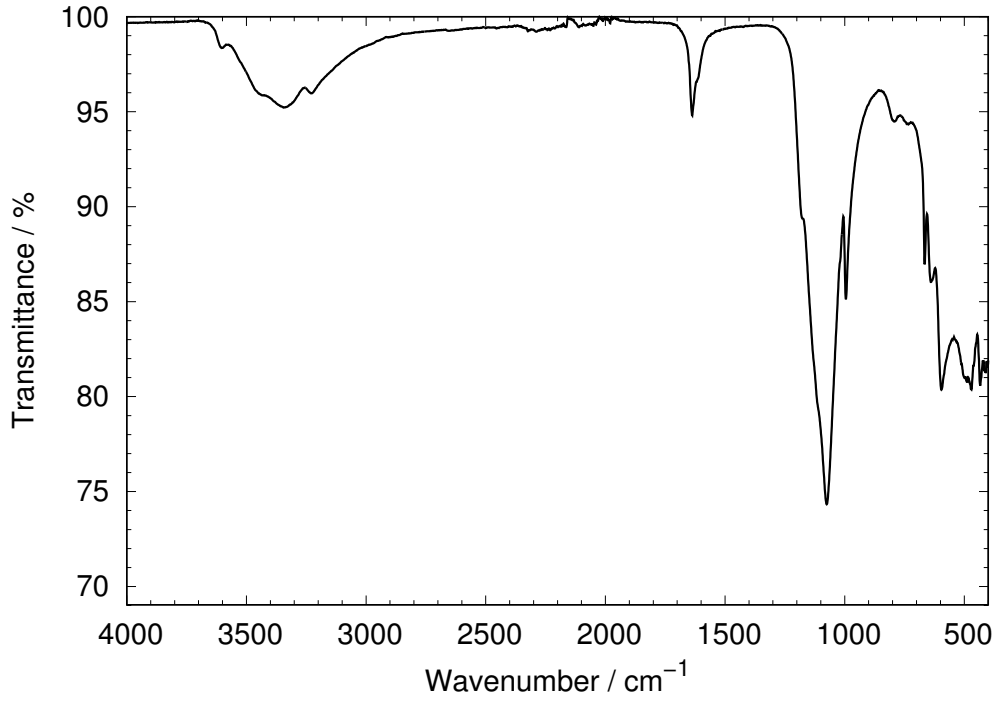


Fig. 70 IR-spectrum of the products obtained by reacting $(TBA)_2S_2O_8$ and $Pr(OTf)_3$ in THF. For experimental details see section 6.2.15.

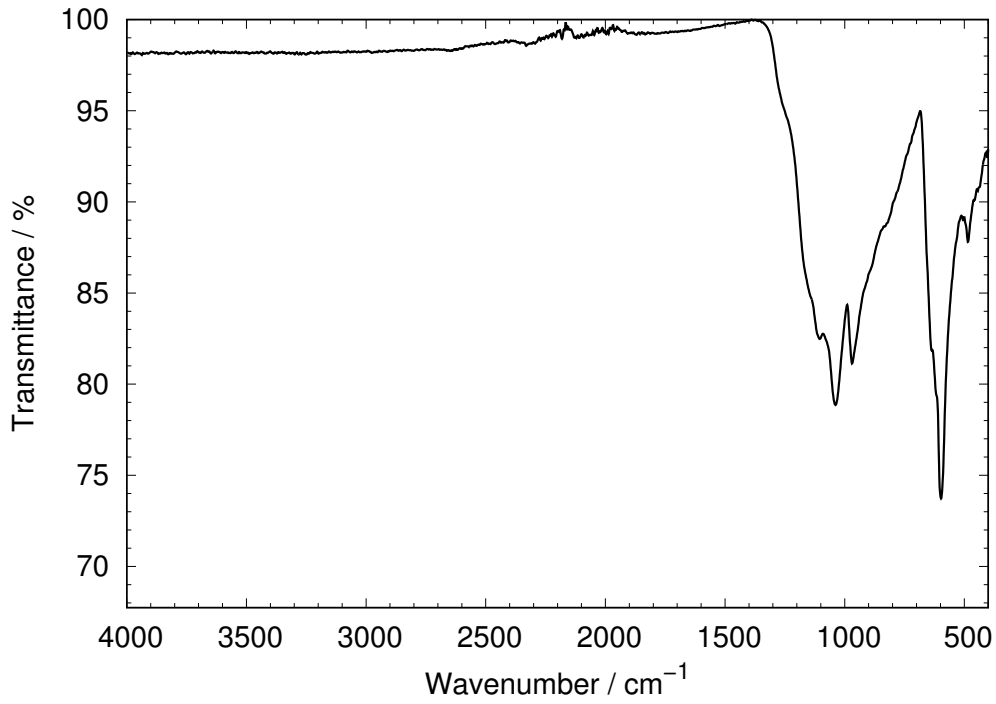


Fig. 71 IR-spectrum of the solids obtained by reacting $K_2S_2O_8$ and $Pr_2(SO_4)_3$ at 11 GPa. For exp. details see section 6.2.16.

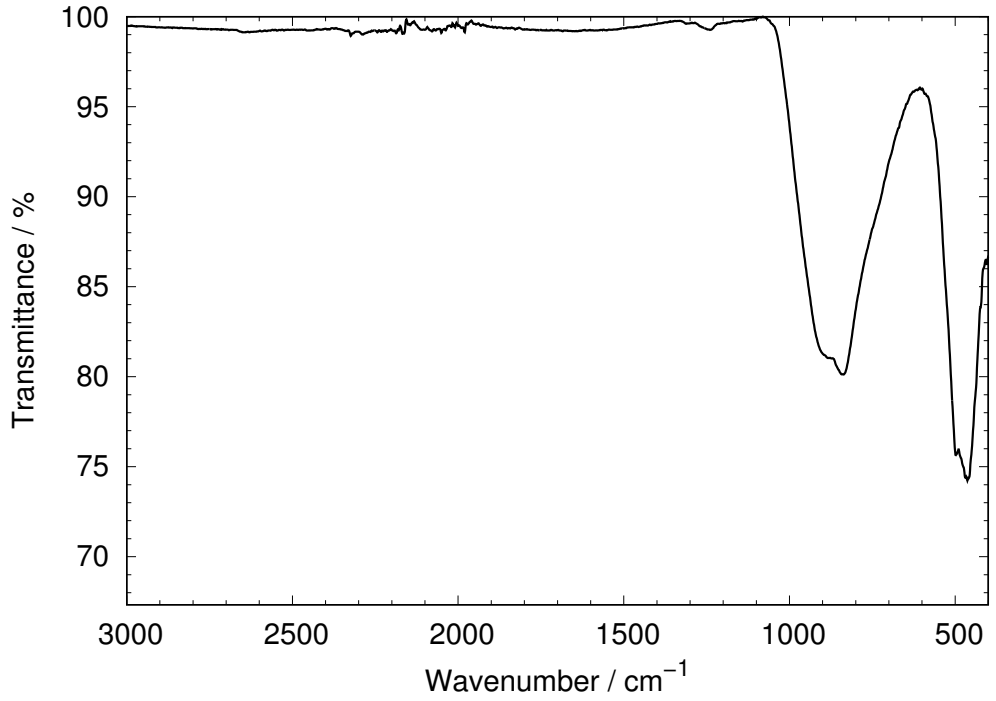


Fig. 72 IR-spectrum of $La_4(SiO_4)_3$. For experimental details see section 6.2.16.

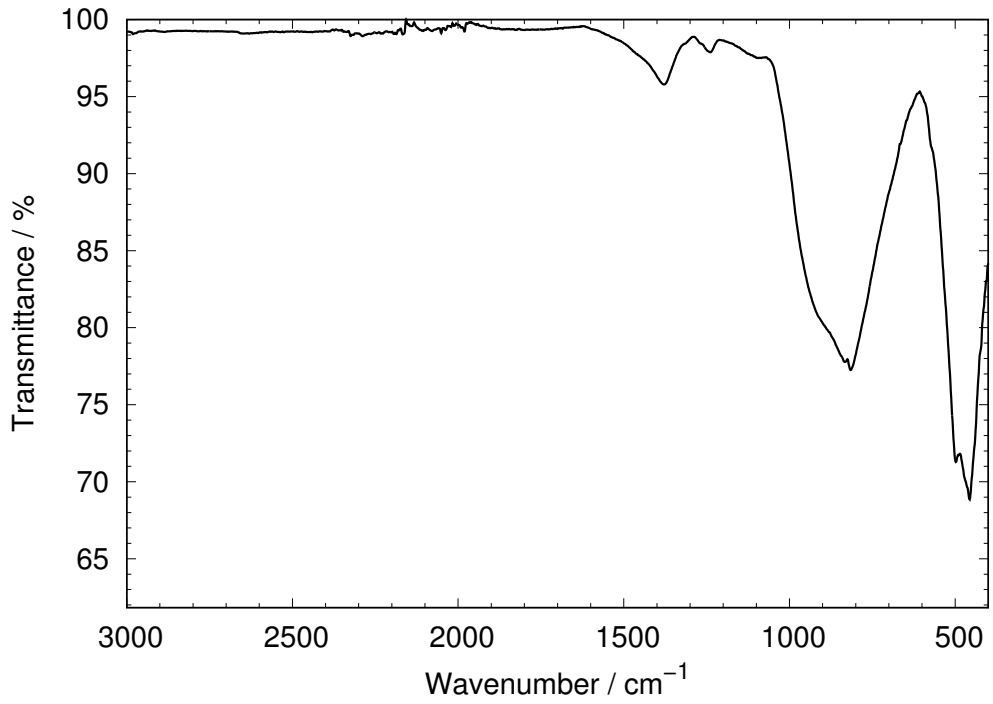


Fig. 73 IR-spectrum of $Nd_4(SiO_4)_3$. For experimental details see section 6.2.16.

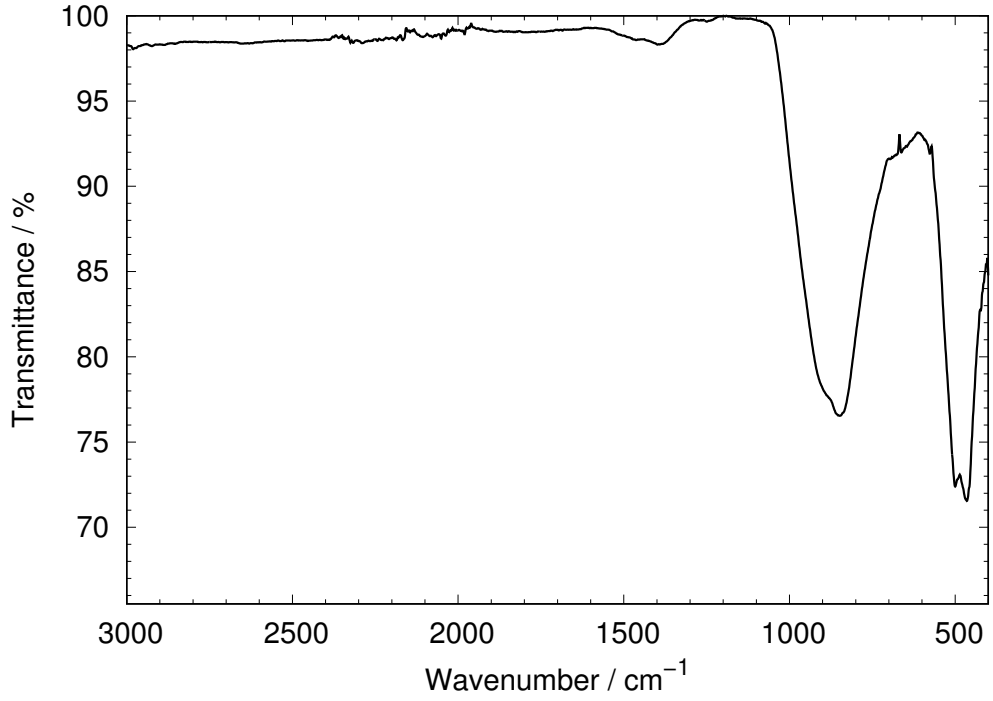


Fig. 74 IR-spectrum of $Pr_4(SiO_4)_3$. For experimental details see section 6.2.16.

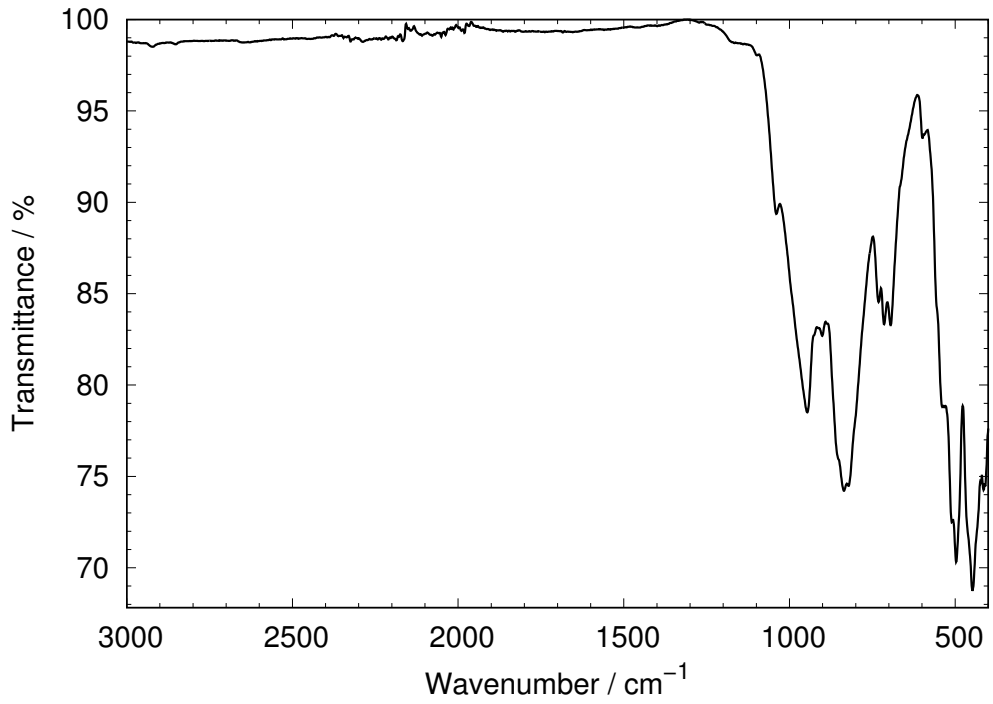


Fig. 75 IR-spectrum of the new polymorph of $Tb_4(SiO_4)(Si_3O_{10})$ (see section 6.2.16 for exp. details).

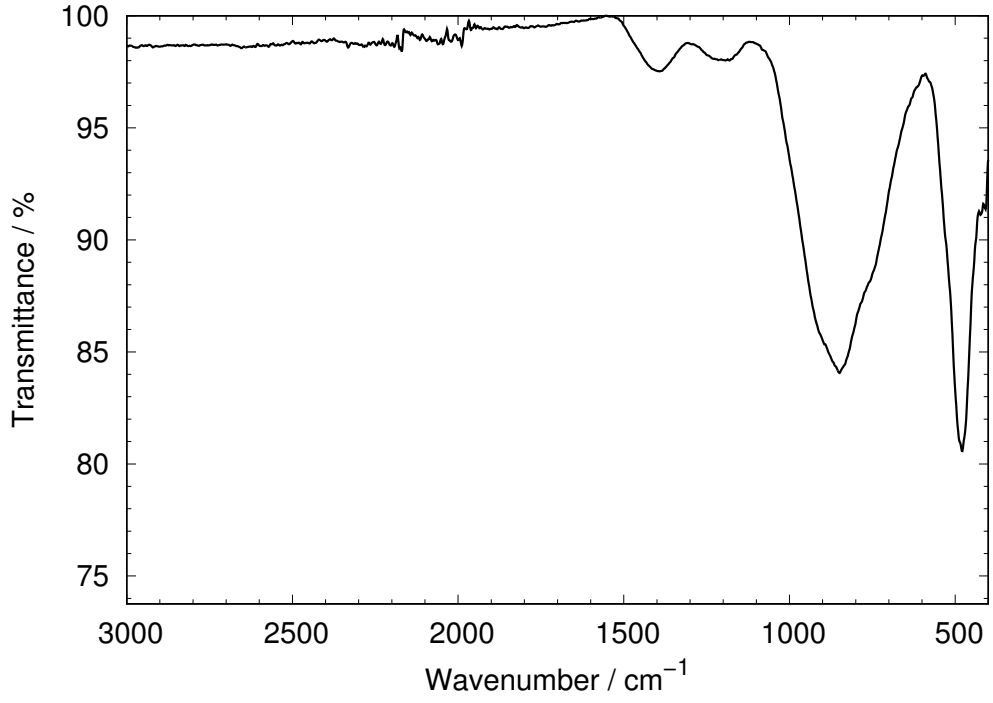


Fig. 76 IR-spectrum of the products obtained by reacting PrO_2, SiO_2 and Na_2O_2 at 11 GPa. See section 6.2.16 for exp. details.

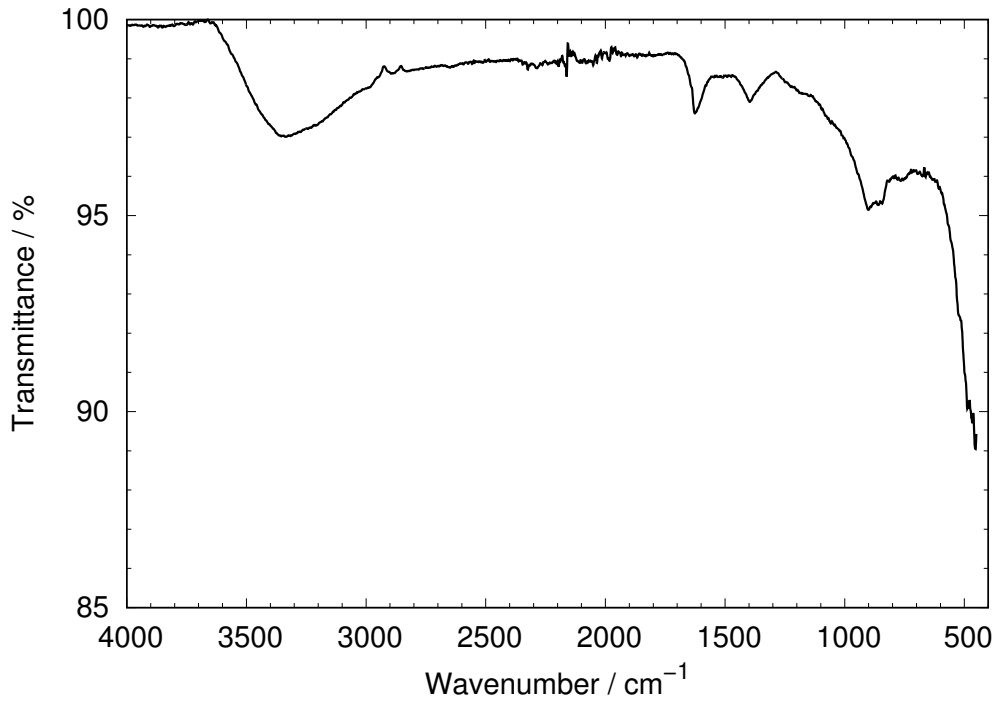


Fig. 77 IR-spectrum of the products obtained by reacting PrO_2, SiO_2 and SrO_2 at 11 GPa. See section 6.2.16 for exp. details.

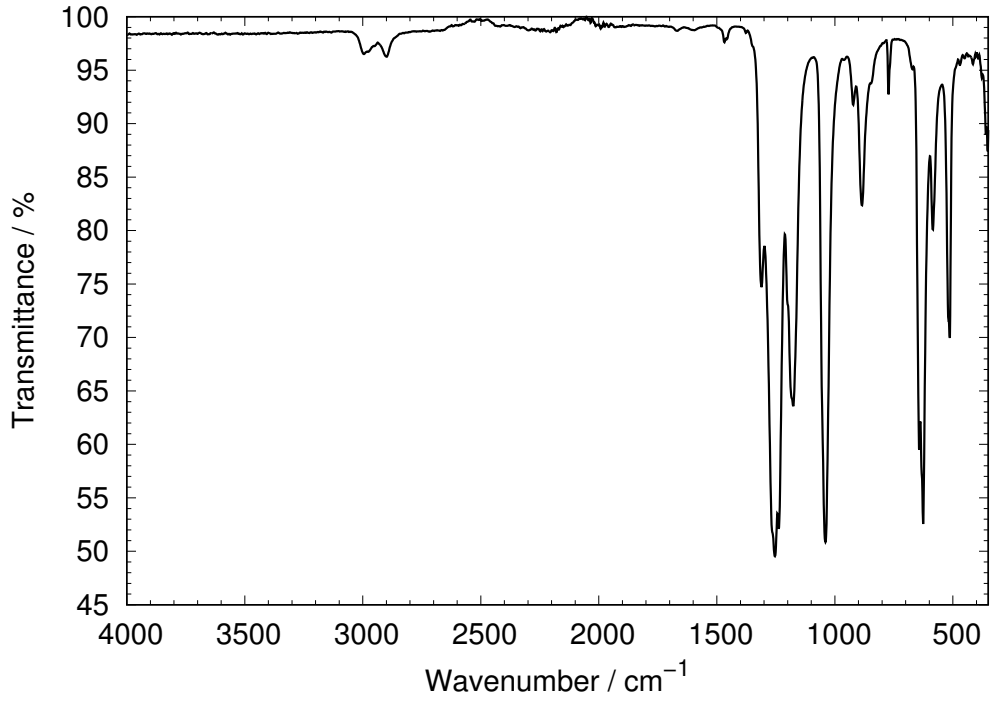


Fig. 78 IR-spectrum of $Eu(OTf)_2(THF)_{1.5}$. For exp. details see section 6.2.21.

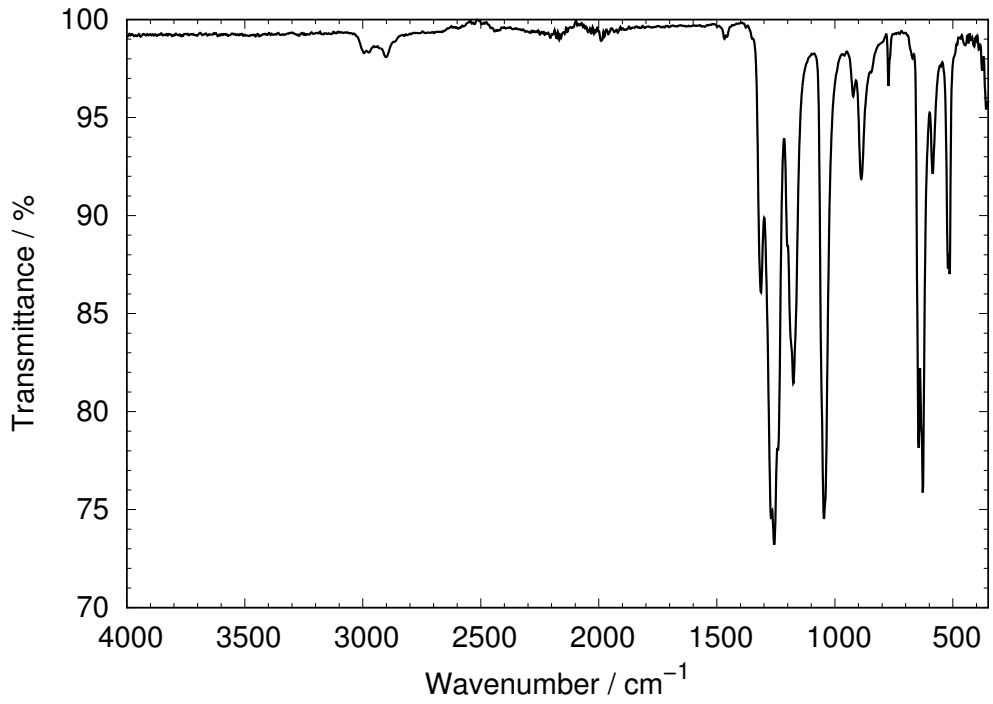


Fig. 79 IR-spectrum of $Sr(OTf)_2(THF)_{1.5}$. For exp. details see section 6.2.22.

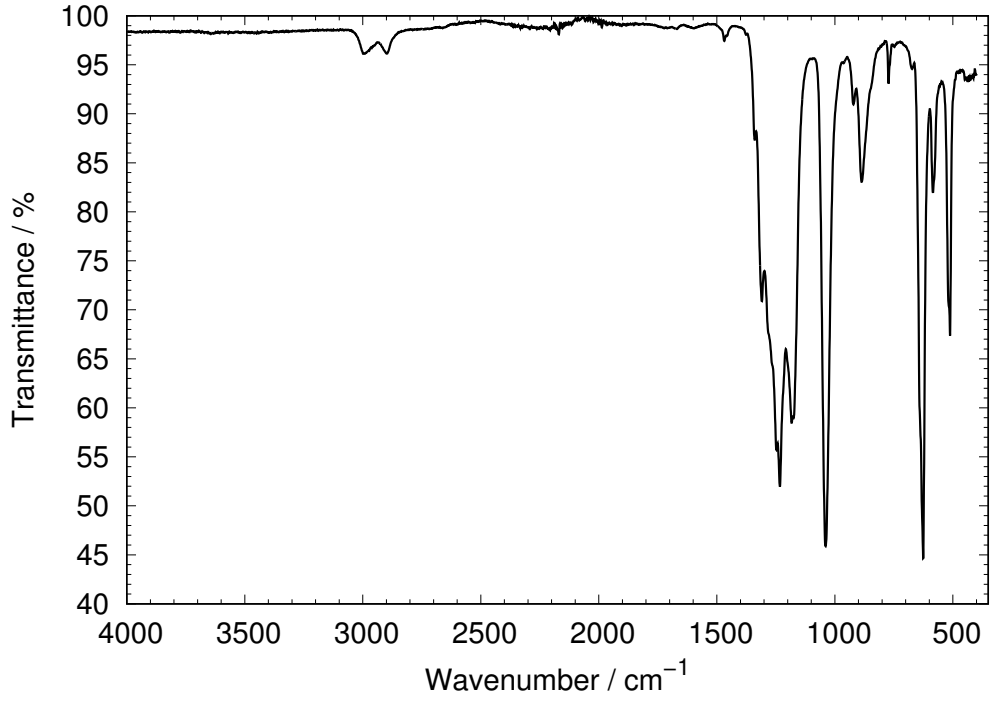


Fig. 80 IR-spectrum of impure $Sm(OTf)_2(THF)_{1.5}$. For exp. details see section 6.2.23.

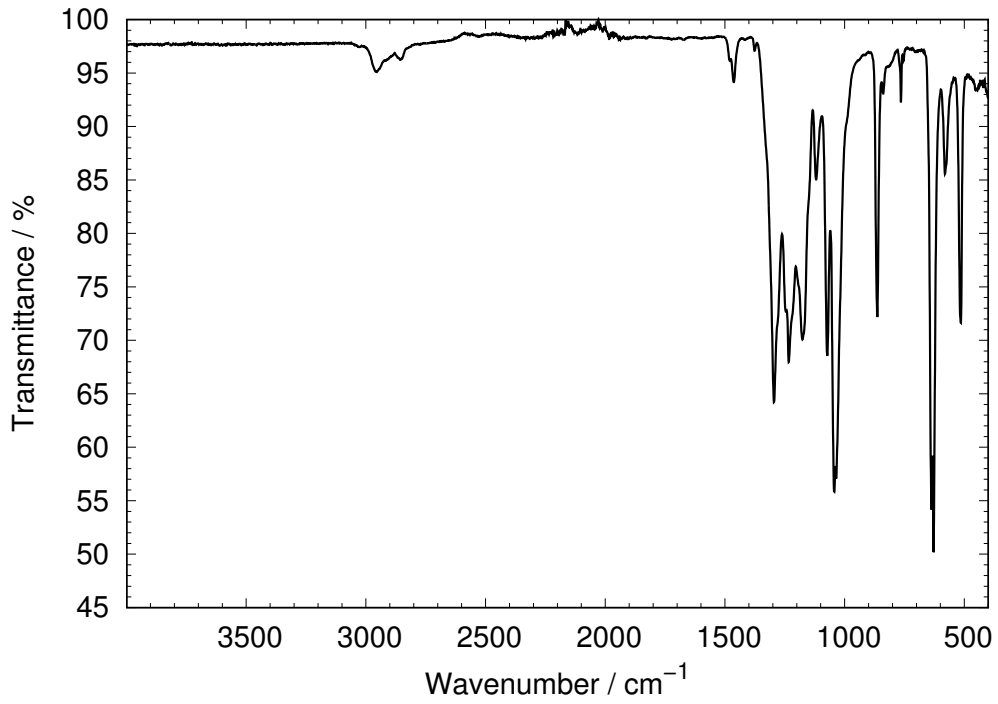


Fig. 81 IR-spectrum of impure $Sm(OTf)_2(DME)_2$. For exp. details see section 6.2.24.

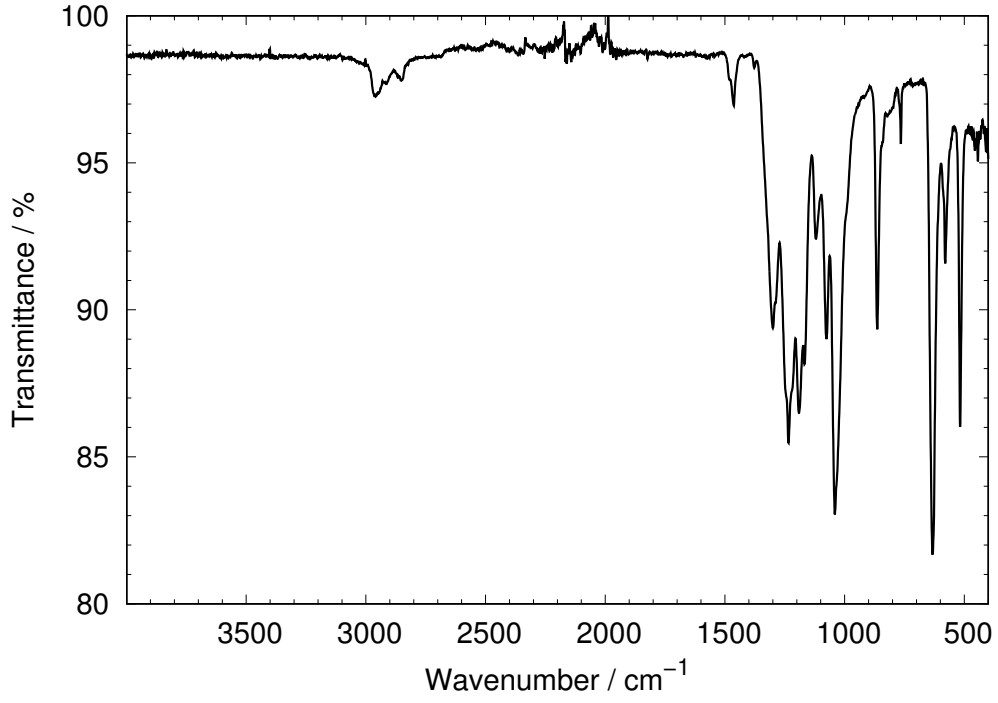


Fig. 82 IR-spectrum of impure $Eu(OTf)_2(DME)_2$. For exp. details see section 6.2.24.

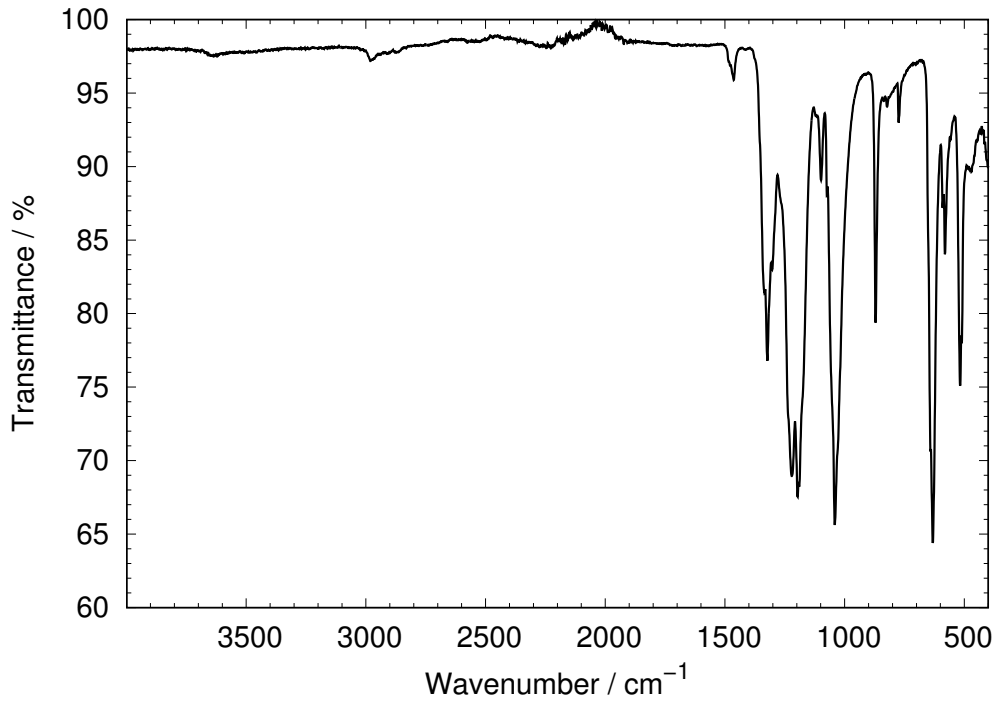


Fig. 83 IR-spectrum of impure $Yb(OTf)_2(DME)_2$. For exp. details see section 6.2.24.

7.2.3 Thermogravimetric Analyses

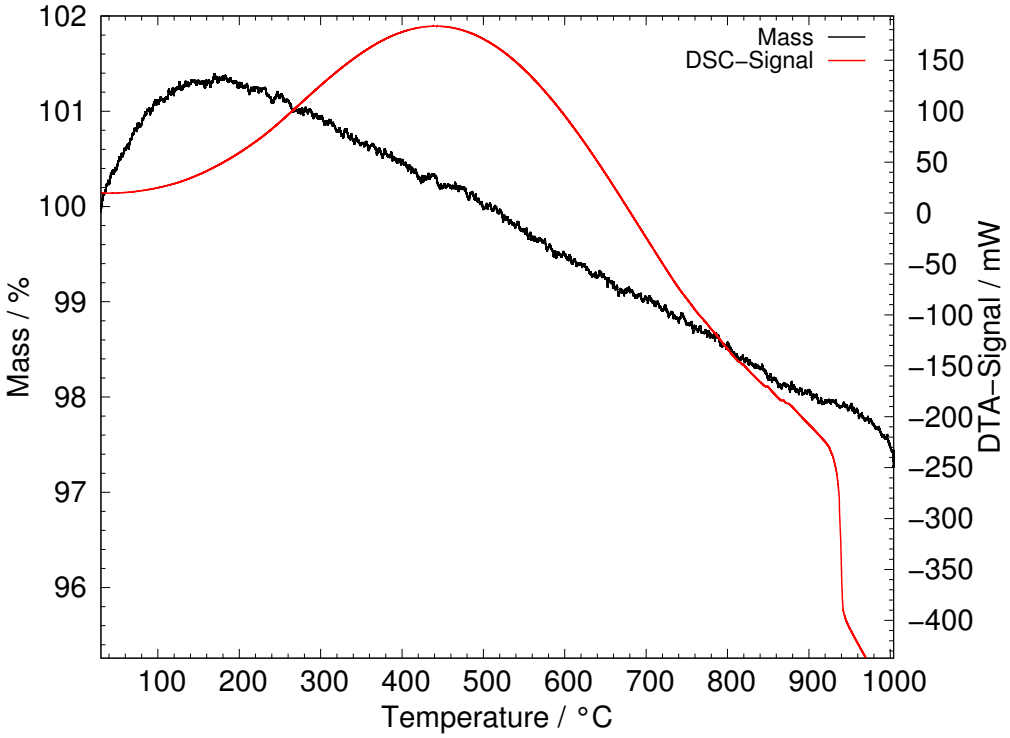


Fig. 84 TGA-DSC of $La_4(SiO_4)_3$ measured in a continuous flow of argon. The temperature was increased with 5 °C /min.

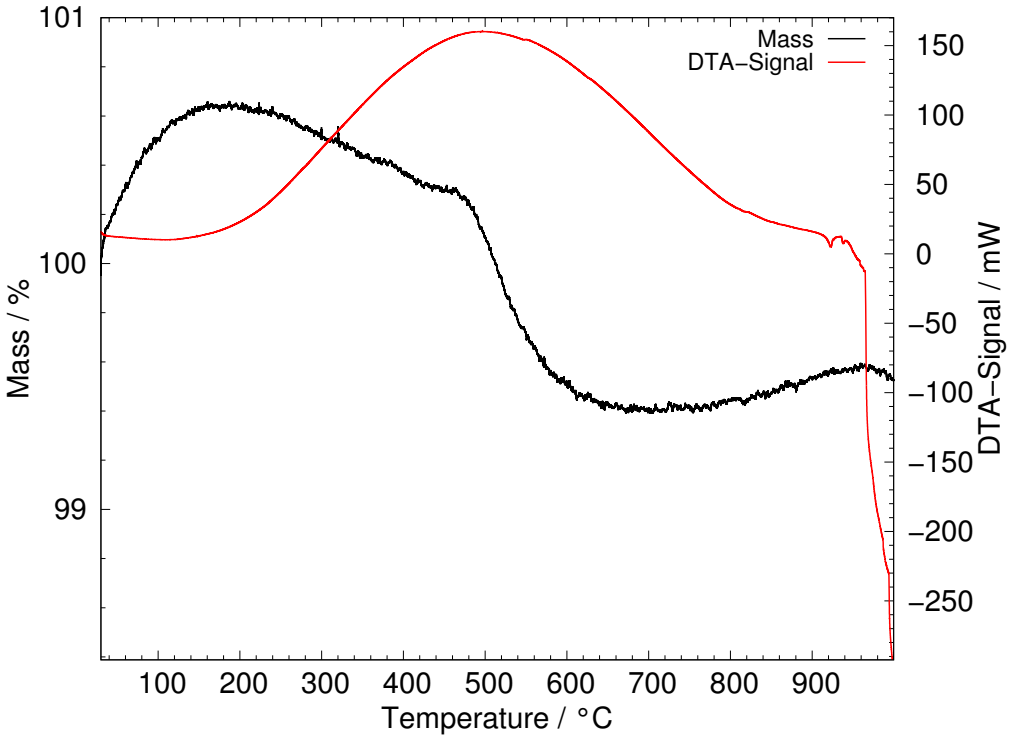


Fig. 85 TGA-DSC of $Nd_4(SiO_4)_3$ measured in a continuous flow of argon. The temperature was increased with 5 °C /min.

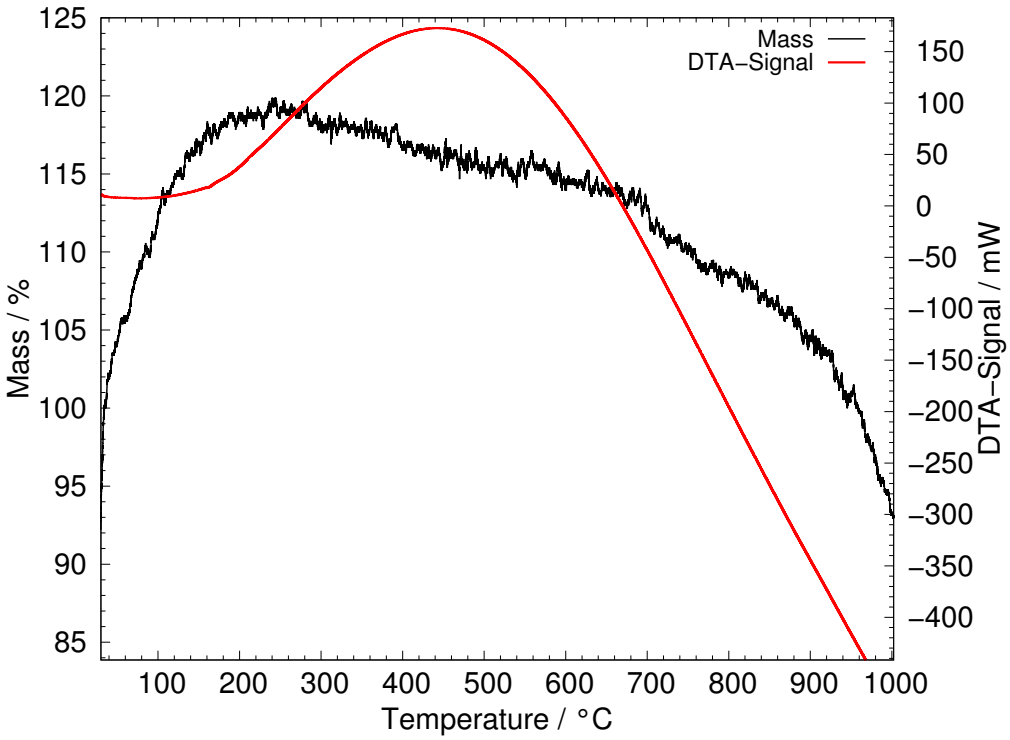


Fig. 86 TGA-DSC of $Pr_4(SiO_4)_3$ measured in a continuous flow of argon. The temperature was increased with 10 °C /min.

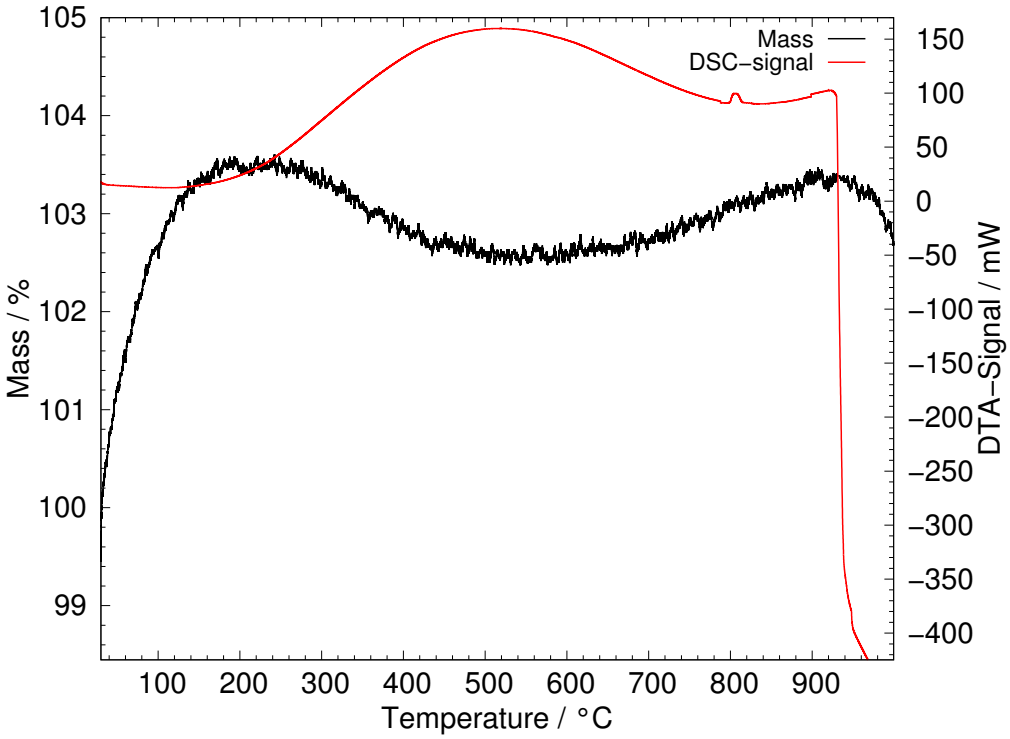


Fig. 87 TGA-DSC of $Tb_4(SiO_4)(Si_3O_{10})$ measured in a continuous flow of argon. The temperature was increased with 5 °C /min.

7.2.4 UV-Vis Spectra

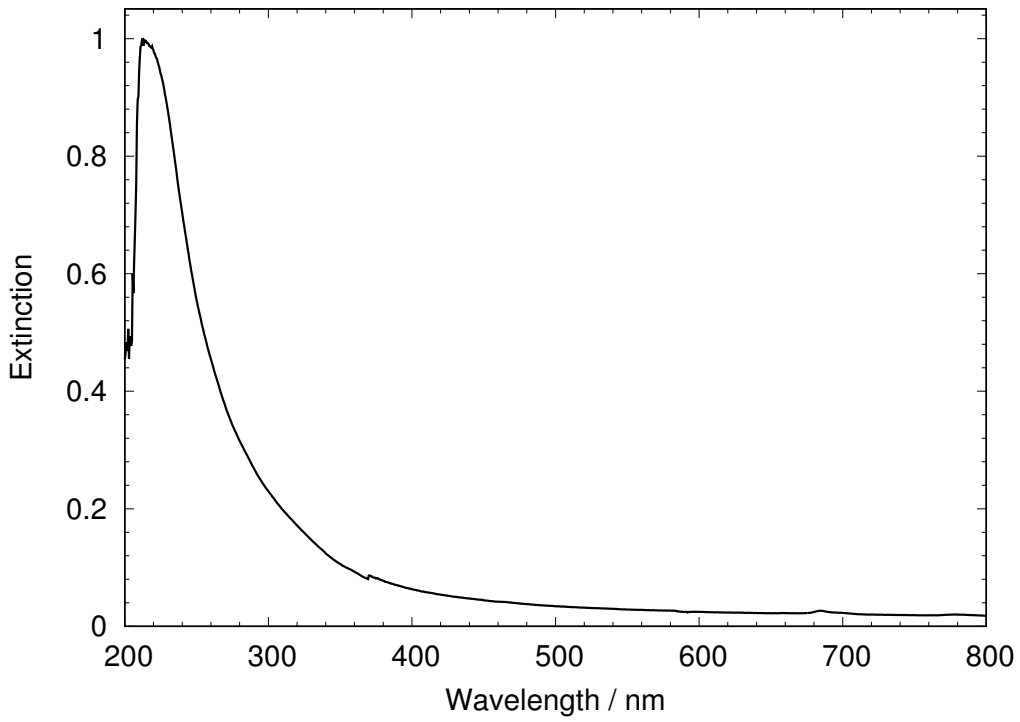


Fig. 88 UV-Vis spectrum of the products from mechanochemical treatment of $Tm(OTf)_3$ with KC_8 measured in acetonitrile (see section 6.2.28 for exp. details.)

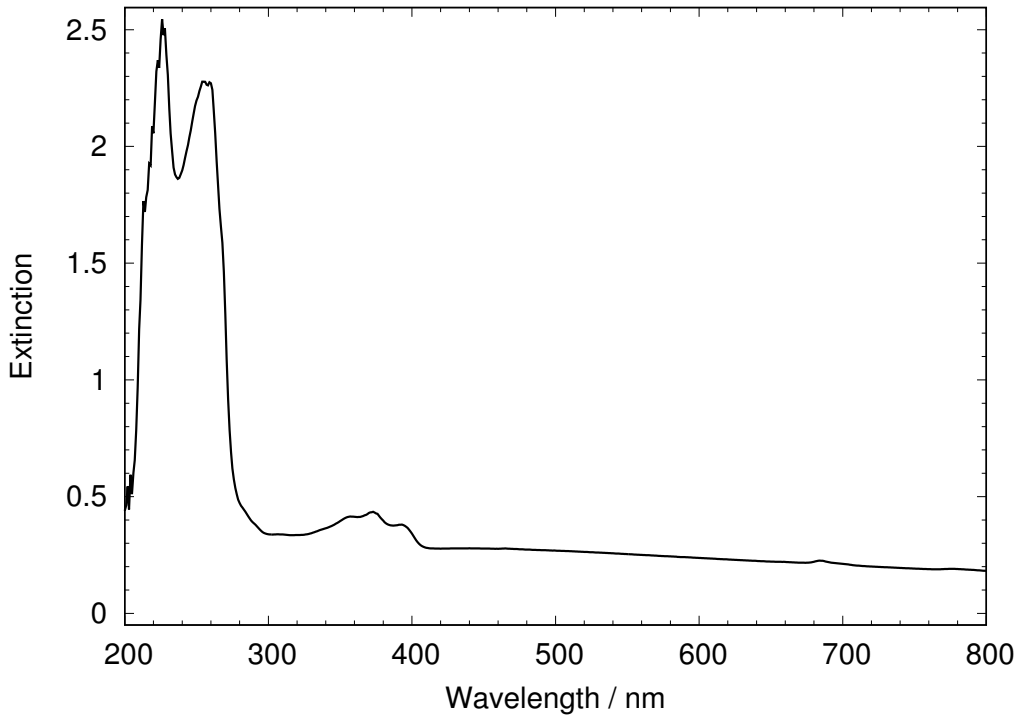


Fig. 89 UV-Vis spectra of the products obtained from attempted mechanochemical comproportionation of $Tm(OTf)_3$ and thulium. See section 6.2.27 for exp. details.

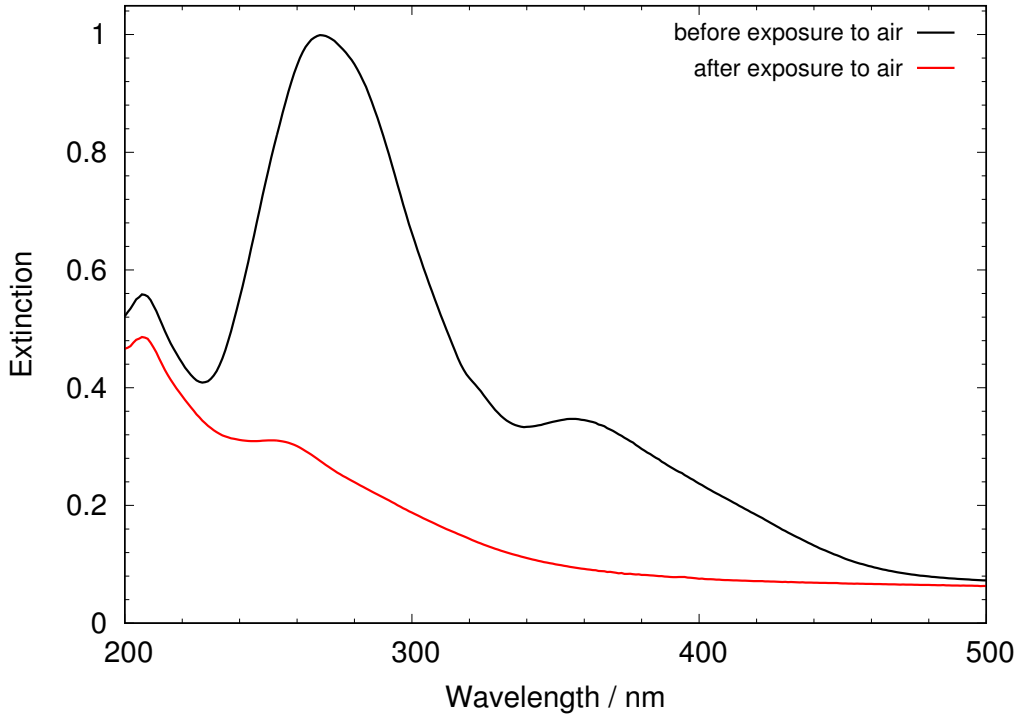


Fig. 90 UV-Vis Spectrum of $Eu(OTf)_2$ obtained from mechanochemical reaction of $Eu(OTf)_3$ and metallic europium. For exp. details see section 6.2.25. The data were measured in THF.

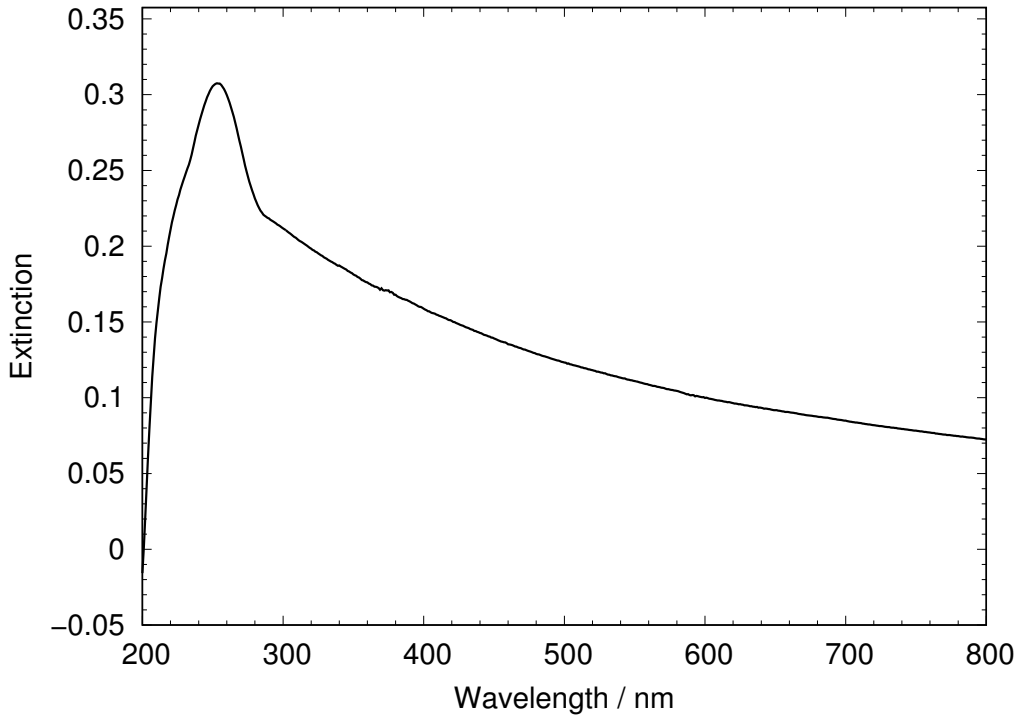


Fig. 91 UV-Vis spectrum of the products from mechanochemical treatment of $Tm(OTf)_3$ with KC_8 measured in acetonitrile. For exp. details refer to section 6.2.31.

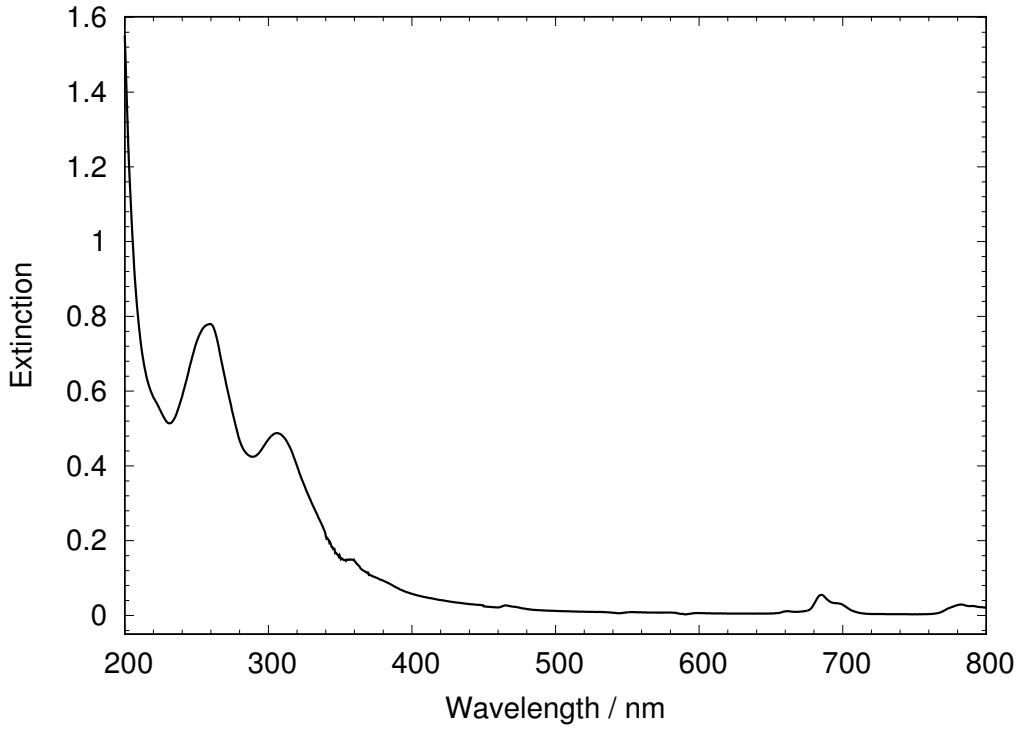


Fig. 92 UV-Vis spectra of products obtained from attempted mechanochemical comproportionation of $Tm(OTf_3)$ and Tm in presence of acetonitrile. See section 6.2.29 for exp. details. The data were collected in acetonitrile as solvent.

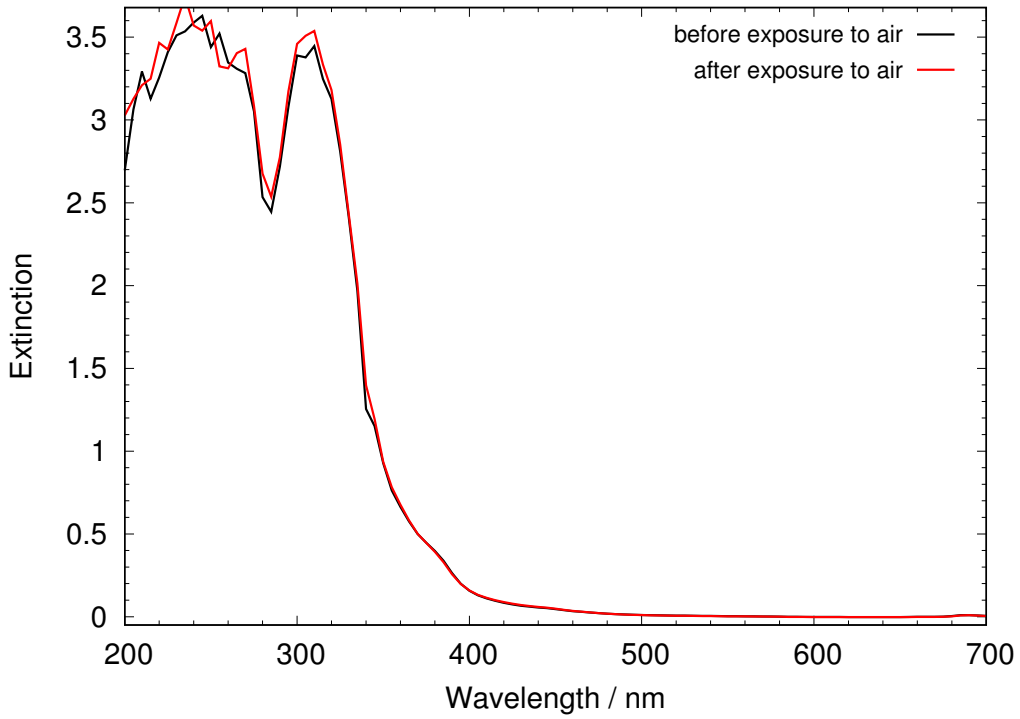


Fig. 93 UV-Vis spectrum of the procucts obtained by treating $Tm(OTf)_3$ with KC_8 in a mixture of DME and acetonitrile. The data were measured in acetonitrile. For exp. data see section 6.2.37.

7.2.5 Luminescence Spectra

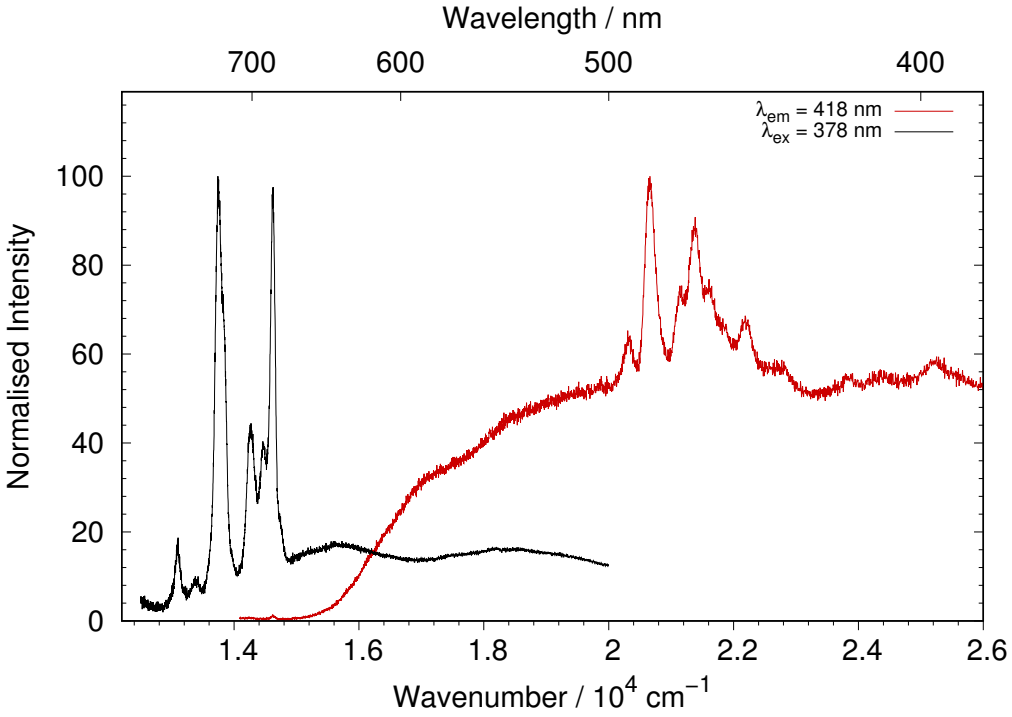


Fig. 94 Luminescence spectrum of $Sm(OTf)_2$ measured at room temperature.

7.2.6 Crystallographic Tables

Tab. 12 Crystallographic data of $Tb(OTf)_3(MeCN)_3$.

Chemical Formula	$C_9H_9F_9N_3O_9S_3Tb$
Molar Mass	729.29 g/mol
Temperature	150.0 K
Crystal System	triclinic
Space Group	$P\bar{1}$
Lattice Parameters	$a = 568.07(4)$ pm
	$b = 1046.38(8)$ pm
	$c = 1910.0(1)$ pm
	$\alpha = 98.533(3)°$
	$\beta = 93.564(2)°$
	$\gamma = 91.541(3)°$
	$V = 1119.86(14) \cdot 10^6$ pm^3
Formula Units	2
Calculated Density	2.163 g/cm^3
Absorption Coefficient	3.558 mm^{-1}
F(000)	700.0
Crystal Size	0.14 × 0.03 × 0.02 mm
Radiation	Mo-Kα_1 (λ = 71.073 pm)
2θ-Range	3.938 to 57.126°
Index Range	$-7 \leq h \leq 7$, $-14 \leq k \leq 14$, $-25 \leq l \leq 25$
Reflections Collected	105841
Absorption Correction	Multi Scan
Independent Reflections	5672 [$R_{int} = 0.0694$, $R_\sigma = 0.0209$]
Data/Restraints/Parameters	5672/0/310
Goodness of Fit	1.193
R_1; wR_2 ($I \geq 2\sigma(I_o)$)	0.0196, 0.0409
R_1; wR_2 (all data)	0.0211, 0.0413
Max./Min. Residual Electron Density	$0.68/-1.37 \cdot 10^{-6}$ e / pm^3

Tab. 13 Crystallographic data of $(NH_4)Pr(SO_4)_2(H_2O)_4$.

Chemical Formula	$H_{12}NO_{12}PrS_2$
Molar Mass	423.14 g/mol
Temperature	150.0 K
Crystal System	monoclinic
Space Group	$P2_1/c$
Lattice Parameters	$a = 665.61(2)$ pm
	$b = 1882.52(9)$ pm
	$c = 878.32(3)$ pm
	$\beta = 97.603(3)°$
	$V = 1090.88(7) \cdot 10^6$ pm^3
Formula Units	4
Calculated Density	2.576 g/cm^3
Absorption Coefficient	4.907 mm^{-1}
F(000)	824.0
Crystal Size	0.1 x 0.1 x 0.1 mm
Radiation	Mo-Kα_1 ($\lambda = 71.073$ pm)
2θ-Range	4.328 to 53.55°
Index Range	$-8 \leq h \leq 8$, $-23 \leq k \leq 23$, $-11 \leq l \leq 11$
Reflections Collected	16301
Absorption Correction	Multi Scan
Independent Reflections	2308 [$R_{int} = 0.0497$, $R_\sigma = 0.0230$]
Data/Restraints/Parameters	2308/12/193
Goodness of Fit	1.068
R_1; wR_2 ($I \geq 2\sigma(I_o)$)	0.0272, 0.0607
R_1; wR_2 (all data)	0.0327, 0.0629
Max./Min. Residual Electron Density	$2.92/-1.64 \cdot 10^{-6}$ e / pm^3

Tab. 14 Crystallographic data of $(TBA)_2S_2O_8$.

Chemical Formula	$C_{16}H_{32}NO_4S$
Molar Mass	963.64 g/mol
Temperature	100.0 K
Crystal System	monoclinic
Space Group	$P2_1/c$
Lattice Parameters	$a = 2274.5(1)$ pm
	$b = 1518.28(9)$ pm
	$c = 2409.9(1)$ pm
	$\beta = 105.959(2)°$
	$V = 8001.4(8) \cdot 10^6$ pm^3
Formula Units	16
Calculated Density	1.103 g/cm^3
Absorption Coefficient	0.177 mm^{-1}
F(000)	2902.0
Crystal Size	0.1 × 0.1 × 0.1 mm
Radiation	Mo-Kα_1 ($\lambda = 71.073$ pm)
2θ-Range	3.944 to 50.698°
Index Range	$-27 \leq h \leq 26$, $-18 \leq k \leq 18$, $-29 \leq l \leq 29$
Reflections Collected	156556
Absorption Correction	Multi Scan
Independent Reflections	14647 [$R_{int} = 0.1853$, $R_\sigma = 0.0988$]
Data/Restraints/Parameters	14647/0/946
Goodness of Fit	1.040
R_1; wR_2 ($I \geq 2\sigma(I_o)$)	0.0772, 0.1992
R_1; wR_2 (all data)	0.1440, 0.2443
Max./Min. Residual Electron Density	$1.03/-0.40 \cdot 10^{-6}$ e / pm^3

Tab. 15 Crystallographic data of $Pr_4(SiO_4)_3$.

Chemical Formula	$O_4Pr_{1.29}Si$
Molar Mass	273.62 g/mol
Temperature	100.0 K
Crystal System	trigonal
Space Group	$R\bar{3}m$
Lattice Parameters	$a = 536.19(3)$ pm
	$c = 1909.8(2)$ pm
	$V = 475.50(7) \cdot 10^6$ pm^3
Formula Units	6
Calculated Density	5.733 g/cm^3
Absorption Coefficient	19.901 mm^{-1}
F(000)	732.0
Crystal Size	0.138 × 0.046 × 0.032 mm
Radiation	Mo-Kα_1 ($\lambda = 71.073$ pm)
2θ-Range	6.4 to 56.518°
Index Range	$-6 \leq h \leq 7$, $-7 \leq k \leq 7$, $-25 \leq l \leq 25$
Reflections Collected	2514
Absorption Correction	Multi Scan
Independent Reflections	169 [$R_{int} = 0.0376$, $R_\sigma = 0.0170$]
Data/Restraints/Parameters	169/0/20
Goodness of Fit	1.178
R_1; wR_2 ($I \geq 2\sigma(I_o)$)	0.0260, 0.0498
R_1; wR_2 (all data)	0.0278, 0.0508
Max./Min. Residual Electron Density	$1.52/-1.42 \cdot 10^{-6}$ e / pm^3

Tab. 16 Crystallographic data of $Tb_4(SiO_4)(Si_3O_{10})$.

Chemical Formula	$O_{14}Si_4Tb_4$
Molar Mass	972.04 g/mol
Temperature	100.0 K
Crystal System	triclinic
Space Group	$P\bar{1}$
Lattice Parameters	$a = 655.61(9)$ pm
	$b = 668.9(1)$ pm
	$c = 2412.3(4)$ pm
	$\alpha = 93.777(6)°$
	$\beta = 90.114(6)°$
	$\gamma = 91.876(6)°$
	$V = 1055.1(3) \cdot 10^6$ pm^3
Formula Units	4
Calculated Density	6.120 g/cm^3
Absorption Coefficient	27.030 mm^{-1}
F(000)	1712.0
Crystal Size	0.2 × 0.2 × 0.5 mm
Radiation	Mo-Kα_1 (λ = 71.073 pm)
2θ-Range	5.078 to 56.604°
Index Range	-8 ≤ h ≤ 8, -8 ≤ k ≤ 8, -32 ≤ l ≤ 32
Reflections Collected	53071
Absorption Correction	Multi Scan
Independent Reflections	5232 [R_{int} = 0.0858, R_σ = 0.0391]
Data/Restraints/Parameters	5232/0/217
Goodness of Fit	1.059
R_1; wR_2 (I≥2σ(I$_o$))	0.0341, 0.0649
R_1; wR_2 (all data)	0.0491, 0.0704
Max./Min. Residual Electron Density	4.07/-2.75 $\cdot 10^{-6}$ e / pm^3

Tab. 17 Crystallographic data of $Yb(OTf)_2(MeCN)_2$.

Chemical Formula	$C_6H_6N_2O_6F_6S_2Yb$
Molar Mass	553.29 g/mol
Temperature	100.0 K
Crystal System	monoclinic
Space Group	$C2/m$
Lattice Parameters	$a = 2520.2(2)$ pm
	$b = 594.65(5)$ pm
	$c = 1039.29(9)$ pm
	$\beta = 99.518(3)°$
	$V = 1536.1(2) \cdot 10^6$ pm^3
Formula Units	4
Calculated Density	2.392 g/cm^3
Absorption Coefficient	6.453 mm^{-1}
F(000)	1040.0
Crystal Size	0.171 × 0.118 × 0.074 mm
Radiation	Mo-Kα_1 ($\lambda = 71.073$ pm)
2θ-Range	3.974 to 50.694°
Index Range	$-30 \leq h \leq 30$, $-7 \leq k \leq 7$, $-12 \leq l \leq 12$
Reflections Collected	34622
Absorption Correction	Multi Scan
Independent Reflections	1554 [$R_{int} = 0.0572$, $R_\sigma = 0.0207$]
Data/Restraints/Parameters	1554/5/141
Goodness of Fit	1.465
R_1; wR_2 ($I \geq 2\sigma(I_o)$)	0.0475, 0.1339
R_1; wR_2 (all data)	0.0475, 0.1340
Max./Min. Residual Electron Density	$2.06/-4.31 \cdot 10^{-6}$ e / pm^3

Tab. 18 Crystallographic data of $Ca(OTf)_2(MeCN)_{0.5}$.

Chemical Formula	$C_6H_3Ca_2F_{12}NO_{12}S_4$
Molar Mass	717.49 g/mol
Temperature	100.0 K
Crystal System	triclinic
Space Group	$P\bar{1}$
Lattice Parameters	$a = 1183.75(8)$ pm
	$b = 1500.54(9)$ pm
	$c = 1506.21(9)$ pm
	$\alpha = 80.520(2)°$
	$\beta = 68.189(2)°$
	$\gamma = 68.725(2)°$
	$V = 2313.2(3) \cdot 10^6$ pm^3
Formula Units	4
Calculated Density	2.060 g/cm^3
Absorption Coefficient	1.004 mm^{-1}
F(000)	1416.0
Crystal Size	0.269 × 0.178 × 0.131 mm
Radiation	Mo-Kα_1 (λ = 71.073 pm)
2θ-Range	4.018 to 70.012°
Index Range	-18 ≤ h ≤ 17, -24 ≤ k ≤ 23, -23 ≤ l ≤ 23
Reflections Collected	73008
Absorption Correction	Numerical
Independent Reflections	16146 [R_{int} = 0.0563, R_σ = 0.0645]
Data/Restraints/Parameters	16146/0/669
Goodness of Fit	1.066
R_1; wR_2 (I≥2σ(I$_o$))	0.0896, 0.2355
R_1; wR_2 (all data)	0.1273, 0.2594
Max./Min. Residual Electron Density	3.06/-1.46 $\cdot 10^{-6}$ e / pm^3

Tab. 19 Crystallographic data of $Ca(OTf)_2(THF)_2$.

Chemical Formula	$C_{10}H_{16}CaF_6O_8S_2$
Molar Mass	482.43 g/mol
Temperature	100.2 K
Crystal System	monoclinic
Space Group	$P2_1/c$
Lattice Parameters	$a = 544.04(5)$ pm
	$b = 1197.7(1)$ pm
	$c = 1450.1(1)$ pm
	$\beta = 99.62(1)°$
	$V = 931.6(2) \cdot 10^6$ pm^3
Formula Units	2
Calculated Density	1.720 g/cm^3
Absorption Coefficient	0.654 mm^{-1}
F(000)	492.0
Crystal Size	0.1 x 0.1 x 0.1 mm
Radiation	Mo-Kα_1 ($\lambda = 71.073$ pm)
2θ-Range	4.436 to 52.958°
Index Range	$-6 \leq h \leq 6$, $-14 \leq k \leq 14$, $-18 \leq l \leq 18$
Reflections Collected	3209
Absorption Correction	Multi Scan
Independent Reflections	3209 [R_{int} =[a], $R_\sigma = 0.4276$]
Data/Restraints/Parameters	3209/6/125
Goodness of Fit	1.206
R_1; wR_2 ($I \geq 2\sigma(I_o)$)	0.1210, 0.2797
R_1; wR_2 (all data)	0.2247, 0.2984
Max./Min. Residual Electron Density	$1.21/-0.85 \cdot 10^{-6}$ e / pm^3

[a] Structure was refined as a two-component twin with the twin law (-1 0 0 0 -1 0 1 0 1).

Tab. 20 Crystallographic data of $Sr(OTf)_2(THF)_{1.5}$.

Chemical Formula	$H_{24}C_{16}F_{12}O_{15}S_4Sr_2$
Molar Mass	963.64 g/mol
Temperature	100.0 K
Crystal System	monoclinic
Space Group	$P2_1/n$
Lattice Parameters	$a = 17.3799(7)$ pm
	$b = 10.1257(2)$ pm
	$c = 20.1552(8)$pm
	$\beta = 109.513(4)°$
	$V = 3343.3(2) \cdot 10^6$ pm^3
Formula Units	4
Calculated Density	1.914 g/cm^3
Absorption Coefficient	3.567 mm^{-1}
F(000)	1856.0
Crystal Size	0.1 × 0.1 × 0.1 mm
Radiation	Mo-Kα_1 ($\lambda = 71.073$ pm)
2θ-Range	3.786 to 50.696°
Index Range	$-20 \leq h \leq 20$, $-12 \leq k \leq 12$, $-24 \leq l \leq 24$
Reflections Collected	217176
Absorption Correction	Multi Scan
Independent Reflections	6113 [$R_{int} = 0.3240$, $R_\sigma = 0.0631$]
Data/Restraints/Parameters	6113/851/653
Goodness of Fit	1.213
R_1; wR_2 ($I \geq 2\sigma(I_o)$)	0.0790, 0.1739
R_1; wR_2 (all data)	0.0920, 0.1789
Max./Min. Residual Electron Density	$0.94/-0.62 \cdot 10^{-6}$ e / pm^3

Tab. 21 Crystallographic data of $Sm(OTf)_2(DME)_2$.

Chemical Formula	$C_{10}H_{20}SmF_6O_{10}S_2$
Molar Mass	628.73 g/mol
Temperature	100.0 K
Crystal System	monoclinic
Space Group	$I2/a$
Lattice Parameters	$a = 1198.05(7)$ pm
	$b = 1075.37(6)$ pm
	$c = 1889.4(1)$ pm
	$\beta = 99.7(5)°$
	$V = 2128.9(2) \cdot 10^6$ pm^3
Formula Units	4
Calculated Density	1.962 g/cm^3
Absorption Coefficient	3.049 mm^{-1}
F(000)	1232.0
Crystal Size	0.136 × 0.095 × 0.036 mm
Radiation	Mo-Kα_1 ($\lambda = 71.073$ pm)
2θ-Range	4.52 to 56.56°
Index Range	$-23 \leq h \leq 25$, $-14 \leq k \leq 14$, $-15 \leq l \leq 15$
Reflections Collected	21458
Absorption Correction	Multi Scan
Independent Reflections	2648 [$R_{int} = 0.0440$, $R_\sigma = 0.0249$]
Data/Restraints/Parameters	2648/0/180
Goodness of Fit	1.054
R_1; wR_2 ($I \geq 2\sigma(I_o)$)	0.0280, 0.0678
R_1; wR_2 (all data)	0.0308, 0.0697
Max./Min. Residual Electron Density	$1.57/-0.58 \cdot 10^{-6}$ e / pm^3

Tab. 22 Crystallographic data of $Eu(OTf)_2(DME)_2$.

Chemical Formula	$C_{10}H_{20}EuF_6O_{10}S_2$
Molar Mass	630.34 g/mol
Temperature	100.0 K
Crystal System	monoclinic
Space Group	$I2/a$
Lattice Parameters	$a = 1198.73(7)$ pm
	$b = 1072.22(7)$ pm
	$c = 1668.8(3)$ pm
	$\beta = 99.51(1)°$
	$V = 2115.4(2) \cdot 10^6$ pm^3
Formula Units	4
Calculated Density	1.979 g/cm^3
Absorption Coefficient	3.257 mm^{-1}
F(000)	1236.0
Crystal Size	0.1 x 0.1 x 0.1 mm
Radiation	Mo-Kα_1 ($\lambda = 71.073$ pm)
2θ-Range	4.534 to 56.564°
Index Range	$-25 \leq h \leq 25$, $-14 \leq k \leq 14$, $-15 \leq l \leq 15$
Reflections Collected	15615
Absorption Correction	Multi Scan
Independent Reflections	2626 [$R_{int} = 0.0390$, $R_\sigma = 0.0262$]
Data/Restraints/Parameters	2626/0/186
Goodness of Fit	1.071
R_1; wR_2 ($I \geq 2\sigma(I_o)$)	0.0249, 0.0570
R_1; wR_2 (all data)	0.0275, 0.0586
Max./Min. Residual Electron Density	$0.95/-0.55 \cdot 10^{-6}$ e / pm^3

Tab. 23 Crystallographic data of $Yb(OTf)_2(DME)_2$.

Chemical Formula	$C_{10}H_{20}YbF_6O_{10}S_2$
Molar Mass	649.40 g/mol
Temperature	100.0 K
Crystal System	monoclinic
Space Group	$I2/a$
Lattice Parameters	$a = 1191.01(7)$ pm
	$b = 1078.43(9)$ pm
	$c = 1827.39(9)$ pm
	$\beta = 102.103(6)°$
	$V = 2082.2(2) \cdot 10^6$ pm^3
Formula Units	4
Calculated Density	2.072 g/cm^3
Absorption Coefficient	4.788 mm^{-1}
F(000)	1256.0
Crystal Size	0.34 × 0.07 × 0.04 mm
Radiation	Mo-Kα_1 ($\lambda = 71.073$ pm)
2θ-Range	4.536 to 56.578°
Index Range	$-24 \leq h \leq 24$, $-14 \leq k \leq 14$, $-15 \leq l \leq 15$
Reflections Collected	22084
Absorption Correction	Multi Scan
Independent Reflections	2593 [$R_{int} = 0.0487$, $R_\sigma = 0.0258$]
Data/Restraints/Parameters	2593/10/186
Goodness of Fit	1.168
R_1; wR_2 ($I \geq 2\sigma(I_o)$)	0.0310, 0.0745
R_1; wR_2 (all data)	0.0325, 0.0753
Max./Min. Residual Electron Density	$1.99/-3.46 \cdot 10^{-6}$ e / pm^3

Tab. 24 Crystallographic data of $Pr(ClO_4)_3(MeCN)_4$.

Chemical Formula	$C_8H_{12}N_4O_{12}Cl_3Pr$
Molar Mass	603.48 g/mol
Temperature	100.0 K
Crystal System	minoclinic
Space Group	Cc
Lattice Parameters	$a = 1201.6(3)$ pm
	$b = 1071.1(2)$ pm
	$c = 1583.4(3)$ pm
	$\beta = 105.464(5)°$
	$V = 1964.2(7) \cdot 10^6$ pm^3
Formula Units	4
Calculated Density	2.041 g/cm^3
Absorption Coefficient	2.953 mm^{-1}
F(000)	1176.0
Crystal Size	0.119 × 0.068 × 0.05 mm
Radiation	Mo-Kα_1 ($\lambda = 71.073$ pm)
2θ-Range	5.18 to 67.076°
Index Range	$-18 \leq h \leq 18$, $-15 \leq k \leq 16$, $-24 \leq l \leq 22$
Reflections Collected	48974
Absorption Correction	Multi Scan
Independent Reflections	6559 [$R_{int} = 0.2359$, $R_\sigma = 0.1733$]
Data/restraints/parameters	6559/2/257
Goodness of Fit	1.228
R_1; wR_2 ($I \geq 2\sigma(I_o)$)	0.1104, 0.2079
R_1; wR_2 (all data)	0.1553, 0.2229
Max./Min. Residual Electron Density	1.15/-2.52 $\cdot 10^{-6}$ e / pm^3
Flack Parameter	-0.02(5)

Tab. 25 Crystallographic data of $Eu(ClO_4)_3(MeCN)_4$.

Chemical Formula	$C_8H_{12}N_4O_{12}Cl_3Eu$
Molar Mass	614.53 g/mol
Temperature	100.0 K
Crystal System	monoclinic
Space Group	Cc
Lattice Parameters	$a = 1201.56(2)$ pm
	$b = 1068.27(1)$ pm
	$c = 1572.70(2)$ pm
	$\beta = 105.575(2)°$
	$V = 1944.58(5) \cdot 10^6$ pm^3
Formula Units	4
Calculated Density	2.099 g/cm^3
Absorption Coefficient	3.703 mm^{-1}
F(000)	1192.0
Crystal Size	0.1 × 0.1 × 0.1 mm
Radiation	Mo-Kα_1 (λ = 71.073 pm)
2θ-Range	5.19 to 72.44°
Index Range	-16 ≤ h ≤ 19, -17 ≤ k ≤ 17, -24 ≤ l ≤ 25
Reflections Collected	90690
Absorption Correction	Multi-Scan
Independent Reflections	7575 [R_{int} = 0.0729, R_σ = 0.0338]
Data/restraints/parameters	7575/2/234
Goodness of Fit	1.269
R_1; wR_2 (I≥2σ(I$_o$))	0.0842, 0.2161
R_1; wR_2 (all data)	0.0850, 0.2163
Max./Min. Residual Electron Density	8.74/-12.55 · 10^{-6} e / pm^3
Flack Parameter	0.057(7)

8 References

[1] G. Tessitore, G. A. Mandl, S. L. Maurizio, M. Kaur, J. A. Capobianco, *RSC Adv.* **2023**, *13*, 17787-17811.

[2] A. A. Yaroshevsky, *Geochem. Int.* **2006**, *44*, 48-55.

[3] E. Fluck, *Pure Appl. Chem.* **1988**, *60*, 431-436.

[4] J.-B. Lu, D. C. Cantu, M.-T. Nguyen, J. Li, V.-A. Glezakou, R. Rousseau, *J. Chem. Theory Comput.* **2019**, *15*, 5987-5997.

[5] P. Pyykko, *Chem. Rev.* **1988**, *88*, 563-594.

[6] J.-C. G. Bünzli, C. Piguet, *Chem. Soc. Rev.* **2005**, *34*, 1048-1077.

[7] J.-C. G. Bünzli, *Acc. Chem. Res.* **2006**, *39*, 53-61.

[8] R. Reisfeld, *AIMS Mater.* **2015**, *2*, 37-60.

[9] I. D. Hughes, M. Däne, A. Ernst, W. Hergert, M. Lüders, J. Poulter, J. B. Staunton, A. Svane, Z. Szotek, W. M. Temmerman, *Nature*, **2007**, *446*, 650-653.

[10] L. Sorace, C. Benelli, D. Gatteschi, *Chem. Soc. Rev.* **2011**, *40*, 3092-3104.

[11] J. Luzon, R. Sessoli, *Dalton Trans.* **2012**, *41*, 13556-13567.

[12] D. N. Woodruff, R. E. P. Winpenny, R. A. Layfield, *Chem. Rev.* **2013**, *113*, 5110-5148.

[13] J.-C. G. Bünzli, S. Comby, A.-S. Chauvin, C. D. B. Vandevyver, *J. Rare Earths* **2007**, *25*, 257-274.

[14] G. Charalampides, K. I. Vatalis, B. Apostoplos, B. Ploutarch-Nikolas, *Procedia Econ. Financ.* **2015**, *24*, 126-135.

[15] J.-C. G. Bünzli, *Eur. J. Inorg. Chem.*, **2017**, *44*, 5058-5063.

[16] J. A. Cotruvo Jr., *ACS Cent. Sci.* **2019**, *5*, 1496–1506.

[17] V. Balaram, *Geosc. Front.* **2019**, *10*, 1285-1303.

[18] L. J. Nugent, R. D. Baybarz, J. L. Burnett, J. L. Ryan, *J. Inorg. Nucl. Chem* **1971**, *33*, 2503-2530.

[19] L. R. Morss, *Chem. Rev.* **1976**, *76*, 827–841.

[20] W. C. Martin, R. Zalubas, L. Hagan, *Atomic Energy Levels: The Rare-Earth Elements*, Department of Commerce, National Bureau of Standards, Institute for Basic Standards, Gaithersburg, **1978**.

[21] P. F. Lang, B. C. Smith, *J. Chem. Educ.* **2010**, *87*, 875-881.

[22] T. P. Gompa, A. Ramanathan, N. T. Rice, H. S. La Pierre, *Dalton Trans.*, **2020**, *49*, 15945-15987.

[23] K. Binnemans in *Handbook on the Physics and Chemistry of the Rare Earths*, Vol. 36 (Eds.: K. A. Gschneidner Jr. J.-C. G. Bunzli,V. K. Pecharsky), Elsevier Science, Amsterdam, **2006**, pp. 281-392.

[24] Y.-M. W-H. Leung, *Coord. Chem. Rev.* **2017**, *340*, 172-197.

[25] Goldschmidt, V. M. Thomassen, L. *Skr. Nor. Vidensk. Akad. Oslo*, **1923**, *5*, 1–48.

[26] R. Schmidt, B. G. Müller, *Z. Anorg. Allg. Chem.* **1999**, *625*, 605-608.

[27] D. L. Rogachev, M. A. Porai-Koshits, V. Ya. Kuznetsov, L. M. Dikareva, *J. Struct. Chem.* **1974**, *15*, 397-401.

[28] J. M. S. Skakle, C. L. Dickson, F. P. Glasser, *Powder Diffr.* **2000**, *15*, 234-238.
[29] T. A. Beineke, J. Delgaudio, *Inorg. Chem.* **1968**, *7*, 715-721.
[30] R. Anwander, M. Dolg, F. T. Edelmann, *Chem. Soc. Rev.* **2017**, *46*, 6697-6709.
[31] A. Ramanathan, J. Kaplan, D.-C. Sergentu, J. A. Branson, M. Ozerov, A. I. Kolesnikov, S. G. Minasian, J. Autschbach, J. W. Freeland, Z. Jiang, M. Mourigal, H. S. La Pierre, *Nat. Commun.* **2023**, *14*, 3134.
[32] H. A. Pagel, P. H. M.-P. Brinton, *J. Am. Chem. Soc.* **1929**, *51*, 42-54.
[33] D. M. Gruen, W. C. Koehler, J. J. Katz, *J. Am. Chem. Soc.* **1951**, *73*, 1475-1479.
[34] G. Brauer, B. Pfeiffer, *J. Less Common Met.* **1963**, *5*, 171-176.
[35] W. Klemm, P. Henkel, *Z. Anorg. Allg. Chem.* **1934**, *220*, 180-182.
[36] B. B. Cunningham, D. C. Feay, M. A. Rollier, *J. Am. Chem. Soc.* **1954**, *76*, 3361-3363.
[37] J. Soriano, M. Givon, J. Shamir, *Inorg. Nucl. Chem.* **1966**, *2*, 13-14.
[38] V. I. Spitzin, L. I. Martynenko, Y. U. M. Kiselev, *Z. Anorg. Allg. Chem.* **1982**, *495*, 39-51.
[39] Y. M. Kiselev, V. B. Sokolov, *Zh. Neorg. Khim.* **1984**, *29*, 857-859.
[40] E. Zintl, W. Morawietz, *Z. anorg. allg. Chemie* **1940**, *245*, 26-31.
[41] R. Hoppe, W. Lidecke, *Naturwissenschaften* **1962**, *49*, 255.
[42] E. Paletta, R. Hoppe, *Naturwissenschaften* **1966**, *53*, 611-612.
[43] K. Seeger, R. Hoppe, *Naturwissenschaften* **1968**, *55*, 297.
[44] H. Brunn, R. Hoppe, *Z. Anorg. Allg. Chem.* **1977**, *433*, 189-199.
[45] R. Wolf, R. Hoppe, *Z. Anorg. Allg. Chem.* **1985**, *522*, 39-47.
[46] R. Wolf, R. Hoppe, *J. Solid State Chem.* **1987**, *70*, 12-18.
[47] R. Wolf, R. Hoppe, *Z. Anorg. Allg. Chem.* **1988**, *556*, 97-108.
[48] R. Hoppe, W. Liebe, *Z. Anorg. Allg. Chem.* **1961**, *313*, 221-227.
[49] K.-M Rödder, R. Hoppe, *Z. Anorg. Allg. Chem.* **1961**, *312*, 277-281.
[50] K.-M Rödder, R. Hoppe, *Z. Anorg. Allg. Chem.* **1961**, *312*, 277-281.
[51] L. B. Asprey, T. K. Keenan, *J. Inorg. Nucl. Chem.* **1961**, *16*, 260-262.
[52] L. B. Asprey, J. S. Coleman M. J. Reisfield in *Lanthanide/Actinide Chemistry*, Vol. 71 (Eds.: P. R. Fields, T. Moeller), ACS, New York, **1967**, pp. 122-126.
[53] A. Delaigue, J. C. Cousseins, *Rev. Chim. Miner.* **1972**, *9*, 789-798.
[54] Y. Laligant, A. Le Bail, G. Férey, D. Avignant, J. C. Cousseins, *Eur. J. Solid State Inorg. Chem.* **1988**, *25*, 551-563.
[55] A. Hoffmann, *Naturwissenschaften* **1934**, *22*, 206.
[56] A. J. Jacobson, B. C. Tofield, B. E. F. Fender, *Acta Cryst.* **1972**, *B28*, 956-961.
[57] Y. Hinatsu, M. Itoh, N. Edelstein, *J. Solid State Chem.* **1997**, *132*, 337-341.
[58] A. Saiki, Y. Seto, H. Seki, H. Ishizawa, M. Kato, *Nippon Kagaku Kaishi* **1991**, *1*, 25-31.
[59] S. W. Pajakoff, *Monatsh. Chem.* **1963**, *94*, 482-496.
[60] S. W. Pajakoff, *Monatsh. Chem.* **1963**, *94*, 527-529.
[61] S. W. Pajakoff, *Monatsh. Chem.* **1964**, *95*, 1002-1004.
[62] S. W. Pajakoff, *Monatsh. Chem.* **1966**, *97*, 733-743.
[63] S. W. Pajakoff, *Monatsh. Chem.* **1968**, *99*, 484-500.

[64] G. Meyer, *Prog. Solid State Chem.* **1982**, *14*, 141-219.
[65] K. Fulle, L. D. Sanjeewa, C. D. McMillen, Y. Wen, A. C. Rajamanthrilage, J. N. Anker, G. Chumanov, J. W. Kolis, *Inorg. Chem.* **2017**, *56*, 6044-6047.
[66] G. Morrison, N. Spagnuolo, S. G. Karakalos, H.-C. zur Loye, *Inorg. Chem.* **2019**, *58*, 8702-8709.
[67] C. T. Palumbo, I. Zivkovic, R. Scopelliti, M. Mazzanti, *J. Am. Chem. Soc.* **2019**, *141*, 9827-9831.
[68] N. T. Rice, I. A. Popov, D. R. Russo, J. Basca, E. R. Batista, P. Yang, J. Telser, H. S. La Pierre, *J. Am. Chem. Soc.* **2019**, *141*, 13222-13233.
[69] A. R. Willauer, C. T. Palumbo, R. Scopeletti, I. Zivkovic, I. Douair, L. Maron, M. Mazzanti, *Angew. Chem. Int. Ed.* **2020**, *59*, 3549-3553.
[70] A. R. Willauer, C. T. Palumbo, F. Fadaei-Tirani, Ivica Zivkovic, I. Douair, L. Maron, M. Mazzanti, *J. Am. Chem. Soc.* **2020**, *142*, 5538-5542.
[71] N. T. Rice, I. A. Popov, D. R. Russo, T. P. Gompa, A. Ramanathan, J. Bacsa, E. R. Batista, P.Yang, H. S. La Pierre, *Chem. Sci.* **2020**, *11*, 6149-6159.
[72] A. R. Willauer, I. Douair, A.-S. Chauvin, F. Fadaei-Tirani, J.-C. G. Bünzli, L. Maron, M. Mazzanti, *Chem. Sci.* **2022**, *13*, 681-691.
[73] T. Vent-Schmidt, Z. Fang, Z. Lee, D. Dixon, S. Riedel, *Chem. Eur. J.* **2016**, *22*, 2406-2416.
[74] L. B. Asprey in *Rare Earth Research*, (Eds.: E. V. Kleber), MacMillan, New York, **1961**.
[75] L. P. Varga, L. B. Asprey, *J. Chem. Phys.* **1968**, *49*, 4674-4679.
[76] G. H. Dieke, *Spectra and Energy Levels of Rare Earth Ions in Crystals*, Interscience Publishers, New York, **1968**.
[77] B. M. van der Ende, L. Aerts, A. Meijerink, *Phys. Chem. Chem. Phys.* **2009**, *11*, 11081-11095.
[78] P. Dorenbos, *J. Phys.: Condens. Matter* **2003**, *15*, 575.
[79] M. Suta, C. Wickleder, *J. Lumin.* **2019**, *210*, 210-238.
[80] J. Becquerel, *Phys. Z.* **1907**, *8*, 632-643.
[81] J. H. Van Vleck, *J. Chem. Phys.* **1937**, *5*, 556-568.
[82] J. H. Van Vleck, *J. Phys. Chem.* **1937**, *41*, 67-80.
[83] X. Qin, X. Liu, W. Huang, M. Bettinelli, X. Liu, *Chem. Rev.* **2017**, *117*, 4488-4527.
[84] L. J. Nugent, R. D. Baybarz, J. L. Burnett, J. L. Ryan, *J. Phys. Chem.* **1973**, *77*, 1528-1539.
[85] G. Beck, W. Nowacki, *Naturwissenschaften* **1938**, *26*, 495-496.
[86] O. Greis, T. Petzel, *Z. Anorg. Allg. Chem.* **1974**, *403*, 1-22.
[87] N. Kunkel, A. Meijerink, H. Kohlmann, *Inorg. Chem.* **2014**, *53*, 4800-4802.
[88] C. Buyer, T. Schleid, *Acta Cryst.* **2021**, *A77*, C1036.
[89] G. Meyer, N. Gerlitzki, S. Hammerich, *J. Alloys Compd.* **2004**, *380*, 71-78.
[90] G. Meyer, *Chem. Rev.* **1988**, *88*, 93-107.
[91] J. D. Corbett, *Rev. Chim. Miner.* **1973**, *10*, 239-257.
[92] J. Felsche, *Naturwissenschaften* **1971**, *58*, 218-219.

[93] C. Funk, J. Koehler, I. Lazar, D. Kajewski, K. Roleder, J. Nuss, A. Bussmann-Holder, H. Bamberger, J. van Slageren, D. Enseling, T. Jüstel, T. Schleid, *Cryst. Growth Des.* **2018**, *18*, 6316-6325.

[94] I. Mayer, E. Levy, A. Glasner, *Acta Cryst.* **1964**, *17*, 1071-1072.

[95] Y. G. Denisenko, A. E. Sedykh, A. S. Oreshonkov, M. S. Molokeev, N. O. Azarapin, E. I. Sal'nikova, O. D. Chimitova, O. V. Andreev, I. A. Razumkova, K. Müller-Buschbaum, *Eur. J. Inorg. Chem.* **2022**, e202200043.

[96] N. T. Flosbach, Master Thesis, University of Cologne (DE), **2020**.

[97] K. Mashima, T. Oshiki, K. Tani, *J. Org. Chem.* **1998**, *63*, 7114-7116.

[98] M. Xémard, A. Jaoul, M. Cordier, F. Molton, O. Cador, B. Le Guennic, C. Duboc, O. Maury, C. Clavaguéra, G. Nocton, *Angew. Chem. Int. Ed.* **2017**, *56*, 4266-4271.

[99] D. Polcari, P. Dauphin-Ducharme, J. Mauzeroll, *Chem. Rev.* **2016**, *116*, 13234-13278.

[100] N. Elgrishi, K. J. Rountree, B. D. McCarthy, E. S. Rountree, T. T. Eisenhart, J. L. Dempsey, *J. Chem. Educ.* **2018**, *95*, 197-206.

[101] S. Tang, A.-V. Mudring, *Cryst. Growth Des.* **2011**, *11*, 1437-1440.

[102] J. Bruns, D. van Gerven, *Angew. Chem. Int. Ed.* **2016**, *128*, 8253-8256.

[103]] C. L. Schmidt, PhD Thesis, Max-Planck-Institute Stuttgart (DE), **2009**.

[104] B. Eriksson, L. O. Larsson, L. Niinisto, *Inorg. Chem.* **1974**, *13*, 290-295.

[105] C. J. Kepert, P. C. Junk, B. W. Skelton, A. H. White, *Aust. J. Chem.* **1999**, *52*, 601-616.

[106] A. Trzesowska, R. Kruszynski, *Acta Cryst.* **2006**, *E62*, i169-i172.

[107] M. Boujelben, M. Toumi, T. Mhiri, *Acta Cryst.* **2007**, *E63*, i144-i145.

[108] S. G. Yang, J. P. Hwang, M. Y. Park, K. Lee, Y. H. Kim, *Tetrahedron* **2007**, *63*, 5184-5188.

[109] P. A. Degtyarev, L. M. Kovba, A. N. Pokrovskii, *Krstallografiya* **1978**, *23*, 840-843.

[110] M. Anenburg, A. D. Burnham, J. L. Hamilton, *Am. Mineral.* **2020**, *105*, 1802-1811.

[111] X. Liu, M. E. Fleet, *J. Phys: Condens. Matter* **2002**, *14*, 11223.

[112] M. E. Fleet, X. Liu, *J. Solid State Chem.* **2005**, *178*, 3275-3283.

[113] A. M. Srivastava, *J. Lumin.* **2016**, *169*, 445-449.

[114] J. Felsche, *Naturwissenschaften* **1972**, *59*, 35-36.

[115] A. N. Christensen, A. F. Jensen, B. K. Themsen, R. G. Hazell, M. Hanfland, E. Dooryhee, *Acta Chem. Scand.* **1997**, *51*, 1178-1185.

[116] H. Müller-Bunz, T. Schleid, *Z. Anorg. Allg. Chem.* **2000**, *626*, 2549-2556.

[117] M. E. Fleet, X. Liu, *Acta Cryst.* **2000**, *B56*, 940-946.

[118] I. Hartenbach, F. Lissner, T. Schleid, *Z. Naturforsch. B* **2003**, *58*, 925-927.

[119] M. E. Fleet, X. Liu, *Z. Kristallogr.* **2003**, *218*, 795-801.

[120] R. J. C. Locke, M. Weis, T. Schleid, *IUCrData* **2023**, *8*, x230591.

[121] M. J. Tribelhorn, M. E. Brown, *Thermochim. Acta* **1995**, *255*, 143-154.

[122] T. A. Rafter, *Analyst* **1950**, *75*, 475-492.

[123] K. -J. Range, M. Stadler, F. Rau, U. Klement, *Angew. Chem. Int. Ed.* **1987**, *26*, 1174-1175.

[124] S. Brieger, Bachelor Thesis, University of Cologne (DE), **2021**.

[125] R. Dinnebier, N. Sofina, L. Hildebrandt, M. Jansen, *Acta Cryst.* **2006**, *B62*, 467-473.

[126] R. D. Shannon, *Acta Cryst.* **1976**, *A32*, 751-767.

[127] S. Fukuzawa, K. Mutoh, T. Tsuchimoto, T. Hiyama, *J. Org. Chem.* **1996**, *61*, 5400-5405.

[128] T. G. Müller, J. Mogk, M. Conrad, F. Kraus *Eur. J. Inorg. Chem.* **2016**, 4162-4169.

[129] K. Rosenstengel, A. Schulz, O. Niehaus, O. Janka, R. Pöttgen, A. Villinger, *Eur. J. Inorg. Chem.* **2018**, 778-790.

[130] O. Reckeweg, A. Simon, *Z. Naturforsch. B* **2003**, *58*, 1097-1104.

[131] D. Walker, M. A. Carpenter, C. M. Hitch, *Am. Mineral.* **1990**, *75*, 1020-1028.

[132] D. Walker, *Am. Mineral.* **1991**, *76*, 1092-1100.

[133] H. Huppertz, *Z. Kristallogr.* **2004**, *219*, 330-338.

[134] C. Schädle, C. Meermann, K. W. Törnroos, R. Anwander, *Eur. J. Inorg. Chem* **2010**, 2841-2852.

[135] M. S. Wickleder, W. Schäfer, *Z. Anorg. Allg. Chem.* **1999**, *625*, 309-312.

[136] M. S. Wickleder, *Z. Anorg. Allg. Chem.* **1999**, *625*, 11-12.

[137] J. D. Bernal, E. Djatlowa, I. Kasarnowsky, S. Reichstein, A. G. Ward, *Z. Kristallogr. – Cryst. Mater.* **1935**, *92*, 344-354.

[138] B. A. Maksimov, M. I. Sirota, R. V. Galiulin, B. P. Sobolev, *Kristallografiya* **1985**, *30*, 284-289.

[139] A. Hirsch, P. Kegler, I. Alencar, J. Ruiz-Fuertes, A. Shelyug, L. Peters, C. Schreinemachers, A. Neumann, S. Neumeier, H.-P. Liermann, A. Navrotsky, G. Roth, *J. Solid State Chem.* **2017**, *245*, 82-88.

[140] D. Guerard, P. Lagrange, A. Herold, *Mat. Sci Eng.* **1977**, *31*, 29-32.

Eidesstattliche Erklärung

Hiermit versichere ich an Eides statt, dass ich die vorliegende Dissertation selbstständig und ohne die Benutzung anderer als der angegebenen Hilfsmittel und Literatur angefertigt habe. Alle Stellen, die wörtlich oder sinngemäß aus veröffentlichten und nicht veröffentlichten Werken dem Wortlaut oder dem Sinn nach entnommen wurden, sind als solche kenntlich gemacht. Ich versichere an Eides statt, dass diese Dissertation noch keiner anderen Fakultät oder Universität zur Prüfung vorgelegen hat; dass sie - abgesehen von unten angegebenen Teilpublikationen und eingebundenen Artikeln und Manuskripten - noch nicht veröffentlicht worden ist sowie, dass ich eine Veröffentlichung der Dissertation vor Abschluss der Promotion nicht ohne Genehmigung des Promotionsausschusses vornehmen werde. Die Bestimmungen dieser Ordnung sind mir bekannt. Darüber hinaus erkläre ich hiermit, dass ich die Ordnung zur Sicherung guter wissenschaftlicher Praxis und zum Umgang mit wissenschaftlichem Fehlverhalten der Universität zu Köln gelesen und sie bei der Durchführung der Dissertation zugrundeliegenden Arbeiten und der schriftlich verfassten Dissertation beachtet habe und verpflichte mich hiermit, die dort genannten Vorgaben bei allen wissenschaftlichen Tätigkeiten zu beachten und umzusetzen. Ich versichere, dass die eingereichte elektronische Fassung der eingereichten Druckfassung vollständig entspricht.

Köln, 31. Januar 2024

Niko Flosbach